TYRE AND VEHICLE DYNAMICS

HANS B. PACEJKA

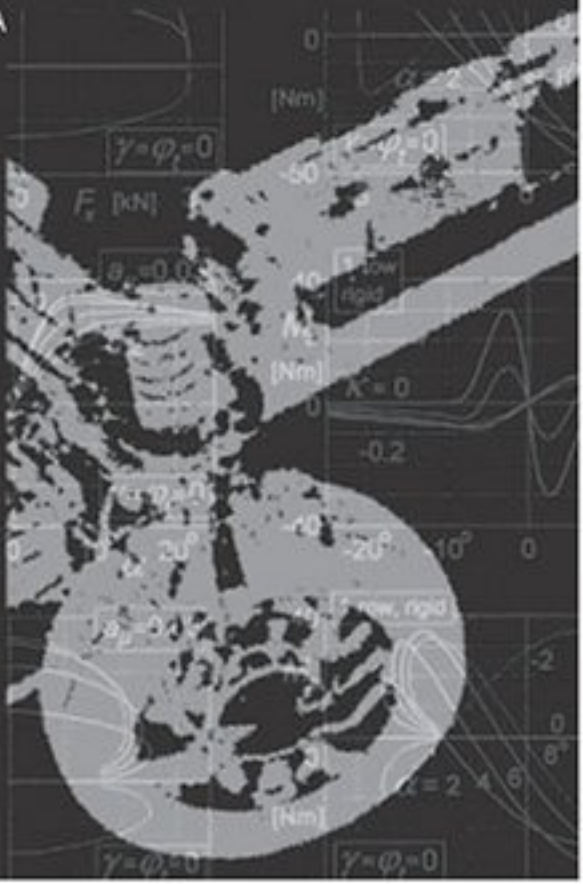

Tyre and Vehicle Dynamics

Hans B. Pacejka

Professor Emeritus
Delft University of Technology
Consultant TNO Automotive Delft
The Netherlands

Chapter 1

TYRE CHARACTERISTICS AND VEHICLE HANDLING AND STABILITY

1.1. Introduction

This chapter is meant to serve as an introduction to vehicle dynamics with emphasis on the influence of tyre properties. Steady-state cornering behaviour of simple automobile models and the transient motion after small and large steering inputs and other disturbances will be discussed. The effects of various shape factors of tyre characteristics (cf. Fig.1.1) on vehicle handling properties will be analysed. The slope of the side force F_y vs slip angle α near the origin (the cornering or side slip stiffness) is the determining parameter for the basic linear handling and stability behaviour of automobiles. The possible offset of the tyre characteristics with respect to their origins may be responsible for the occurrence of the so-called tyre-pull phenomenon. The further non-linear shape of the side (or cornering) force characteristic governs the handling and stability properties of the vehicle at higher lateral accelerations. The load dependency of the curves, notably the non-linear relationship of cornering stiffness with tyre normal load has a considerable effect on the handling characteristic of the car. For the (quasi)

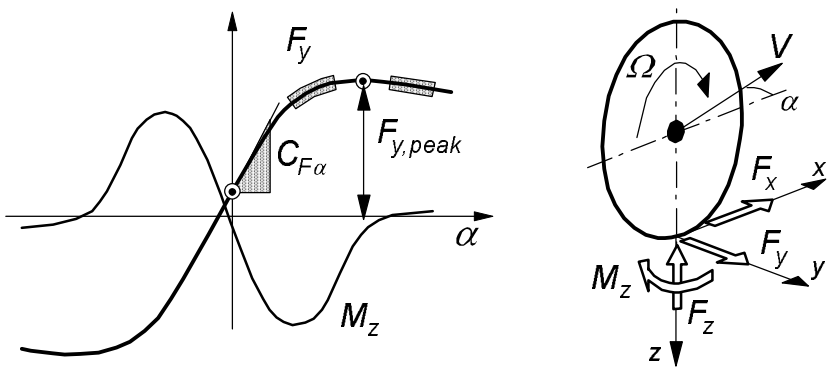

Fig. 1.1 Characteristic shape factors (indicated by points and shaded areas) of tyre or axle chacteristics that may influence vehicle handling and stability properties. Slip angle and force and moment positive directions, cf. App.1.

steady-state handling analysis simple single track (two-wheel) vehicle models will be used. Front and rear axle effective side force characteristics are introduced to represent effects that result from suspension and steering system design factors such as steering compliance, roll steer and lateral load transfer. Also the effect of possibly applied (moderate) braking and driving forces may be incorporated in the effective characteristics. Large braking forces may result in wheel-lock and possibly large deviations from the undisturbed path. The motion resulting from wheel lock will be dealt with in an application of the theory of a simple physical tyre model in Chapter 3 (the brush model). The application of the handling and stability theory to the dynamics of heavy trucks will also be briefly dealt with in the present chapter. Special attention will be given to the phenomenon of oscillatory instability that may show up with the car trailer combination.

When the wavelength of an oscillatory motion of the vehicle that may arise from road unevenness, brake torque fluctuations, wheel unbalance or instability (shimmy), is smaller than say 5m, a non-steady-state or transient description of tyre response is needed to properly analyse the phenomenon. In Chapters 5-8 these matters will be addressed. Applications demonstrate the use of transient and oscillatory tyre models and provide insight into the vehicle dynamics involved. Chapter 10 is specially devoted to the analysis of motorcycle cornering behaviour and stability.

1.2. Tyre and Axle Characteristics

Tyre characteristics are of crucial importance for the dynamic behaviour of the road vehicle. In this section an introduction is given to the basic aspects of the force and moment generating properties of the pneumatic tyre. Both the pure and combined slip characteristics of the tyre are discussed and typical features presented. Finally, the so-called effective axle characteristics are derived from the individual tyre characteristics and the relevant properties of the suspension and steering system.

1.2.1. Introduction to Tyre Characteristics

The upright wheel rolling freely, that is without applying a driving torque, over a flat level road surface along a straight line at zero side slip, may be defined as the starting situation with all components of slip equal to zero. A relatively small pulling force is needed to overcome the tyre rolling resistance and a side force

and (self) aligning torque may occur as a result of the not completely symmetric structure of the tyre. When the wheel motion deviates from this by definition zero slip condition, wheel slip occurs that is accompanied by a build-up of additional tyre deformation and possibly partial sliding in the contact patch. As a result, (additional) horizontal forces and the aligning torque are generated. The mechanism responsible for this is treated in detail in the subsequent chapters. For now, we will suffice with some important experimental observations and define the various slip quantities that serve as inputs into the tyre system and the moment and forces that are the output quantities (positive directions according to Fig.1.1). Several alternative definitions are in use as well. In Appendix 1 various sign conventions of slip, camber and output forces and moments together with relevant characteristics have been presented.

For the freely rolling wheel the forward speed V_x (longitudinal component of the total velocity vector V of the wheel centre) and the angular speed of revolution Ω_o can be taken from measurements. By dividing these two quantities the so-called effective rolling radius r_e is obtained:

$$r_e = \frac{V_x}{\Omega_o} \tag{1.1}$$

Although the effective radius may be defined also for a braked or driven wheel, we restrict the definition to the case of free rolling. When a torque is applied about the wheel spin axis a longitudinal slip arises that is defined as follows:

$$\kappa = -\frac{V_x - r_e\Omega}{V_x} = -\frac{\Omega_o - \Omega}{\Omega_o} \tag{1.2}$$

The sign is taken such that for a positive κ a positive longitudinal force F_x arises, that is: a driving force. In that case, the wheel angular velocity Ω is increased with respect to Ω_o and consequently $\Omega > \Omega_o = V_x/r_e$. During braking, the fore and aft slip becomes negative. At wheel lock, obviously, $\kappa = -1$. At driving on slippery roads, κ may attain very large values. To limit the slip to a maximum equal to one, in some texts the longitudinal slip is defined differently in the driving range of slip: in the denominator of (1.2) Ω_o is replaced by Ω. This will not be done in the present text.

Lateral wheel slip is defined as the ratio of the lateral and the forward velocity of the wheel. This corresponds to minus the tangent of the slip angle α (Fig.1.1). Again, the sign of α has been chosen such that the side force becomes positive at positive slip angle.

$$\tan\alpha = -\frac{V_y}{V_x} \tag{1.3}$$

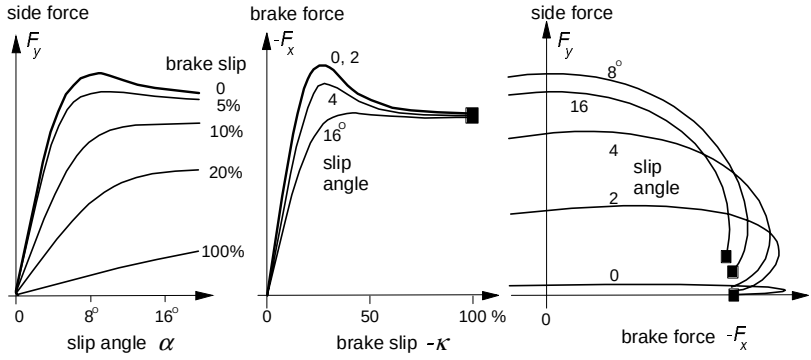

Fig. 1.2. Combined side force and brake force characteristics.

The third and last slip quantity is the so-called spin which is due to rotation of the wheel about an axis normal to the road. Both the yaw rate resulting in path curvature when α remains zero, and the wheel camber or inclination angle γ of the wheel plane about the x axis contribute to the spin. The camber angle is defined positive when looking from behind the wheel is tilted to the right. In Chapter 2 more precise definitions of the three components of wheel slip will be given. The forces F_x and F_y and the aligning torque M_z are results of the input slip. They are functions of the slip components and the wheel load. For steady-state rectilinear motions we have in general:

$$F_x = F_x(\kappa, \alpha, \gamma, F_z)\,,\ \ F_y = F_y(\kappa, \alpha, \gamma, F_z)\,,\ \ M_z = M_z(\kappa, \alpha, \gamma, F_z) \qquad (1.4)$$

The vertical load F_z may be considered as a given quantity that results from the normal deflection of the tyre. The functions can be obtained from measurements for a given speed of travel and road and environmental conditions.

Figure 1.1 shows the adopted system of axes (x, y, z) with associated positive directions of velocities and forces and moments. The exception is the vertical force F_z acting from road to tyre. For practical reasons, this force is defined to be positive in the upward direction and thus equal to the normal load of the tyre. Also Ω (not provided with a y subscript) is defined positive with respect to the negative y axis. Note, that the axes system is in accordance with SAE standards (SAE J670e, 1976). The sign of the slip angle, however, is chosen opposite with respect to the SAE definition, cf. Appendix 1.

In Fig.1.2 typical pure lateral (κ =0) and longitudinal (α =0) slip characteristics have been depicted together with a number of combined slip curves. The camber angle γ was kept equal to zero. We define pure slip to be the situation when either longitudinal or lateral slip occurs in isolation. The figure indicates that a drop in force arises when the other slip component is added. The resulting situation is designated as combined slip. The decrease in force can be simply

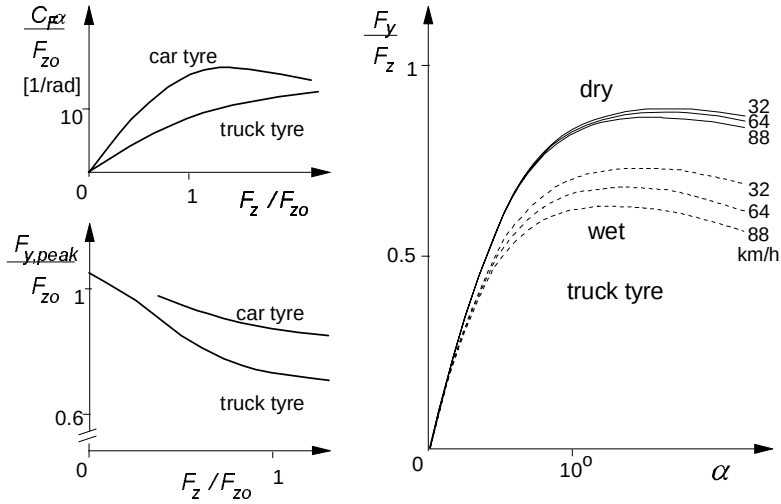

Fig. 1.3. Typical characteristics for the normalised cornering stiffness, peak side force and side force vs normalised vertical load and slip angle respectively. F_{zo} is the rated load.

explained by realising that the total horizontal frictional force F cannot exceed the maximum value (radius of 'friction circle') which is dictated by the current friction coefficient and normal load. Later, in Chapter 3 this becomes clear when considering the behaviour of a simple physical tyre model. The diagrams include the situation when the brake slip ratio has finally attained the value 100% (κ = -1) which corresponds to wheel lock.

The slopes of the pure slip curves at vanishing slip are defined as the longitudinal and lateral slip stiffnesses respectively. The longitudinal slip stiffness is designated as $C_{F\kappa}$. The lateral slip or cornering stiffness of the tyre, denoted with $C_{F\alpha}$, is one of the most important property parameters of the tyre and is crucial for the vehicle's handling and stability performance. The slope of minus the aligning torque versus slip angle curve (Fig.1.1) at zero slip angle is termed as the aligning stiffness and is denoted with $C_{M\alpha}$. The ratio of minus the aligning torque and the side force is the pneumatic trail t (if we neglect the so-called residual torque to be dealt with in Chapter 4). This length is the distance behind the contact centre (projection of wheel centre onto the ground in wheel plane direction) to the point where the resulting lateral force acts. The linearised force and moment characteristics (valid at small levels of slip) can be represented by the following expressions in which the effect of camber has been included:

$$\begin{aligned} F_x &= C_{F\kappa}\kappa \\ F_y &= C_{F\alpha}\alpha + C_{F\gamma}\gamma \\ M_z &= -C_{M\alpha}\alpha + C_{M\gamma}\gamma \end{aligned} \tag{1.5}$$

These equations have been arranged in such a way that all the coefficients (the force and moment slip and camber stiffnesses) become positive quantities (excluding some exceptional cases).

It is of interest to note that the order of magnitude of the tyre cornering stiffness ranges from about 6 to about 30 times the vertical wheel load when the cornering stiffness is expressed as force per radian. The lower value holds for the older bias-ply tyre construction and the larger value for modern racing tyres. The longitudinal slip stiffness has been typically found to be about 50% larger than the cornering stiffness. The pneumatic trail is of an order of magnitude equal to a quarter of the contact patch length.

For the side force which is the more important quantity in connection with automobile handling properties, a number of interesting diagrams have been presented in Fig.1.3. These characteristics are typical for truck and car tyres and are based on experiments conducted at the University of Michigan Transportation Research Institute (UMTRI, formerly HSRI), cf. Ref. (Segel et al. 1981). The car tyre cornering stiffness data stems from newer findings. It is seen that the cornering stiffness changes in a less than proportional fashion with the normal wheel load. The maximum normalised side force $F_{y,peak}/F_z$ appears to decrease with increasing wheel load. Marked differences in level and slope occur for the car and truck tyre curves also when normalised with respect to the rated or nominal load. The cornering force vs slip angle characteristic shown at different speeds and road conditions indicate that the slope at zero slip angle is not or hardly affected by the level of speed and by the condition wet or dry. The peak force level shows only little variation if the road is dry. On a wet road a more pronounced peak occurs and the peak level drops significantly with increasing speed.

Curves which exhibit a shape like the side force characteristics of Fig.1.3 can be represented by a mathematical formula that has become known by the name 'Magic Formula'. A full treatment of the empirical tyre model associated with this formula is given in Chapter 4. For now we can suffice with showing the basic expressions for the side force and the cornering stiffness:

$$F_y = D \sin[C \arctan\{B\alpha - E(B\alpha - \arctan(B\alpha))\}]$$

with stiffness factor

$$B = C_{F\alpha}/(CD)$$

peak factor (1.6)

$$D = \mu F_z \quad (= F_{y,peak})$$

and cornering stiffness

$$C_{F\alpha}\,(= BCD) = c_1 \sin\{2 \arctan(F_z/c_2)\}$$

The shape factors C and E as well as the parameters c_1 and c_2 and the friction coefficient μ (possibly depending on the vertical load and speed) may be estimated or determined through regression techniques.

1.2.2. Effective Axle Cornering Characteristics

For the basic analysis of (quasi) steady-state turning behaviour a simple two-wheel vehicle model may be used successfully. Effects of suspension and steering system kinematics and compliances such as steer compliance, body roll and also load transfer may be taken into account by using effective axle characteristics. The restriction to (quasi) steady state becomes clear when we realise that for transient or oscillatory motions, exhibiting yaw and roll accelerations and differences in phase, variables like roll angle and load transfer can no longer be written as direct algebraic functions of one of the lateral axle forces (front or rear). Consequently, we should drop the simple method of incorporating the effects of a finite centre of gravity height if the frequency of input signals such as the steering wheel angle cannot be considered small relative to the body roll natural frequency. Since the natural frequency of the wheel suspension and steering systems are relatively high, the restriction to steady-state motions becomes less critical in case of the inclusion of e.g. steering compliance in the effective characteristic. Chiesa and Rinonapoli (1967) were among the first to employ effective axle characteristics or 'working curves' as these were referred to by them. Vågstedt (1995) determined these curves experimentally.

Before assessing the complete non-linear effective axle characteristics we will first direct our attention to the derivation of the effective cornering stiffnesses which are used in the simple linear two-wheel model. For these to be determined, a more comprehensive vehicle model has to be defined.

Figure 1.4 depicts a vehicle model with three degrees of freedom. The forward velocity u may be kept constant. As motion variables we define the lateral velocity v of reference point A, the yaw velocity r and the roll angle φ. A moving axes system (A,x,y,z) has been introduced. The x axis points forwards and lies both in the ground plane and in the plane normal to the ground that passes through the so-called roll axis. The y axis points to the right and the z axis points downwards. This latter axis passes through the centre of gravity when the the roll angle is equal to zero. In this way the location of the point of reference A has been defined. The longitudinal distance to the front axle is a and the distance to the rear axle is b. The sum of the two distances is the wheel base l. For convenience we may write: $a=a_1$ and $b=a_2$.

In a curve, the vehicle body rolls about the roll axis. The location and

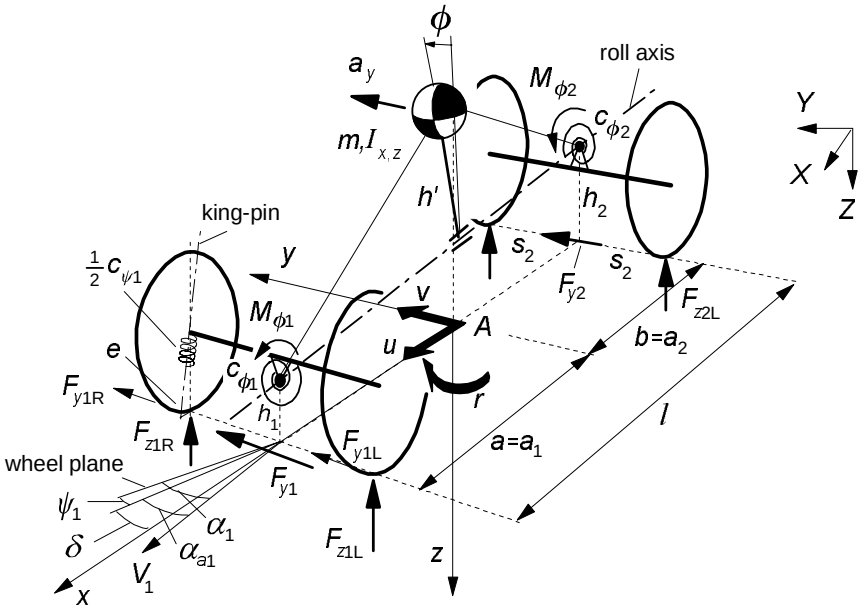

Fig. 1.4. Vehicle model showing three degrees of freedom: lateral, yaw and roll.

attitude of this virtual axis is defined by the heights $h_{1,2}$ of the front and rear roll centres. The roll axis is assessed by considering the body motion with respect to the four contact centres of the wheels on the ground under the action of an external lateral force that acts on the centre of gravity. Due to the symmetry of the vehicle configuration and the linearisation of the model these locations can be considered as fixed. The roll centre locations are governed by suspension kinematics and possibly suspension lateral compliances. The torsional springs depicted in the figure represent the front and rear roll stiffnesses $c_{\varphi 1,2}$ which result from suspension springs and anti-roll bars.

The fore and aft position of the centre of gravity of the body is defined by a and b; its height follows from the distance h' to the roll axis. The body mass is denoted by m and the moments of inertia with respect to the centre of mass and horizontal and vertical axes by I_x, I_z and I_{xz}. These latter quantities will be needed in a later phase when the differential equations of motion are established. The unsprung masses will be neglected or they may be included as point masses attached to the roll axis and thus make them part of the sprung mass, that is, the vehicle body.

Furthermore, the model features torsional springs around the steering axes. The king-pin is positioned at a small caster angle that gives rise to the caster length e as indicated in the drawing. The total steering torsional stiffness, left plus right, is denoted by $c_{\psi 1}$.

Effective Axle Cornering Stiffness

Linear analysis, valid for relatively small levels of lateral accelerations allows the use of approximate tyre characteristics represented by just the slopes at zero slip. We will first derive the effective axle cornering stiffness that may be used under these conditions. The effects of load transfer, body roll, steer compliance, side force steer and initial camber and toe angles will be included in the ultimate expression for the effective axle cornering stiffness.

The linear expressions for the side force and the aligning torque acting on a tyre have been given by Eqs.(1.5). The coefficients appearing in these expressions are functions of the vertical load. For small variations with respect to the average value (designated with subscript o) we write for the cornering and camber force stiffnesses the linearised expressions:

$$\begin{aligned} C_{F\alpha} &= C_{F\alpha o} + \zeta_\alpha \Delta F_z \\ C_{F\gamma} &= C_{F\gamma o} + \zeta_\gamma \Delta F_z \end{aligned} \tag{1.7}$$

where the increment of the wheel vertical load is denoted by ΔF_z and the slopes of the coefficient versus load curves at $F_z = F_{zo}$ are represented by $\zeta_{\alpha\gamma}$.

When the vehicle moves steadily around a circular path a centripetal acceleration a_y occurs and a centrifugal force $K = ma_y$ can be said to act on the vehicle body at the centre of gravity in the opposite direction. The body roll angle φ, that is assumed to be small, is calculated by dividing the moment about the roll axis by the apparent roll stiffness which is reduced with the term mgh' due to the additional moment $mgh'\varphi$:

$$\varphi = \frac{-ma_y h'}{c_{\varphi 1} + c_{\varphi 2} - mgh'} \tag{1.8}$$

The total moment about the roll axis is distributed over the front and rear axles in proportion to the front and rear roll stiffnesses. The load transfer ΔF_{zi} from the inner to the outer wheels that occurs at axle i (= 1 or 2) in a steady-state cornering motion with centripetal acceleration a_y follows from the formula:

$$\Delta F_{zi} = \sigma_i m a_y \tag{1.9}$$

with the load transfer coefficient of axle i

$$\sigma_i = \frac{1}{2s_i}\left(\frac{c_{\varphi i}}{c_{\varphi 1} + c_{\varphi 2} - mgh'} h' + \frac{l - a_i}{l} h_i \right) \tag{1.10}$$

The attitude angle of the roll axis with respect to the horizontal is considered small. In the formula, s_i denotes half the track width, h' is the distance from the

centre of gravity to the roll axis and $a_1=a$ and $a_2=b$. The resulting vertical loads at axle i for the left (L) and right (R) wheels become after considering the left and right increments in load:

$$\begin{aligned} \Delta F_{ziL} &= \Delta F_{zi} \quad , \quad \Delta F_{ziR} = -\Delta F_{zi} \\ F_{ziL} &= \tfrac{1}{2} F_{zi} + \Delta F_{zi} \quad , \quad F_{ziR} = \tfrac{1}{2} F_{zi} - \Delta F_{zi} \end{aligned} \tag{1.11}$$

The wheels at the front axle are steered about the king-pins with the angle δ. This angle relates directly to the imposed steering wheel angle δ_{stw} through the steering ratio n_{st}.

$$\delta = \frac{\delta_{stw}}{n_{st}} \tag{1.12}$$

In addition to this imposed steer angle the wheels may show a steer angle and a camber angle induced by body roll through suspension kinematics. The functional relationships with the roll angle may be linearised. For axle i we define:

$$\begin{aligned} \psi_{ri} &= \varepsilon_i \varphi \\ \gamma_{ri} &= \tau_i \varphi \end{aligned} \tag{1.13}$$

Steer compliance gives rise to an additional steer angle due to the external torque that acts about the king-pin (steering axis). For the pair of front wheels this torque results from the side force (of course also from the here not considered driving or braking forces) that exerts a moment about the king-pin through the moment arm which is composed of the caster length e and the pneumatic trail t_1. With the total steering stiffness $c_{\psi 1}$ felt about the king-pins with the steering wheel held fixed, the additional steer angle becomes when for simplicity the influence of camber on the pneumatic trail is disregarded:

$$\psi_{c1} = -\frac{F_{y1}(e + t_1)}{c_{\psi}} \tag{1.14}$$

In addition, the side force (but also the fore and aft force) may induce a steer angle due to suspension compliance. The so-called side force steer reads:

$$\psi_{sfi} = c_{sfi} F_{yi} \tag{1.15}$$

For the front axle, we should separate the influences of moment steer and side force steer. For this reason, side force steer at the front is defined to occur as a result of the side force acting in a point on the king-pin axis.

Beside the wheel angles indicated above, the wheels may have been given initial angles that already exist at straight ahead running. These are the toe angle

ψ_o (positive pointing outwards) and the initial camber angle γ_o (positive: leaning outwards). For the left and right wheels we have the initial angles:

$$\begin{aligned} \psi_{iLo} &= -\psi_{io} \quad , \quad \psi_{iRo} = \psi_{io} \\ \gamma_{iLo} &= -\gamma_{io} \quad , \quad \gamma_{iRo} = \gamma_{io} \end{aligned} \tag{1.16}$$

Adding all relevant contributions (1.12) to (1.16) together yields the total steer angle for each of the wheels.

The effective cornering stiffness of an axle $C_{eff,i}$ is now defined as the ratio of the axle side force and the virtual slip angle. This angle is defined as the angle between the direction of motion of the centre of the axle i (actually at road level) when the vehicle velocity would be very low and approaches zero (then also $F_{yi} \rightarrow 0$) and the direction of motion at the actual speed considered. The virtual slip angle of the front axle has been indicated in Fig.1.4 and is designated as α_{a1}. We have in general:

$$C_{eff,i} = \frac{F_{yi}}{\alpha_{ai}} \tag{1.17}$$

The axle side forces in the steady-state turn can be derived by considering the lateral force and moment equilibrium of the vehicle:

$$F_{yi} = \frac{l - a_i}{l} m a_y \tag{1.18}$$

The axle side force is the sum of the left and right individual tyre side forces. We have

$$\begin{aligned} F_{yiL} &= (\tfrac{1}{2}C_{F\alpha i} + \zeta_{\alpha i}\Delta F_{zi})(\alpha_i - \psi_{io}) + (\tfrac{1}{2}C_{F\gamma i} + \zeta_{\gamma i}\Delta F_{zi})(\gamma_i - \gamma_{io}) \\ F_{yiR} &= (\tfrac{1}{2}C_{F\alpha i} - \zeta_{\alpha i}\Delta F_{zi})(\alpha_i + \psi_{io}) + (\tfrac{1}{2}C_{F\gamma i} - \zeta_{\gamma i}\Delta F_{zi})(\gamma_i + \gamma_{io}) \end{aligned} \tag{1.19}$$

where the average wheel slip angle α_i indicated in the figure is

$$\alpha_i = \alpha_{ai} + \psi_i \tag{1.20}$$

and the average additional steer angle and the average camber angle are:

$$\begin{aligned} \psi_i &= \psi_{ri} + \psi_{ci} + \psi_{sfi} \\ \gamma_i &= \gamma_{ri} \end{aligned} \tag{1.21}$$

The unknown quantity is the virtual slip angle α_{ai} which can be determined for a given lateral acceleration a_y. Next, we use the equations (1.8, 1.9, 1.13, 1.18, 1.14, 1.15), substitute the resulting expressions (1.21) and (1.20) in (1.19) and add up these two equations. The result is a relationship between the axle slip angle α_{ai} and the axle side force F_{yi}. We obtain for the slip angle of axle i:

$$\alpha_{ai} = \frac{F_{yi}}{C_{eff,i}} = \tag{1.22}$$
$$= \frac{F_{yi}}{C_{F\alpha i}}\left(1 + \frac{l(\varepsilon_i C_{F\alpha i} + \tau_i C_{F\gamma i})h'}{(l-a_i)(c_{\varphi 1} + c_{\varphi 2} - mgh')} + \frac{C_{F\alpha i}(e_i + t_i)}{c_{\psi i}} - C_{F\alpha i} c_{sfi} + \frac{2l\sigma_i}{l-a_i}(\zeta_{\alpha i}\psi_{io} + \zeta_{\gamma i}\gamma_{io})\right)$$

The coefficient of F_{yi} constitutes the effective axle cornering compliance, which is the inverse of the effective axle cornering stiffness (1.17). The quantitative effect of each of the suspension, steering and tyre factors included can be easily assessed. The subscript i refers to the complete axle. Consequently, the cornering and camber stiffnesses appearing in this expression are the sum of the stiffnesses of the left and right tyre:

$$\begin{aligned} C_{F\alpha i} &= C_{F\alpha iL} + C_{F\alpha iR} = C_{F\alpha iLo} + C_{F\alpha iRo} \\ C_{F\gamma i} &= C_{F\gamma iL} + C_{F\gamma iR} = C_{F\gamma iLo} + C_{F\gamma iRo} \end{aligned} \tag{1.23}$$

in which (1.7) and (1.11) have been taken into account. The load transfer coefficient σ_i follows from Eq.(1.10). Expression (1.22) shows that the influence of lateral load transfer only occurs if initially, at straight ahead running, side forces are already present through the introduction of e.g. opposite steer and camber angles. If these angles are absent, the influence of load transfer is purely non-linear and is only felt at higher levels of lateral accelerations. In the next subsection, this non-linear effect will be incorporated in the effective axle characteristic.

Effective Non-Linear Axle Characteristics

To illustrate the method of effective axle characteristics we will first discuss the determination of the effective characteristic of a front axle showing steering compliance. The steering wheel is held fixed. Due to tyre side forces and self-aligning torques (left and right) distortions will arise resulting in an incremental steer angle ψ_{c1} of the front wheels (ψ_{c1} will be negative in Fig.1.5 for the case of just steer compliance). Since load transfer is not considered in this example, the situation at the left and right wheels are identical (initial toe and camber angles being disregarded). The front tyre slip angle is denoted with α_1. The 'virtual' slip angle of the axle is denoted with α_{a1} and equals (cf. Fig.1.5):

$$\alpha_{a1} = \alpha_1 - \psi_{c1} \tag{1.24}$$

where both α_1 and ψ_{c1} are related with F_{y1} and M_{z1}. The subscipt 1 refers to the front axle and thus to the pair of tyres. Consequently, F_{y1} and M_{z1} denote the sum of the left and right tyre side forces and moments. The objective is, to find the

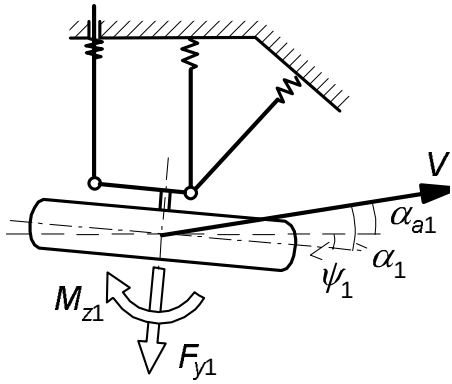

Fig. 1.5. Wheel suspension and steering compliance resulting in additional steer angle ψ_1.

function $F_{y1}(\alpha_{a1})$ which is the effective front axle characteristic. Figure 1.6 shows a graphical approach. According to Eq.(1.24) the points on the $F_{y1}(\alpha_1)$ curve must be shifted horizontally over a length ψ_{c1} to obtain the sought $F_{y1}(\alpha_{a1})$. The slope of the curve at the origin corresponds to the effective axle cornering stiffness found in the preceding subsection. Although the changes with respect to the original characteristic may be small, they can still be of considerable importance since it is the difference of slip angles front and rear which largely determines the vehicle's handling behaviour.

The effective axle characteristic for the case of roll steer can be easily established by subtracting ψ_{ri} from α_i. Instead of using the linear relationships (1.8) and (1.13) non-linear curves may be adopted, possibly obtained from measurements. For the case of roll camber, the situation becomes more complex.

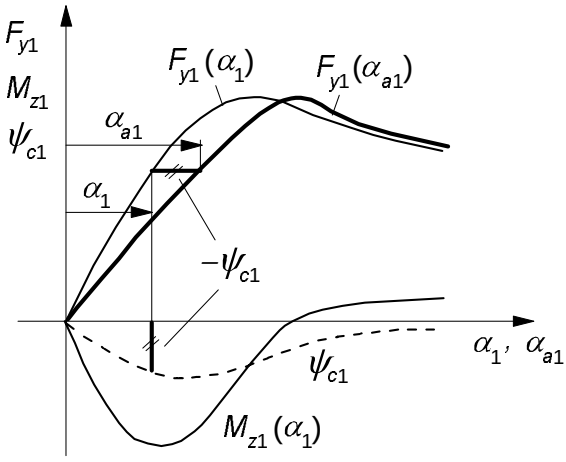

Fig. 1.6. Effective front axle characteristic $F_{y1}(\alpha_{a1})$ influenced by steering compliance.

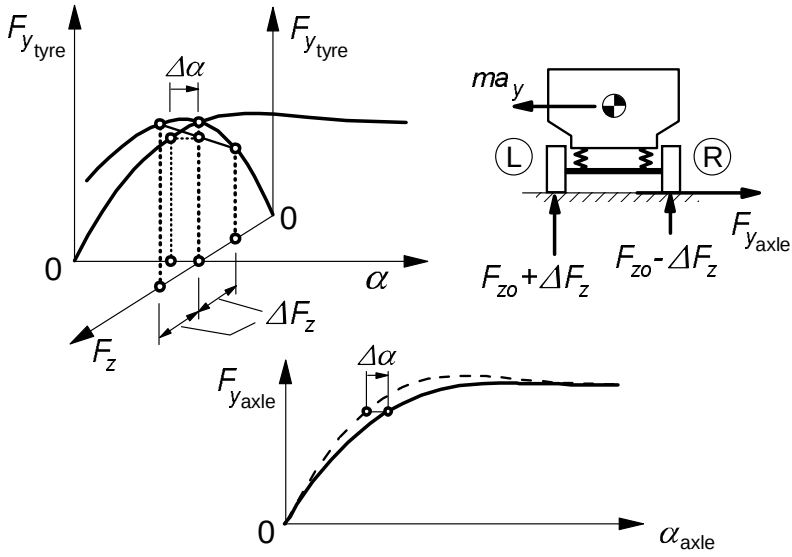

Fig. 1.7. The influence of load transfer on the resulting axle characteristic.

At a given axle side force the roll angle and the associated camber angle can be found. The cornering characteristic of the pair of tyres at that camber angle is needed to find the slip angle belonging to the side force considered.

Load transfer is another example that is less easy to handle. In Fig.1.7 a three dimensional graph is presented for the variation of the side force of an individual tyre as a function of the slip angle and of the vertical load. The former at a given load and the latter at a given slip angle. The diagram illustrates that at load transfer the outer tyre exhibiting a larger load will generate a larger side force than the inner tyre. Because of the non-linear degressive F_y vs F_z curve, however, the average side force will be smaller than the original value it had in the absence of load transfer. The graph indicates that an increase $\Delta\alpha$ of the slip angle would be needed to compensate for the adverse effect of load transfer. The lower diagram gives a typical example of the change in characteristic as a result of load transfer. At the origin the slope is not affected but at larger slip angles an increasingly lower derivative appears to occur. The peak diminishes and may even disappear completely. The way to determine the resulting characteristic is the subject of the next exercise.

Exercise 1.1. Construction of effective axle characteristic at load transfer

For a series of tyre vertical loads F_z the characteristics of the two tyres mounted on, say, the front axle of an automobile are given. In addition, it is known how the load transfer ΔF_z at the front axle depends on the centrifugal force K ($= mg\,F_{y1}/F_{z1} = mg\,F_{y2}/F_{z2}$) acting at the centre of gravity. From this data the resulting cornering charac-

teristic of the axle considered (at steady-state cornering) can be determined.

1. Find the resulting characteristic of one axle from the set of individual tyre characteristics at different tyre loads F_z and the load transfer characteristic both shown in Fig.1.8.
   Hint: First draw in the lower diagram the axle characteristics for values of ΔF_z = 1000, 2000, 3000 and 4000 N and then determine which point on each of these curves is valid considering the load transfer characteristic (left-hand diagram). Draw the resulting axle characteristic.
   It may be helpful to employ the Magic Formula (1.6) and the parameters shown below:
   side force: $F_y = D \sin[C \arctan\{B\alpha - E(B\alpha - \arctan(B\alpha))\}]$
   with factors: $B = C_{F\alpha}/(CD)$, $C = 1.3$, $D = \mu F_z$, $E = -3$, with $\mu = 1$
   cornering stiffness: $C_{F\alpha} = c_1 \sin[2 \arctan\{F_z / c_2\}]$
   with parameters: $c_1 = 60000$ [N/rad], $c_2 = 4000$ [N]
   In addition, we have given for the load transfer: $\Delta F_z = 0.52 F_{y,axle}$ (up to lift-off of the inner tyre, after which the other axle may take over to accommodate the increased total load transfer).
2. Draw the individual curves of F_{yL} and F_{yR} (for the left and right tyre) as a function of α which appear to arise under the load transfer condition considered here.
3. Finally, plot these forces as a function of the vertical load F_z (ranging from 0-8000N). Note the variation of the lateral force of an individual (left or right) tyre in this same range of vertical load which may be covered in a left and in a right-hand turn at increasing speed of travel until (and possibly beyond) the moment that one of the wheels (the inner wheel) lifts from the ground.

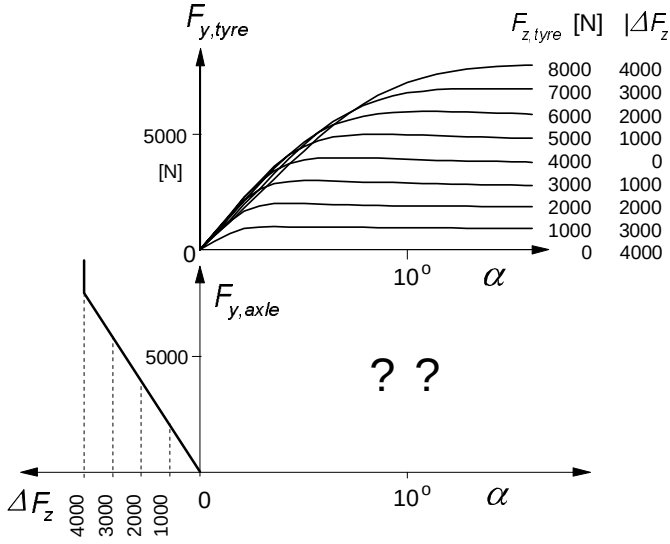

Fig. 1.8. The construction of the resulting axle cornering characteristics at load transfer (Exercise 1.1).

1.3. Vehicle Handling and Stability

In this section attention is paid to the more fundamental aspects of vehicle horizontal motions. Instead of discussing results of computer simulations of complicated vehicle models we rather take the simplest possible model of an automobile that runs at constant speed over an even horizontal road and thereby gain considerable insight into the basic aspects of vehicle handling and stability. Important early work on the linear theory of vehicle handling and stability has been published by Riekert and Schunck (1940), Whitcomb and Milliken (1956) and Segel (1956). Pevsner (1947) studied the non-linear steady-state cornering behaviour at larger lateral accelerations and introduced the handling diagram. One of the first more complete vehicle model studies has been conducted by Pacejka (1958) and by Radt and Pacejka (1963).

For more introductory or specialised study the reader may be referred to books on the subject published earlier, cf. e.g.: Gillespie (1992), Mitschke (1990), Milliken (1995) and Kortüm and Lugner (1994).

The derivation of the equations of motion for the three degree of freedom model of Fig.1.4 will be treated first after which the simple model with two degrees of freedom is considered and analysed. This analysis comprises the steady-state response to steering input and the stability of the resulting motion. Also, the frequency response to steering fluctuations and external disturbances will be discussed, first for the linear vehicle model and subsequently for the non-linear model where large lateral accelerations and disturbances are introduced.

The simple model to be employed in the analysis is presented in Fig.1.9. The track width has been neglected with respect to the radius of the cornering motion

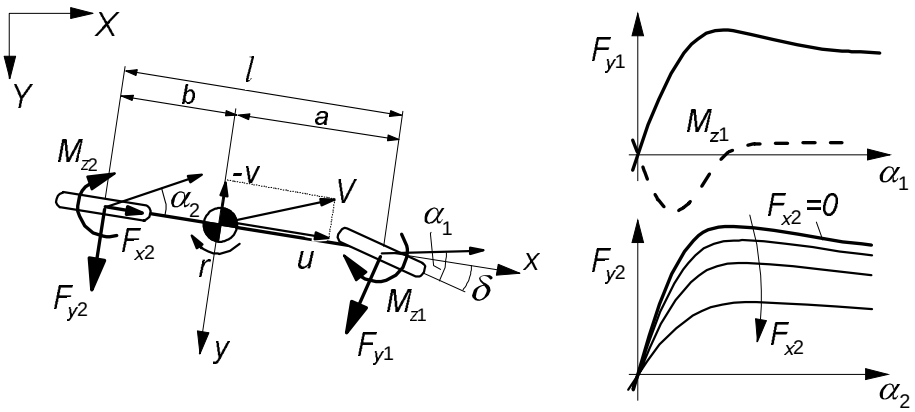

Fig. 1.9. Simple car model with side force characteristics for front and rear (driven) axle.

which allows the use of a two-wheel vehicle model. The steer and slip angles will be restricted to relatively small values. Then, the variation of the geometry may be regarded to remain linear, that is: $\cos\alpha \approx 1$ and $\sin\alpha \approx \alpha$ and similarly for the steer angle δ. Moreover, the driving force required to keep the speed constant is assumed to remain small with respect to the lateral tyre force. Considering combined slip curves like those shown in Fig.1.2 (right), we may draw the conclusion that the influence of F_x on F_y may be neglected in that case.

In principle, a model as shown in Fig.1.9 lacks body roll and load transfer. Therefore, the theory is actually limited to cases where the roll moment remains small, that is at low friction between tyre and road or a low centre of gravity relative to the track width. This restriction may be overcome by using the effective axle characteristics in which the effects of body roll and load transfer have been included while still adhering to the simple (rigid) two-wheel vehicle model. As has been mentioned before, this is only permissible when the frequency of the imposed steer angle variations remains small with respect to the roll natural frequency. Similarly, as has been demonstrated in the preceding section, effects of other factors like compliance in the steering system and suspension mounts may be accounted for.

The speed of travel is considered to be constant. However, the theory may approximately hold also for quasi-steady-state situations for instance at moderate braking or driving. The influence of the fore-and-aft force F_x on the tyre or axle cornering force vs slip angle characteristic (F_y, α) may then be regarded (cf. Fig.1.9). The forces F_{y1} and F_{x1} and the moment M_{z1} are defined to act upon the single front wheel and similarly we define F_{y2} etc. for the rear wheel.

1.3.1. Differential Equations for Plane Vehicle Motions

In this section, the differential equations for the three degree of freedom vehicle model of Fig.1.4 will be derived. In first instance, the fore and aft motion will also be left free to vary. The resulting set of equations of motion may be of interest for the reader to further study the vehicle's dynamic response at somewhat higher frequencies where the roll dynamics of the vehicle body may become of importance. From these equations, the equations for the simple two-degree of freedom model of Fig.1.9 used in the subsequent section can be easily assessed. In Subsection 1.3.6 the equations for the car with trailer will be established. The possible instability of the motion will be studied.

We will employ Lagrange's equations to derive the equations of motion. For a system with n degrees of freedom n (generalised) coordinates q_i are selected which are sufficient to completely describe the motion while possible kinematic

constraints remain satisfied. The moving system possesses kinetic energy T and potential energy U. External generalised forces Q_i associated with the generalised coordinates q_i may act on the system and do work W. Internal forces acting from dampers to the system structure may be regarded as external forces taking part in the total work W. The equation of Lagrange for coordinate q_i reads:

$$\frac{d}{dt}\frac{\partial T}{\partial \dot{q}_i} - \frac{\partial T}{\partial q_i} + \frac{\partial U}{\partial q_i} = Q_i \tag{1.25}$$

The system depicted in Fig.1.4 and described in the preceding subsection performs a motion over a flat level road. Proper coordinates are the Cartesian coordinates X and Y of reference point A, the yaw angle ψ of the moving x axis with respect to the inertial X axis and finally the roll angle φ about the roll axis. For motions near the X axis and thus small yaw angles, Eq.(1.25) is adequate to derive the equations of motion. For cases where ψ may attain large values, e.g. when moving along a circular path, it is preferred to use modified equations where the velocities u, v and r of the moving axes system are used as generalised motion variables in addition to the coordinate φ. The relations between the two sets of variables are (the dots referring to differentiation with respect to time):

$$\begin{aligned} u &= \dot{X}\cos\psi + \dot{Y}\sin\psi \\ v &= -\dot{X}\sin\psi + \dot{Y}\cos\psi \\ r &= \dot{\psi} \end{aligned} \tag{1.26}$$

The kinetic energy can be expressed in terms of u, v and r. Preparation of the first terms of Eq. (1.25) for the coordinates X, Y and ψ yields:

$$\begin{aligned} \frac{\partial T}{\partial \dot{X}} &= \frac{\partial T}{\partial u}\frac{\partial u}{\partial \dot{X}} + \frac{\partial T}{\partial v}\frac{\partial v}{\partial \dot{X}} = \frac{\partial T}{\partial u}\cos\psi - \frac{\partial T}{\partial v}\sin\psi \\ \frac{\partial T}{\partial \dot{Y}} &= \frac{\partial T}{\partial u}\frac{\partial u}{\partial \dot{Y}} + \frac{\partial T}{\partial v}\frac{\partial v}{\partial \dot{Y}} = \frac{\partial T}{\partial u}\sin\psi + \frac{\partial T}{\partial v}\cos\psi \\ \frac{\partial T}{\partial \dot{\psi}} &= \frac{\partial T}{\partial r} \\ \frac{\partial T}{\partial \psi} &= \frac{\partial T}{\partial u}v - \frac{\partial T}{\partial v}u \end{aligned} \tag{1.27}$$

The yaw angle ψ may now be eliminated by multiplying the final equations for X and Y successively with $\cos\psi$ and $\sin\psi$ and subsequently adding and subtracting them. The resulting equations represent the equilibrium in the x and y (or u and v) directions respectively.

We obtain the following set of modified Lagrangean equations for the first three variables u, v and r and subsequently for the remaining real coordinates

(for our system only φ) :

$$\begin{aligned}
&\frac{d}{dt}\frac{\partial T}{\partial u} - r\frac{\partial T}{\partial v} = Q_u \\
&\frac{d}{dt}\frac{\partial T}{\partial v} + r\frac{\partial T}{\partial u} = Q_v \\
&\frac{d}{dt}\frac{\partial T}{\partial r} - v\frac{\partial T}{\partial u} + u\frac{\partial T}{\partial v} = Q_r \\
&\frac{d}{dt}\frac{\partial T}{\partial \dot{\varphi}} - \frac{\partial T}{\partial \varphi} + \frac{\partial U}{\partial \varphi} = Q_\varphi
\end{aligned} \tag{1.28}$$

The generalised forces are found from the virtual work:

$$\delta W = \sum_{j=1}^{4} Q_j \, \delta q_j \tag{1.29}$$

with q_j referring to the quasi coordinates x and y and the coordinates ψ and φ. Note that x and y can not be found from integrating u and v. For that reason the term 'quasi' coordinate is used. For the vehicle model we find for the virtual work as a result of the virtual displacements δx, δy, $\delta\psi$ and $\delta\varphi$:

$$\delta W = \sum F_x \, \delta x + \sum F_y \, \delta y + \sum M_z \delta\psi + \sum M_\varphi \delta\varphi \tag{1.30}$$

where apparently

$$\begin{aligned}
Q_u &= \sum F_x = F_{x1}\cos\delta - F_{y1}\sin\delta + F_{x2} \\
Q_v &= \sum F_y = F_{x1}\sin\delta + F_{y1}\cos\delta + F_{y2} \\
Q_r &= \sum M_z = aF_{x1}\sin\delta + aF_{y1}\cos\delta + M_{z1} - bF_{y2} + M_{z2} \\
Q_\varphi &= \sum M_\varphi = -(k_{\varphi 1} + k_{\varphi 2})\dot{\varphi}
\end{aligned} \tag{1.31}$$

The longitudinal forces are assumed to be the same at the left and right wheels and the effect of additional steer angles ψ_i are neglected here. Shock absorbers in the wheel suspensions are represented by the resulting linear moments about the roll axes with damping coefficients $k_{\varphi i}$ at the front and rear axles.

With the roll angle φ and the roll axis inclination angle $\theta_r \approx (h_2 - h_1)/l$ assumed small, the kinetic energy becomes:

$$\begin{aligned}
T = {}&\tfrac{1}{2} m\{(u - h'\varphi r)^2 + (v + h'\dot{\varphi})^2\} + \\
&+\tfrac{1}{2} I_x \dot{\varphi}^2 + \tfrac{1}{2} I_y (\varphi r)^2 + \tfrac{1}{2} I_z (r^2 - \varphi^2 r^2 + 2\theta_r r\dot{\varphi}) - I_{xz} r\dot{\varphi}
\end{aligned} \tag{1.32}$$

The potential energy U is built up in the suspension springs (including the radial tyre compliances) and through the height of the centre of gravity. We have, again for small angles:

$$U = \tfrac{1}{2}(c_{\varphi 1} + c_{\varphi 2})\varphi^2 - \tfrac{1}{2}mgh'\varphi^2 \tag{1.33}$$

The equations of motion are finally established by using the expressions (1.31), (1.32) and (1.33) in the equations (1.28). The equations will be linearised in the assumedly small angles φ and δ. For the variables u, v, r and φ we obtain successively:

$$m(\dot{u} - rv - h'\varphi\dot{r} - 2h'r\dot{\varphi}) = F_{x1} - F_{y1}\delta + F_{x2} \tag{1.34a}$$

$$m(\dot{v} + ru + h'\ddot{\varphi} - h'r^2\varphi) = F_{x1}\delta + F_{y1} + F_{y2} \tag{1.34b}$$

$$I_z\dot{r} + (I_z\theta_r - I_{xz})\ddot{\varphi} - mh'(\dot{u} - rv)\varphi = aF_{x1}\delta + aF_{y1} + M_{z1} - bF_{y2} + M_{z2} \tag{1.34c}$$

$$(I_x + mh'^2)\ddot{\varphi} + mh'(\dot{v} + ru) + (I_z\theta_r - I_{xz})\dot{r} - (mh'^2 + I_y - I_z)r^2\varphi + \\ + (k_{\varphi 1} + k_{\varphi 2})\dot{\varphi} + (c_{\varphi 1} + c_{\varphi 2} - mgh')\varphi = 0 \tag{1.34d}$$

Note that the small additional roll and compliance steer angles ψ_i have been neglected in the assessment of the force components. The tyre side forces depend on the slip and camber angles front and rear and on the tyre vertical loads. We may need to take the effect of combined slip into account. The longitudinal forces are either given as a result of brake effort or imposed propulsion torque or they depend on the wheel longitudinal slip which follows from the wheel speed of revolution requiring four additional wheel rotational degrees of freedom. The first equation (1.34a) may be used to compute the propulsion force needed to keep the forward speed constant.

The vertical loads and more specifically the load transfer can be obtained by considering the moment equilibrium of the front and rear axle about the respective roll centres. For this, the roll moments $M_{\varphi i}$ (cf. Fig.1.4) resulting from suspension springs and dampers as appear in Eq.(1.34d) through the terms with subscript 1 and 2 respectively, and the axle side forces appearing in Eq.(1.34b) are to be regarded. For a linear model the load transfer can be neglected if initial (left/right opposite) wheel angles are disregarded. We have at steady-state (effect of damping vanishes):

$$\Delta F_{zi} = \frac{-c_{\varphi i}\varphi + F_{yi}h_i}{2s_i} \tag{1.35}$$

The front and rear slip angles follow from the lateral velocities of the wheel axles and the wheel steer angles with respect to the moving longitudinal x axis. The longitudinal velocities of the wheel axles may be regarded the same left and right

and equal to the vehicle longitudinal speed u. This is allowed when $s_i|r| \ll u$. Then the expressions for the assumedly small slip angles read:

$$\begin{aligned} \alpha_1 &= \delta + \psi_1 - \frac{v + ar - e\dot{\delta}}{u} \\ \alpha_2 &= \psi_2 - \frac{v - br}{u} \end{aligned} \tag{1.36}$$

The additional roll and compliance steer angles ψ_i and the wheel camber angles γ_i are obtained from Eq.(1.21) with (1.13-15) or corresponding non-linear expressions. Initial wheel angles are assumed to be equal to zero. The influence of the steer angle velocity appearing in the expression for the front slip angle is relatively small and may be disregarded. The small products of the caster length e and the time rate of change of ψ_i have been neglected in the above expressions.

Equations (1.34) may be further linearised by assuming that all the deviations from the rectilinear motion are small. This allows the neglection of all products of variable quantities which vanish when the vehicle moves straight ahead. The side forces and moments are then written as in Eq.(1.5) with the subscripts i=1 or 2 provided. If the moment due to camber is neglected and the pneumatic trail is introduced in the aligning torque we have:

$$\begin{aligned} F_{yi} &= F_{y\alpha i} + F_{y\gamma i} = C_{F\alpha i}\alpha_i + C_{F\gamma i}\gamma_i \\ M_{zi} &= M_{z\alpha i} = -C_{M\alpha i}\alpha_i = -t_i F_{y\alpha i} = -t_i C_{F\alpha i}\alpha_i \end{aligned} \tag{1.37}$$

The three linear equations of motion for the system of Fig.1.4 with the forward speed u kept constant finally turn out to read expressed solely in terms of the three motion variables v, r and φ:

$$\begin{aligned} m(\dot{v} + ur + h'\ddot{\varphi}) = {} & C_{F\alpha 1}\{(1 + c_{sc1})(u\delta + e\dot{\delta} - v - ar)/u + c_{sr1}\varphi\} + \\ & + C_{F\alpha 2}\{(1 + c_{sc2})(-v + br)/u + c_{sr2}\varphi\} + (C_{F\gamma 1}\tau_1 + C_{F\gamma 2}\tau_2)\varphi \end{aligned} \tag{1.38a}$$

$$\begin{aligned} I_z\dot{r} + (I_z\theta_r - I_{xz})\ddot{\varphi} = {} & (a - t_1)C_{F\alpha 1}\{(1 + c_{sc1})(u\delta + e\dot{\delta} - v - ar)/u + c_{sr1}\varphi\} + \\ & - (b + t_2)C_{F\alpha 2}\{(1 + c_{sc2})(-v + br)/u + c_{sr2}\varphi\} + (aC_{F\gamma 1}\tau_1 - bC_{F\gamma 2}\tau_2)\varphi \end{aligned} \tag{1.38b}$$

$$\begin{aligned} (I_x + mh'^2)\ddot{\varphi} + mh'(\dot{v} + ur) + (I_z\theta_r - I_{xz})\dot{r} + (k_{\varphi 1} + k_{\varphi 2})\dot{\varphi} + \\ + (c_{\varphi 1} + c_{\varphi 2} - mgh')\varphi = 0 \end{aligned} \tag{1.38c}$$

In these equations the additional steer angles ψ_i have been eliminated by using expressions (1.21) with (1.13-15). Furthermore, the resulting compliance steer

and roll steer coefficients for $i = 1$ or 2 have been introduced:

$$c_{sci} = \frac{\left(c_{sfi} - \dfrac{e_i + t_i}{c_{\psi i}}\right) C_{F\alpha i}}{1 - \left(c_{sfi} - \dfrac{e_i + t_i}{c_{\psi i}}\right) C_{F\alpha i}}, \quad c_{sri} = \frac{\varepsilon_i + \tau_i \left(c_{sfi} - \dfrac{e_i + t_i}{c_{\psi i}}\right) C_{F\gamma i}}{1 - \left(c_{sfi} - \dfrac{e_i + t_i}{c_{\psi i}}\right) C_{F\alpha i}} \tag{1.39}$$

where the steer stiffness at the rear $c_{\psi 2}$ may be taken equal to infinity. Furthermore, we have the roll axis inclination angle:

$$\theta_r = \frac{h_2 - h_1}{l} \tag{1.40}$$

In Chapters 7 and 8 the transient properties of the tyre will be addressed. The relaxation length denoted by σ_i is an important parameter that controls the lag of the response of the side force to the input slip angle. For the Laplace transformed version of the equations (1.38) with the Laplace variable s representing differentiation with respect to time, we may introduce tyre lag by replacing the slip angle α_i by the filtered transient slip angle. This may be accomplished by replacing the cornering stiffnesses $C_{F\alpha i}$ appearing in (1.38) and (1.39) by the 'transient stiffnesses':

$$C_{F\alpha i} \rightarrow \frac{C_{F\alpha i}}{1 + s\sigma_i / u} \tag{1.41}$$

A similar procedure may be followed to include the tyre transient response to wheel camber variations. The relaxation length concerned is about equal to the one used for the response to side slip variations. At nominal vertical load the relaxation length is of the order of magnitude of the wheel radius. A more precise model of the aligning torque may be introduced by using a transient pneumatic trail with a similar replacement as indicated by (1.41) but with a much smaller relaxation length approximately equal to half the contact length of the tyre. For more details we refer to Chapter 9 that is dedicated to short wavelength force and moment response.

1.3.2. Linear Analysis of the Two-Degree of Freedom Model

From the equations (1.34b and c) the reduced set of equations for the two-degree of freedom model can be derived immediately. The roll angle φ and its derivative are set equal to zero and furthermore, we will assume the forward speed u ($\approx V$) to remain constant and neglect the influence of the lateral component of the longitudinal forces F_{xi}. The equations of motion of the simple model of Fig.1.9 for v and r now read:

$$m(\dot{v} + ur) = F_{y1} + F_{y2} \tag{1.42a}$$

$$I\dot{r} = aF_{y1} - bF_{y2} \tag{1.42b}$$

with v denoting the lateral velocity of the centre of gravity and r the yaw velocity. The symbol m stands for the vehicle mass and I ($=I_z$) denotes the moment of inertia about the vertical axis through the centre of gravity. For the matter of simplicity, the rearward shifts of the points of application of the forces F_{y1} and F_{y2} over a length equal to the pneumatic trail t_1 and t_2 respectively (that is the aligning torques) have been disregarded. Later, we come back to this. The side forces are functions of the respective slip angles:

$$F_{y1} = F_{y1}(\alpha_1) \quad \text{and} \quad F_{y2} = F_{y2}(\alpha_2) \tag{1.43}$$

and the slip angles are expressed by

$$\alpha_1 = \delta - \frac{1}{u}(v + ar) \quad \text{and} \quad \alpha_2 = -\frac{1}{u}(v - br) \tag{1.44}$$

neglecting the effect of the time rate of change of the steer angle appearing in Eq.(1.36). For relatively low frequency motions the effective axle characteristics or effective cornering stiffnesses according to Eqs.(1.17, 1.22) may be employed.

When only small deviations with respect to the undisturbed straight-ahead motion are considered, the slip angles may be assumed to remain small enough to allow linearisation of the cornering characteristics. For the side force the relationship with the slip angle reduces to the linear equation:

$$F_{yi} = C_i\alpha_i = C_{F\alpha i}\alpha_i \tag{1.45}$$

where C_i denotes the cornering stiffness. This can be replaced by the symbol $C_{F\alpha i}$ which may be preferred in more general cases where also camber and aligning stiffnesses play a role.

The two linear first-order differential equations now read:

$$
\begin{aligned}
m\dot{v} + \frac{1}{u}(C_1 + C_2)v + \left\{mu + \frac{1}{u}(aC_1 - bC_2)\right\}r &= C_1\delta \\
I\dot{r} + \frac{1}{u}(a^2C_1 + b^2C_2)r + \frac{1}{u}(aC_1 - bC_2)v &= aC_1\delta
\end{aligned}
\tag{1.46}
$$

After elimination of the lateral velocity v we obtain the second-order differential equation for the yaw rate r:

$$
\begin{aligned}
Imu\ddot{r} + \{I(C_1 + C_2) + m(a^2C_1 + b^2C_2)\}\dot{r} + \\
+ \frac{1}{u}\{C_1C_2l^2 - mu^2(aC_1 - bC_2)\}r = muaC_1\dot{\delta} + C_1C_2l\delta
\end{aligned}
\tag{1.47}
$$

Here, as before, the dots refer to differentiation with respect to time, δ is the steer angle of the front wheel and l ($=a+b$) represents the wheel base. The equations may be simplified by introducing the following quantities:

$$
\begin{aligned}
C &= C_1 + C_2 \\
Cs &= C_1a - C_2b \\
Cq^2 &= C_1a^2 + C_2b^2 \\
mk^2 &= I
\end{aligned}
\tag{1.48}
$$

Here, C denotes the total cornering stiffness of the vehicle, s is the distance from the centre of gravity to the so-called neutral steer point S (Fig. 1.11), q is a length corresponding to an average moment arm and k is the radius of gyration. Equations (1.46) and (1.47) now reduce to:

$$
\begin{aligned}
m(\dot{v} + ur) + \frac{C}{u}v + \frac{Cs}{u}r &= C_1\delta \\
mk^2\dot{r} + \frac{cq^2}{u}r + \frac{Cs}{u}v &= C_1a\delta
\end{aligned}
\tag{1.49}
$$

and with v eliminated:

$$
m^2k^2u^2\ddot{r} + mC(q^2 + k^2)u\dot{r} + (C_1C_2l^2 - mu^2Cs)r = mu^2aC_1\dot{\delta} + uC_1C_2l\delta
\tag{1.50}
$$

The neutral steer point S is defined as the point on the longitudinal axis of the vehicle where an external side force can be applied without changing the vehicle's yaw angle. If the force acts in front of the neutral steer point, the vehicle is expected to yaw in the direction of the force; if behind, then against the force. The point is of interest when discussing the steering characteristics and stability.

Linear Steady-State Cornering Solutions

We are interested in the path curvature ($1/R$) that results from a constant steer angle δ at a given constant speed of travel V. Since we have at steady state:

$$\frac{1}{R} = \frac{r}{V} \approx \frac{r}{u} \tag{1.51}$$

the expression for the path curvature becomes using (1.47) with u replaced by V and the time derivatives omitted:

$$\frac{1}{R} = \frac{C_1 C_2 l}{C_1 C_2 - m V^2 (a C_1 - b C_2)} \delta \tag{1.52}$$

By taking the inverse, the expression for the steer angle required to negotiate a curve with a given radius R is obtained:

$$\delta = \frac{1}{R}\left(l - m V^2 \frac{a C_1 - b C_2}{l C_1 C_2} \right) \tag{1.53}$$

It is convenient to introduce the so-called understeer coefficient or gradient η. For our model, this quantity is defined as

$$\eta = -\frac{mg}{l} \frac{a C_1 - b C_2}{C_1 C_2} = -\frac{s}{l} \frac{mgC}{C_1 C_2} \tag{1.54}$$

with g denoting the acceleration due to gravity. After having defined the lateral acceleration which in the present linear analysis equals the centripetal acceleration:

$$a_y = V r = \frac{V^2}{R} \tag{1.55}$$

Eq.(1.53) can be written in the more convenient form

$$\delta = \frac{l}{R}\left(1 + \eta \frac{V^2}{g l} \right) = \frac{l}{R} + \eta \frac{a_y}{g} \tag{1.56}$$

The meaning of understeer versus oversteer becomes clear when the steer angle is plotted against the centripetal acceleration while the radius R is kept constant. In Fig.1.10 (left-hand diagram) this is done for three types of vehicles showing understeer, neutral steer and oversteer. Apparently, for an understeered vehicle, the steer angle needs to be increased when the vehicle is going to run at a higher speed. At neutral steer the steer angle can be kept constant while at oversteer a reduction in steer angle is needed when the speed of travel is increased and at the same time a constant turning radius is maintained.

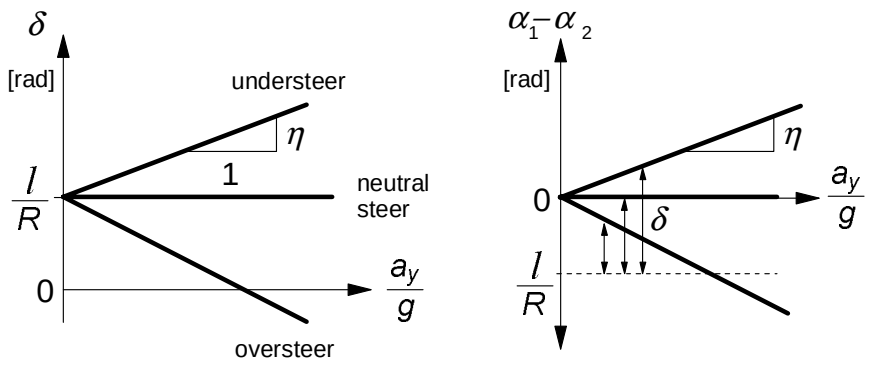

Fig. 1.10. The steer angle versus lateral acceleration at constant path curvature (left graph). The difference in slip angle versus lateral acceleration and the required steer angle at a given path curvature (right graph). The understeer gradient η.

According to Eq.(1.56) the steer angle changes sign when for an oversteered car the speed increases beyond the critical speed that is expressed by:

$$V_{crit} = \sqrt{\frac{gl}{-\eta}} \qquad (\eta < 0) \tag{1.57}$$

As will be shown later, the motion becomes unstable when the critical speed is surpassed. Apparently, this can only happen when the vehicle shows oversteer.

For an understeered car a counterpart has been defined which is the so-called characteristic speed. It is the speed where the steer angle required to maintain the same curvature increases to twice the angle needed at speeds approaching zero. We may also say that at the characteristic speed the path curvature response to steer angle has decreased to half its value at very low speed. Also interesting is the fact that at the characteristic speed the yaw rate response to steer angle r/δ reaches a maximum (the proof of which is left to the reader). We have for the characteristic velocity:

$$V_{char} = \sqrt{\frac{gl}{\eta}} \qquad (\eta > 0) \tag{1.58}$$

Expression (1.54) for the understeer gradient η is simplified when the following expressions for the front and rear axle loads are used:

$$F_{z1} = \frac{b}{l} mg \quad \text{and} \quad F_{z2} = \frac{a}{l} mg \tag{1.59}$$

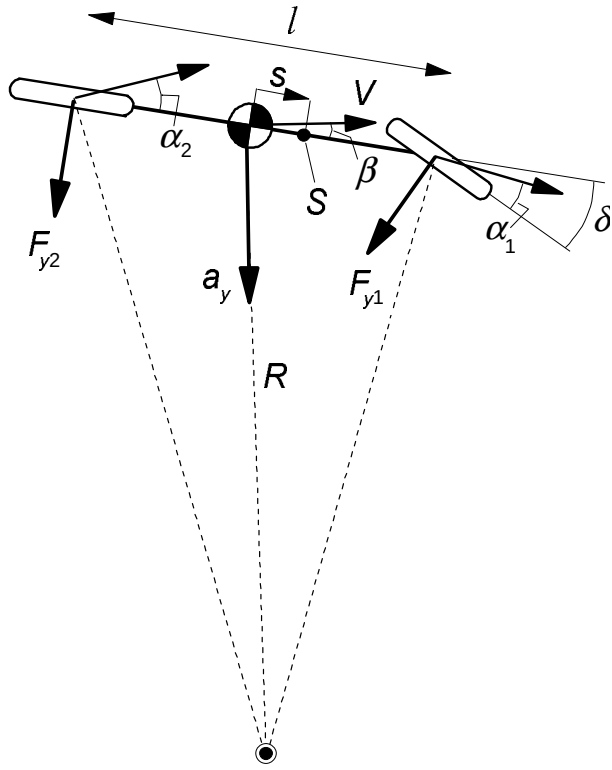

Fig. 1.11. Two-wheel vehicle model in a cornering manoeuvre.

We obtain:

$$\eta = \frac{F_{z1}}{C_1} - \frac{F_{z2}}{C_2} \tag{1.60}$$

which says that a vehicle exhibits an understeer nature when the relative cornering compliance of the tyres at the front is larger than at the rear. It is important to note that in (1.59) and (1.60) the quantities $F_{z1,2}$ denote the vertical axle loads that occur at stand-still and thus represent the mass distribution of the vehicle. Changes of these loads due to aerodynamic down forces and fore and aft load transfer at braking or driving should not be introduced in expression (1.60).

In the same diagram the difference in slip angle front and rear may be indicated. We find for the side forces

$$F_{y1} = \frac{b}{l} m a_y = F_{z1} \frac{a_y}{g}, \qquad F_{y2} = \frac{a}{l} m a_y = F_{z2} \frac{a_y}{g} \tag{1.61}$$

and hence for the slip angles

$$\alpha_1 = \frac{F_{z1}}{C_1}\frac{a_y}{g}, \qquad \alpha_2 = \frac{F_{z2}}{C_2}\frac{a_y}{g} \tag{1.62}$$

The difference now reads when considering the relation (1.59)

$$\alpha_1 - \alpha_2 = \eta\frac{a_y}{g} \tag{1.63}$$

Apparently, the sign of this difference is dictated by the understeer coefficient. Consequently, it may be stated that according to the linear model an understeered vehicle ($\eta > 0$) moves in a curve with slip angles larger at the front than at the rear ($\alpha_1 > \alpha_2$). For a neutrally steered vehicle the angles remain the same ($\alpha_1 = \alpha_2$) and with an oversteered car the rear slip angles are bigger ($\alpha_2 > \alpha_1$). As is shown by the expressions (1.54), the signs of η and s are different. Consequently, as one might expect when the centrifugal force is considered as the external force, a vehicle acts oversteered when the neutral steer point lies in front of the centre of gravity and understeered when S lies behind the c.g.. As we will see later on, the actual non-linear vehicle may change its steering character when the lateral acceleration increases. It appears then that the difference in slip angle is no longer directly related to the understeer gradient.

Consideration of Eq.(1.56) reveals that in the left-hand graph of Fig.1.10 the difference in slip angle can be measured along the ordinate starting from the value l/R. It is of interest to convert the diagram into the graph shown on the right-hand side of Fig.1.10 with ordinate equal to the difference in slip angle. In that way, the diagram becomes more flexible because the value of the curvature $1/R$ may be selected afterwards. The horizontal dotted line is then shifted vertically according to the value of the relative curvature l/R considered. The distance to the handling line represents the magnitude of the steer angle.

Figure 1.11 depicts the resulting steady-state cornering motion. The vehicle side slip angle β has been indicated. It is of interest to note that at low speed this angle is negative for right-hand turns. Beyond a certain value of speed the tyre slip angles have become sufficiently large and the vehicle slip angle changes into positive values. In Exercise 1.2 the slip angle β will be used.

Influence of the Pneumatic Trail

The direct influence of the pneumatic trails t_i may not be negligible. In reality, the tyre side forces act a small distance behind the contact centres. As a consequence, the neutral steer point should also be considered to be located at a distance approximately equal to the average value of the pneumatic trails, more

to the rear, which means actually more understeer. The correct values of the position s of the neutral steer point and of the understeer coefficient η can be found by using the effective axle distances $a' = a - t_1$, $b' = b + t_2$ and $l' = a' + b'$ in the Eqs. (1.48) and (1.59) instead of the original quantities a, b and l.

Stability of the Motion

Stability of the steady-state circular motion can be examined by considering the differential equation (1.47) or (1.50). The steer angle is kept constant so that the equation gets the form

$$a_0 \ddot{r} + a_1 \dot{r} + a_2 r = b_1 \delta \tag{1.64}$$

For this second-order differential equation stability is assured when all coefficients a_i are positive. Only the last coefficient a_2 may become negative which corresponds to divergent instability (spin-out without oscillations). As already indicated, this will indeed occur when for an oversteered vehicle the critical speed (1.57) is exceeded. The condition for stability reads:

$$a_2 = C_1 C_2 l^2 \left(1 + \eta \frac{V^2}{gl} \right) = C_1 C_2 l^2 \left(\frac{\delta}{l/R} \right)_{ss} > 0 \tag{1.65}$$

with the subscript $_{ss}$ referring to steady-state conditions, or

$$V < V_{crit} = \sqrt{\frac{gl}{-\eta}} \qquad (\eta < 0) \tag{1.66}$$

The next section will further analyse the dynamic nature of the stable and unstable motions.

It is of importance to note that when the condition of an automobile subjected to driving or braking forces is considered, the cornering stiffnesses front and rear will change due to the associated fore and aft axle load transfer and the resulting state of combined slip. In expression (1.60) for the understeer coefficient η the quantities F_{zi} represent the static vertical axle loads obtained through Eqs.(1.59) and are to remain unchanged! In Subsection 1.3.4 the effect of longitudinal forces on vehicle stability will be further analysed.

Free Linear Motions

To study the nature of the free motion after a small disturbance in terms of natural frequency and damping, the eigenvalues, that is the roots of the characteristic equation of the linear second-order system, are to be assessed. The

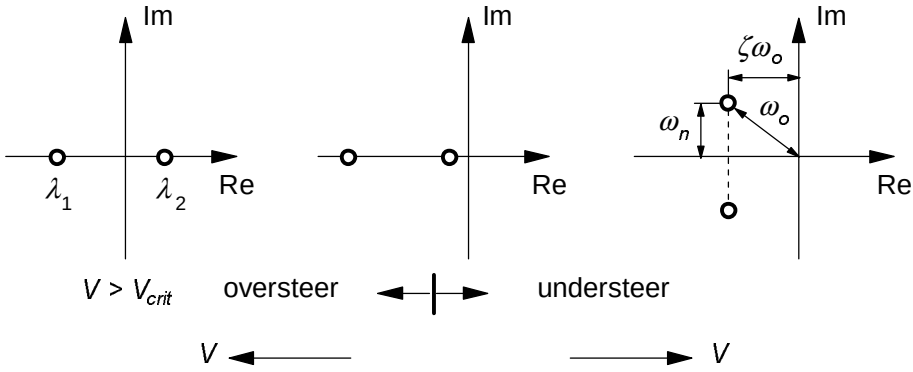

Fig. 1.12. Possible eigenvalues for the over and understeered car at lower and higher speeds.

characteristic equation of the system described by the equations (1.49) or (1.50) reads after using the relation (1.54) between s and η:

$$m^2k^2V^2\lambda^2 + mC(q^2 + k^2)V\lambda + C_1C_2l^2\left(1 + \frac{\eta}{gl}V^2\right) = 0 \qquad (1.67)$$

For a single mass-damper-spring system shown in Fig.1.13 with r the mass displacement, δ the forced displacement of the support, M the mass, D the sum of the two damping coefficients D_1 and D_2 and K the sum of the two spring stiffnesses K_1 and K_2 a differential equation similar in structure to Eq.(1.50) arises:

$$M\ddot{r} + D\dot{r} + Kr = D_1\dot{\delta} + K_1\delta \qquad (1.68)$$

and the corresponding characteristic equation:

$$M\lambda^2 + D\lambda + K = 0 \qquad (1.69)$$

When an oversteered car exceeds its critical speed, the last term of (1.67) becomes negative which apparently corresponds with a negative stiffness K. An inverted pendulum is an example of a second-order system with negative last coefficient showing monotonous (diverging) instability.

The roots λ of equation (1.67) may have loci in the complex plane as shown in Fig.1.12. For positive values of the cornering stiffnesses only the last coefficient of the characteristic equation can become negative which is responsible for the limited types of eigenvalues that can occur. As we will see in Subsection 1.3.3, possible negative slopes beyond the peak of the non-linear axle characteristics may give rise to other types of unstable motions connected with two positive real roots or two conjugated complex roots with a positive real part. For the linear vehicle model we may have two real roots in the oversteer case and

a pair of complex roots in the understeer case, except at low speeds where the understeered vehicle can show a pair of real negative roots.

As indicated in the figure, the complex root is characterised by the natural frequency ω_o of the undamped system ($D = 0$), the damping ratio ς and the resulting actual natural frequency ω_n. Expressions for these quantities in terms of the model parameters are rather complex. However, if we take into account that in normal cases $|s| \ll l$ and $q \approx k \approx \frac{1}{2} l$ we may simplify these expressions and find the following useful formulae:

The natural frequency of the undamped system:

$$\omega_o^2 = \frac{K}{M} \approx \left(\frac{C}{mV}\right)^2 \cdot \left(1 + \frac{\eta}{gl} V^2\right) \tag{1.70}$$

The damping ratio:

$$\zeta = \frac{D}{2M\omega_o} \approx \frac{1}{\sqrt{1 + \frac{\eta}{gl} V^2}} \tag{1.71}$$

The natural frequency:

$$\omega_n^2 = \omega_o^2 (1 - \zeta^2) \approx \left(\frac{C}{m}\right)^2 \frac{\eta}{gl} \tag{1.72}$$

The influence of parameters has been indicated in Fig.1.13. An arrow pointing upwards represents an increase of the quantity in the same column of the matrix.

The yaw rate response to a step change in steer angle is typified by the rise

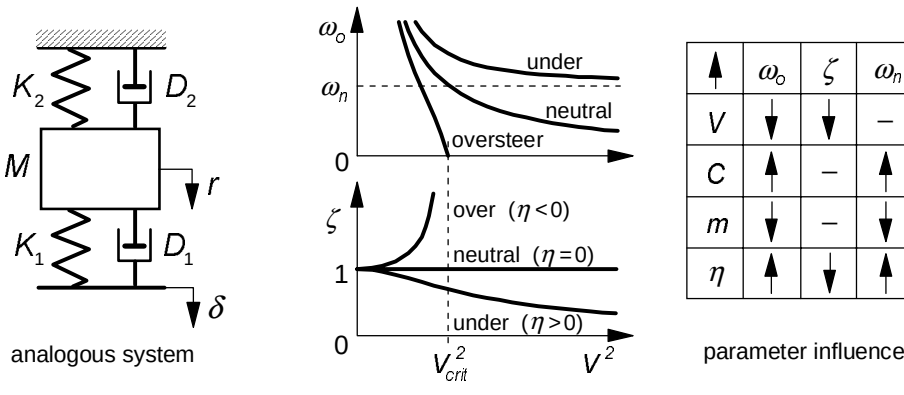

↑	ω_o	ζ	ω_n
V	↓	↓	–
C	↑	–	↑
m	↓	–	↓
η	↑	↓	↑

Fig. 1.13. The influence of parameters on natural frequency and damping.

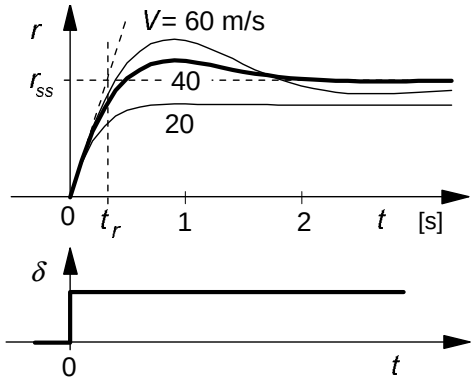

	t_r
$V<V_{char}$	↑
$V>V_{char}$	↓
η	↓
C_1	↓
m	↑
k	↑

Fig. 1.14. Step response of yaw rate to steer angle. Parameters according to Table 1.1. Parameter influence on the rise time t_r.

time t_r indicated in Fig. 1.14 and expressed in terms of the parameters as follows:

$$t_r = \frac{mk^2V}{aC_1l\left(1+\frac{\eta}{gl}V^2\right)} = \frac{mk^2V}{\frac{a}{l}\left\{C_1l^2+\left(b-a\frac{C_1}{C_2}\right)mV^2\right\}} \tag{1.73}$$

The parameter influence has been indicated in the figure. The results correspond qualitatively well with the 90% response times found in vehicle model simulation studies. A remarkable result is that for an understeered automobile the response time is smaller than for an oversteered car.

Forced Linear Vibrations

The conversion of the equations of motion (1.46) into the standard state space representation is useful when the linear system properties are the subject of investigation. The system at hand is of the second order and hence possesses two state variables for which we choose: v and r. The system is subjected to a single input signal: the steer angle δ. Various variables may be of interest to analyse the vehicle's response to steering input oscillations. The following quantities are selected to illustrate the method and to study the dynamic behaviour of the vehicle: the lateral acceleration a_y of the centre of gravity of the vehicle, the yaw rate r and the vehicle slip angle β defined at the centre of gravity. In matrix notation the equation becomes:

$$\begin{aligned} \dot{\boldsymbol{x}} &= \boldsymbol{A}\boldsymbol{x} + \boldsymbol{B}\boldsymbol{u} \\ \boldsymbol{y} &= \boldsymbol{C}\boldsymbol{x} + \boldsymbol{D}\boldsymbol{u} \end{aligned} \tag{1.74}$$

with

$$\dot{\boldsymbol{x}} = \begin{pmatrix} \dot{v} \\ \dot{r} \end{pmatrix}, \quad \boldsymbol{u} = \delta, \quad \boldsymbol{y} = \begin{pmatrix} a_y \\ r \\ \beta \end{pmatrix} = \begin{pmatrix} \dot{v} + Vr \\ r \\ -v/V \end{pmatrix} \tag{1.75}$$

and

$$\boldsymbol{A} = -\begin{pmatrix} \dfrac{C}{mV} & V + \dfrac{Cs}{mV} \\ \dfrac{Cs}{mk^2V} & \dfrac{Cq^2}{mk^2V} \end{pmatrix}, \quad \boldsymbol{B} = \begin{pmatrix} \dfrac{C_1}{m} \\ \dfrac{C_1 a}{mk^2} \end{pmatrix}$$

$$\boldsymbol{C} = -\begin{pmatrix} \dfrac{C}{mV} & \dfrac{Cs}{mV} \\ 0 & -1 \\ 1/V & 0 \end{pmatrix}, \quad \boldsymbol{D} = \begin{pmatrix} \dfrac{C_1}{m} \\ 0 \\ 0 \end{pmatrix} \tag{1.76}$$

The frequency response functions have been computed using Matlab software. Figure 1.15 presents the amplitude and phase response functions for each of the three output quantities and at three different values of speed of travel. The values of the chosen model parameters and a number of characteristic quantities have been listed in Table 1.1.

Explicit expressions of the frequency response functions in terms of model parameters are helpful to understand and predict the characteristic aspects of these functions which may be established by means of computations or possibly through full scale experiments.

From the differential equation (1.50) the frequency response function is easily derived. Considering the quantities formulated by (1.70) and (1.71) and the steady-state response $(r/\delta)_{ss} = (V/R)/\delta$ obtained from (1.56) we find:

Table 1.1. Parameter values and typifying quantities

parameters		derived typifying quantities					
a	1.4 m	l	3 m	V [m/s]	20	40	60
b	1.6 m	F_{z1}	8371 N	ω_o [rad/s]	4.17	2.6	2.21
C_1	60000N/rad	F_{z2}	7325 N	ζ [-]	0.9	0.7	0.57
C_2	60000N/rad	q	1.503 m	ω_n [rad/s]	1.8	1.8	1.82
m	1600 kg	s	-0.1 m	t_r [s]	0.23	0.3	0.27
k	1.5 m	η	0.0174 rad (~1° extra steer / g lateral accel.)				

$$\frac{r}{\delta}(j\omega) = \left(\frac{r}{\delta}\right)_{ss} \cdot \frac{1 + \dfrac{mVa}{C_2 l} j\omega}{1 - \left(\dfrac{\omega}{\omega_o}\right)^2 + 2\zeta\left(\dfrac{j\omega}{\omega_o}\right)} \quad ; \quad \left(\frac{r}{\delta}\right)_{ss} = \frac{V/l}{1 + \dfrac{\eta}{gl}V^2} \tag{1.77}$$

Similarly, the formula for the response of lateral acceleration a_y can be derived:

$$\frac{a_y}{\delta}(j\omega) = \left(\frac{a_y}{\delta}\right)_{ss} \cdot \frac{1 - \dfrac{mk^2}{C_2 l}\omega^2 + \dfrac{b}{V} j\omega}{1 - \left(\dfrac{\omega}{\omega_o}\right)^2 + 2\zeta\left(\dfrac{j\omega}{\omega_o}\right)} \quad ; \quad \left(\frac{a_y}{\delta}\right)_{ss} = \frac{V^2/l}{1 + \dfrac{\eta}{gl}V^2} \tag{1.78}$$

and for the slip angle β:

$$\frac{\beta}{\delta}(j\omega) = \left(\frac{\beta}{\delta}\right)_{ss} \cdot \frac{1 - \dfrac{mk^2 V}{amV^2 - bC_2 l} j\omega}{1 - \left(\dfrac{\omega}{\omega_o}\right)^2 + 2\zeta\left(\dfrac{j\omega}{\omega_o}\right)} \quad ; \quad \left(\frac{\beta}{\delta}\right)_{ss} = -\frac{b}{l}\,\frac{1 - \dfrac{a}{b}\dfrac{m}{C_2 l}V^2}{1 + \dfrac{\eta}{gl}V^2} \tag{1.79}$$

By considering Eq.(1.77) it can now be explained for instance that at higher frequencies the system shows features of a first-order system: because of the $j\omega$ term in the numerator the yaw rate amplitude response tends to a decay at a 6dB per octave rate (if plotted in log-log scale) and the phase lag approaches

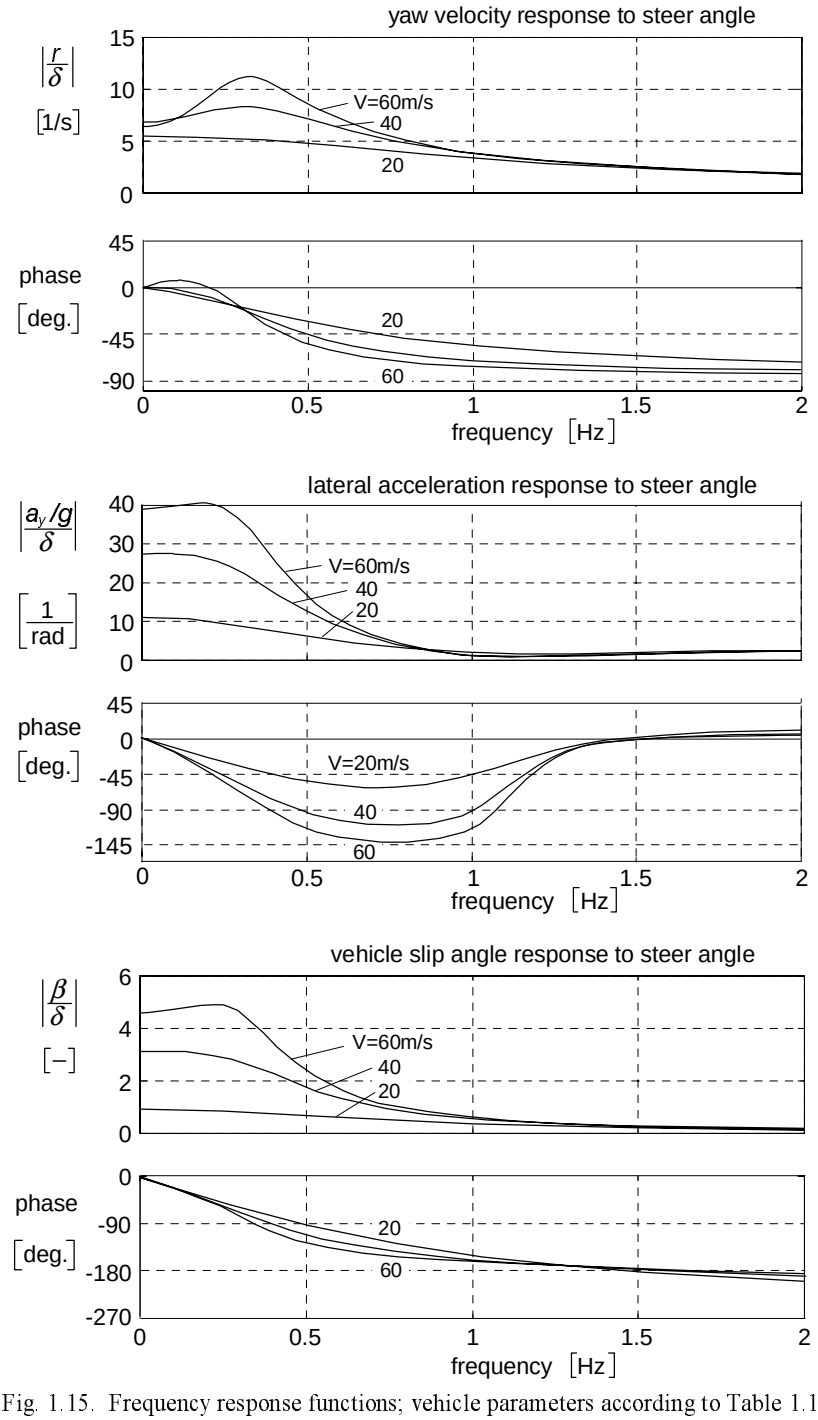

Fig. 1.15. Frequency response functions; vehicle parameters according to Table 1.1.

90 degrees. The phase increase at low frequencies and higher speeds is due to the presence of the speed V in that same term. At speeds beyond approximately the characteristic speed, the corresponding (last) term in the denominator has less influence on the initial slope of the phase characteristic. The lateral acceleration response (1.78) shown in the centre graph of Fig.1.15 gives a finite amplitude at frequencies tending to infinity because of the presence of ω^2 in the numerator. For the same reason, the phase lag goes back to zero at large frequencies. The side slip phase response tends to -270 degrees (at larger speeds) which is due to the negative coefficient of $j\omega$ in the numerator of (1.79). This in contrast to that coefficient of the yaw rate response (1.77).

It is of interest to see that the steady-state slip angle response, indicated in (1.79), changes sign at a certain speed V. At low speeds where the tyre slip angles are still very small, the vehicle slip angle obviously is negative for positive steer angle (considering positive directions as adopted in Fig.1.11). At larger velocities the tyre slip angles increase and as a result, β changes into the positive direction.

Exercise 1.2. Four wheel steer, condition that the vehicle slip angle vanishes

Consider the vehicle model of Fig.1.16. Both the front and the rear wheels can be steered. The objective is to have a vehicle moving with a slip angle β remaining equal to zero. In practice, this may be done to improve handling qualities of the automobile (reduces to first-order system!) and to avoid excessive side slipping motions of the rear axle in lane change manoeuvres. Adapt the equations of motion (1.46) and assess the required relationship between the steer angles δ_1 and δ_2. Do this in terms of the transfer function between δ_2 and δ_1 and the associated differential equation. Find the steady-state ratio $(\delta_2/\delta_1)_{ss}$ and plot this as a function of the speed V. Show also the frequency response function $\delta_2/\delta_1\,(j\omega)$ for the amplitude and phase at a speed $V = 30$ m/s. Use the vehicle parameters supplied in Table 1.1.

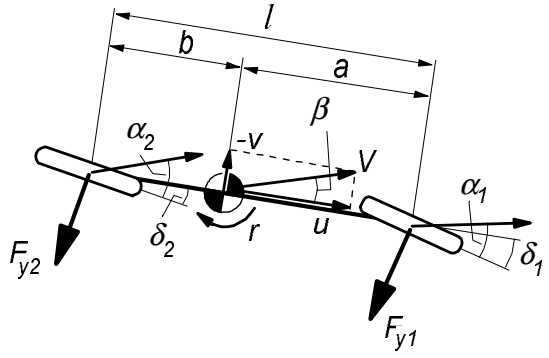

Fig. 1.16. 'Four-wheel' steering to make slip angle $\beta = 0$ (Exercise 1.2).

1.3.3. Non-Linear Steady-State Cornering Solutions

From Eqs.(1.42) and (1.59) with the same restrictions as stated below Eq.(1.60), the following force balance equations can be derived (follows also from Eqs.(1.61)). The effect of the pneumatic trails will be dealt with later on.

$$\frac{F_{y1}}{F_{z1}} = \frac{F_{y2}}{F_{z2}} = \frac{a_y}{g} \quad \left(= \frac{K}{mg} \right) \tag{1.80}$$

Where $K = ma_y$ represents the centrifugal force. The kinematic relationship

$$\delta - (\alpha_1 - \alpha_2) = \frac{l}{R} \tag{1.81}$$

follows from Eqs.(1.44) and (1.51). In Fig.1.11 the vehicle model has been depicted in a steady-state cornering manoeuvre. It can easily be observed from this diagram that relation (1.44) holds approximately when the angles are small.

The ratio of the side force and vertical load as shown in (1.80) plotted as a function of the slip angle may be termed as the normalised tyre or axle characteristic. These characteristics subtracted horizontally from each other produce the 'handling curve'. Considering the equalities (1.80) the ordinate may be replaced by a_y/g. The resulting diagram with abscissa α_1-α_2 is the non-linear version of the right-hand diagram of Fig.1.10 (rotated 90° anti-clockwise). The diagram may be completed by attaching the graph that shows for a series of speeds V the relationship between lateral acceleration (in g units) a_y/g and the relative path curvature l/R according to Eq.(1.55).

Figure 1.17 shows the normalised axle characteristics and the completed handling diagram. The handling curve consists of a main branch and two side lobes. The different portions of the curves have been coded to indicate the corresponding parts of the original normalised axle characteristics they originate from. Near the origin the system may be approximated by a linear model. Consequently, the slope of the handling curve in the origin with respect to the vertical axis is equal to the understeer coefficient η. In contrast to the straight handling line of the linear system (Fig.1.10), the non-linear system shows a curved line. The slope changes along the curve which means that the degree of understeer changes with increasing lateral acceleration. The diagram of Fig.1.17 shows that the vehicle considered changes from understeer to oversteer. We define:

$$\begin{aligned} &\textit{understeer} \text{ if: } \left(\frac{\partial\delta}{\partial V}\right)_R > 0 \\ &\textit{oversteer} \text{ if: } \left(\frac{\partial\delta}{\partial V}\right)_R < 0 \end{aligned} \tag{1.82}$$

The family of straight lines represents the relationship between acceleration and curvature at different levels of speed. The speed line belonging to V= 50km/h has been indicated (wheel base l= 3m). This line is shifted to the left over a distance equal to the steer angle δ = 0.04rad and three points of intersection with the handling curve arise. These points I, II and III indicate the possible equilibrium conditions at the chosen speed and steer angle. The connected values of the relative path curvature l/R can be found by going back to the speed line. As will

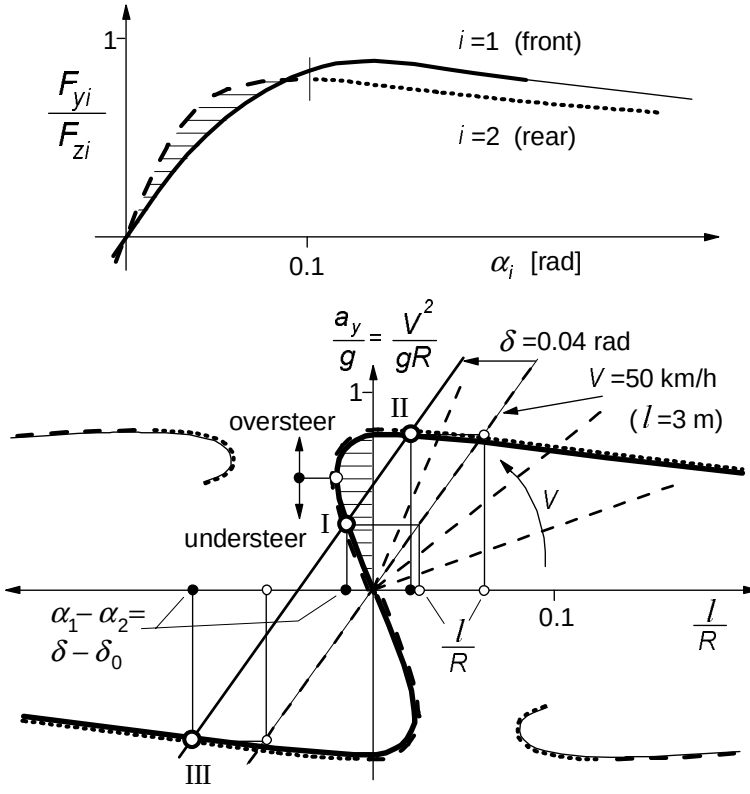

Fig. 1.17. Handling diagram resulting from normalized tyre characteristics. Equilibrium points I, II and III (steady turns) of which only I is stable, arise for speed V= 50 km/h and steer angle δ = 0.04 rad. From the different line types the manner in which the curves are obtained from the upper diagram may be retrieved.

be shown further on, only point I refers to a stable cornering motion. In points II and III ($R<0$!) the motion is unstable.

At a given speed V, a certain steer angle δ is needed to negotiate a circular path with given radius R. The steer angle required can be read directly from the handling diagram. The steer angle needed to negotiate the same curve at very low speed ($V\to 0$) tends to l/R. This steer angle is denoted with δ_0. Consequently, the abscissa of the handling curve α_1-α_2 may as well be replaced by δ-δ_0. This opens the possibility to determine the handling curve with the aid of simple experimental means, i.e. measuring the steering wheel input (reduced to equivalent road wheel steer angle by means of the steering ratio, which method automatically includes steering compliance effects) at various speeds running over the same circular path.

Subtracting normalized characteristics may give rise to very differently

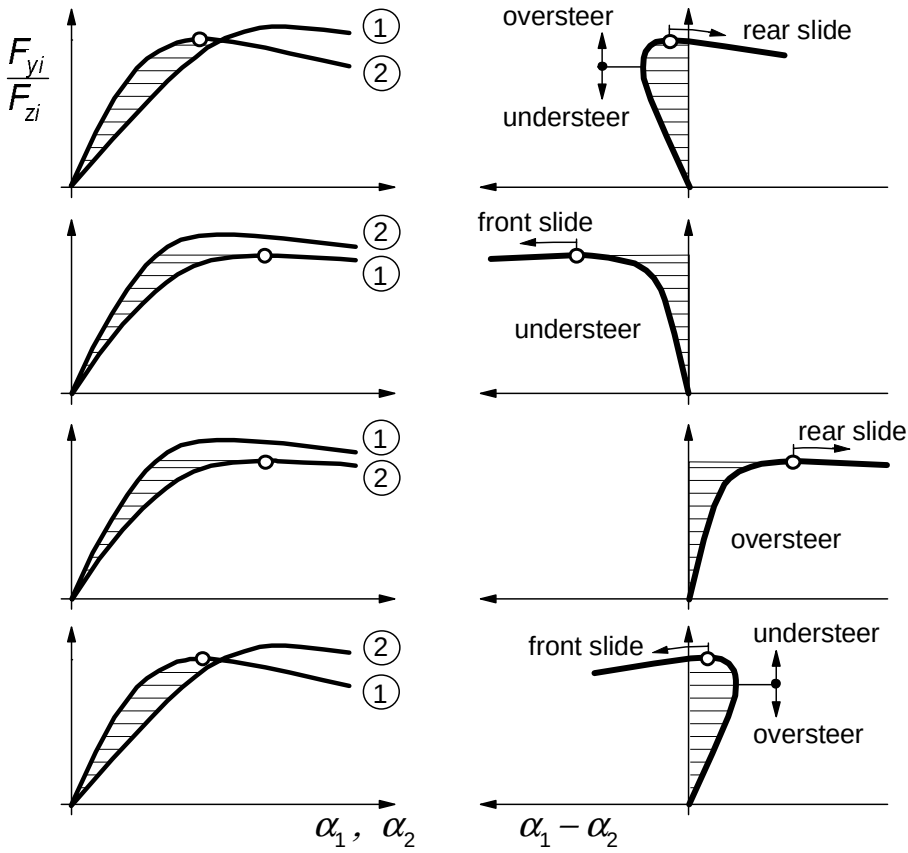

Fig. 1.18. A number of handling curves arising from the pairs of normalized tyre characteristics shown left. Only the main branch of handling curve is drawn (1: front, 2: rear).

shaped handling curves only by slightly modifying the original characteristics. As Fig.1.17 shows, apart from the main branch passing through the origin, isolated branches may occur. These are associated with at least one of the decaying ends of the pair of normalized tyre characteristics.

In Fig.1.18 a set of four possible combinations of axle characteristics have been depicted together with the resulting handling curves. This collection of characteristics shows that the nature of steering behaviour is entirely governed by the normalised axle characteristics and in particular their relative shape with respect to each other.

The way in which we can use the handling diagram is presented in Fig.1.19. The speed of travel may be kept constant and the lateral acceleration is increased be running over a spiral path with decreasing radius. The required variation of the steer angle follows from the distance between the handling curve and the speed line. Similarly we can observe what happens when the path curvature is kept constant and the speed is increased. Also, the resulting variation of the curvature at a constant steer angle and increasing speed can be found. More general cases of quasi steady-state motions may be studied as well.

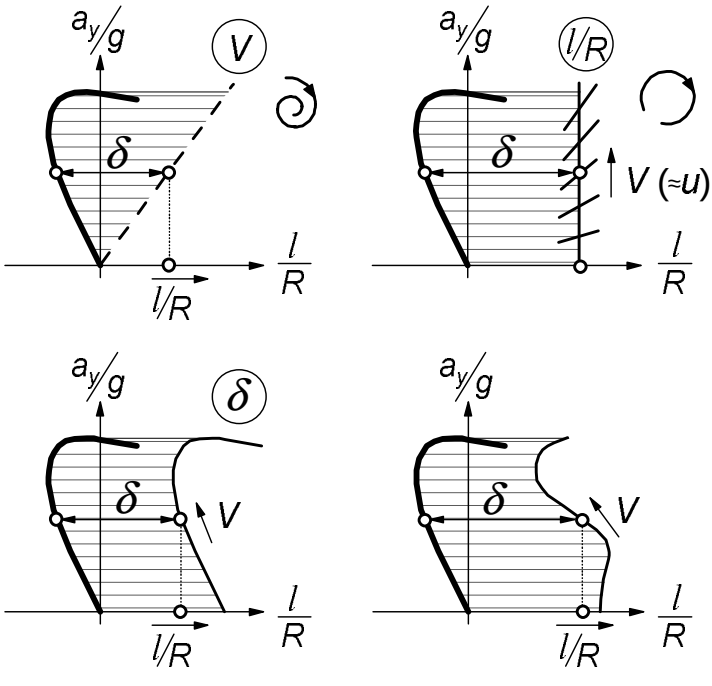

Fig. 1.19. Types of quasi steady-state manoeuvres.

Stability of the Motion at Large Lateral Accelerations

The non-linear set of equations (1.42-44) may be linearised around the point of operation, that is one of the equilibrium states indicated above. The resulting second-order differential equation has a structure similar to Eq.(1.64) or (1.47) but with the variables replaced by their small variations with respect to the steady-state condition considered. Analysis of the coefficients of the characteristic equation reveals if stability exists. Also the nature of stability (monotonous, oscillatory) follows from these coefficients. This is reflected by the type of singular points (node, spiral, saddle) representing the equilibrium solutions in the phase plane as treated in the next section.

It now turns out that not only the last coefficient can become negative but also the second coefficient a_1. Instead of the cornering stiffnesses C defined in the origin of the tyre cornering characteristics, the slope of the normalised characteristics at a given level of a_y/g becomes now of importance. We define

$$\Phi_i = \frac{1}{F_{zi}} \frac{\partial F_{yi}}{\partial \alpha_i} \qquad (i = 1, 2) \tag{1.83}$$

The conditions for stability, that is: second and last coefficient of equation comparable with Eq.(1.47) must be positive, read after having introduced the radius of gyration k ($k^2 = I/m$):

$$(k^2 + a^2)\Phi_1 + (k^2 + b^2)\Phi_2 > 0 \tag{1.84}$$

$$\Phi_1 \Phi_2 \left(\frac{\partial \delta}{\partial\, 1/R} \right)_V > 0 \tag{1.85}$$

The subscript V refers to the condition of differentiation with V kept constant, that is while staying on the speed line of Fig.1.17. The first condition (1.84) may be violated when we deal with tyre characteristics showing a peak in side force and a downwards sloping further part of the characteristic. The second condition corresponds to condition (1.65) for the linear model. Accordingly, instability is expected to occur beyond the point where the steer angle reaches a maximum while the speed is kept constant. This, obviously, can only occur in the oversteer range of operation. In the handling diagram the stability boundary can be assessed by finding the tangent to the handling curve that runs parallel to the speed line considered.

In the upper diagram of Fig.1.20 the stability boundary, that holds for the right part of the diagram (a_y vs l/R), has been drawn for the system of Fig.1.17 that changes from initial understeer to oversteer. In the middle diagram a number

of shifted V-lines, each for a different steer angle δ, has been indicated. In each case the points of intersection represent possible steady-state solutions. The highest point represents an unstable solution as the corresponding point on the speed line lies in the unstable area. When the steer angle is increased the two points of intersections move towards each other. It turns out that for this type of handling curve a range of δ values exists without intersections with the positive half of the curve. The fact that both right-hand turn solutions may vanish has serious implications which follows from the phase plot. At increased steer angle, however, new solutions may show up. At first, these solutions appear to be unstable, but at rather large steer angles of more than about 0.2 rad we find again stable solutions. These occur on the isolated branch where α_2 is small and α_1 is large. Apparently, we find that the vehicle that increases its speed while running at a constant turning radius will first cross the stability boundary and may then

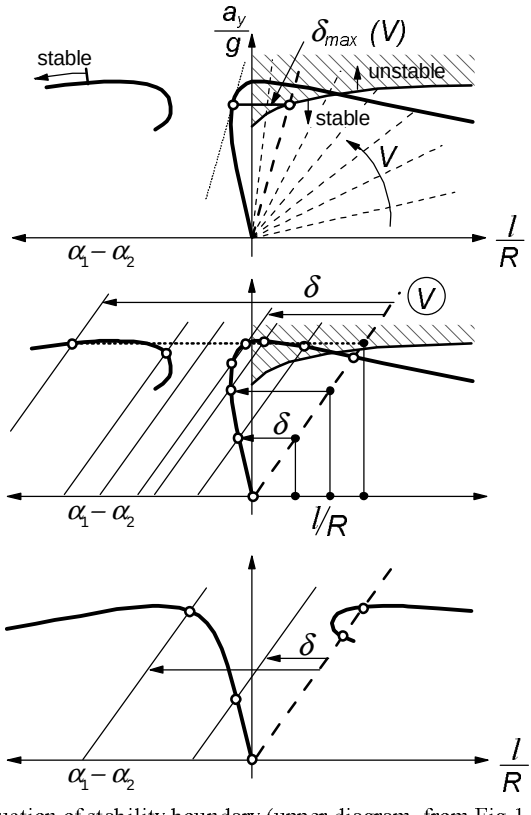

Fig. 1.20. Construction of stability boundary (upper diagram, from Fig. 1.17). On the isolated branch a stable range may occur (large steer angle as indicated in middle diagram). The lower diagram shows the case with complete understeer featuring a stable main branch.

recover its stability by turning the steering wheel to a relatively large angle. In the diagram the left part of the isolated branch is reached where stable spirals appear to occur. This phenomenon may correspond to similar experiences in the racing practice, cf. Jenkinson (1958).

The lower diagram depicts the handling curve for a car that remains understeered throughout the lateral acceleration range. Everywhere the steady-state cornering motion remains stable. Up to the maximum of the curve the tangents slope to the left and cannot run parallel to a speed line. Beyond the peak, however, we can find a speed line parallel to the tangent, but at the same time one of the slopes (Φ_1) of the normalised axle characteristics starts to show a negative sign so that condition (1.85) is still satisfied. Similarly, the limit oversteer vehicle of the upper graph remains unstable beyond the peak. On the isolated part of the handling curve of the lower diagram the motion remains unstable. It will be clear that the isolated branches vanish when we deal with axle characteristics that do not show a peak and decaying part of the curve.

It may seem that the establishment of unstable solutions has no particular value. It will become clear, however, that the existence and the location of both stable and unstable singular points play an important role in shaping the trajectories in the phase-plane. Also, the nature of stability or instability in the singular points are of importance.

Exercise 1.3. Construction of the complete handling diagram from pairs of axle characteristics

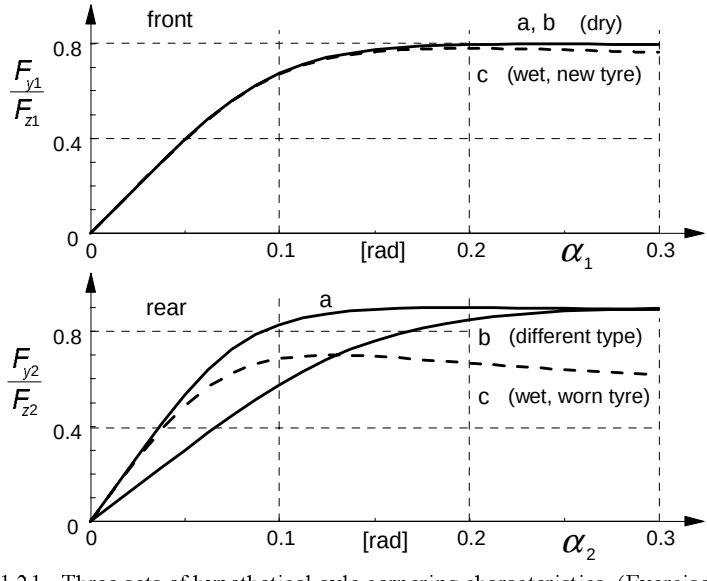

Fig. 1.21. Three sets of hypothetical axle cornering characteristics (Exercise 1.3).

We consider three sets of hypothetical axle characteristics (a, b and c) shown in the graph of Fig.1.21. The dimensions of the vehicle model are: $a = b = \frac{1}{2}l = 1.5$ m. For the tyres we may employ axle characteristics described by the Magic Formula (1.6):

$$F_y = D \sin[C \arctan\{B\alpha - E(B\alpha - \arctan(B\alpha))\}]$$

We define: the peak side force $D = \mu F_z$ and the cornering stiffness $C_{F\alpha} = BCD = c_{F\alpha} F_z$ so that $B = c_{F\alpha}/(C\mu)$. For the six tyre/axle configurations the parameter values have been given in the table below.

axle	case	μ	$c_{F\alpha}$	C	E
front	a, b	0.8	8	1.2	-2
	c	0.78	8	1.3	-2
rear	a	0.9	11	1.2	-2
	b	0.9	6	1.2	-2
	c	0.65	11	1.5	-1

Determine for each of the three combinations (two dry, one wet):

1. The handling curve (cf. Fig. 1.17).
2. The complete handling diagram (cf. Fig. 1.17).
3. The portion of the curves where the vehicle shows an oversteer nature.
4. The stability boundary (associated with these oversteer ranges) in the (a_y/g versus l/R) diagram (= right-hand side of the handling diagram) (cf. Fig.1.20).
5. Indicate in the diagram (or in a separate graph):
   a. the course of the steer angle δ required to negotiate a curve with radius $R = 60$m as a function of the speed V. If applicable, indicate the stability boundary, that is the critical speed V_{crit}, belonging to this radius.
   b. the course of steer angle δ as a function of relative path curvature l/R at a fixed speed $V = 72$ km/h and if applicable assess the critical radius R_{crit}.

For the vehicle systems considered so far a unique handling curve appears to suffice to describe the steady-state turning behaviour. Cases may occur, however, where more curves are needed, one for each velocity. A simple example is the situation when the car runs over a wet surface where the tyre characteristics change considerably with speed. Also, as a result of the down forces acting on e.g. the body of a racing car, the tyre loads increase with speed. Consequently, the tyre characteristics change accordingly which requires an adaptation of the handling curve.

A more difficult and fundamentally different situation occurs when the vehicle is equipped with a third axle. Also in this case multiple handling curves arise. A tandem rear axle configuration of a heavy truck for example, strongly opposes

movement along a curved track. The slip angles of the two rear axles are different so that a counteracting torque arises. This torque gets larger when the turning radius becomes smaller. This may for instance occur at a given level of lateral acceleration. When at this level the speed becomes lower, the curvature must become larger and the opposing torque will increase which entails an increased front steer angle to generate a larger side force needed to balance the vehicle. This increased steer angle goes on top of the steer angle which was already larger because of the increased l/R. Here, l is the average wheel base. Consequently, in the handling diagram, the points on the handling curve belonging to the lower speed lie more to the left. For a detailed study on this special subject we refer to Winkler (1998).

Assessment of the Influence of the Pneumatic Trail on the Handling Curve

So far the direct influence of the pneumatic trails have not been taken into account. As with the linear analysis we may do this by considering the effective axle positions

$$a'=a-t_1\,,\quad b'=b+t_2 \qquad \text{and} \qquad l'=a'+b' \tag{1.86}$$

The difficulty we have to face now is the fact that these pneumatic trails t_i will vary with the respective slip angles. We have if the residual torques are neglected:

$$t_i(\alpha_i) = -\frac{M_{zi}(\alpha_i)}{F_{yi}(\alpha_i)} \tag{1.87}$$

Introducing the effective axle loads

$$F'_{z1} = \frac{b'}{l'}mg\,,\quad F'_{z2} = \frac{a'}{l'}mg \tag{1.88}$$

yields for the lateral force balance instead of (1.80):

$$\frac{F_{y1}}{F'_{z1}} = \frac{F_{y2}}{F'_{z2}} = \frac{a_y}{g} \tag{1.89}$$

or after some rearrangements:

$$\frac{a'}{a}\frac{F_{y1}}{F_{z1}} = \frac{b'}{b}\frac{F_{y2}}{F_{z2}} = Q\frac{a_y}{g} \tag{1.90}$$

with

$$Q = \frac{l}{l'}\frac{a'b'}{a\,b} \approx 1 \tag{1.91}$$

The corrected normalised side force characteristics as indicated in (1.90) can be computed beforehand and drawn as functions of the slip angles and the normal procedure to assess the handling curve can be followed. This can be done by taking the very good approximation $Q = 1$ or we might select a level of Qa_y/g then assess the values of the slip angles that belong to that level of the corrected normalised side forces and compute Q according to (1.91) and from that the correct value of a_y/g.

Large Deviations with Respect to the Steady-state Motion

The variables r and v may be considered as the two state variables of the second-order non-linear system represented by the equations (1.42). Through computer numerical integration the response to a given arbitrary variation of the steer angle can be easily obtained. For motions with constant steer angle δ (possibly after a step change), the system is autonomous and the phase-plane representation may be used to find the solution. For that, we proceed by eliminating the time from Eqs. (1.42). The result is a first-order non-linear equation (using $k^2 = I/m$):

$$\frac{dv}{dr} = k^2 \frac{F_{y1} + F_{y2} - mVr}{aF_{y1} - bF_{y2}} \tag{1.92}$$

Since F_{y1} and F_{y2} are functions of α_1 and α_2 it may be easier to take α_1 and α_2 as the state variables. With (1.44) we obtain:

$$\frac{d\alpha_2}{d\alpha_1} = \frac{dv/dr - b}{dv/dr + a} \tag{1.93}$$

which becomes with (1.92):

$$\frac{d\alpha_2}{d\alpha_1} = \frac{F_{y2}(\alpha_2)/F_{z2} - (\delta - \alpha_1 + \alpha_2)V^2/gl}{F_{y1}(\alpha_1)/F_{z1} - (\delta - \alpha_1 + \alpha_2)V^2/gl} \tag{1.94}$$

For the sake of simplicity we have assumed $I/m = k^2 = ab$.

By using Eq.(1.94) the trajectories (solution curves) can be constructed in the (α_1, α_2) plane. The isocline method turns out to be straightforward and simple to employ. The pattern of the trajectories is strongly influenced by the so-called singular points. In these points the motion finds an equilibrium. In the singular points the motion is stationary and consequently, the differentials of the state variables vanish.

From the handling diagram K/mg and l/R are readily obtained for given combinations of V and δ. Used in combination with the normalized tyre

characteristics F_{y1}/F_{z1} and F_{y2}/F_{z2} the values of α_1 and α_2 are found, which form the coordinates of the singular points. The manner in which a stable turn is approached and from what collection of initial conditions such a motion can or cannot be attained may be studied in the phase-plane. One of the more interesting results of such an investigation is the determination of the boundaries of the domain of attraction in case such a domain with finite dimensions exists. The size of the domain may give indications as to the so-called stability in the large. In other words the question may be answered: does the vehicle return to its original steady-state condition after a disturbance and to what degree does this depend on the magnitude and point of application of the disturbance impulse?

For the construction of the trajectories we draw isoclines in the (α_1, α_2) plane. These isoclines are governed by Eq.(1.94) with slope $d\alpha_2/d\alpha_1$ kept constant. The following three isoclines may already provide sufficient information to draw estimated courses of the trajectories. We have for $k^2 = ab$:

vertical intercepts $(d\alpha_2/d\alpha_1 \to \infty)$:

$$\alpha_2 = \frac{gl}{V^2}\frac{F_{y1}(\alpha_1)}{F_{z1}} + \alpha_1 - \delta \tag{1.95}$$

horizontal intercepts $(d\alpha_2/d\alpha_1 \to 0)$:

$$\alpha_1 = -\frac{gl}{V^2}\frac{F_{y2}(\alpha_2)}{F_{z2}} + \alpha_2 + \delta \tag{1.96}$$

intercepts under 45⁰ $(d\alpha_2/d\alpha_1 = 1)$:

$$\frac{F_{y1}(\alpha_1)}{F_{z1}} = \frac{F_{y2}(\alpha_2)}{F_{z2}} \tag{1.97}$$

Figure 1.22 illustrates the way these isoclines are constructed. The system of Fig.1.17 with $k = a = b$, $\delta = 0.04$ rad and $V = 50$ km/h has been considered. Note, that the normalised tyre characteristics appear in the left-hand diagram for the construction of the isoclines. The three points of intersection of the isoclines are the singular points. They correspond to the points I, II and III of Fig.1.17. The stable point is a focus (spiral) point with a complex pair of solutions of the characteristic equation with a negative real part. The two unstable points are of the saddle type corresponding to a real pair of solutions, one of which is positive. The direction in which the motion follows the trajectories is still a question to be examined. Also for this purpose the alternative set of axes with r and v as coordinates (multiplied with a factor) has been introduced in the diagram after using the relations (1.44).

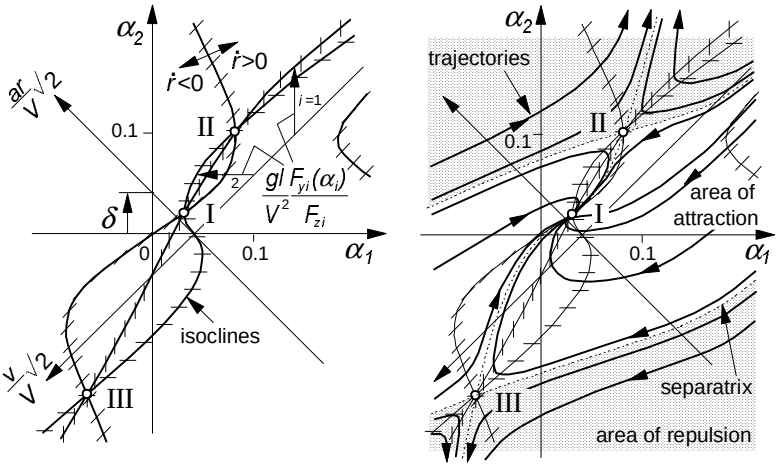

Fig. 1.22. Isoclines for the construction of trajectories in the phase-plane. Also shown: the three singular points I, II and III (cf. Fig.1.17) and the separatrices constituting the boundary of the domain of attraction. Point I represents the stable cornering motion at steer angle δ.

From the original equations (1.42) it can be found that the isocline (1.97) forms the boundary between areas with $\dot{r} > 0$ and $\dot{r} < 0$ (indicated in Fig.1.22). Now it is easy to ascertain the direction along the trajectories. We note that the system exhibits a bounded domain of attraction. The boundaries are called separatrices. Once outside the domain, the motion finds itself in an unstable situation. Remains the disturbance limited so that resulting initial conditions of the state variables stay within the boundaries, then ultimately the steady-state condition is reached again.

For systems with normalized characteristics showing everywhere a positive slope, a handling curve arises that consists of only the main branch through the origin. If the rear axle characteristic (at least in the end) is higher than the front axle characteristic, the vehicle will show (at least in the limit) an understeer nature and unstable singular points cannot occur. This at least if for the case of initial oversteer the speed remains under the critical speed. In such cases, the domain of attraction is theoretically unbounded so that for all initial conditions ultimately the stable equilibrium is attained. The domain of Fig.1.22 appears to be open on two sides which means that initial conditions, in a certain range of (r/v) values, do not require to be limited in order to reach the stable point. Obviously, disturbance impulses acting in front of the centre of gravity may give rise to such combinations of initial conditions.

In Figs.1.23 and 1.24 the influence of an increase in steer angle δ on the stability margin (distance between stable point and separatrix) has been shown

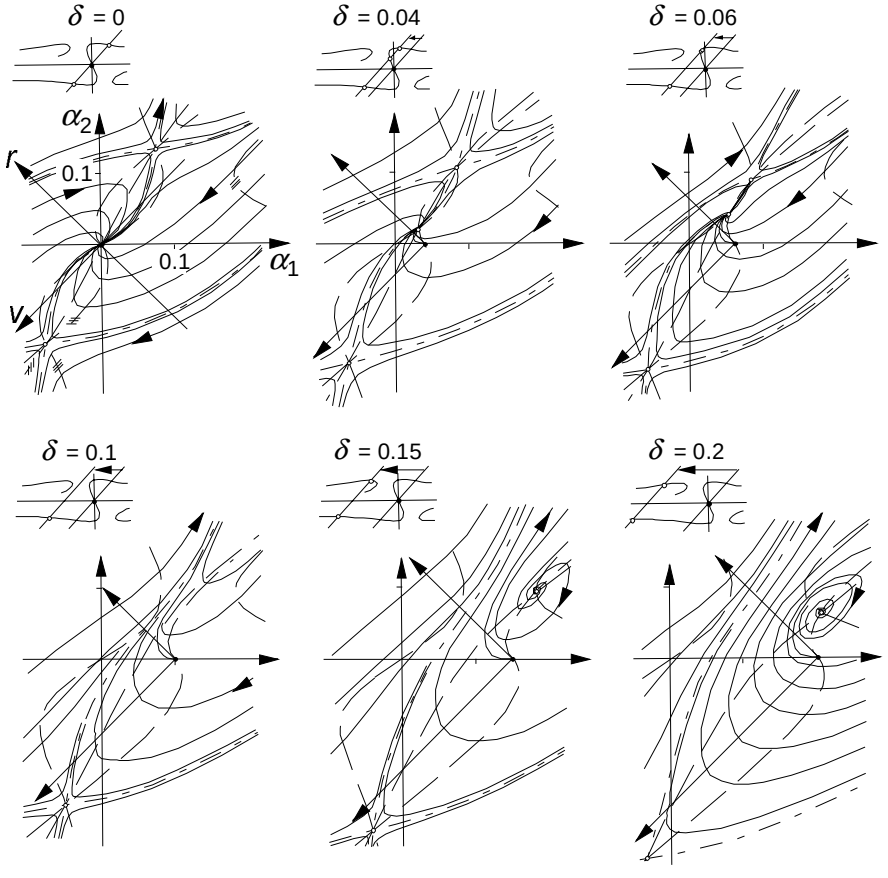

Fig. 1.23. Influence of steering on the stability margin (system of Fig. 1.20 (top)).

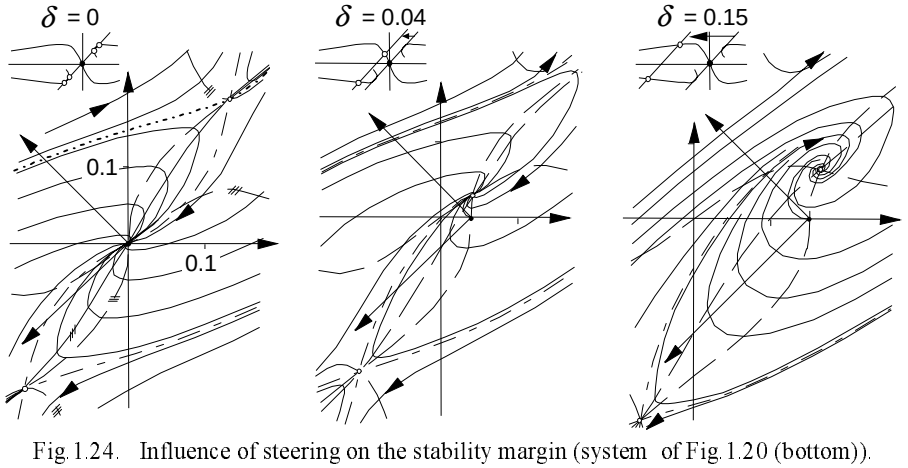

Fig. 1.24. Influence of steering on the stability margin (system of Fig. 1.20 (bottom)).

for the two vehicles considered in Fig.1.20. The system of Fig.1.23 is clearly much more sensitive. An increase in δ (but also an increase in speed V) reduces the stability margin until it is totally vanished as soon as the two singular points merge (also the corresponding points I and II on the handling curve of Fig.1.17) and the domain breaks open. As a result, all trajectories starting above the lower separatrix tend to leave the area. This can only be stopped by either quickly reducing the steer angle or enlarging δ to around 0.2rad or more. The latter situation appears to be stable again (focus) as has been stated before. For the understeered vehicle of Fig.1.24 stability is practically always ensured.

For a further appreciation of the phase diagram it is of interest to determine the new initial state (r_o, v_o) after the action of a lateral impulse to the vehicle (cf. Fig.1.25). For an impulse S acting at a distance x in front of the centre of gravity the increase in r and v becomes:

$$\Delta r = \frac{Sx}{I}, \qquad \Delta v = \frac{S}{m} \tag{1.98}$$

which results in the direction

$$\frac{a\Delta r}{\Delta v} = \frac{x}{b}\frac{ab}{k^2} \tag{1.99}$$

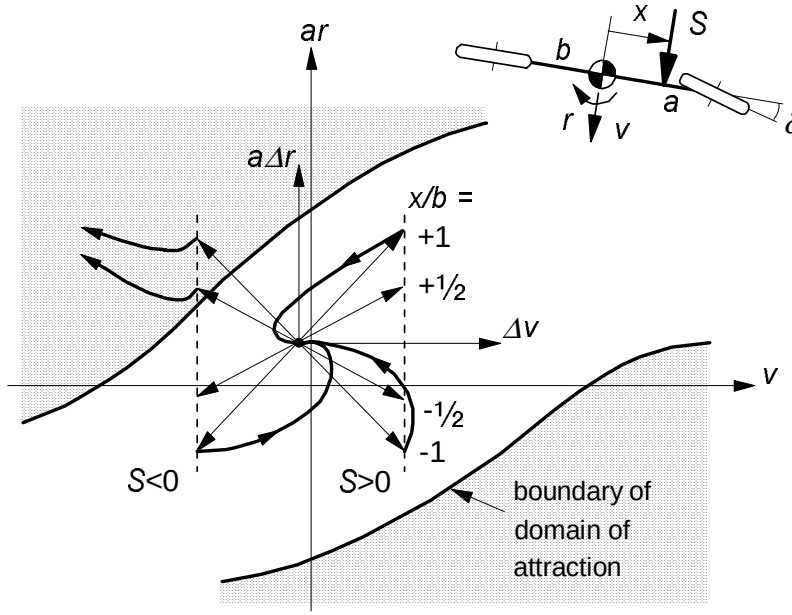

Fig. 1.25. Large disturbance in a curve. New initial state vector (Δv, Δr) after the action of a lateral impulse S. Once outside the domain of attraction the motion becomes unstable and may get out of control.

The figure shows the change in state vector for different points of application and direction of the impulse S ($k^2 = I/m = ab$). Evidently, an impulse acting at the rear (in outward direction) constitutes the most dangerous disturbance. On the other hand, an impulse acting in front of the centre of gravity about half way the front axle does not appear to be able to get the new starting point outside of the domain of attraction no matter the intensity of the impulse.

When the slip angles become larger, the forward speed u may no longer be considered as a constant quantity. Then, the system is described by a third-order set of equations. In the paper (Pacejka, 1986) the solutions for the simple automobile model have been presented also for yaw angles > 90°.

1.3.4. The Vehicle at Braking or Driving

When the vehicle is subjected to longitudinal forces that may result from braking or driving actions possibly to compensate for longitudinal wind drag forces or down or upward slopes, fore and aft load transfer will arise (Fig.1.26). The resulting change in tyre normal loads causes the cornering stiffnesses and the peak side forces of the front and rear axles to change. Since, as we assume here, the fore and aft position of the centre of gravity is not affected (no relative car body motion), we may expect a change in handling behaviour indicated by a rise or drop of the understeer gradient. In addition, the longitudinal driving or braking forces give rise to a state of combined slip, thereby affecting the side force in a way as shown in Fig.1.2.

For moderate driving or braking forces the influence of these forces on the side force F_y is relatively small and may be neglected for this occasion. This means that, for now, the cornering stiffness may be considered to be dependent on the normal load only. The upper left diagram of Fig.1.3 depicts typical

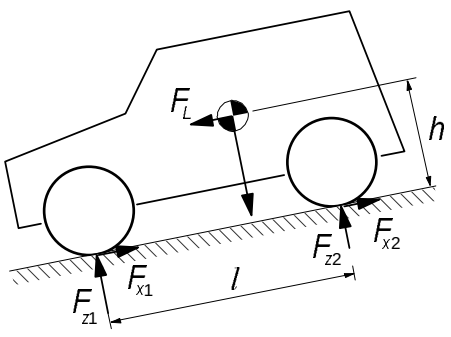

Fig. 1.26. The automobile subjected to longitudinal forces and the resulting load transfer.

variations of the cornering stiffness with vertical load.

The load transfer from the rear axle to the front axle that results from a forward longitudinal force F_L acting at the centre of gravity at a height h above the road surface (F_L possibly corresponding to the inertial force at braking) becomes:

$$\Delta F_z = \frac{h}{l} F_L \tag{1.100}$$

The understeer gradient reads according to Eq.(1.60):

$$\eta = \frac{F_{z1o}}{C_1(F_{z1})} - \frac{F_{z2o}}{C_2(F_{z2})} \tag{1.101}$$

The static axle loads F_{zio} (i=1 or 2) are calculated according to Eq.(1.59), while the actual loads F_{zi} front and rear become:

$$F_{z1} = F_{z1o} + \Delta F_z \ , \quad F_{z2} = F_{z2o} - \Delta F_z \tag{1.102}$$

At moderate braking with deceleration $-a_x = F_L/m$ the load transfer remains small and we may use the linearised approximation of the variation of cornering stiffness with vertical load:

$$C_i = C_{io} + \zeta_{\alpha i} \Delta F_{zi} \quad \text{with } \zeta_{\alpha i} = \left.\frac{\partial C_i}{\partial F_{zi}}\right)_{F_{zio}} \tag{1.103}$$

The understeer gradient (1.101) can now be expressed in terms of the longitudinal acceleration a_x (which might be: minus the forward component of the acceleration due to gravity parallel to the road). We obtain:

$$\eta = \eta_o + \lambda \frac{a_x}{g} \tag{1.104}$$

with the determining factor λ approximately expressed as:

$$\lambda = \zeta_{\alpha 1} \frac{h}{b} \left(\frac{F_{z1o}}{C_{1o}} \right)^2 + \zeta_{\alpha 2} \frac{h}{a} \left(\frac{F_{z2o}}{C_{2o}} \right)^2 \tag{1.105}$$

and η_o denoting the original value not including the effect of longitudinal forces. Obviously, since $\zeta_{\alpha 1,2}$ is usually positive, negative longitudinal accelerations a_x, corresponding to braking, will result in a decrease of the degree of understeer.

To illustrate the magnitude of the effect we use the parameter values given in Table 1.1 (above Eq.(1.77)) and add the c.g. height h=0.6m and the cornering stiffness versus load gradients $\zeta_{\alpha i} = 0.5C_{io}/F_{zio}$. The resulting factor appears to take the value $\lambda = 0.052$. This constitutes an increase of η equal to $0.052a_x/g$. Apparently, the effect of a_x on the understeer gradient is considerable when

regarding the original value $\eta_o = 0.0174$.

As illustrated by Fig.1.9 the peak side force will be diminished if a longitudinal driving or braking force is transmitted by the tyre. This will have an impact on the resulting handling diagram in the higher range of lateral acceleration. The resulting situation may be represented by the second and third diagrams of Fig.1.18 corresponding to braking (or driving) at the front or rear respectively. The problem becomes considerably more complex when we realise that at the front wheels the components of the longitudinal forces perpendicular to the x axis of the vehicle are to be taken into account. Obviously, we find that at braking of the front wheels these components will counteract the cornering effect of the side forces and thus will make the car more understeer. The opposite occurs when these wheels are driven (more oversteer). For a more elaborate discussion on this item we may refer to Pacejka (1973b).

At hard braking, possibly up to wheel lock, stability and steerability may deteriorate severely. This more complex situation will be discussed in Chapter 3 where more information on the behaviour of tyres at combined slip is given.

1.3.5. The Moment Method

Possible steady-state cornering conditions, stable or unstable, has been portrayed in the handling diagram of Fig.1.17. In Fig.1.22 motions tending to or departing from these steady-state conditions have been depicted. These motions are considered to occur after a sudden change in steer angle. The potential available to deviate from the steady turn depends on the margin of the front and rear side forces to increase in magnitude. For each point on the handling curve it is possible to assess the degree of manoeuverability in terms the moment that can be generated by the tyre side forces about the vehicle centre of gravity. Note that at the steady-state equilibrium condition the tyre side forces are balanced with the centrifugal force and the moment equals zero.

In general, the handling curve holds for a given speed of travel. That is so, when e.g. the aerodynamic down forces are essential in the analysis. In Fig.1.27 a diagram has been presented that is designated as the *MMM* diagram (the Milliken Moment Method diagram) and is computed for a speed of 60 mph. The force-moment concept was originally proposed by W.F.Milliken in 1952 and thereafter continuously further developed by the Cornell Aeronautical Laboratory staff and by Milliken Research Associates. A detailed description is given in Milliken's book (1995).

The graph shows curves of the resulting tyre moment N versus the resulting tyre side force Y in non-dimensional form. The resulting force and moment result

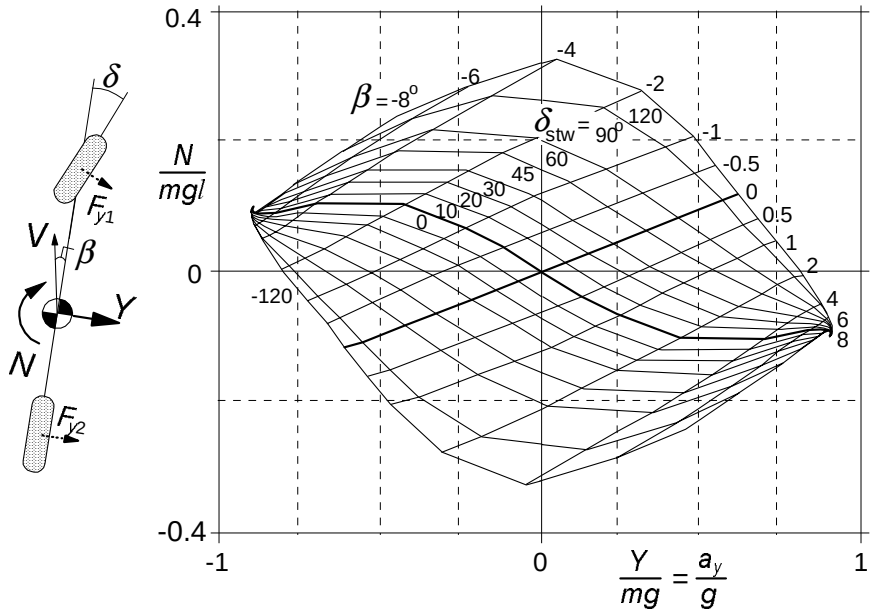

Fig. 1.27. The *MMM* diagram portraying the car's potential manoeuvring capacity.

from the individual side forces and act from ground to vehicle. For greater accuracy, one may take the effect of the pneumatic trails into consideration. Two sets of curves have been plotted: one set for constant values of the vehicle side slip angle β with the steering wheel angle δ_{stw} as parameter and the other set for contant steer angle and varying slip angle. Along the horizontal axis the moment is zero and we have the steady-state equilibrium cornering situation that corresponds with the handling curve. It is observed that for the constant speed considered in the diagram, the steer angle increases when the total side force Y or lateral acceleration a_y is chosen larger which indicates that the motion remains stable. At the limit (near number 2) the maximum steady-state lateral acceleration is attained. At that point the ability to generate a positive moment is exhausted. Only a negative moment may still be developed by the car that tends to straighten the curve that is being negotiated. As we have seen in Fig.1.18, second diagram, there is still some side force margin at the rear tyre which can be used to increase the lateral acceleration in a transient fashion. At the same time, however, the car yaws outwards because the associated moment is negative (cf. diagram near number 8). How to get at points below the equilibrium point near the number 2 is a problem. Rear wheel steering is an obvious theoretical option. In that way, the vehicle slip angle β and front steer angle δ can remain unchanged while the rear steer angle produce the desired rear tyre slip angle. Of course, the diagram needs to be adapted in case of rear wheel

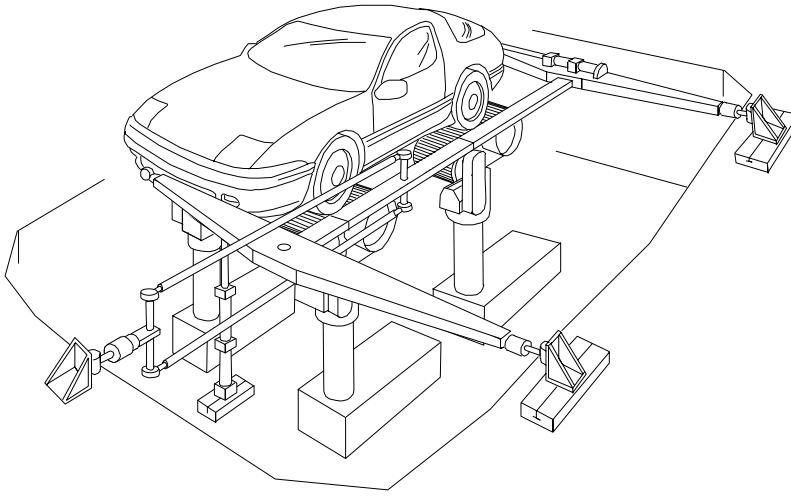

Fig. 1.28. The MTS Flat-Trac Roadway Simulator™, Milliken (1995).

steering. Another more practicle solution would be to bring the vehicle in the desired attitude ($\beta \to 8°$) by briefly inducing large brake or drive slip at the rear that lowers the cornering force and lets the car swing to the desired slip angle while at the same time the steering wheel is turned backwards to even negative values.

The *MMM* diagram, which is actually a Gough plot (for a single tyre, cf. Figs.3.5 and 3.29) established for the whole car at different steer angles, may be assessed experimentally either through outdoor or indoor experiments. On the proving ground a vehicle may be attached at the side of a heavy truck or railway vehicle and set at different slip angles while the force and moment are being measured (tethered testing), cf. Milliken (1995). Figure 1.28 depicts the remarkable laboratory MMM test machine. This MTS Flat-Trac Roadway Simulator™ uses four flat belts which can be steered and driven independently. The car is constraint in its centre of gravity but is free to roll and pitch.

1.3.6. The Car Trailer Combination

In this section we will discuss the role of the tyre in connection with the dynamic behaviour of a car that tows a trailer. More specifically, we will study the possible unstable motions that may show up with such a combination. Linear differential equations are sufficient to analyse the stability of the straight ahead motion. We will again employ Lagrange's equations to set up the equations of motion. The original equations (1.25) may be employed because the yaw angle

is assumed to remain small. The generalised coordinates Y, ψ and θ are used to describe the car's lateral position and the yaw angles of car and trailer respectively. The forward speed dX/dt ($\approx V \approx u$) is considered to be constant. Figure 1.29 gives a top view of the system with three degrees of freedom. The alternative set of three variables v, r and the articulation angle φ and the vehicle velocity V (a parameter) which are not connected to the inertial axes system (0, X, Y) has been indicated as well and will be employed later on. The kinetic energy for this system becomes, if we neglect all the terms of the second order of magnitude (products of variables):

$$T = \tfrac{1}{2}m(\dot{X}^2 + \dot{Y}^2) + \tfrac{1}{2}I\dot{\psi}^2 + \tfrac{1}{2}m_c\{\dot{X}^2 + (\dot{Y} - h\dot{\psi} - f\dot{\theta})^2\} + \tfrac{1}{2}I_c\dot{\theta}^2 \qquad (1.106)$$

The potential energy remains zero:

$$U = 0 \qquad (1.107)$$

and the virtual work done by the external road contact forces acting on the three axles reads:

$$\delta W = F_{y1}\delta(Y + a\psi) + F_{y2}\delta(Y - b\psi) + F_{y3}\delta(Y - h\psi - g\theta) \qquad (1.108)$$

With the use of the equations (1.25) and (1.29) the following equations of motion are established for the generalised coordinates Y, ψ and θ:

$$(m + m_c)\ddot{Y} - m_c(h\ddot{\psi} + f\ddot{\theta}) = F_{y1} + F_{y2} + F_{y3} \qquad (1.109)$$

$$(I_c + m_c f^2)\ddot{\theta} - m_c f(\ddot{Y} - h\ddot{\psi}) = -gF_{y3} \qquad (1.110)$$

$$(I + m_c h^2)\ddot{\psi} - m_c h(\ddot{Y} - f\ddot{\theta}) = aF_{y1} - bF_{y2} - hF_{y3} \qquad (1.111)$$

This constitutes a system of the sixth order. By introducing the velocities v and

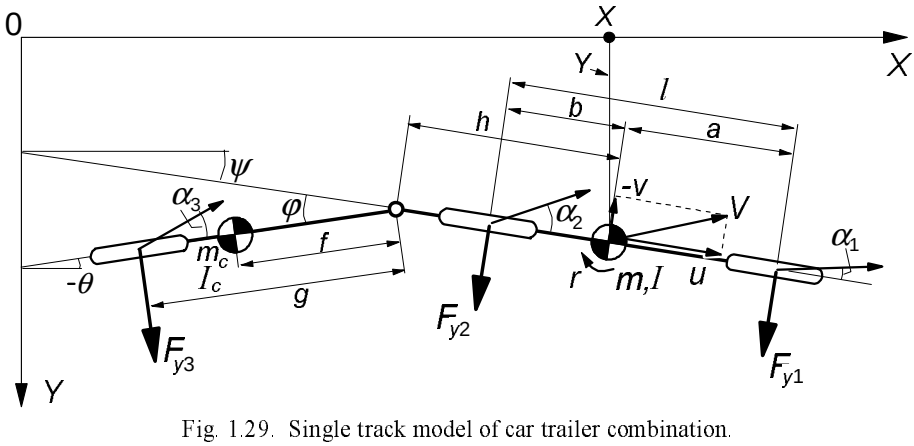

Fig. 1.29. Single track model of car trailer combination.

r the order can be reduced to four. In addition, the angle of articulation φ will be used. We have the relations:

$$\dot{Y} = V\psi + v \quad , \quad \dot{\psi} = r \quad , \quad \theta = \psi - \varphi \tag{1.112}$$

and with these the equations for v, r and φ:

$$(m + m_c)(\dot{v} + Vr) - m_c\{(h+f)\dot{r} - f\ddot{\varphi}\} = F_{y1} + F_{y2} + F_{y3} \tag{1.113}$$

$$\{I + m_c h(h+f)\}\dot{r} - m_c h(\dot{v} + Vr + f\ddot{\varphi}) = aF_{y1} - bF_{y2} - hF_{y3} \tag{1.114}$$

$$(I_c + m_c f^2)(\ddot{\varphi} - \dot{r}) + m_c f(\dot{v} + Vr - h\dot{r}) = gF_{y3} \tag{1.115}$$

The right-hand members are still to be expressed in terms of the motion variables. With the axle cornering stiffnesses C_1, C_2 and C_3 we have:

$$\begin{aligned} F_{y1} &= C_1\alpha_1 = -C_1\frac{v + ar}{V} \\ F_{y2} &= C_2\alpha_2 = -C_2\frac{v - br}{V} \\ F_{y3} &= C_3\alpha_3 = -C_3\left(\frac{v - hr - g(r - \dot{\varphi})}{V} + \varphi\right) \end{aligned} \tag{1.116}$$

From the resulting set of linear differential equations the characteristic equation may be derived which is of the fourth degree. Its general structure is:

$$a_0 s^4 + a_1 s^3 + a_2 s^2 + a_3 s + a_4 = 0 \tag{1.117}$$

The stability of the system can be investigated by considering the real parts of the roots of this equation or we might employ the criterium for stability according to Routh-Hurwitz. According to this criterium, the system of order n is stable when all the coefficients a_i are positive and the Hurwitz determinants H_{n-1}, H_{n-3} etc. are positive. For our fourth-order system the complete criterium for stability reads:

$$H_3 = \begin{bmatrix} a_1 & a_0 & 0 \\ a_3 & a_2 & a_1 \\ 0 & a_4 & a_3 \end{bmatrix} = a_1 a_2 a_3 - a_1^2 a_4 - a_0 a_3^2 > 0 \tag{1.118}$$

$$a_i > 0 \qquad \text{for } i = 0, 1, \ldots..4$$

In Fig.1.30, the boundaries of stability have been presented in the caravan axle cornering stiffness vs speed parameter plane. The three curves belong to the

three different sets of parameters for the position f of the caravan's centre of gravity and the caravan's mass m_c as indicated in the figure. An important result is that a lower cornering stiffness promotes oscillatory instability: the critical speed beyond which instability occurs decreases. Furthermore, it appears from the diagram that moving the caravans centre of gravity forward (f smaller) stabilises the system which is reflected by the larger critical speed. A heavier caravan (m_c larger) appears to be bad for stability. Furthermore, it has been found that a larger draw bar length g is favourable for stability.

It turns out that a second type of instability may show up. This occurs when the portion of the weight of the caravan supported by the coupling point becomes too large. This extra weight is felt by the towing vehicle and makes it more oversteer. The critical speed associated with this phenomenon is indicated in the diagram by the vertical lines. This divergent instability occurs when (starting out from a stable condition) the last coefficient becomes negative, that is $a_n = a_4 < 0$.

The oscillatory instability connected with the 'snaking' phenomenon arises as soon as (from a stable condition) the second highest Hurwitz determinant becomes negative, $H_{n-1} = H_3 < 0$ (then also $H_n < 0$), cf. Klotter (1960) or Leipholz (1987). When the critical speed is surpassed self-excited oscillations are created which shows an amplitude that in the actual non-linear case does not appear to limit itself. This is in contrast to the case of the wheel shimmy phenomenon to

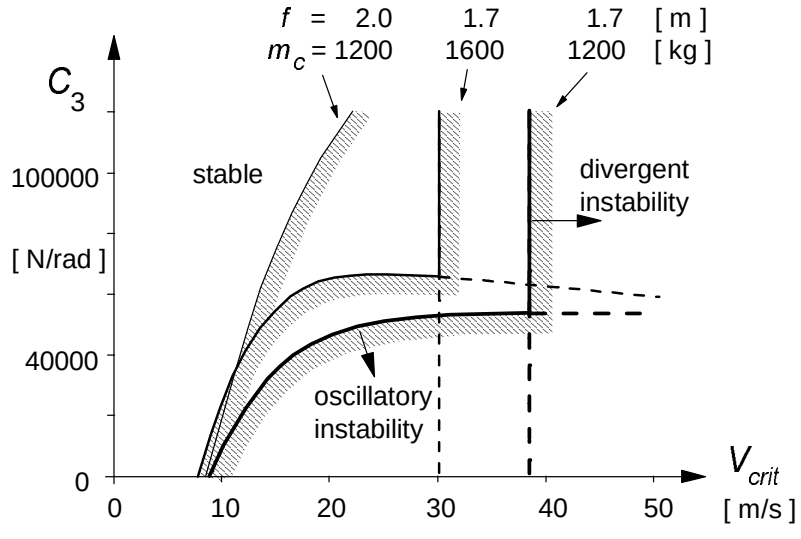

Fig. 1.30. Stability boundaries for the car caravan combination in the caravan cornering stiffness versus critical speed diagram. Vehicle parameters according to Table 1.1, in addition: h = 2m, g= 2m, k_c= 1.5m ($I_c = m_c k_c^2$), cf. Fig.1.29.

be treated in Chapter 5 where a stable limited oscillation appears to arise. The cause of the unlimited snaking oscillation is that with increasing amplitudes also the slip angle increases which lowers the average cornering stiffness as a consequence of the degressively non-linear cornering force characteristic. From the diagram we found that this will make the situation increasingly worse. As has been seen from full vehicle/caravan model simulations, the whole combination will finally overturn. Another effect of this reduction of the average cornering stiffness is that when the vehicle moves at a speed lower than the critical speed, the originally stable straight ahead motion may become unstable if through the action of an external disturbance (side wind gust) the slip angle of the caravan axle becomes too large (surpassing of the associated unstable limit-cycle). This is an unfortunate, possibly dangerous situation! We refer to Troger (1984) for further details.

Exercise 1.4. Stability of a trailer

Consider the trailer of Fig.1.31 that is towed by a heavy steadily moving vehicle at a forward speed V along a straight line. The trailer is connected to the vehicle by means of a hinge. The attachment point shows a lateral flexibility that is represented by the lateral spring with stiffness c_y. Furthermore, a yaw torsional spring and damper are provided with coefficients c_φ and k_φ .

Derive the equations of motion of this system with generalised coordinates y and φ. Assume small displacements so that the equations can be kept linear. The damping couple $k_\varphi \dot{\varphi}$ may be considered as an external moment acting on the trailer or we may use the dissipation function $D = ½\, k_\varphi \dot{\varphi}^2$ and add $+\partial D/\partial \dot{q}_i$ to the left-hand side of Lagrange's equation (1.25). Obviously, the introduction of this extra term will be beneficial particularly when the system to be modelled is more complex.

Assess the condition for stability for this fourth-order system. Simplify the system by putting $g = f$ and $c_\varphi = k_\varphi = 0$. Now find the explicit conditional statement for the cornering stiffness C.

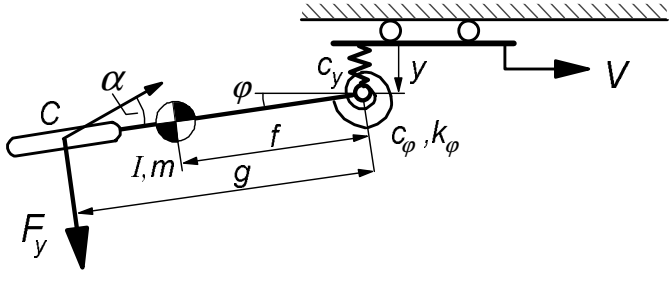

Fig. 1.31. On the stability of a trailer (Exercise 1.4).

1.3.7. Vehicle Dynamics at More Complex Tyre Slip Conditions

So far, relatively simple vehicle dynamics problems have been studied in which the basic steady-state cornering force versus slip angle characteristic plays the dominant role. The situation becomes more complex when matters like combined slip at hard braking, wheel camber, tyre transient and vibrational properties and e.g. obstacle crossings are to be considered.

In the subsequent chapters tyre performance and modelling will be treated in greater detail which enables us to introduce relevant tyre properties in the analysis. The following specific subjects will be studied as applications of the tyre modelling theory:

- Vehicle stability at excessive braking and wheel lock (Chapter 3)
- Motorcycle steady-state cornering (Chapter 10)
- Wheel shimmy (Chapter 6)
- Steering vibrations (Chapter 8)
- Motorcycle weave and wobble (Chapter 10)
- Tyre out-of-roundness (Chapter 8)
- Cornering on uneven roads (Chapters 5,8)
- ABS on uneven roads (Chapter 8)
- Traversing short obstacles (Chapter 9)
- Parking (Chapter 9)

Chapter 2

BASIC TYRE MODELLING CONSIDERATIONS

2.1. Introduction

The performance of a tyre as a force and moment generating structure is a result of a combination of several aspects. Factors which concern the primary tasks of the tyre may be distinguished from factors which involve (often important) secondary effects.

In Table 2.1 these factors are presented in matrix form. A further distinction is made between (quasi) steady-state and vibratory behaviour and, additionally, between symmetric (or in-plane) and anti-symmetric (or out-of-plane) aspects. The primary task factors appear in bold letters. The remaining factors are considered as secondary factors.

The primary requirements to transmit forces in the three perpendicular directions (F_x, F_y, F_z) and to cushion the vehicle against road irregularities involve secondary factors like lateral and longitudinal distortions and slip. Although regarded as secondary phenomena, some of the quantities involved are crucial for the generation of the deformations and the associated forces and will

Table 2.1. Tyre factors.

	primary task functions and secondary effects		
	(quasi) steady-state ⇔ transient/vibratory state		
symmetric (in-plane)	**load carrying** **braking/driving** rolling resistance	radial deflection tangential slip and distorsion	**cushioning** dynamic coupling natural vibrations
anti-symmetric (out-of-plane)	**cornering** pneumatic trail overturning couple	lateral and spin/turn slip and distorsion	phase lag destabilisation natural vibrations

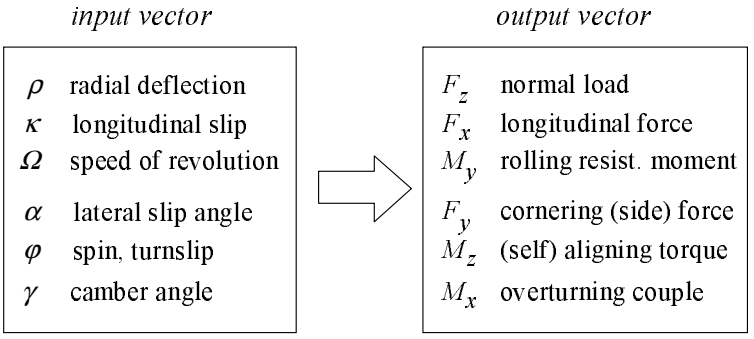

Fig. 2.1. Input/output quantities (road surface considered flat).

be treated as input variables into the system. Figure 2.1 presents the 'vectors' of input and output components. In this diagram the tyre is assumed to be uniform and to move over a flat road surface. The input vector stems from motions of the wheel relative to the road. A precise definition of these input quantities is given in the next section.

For small deviations from the straight ahead motion a linear description of the behaviour may be given. Then, it is advantageous to recognize the fact that the responses to the symmetric and anti-symmetric motions of the assumedly symmetric wheel-tyre system can be considered as uncoupled. Figure 2.2 shows the separate function blocks with the input and output quantities. Here we have also considered the possibility of input from variations in road surface geometry and from tyre non-uniformities resulting in e.g. out-of-roundness, stiffness variations and 'built-in' forces.

The forces and moments are considered as output quantities. It is sometimes beneficial to assume these forces to act on a rigid disc with inertial properties equal to those of the tyre when considered rigid. These forces may differ from the forces acting between road and tyre because of the dynamic forces acting on the tyre when vibrating relative to the wheel rim. The motions of the wheel rim and the profile of the road, represented by its height w and its forward and transverse slope at or near the contact centre, are regarded as input quantities to the tyre. Braking and driving torques M_a are considered to act on the rotating wheel inertia I_w. For the freely rolling tyre (then, by definition $M_a = 0$), the wheel angular motion about the spindle axis is governed by only the internal moment M_η acting between rim and tyre. The five motion components of the wheel spin axis may then remain to serve as input vector.

The discussion on the force generation and dynamic properties of the tyre will be conducted along the two main lines: symmetric and anti-symmetric behaviour. Interaction between these main groups of input motions complicates the situation

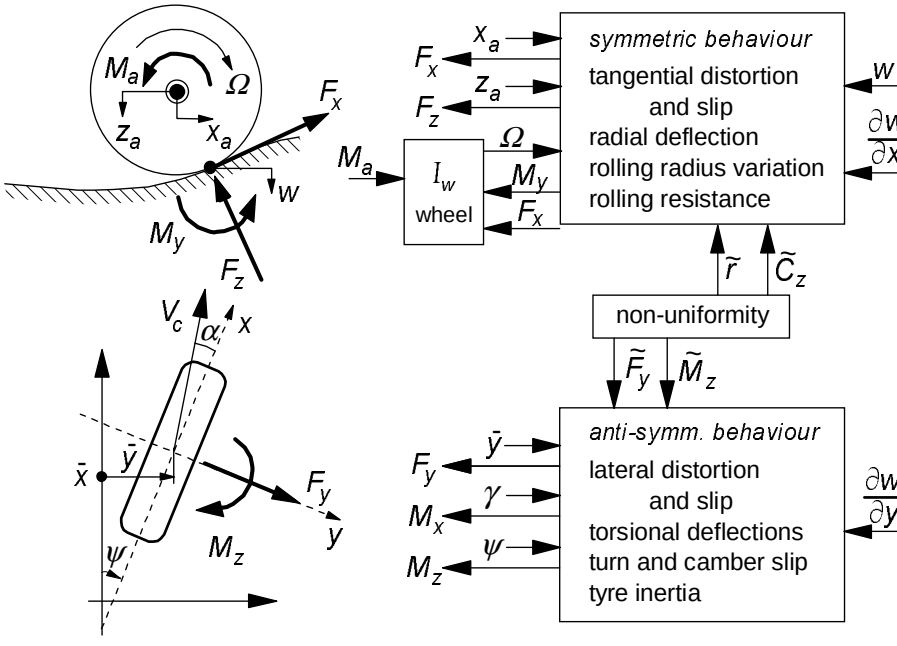

Fig. 2.2. Wheel axle motion and road surface coordinates and possibly uncoupled tyre system blocks valid for small deviations from the steady-state straight ahead motion.

(combined slip). These interactions become important if at least one of the input motions, or more precisely, one of the associated slip components becomes relatively large. Because of its relative simplicity, the steady-state behaviour will be treated first (Chapter 3). The discussion on tyre dynamic behaviour starts in Chapter 5.

2.2. Definition of Tyre Input Quantities

If the problem which is going to be investigated involves road irregularities, then the location and the orientation of the stub axle (spindle axis) must be known with respect to the specific irregularity met on the road. The road surface is defined with respect to a coordinate system of axes attached to the road. If the position and orientation of the axle is known with respect to the fixed triad then the exact position of the wheel with respect of the possibly irregular road surface can be determined. This relative position and orientation of the wheel with respect to the road is important to derive the radial tyre deflection and the relative attitude (camber) and to assess the current value of the friction coefficient which may vary due to e.g. slippery spots or non-homogeneous

surface conditions (grooves). The time rate of change of this relative position is needed not only for possible hysteresis effects but mainly for the determination of the so-called 'slip' of the wheel with respect to the ground.

If the road surface near the contact patch can be approximated by a flat plane (that is, when the smallest considered wavelength of the decomposed surface vertical profile is large with respect to the contact length and its amplitude small) the distance of the wheel centre to the road plane and the angle between wheel plane and the normal to the road surface will suffice in addition to the several slip quantities and the running speed of the wheel.

For the definition of the various motion and position input quantities listed in Fig.2.1, it is helpful to consider Fig.2.3. A number of planes have been drawn. The road plane and the wheel-centre-plane (with line of intersection along the unit vector $\boldsymbol{l}$) and two planes normal to the road plane, one of which contains the vector $\boldsymbol{l}$ and the other the unit vector $\boldsymbol{s}$ which is defined along the wheel spin axis. From the figure follows the definition of the contact centre C also designated as the point of intersection (of the three planes). The unit vector $\boldsymbol{t}$ lies in the road plane and is directed perpendicular to $\boldsymbol{l}$. Vector $\boldsymbol{r}$ forms the connection between wheel centre A and contact centre C. Its length, r, is defined as the loaded radius of the tyre. The position and attitude of the wheel with respect to the inertial triad is completely described by the vectors $\boldsymbol{b} + \boldsymbol{a}$ and $\boldsymbol{s}$.The road plane is defined at the contact centre by the position vector of that point $\boldsymbol{c}$ and the normal to the

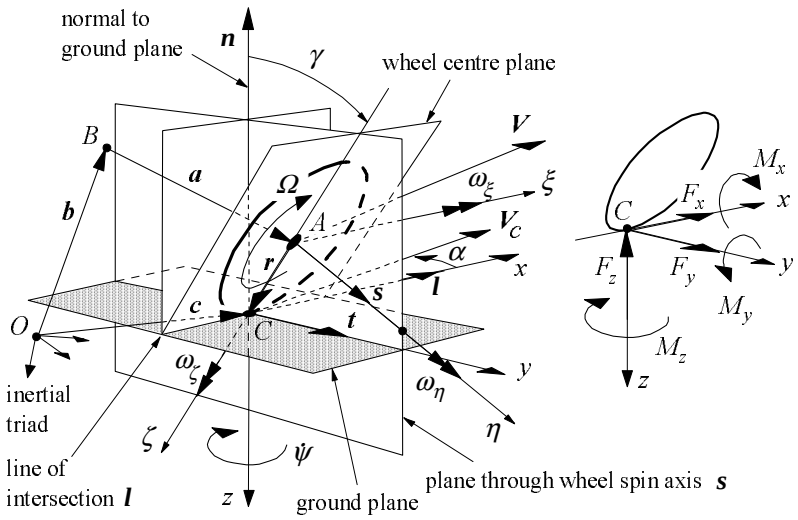

Fig. 2.3. Definition of position, attitude and motion of the wheel and the forces and moments acting from the road on the wheel. Directions shown are defined as positive.

road in that point represented by the unit vector $\boldsymbol{n}$ (positive upwards). Figure 2.3 also shows two systems of axes (besides the inertial triad). Firstly, we have introduced the road contact axes system (C, x, y, z) of which the x-axis points forwards along the line of intersection ($\boldsymbol{l}$), the z-axis points downwards normal to the road plane ($-\boldsymbol{n}$) and the y-axis points to the right along the transverse unit vector $\boldsymbol{t}$. Secondly, the wheel axle system of axes (A, ξ, η, ζ) has been defined with the ξ axis parallel to the x axis, the η axis along the wheel spindle axis ($\boldsymbol{s}$) and the ζ axis along the radius ($\boldsymbol{r}$).

Sign conventions in the literature are not uniform. For the sake of convenience and to reduce sources of making errors, we have chosen a sign convention that avoids working with negative quantities as much as possible.

The radial deflection of the tyre ρ is defined as the reduction of the tyre radius from the unloaded situation r_f to the loaded case r:

$$\rho = r_f - r \tag{2.1}$$

For positive ρ the wheel load F_z (positive upwards) is positive as well.

The tangential or longitudinal slip κ requires deeper analysis. For the sake of properly defining the longitudinal slip, the so-called slip point S is introduced. This point is thought to be attached to the rim or wheel body at a radius equal to the slip radius r_s and forms the centre of rotation when the wheel rolls at longitudinal slip equal to zero. The slip radius is the radius of the slip circle. At vanishing longitudinal slip, this slip circle rolls purely over an imaginary surface parallel to the road plane. The length of the slip radius depends on the definition of longitudinal slip that is adopted. A straight forward definition would be to make the slip radius equal to the loaded wheel radius. This, however, would already lead to a considerable magnitude of the longitudinal force F_x that would be generated at longitudinal slip equal to zero. A more convenient and physically proper definition corresponds to the situation that F_x=0 at zero longitudinal slip. Because of the occurrence of rolling resistance, measurements of tyre characteristics would then require the application of a driving torque to reach the condition of slip equal to zero! This may become of importance especially when experiments are conducted at large camber angles where the drag may become considerable (motorcycle tyres). An alternative, often used definition takes the effective rolling radius r_e defined at free rolling (M_a = 0), as the slip radius. Under normal conditions, the resulting F_x vs κ diagrams according to the latter two definitions are very close. A small horizontal shift of the curves is sufficiently accurate to change from one definition to the other. The drawback of the last definition is that when testing on very low friction (icy) surfaces, the rolling resistance may be too large to let the wheel rotate without the application of a driving torque. Consequently, the state of free rolling cannot be realised

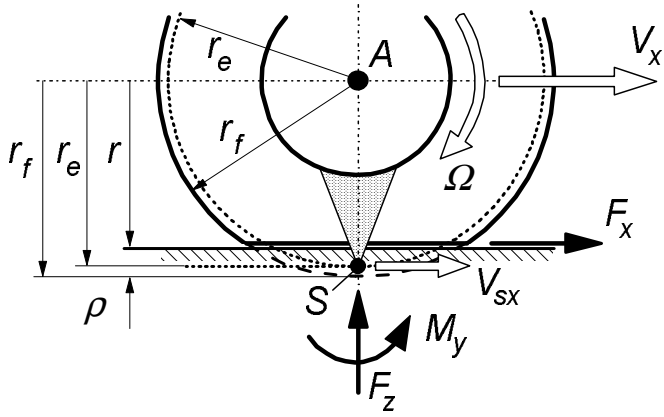

Fig. 2.4. Effective rolling radius and longitudinal slip velocity.

under these conditions. Nevertheless, we will adopt the last definition where $r_s = r_e$ and consequently, point S is located at a distance r_e from the wheel centre. Figure 2.4 depicts this configuration.

According to this definition we will have the situation that when a wheel rolls freely (that is: at $M_a = 0$) at constant speed over a flat even road surface, the longitudinal slip κ is equal to zero. This notwithstanding the fact that at free rolling some fore and aft deformations will occur because of the presence of hysteresis in the tyre that generates a rolling resistance moment M_y. Through this a rolling resistance force $F_r = M_y/r$ arises which necessarily is accompanied by tangential deformations. We may agree that at the instant of observation, point S, that lies on the slip circle and is attached to the wheel rim, has reached its lowest position, that is: on the line along the radius vector $\boldsymbol{r}$. At free rolling, its velocity has then become equal to zero and point S has become the centre of rotation of the motion of the wheel rim. We have at free rolling on a flat road for a wheel in upright position ($\gamma = 0$) and/or without wheel yaw rate ($\dot{\psi} = 0$), cf. Fig.2.3, a velocity of the wheel centre in forward (x or ξ) direction:

$$V_x = r_e \Omega \tag{2.2}$$

with Ω denoting the speed of revolution of the wheel body to be defined hereafter. By using this relationship, the value of the effective rolling radius can be assessed from an experiment. The forward speed and the wheel speed of revolution are both measured while the wheel axle is moved along a straight line over a flat road. Division of both quantities leads to the value of r_e. The effective rolling radius will be a function of the normal load and the speed of travel. We may possibly have to take into account the dependency on the camber angle and the slip angle.

If at braking or driving the longitudinal slip is no longer zero, point S will move with a longitudinal slip speed V_{sx} which differs from zero. We obviously obtain if again $\gamma\dot{\psi} = 0$:

$$V_{sx} = V_x - \Omega r_e \tag{2.3}$$

The longitudinal slip (sometimes called the slip ratio) is denoted by κ and may be tentatively defined as the ratio of longitudinal slip velocity $-V_{sx}$ of point S and the forward speed of the wheel centre V_x:

$$\kappa = -\frac{V_{sx}}{V_x} \tag{2.4}$$

or with (2.3):

$$\kappa = -\frac{V_x - \Omega r_e}{V_x} \tag{2.5}$$

This again holds for a wheel on a flat road and with $\gamma\dot{\psi} = 0$. A more general and precise definition of κ will be given later on. The sign of the longitudinal slip κ has been chosen such that at driving, when $F_x > 0$, κ is positive and at braking, when $F_x < 0$, κ is negative. When the wheel is locked ($\Omega = 0$) we obviously have $\kappa = -1$. In the literature, the symbol s (or S) is more commonly used to denote the slip ratio.

The angular speed of rolling Ω_r more precisely defined for the case of moving over undulated road surfaces, is the time rate of change of the angle between the radius connecting S and A (this radius is thought to be attached to the wheel) and the radius $\boldsymbol{r}$ defined in Fig.2.3 (always lying in the plane normal to the road through the wheel spin axis). Figure 2.5 illustrates the situation.

The linear speed of rolling V_r is defined as the velocity with which an imaginary point C^* that is positioned on the line along the radius vector $\boldsymbol{r}$ and coincides with point S at the instant of observation, moves forward (in x direction) with respect to point S that is fixed to the wheel rim:

$$V_r = r_e \Omega_r \tag{2.6}$$

For a tyre freely rolling over a flat road we have: $\Omega_r = \Omega$ and with $\gamma\dot{\psi} = 0$ in addition: $V_r = V_x$. Note, that at wheel lock ($\Omega = 0$) the angular speed of rolling Ω_r is not equal to zero when the wheel moves over a road with a curved vertical profile (then not always the same point of the wheel is in contact with the road). For a cambered wheel showing a yaw rate $\dot{\psi}$, pure rolling can occur on a flat road even when the speed of the wheel centre $V_x = 0$. In that case a linear speed of rolling arises that is equal to $V_r = r_e\dot{\psi}\sin\gamma$ and consequently an angular speed

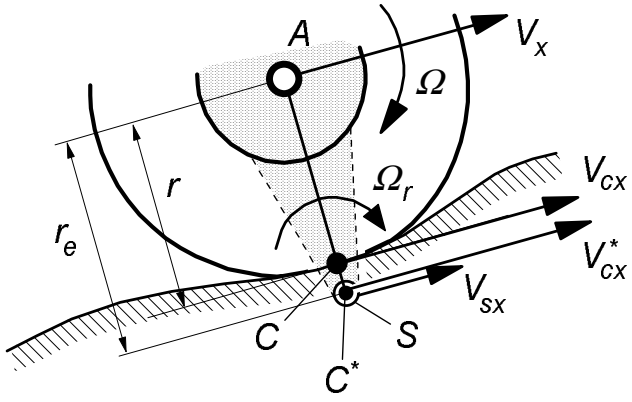

Fig. 2.5. Rolling and slipping of a tyre over an undulated road surface.

of rolling $\Omega_r = \dot{\psi} \sin\gamma$.

In the normal case of an approximately horizontal road surface, the wheel speed of revolution Ω may be defined as the angular speed of the wheel body (rim) seen with respect to a vertical plane that passes through the wheel spindle axis. On a flat level road, the angular speed of rolling Ω_r and the speed of revolution of the wheel Ω are equal to each other. The absolute speed of rotation of the wheel about the spindle axis ω_η will be different from $-\Omega$ when the wheel is cambered and a yaw rate occurs of the plane through the spindle axis and normal to the road about the normal to the road. Then (cf. Fig. 2.6)

$$\omega_\eta = -\Omega + \dot{\psi} \sin\gamma \tag{2.7}$$

This equation forms a correct basis for a general definition of Ω also on non-level road surfaces. Its computation is straight forward if ω_η is available from wheel dynamics calculations.

The longitudinal running speed V_{cx}^* is defined as the longitudinal component of the velocity of propagation of the imaginary point C^* (on radius vector $\boldsymbol{r}$) in the direction of the x-axis (vector $\boldsymbol{l}$). In case the wheel is moved in such a way that the same point remains in contact with the road we would have $V_{cx}^* = V_{sx}$. This corresponds to wheel-lock when the road is flat and the vehicle pitch rate is zero. For a freely rolling tyre the longitudinal running speed equals the linear speed of rolling: $V_{cx}^* = V_r$. On a flat road and at zero camber or zero yaw rate ($\gamma\dot{\psi} = 0$) we obtain $V_{cx}^* = V_x$. The general definition for longitudinal slip now reads:

$$\kappa = -\frac{V_{sx}}{V_{cx}^*} \tag{2.8}$$

The lateral slip is defined as the ratio of the lateral velocity $-V_{cy}$ of the contact centre C and the longitudinal running speed V_{cx}^*. We have in terms of the slip angle α:

$$\tan\alpha = -\frac{V_{cy}}{V_{cx}^*} \tag{2.9}$$

which for a wheel, not showing camber rate $\dot{\gamma}$ nor radial deflection rate $\dot{\rho}$ and yaw rate $\dot{\psi}$ at non-zero camber angle γ, when running on a flat road reduces to the ratio of lateral and forward speed of the wheel centre:

$$\tan\alpha = -\frac{V_y}{V_x} \tag{2.10}$$

In practice, points C and C^* lie closely together and making distinction between the longitudinal or the lateral velocities of these points is only of academic interest and may be neglected. Instead of V_{cx}^* in the denominator we may write V_{cx} and if we wish, instead of V_{cy} in the numerator the lateral speed of point S (parallel to road plane) which is V_{sy}. This may even be a better choice if large values of camber are considered while a vertical tyre deflection rate occurs. The definitions of the slip components then reduce to:

$$\kappa = -\frac{V_{sx}}{V_{cx}} \tag{2.11}$$

$$\tan\alpha = -\frac{V_{sy}}{V_{cx}} \tag{2.12}$$

The slip velocities V_{sx} and V_{sy} form the components of the slip speed vector $\boldsymbol{V}_s$ and κ and $\tan\alpha$ the components of the slip vector $\boldsymbol{s}_s$. We have:

$$\boldsymbol{V}_s = \begin{pmatrix} V_{sx} \\ V_{sy} \end{pmatrix} \tag{2.13}$$

and

$$\boldsymbol{s}_s = \begin{pmatrix} \kappa \\ \tan\alpha \end{pmatrix} \tag{2.14}$$

The 'spin' slip φ is defined as the component $-\boldsymbol{\omega}_z$ of the absolute speed of rotation vector $\boldsymbol{\omega}$ of the wheel body along the normal to the road plane $\boldsymbol{n}$ divided by the forward running speed. We obtain the expression in terms of yaw rate $\dot{\psi}$ and camber angle γ (cf. Fig.2.6):

$$\varphi = -\frac{\omega_z}{V_{cx}^*} = -\frac{\dot{\psi} - \Omega \sin\gamma}{V_{cx}^*} \tag{2.15}$$

The minus sign is introduced again to remain consistent with the definitions of longitudinal and lateral slip (2.11, 2.12). Then, we will have as a result of a positive φ a positive moment M_z. It turns out that then also the resulting side force F_y is positive. The yaw rate $\dot{\psi}$ is defined as the speed of rotation of the line of intersection (unit vector $\boldsymbol{l}$) about the z axis normal to the road (cf. Fig.2.3). If side slip does not occur ($\alpha \equiv 0$) and the wheel moves over a flat road, equation (2.15) may be written as

$$\varphi = -\frac{1}{R} + \frac{\Omega_r}{V_{cx}^*}\sin\gamma = -\frac{1}{R} + \frac{1}{r_e}\frac{V_r}{V_{cx}^*}\sin\gamma \tag{2.16}$$

When the tyre rolls freely (then $V_{sx} = 0$, $V_{cx}^* = V_r$) we obviously obtain:

$$\varphi = -\frac{1}{R} + \frac{1}{r_e}\sin\gamma \tag{2.17}$$

with $1/R$ denoting the momentary curvature of the path of C^* or approximately

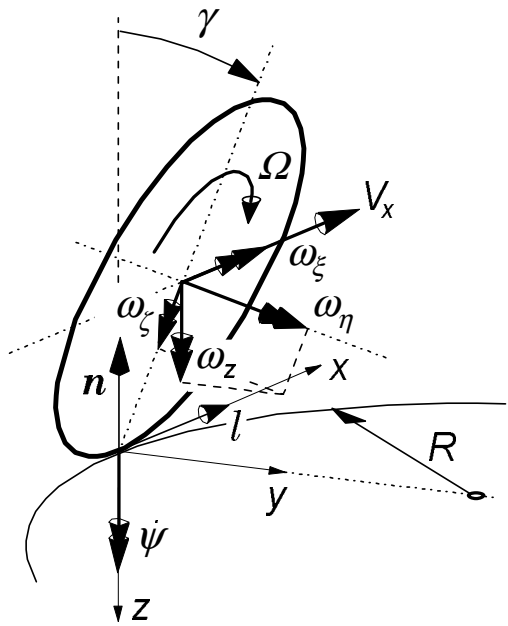

Fig. 2.6. Rotational slip resulting from path curvature and wheel camber (slip angle = 0).

of the contact centre C.

For a tyre we shall distinguish between spin due to path curvature and spin due to wheel camber. For a homogeneous ball the effect of both input quantities is the same. For further use we define turn slip as

$$\varphi_t = -\frac{\dot{\psi}}{V_{cx}^*} \qquad \left(= -\frac{1}{R} \quad \text{if } \alpha \text{ is constant} \right) \tag{2.18}$$

Wheel camber or wheel inclination angle γ is defined as the angle between the wheel-centre-plane and the normal to the road. With Fig.2.3 we find:

$$\sin\gamma = -\boldsymbol{n}\cdot\boldsymbol{s} \tag{2.19}$$

or on level roads:

$$\sin\gamma = s_z \tag{2.20}$$

where s_z represents the vertical component of the unit vector $\boldsymbol{s}$ along the wheel spin axis.

2.3. Assessment of Tyre Input Motion Components

The location of the contact centre C and the magnitude of the wheel radius r result from the road geometry and the position of the wheel axle. We consider the approximate assumption that the road plane is defined by the plane touching the surface at point Q located vertically below the wheel centre A. The position of point Q with respect to the inertial frame (O°, x°, y°, z°) is given by vector $\boldsymbol{q}$. The normal to the road plane is defined by unit vector $\boldsymbol{n}$. The location of a reference point B of the vehicle is defined by vector $\boldsymbol{b}$ and the location of the wheel centre A by $\boldsymbol{b} + \boldsymbol{a}$ (cf. Fig.2.3). The orientation of the wheel spin axis is given by unit vector $\boldsymbol{s}$ and the location of the contact centre C by

$$\boldsymbol{c} = \boldsymbol{b} + \boldsymbol{a} + \boldsymbol{r} \tag{2.21}$$

where $\boldsymbol{r}$ is still to be determined. The expression for $\boldsymbol{r}$ is derived from the equations:

$$\boldsymbol{r} = r\boldsymbol{l} \times \boldsymbol{s} \tag{2.22}$$

with

$$\boldsymbol{l} = \lambda\, \boldsymbol{n} \times \boldsymbol{s} \tag{2.23}$$

(with λ resulting from the condition that $|\boldsymbol{l}| = 1$) and with (2.21) in order to

obtain the magnitude of the loaded radius r:

$$\boldsymbol{c}\cdot\boldsymbol{n} = \boldsymbol{q}\cdot\boldsymbol{n} \tag{2.24}$$

which indicates that contact point C and road point Q lie on the same plane perpendicular to $\boldsymbol{n}$. On flat level roads the above equations become a lot simpler since in that case $\boldsymbol{n}^{\mathrm{T}} = (0, 0, -1)$ and the z components of $\boldsymbol{c}$ and $\boldsymbol{q}$ become zero.

The radial tyre deflection ρ is now readily obtained from

$$\rho = r_f - r \tag{2.25}$$

with r_f the free unloaded radius. For a given tyre the effective rolling radius r_e is a function of amongst other things the unloaded radius, the radial deflection, the camber angle and the speed of travel.

The vector for the speed of propagation of the contact centre V_c representing the magnitude and direction of the velocity with which point C moves over the road surface, is obtained by differentiation with respect to time of position vector $\boldsymbol{c}$ (2.21):

$$\boldsymbol{V}_c = \dot{\boldsymbol{c}} = \dot{\boldsymbol{b}} + \dot{\boldsymbol{a}} + \dot{\boldsymbol{r}} = \boldsymbol{V} + \dot{\boldsymbol{r}} \tag{2.26}$$

With $\boldsymbol{V}$ the velocity vector of the wheel centre A (Fig.2.3). The speed of propagation of point C^* represented by the vector $\boldsymbol{V}_c^*$ becomes (cf. Fig.2.5 and assume r_e/r constant):

$$\boldsymbol{V}_c^* = \boldsymbol{V} + \frac{r_e}{r}\dot{\boldsymbol{r}} \tag{2.27}$$

The velocity vector of point S that is fixed to the wheel body results from

$$\boldsymbol{V}_s = \boldsymbol{V} + \frac{r_e}{r}\boldsymbol{\omega}\times\boldsymbol{r} \tag{2.28}$$

with ω being the the angular velocity of the wheel body with respect to the inertial frame. On the other hand, this velocity is equal to the speed of point C^* minus the linear speed of rolling

$$\boldsymbol{V}_s = \boldsymbol{V}_c^* - V_r\,\boldsymbol{l} \tag{2.29}$$

from which V_r follows:

$$V_r = \boldsymbol{l}\cdot(\boldsymbol{V}_c^* - \boldsymbol{V}_s) \tag{2.30}$$

or

$$V_r = V_{cx}^* - V_{sx} \tag{2.31}$$

The linear speed of rolling is according to (2.6) related to the angular speed of

rolling:

$$\Omega_r = \frac{1}{r_e} V_r \tag{2.32}$$

Of course, on flat roads $\Omega_r = \Omega$ which is the wheel speed of revolution and may be directly calculated by using the relationship (2.7).

The lateral slip speed V_{cy} is obtained by taking the lateral component of $\boldsymbol{V}_c$ (2.26):

$$V_{cy} = \boldsymbol{V}_c \cdot \boldsymbol{t} \tag{2.33}$$

with

$$\boldsymbol{t} = \boldsymbol{l} \times \boldsymbol{n} \tag{2.34}$$

The lateral slip $\tan\alpha$ reads:

$$\tan\alpha = -\frac{V_{cy}}{V^*_{cx}} = -\frac{\boldsymbol{V}_c \cdot \boldsymbol{t}}{\boldsymbol{V}^*_c \cdot \boldsymbol{l}} \tag{2.35}$$

The longitudinal slip speed V_{sx} is obtained in a similar way:

$$V_{sx} = \boldsymbol{V}_s \cdot \boldsymbol{l} \tag{2.36}$$

The longitudinal slip κ now becomes:

$$\kappa = -\frac{V_{sx}}{V^*_{cx}} = -\frac{\boldsymbol{V}_s \cdot \boldsymbol{l}}{\boldsymbol{V}^*_c \cdot \boldsymbol{l}} \tag{2.37}$$

The turn slip according to definition (2.18) is derived as follows

$$\varphi_t = -\frac{\dot{\psi}}{V^*_{cx}} = -\frac{\dot{\boldsymbol{l}} \cdot \boldsymbol{t}}{\boldsymbol{V}^*_c \cdot \boldsymbol{l}} \tag{2.38}$$

with in the numerator the time derivative of the unit vector $\boldsymbol{l}$. The wheel camber angle is obtained as indicated before:

$$\sin\gamma = -\boldsymbol{n} \cdot \boldsymbol{s} \tag{2.39}$$

Exercise 2.1. Slip and rolling speed of a wheel steered about a vertical axis

The vehicle depicted in Fig.2.7 runs over a flat level road. The rear frame moves with velocities u, v and r with respect to an inertial triad (choose (O^o, x^o, y^o, z^o) which at the instant considered is positioned parallel to the moving triad (B, x, y, z) attached to the rear frame). The front frame can be turned with a rate $\dot{\delta}(= \mathrm{d}\delta/\mathrm{d}t)$ with respect to the rear frame. At the instant considered the front frame is steered over an angle δ.

It is assumed that the effective rolling radius is equal to the loaded radius ($r_e = r$,

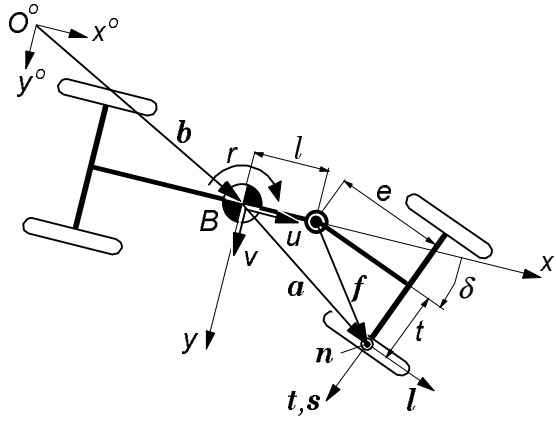

Fig. 2.7. Top-view of vehicle (Exercise 2.1).

$C^* = C$). The longitudinal slip at the front wheels is assumed to be equal to zero (V_{sx} = 0).

Derive expressions for the lateral slip speed V_{cy}, the linear speed of rolling V_r and the lateral slip tanα for the right front wheel.

Exercise 2.2. Slip and rolling speed of a wheel steered about an inclined axis (motorcycle)

The wheel shown in Fig.2.8 runs over a flat level road surface. Its centre A moves along a horizontal straight line at a height H with a speed u. The rake angle ε is 45°. The steer axis BA (vector $\boldsymbol{a}$) translates with the same speed u. There is no wheel slip in longitudinal direction (V_{sx} = 0). Again we assume $r_e = r$. For the sake of simplifying the complex problem, it is assumed that the wheel centre height H is a given constant.

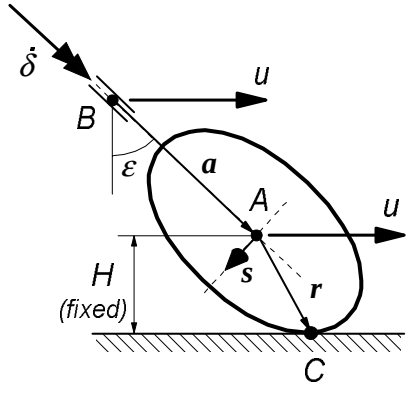

Fig. 2.8. Side view of front part of vehicle (motorcycle) with wheel turned over angle δ about steer axis ($\boldsymbol{a}$) (Exercise 2.2).

Derive expressions for the lateral slip speed V_{cy}, the linear speed of rolling V_r and the turn slip speed $\dot{\psi}$ in terms of H, u and $\dot{\delta}$ for $\delta = 0°$, 30° and 90°. Also show the expressions for the slip angle α, the camber angle γ and the spin slip φ with contributions both from turning and camber. Note, that in reality height H depends on δ and changes due to $\dot{\delta}$.

2.4. Fundamental Differential Equations for a Rolling and Slipping Body

A wheel with tyre that rolls over a smooth level surface and at the same time performs longitudinal and lateral slipping motions, will develop horizontal deformations as a result of the presence of frictional forces which attempt to prevent the tyre particles, that have entered the contact area, from sliding over the road. Besides areas of adhesion, areas of sliding may occur in the contact patch. The latter condition will arise when the deflection generated in the range of adhesion would have become too large to be maintained by the available frictional forces. In the following, a set of partial differential equations will be derived that governs the horizontal tyre deflections in the contact area in connection with possibly occurring velocities of sliding of the tyre particles. For a given physical structure of the tyre, these equations can be used to develop the complete mathematical description of tyre model behaviour as will be demonstrated in subsequent chapters.

Consider a rotationally symmetric elastic body representing a wheel and tyre rolling over a smooth horizontal rigid surface representing the road. As indicated in Fig.2.9 a system of axes ($O°$, $x°$, $y°$, $z°$) is assumed to be fixed to the road. The $x°$ and $y°$ axes lie in the road surface and the $z°$ axis points downwards. Another coordinate system (C, x, y, z) is introduced of which the axes x and y lie in the ($x°$, $O°$, $y°$) plane and z points downwards. The x axis is defined to lie in the wheel centre plane and the y axis forms the vertical projection of the wheel spindle axis. The origin C which is the so-called contact centre or, perhaps better: the point of intersection, travels with an assumedly constant speed V_c over the ($x°$, $O°$, $y°$) plane. The travelled distance s is

$$s = V_c t \tag{2.40}$$

where t denotes the time. The tangent to the orbit of C makes an angle β with the fixed $x°$ axis. With respect to this tangent the x axis is rotated over an angle α, defined as the slip angle. The angular deviation of the x axis with respect to the $x°$ axis (that is the yaw angle) becomes

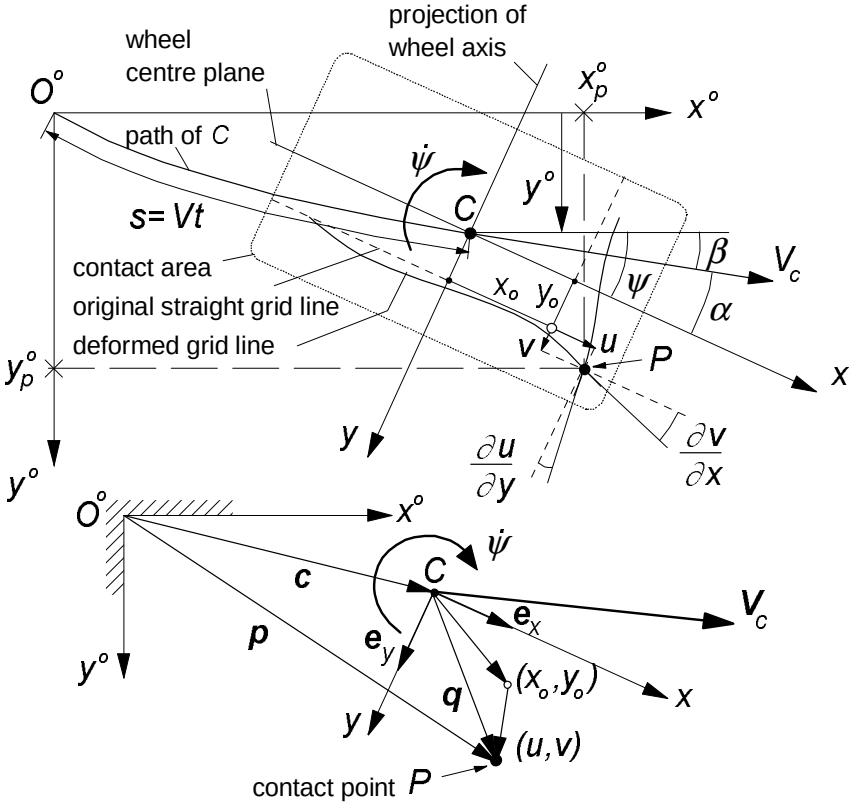

Fig. 2.9. Top view of tyre contact area showing its position with respect to the system of axes (O^o, x^o, y^o, z^o) fixed to the road and its deformations (u, v) with respect to the moving triad (C, x, y, z).

$$\psi = \beta + \alpha \tag{2.41}$$

For the angle β the following relation with $y°$, the lateral displacement of C, holds

$$\sin\beta = \frac{\mathrm{d}y^o}{\mathrm{d}s} \tag{2.42}$$

As a result of friction, horizontal deformations may occur in the contact patch. The corresponding displacements of a contact point with respect to the position this material point would have in the horizontally undisturbed state (defined to occur when rolling on a frictionless surface), with coordinates (x_o, y_o), are indicated by u and v in x and y direction respectively. These displacements are functions of coordinates x and y and of the travelled distance s or the time t.

The position in space of a material point of the rolling and slipping body in contact with the road (cf. Fig.2.9) is indicated by the vector

$$\boldsymbol{p} = \boldsymbol{c} + \boldsymbol{q} \tag{2.43}$$

where $\boldsymbol{c}$ indicates the position of the contact centre C in space and $\boldsymbol{q}$ the position of the material point with respect to the contact centre. We have for the latter vector:

$$\boldsymbol{q} = (x_o + u)\,\boldsymbol{e}_x + (y_o + v)\,\boldsymbol{e}_y \tag{2.44}$$

with $\boldsymbol{e}_x$ $(=\boldsymbol{l})$ and $\boldsymbol{e}_y$ $(=\boldsymbol{t})$ representing the unit vectors in x and y directions. The vector of the sliding velocity of the material point relative to the road obviously becomes:

$$\boldsymbol{V}_g = \dot{\boldsymbol{p}} = \dot{\boldsymbol{c}} + \dot{\boldsymbol{q}} = \boldsymbol{V}_c + (\dot{x}_o + \dot{u})\,\boldsymbol{e}_x + (\dot{y}_o + \dot{v})\,\boldsymbol{e}_y + \dot{\psi}\{(x_o + u)\,\boldsymbol{e}_y - (y_o + v)\,\boldsymbol{e}_x\} \tag{2.45}$$

where $\boldsymbol{V}_c = \dot{\boldsymbol{c}}$ denotes the vector of the speed of propagation of contact centre C.

The coordinates x_o and y_o of the material contact point of the horizontally undisturbed tyre (zero friction) will change due to rolling. Then, the point will move through the contact area from the leading edge to the trailing edge. In the general case, e.g. of an elastic ball rolling over the ground, we may have rolling both in the forward and lateral directions. Then, both coordinates of the material point will change with time. In the present analysis of the rolling wheel we will disregard the possibility of sideways rolling.

To assess the variation of the coordinates of the point on the zero friction surface let us first consider an imaginary road surface that is in the same position as the actual surface but does not transmit forces to the wheel. Then, the tyre penetrates the imaginary surface without deformation. When the general situation is considered of a wheel-spin-axis that is inclined with respect to the imaginary road surface, i.e. rolling at a camber angle γ, the coordinates x and y of the material point change with time as follows:

$$\begin{aligned} \dot{x} &= \frac{\mathrm{d}x}{\mathrm{d}t} = -r_o(y)\cdot\Omega \\ \dot{y} &= \frac{\mathrm{d}y}{\mathrm{d}t} = -x\,\sin\gamma\cdot\Omega \end{aligned} \tag{2.46}$$

If $\frac{1}{2}a|\dot{\gamma}| \ll r_o|\gamma|\Omega$ the effect of the time rate of change of the camber angle (wheel plane rotation about the x axis) on the partial derivative $\partial y/\partial t$ and thus on $\dot{y}$ may be neglected. This effect is directly connected with the small instantaneous or so-called non-lagging response to camber changes. Similar instantaneous responses may occur as a result of normal load changes when the tyre shows conicity or ply-steer. The terms associated with $\partial y/\partial t$ have been neglected in the above equation and related neglections will be performed in subsequent formulae for $\dot{y}_o$.

The radius of the outer surface in the undeformed state r_o may depend on the lateral coordinate y. If the rolling body shows a touching surface that is already parallel to the road before it is deformed, we would have in the neighbourhood of the centre of contact: $r_o(y) = r_o(0) - y \sin\gamma$. In case of a cambered car tyre a distortion of belt and carcass is needed to establish contact over a finite area with the ground. The shape of the tyre cross section in the undeformed state governs the dependency of the free radius with the distance to the wheel centre plane.

In Fig.2.10 an example is given of two different cases. The upper part corresponds to a rear view and the lower one to a plan view of a motorcycle tyre and of a car tyre pressed against an assumedly frictionless surface (μ=0). It may be noted that in case of a large camber angle like with the motorcycle tyre, one might decide to redefine the position of the x and z axes. The contact line which is the part of the peripheral line that touches the road surface has been indicated in the figure.

When the tyre is loaded against an assumedly frictionless rigid surface, deformations of the tyre will occur. These will be due to: (1) lateral and longitudinal compression in the contact region, (2) a possibly not quite symmetric structure of the tyre resulting in effects known as ply-steer and conicity and (3) loading at a camber angle which will result in distortion of the carcass and belt. The deformations occurring in the contact plane will be denoted with u_o and v_o. We will introduce the functions $\theta_{x,y}(x, y)$ representing the partial derivatives of these normal-load-induced longitudinal and lateral deformations with respect to x. We have:

$$\theta_x(x,y) = \frac{\partial u_o}{\partial x} \quad \text{and} \quad \theta_y(x,y) = \frac{\partial v_o}{\partial x} \tag{2.47}$$

These functions depend on the vertical load and on the camber angle.

If the tyre is considered to roll on a frictionless flat surface at a camber angle or with non-zero θ's , lateral and longitudinal sliding of the contact points will occur even when the wheel does not exhibit lateral, longitudinal or turn slip. Since horizontal forces do not occur in this imaginary case, u and v are defined to be zero. The coordinates with respect of the moving axes system (C, x, y, z) of the contact point sliding over the hypothetical frictionless surface were denoted as x_o and y_o. The time rates of change of x_o and y_o depend on the position in the contact patch, on the speed of rolling Ω and on the camber angle γ. We find after disregarding the effect of $\partial y_o/\partial t$:

$$\begin{aligned} \dot{x}_o &= \dot{x} + \dot{u}_o = -\{1 + \theta_x(x,y)\} \cdot r_o(y) \cdot \Omega \\ \dot{y}_o &= \dot{y} + \dot{v}_o = -\{x_o \sin\gamma + \theta_y(x,y)\, r_o(y)\} \cdot \Omega \end{aligned} \tag{2.48}$$

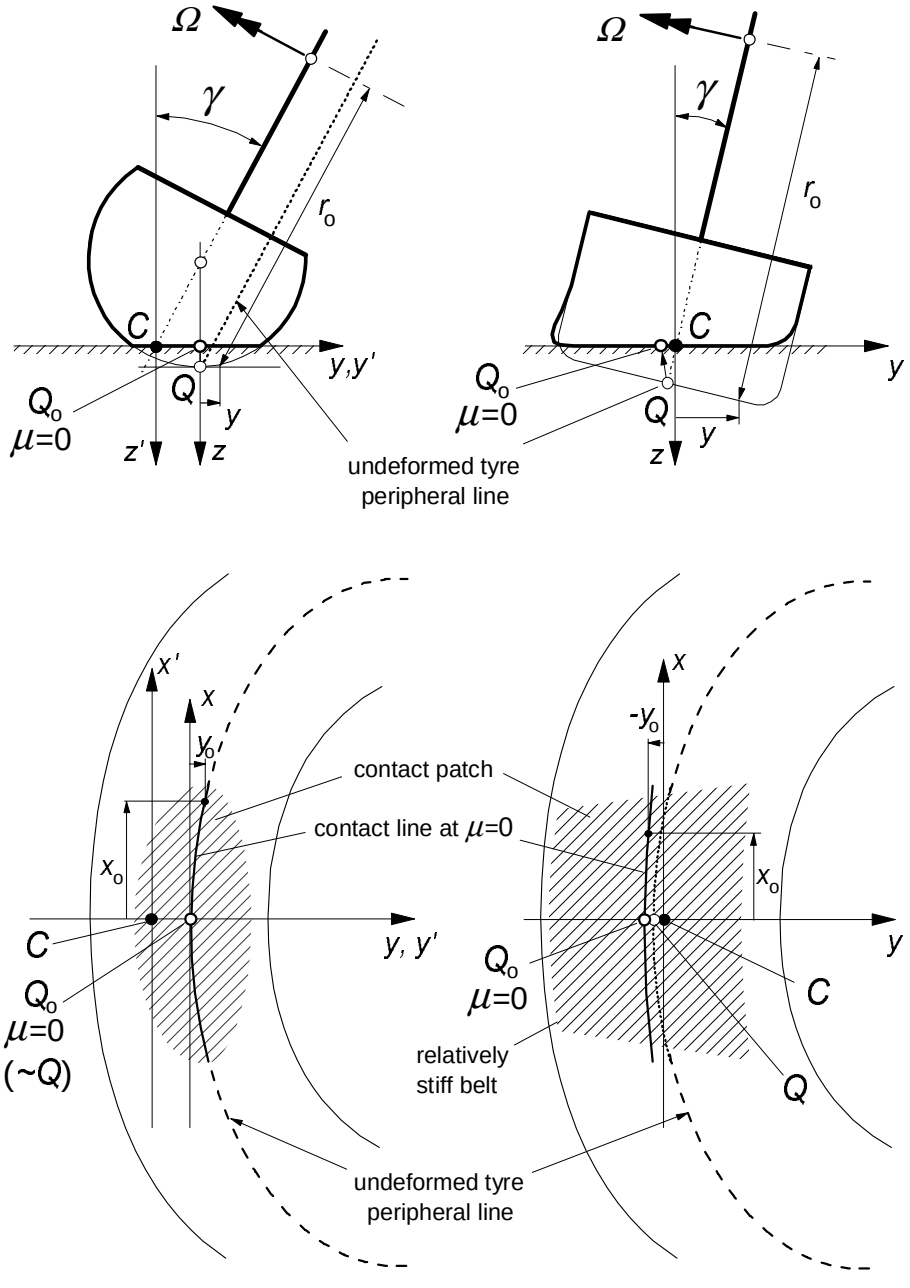

Fig. 2.10. A motorcycle tyre (left) and a car tyre (right) in cambered position touching the assumedly frictionless road surface. The former without and the latter with torsion and bending of the carcass and belt. Top: rear view; bottom: top view.

For homogeneous rolling bodies (e.g. a railway wheel or a rubber ball) with counter surfaces already parallel before touching, torsion about the longitudinal axis and lateral bending do not occur, ply-steer and conicity are absent and horizontal compression may be neglected (θ's vanish). Moreover, we then had: $r_o(y) = r_o(0) - y \sin\gamma$ so that for this special case (2.48) reduces to:

$$\begin{aligned} \dot{x}_o &= \dot{x} = -\{r_o(0) - y\sin\gamma\}\cdot\Omega \\ \dot{y}_o &= \dot{y} = -x\sin\gamma\cdot\Omega \end{aligned} \tag{2.49}$$

For a tyre the terms with θ are appropriate. Circumferential compression ($\theta_x < 0$) decreases the effective rolling radius r_e that is defined at free rolling. At camber, due to the structure of a car tyre with a belt that is relatively stiff in lateral bending, the compression/extension factor θ_x will not be able to compensate for the fact that a car tyre shows only a relatively small variation of the free radius $r_o(y)$ across the width of the tread, while for the same reason the lateral distorsion factor θ_y appears to be capable of considerably counteracting the effect of the term with $\sin\gamma$ in the second equation (2.48). For a motorcycle tyre with a cross section approximately forming a sector of a circle, touching at camber is accomplished practically without torsion about a longitudinal axis and the associated lateral bending of the tyre near the contact zone. Figure 2.10 illustrates the expected deformations and the resulting much smaller curvature of the contact line on a frictionless surface for the car tyre relative to the curvature exhibited by the motorcycle tyre. Since on a surface with friction the rolling tyre will be deformed to acquire a straight contact line, this observation may explain the relatively low camber stiffness of the car and truck tyre.

As mentioned above, circumferential compression of belt and tread resulting from the normal loading process (somewhat counteracted by the presence of hysteresis also represented by the factor θ_x) gives rise to a decrease of the effective rolling radius. The compression may not be uniform along the x axis. For our purposes, however, we will disregard the resulting secondary effects. The coefficient in (2.48) that relates the passage velocity $-\dot{x}_o$ and the speed of revolution Ω of the wheel is designated as the local effective rolling radius r_{ej} at e.g. row j of tread elements. This radius depends on the lateral position y_j and will change with the vertical load F_z and the camber angle γ. The velocity through the contact zone of the elements of row j is: $-\dot{x}_o = r_{ej}\Omega$. We may write:

$$r_{ej} = \{1 + \theta_x(y_j)\}\, r_o(y_j) = r_e + \Delta r_{ej}(y_j) \tag{2.50}$$

in which use has been made of the overall tyre effective rolling radius r_e defined according to Eqs.(2.2, 2.6) and $\Delta r_{ej}(y_j)$ the possibly anti-symmetric variation of the local effective rolling radius over the tread width with respect to r_e due to

loading at camber or conicity. The (average) effective rolling radius r_e is expected to depend on the camber angle as well.

We will now try to make a distinction between the contributions to the anti-symmetric variation originating from conicity and from camber. We write for the local passage velocity:

$$\dot{x}_o = -[\{1+\theta_{\mathrm{con}x}(y)\}\, r_e - \{1+\theta_{\gamma x}(y)\}\, y_o \sin\gamma]\cdot\Omega \tag{2.51}$$

In this way we have achieved a structure closely related to the first equation of (2.49). For a rolling elastic body like a ball or a motorcycle tyre, $\theta_{\gamma x}$ will be (close to) zero, while a car, truck or racing car tyre is expected to have a $\theta_{\gamma x}$ closer to the value -1. A bias-ply tyre featuring a more compliant carcass and tread band and a rounder cross section profile is expected to better 'recover' from the torsion effects, resulting in a value in between the two extremes. It is true that in general bias-ply tyres show considerably larger side forces as a result of camber than radial ply car tyres.

When the product of θ_y and r_o - r_e is considered to be negligible we write for the lateral velocity of the points over a frictionless surface with respect to the x axis instead of (2.48):

$$\dot{y}_o = -\{x_o \sin\gamma + \theta_y(x,y)\cdot r_e\}\cdot\Omega \tag{2.52}$$

The resulting expressions (2.51, 52) may now be substituted in expression (2.45) for the sliding speed components.

For a given material point of the tyre outer surface that now rolls on a road surface with friction reintroduced, the associated deflections u and v (which occur on top of the initial load induced deflections u_o and v_o) are functions of its location in the contact patch and of the time: $u = u(x_o, y_o, t)$ and $v = v(x_o, y_o, t)$. Hence we have for the time rates of change:

$$\begin{aligned} \dot{u} &= \frac{\mathrm{d}u}{\mathrm{d}t} = \frac{\partial u}{\partial x_o}\frac{\mathrm{d}x_o}{\mathrm{d}t} + \frac{\partial u}{\partial y_o}\frac{\mathrm{d}y_o}{\mathrm{d}t} + \frac{\partial u}{\partial t} \\ \dot{v} &= \frac{\mathrm{d}v}{\mathrm{d}t} = \frac{\partial v}{\partial x_o}\frac{\mathrm{d}x_o}{\mathrm{d}t} + \frac{\partial v}{\partial y_o}\frac{\mathrm{d}y_o}{\mathrm{d}t} + \frac{\partial v}{\partial t} \end{aligned} \tag{2.53}$$

in which the expressions (2.51, 52) apply. If we disregard sideways rolling and neglect a possible small effect of the variation of y_o that occurs at camber, conicity or ply-steer, the second terms of the right-hand members disappear. The remaining expressions are substituted in (2.45).

According to Eq.(2.29) the linear speed of rolling and the velocity of the contact centre are related through the slip speed. We have (when disregarding the

generally very small difference between the velocities of C^* and C) the vector relationship:

$$\boldsymbol{V}_c = \boldsymbol{V}_s + V_r\,\boldsymbol{e}_x \qquad \text{with} \qquad V_r = r_e\Omega \tag{2.54}$$

After simplifying the equations by neglecting products of assumedly small quantities (i.e. deflections and input (slip) quantities) and using the expression for ω_z which is the absolute angular velocity of the wheel body about the z axis as indicated in Eq.(2.15), components of the sliding velocity become:

$$V_{gx} = V_{sx} - \left(\frac{\partial u}{\partial x} + \theta_{\mathrm{con}x}(y)\right)\cdot V_r + \frac{\partial u}{\partial t} - y_o\omega_z + \theta_{\gamma x}(y)\cdot y_o \sin\gamma\cdot\Omega \tag{2.55}$$

$$V_{gy} = V_{sy} - \left(\frac{\partial v}{\partial x} + \theta_y(x,y)\right)\cdot V_r + \frac{\partial v}{\partial t} + x_o\omega_z \tag{2.56}$$

With all θ's omitted we would return to the basic case of e.g. a ball rolling and slipping over a flat rigid surface. In Chapter 3 a physical tyre model is developed using the above equations. There, the θ's are expressed in terms of the camber angle and of equivalent camber and slip angles γ_{con} and α_{ply} to account for conicity and ply-steer (cf. Eqs.(3.108,109)).

Let us now consider the special case of a freely rolling tyre subjected to only small lateral slip and spin ($\kappa=0$, $|\alpha|\ll 1$, $|\gamma|\ll 1$, $r_e \ll |R|$, with R : the instantaneous radius of path curvature, and thus $|\varphi_t|\ll 1/r_e$) and neglect effects of initial non-parallellity of touching surfaces as well as 'built-in' load and camber induced deformation effects (all θ's =0). We then have (approximately):

$$V_{sx} = 0\,,\ V_{sy} = -V_c\alpha\,,\ V_r = V_c\,,\ \omega_z\,(=\dot{\psi} - \Omega\sin\gamma) = -V_c\varphi \tag{2.57}$$

Using the travelled distance s (2.40) instead of the time t as an independent variable, we obtain the following expressions for the sliding velocities of a contact point with coordinates (x, y) of a freely rolling tyre at small lateral slip and spin:

$$V_{gx} = V_c\left(y\varphi - \frac{\partial u}{\partial x} + \frac{\partial u}{\partial s}\right) \tag{2.58}$$

$$V_{gy} = V_c\left(-\alpha - x\varphi - \frac{\partial v}{\partial x} + \frac{\partial v}{\partial s}\right) \tag{2.59}$$

In the contact area regions of adhesion may occur as well as regions where sliding takes place. In the region of adhesion the tyre particles touching the road do not move and we have $V_{gx} = V_{gy} = 0$. In this part of the contact area, the frictional shear forces acting from road to tyre on a unit area (with components

denoted by q_x and q_y not to be confused with the components of the position vector (2.44) used earlier) do not exceed the maximum available frictional force per unit area. The maximum frictional shear stress is governed by the coefficient of friction μ and the normal contact pressure q_z. In the adhesion region Eqs.(2.58, 59) reduce to:

$$\frac{\partial u}{\partial x} - \frac{\partial u}{\partial s} = -y\varphi \tag{2.60}$$

$$\frac{\partial v}{\partial x} - \frac{\partial v}{\partial s} = -\alpha - x\varphi \tag{2.61}$$

Furthermore we have the condition:

$$\sqrt{q_x^2 + q_y^2} < \mu q_z \tag{2.62}$$

In the region of sliding, equations (2.58, 59) hold. If the deformation gradients were known, the velocity components V_{gx} and V_{gy} might be obtained from these equations. For the frictional stress vector we obtain:

$$(q_x, q_y) = -\mu\, q_z (V_{gx}, V_{gy})/V_g \tag{2.63}$$

with

$$V_g = \sqrt{V_{gx}^2 + V_{gy}^2} \tag{2.64}$$

For the simpler case that only lateral slip occurs ($\varphi = 0$) the equations for the lateral deformations reduce to:

in adhesion region:

$$\left.\begin{aligned} &\frac{\partial v}{\partial x} - \frac{\partial v}{\partial s} = -\alpha \\ &|q_y| < \mu q_z \end{aligned}\right\} \tag{2.65}$$

in sliding region:

$$\left.\begin{aligned} &\frac{\partial v}{\partial x} - \frac{\partial v}{\partial s} = -\alpha - \frac{V_{gy}}{V_c} \\ &q_y = -\mu q_z \operatorname{sgn} V_{gy} \end{aligned}\right\} \tag{2.66}$$

The equations (2.55, 56) apply in general. Their solutions contain constants of

integration which depend on the selected physical model description of the tyre. Applications of the differential equations derived above will be demonstrated in subsequent chapters both for steady-state and non-steady-state conditions. In the case of steady-state motion of the wheel, the partial derivatives with respect to time t or travelled distance s become equal to zero ($\partial v/\partial s = \partial u/\partial s = 0$). Then, the deformation gradients in the area of adhesion ($V_g = 0$) follow easily from the then ordinary differential equations. In the last simple case (2.66) we would obtain: $dv/dx = -\alpha$ which means that the contact line is straight and runs parallel to the speed vector V_c.

Exercise 2.3. Partial differential equations with longitudinal slip included

Establish the differential equations for the sliding velocities similar to the Eqs.(2.58, 59) but now with longitudinal slip κ included (α and φ remain small). Note that in that case $V_r \neq V_c$ and that V_r may be expressed in terms of V_{cx} ($\sim V_c$) and κ. Also, find the partial differential equations governing the deflections in the adhesion zone similar to the Eqs.(2.60, 61).

2.5. Tyre Models (Introductory Discussion)

Several types of mathematical models of the tyre have been developed during the last half century. Each type for a specific purpose. Different levels of accuracy and complexity may be introduced in the various categories of utilization. This often involves entirely different ways of approach. Figure 2.11 roughly illustrates how the intensity of various consequences associated with different ways of attacking the problem tend to vary. From left to right the model is based less on full scale tyre experiments and more on the theory of the behaviour of the physical structure of the tyre. In the middle, the model will be simpler but possibly less accurate while at the far right the descriptions becomes complex and less suitable for application in the simulation of vehicle motions and may be more appropriate for the analysis of detailed tyre performance in relation to its construction.

At the left-hand category, we have mathematical tyre models which describe measured tyre characteristics through tables or mathematical formulae and certain interpolation schemes. These formulae have a given structure and possess parameters which are usually assessed with the aid of regression procedures to yield a best fit to the measured data. A well-known empirical model is the Magic Formula tyre model treated in Chapter 4. This model is based on a sin(arctan) formula which not only provides an excellent fit for the F_y, F_x and M_z curves but in addition features coefficients which have clear relationships with typical shape

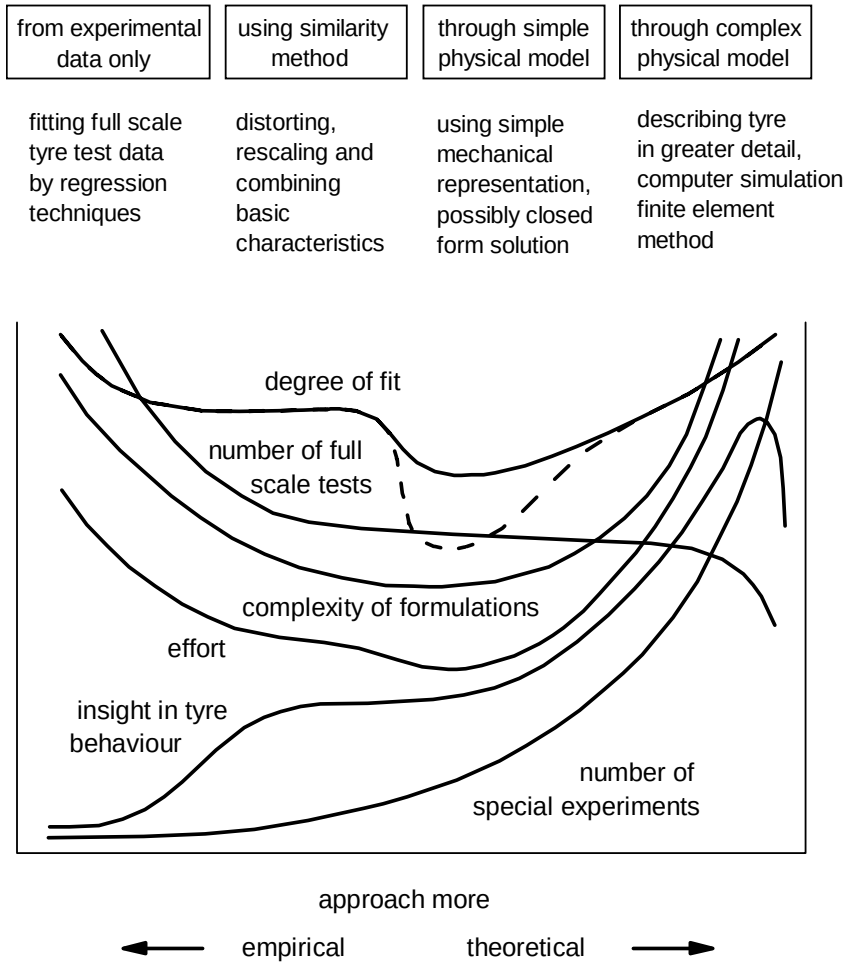

Fig. 2.11. Four categories of possible types of approach to develop a tyre model.

and magnitude factors of the curves to be fitted.

The similarity approach (second category) is based on the use of a number of basic characteristics typically obtained from measurements. Through distortion, rescaling and multiplications, new relationships are obtained to describe certain off-nominal conditions. Chapter 4 introduces this method which is particularly useful for application in vehicle simulation models that requires rapid (e.g. real time) computations.

Depending on the type of the physical model chosen, a simple formulation may already provide sufficient accuracy for limited fields of application. The HSRI model depicted in Fig.2.12 developed by Dugoff, Fancher and Segel

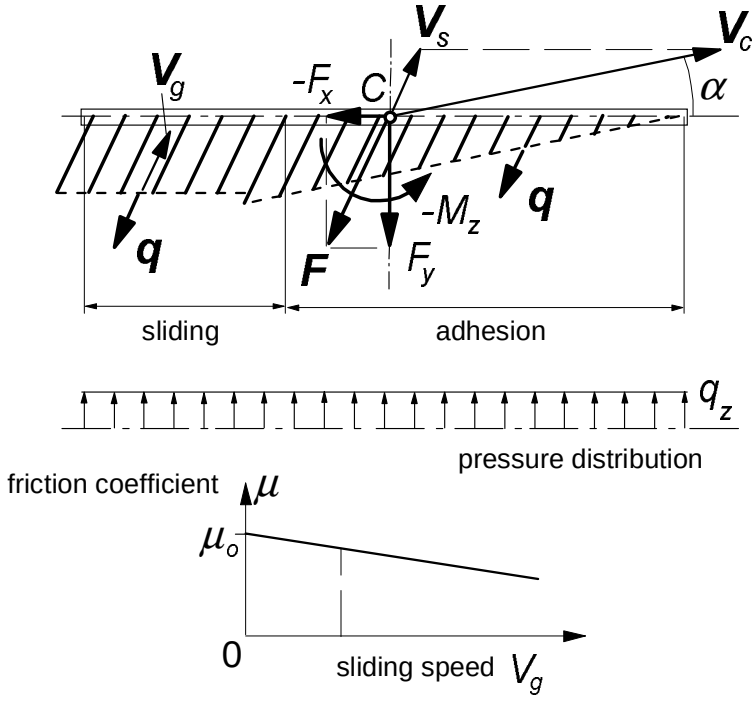

Fig. 2.12. a. The brush type tyre model at combined longitudinal (brake) slip and lateral slip in case of equal longitudinal and lateral stiffnesses.
b. The linearly decaying friction coefficient.

(1970) and later corrected and improved by Bernard et al. (1977) is a good example. The figure illustrates the considerable simplification with respect to a more realistic representation of tyre deformation (Fig.2.13) that is needed to keep the resulting mathematical formulation manageable for vehicle dynamics simulation purposes and still include important matters like the representation of combined slip and a coefficient of friction that may drop with speed of sliding.

The model of Fig.2.13 exhibits carcass flexibility and shows a more realistic parabolic pressure distribution. For such a model, (approximate) analytical solutions are feasible only when pure side slip (possibly including camber) occurs and the friction coefficient is considered constant (e.g. Fiala, 1954).

Relatively simple physical models of this third category like the 'brush model' of Fig.2.12 are especially useful to get a better understanding of tyre behaviour. The brush model with a parabolic pressure distribution will be discussed at length in Chapter 3.

The right-most group of Fig.2.11 is aimed primarily at more detailed analysis of the tyre. The complex finite element based models belongs to this category.

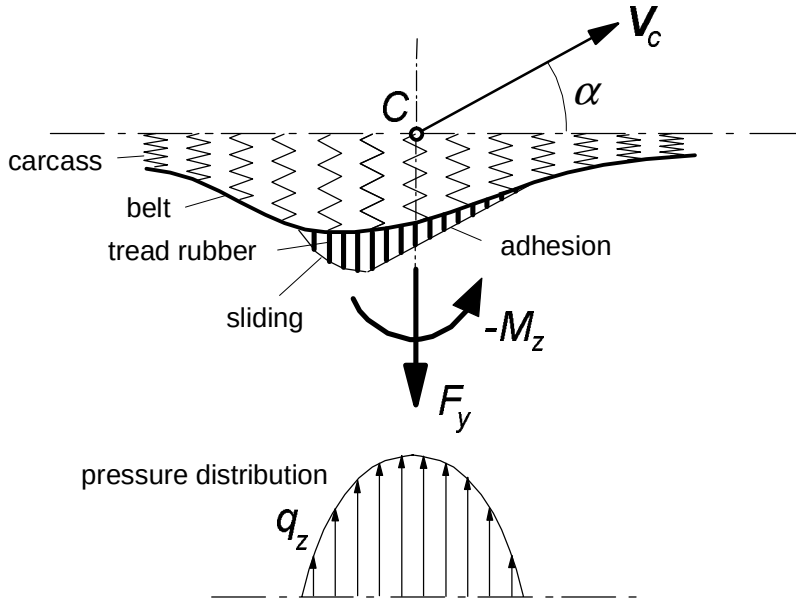

Fig. 2.13. Tyre model with flexible carcass at steady-state rolling with slip angle α.

A simpler representation of carcass complance that is experienced in the lower part of the tyre near the contact patch considerably speeds up the computation. Also the way in which the tread elements are handled is crucial. The computer simulation tread-element-following method is attractive and allows considerable freedom to choose pressure distribution and friction coefficient functions of sliding velocity and local contact pressure. The physical model that forms the basis of the latter method has been depicted in Fig.2.14. Influence (Green) functions may be used to describe the carcass horizontal compliance in the contact zone and possibly several rows of tread elements may be considered to move through the contact patch. One element per row is followed while it travels through the length of contact (or several elements through respective sub-zones). During such a passage the carcass deflection is kept constant, the motion of the single mass-spring (tread element) system that is dragged over the ground is computed, the frictional forces are integrated, the total forces and moment determined and the carcass deflection is up-dated. Instead of using the dynamic way of solving for the deflection of the tread element while it runs through the contact patch, an iteration process may be employed. The model is capable of handling non-steady state conditions. A relatively simple application of the tread-element-following method will be shown in the subsequent chapter when dealing with the 'brush model' subjected to combined slip with camber, a condition that

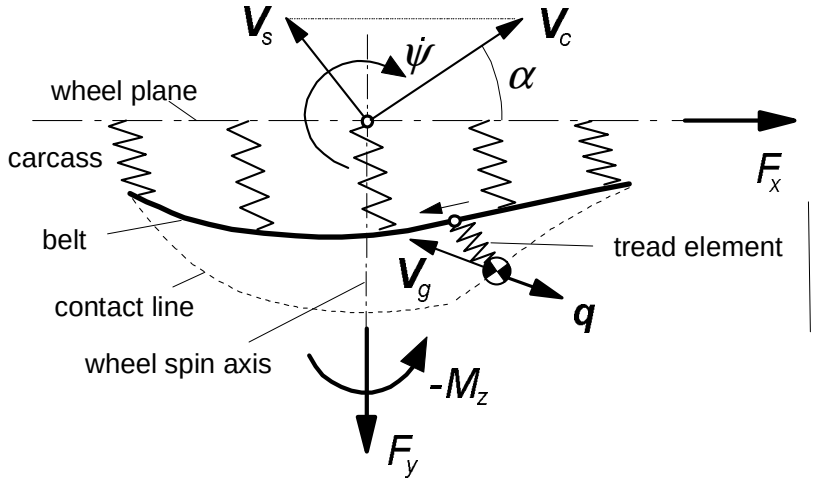

Fig. 2.14. Computer simulation tyre model with flexible carcass, arbitrary pressure distribution and friction coefficient functions. Forces acting on a single tread element mass during one passage through the contact length are integrated to obtain the total forces and moment F_x, F_y and M_z.

is too difficult to deal with analytically. Also the introduction of carcass compliance will be demonstrated. For further study we refer to the original work of Willumeit (1969), Pacejka (1972a), Sharp (1986), Gipser (1997), Guo (1997) and Mastinu (1997) and the state-of-the-art paper of Pacejka and Sharp (1991).

Although it is possible to develop a model for non-steady-state conditions by purely empirical means, most relatively simple and more complex transient and dynamic tyre models are based on the physical nature of the tyre. It is of interest to note that for a proper description of tyre behaviour at time-varying conditions an essential property must be represented in the physical models belonging to both right-hand categories of Fig.2.11. That is the lateral and sometimes also the fore and aft compliance of the carcass. Less complex non-steady-state tyre models feature only carcass compliance without the inclusion of elastic tread elements. In steady-state models the introduction of such a flexibility is often not required. Only to properly represent the self-aligning torque in case of a braked or driven wheel, carcass lateral compliance is needed. Tyre inertia becomes important at higher speeds and frequencies of the wheel motion. The problem of establishing non-steady-state tyre models is addressed in Chapters 5,7,8 and 9 in successive levels of complexity to meet conditions of increasing difficulty.

Conditions become more demanding when for example: (1) the wheel motion gives rise to larger values of slip which no longer permits an approximate linear description of the force and moment generating properties; (2) combined slip

occurs, possibly including wheel camber and turn slip; (3) large camber occurs which may necessitate the consideration of the dimensions of the tyre cross section; (4) the friction coefficient can not be approximated as a constant quantity but may vary with sliding velocity and speed of travel as occurs on wet or icy surfaces; (5) the wavelength of the path of contact points at non-steady-state conditions can no longer be considered large, which may require the introduction of the lateral and longitudinal compliance of the carcass; (6) the wavelength becomes relatively short which may necessitate the consideration of a finite contact length (retardation effect) and possibly the contact width (at turn slip and camber); (7) the speed of travel is large so that tyre inertia becomes of importance in particular its gyroscopic effect; (8) the frequency of the wheel motion has reached a level that requires the inclusion of the first or even higher modes of vibration of the belt; (9) the vertical profile of the road surface contains very short wavelengths with appreciable amplitudes as would occur in the case of rolling over a short obstacle or cleat, then amongst other things the tyre enveloping properties should be accounted for; (10) motions become severe (large slip and high speed) which may necessitate modelling the effect of the warming up of the tyre involving possibly the introduction of the tyre temperature as a model parameter. All items mentioned (except the last one) will be accounted for in the remainder of this book.

Chapter 3

THEORY OF STEADY-STATE SLIP FORCE AND MOMENT GENERATION

3.1. Introduction

This chapter is devoted to the analysis of the properties of a relatively simple theoretical tyre model belonging to the third category of Fig.2.11. The mathematical modelling of the physical model shown in Fig.2.13 has been a challenge to various investigators. Four fundamental factors play a role: frictional properties in the road-tyre interface, distribution of the normal contact pressure, compliance of the tread rubber and compliance of the belt/carcass.

Models of the carcass with belt and side walls with encapsulated pressurised air that are commonly encountered in the tyre modelling literature, are either based on an elastic beam or on a stretched string both suspended on an elastic foundation with respect to the wheel rim. The representation of the belt by a beam instead of by a stretched string is more difficult because of the fact that the differential equation that governs the lateral deflection of the belt under the action of a lateral force becomes of the fourth instead of the second order. For the study of steady-state tyre behaviour, most authors approximate the more or less exact expressions for the lateral deflection of the beam or string.

As an extension to the original 'brush' model of Fromm and of Julien (cf. Hadekel (1952) for references) who did not consider carcass compliance, Fiala (1954) and Freudenstein (1961) developed theories in which the carcass deflection is approximated by a symmetric parabola. Böhm (1963) and Borgmann (1963), the latter without the introduction of tread elements, used asymmetric approximate shapes determined by both the lateral force and the aligning torque. Pacejka (1966, 1981) established the steady-state side slip characteristics for a stretched-string tyre model without and with the inclusion of tread elements attached to the string. The lateral stiffness distribution as measured on a slowly rolling tyre in terms of influence or Green's functions (cf. Savkoor, 1970) may be employed in a model for the side slipping tyre possibly in connection with the tread-element-following method that was briefly discussed

in the preceding section (cf. Pacejka 1972, 1974) and will be demonstrated later on in Section 3.3 of the present chapter.

Frank (1965a) has carried out a thorough comparative investigation of the various one-dimensional models. He employed a general fourth-order differential equation with which tyre models can be examined that feature a stretched string, a beam or a stretched beam provided with elastic tread elements. Frank obtained a solution of the steady-state slip problem with the aid of a special analogue computer circuit. A correlation with Fourier components of the measured deformation of real tyres reveals that the stretched string type model seems more suitable for the simulation of a bias ply tyre, whereas the beam model is probably more appropriate for representing the radial ply tyre.

Figure 3.1 (from Frank, 1965b) presents the calculated characteristics of several types of carcass models provided with tread elements. The curves represent: *a*. stretched string model, *b*. beam model, *c*. approximation based on Fiala's model (symmetric parabolic carcass deflection), *d*. model of Fromm (brush model with rigid carcass). The tread element stiffness is the same for each model. The parameters in the cases *a*, *b* and *c* have been chosen in such a way

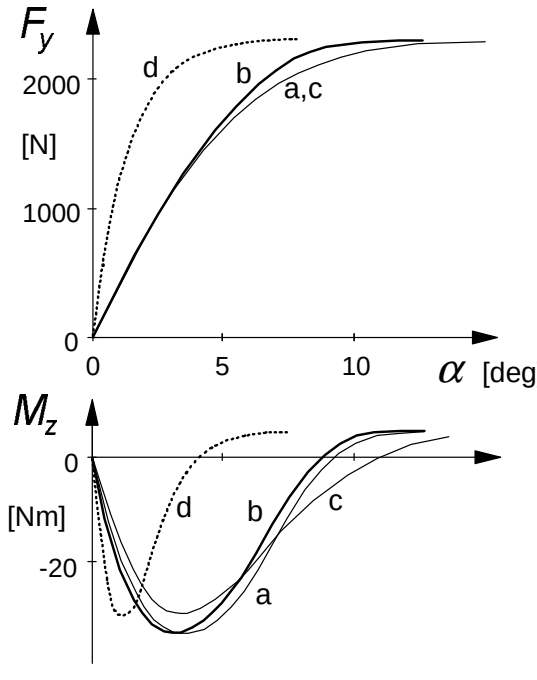

Fig. 3.1. Comparison of calculated characteristics for four different tyre models with tread elements and non-symmetrical pressure distribution at a given wheel vertical load (a: string, b: beam, c: Fiala, d: brush i.e. with rigid carcass) (from Frank 1965).

as to give a best fit to experimental data for the peak side force and the cornering force at small slip angles (that is: same cornering stiffness). It appears then that model *c* shows close correspondence with curve *a* for the side force. Curves *d* show the result when the carcass elasticity is neglected and only the flexibility of the tread elements is taken into account. When the tread element stiffness of model *d* is adapted (i.e. lowered) in such a way that the cornering stiffness becomes equal to that of the other three models, no difference between the side force characteristics according to Fromm's and Fiala's models appear to occur. Due to approximations introduced by Fiala, the coefficients in the expression for the side force versus slip angle (if parabolic pressure distribution is adopted) become equal to those obtained directly by Fromm.

In the calculations for Fig.3.1, Frank employed a constant coefficient of friction μ and a slightly asymmetric vertical pressure distribution $q_z(x)$, found from measurements. The positive aligning torque obtained at larger values of the slip angle α arises as a result of this asymmetry. The phenomenon that in practice the aligning torque indeed varies in this way is due to a combination of several effects.The main cause is probably connected with the asymmetric pressure distribution of the rolling tyre (due to hysteresis of the tyre compound) resulting in a small forward shift of the point of application of the normal load (giving rise to rolling resistance) and, consequently, at full sliding also of the resulting side force. Another important factor causing the moment to become positive is the fact that the coefficient of friction is not a constant but tends to decrease with sliding velocity. As may be derived from e.g. Eq.(2.59) the sliding velocity attains its largest values in the rear portion of the contact area where the slope $\partial v/\partial x$ becomes largest. Consequently, we expect to have larger side forces acting in the front half of the contact area at full sliding conditions than in the rear half. The rolling resistance force that due to the lateral distortion acts slightly beside the wheel plane, may also contribute to the sign change of M_z. A with sliding velocity decreasing μ (not considered by Frank) causes the creation of a peak in the $F_y(\alpha)$ curves and a further slight decay. This has often been observed to occur in practice, especially on wet and icy roads. In the longitudinal force characteristic the peak is usually more pronounced.

The influence of different but symmetric shapes for the vertical force distribution along the x-axis has been theoretically investigated by Borgman (1963). He finds that, especially for tyres exhibiting a relatively large carcass compliance, the influence of the pressure distribution is of importance. Non-symmetric more general distributions were studied by Guo (1994). Many authors adopt for the purpose of mathematical simplicity the parabolic distribution (Fiala 1954, Freudenstein 1961, Bergman 1965, Pacejka 1958, Sakai (also n-th degree parabola, 1989), Dugoff et al. 1970 (uniform, rectangular distribution) and

Bernard et al. 1977 (trapezium shape)). Models of Fiala and Freudenstein feature a flexible carcass while the remaining authors have restricted themselves to a rigid carcass or a uniformly deflected belt. That, however, enabled them to include the description of the more difficult case of combined slip. The introduction of a non-constant friction coefficient has been treated by amongst others: Böhm (1963), Borgmann (1963), Dugoff e.a. (1970), Sakai (1981) and Bernard e.a. (1977).

Figure 3.1 shows that, when the model parameters are chosen properly, the choice of the type of carcass model (beam, string or rigid) has only a limited effect. Qualitatively, the resulting curves are identical. The rigid carcass model with elastic tread elements is often referred to as the brush tyre model. Because of its simplicity and qualitative correspondence with experimental tyre behaviour we will give a full treatment of its properties, mainly to provide understanding of steady-state tyre slipping properties which may also be helpful in the development of more complex models. A uniform carcass deflection will be considered to improve the aligning torque representation at combined slip.

In Section 3.3 of this chapter we will deal with the effect of non-uniform carcass deflection, non-constant friction coefficient and the inclusion of camber and turning (path curvature) combined with side slip and braking/driving. For this purpose, the tread simulation model will be employed.

3.2. Tyre Brush Model

The brush model consists of a row of elastic bristles that touches the road plane and can deflect in a direction parallel to the road surface. These bristles may be called tread elements. Their compliance represents the elasticity of the combination of carcass, belt and actual tread elements of the real tyre. As the tyre rolls, the first element that enters the contact zone is assumed to stand perpendicularly with respect to the road surface. When the tyre rolls freely (that is without the action of a driving or braking torque) and without side slip, camber or turning, the wheel moves along a straight line parallel to the road and in the direction of the wheel plane. In that situation, the tread elements remain vertical and move from the leading edge to the trailing edge without developing a horizontal deflection and consequently without generating a fore and aft or side force. A possible presence of rolling resistance is disregarded. When the wheel speed vector V shows an angle with respect to the wheel plane, side slip occurs. When the wheel velocity of revolution Ω multiplied with the effective rolling radius r_e is not equal to the forward component of the wheel speed $V_x = V\cos\alpha$ we have fore and aft slip. Under these conditions, depicted in Fig.3.2, horizontal

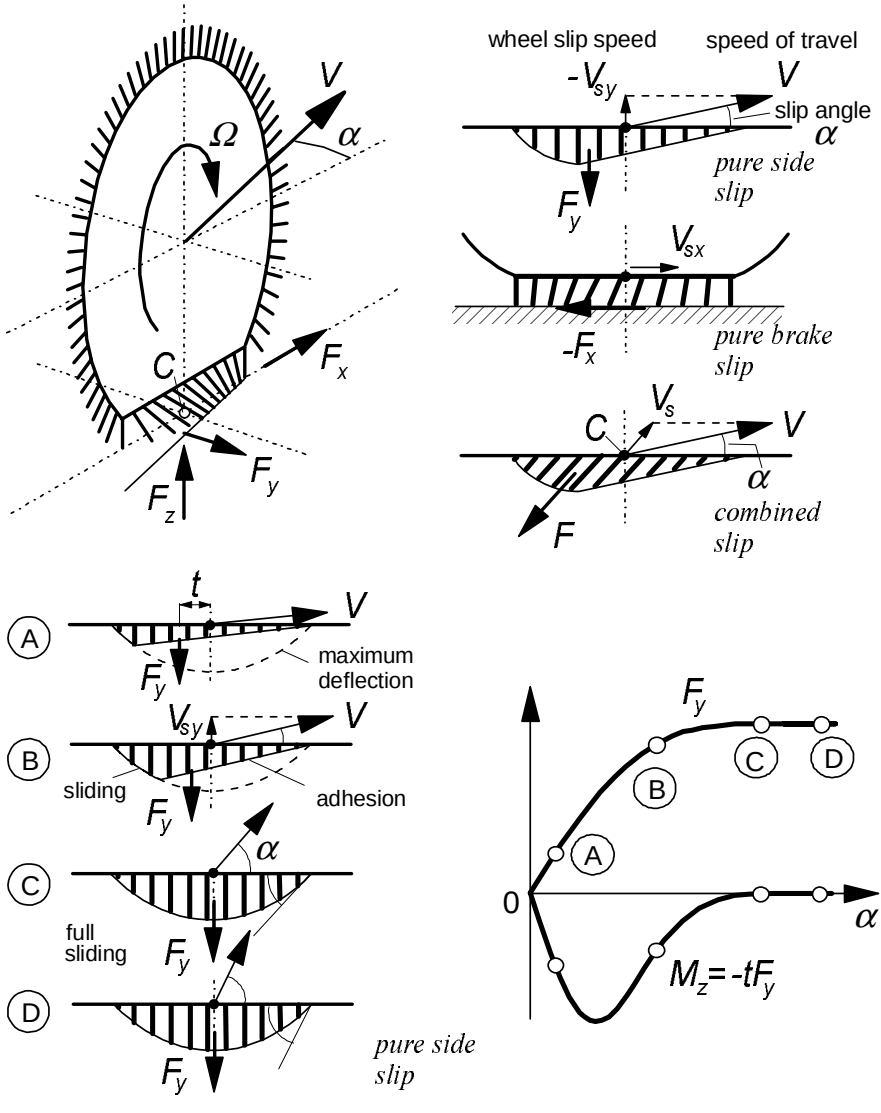

Fig. 3.2. The brush tyre model.
Top left: view of driven and side slipping tyre.
Top right: the tyre at different slip conditions.
Bottom left: the tyre at pure side slip, from small to large slip angle.
Bottom right: the resulting side force and aligning torque characteristics.

deflections are developed and corresponding forces and moment arise. The tread elements move from the leading edge (at the right hand side of the pictures) to the trailing edge. The tip of the element will as long as the available friction allows adhere to the ground (that is, it will not slide over the road surface). At the same time, the base point of the element remains in the wheel plane and moves backwards with the linear speed of rolling V_r (that is equal to Ωr_e) with respect to wheel axis or better: with respect to the contact centre C. With respect to the road, the base point of the element moves with a velocity that is designated as the slip speed V_s of the wheel.

In the lower part of the figure the model is shown at pure side slip. The slip changes from very small to relatively large. We observe that the deflection increases while the element moves further through the contact patch. The deflection rate is equal to the assumedly constant slip speed. The resulting deflection varies linearly with the distance to the leading edge and the tips form a straight contact line that lies in a direction parallel to the wheel speed vector V. The figure also shows the maximum possible deflection that can be reached by the element depending on its position in the contact region. This maximum is governed by the (constant) coefficient of friction μ, the vertical force distribution q_z and the stiffness of the element c_{py}. The pressure distribution and consequently also the maximum deflection v_{max} have been assumed to vary according to a parabola. As soon as the straight contact line intersects the parabola, sliding will start. The remaining part of the contact line will coincide with the parabola for the maximum possible deflection. At increasing slip angle, the side force that is generated will increase. The distance of its line of action behind the contact centre is termed the pneumatic trail t. The aligning torque arises through the non-symmetric shape of the deflection distribution and will be found by multiplying the side force with the pneumatic trail. As the slip increases, the deformation shape becomes more symmetric and, as a result, the trail gets smaller. This is because the point of intersection moves forward, thereby increasing the sliding range and decreasing the range of adhesion. This continues until the wheel speed vector runs parallel to the tangent to the parabola at the foremost point. Then, the point of intersection has reached the leading edge and full sliding starts to occur. The shape has now become fully symmetric. The side force attains its maximum and acts in the middle so that the moment vanishes. That situation remains unchanged when the slip angle increases further. The resulting characteristics for the side force and the aligning torque have been depicted in the same figure. In the part to follow next, the mathematical expressions for these relationships will be derived, first for the case of pure side slip.

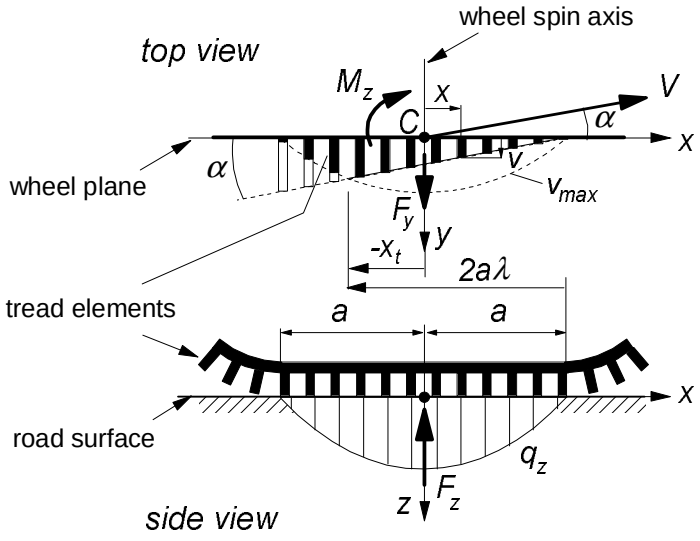

Fig. 3.3. Brush model moving at pure side slip shown in top and side view.

3.2.1. Pure side slip

The brush model moving at a constant slip angle has been depicted in greater detail in Fig.3.3. It shows a contact line which is straight and parallel to the velocity vector V in the adhesion region and curved in the sliding region where the available frictional force becomes lower than the force which would be required for the tips of the tread elements to follow the straight line further. In the adhesion region the linear variation of the deformation is in accordance with the general equation (2.65) (where $\tan\alpha$ has been assumed small and replaced by α) with at steady state $\partial v/\partial s = 0$. For this simple model, the deformation of the tread element at the leading edge vanishes. Consequently, the lateral deformation in the adhesion region reads

$$v = (a-x)\tan\alpha \tag{3.1}$$

where a denotes half the contact length.

In case of vanishing sliding, which will occur for $\alpha \to 0$ or for $\mu \to \infty$, expression (3.1) is valid for the entire region of contact. With the lateral stiffness c_{py} of the tread elements per unit length of the assumedly rectangular contact area the following integrals and expressions for the cornering force F_y and the aligning torque M_z hold:

$$F_y = c_{py} \int_{-a}^{a} v\,dx = 2\,c_{py} a^2 \alpha$$
$$M_z = c_{py} \int_{-a}^{a} v x\,dx = -\tfrac{2}{3}\,c_{py} a^3 \alpha \tag{3.2}$$

Consequently, the cornering stiffness and the aligning stiffness become respectively:

$$C_{F\alpha} = (\partial F_y/\partial\alpha)_{\alpha=0} = 2\,c_{py} a^2$$
$$C_{M\alpha} = -(\partial M_z/\partial\alpha)_{\alpha=0} = \tfrac{2}{3} c_{py} a^3 \tag{3.3}$$

Next, we will consider the case of finite μ and a pressure distribution which gradually drops to zero at both edges. For the purpose of simplicity we assume a parabolic distribution of the vertical force per unit length as expressed by

$$q_z = \frac{3F_z}{4a} \cdot \left\{ 1 - \left(\frac{x}{a} \right)^2 \right\} \tag{3.4}$$

where F_z represents the vertical wheel load. Hence, the largest possible side force distribution becomes:

$$|q_{y,\,max}| = \mu\, q_z = \tfrac{3}{4} \mu F_z \frac{(a^2 - x^2)}{a^3} \tag{3.5}$$

In Fig.3.3 the maximum possible lateral deformation $v_{max} = q_{y,max}/c_{py}$ has been indicated. For the sake of abbreviation the following composite tyre model parameter is introduced:

$$\theta_y = \frac{2 c_{py} a^2}{3 \mu F_z} \tag{3.6}$$

The distance from the leading edge to the point where the transition from the adhesion to the sliding region occurs is written as $2a\lambda$ and is determined by the factor λ. The value of this non-dimensional quantity is found by realising that at this point, where $x=x_t$, the deflection in the adhesion range becomes equal to that of the sliding range. Hence, with Eqs.(3.1, 5, 6) the following equality holds:

$$|q_y| = c_{py}(a - x_t)\,|\tan\alpha| = |q_{y,max}| = \frac{c_{py}}{2a\theta_y}(a - x_t)(a + x_t) \tag{3.7}$$

and thus for $\lambda = (a - x_t)/2a$ we obtain the relationship with the slip angle α:

$$\lambda = 1 - \theta_y\,|\tan\alpha| \tag{3.8}$$

From this equation, the angle α_{sl}, where total sliding starts ($\lambda = 0$), can be calculated:

$$\tan\alpha_{sl} = \frac{1}{\theta_y} \tag{3.9}$$

As the distribution of the deflections of the elements has now been established, the total force F_y and the moment M_z can be assessed by integration over the contact length (like in Eq.(3.2) but now separate for the sliding range $-a<x<x_t$ and the adhesion range $x_t<x<a$). For convenience we introduce the notation for the slip:

$$\sigma_y = \tan\alpha \tag{3.10}$$

The resulting formula for the force reads:
if $|\alpha| \le \alpha_{sl}$

$$\begin{aligned} F_y &= \mu F_z(1-\lambda^3)\,\mathrm{sgn}\,\alpha \\ &= 3\mu F_z\theta_y\sigma_y\left\{1-|\theta_y\sigma_y|+\tfrac{1}{3}(\theta_y\sigma_y)^2\right\} \end{aligned} \tag{3.11}$$

and if $|\alpha| \ge \alpha_{sl}$ (but $< \frac{1}{2}\pi$)

$$F_y = \mu F_z\,\mathrm{sgn}\,\alpha \tag{3.11a}$$

and for the moment:
if $|\alpha| \le \alpha_{sl}$

$$\begin{aligned} M_z &= -\mu F_z\lambda^3 a(1-\lambda)\,\mathrm{sgn}\,\alpha \\ &= -\mu F_z a\theta_y\sigma_y\left\{1-3|\theta_y\sigma_y|+3(\theta_y\sigma_y)^2-|\theta_y\sigma_y|^3\right\} \end{aligned} \tag{3.12}$$

with peak value (27/256) μF_z at $\sigma_y = 1/(4\theta_y)$. If $|\alpha| \ge \alpha_{sl}$ (but $< \frac{1}{2}\pi$)

$$M_z = 0 \tag{3.12a}$$

The pneumatic trail t, which indicates the distance behind the contact centre C where the resultant side force F_y is acting, becomes:
if $|\alpha| \le \alpha_{sl}$

$$t = -\frac{M_z}{F_y} = \frac{1}{3}a\frac{1-3|\theta_y\sigma_y|+3(\theta_y\sigma_y)^2-|\theta_y\sigma_y|^3}{1-|\theta_y\sigma_y|+\frac{1}{3}(\theta_y\sigma_y)^2} \tag{3.13}$$

and if $|\alpha| \ge \alpha_{sl}$ (but $< \frac{1}{2}\pi$)

$$t = 0 \tag{3.13a}$$

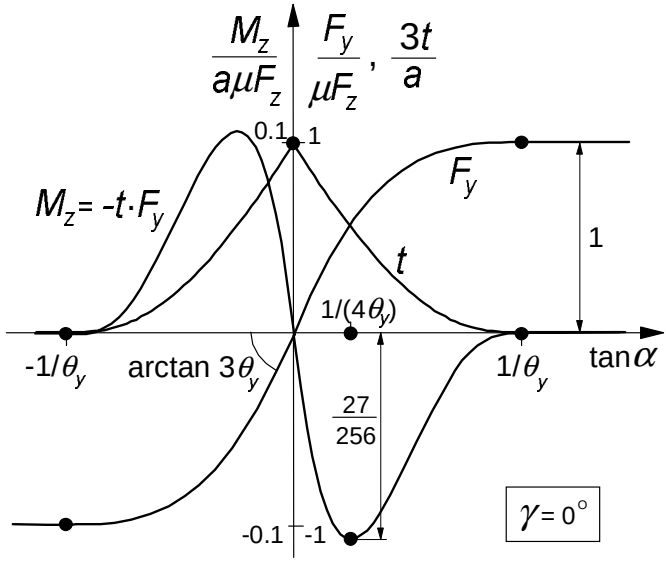

Fig. 3.4. Characteristics of the simple brush model: side force, aligning torque and pneumatic trail vs slip angle.

These relationships have been shown graphically in Fig.3.4. At vanishing slip angle expression (3.13) reduces to

$$t = t_o = -\left(\frac{M_z}{F_y}\right)_{\alpha \to 0} = \frac{1}{3}a \tag{3.14}$$

This value is smaller than normally encountered in practice. The introduction of an elastic carcass will improve this quantitative aspect. Then, the more realistic value of $t \approx 0.5a$ may be achieved (cf. Pacejka 1966 for a stretched string model to represent the elastic carcass and Section 3.3 for a more generally applicable way of approach to account for the carcass compliance). Another point in which the simple model deviates considerably from experimental results concerns the effect of changing the vertical wheel load F_z. With the assumption that the contact length $2a$ changes quadratically with radial tyre deflection ρ and that F_z depends linearly on ρ, so that $a^2 \sim F_z$, it can be easily shown that for the brush model F_y and M_z vary proportionally with F_z and $F_z^{3/2}$ respectively. Experiments, however, show that F_y varies less than linearly with F_z. In most cases, the F_y vs F_z characteristic, obtained at a small value of the slip angle, even shows a maximum after which the cornering force drops with increasing wheel load. Obviously, the same holds for the cornering stiffness $C_{F\alpha}$ (cf. Fig.1.3). Also in this respect the introduction of an elastic carcass (in particular when its lateral

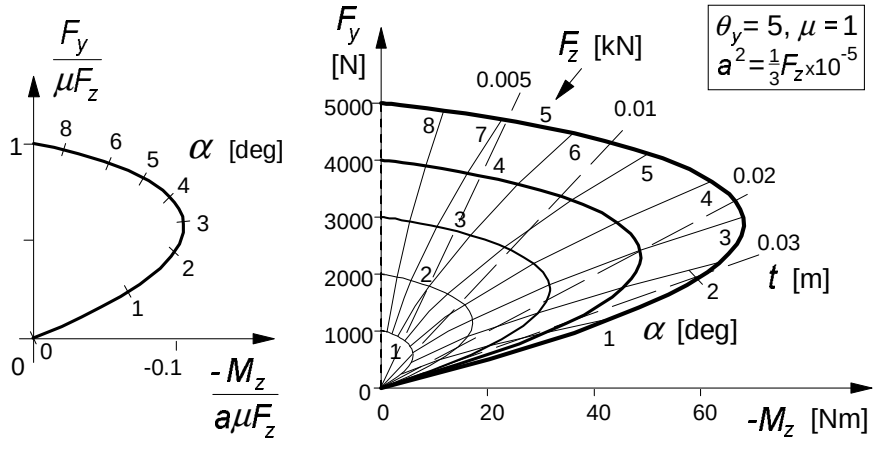

Fig. 3.5. The so-called Gough plot for the brush model, non-dimensional and with dimension using an assumed load vs contact length relationship.

stiffness decreases with increasing normal load) improves the agreement with experiments. When considering a deflected cross section of a tyre with side walls modelled as membranes under tension encapsulating pressurised air, such a decrease in lateral stiffness can be found to occur in theory (cf. Pacejka 1981, p.729 and 730).

An interesting diagram is the so-called Gough-plot, in which F_y is plotted vs M_z for a series of constant values of F_z (or possibly of μ at constant F_z) and of α respectively. This produces two sets of curves shown in Figs.3.5 and 3.6. In the first figure, the characteristics for the brush model have been presented. The

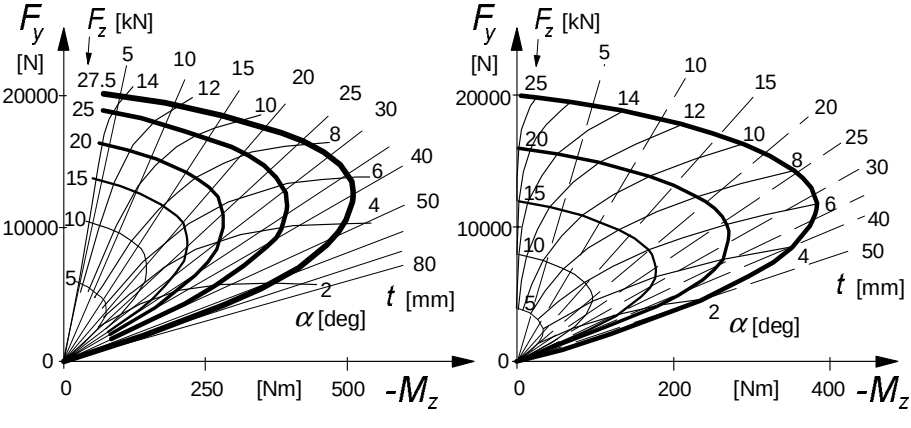

Fig. 3.6. Left: Gough plot of truck tyre 9.00-20, measured on a dry road surface (Freudenstein, 1961). Right: brush model with tread element stiffness c_p decaying linearly with F_z.

left-hand diagram shows that when made non-dimensional, a single curve results. The second figure presents the measured curves for a truck tyre and in addition a diagram according to the brush model. The model has been adapted to include the non-linear relationship of the cornering stiffness versus vertical load by making the tread element stiffness decrease linearly with vertical load. As can be seen from the left-hand plot (at large values of α where saturation of F_y occurs), the truck tyre also exhibits a decay in friction coefficient with increasing vertical load (not included in the model calculations), cf. also Fig.1.3. Further, as expected, the actual tyre generates an aligning torque larger than according to the model.

3.2.2. Pure Longitudinal Slip

For the brush-type tyre model with tread elements flexible in longitudinal direction, the theory for longitudinal (braking or driving) force generation develops along similar lines as those set out in Section 3.2.1 where the side force and aligning torque response to slip angle has been derived. To simplify the discussion, we restrict ourselves here to non-negative values of the forward speed V_x and of the speed of revolution Ω.

In Fig.3.7 a side-view of the brush model has been shown. As was indicated before, the so-called slip point S is introduced. This is an imaginary point attached to the wheel rim and is located, at the instant considered, a distance equal to the effective rolling radius r_e (defined at free rolling) below the wheel centre. At free rolling, by definition, the slip point S has a velocity equal to zero.

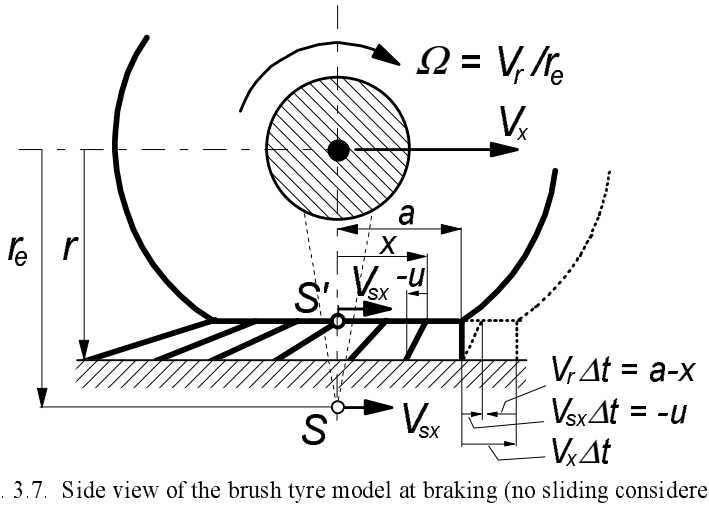

Fig. 3.7. Side view of the brush tyre model at braking (no sliding considered).

Then, it forms the instantaneous centre of rotation of the wheel rim. We may think of a slip circle with radius r_e that in case of free rolling rolls perfectly, that is: without sliding, over an imaginary road surface that touches the slip circle in point S. When the wheel is being braked, point S moves forward with the longitudinal slip velocity V_{sx}. When driven, the slip point moves backwards with consequently a negative slip speed. In the model, a point S' is defined that is attached to the base line at its centre (that is, at the base point of the tread element below the wheel centre, cf. Fig.3.7). By definion, the velocity of this point is the same as that of point S. That means that S' also moves with the same slip speed V_{sx}. It is assumed that the tread elements attached at their base points to the circumferentially rigid carcass, enter the contact area in vertical position. At free rolling with slip speed V_{sx} (of both points S and S') equal to zero, the orientation of the elements remains vertical while moving from front to rear through the contact zone. Consequently, no longitudinal force is being transmitted and we have a wheel speed of revolution:

$$\Omega = \Omega_o = \frac{V_x}{r_e} \tag{3.15}$$

Here it is assumed that the longitudinal component of the speed of propagation of the contact centre C is equal to the longitudinal component of the speed of the wheel centre ($V_{cx} = V_x$). As has been seen in the previous chapter this will occur on a flat road surface at vanishing $\gamma\dot{\psi}$. When Ω differs from its value at free rolling Ω_o the wheel is being braked or driven and the longitudinal slip speed V_{sx} becomes:

$$V_{sx} = V_x - \Omega r_e \tag{3.16}$$

In the model, the base points of all the tread elements move with the same speed V_{sx}. A base point progresses backwards through the contact zone with a speed V_r called the linear speed of rolling. Apparently, we have:

$$V_r = \Omega r_e = V_x - V_{sx} \tag{3.17}$$

An element the tip of which adheres to the ground and the base point is moved towards the rear over a distance a-x from the leading edge (for which a time span $\Delta t = (a - x)/V_r$ is needed) has developed a deflection in longitudinal direction:

$$u = -V_{sx} \frac{a - x}{V_r} \tag{3.18}$$

The same expression may be obtained by integration of the fundamental equation (2.55) and noting that $V_{gx} = \omega_z = \partial u/\partial t = \theta$'s $= 0$ and finally using the boundary condition $u = 0$ at $x = a$.

We may write the longitudinal deflection u in terms of the 'practical' longitudinal slip $\kappa = -V_{sx}/V_x$:

$$u = -(a-x)\frac{V_{sx}}{V_x - V_{sx}} = (a-x)\frac{\kappa}{1+\kappa} \tag{3.19}$$

In terms of the alternative definition of longitudinal slip: the 'theoretical' slip, to be used in the subsequent section and defined as

$$\sigma_x = -\frac{V_{sx}}{V_r} = \frac{\kappa}{1+\kappa} \tag{3.20}$$

(note, we restrict ourselves to non-negative speeds of rolling: $V_r \geq 0$ and $\kappa \geq -1$) we obtain:

$$u = (a-x)\sigma_x \tag{3.21}$$

In Section 3.2.1 we found with Eqs.(3.1) and (3.10) for the lateral deflection at pure side slip ($\sigma_y = \tan\alpha$):

$$v = (a-x)\sigma_y \tag{3.22}$$

Comparison of the equations (3.21) and (3.22) shows that the longitudinal deformations u will be equal in magnitude to the lateral deformations v if $\sigma_y = \tan\alpha$ equals $\sigma_x = \kappa/(1+\kappa)$. For equal tread element stiffnesses ($c_{px} = c_{py}$) and friction coefficients ($\mu_x = \mu_y$) in lateral and longitudinal directions, the slip force characteristics in both directions are identical when $\tan\alpha$ and $\kappa/(1+\kappa)$ are used as abscissa, cf. Fig.3.8. Also, Eq.(3.11) holds for the longitudinal force F_x if the subscripts y are replaced by x and $\tan\alpha$ by κ.

Obviously, total sliding will start at $\sigma_x = \kappa/(\kappa+1) = \pm 1/\theta_x$ or in terms of the practical slip at:

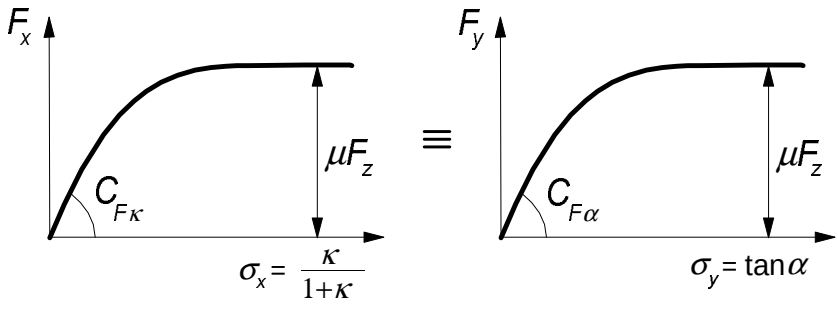

Fig.3.8. Equality of the two pure slip characteristics for an isotropic tyre model if plotted against the theoretical slip.

$$\kappa = \kappa_{sl} = \frac{-1}{1 \pm \theta_x} \tag{3.23}$$

with

$$\theta_x = \frac{2}{3} \frac{c_{px} a^2}{\mu F_z} \tag{3.24}$$

Linearization for small values of slip κ yields a deflection at coordinate x:

$$u = (a - x)\kappa \tag{3.25}$$

and a fore and aft force

$$F_x = 2 c_{px} a^2 \kappa \tag{3.26}$$

with c_{px} the longitudinal tread element stiffness per unit length. This relation contains the longitudinal slip stiffness

$$C_{F\kappa} = (\partial F_x / \partial \kappa)_{\kappa = 0} = 2 c_{px} a^2 \tag{3.27}$$

For equal longitudinal and lateral stiffnesses ($c_{px} = c_{py}$) we obtain equal slip stiffnesses $C_{F\kappa} = C_{F\alpha}$. In reality, however, appreciable differences between the measured values of $C_{F\kappa}$ and $C_{F\alpha}$ may occur (say $C_{F\kappa}$ about 50% larger than $C_{F\alpha}$) which is due to the lateral (torsional) compliance of the carcass of the actual tyre. Still, it is expected that qualitative similarity of both pure slip characteristics remains.

3.2.3. Interaction between Lateral and Longitudinal Slip (combined slip)

For the analysis of the influence of longitudinal slip (or longitudinal force) on the lateral force and moment generation properties we shall, for the sake of mathematical simplicity, restrict ourselves to the case of equal longitudinal and lateral stiffnesses of the tread elements (isotropic model), i.e.:

$$c_p = c_{px} = c_{py} \tag{3.28}$$

and equal and constant friction coefficients

$$\mu = \mu_x = \mu_y \tag{3.29}$$

Again a parabolic pressure distribution is considered.

Figure 3.9 depicts the deformations which arise when the tyre model which runs at a given slip angle α is driven or braked. Due to the equal stiffness in all

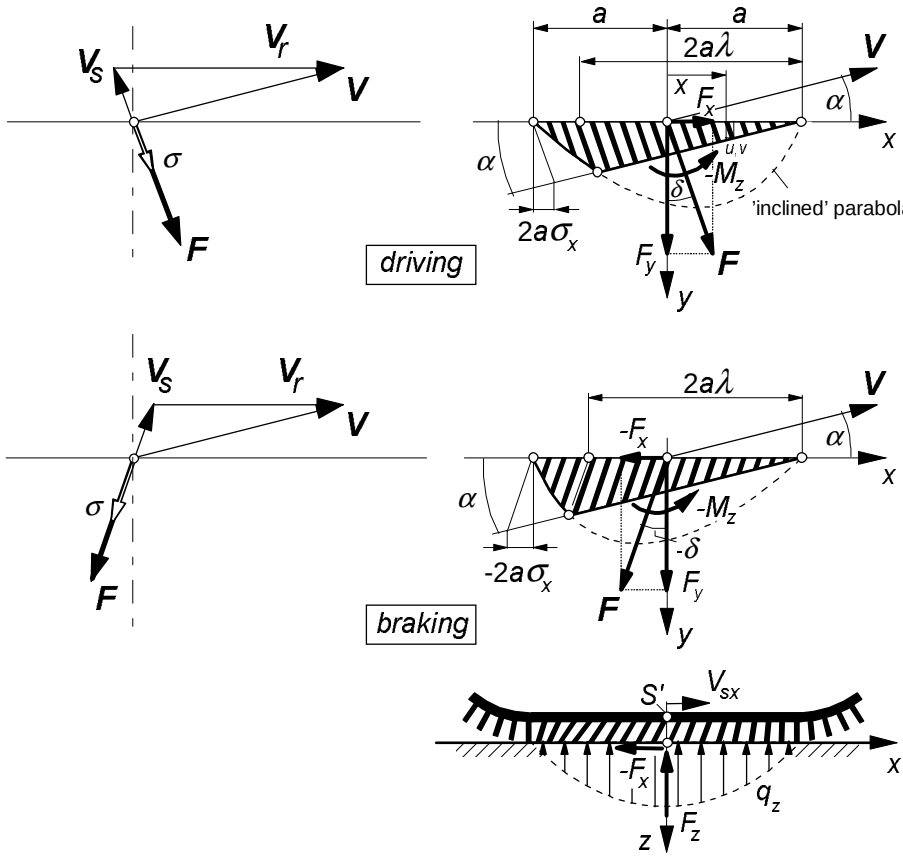

Fig. 3.9. Vector diagram and deformation of the brush model running at a given slip angle for the cases of driving and braking.

horizontal directions and the isotropic friction properties, the deflections are directed opposite to the slip speed vector V_s, also in the sliding region. In this latter region, the tips of the elements slide over the road with sliding speed V_g directed opposite to the local friction force q (per unit contact length). The whole deformation history of a tread element while running through the contact area is a one-dimensional process along the direction of V_s.

The velocity of progression of a base point through the contact length is the rolling speed V_r (again assumed non-negative). The deflection rate of an element in the adhesion region is equal to the slip speed V_s. The time which elapses from the point of entrance to the point a distance x in front of the contact centre equals

$$\Delta t = \frac{a - x}{V_r} \tag{3.30}$$

In this position, the deflection of an element that is still in adhesion becomes in vectorial form

$$\boldsymbol{e} = \begin{pmatrix} u \\ v \end{pmatrix} = \boldsymbol{V}_s \Delta t = -\frac{\boldsymbol{V}_s}{V_r}(a - x) \tag{3.31}$$

It seems natural at this stage to introduce the alternative (theoretical) slip quantity again, but now in vectorial form:

$$\boldsymbol{\sigma} = \begin{pmatrix} \sigma_x \\ \sigma_y \end{pmatrix} = -\frac{\boldsymbol{V}_s}{V_r} = -\frac{1}{V_r}\begin{pmatrix} V_{sx} \\ V_{sy} \end{pmatrix} \tag{3.32}$$

with the linear speed of rolling

$$V_r = V_x - V_{sx} \tag{3.33}$$

The relations of these theoretical slip quantities with the practical slip quantities κ (= $-V_{sx}/V_x$) and $\tan\alpha$ (= $-V_{sy}/V_x$) are:

$$\sigma_x = \frac{\kappa}{1 + \kappa}$$
$$\sigma_y = \frac{\tan\alpha}{1 + \kappa} \tag{3.34}$$

The deflection of an element in the adhesion region now reads

$$\boldsymbol{e} = (a - x)\boldsymbol{\sigma} \tag{3.35}$$

from which it is apparent that longitudinal and lateral deflections are governed by σ_x and σ_y respectively and independent of each other. This would not be the case if expressed in terms of the practical quantities κ and α!

The local horizontal contact force acting on the tips of the elements (per unit contact length) reads

$$\boldsymbol{q} = c_p(a - x)\boldsymbol{\sigma} \qquad (\textit{adhesion region}) \tag{3.36}$$

As soon as

$$q = |\boldsymbol{q}| = \sqrt{q_x^2 + q_y^2} > \mu q_z \tag{3.37}$$

the sliding region is entered. Then the friction force vector becomes

$$\boldsymbol{q} = -\frac{\boldsymbol{V}_s}{V_s}\mu q_z = \frac{\boldsymbol{\sigma}}{\sigma}\mu q_z \qquad (\textit{sliding region}) \tag{3.38}$$

where

$$V_s = \sqrt{V_{sx}^2 + V_{sy}^2} \tag{3.39}$$

and

$$\sigma = \sqrt{\sigma_x^2 + \sigma_y^2} \tag{3.40}$$

Similarly, the magnitude of the deflection of an element becomes:

$$e = |\boldsymbol{e}| = \sqrt{u^2 + v^2} \tag{3.41}$$

The point of transition from adhesion to sliding region is obtained from the condition:

$$c_p e = \mu q_z \tag{3.42}$$

or

$$c_p \sigma (a - x_t) = \frac{3}{4} \mu F_z \frac{a^2 - x_t^2}{a^3} \tag{3.43}$$

which yields

$$x_t = \frac{4}{3} \frac{c_p a^3 \sigma}{\mu F_z} - a = a(2\theta\sigma - 1) \tag{3.44}$$

or in similar terms as Eq. (3.8):

$$\lambda = 1 - \theta\sigma \tag{3.45}$$

where analogous to expressions (3.6) and (3.24) for the isotropic model parameter θ reads:

$$\theta = \theta_y = \theta_x = \frac{2}{3} \frac{c_p a^2}{\mu F_z} \tag{3.46}$$

From Eq.(3.45) the slip σ_{sl} at which total sliding starts can be calculated. We get analogous to (3.9)

$$\sigma_{sl} = \frac{1}{\theta} \tag{3.47}$$

The magnitude of the total force $F = |\boldsymbol{F}|$ now easily follows in accordance with (3.11):

$$F = \mu F_z (1 - \lambda^3) = \mu F_z \{3\theta\sigma - 3(\theta\sigma)^2 + (\theta\sigma)^3\} \quad \text{for } \sigma \le \sigma_{sl}$$

$$F = \mu F_z \qquad \text{for } \sigma \ge \sigma_{sl} \tag{3.48}$$

and obviously follows the same course as those shown in Fig.3.8. The force vector $\boldsymbol{F}$ acts in a direction opposite to $\boldsymbol{V}_s$ or $-\boldsymbol{\sigma}$. Hence

$$\boldsymbol{F} = F\frac{\boldsymbol{\sigma}}{\sigma} \tag{3.49}$$

from which the components F_x and F_y may be obtained.

The moment $-M_z$ is obtained by multiplication of F_y with the pneumatic trail t. This trail is easily found when we realize that the deflection distribution over the contact length is identical with the case of pure side slip if $\tan\alpha_{eq} = \sigma$ (cf. Fig. 3.10). Consequently, the formula (3.13) represents the pneumatic trail at combined slip as well if $\theta_y\sigma_y$ is replaced by $\theta\sigma$. We have with (3.13):

$$M_z = -t(\sigma)\cdot F_y \tag{3.50}$$

In Figs.3.11 and 3.12 the dramatic reduction of the pure slip forces (the side force and the longitudinal force respectively) that occurs as a result of the simultaneous introduction of the other slip component (the longitudinal slip and the side slip respectively) have been indicated. We observe an (almost) symmetric shape of these interaction curves. The peak of the side force versus longitudinal slip curves at constant values of the slip angle appears to be slightly shifted towards the braking side. This phenomenon will be further discussed in connection with the alternative representation of the same results according to Fig.3.13. At very large longitudinal slip that is when $|V_{sx}|/V_x \to \infty$ the side force approaches zero and the same occurs for the longitudinal force when the lateral slip $\tan\alpha$ goes to infinity ($\alpha \to 90°$) at a given value of the longitudinal slip because obviously in that case with $V_x \to 0$ also the longitudinal slip speed must vanish. For a locked wheel with $V_{sx} = V_x$ and $\kappa = -1$ we have $F_y = \mu F_z \sin\alpha$ and $F_x = -\mu F_z \cos\alpha$.

In the diagram of Fig.3.13 the calculated variations of F_y and M_z with F_x have been plotted for several fixed values of α. Also the curves for constant κ have

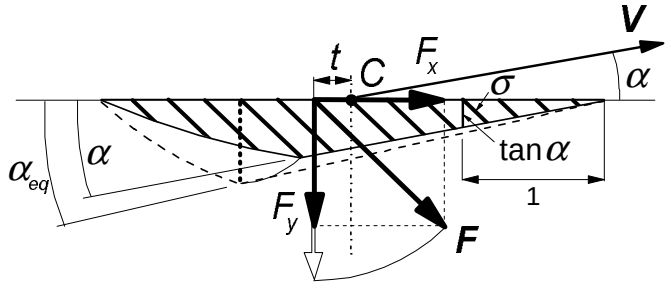

Fig. 3.10. Equivalent side slip angle producing the same pneumatic trail t.

been depicted. For clarification of the nature of the F_y - F_x diagram the deflection of an element near the leading edge has been shown in Fig.3.14. Since the distance from the leading edge has been defined for this occasion to be equal to unity the deflection e of the element equals the slip σ. The radius of the circle denoting maximum possible deflections is equal to σ_{sl}. The two points on the

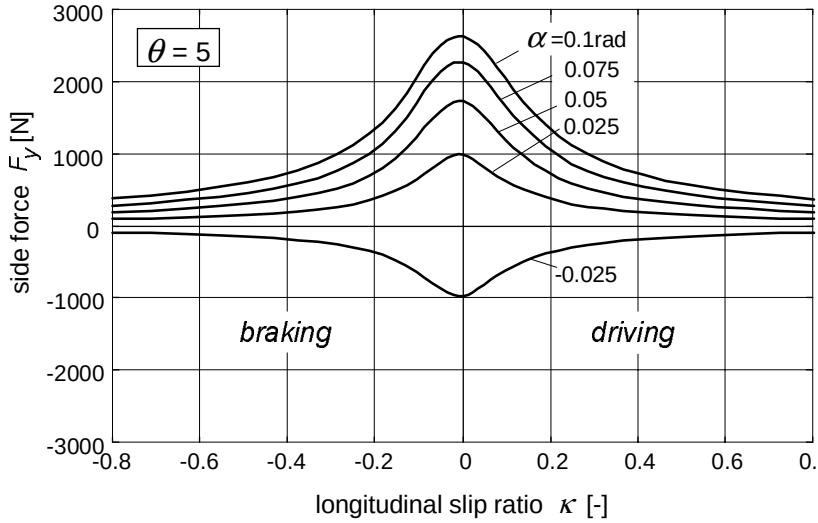

Fig. 3.11. Reduction of side force due to the presence of longitudinal slip.

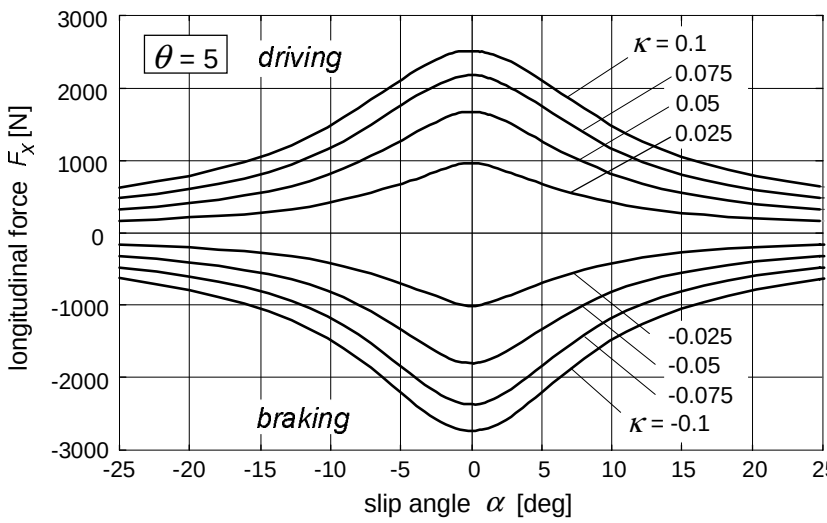

Fig. 3.12. Reduction of longitudinal force due to the presence of side slip.

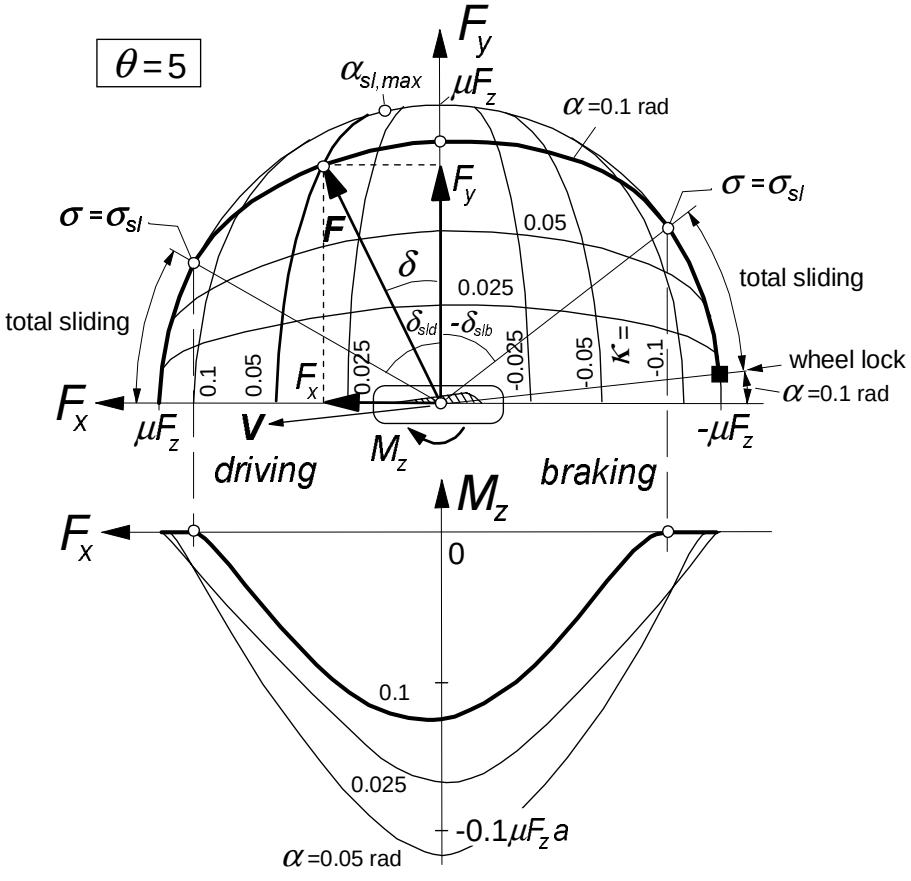

Fig. 3.13. Cornering force and aligning torque as functions of longitudinal force at constant slip angle α or longitudinal slip κ.

circle where at the α considered the sliding boundary σ_{sl} is attained correspond to the points on the α curve of the force diagram of Fig.3.13. This also explains the slightly inclined nature of the α curves. At braking, F_y appears to be a little larger than at driving. This is at least true for the two cases of Fig.3.9, one at driving and the other at braking, showing the same slip angle and the same magnitude of the deviation angle δ of the slip velocity vector and thus of the force vector with respect to the y axis. Then, the slip speeds V_s are equal in magnitude, but at braking the speed of rolling V_r is obviously smaller. When considering the definition of the theoretical slip σ (3.32) and the functional relationship (3.48) with the force F it becomes clear that F must be larger for the case of braking because of the then larger magnitude of σ. Finally, the case of wheel lock is pointed at. Then, the force vector $\boldsymbol{F}$ which in magnitude is equal

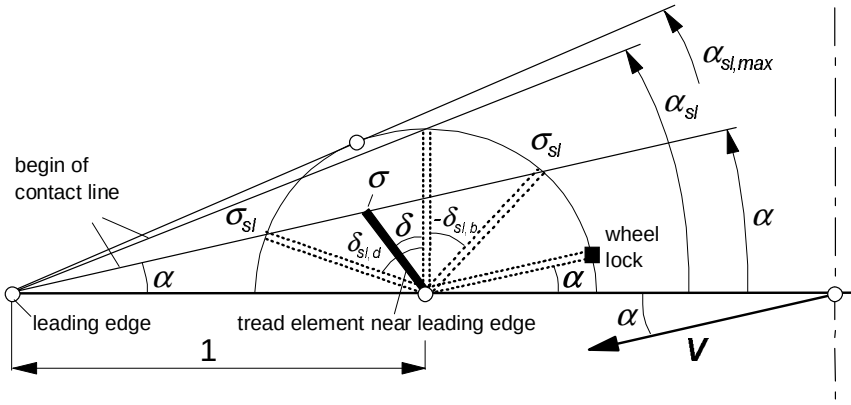

Fig.3.14. The situation near the leading edge. Various deflections of an element at a distance equal to 1 from the leading edge are shown corresponding with points in the upper diagram of Fig.3.13.

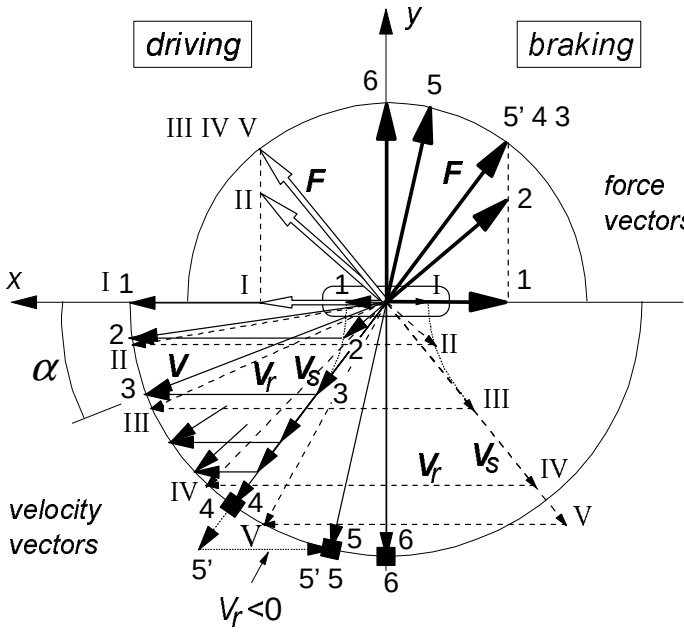

Fig. 3.15. The F_x - F_y diagram extended with the corresponding velocity diagram. The brake (pedal) force is kept constant while the slip angle is increased. The same is done at a constant driving effort. In the case of braking the speed of rolling V_r decreases until the wheel gets locked. In the special case 5' the wheel is rotated backwards to keep the slip speed V_s and thus the force vector $\boldsymbol{F}$ in the original direction.

to μF_z, is directed opposite to the speed vector of the wheel V which then coincides with the slip speed vector V_s.

Experimental evidence (e.g. Fig.3.17) supports the nature of the theoretical curves for the forces as shown in Fig.3.13. Often, the shape appears to be more asymmetric than predicted by the simple brush model. This may be due to a slight increase in the contact length while braking (making the tyre stiffer) and by the brake force induced slip angle of the contact patch at side slip. This is accomplished through the torsion of the carcass induced by the moment about the vertical axis that is exerted by the braking force which has shifted its line of action due to the lateral deflection connected with the side force. The more advanced model to be developed further on in this chapter will take the latter effect into account.

The moment curves presented in the lower diagram of Fig.3.13 show a more or less symmetrical bell shape. As expected, the aligning torque becomes equal to zero when total sliding occurs ($\sigma \geq \sigma_{sl}$). Later on, we will see that these computed moment characteristics may appreciably deviate from experimentally obtained curves.

At this stage, we will first apply the knowledge gained sofar to the analysis of a practical situation that occurs with a wheel that is braked or driven (at constant brake pressure and throttle respectively) while its slip angle is varied.

In Fig.3.15 the force diagram is shown in combination with the corresponding

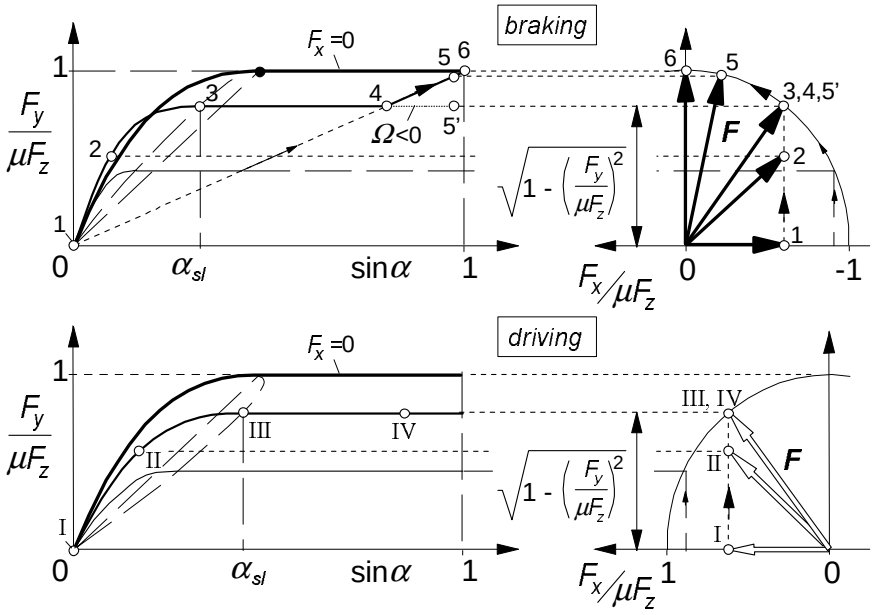

Fig. 3.16. Tyre characteristics at constant brake (pedal) force and driving force. Numerals correspond to those of Fig. 3.15.

velocity diagram. At a given braking force $-F_x$ and wheel speed of travel V, the slip angle α is changed from zero to $90°$. The variation of slip speed V_s and rolling speed V_r may be followed from case 1 where $\alpha = 0$ to case 3 where total sliding starts and further to case 4 where V_r and thus Ω vanishes and the wheel becomes locked. A further increase of α (at constant brake pedal force) as in case 5 will necessarily lead to a reduction in braking force $-F_x$ unless the wheel is rotated in opposite direction ($\Omega < 0$) as represented by case 5'. In the cases of driving indicated by Roman numerals the driving force F_x can be maintained irrespective of the value of α (with $|\alpha| < 90°$).

The nature of the resulting F_y - α characteristics at given driving or braking effort is shown in Fig.3.16. Plotting of F_y versus $\sin\alpha$ is advantageous because the portion where wheel lock occurs is then represented by a straight line.

Another important advantage of putting $\sin\alpha$ instead of $\tan\alpha$ along the abscissa is that (after having completed the diagram for negative values of $\sin\alpha$ resulting in an oddly symmetric graph) the complete range of α is covered: the speed vector V may swing around over the whole range of $360°$. An application in vehicle dynamics will be discussed in Section 3.4 of this chapter (yaw instability at locked rear wheels).

For illustration we have shown in Figs.3.17 and 18 experimentally assessed characteristics. The force diagrams correspond reasonably well with the theoretical observations. The moment curves, however, deviate considerably from the theoretical predictions (compare Fig.3.18 with Fig.3.13). It appears that according to this figure M_z changes its sign in the braking half of the diagram. This phenomenon can not be explained with the simple tyre brush model that has been employed thus far.

The introduction of a laterally flexible carcass seems essential for a proper on a driven or braked wheel. In Fig.3.19 a possible extension of the brush model is depicted. The carcass line is assumed to remain straight and parallel to the wheel plane in the contact region. A lateral and longitudinal compliance with respect to the wheel plane is introduced. In addition, a possible initial off set of the line of action of the longitudinal force with respect to the wheel centre plane is regarded. Such an off set is caused by asymmetry of the construction of the tyre or by the presence of a camber angle.

With this model the moment M_z is composed of the original contribution M_z' established by the brush model and those due to the forces F_y and F_x which show lines of action shifted with respect to the contact centre C over the distances u_c and $v_o + v_c$ respectively. The self-aligning torque now reads:

$$\begin{aligned} M_z &= M_z' - F_x(v_o + v_c) + F_y u_c \\ &= M_z' - c\,F_x F_y - F_x v_o \end{aligned} \tag{3.51}$$

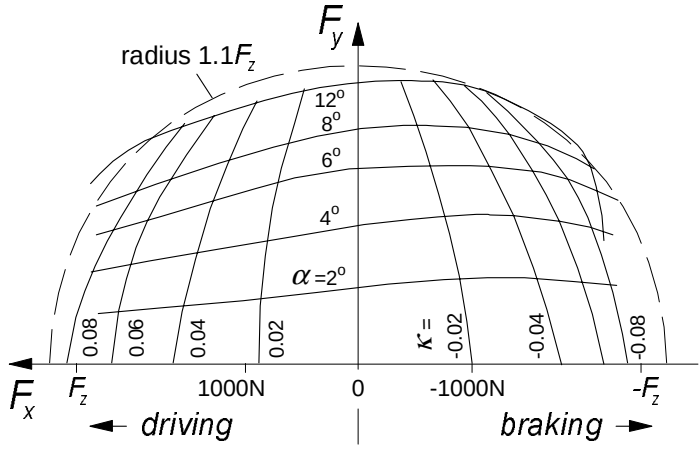

Fig. 3.17. F_y - F_x characteristics for 6.00-13 tyre measured on dry internal drum with diameter of 3.8m (from Henker 1968).

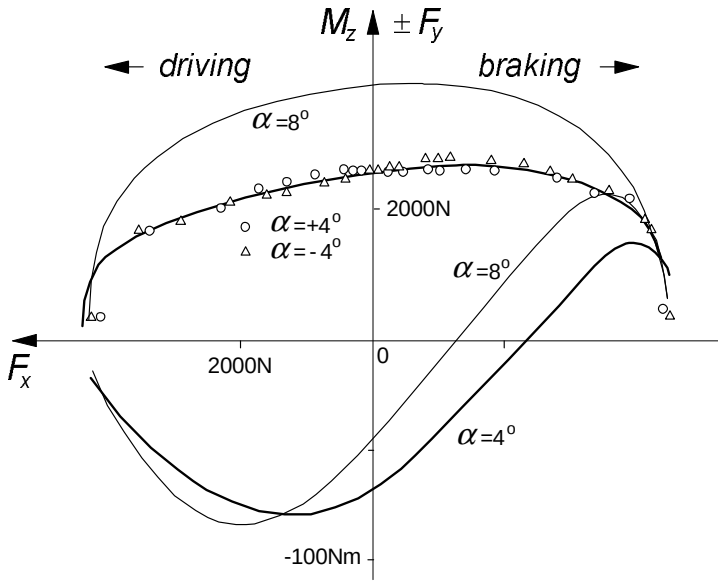

Fig. 3.18. Combined slip side force and moment versus longitudinal force characteristics measured at two values of the slip angle for a 7.60-15 tyre on a dry flat surface (from Nordeen and Cortese (1963)).

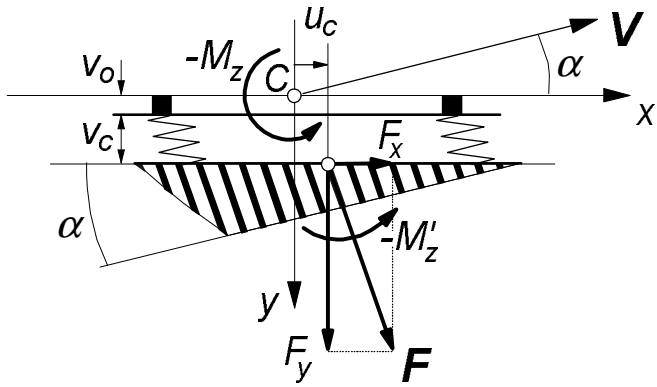

Fig. 3.19. Extended tyre brush model showing off set and deflection of carcass line (straight and parallel to wheel plane).

where the compliance coefficient c has been introduced that is defined by:

$$c = \frac{\varepsilon_y}{C_{cy}} - \frac{\varepsilon_x}{C_{cx}} \tag{3.52}$$

Here, C_{cx} and C_{cy} denote the longitudinal and lateral carcass stiffnesses respectively and ε_x and ε_y the effective fractions of the actual displacements. These fractions must be considered because of concurrent lateral and longitudinal rolling of the tyre lower section against the road surface under the action of a lateral and fore and aft force respectively which will change the normal force distribution in the contact patch and thereby reduce the actual displacements of the lines of action of both horizontal forces. The resulting calculations can be performed in a direct straightforward manner because the slip angle of the extended model is the same as the one for the internal brush model. Later on, in Section 3.3, the effect of the introduction of a torsional and bending stiffness of the carcass and belt will be discussed. The resulting model, however, is a lot more complex and closed form solutions are no longer possible. In Sec.3.3 the technique of the tread element following method will be employed in the tread simulation model to determine the response.

The combined slip response of the simple extended model of Fig.3.19 is given in the Figs.3.20 and 3.21. It is observed that in Fig.3.20 the aligning torque changes its sign in the braking range. This is due to the term in Eq.(3.51) with the compliance coefficient c. The resulting qualitative shape is quite similar to the experimentally found curves of Fig.3.18. In Fig.3.21 the effect of an initial off set of v_o=5mm has been depicted.

Here carcass compliance has been disregarded and only the last term of (3.51) has been added. We see that a moment is generated already at zero slip

angle. The curves found in Fig.3.13 for non-zero side slip are then simply added to the inclined straight line belonging to $\alpha = 0$. The type of curves that result are often found experimentally. The effect of lateral compliance may then be very

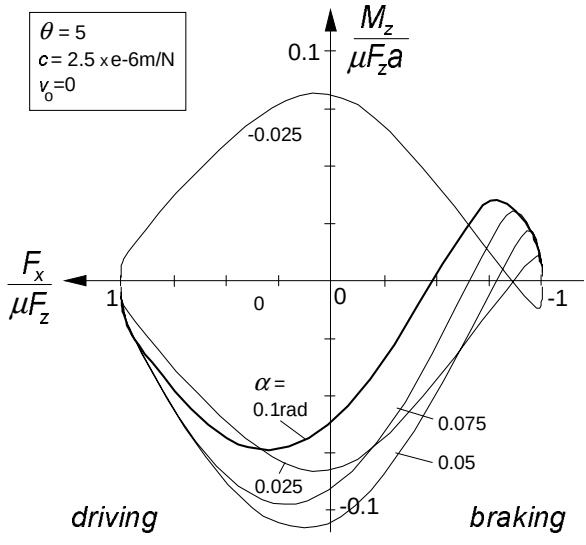

Fig. 3.20. The influence of lateral carcass compliance on the aligning torque for a braked or driven wheel according to the extended brush model.

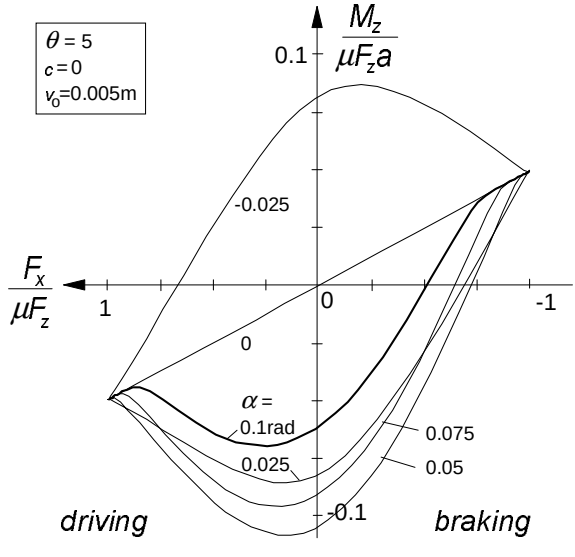

Fig. 3.21. The influence of an initial lateral off set v_o of F_x on the aligning torque for a braked or driven wheel according to the extended brush model.

small or cancelled out by the effect of the fore and aft compliance of the carcass (second term of right-hand member of (3.52)).

Exercise 3.1. Characteristics of the brush model

Consider the brush tyre model as treated in Section 3.2. Elastic and frictional properties are the same in all horizontal directions and Eq.(3.46) holds.
For $0 \leq \alpha \leq \frac{1}{2}\pi$ the side force characteristic is described by (according to Eq.(3.11))

$$F_y = \mu F_z(3\theta \tan\alpha - 3\theta^2 \tan^2\alpha + \theta^3 \tan^3\alpha) \qquad (\alpha \leq \alpha_{sl})$$
$$F_y = \mu F_z \qquad (\alpha \geq \alpha_{sl})$$

1. Calculate the value of θ and $\tan\alpha_{sl}$ for
   $\mu F_z = 2000$ N
   $C_{F\alpha} = 18000$ N/rad
2. Sketch the $F_y(\tan\alpha)$ characteristic and also the $M_z(\tan\alpha)$ and $t(\tan\alpha)$ curves (according to Eqs.(3.12, 13)) for
   $a = 0.1$ m
3. Replace in the $F_y(\tan\alpha)$ diagram the ordinate F_y by F and the abscissa $\tan\alpha$ by σ thereby assessing the total force vs slip diagram. Calculate the slip values σ_x, σ_y and σ using equations (3.34) and (3.40) for one value of $\tan\alpha = 0.15$ and a number of values of κ in a suitable range (e.g. from $-1/\theta$ to $+1/\theta$). Determine the force vector $\boldsymbol{F}$ for each of the κ values and sketch the F_y - F_x curve for $\tan\alpha = 0.15$. Draw the friction circle with radius $F_{max} = \mu F_z$ in which the curve will appear. Note the two points where $\sigma = \sigma_{sl}$ (= $\tan\alpha_{sl}$) where the curve touches the circle. Indicate the point where wheel lock occurs.
4. Replace in the $t(\tan\alpha)$ diagram the abscissa by σ thereby establishing the $t(\sigma)$ diagram. Determine the values of $M_z' = -tF_y$ for the same series of κ values and $\tan\alpha = 0.15$.
5. Now use Eq.(3.51) and calculate the torque M_z for a lateral carcass stiffness $C_{cy} = 60000$ N/m ($C_{cx} \to \infty$) and disregard the correction factor ε_y (=1).
6. Draw for the cases mentioned in question 3 where the α curve touches the friction circle ($\sigma = \sigma_{sl}$), the force and velocity diagram according to Fig.3.15. Do the same for the case of wheel lock.
7. Sketch the $F_y(\sin\alpha)$ characteristics (Fig.3.16) for $F_x = 0$ and also for that constant brake pedal force corresponding to the value of $-F_x$ where the $\tan\alpha = 0.15$ curve touches the friction circle ($\sigma = \sigma_{sl}$).

3.2.4. Camber and Turning (Spin)

For the study of horizontal cornering, one should not only consider side slip but also the influence of two other effects, which in most cases (except for the motorcycle) are of much less importance than side slip. The introduction of these two input variables which completes the description of the out-of-plane tyre force and moment generation, are firstly the wheel camber or tilt angle γ between the wheel plane and the normal to the road (cf. Fig. 2.6), and secondly the turn slip $\dot{\psi}/V_x$. Both are components of the total spin φ. First, we will analyse the situation in the absence of lateral and longitunal wheel slip.

Pure spin

In the steady state case the turn slip equals the curvature $1/R$ of a circular path with radius R. For homogeneous rolling bodies (solid rubber ball, steel railway wheel) the mechanisms to produce side force and moment as a result of camber and turning are equal as they both originate from the same spin motion (cf. Eq. (2.17)). For a tyre with its rather complex structure the situation may be quantitatively different for the two components of spin.

As depicted in Fig.3.22, the wheel is considered to move tangentially to a circular horizontal path with radius R while the wheel plane shows a constant camber angle γ and apparently the slip angle is kept equal to zero. The wheel is picturised here as a part of an imaginary ball. When lifted from the ground, the

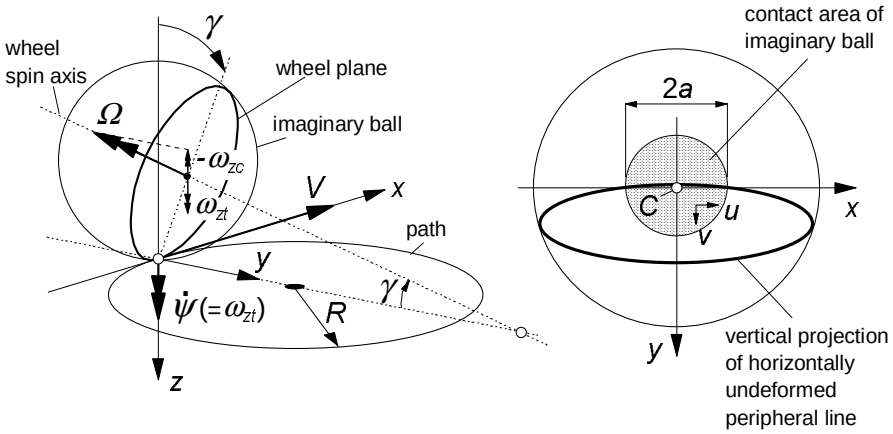

Fig. 3.22. Wheel rolling at a camber angle while turning along a circular path without side slip. At the right: a top-view of the peripheral line of the non-rolling wheel considered as being a part of an imaginary ball pressed against a flat surface.

intersection of wheel plane and ball outer surface forms the peripheral line of the tyre. When loaded vertically, the ball and consequently the peripheral line are assumed to show no horizontal deformations, which in reality will approximately be the case for a homogeneous ball showing a relatively small contact area.

We apply the theory of a rolling and slipping body and consider equations (2.55, 56) and restrict ourselves to the case of steady-state pure spin, that is: with $\alpha = \kappa = 0$. Then with turn slip velocity $\omega_{zt} = \dot{\psi}$ in Fig.3.22 we find

$$V_{sx} = 0\,,\ V_{sy} = 0\,,\ V_r = V_c\,,\ \omega_z = \dot{\psi} - \Omega \sin\gamma = V_c\left(\frac{1}{R} - \frac{1}{r_e}\sin\gamma\right) \tag{3.53}$$

Furthermore, the difference between (x,y) and (x_o,y_o) will be neglected and tyre conicity and ply-steer disregarded.. The correction factors θ attributed to camber may be approximated by:

$$\theta_{\gamma x}(y) = -\varepsilon_{\gamma x}\,,\quad \theta_y(x,y) = -\varepsilon_{\gamma y}\frac{x}{r_e}\sin\gamma \tag{3.54}$$

with both reduction factors ε equal or close to zero for a railway wheel or a motorcycle tyre and expected to be closer to unity for a steel belted car or truck tyre, cf. discussion below Eq. (3.117). With both factors assumed equal and denoted as ε_γ we may define a total actual spin

$$\varphi = -\frac{1}{V_c}\{\dot{\psi} - (1 - \varepsilon_\gamma)\Omega \sin\gamma\} = -\frac{1}{R} + \frac{1 - \varepsilon_\gamma}{r_e}\sin\gamma \tag{3.55}$$

The last term represents the curvature $-1/R_\gamma$ of the tyre peripheral line touching a frictionless surface at a cambered position. When disregarding a possible uniform offset of this line we obtain when integrating (2.52) by using (3.54) and approximating (2.51) by taking $\dot{x}_o = \dot{x} = r_e\Omega$:

$$y_o = y_{\gamma o} = -\frac{1 - \varepsilon_\gamma}{2r_e}(a^2 - x^2)\sin\gamma \tag{3.56}$$

which reduces expressions (2.55, 56) for the sliding velocities with (3.53-55) to:

$$\begin{aligned} V_{gx} &= -\left(\frac{\partial u}{\partial x} - y\varphi\right)V_c \\ V_{gy} &= -\left(\frac{\partial v}{\partial x} + x\varphi\right)V_c \end{aligned} \tag{3.57}$$

In the range of adhesion where the sliding velocities vanish, the deflection gradients become:

$$\frac{\mathrm{d}u}{\mathrm{d}x} = y\varphi\ , \qquad \frac{\mathrm{d}v}{\mathrm{d}x} = -x\varphi \tag{3.58}$$

Integration yields the following expressions for the horizontal deformations in the contact area:

$$\begin{aligned} u &= yx\varphi + C_1 \\ v &= -\tfrac{1}{2}x^2\varphi + C_2 \end{aligned} \tag{3.59}$$

The second expression is, of course, an approximation of the actual variation which is according to a circle. The approximation is due to the assumption made that the deflections v are much smaller than the path radius R. The constants of integration follow from boundary conditions which depend on the tyre model employed and on the slip level. As an example, consider the simple brush model with horizontal deformations through elastic tread elements only. The contact area is assumed to be rectangular with length $2a$ and width $2b$ and filled with an infinite number of tread elements. In Fig.3.23 three rows of tread elements have been shown in the deformed situation. For this model the following boundary conditions apply:

$$x = a: \quad v = u = 0 \tag{3.60}$$

With the use of (3.59) the formulae for the deformations in the adhesion zone starting at the leading edge read:

$$\begin{aligned} u &= -y(a - x)\varphi \\ v &= \tfrac{1}{2}(a^2 - x^2)\varphi \end{aligned} \tag{3.61}$$

After introducing c'_{px} and c'_{py} denoting the stiffness of the tread rubber per unit area in x and y direction respectively and assuming small spin and hence vanishing sliding, we can calculate the lateral force and the moment about the vertical axis by integration over the contact area. We obtain:

$$\begin{aligned} F_y &= \tfrac{4}{3}c'_{py}a^3 b\varphi = C_{F\varphi}\varphi \\ M_z &= \tfrac{4}{3}c'_{px}a^2 b^3\varphi = C_{M\varphi}\varphi \end{aligned} \tag{3.62}$$

or in terms of path curvature (if $\alpha \equiv 0$ or constant) and camber angle (γ small):

$$\begin{aligned} F_y &= -C_{F\varphi}\left(\frac{1}{R} - \frac{1-\varepsilon_\gamma}{r_e}\gamma\right) = C_{F\varphi}\frac{-1}{R} + C_{F\gamma}\gamma \\ M_z &= -C_{M\varphi}\left(\frac{1}{R} - \frac{1-\varepsilon_\gamma}{r_e}\gamma\right) = C_{M\varphi}\frac{-1}{R} + C_{M\gamma}\gamma \end{aligned} \tag{3.63}$$

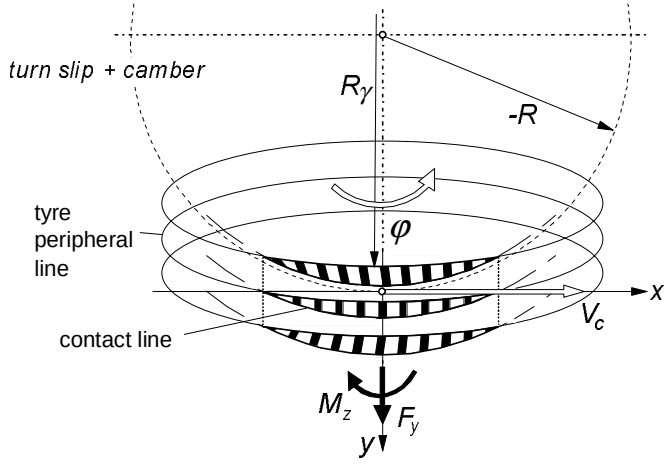

Fig.3.23. Top-view of cambered tyre model rolling in a curve with radius -*R*.

In case of pure turning, the force acting on the tyre is directed away from the path centre and the moment acts opposite to the sense of turning. Consequently both the force and the moment try to reduce the curvature $1/|R|$. In case of pure camber, the force on the wheel is directed towards the point of intersection of the wheel axis and the road plane, while the moment tries to turn the rolling wheel towards this point of intersection. No resulting force or torque is expected to occur when $(1-\varepsilon_\gamma)\sin\gamma = r_e/R$. For the special case that $\varepsilon_\gamma = 0$, this will occur when the point of intersection and the path centre coincide. As the lateral deflection shows a symmetric distribution, the moment must be caused solely by the longitudinal forces. The generation of the moment may be explained by considering three wheels rigidly connected to each other, mounted on one axle. The wheels rotate at the same rate but in a curve the wheel centres travel different distances in a given time interval and when cambered, these distances are equal but the effective rolling radii are different. In both situations opposite longitudinal slip occurs, which results in a braked and a driven wheel (in Fig.3.23 the right and the left-hand wheel respectively) and consequently in a couple M_z.

Up to now we have dealt with the relatively simple case of complete adhesion. When sliding is allowed by introducing a limited value of the coefficient of friction μ, the calculations become quite complicated. When a finite width $2b$ is considered, complete adhesion will only occur for vanishing values of spin. We expect that sliding will start at the left and right rear corners of the contact area, since in these points the available horizontal contact forces reduce to zero and the longitudinal deformations u would become maximal in the hypothetical case

that $\mu \to \infty$. The zones of sliding grow with increasing spin and will thereby cause a less than proportional variation of F_y and M_z with φ. The case of finite contact width is too difficult to handle by a simple analysis. It will be dealt with later on in Sec.3.3 when the tread element following simulation method is introduced.

For now we assume a thin tyre model with $b = 0$. If, as before, a parabolic pressure distribution is assumed with a similar variation of the maximum possible lateral deflection v_{max}, it is obvious from Eq.(3.61) showing that the lateral deflection is also (approximately) parabolic, that no sliding will occur up to a certain critical value of spin φ_{sl}, where the adhesion limit is reached throughout the contact length. Up to this point F_y varies linearly with φ and M_z remains equal to zero.

According to Eq. (3.63) with ε_γ assumed to take a value that is minimally equal to zero, spin due to camber theoretically cannot exceed the value $1/r_e$. Consequently, at larger values of spin turn slip must be involved. Beyond the critical value φ_{sl} the situation becomes quite complex. The discussion may be simplified by considering a turn table on top of which the wheel rolls with its spin axis fixed. The condition of adhesion is satisfied when the deflections remain within the boundaries given by the parabola's $\pm v_{max}$ as indicated in Fig.3.24a. In the same figure the corresponding situation at camber has been indicated at the same value of spin with curvature $1/R_\gamma$ of the deflected peripheral line ($y_{\gamma o}$, Eq.(3.56)) on a $\mu = 0$ surface equal to the path curvature $1/R$.

Sliding occurs as soon as the points of the table surface can cross the adhesion boundary $\pm v_{max}$. This occurs simultaneously for all the points in the front half of the contact line when the path curvature exceeds the curvature of the adhesion boundary. Once the contact point arrives in the rear half of the contact zone (at $x = 0$), the point can maintain adhesion because now the point on the table moves towards the inside of the adhesion boundaries. The point follows a circle until the opposite boundary is reached at $x = x_{s2}$ (cf. Fig.3.24b,c) where the deformation v is opposite in sign and reaches its maximum value v_{max}, after which sliding occurs again. With increasing turn slip φ (= -1/R) this latter sliding zone grows. At the same time the side force F_y decreases and the torque M_z, that arises for $\varphi > \varphi_{sl}$, increases until the situation is reached where R and F_y approach zero and M_z attains its maximum value (tyre standing still and rotating about its vertical axis). In Fig.3.24c the radius R has been considered large with respect to half the contact length a. Then the circle segments may be approximated by parabola's which makes the analysis a lot simpler. In the lower part of the figure a camber equivalent graph has been depicted. The curved contact line in the adhesion range is then converted to a straight (horizontal) line. The graph is obtained from the turn slip graph by subtracting from all the curves the deflection $v_{\varphi\infty}$ that would occur if full adhesion can be maintained (e.g. at μ

$\to \infty$). We use this graph as the basis for the calculation of the force and moment response to spin. First for the case of pure spin and then for the case of combined spin and side slip.

The parameter θ_y defined by Eq.(3.6) is used again and the maximum possible lateral deflection reads according to (3.5):

$$v_{max} = \frac{a^2 - x^2}{2a\theta_y} \tag{3.64}$$

The deflection at assumed full adhesion would become:

$$v_{\varphi\infty} = \tfrac{1}{2}\varphi(a^2 - x^2) \tag{3.65}$$

Equating the deflection at full sliding to the one at full adhesion yields the spin at the verge of sliding:

$$\varphi_{sl} = \frac{\operatorname{sgn}\varphi}{a\theta_y} \tag{3.66}$$

The locations of the transition points indicated in Fig.3.24c are found to be given by the coordinates:

$$x_{s1} = 0,\ x_{s2} = \frac{-a}{\sqrt{\tfrac{1}{2}(a\theta_y|\varphi| + 1)}},\quad y_{s1} = y_{s2} = -\frac{a\theta_y|\varphi| - 1}{2\theta_y}a\operatorname{sgn}\varphi \tag{3.67}$$

The deflections become in the first and second sliding regions and in the adhesion region respectively:

$$v_1 = -v_3 = v_{max}\operatorname{sgn}\varphi\ ,\quad v_2 = y_{sl} + v_{\varphi\infty} \tag{3.68}$$

Integration over the contact length yields for the side force:

$$F_y = \mu F_z\sqrt{2}\frac{\operatorname{sgn}\varphi}{\sqrt{a\theta_y|\varphi| + 1}} \tag{3.69}$$

and for the moment:

$$M_z = \tfrac{3}{8}\mu F_z a\frac{a\theta_y|\varphi| - 1}{a\theta_y|\varphi| + 1}\operatorname{sgn}\varphi \tag{3.70}$$

At $\varphi = \varphi_{sl}$ the force reduces to $\mu F_z \operatorname{sgn}\varphi$ and the moment to zero. The same can be obtained from the expressions (3.62) holding for the case of full adhesion when $2c'_{py}b$ is replaced by c_{py} and the width $2b$ is taken equal to zero.

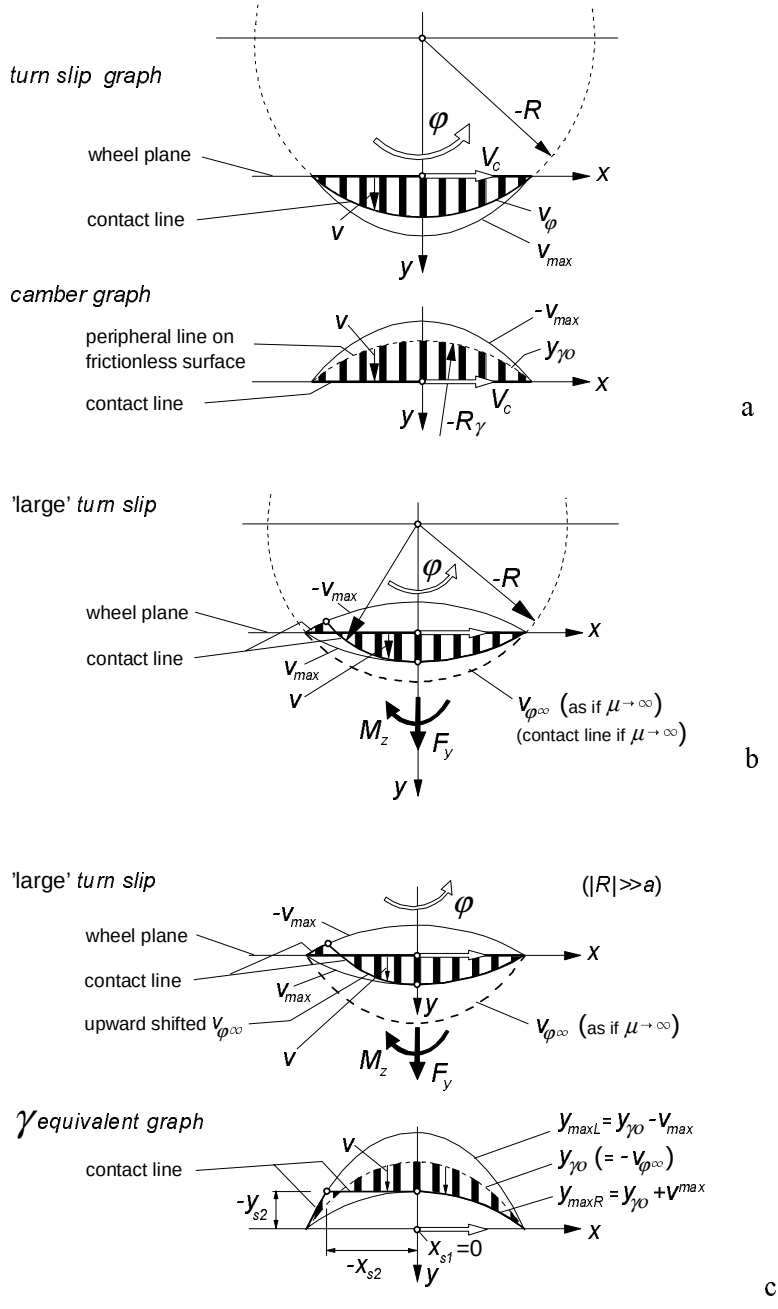

Fig. 3.24. The tyre brush model with zero width rolling while turning or at a camber angle (a) at full adhesion. Turning at large spin showing sliding at the front half and at the rear end (b,c), with parabolic approximation of the circular path in (c).

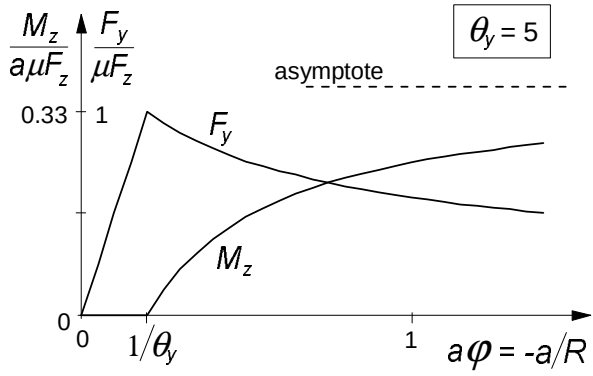

Fig. 3.25. Force and moment versus non-dimensional spin for single row brush model.

For spin approaching infinity, that is when the radius $R \to 0$, the force F_y vanishes while the moment reaches its maximum value:

$$F_y = 0 \ , \quad M_z = M_{z,max} = \frac{3}{8}\mu F_z a \ \mathrm{sgn}\varphi \tag{3.71}$$

In Fig.3.25 the pure spin characteristics have been presented according to the above expressions. It is of interest to note that although the parabola does not resemble the circular path so well at smaller radii, the resulting response seems to be acceptable at least if the deflections remain sufficiently small.

Spin and side slip

In the analysis of combined spin and side slip we may distinguish again between the cases of small and large spin. As before, at small spin we have only a sliding range that starts at the rear end of the contact line, whereas at large spin we have an additional sliding zone that starts at the leading edge. First we will consider the simpler case of small spin.

In Fig.3.26 an example is shown of the single row brush model, both for the cases of turning and (equivalent) camber. In the camber graph, the curves y_{maxL} and y_{maxR} have been drawn which indicate the maximum possible displacements of the tips of the elements to the left and to the right with respect to the $y_{\gamma o}$ line. The shaded area corresponds to the deformation of the brush model when subjected solely to the slip angle with the maximum possible deflection $-v_{max}$ replaced by (in this case with negative slip angle) y_{maxL}. This would correspond to the introduction of an adapted friction coefficient μ or parameter θ_y. Apparently, the actual deflection of the elements at camber and side slip is then obtained by adding the deflection $v_{\varphi\infty}$ that would occur when the model would be subjected to spin only and full adhesion is assumed. The adapted parameter θ_y

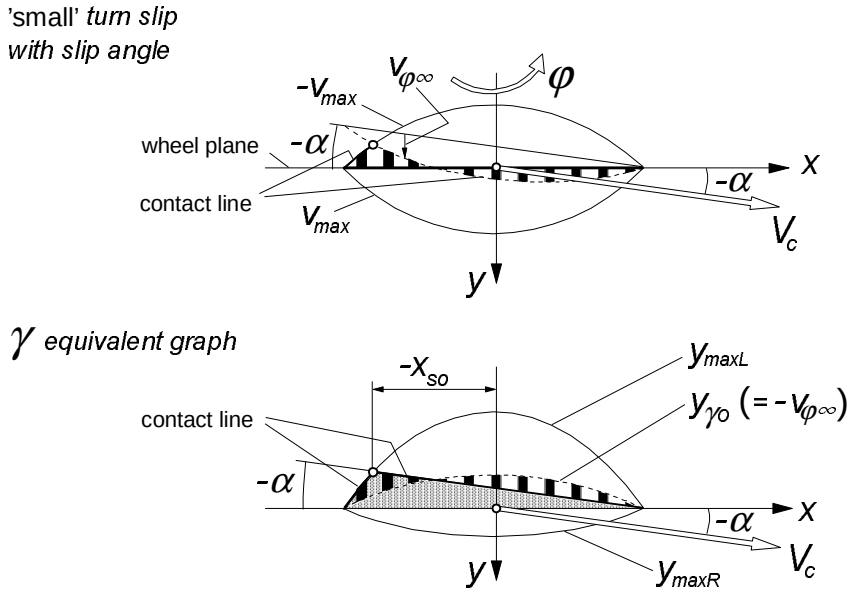

Fig. 3.26. The brush model turning at 'small' spin or subjected to camber at the same level of spin while running at a slip angle.

turns out to read:

$$\theta_y^* = \frac{\theta_y}{1 - a\varphi\theta_y \operatorname{sgn}\alpha} \quad \text{with} \quad \theta_y = \frac{2c_{py}a^2}{3\mu F_z} \tag{3.72}$$

with the condition for the spin to be 'small':

$$|\varphi| < \varphi_l = \frac{1}{a\theta_y} \tag{3.73}$$

The side force becomes similar to Eq.(3.11) with the camber force at full adhesion added:
if $|\tan\alpha| = |\sigma_y| \le \sigma_{y,sl} = 1/\theta_y^*$

$$F_y = 3\mu F_z \theta_y \sigma_y \left\{1 - \left|\theta_y^* \sigma_y\right| + \tfrac{1}{3}\left(\theta_y^* \sigma_y\right)^2\right\} + \tfrac{2}{3} c_{py} a^3 \varphi \tag{3.74}$$

and if $|\tan\alpha| = |\sigma_y| > \sigma_{y,sl}$

$$F_y = \mu F_z \operatorname{sgn}\alpha \tag{3.74a}$$

For the moment we obtain:

if $|\tan\alpha| = |\sigma_y| \le \sigma_{y,sl} = 1/\theta_y^*$

$$M_z = -\mu F_z a\theta_y\sigma_y\left\{1 - 3\left|\theta_y^*\sigma_y\right| + 3\left(\theta_y^*\sigma_y\right)^2 - \left|\theta_y^*\sigma_y\right|^3\right\} \tag{3.75}$$

and if $|\tan\alpha| = |\sigma_y| > \sigma_{y,sl}$

$$M_z = 0 \tag{3.75a}$$

We may introduce a pneumatic trail t_α that multiplied with the force $F_{y\alpha}$ due to the slip angle (with the last term of (3.74) omitted) produces the moment $-M_z$:

if $|\tan\alpha| = |\sigma_y| \le \sigma_{y,sl} = 1/\theta_y^*$

$$t_\alpha = -\frac{M_z}{F_{y\alpha}} = \frac{1}{3}a\frac{1 - 3\left|\theta_y^*\sigma_y\right| + 3\left(\theta_y^*\sigma_y\right)^2 - \left|\theta_y^*\sigma_y\right|^3}{1 - \left|\theta_y^*\sigma_y\right| + \frac{1}{3}\left(\theta_y^*\sigma_y\right)^2} \tag{3.76}$$

and else: $t_\alpha = 0$.

The graph of Fig.3.27 clarifies the configuration of the various curves and their mutual relationship. For different values of the camber angle γ the characteristics for the force and the moment versus the slip angle have been calculated with the above equations and presented in Fig.3.28. The corresponding Gough plot has been depicted in Fig.3.29. The relationship between γ and the spin φ follows from Eq.(3.55).

The curves established show good qualitative agreement with measured

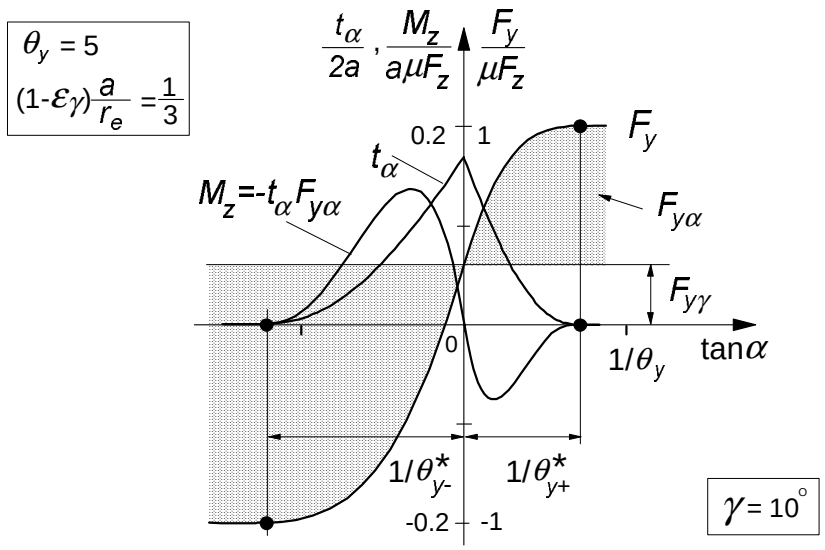

Fig. 3.27. Basic configuration of the characteristics vs side slip at camber angle γ=10 deg..

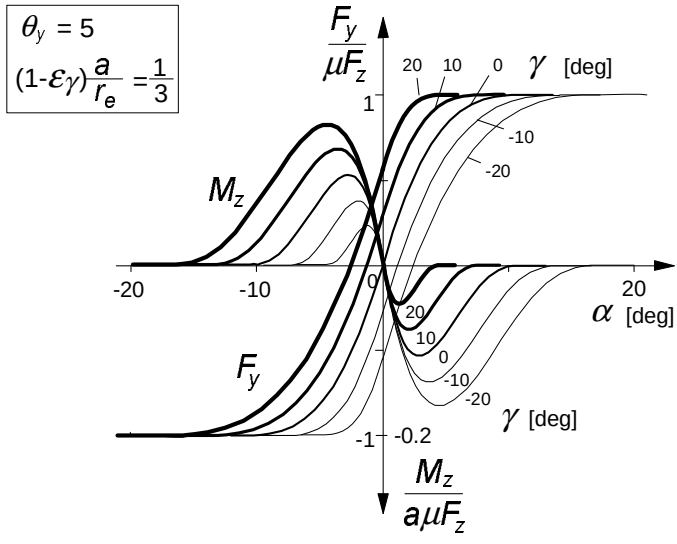

Fig. 3.28. The calculated side force and moment characteristics at various camber angles

characteristics. Some details in their features may be different with respect to experimental evidence. In the next section where the simulation model is introduced, the effect of various other parameters like the width of the contact patch and the possibly camber dependent average friction coefficient on the peak side force will be discussed.

The next item to be addressed is the response to large spin in the presence of side slip. Figures 3.30a,b refer to this situation. Large spin with two sliding ranges occurs when the following two conditions are fulfilled.

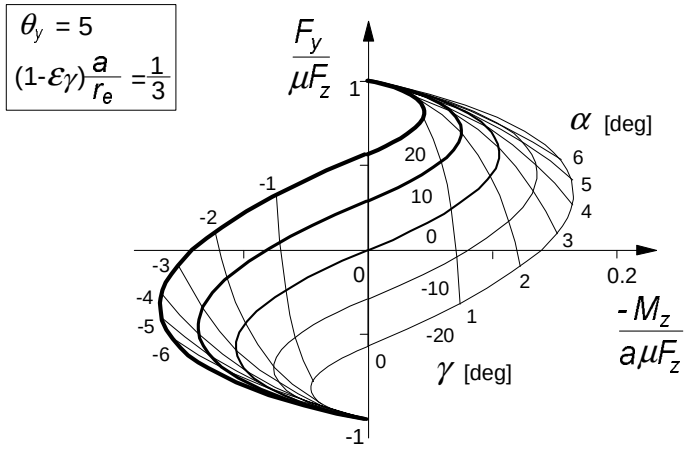

Fig. 3.29. The corresponding Gough plot

$$|\varphi| \geq \varphi_l = \frac{1}{a\theta_y} \quad \text{and} \quad \tan|\alpha| \leq a|\varphi| - \frac{1}{\theta_y} \quad (>0) \tag{3.77}$$

If the second condition is not satisfied we have a relatively large slip angle and the equations (3.74,75) hold again. This situation is illustrated in Fig.3.30c.

For the development of the equations for the deflections we refer to Fig.3.30a with the camber equivalent graph. First, the distances y will be established and then the deflections $v_{\varphi\infty}$ will be added to obtain the actual deflections v. Adhesion occurs in between the two sliding ranges. The straight line runs parallel to the speed vector and touches the boundary y_{maxR}. The tangent point forms the first transition point from sliding to adhesion. More to the rear, the straight line intersects the other boundary y_{maxL}. With the following two quantities introduced

$$A_1 = \tfrac{1}{2}\left(a|\varphi| - \frac{1}{\theta_y}\right), \quad A_2 = \tfrac{1}{2}\left(a|\varphi| + \frac{1}{\theta_y}\right) \tag{3.78}$$

we derive for the x-coordinates of the transition points:

$$x_{s1} = \frac{a \tan\alpha \operatorname{sgn}\varphi}{2A_1} \tag{3.79}$$

and

$$x_{s2} = -\frac{q + \operatorname{sgn}\varphi\sqrt{q^2 + 4pr}}{2p} \tag{3.80}$$

with

$$p = \frac{A_2}{a}\operatorname{sgn}\varphi, \quad q = \tan\alpha, \quad r = aA_2\operatorname{sgn}\varphi + y_{s1} + x_{s1}\tan\alpha \tag{3.81}$$

The distances y in the first sliding region ($x_{s1} < x < a$) read:

$$y_1 = -A_1\frac{a^2 - x^2}{a}\operatorname{sgn}\varphi \tag{3.82}$$

in the adhesion region ($x_{s2} < x < x_{s1}$):

$$y_2 = y_{s1} + (x_{s1} - x)\tan\alpha \tag{3.83}$$

with

$$y_{s1} = y_1(x_{s1}) \tag{3.84}$$

and in second sliding range ($-a < x < x_{s2}$):

$$y_3 = -A_2\frac{a^2 - x^2}{a}\operatorname{sgn}\varphi \tag{3.85}$$

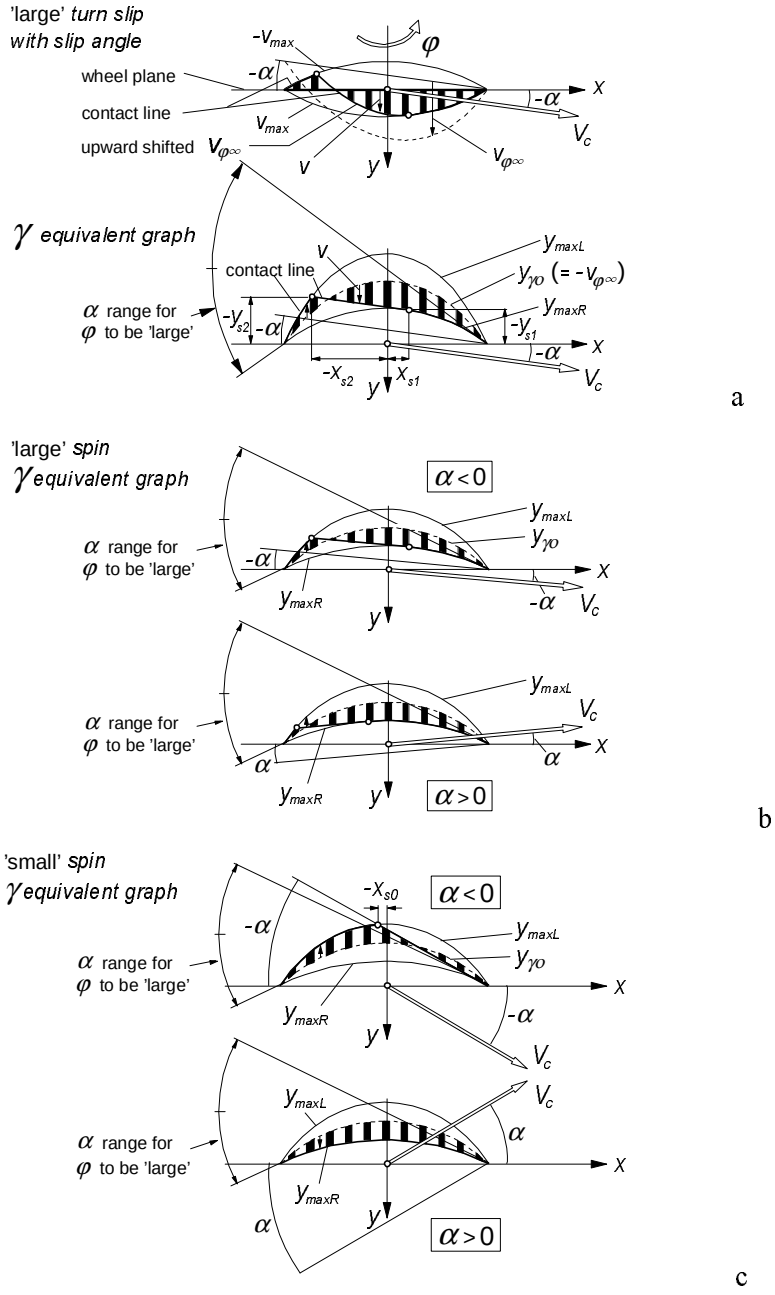

Fig. 3.30. The model running at large spin (turning and equivalent camber) at a relatively small (a,b) or large positive or negative slip angle (c).

Integration over the contact length after addition of $v_{\varphi\infty}$ and multiplication with the stiffness per unit length c_{py} gives the side force and after first multiplying with x the aligning torque. We obtain the formulae:

$$F_y = c_p \frac{\operatorname{sgn}\varphi}{a}\left\{A_1(a^2 x_{s1} - \tfrac{1}{3}x_{s1}^3) - A_2(a^2 x_{s2} - \tfrac{1}{3}x_{s2}^3)\right\} + \\ + c_p\left\{(y_{s1} + x_{s1}\tan\alpha)(x_{s1} - x_{s2}) - \tfrac{1}{2}\tan\alpha\,(x_{s1}^2 - x_{s2}^2)\right\} \tag{3.86}$$

$$M_z = -\tfrac{1}{2}c_p \frac{\operatorname{sgn}\varphi}{a}\left\{A_1\left(\tfrac{1}{2}a^4 - a^2 x_{s1}^2 + \tfrac{1}{2}x_{s1}^4\right) - A_2\left(\tfrac{1}{2}a^4 - a^2 x_{s2}^2 + \tfrac{1}{2}x_{s2}^4\right)\right\} + \\ + c_p\left\{\tfrac{1}{2}(y_{s1} + x_{s1}\tan\alpha)(x_{s1}^2 - x_{s2}^2) - \tfrac{1}{3}\tan\alpha\,(x_{s1}^3 - x_{s2}^3)\right\} \tag{3.87}$$

The resulting characteristics have been presented in Figs.3.31 and 3.32. The graphs form an extension of the diagram of Fig.3.28 where the level of camber correspond to 'small' spin. It can be observed that in accordance with Fig.3.25 the force at zero side slip first increases with increasing spin and then decays. As was the case with smaller spin for the case where spin and side slip have the same sign, the slip angle where the peak side force is reached becomes larger. When the signs of both slip components have opposite signs, the level of side slip where the force saturates may become very large. As can be seen from Fig.3.30b the deflection pattern becomes more anti-symmetric when with positive spin the slip angle is negative. This explains the fact that at higher levels of spin the torque attains its maximum at larger slip angles with a sign opposite to that of the spin. The observation concerning the peak side force, of course, also holds for the slip angle where the torque reduces to zero.

Spin, longitudinal and side slip, the width effect

The width of the contact patch has a considerable effect on the torque and indirectly on the side force because of the consumption of some of the friction by the longitudinal forces involved. Furthermore, for the actual tyre with carcass compliance, the spin torque will generate an additional distortion of the carcass which results in a further change of the effective slip angle (beside the distortion already brought about by the aligning torque that results from lateral forces). Amongst other things, these matters can be taken into account in the tread simulation model to be dealt with in Section 3.3.

In the part that follows now, we will show the complexity involved when longitudinal slip is considered beside spin and side slip. To include the effect of the width of the contact patch we consider a model with a left and a right row of tread elements positioned at a distance $y_L = -b_{row}$ and $y_R = b_{row}$ from the wheel

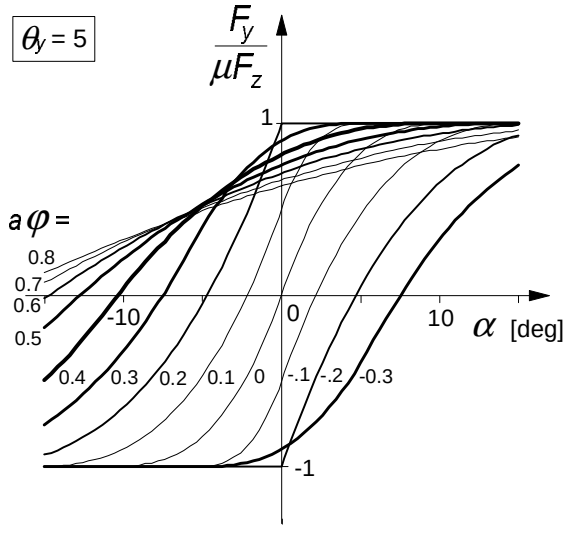

Fig. 3.31. Side force characteristics of the single row brush model up to large levels of spin. (Compare with Fig.3.28 where spin is small and $a\varphi = 0.33 \sin\gamma$).

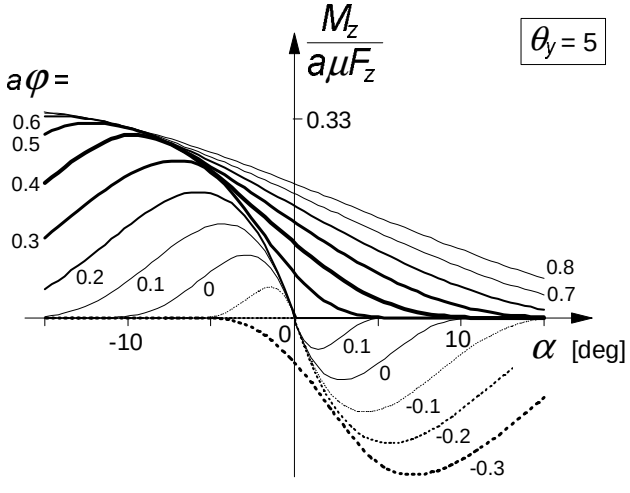

Fig. 3.32. Aligning torque characteristics of the single row brush model up to large levels of spin. (Compare with Fig.3.28 where spin is small and $a\varphi = 0.33 \sin\gamma$).

centre plane. In fact, we may assume that we deal with two wheels attached to each other on the same shaft at a distance $2b_{row}$ from each other. The wheels are subjected to the same side slip and turn slip velocities, V_{sy} and $\dot{\psi}$, and show the same camber angle γ. However, the longitudinal slip velocities are different, for the case of camber because of a difference in effective rolling radii. We have for

the longitudinal slip velocity of the left or right wheel positioned at a distance $y_{L,R}$ from the centre plane:

$$V_{sxL,R} = V_{sx} - y_{L,R}\{\dot{\psi} - (1-\varepsilon_\gamma)\Omega\sin\gamma\} \tag{3.88}$$

This expression is obtained by considering Eq.(2.55) in which conicity is disregarded, steady-state is assumed to occur and the camber reduction factor ε_γ is introduced. The factors θ are defined as (like in (3.54, 55)):

$$\theta_{\gamma x}(y) = -\varepsilon_\gamma\ , \quad \theta_y(x,y) = -\varepsilon_\gamma \frac{x}{r_e}\sin\gamma \tag{3.89}$$

From Eqs.(2.55, 56) using (3.88) the sliding velocity components are obtained

$$V_{gxL,R} = V_{sxL,R} - \frac{\partial u_{L,R}}{\partial x} V_r \tag{3.90}$$

$$V_{gy} = V_{sy} - \frac{\partial v}{\partial x} V_r + x\{\dot{\psi} - (1-\varepsilon_\gamma)\Omega\sin\gamma\} \tag{3.91}$$

After introducing the theoretical slip quantities for the two attached wheels

$$\sigma_{xL,R} = -\frac{V_{sxL,R}}{V_r}\ , \quad \sigma_y = -\frac{V_{sy}}{V_r}\ , \quad \sigma_\psi = -\frac{\dot{\psi}}{V_r} \tag{3.92}$$

we find for the gradients of the deflections in the adhesion zone (where $V_g = 0$) if small spin is considered (sliding only at the rear):

$$\frac{\partial u_{L,R}}{\partial x} = -\sigma_{sxL,R} \tag{3.93}$$

$$\frac{\partial v}{\partial x} = -\sigma_y - x\left\{\sigma_\psi + (1-\varepsilon_\gamma)\frac{1}{r_e}\sin\gamma\right\} \tag{3.94}$$

which yields after integration for the deflections in the adhesion zone ($x < x_t$):

$$u_{L,R} = (a-x)\sigma_{xL,R} \tag{3.95}$$

$$v = (a-x)\,\sigma_y + \tfrac{1}{2}(a^2 - x^2)\left\{\sigma_\psi + (1-\varepsilon_\gamma)\frac{1}{r_e}\sin\gamma\right\} \tag{3.96}$$

The transition point from adhesion to sliding, at $x = x_t$, can be assessed with the aid of the condition

$$c_p e_{L,R} = \mu q_z \tag{3.97}$$

with the magnitude of the deflection

$$e_{L,R} = |\boldsymbol{e}_{L,R}| = \sqrt{u_{L,R}^2 + v^2} \tag{3.98}$$

Solving for x_t and performing the integration over the adhesion range may be carried out numerically. In the sliding range, the direction of the deflections vary with x. As an approximation one may assume that these deflections $\boldsymbol{e}$ (for an isotropic model) are all directed opposite to the slip speed $V_{sL,R}$. Results of such integrations yielding the values of F_x, F_y and M_z will not be shown here. We refer to Sakai (1990) for analytical solutions of the single row brush model at combined slip with camber.

3.3. The Tread Simulation Model

In this section a methodology is developed that enables us to investigate effects of elements in the tyre model which were impossible to include in the analytical brush model dealt with in the preceding Section 3.2. Examples of such complicating features are: arbitrary pressure distribution; velocity and pressure dependent friction coefficient; anisotropic stiffness properties; combined lateral, longitudinal and camber or turn slip; lateral, bending and yaw compliance of the carcass and belt; finite tread width at turn slip or camber.

The method is based on the time simulation of the deformation history of one or more tread elements while moving through the contact zone. The method is

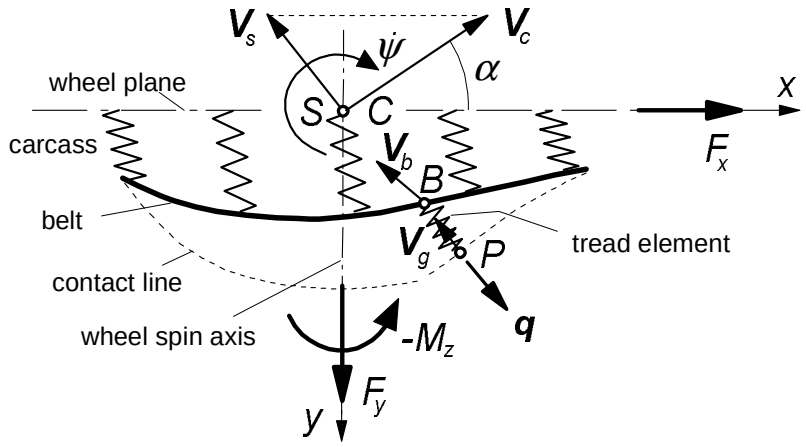

Fig. 3.33. Enhanced model with deflected carcass and tread element that is followed from front to rear.

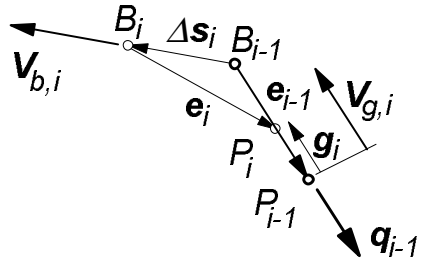

Fig. 3.34. The isotropic tread element with deflection $\boldsymbol{e}$ in two successive positions i-1 and i. Its base point B moves with speed V_b and its tip P slides with speed V_g.

very powerful and can be used either under steady-state or time varying conditions. In the latter non-steady situation we may divide the contact length into a number of zones of equal length in each of which a tread element is followed. In case of turning or camber the contact patch should be divided into several parallel rows of elements. While moving through the zones the forces acting on the elements are calculated and integrated. After having moved completely through a zone the integration produces the zone forces. These forces act on the belt and the corresponding distortion is calculated. With the updated belt deflection the next passage through the zones is performed and the calculation is repeated.

Here, we will restrict the discussion to steady-state slip conditions and take a single zone with length equal to the contact length. In Section 2.5 an introductory discussion has been given and reference has been made to a number of sources in the literature. The complete listing of the simulation program *TreadSim* written in Matlab code is given in Appendix 2. For details we may refer to this program.

Figure 3.33 depicts the model with deflected belt and the tread element that has moved from the leading edge to a certain position in the contact zone. In Fig.3.34 the tread element deflection vector $\boldsymbol{e}$ has been shown. The tread element is assumed to be isotropic thus with equal stiffnesses in x and y direction. Then, when the element is sliding, the sliding speed vector V_g, that has a sense opposite to the friction force vector $\boldsymbol{q}$, is directed opposite to the deflection vector $\boldsymbol{e}$. The figure depicts the deflected element at the ends of two successive time steps i-1 and i. The first objective is now to find an expression for the displacement $\boldsymbol{g}$ of the tip of the element while sliding over the ground.

The contact length is divided into n intervals. Over each time step Δt the base point B moves over an interval length towards the rear. With given length:

$$\Delta x = \frac{2a}{n} \tag{3.99}$$

and the linear speed of rolling $V_r = r_e \Omega$ the time step Δt is obtained:

$$\Delta t = \frac{\Delta x}{V_r} \tag{3.100}$$

With the velocity vector $\boldsymbol{V}_b$ of point B the displacement vector $\Delta \boldsymbol{s}$ of this point over the time step becomes:

$$\Delta \boldsymbol{s} = \boldsymbol{V}_b \Delta t \tag{3.101}$$

The base point B moves along the belt peripheral line or a line parallel to this line. With the known lateral coordinate y_b of this line of base points with respect to the wheel centre plane, the local slope $\partial y_b / \partial x$ can be assessed. Then, with the slip velocity $\boldsymbol{V}_s$ of the slip point S, the yaw rate of the line of intersection $\dot{\psi}$ and the rolling speed V_r, the components of $\boldsymbol{V}_b$ can be found.

The velocity of point B may be considered as the sliding velocity of this point with respect to the ground and we may employ the equations (2.55,56) for its assessment. In these equations, at steady state, the time derivatives of u and v vanish, the slope $\partial u / \partial x$ is replaced by zero and for $\partial v / \partial x$ we take the gradient of the belt deflection caused by the external force and moment. We have with average x position $x_b = x + 0.5 \Delta x$:

$$V_{bx} = V_{sx} - y_{bo}(\dot{\psi} - \Omega \sin\gamma) - \theta_{con,x}(y)\, V_r + \theta_{yx}(y)\, y_{bo} \Omega \sin\gamma \tag{3.102}$$

and

$$V_{by} = V_{sy} + x_b \dot{\psi} - \frac{\partial y_b}{\partial x_b} V_r \tag{3.103}$$

with the slip and roll velocities

$$V_{sx} = -V_{cx} \kappa \ , \quad V_r = r_e \Omega = V_{cx} - V_{sx} \ , \quad V_{sy} = -V_{cx} \tan\alpha \tag{3.104}$$

The lateral displacement y_b of the belt at the contact centre is attributed to camber, conicity and the lateral external force (through the lateral compliance of the carcass). The gradient $\partial y_b / \partial x_b$ may be approximately assessed by assuming a parabolic base line $y_b(x_b)$ exhibiting an average slope c_s influenced by the aligning torque (through the yaw compliance) and ply-steer, and a curvature c_c influenced by the side force (through the bending stiffness) and camber and conicity (cf. (3.56)). We have for the lateral coordinate:

$$y_b = -\frac{a^2}{2r_e}\left(1 - \varepsilon_{yy}\right)(\gamma_{con} + \sin\gamma) + \frac{F_y}{c_{lat}} + c_s x_b + \tfrac{1}{2} c_c x_b^2 \pm b_{row} \tag{3.105}$$

and for its approximation used in (3.102):

$$y_{bo} = \pm b_{row} \tag{3.106}$$

and the slope:

$$\frac{\partial y_b}{\partial x_b} = c_s + c_c x_b = \frac{M'_z}{c_{yaw}} - \frac{x_b F_y}{c_{bend}} + \frac{x_b}{r_e}\sin\gamma + \theta_y(x_b, y_b) \tag{3.107}$$

Conicity and ply-steer will be interpreted here to be caused by 'built-in' camber and slip angles. These equivalent camber and slip angles γ_{con} and α_{ply} are introduced in the expressions of the quantities θ. We define:

$$\theta_{\gamma x}(y_b) = -\varepsilon_{\gamma x} \;, \quad \theta_{con,x}(y_b) = -\frac{y_b}{r_e}\left(1 - \varepsilon_{\gamma x}\right)\gamma_{con} \tag{3.108}$$

and

$$\theta_y(x_b, y_b) = -\varepsilon_{\gamma y}\frac{x_b}{r_e}\sin\gamma + \left(1 - \varepsilon_{\gamma y}\right)\frac{x_b}{r_e}\gamma_{con} + \alpha_{ply} \tag{3.109}$$

The coefficients $\varepsilon_{\gamma x}$ and $\varepsilon_{\gamma y}$ may be taken equal to each other. The first term of the displacement (3.105) is just a guess. It constitutes the lateral displacement of the base line at the contact centre when the tyre is pressed on a frictionless surface in the presence of conicity and camber. The displacements at the contact leading and trailing edges are assumed to be zero under these conditions.The approximation y_{bo} (3.106) is used in (3.102) to avoid apparent changes in the effective rolling radius at camber. The actual lateral coordinate y_b (3.105) plus a term $y_{r\gamma}$ is used to calculate the aligning torque. With this additional term the lateral shift of F_x due to sideways rolling when the tyre is being cambered is accounted for. We have $y_{b,eff} = y_b + y_{r\gamma}$ with $y_{r\gamma} = \varepsilon_{yr\gamma} b \sin\gamma$ with an upper limit of its magnitude equal to b. The moment M'_z causes the torsion of the contact patch and is assumed to act around a point closer to its centre like depicted in Fig.3.19. A reduction parameter ε'_y is used for this purpose. More refinements may be introduced. For details we refer to the complete listing of the program *TreadSim* included in the Appendix.

With the displacement vector $\Delta\boldsymbol{s}$ (3.101) established we can derive the change in deflection $\boldsymbol{e}$ over one time step. By keeping the directions of motion of the points B and P in Fig.3.34 constant during the time step, an approximate expression for the new deflection vector is obtained. After the base point B has moved according to the vector $\Delta\boldsymbol{s}$ we have:

$$\boldsymbol{e}_i = \boldsymbol{e}_{i-1} + \boldsymbol{g}_i - \Delta\boldsymbol{s}_i \qquad \text{with} \quad \boldsymbol{g}_i = -\frac{g_i}{e_{i-1}}\boldsymbol{e}_{i-1} \tag{3.110}$$

Here, e_{i-1} denotes the absolute value of the deflection and g_i the distance P has slided in the direction of $-\boldsymbol{e}_{i-1}$. In case of adhesion, the sliding distance $g_i = 0$. When the tip slides, the deflection becomes:

$$e_i = \frac{\mu_i q_{z,i}}{c_p} \tag{3.111}$$

From (3.110) an approximate expression for g_i can be established, considering that g is small with respect to the deflection e. We obtain:

$$g_i = \frac{1}{2} e_{i-1} \frac{(e_{x,i-1} - \Delta s_{x,i})^2 + (e_{y,i-1} - \Delta s_{y,i})^2 - e_i^2}{e_{x,i-1}(e_{x,i-1} - \Delta s_{x,i}) + e_{y,i-1}(e_{y,i-1} - \Delta s_{y,i})} \tag{3.112}$$

in which expression (3.111) is to be substituted. If g_i is positive, sliding remains. If not, adhesion commences. In the case of sliding, the deflection components can be found from (3.110) using (3.112). Then, the force vector per unit length is:

$$\boldsymbol{q}_i = \mu q_{z,i} \frac{\boldsymbol{e}_i}{e_i} \tag{3.113}$$

If adhesion occurs, $g_i = 0$ and with (3.110) the deflection is determined again. The force per unit length now reads:

$$\boldsymbol{q}_i = c_p \boldsymbol{e}_i \tag{3.114}$$

As soon as the condition for adhesion

$$q_i = |\boldsymbol{q}_i| \le \frac{\mu_i q_{z,i}}{c_p} \tag{3.115}$$

is violated, sliding begins. The sliding distance g_i is calculated again and its sign checked.until adhesion may show up again.

In (3.113) the friction coefficient appears. This quantity may be expressed as a function of the sliding velocity of the tip of the element over the ground. However, this velocity is not available at this stage of the calculation. Through iterations we may be able to assess the sliding speed at the position considered. Instead, we will adopt an approximation and use the velocity of the base point (3.102, 103) to determine the current value of the friction coefficient. The following functional relationship may be used for the friction coefficient versus the magnitude of the approximated sliding speed V_b:

$$\mu = \frac{\mu_o}{1 + a_\mu V_b} \tag{3.116}$$

During the passage of the element through the contact zone the forces $\Delta \boldsymbol{F}_i$ are calculated by multiplying $\boldsymbol{q}_i$ with the part of the contact length Δx covered over the time step Δt.

Subsequently, the total force components and the aligning moment are found

by adding together all the contributions ΔF_{xi} , ΔF_{yi} , and $x_{bi}\Delta F_{yi}$ - $y_{bi,eff}\Delta F_{xi}$ respectively. A correction to the moment arm may be introduced to account for the side ways rolling of the tyre cross section while being cambered and deflected (causing lateral shift of point of action of the resulting normal load F_z and similarly of the longitudinal force F_x). Also, the counter effect of the longitudinal deflection u_c may contribute to this correction factor, cf. Eq.(3.51).

In the sequel a number of example results of using the tread simulation model have been presented. The following cases have been investigated:

1. Sliding velocity dependent friction coefficient (rigid carcass but parameter c of Eq.(3.52) is included). (Fig.3.35a)
2. Flexible carcass, without and with camber. (Fig.3.35b)
3. Finite tread width (two rows of tread elements, flexible carcass), with and without camber. (Fig.3.35c)
4. Combined lateral and turn slip (two rows, flexible carcass). (Fig.3.35d)
5. Pneumatic trail at pure side slip (flexible and rigid carcass). (Fig.3.36)

The computations have been conducted with the set of parameter values listed in Table 3.1.

Table 3.1. Parameter values used in the tread simulation model. (Figs. 3.35-37)

a	0.1m	F_z	3000 N	c_{lat}	100 kN/m	$C_{F\kappa}$	$15F_z$
b	0.08m	V_c	30 m/s	c_{bend}	4 kNm	y_o	0 :v_o Eq.3.51
b_{row}	0.05m	μ_o	1.0	c_{yaw}	6 kNm/rad	α_{ply}	0
r_e	0.3 m	a_μ	0, 0.03s/m	c	$1/c_{lat}$	γ_{con}	0
$\varepsilon_{y\gamma\gamma}$	4.0	other ε's = 0		$c_p = C_{F\kappa}/(2a^2 n_{row})$		$\theta = C_{F\kappa}/(3\ \mu_o\ F_z)$	

In case of a 'rigid' carcass, parameter c (=0.01m/kN), Eq.(3.52), is used while c_{lat}, c_{bend}, $c_{yaw} \to \infty$. As indicated, quantities c_p and θ follow from the model parameters.

The graphs of the lower half of Fig.3.35a relative to the upper half show the most prominent effect of a with sliding velocity decreasing friction coefficient. At $a_\mu = 0.03$ the side force F_y exhibits a clear peak at a slip angle of about seven degrees when the wheel is rolling freely ($\kappa = 0$). Also the fore and aft force F_x tends to decrease after having reached its peak value. The inward endings of the curves at constant values of slip angle shown in the bottom diagram are typical especially for a tyre running on wet road surfaces. The peak values themselves will decrease when the speed of travel is increased (not shown) while the initial

slopes (slip stiffnesses) remain unchanged. The change in sign of the aligning torque in the braking range of its diagram occurs because of the retained parameter c that produces the effect of the flexible carcass according to Eqs.(3.51,52). The expected change in sign of the aligning torque curve at pure side slip at higher levels of side slip does not occur due to the limitation of the estimation of the sliding speed for which the speed of a point of the belt is taken (here rigid). In Fig.3.35b with the carcass considered flexible this sign change does show up as illustrated in the upper right diagram.

A more important effect of the flexible carcass presented in Fig.3.35b is the decreased cornering stiffness while the fore and aft slip stiffness remains the same. The lower value of F_y at $\alpha = 2°$ in the F_y vs F_x diagram clearly demonstrates this effect. The aligning torque, however, is not so much affected. This due to the larger pneumatic trail which is a result of the curved deflection line of the belt. Figure 3.36 shows the pneumatic trail diagram for the model with and without carcass compliance (the number of rows has no influence in case of zero spin). As expected, the simple brush model with rigid carcass has a trail of $0.33a$ when the slip angle approaches zero. The flexible carcass model considered features a pneumatic trail of about $0.46a$. See Fig.3.38 for the deflection pattern.

The influence on the curves of the introduction of the relatively large camber angle of 10° is indicated in the lower half of Fig.3.35b. The effect is most clearly demonstrated in the lower left diagram. The camber thrust is accompanied by a lateral deflection that causes a shift of the line of action of the longitudinal force. The resulting torque tends to rotate the lower part of the belt about the vertical axis which now can be accomplished through the yaw compliance of the carcass. At braking, the rotation is such that an apparent slip angle arises that increases the camber side force. At driving, the opposite occurs. As a result, the constant slip angle curves plotted in the diagram show an inclination. The corresponding influence diagram of κ on F_y shows distorted curves when compared with those of Fig.3.11. The inversed S shape of the curves at small slip angle is a feature that is commonly encountered in measured characteristics. The aligning torque diagram (lower right picture) is considerably changed as a result of the action of the torque mentioned above that originates from F_x.

In Fig.3.35c the effect of a finite width of the contact patch is demonstrated. Two rows of tread elements have been considered. At the camber angle of 10° a spin torque is generated that appears to rotate the lower part of the belt in such a way that an apparent slip angle arises that increases the camber thrust. The upper left hand diagram shows the increase in side force. The right-hand diagram indicates the considerable rise in the aligning torque as a result of the spin torque in the range of small longitudinal force F_x.

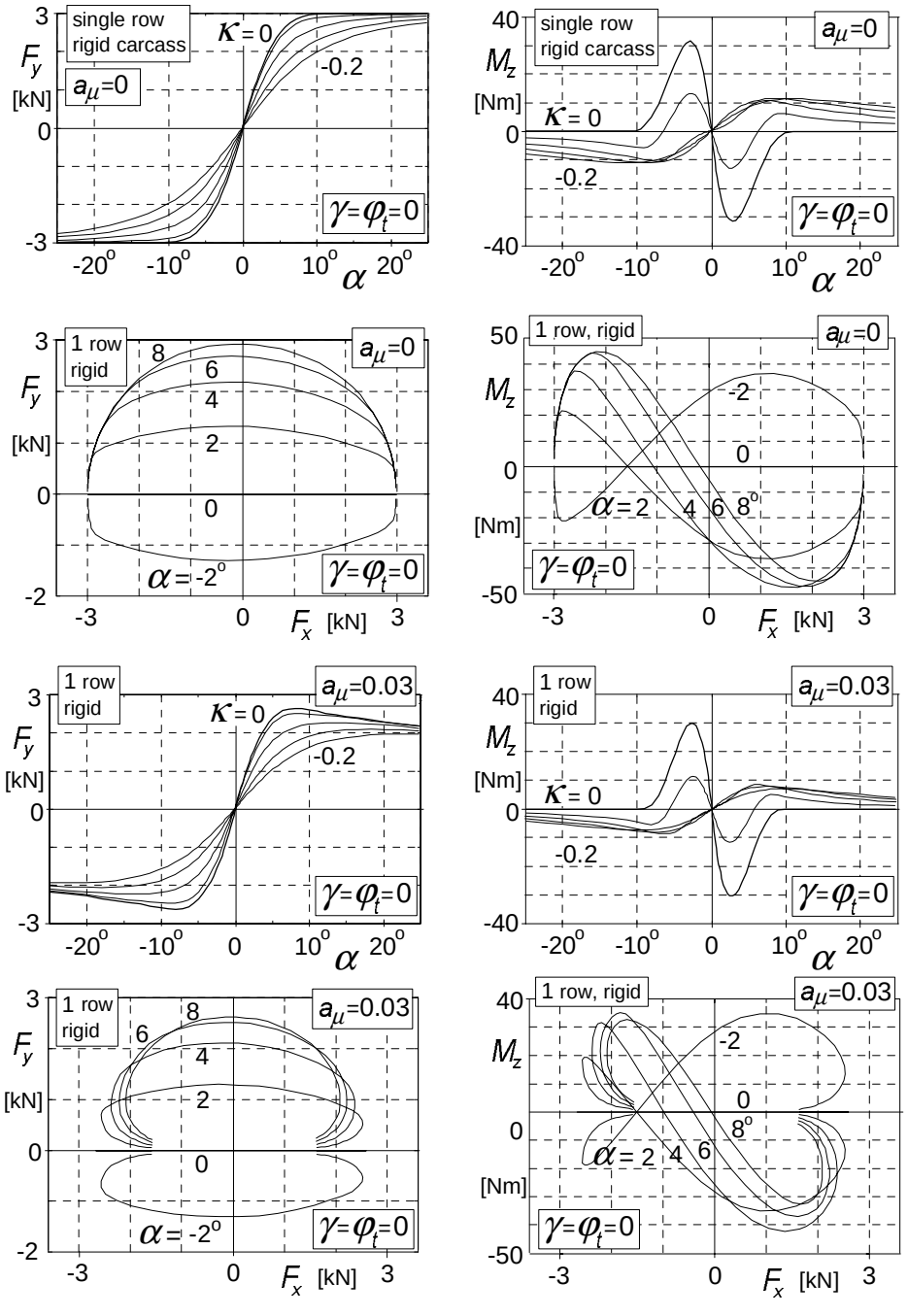

Fig. 3.35a. Characteristics computed with tread simulation model.

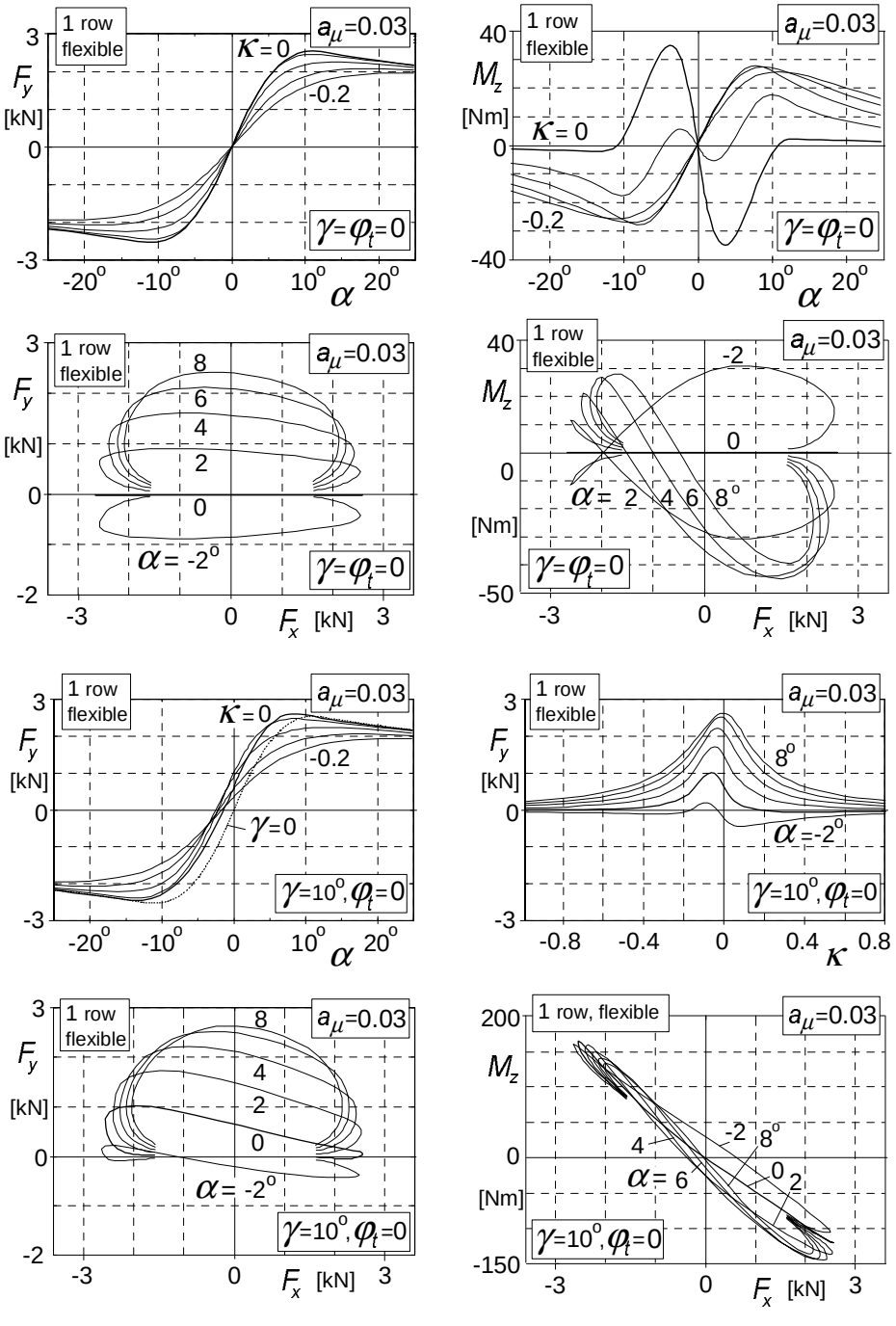

Fig. 3.35b. Characteristics computed with tread simulation model.

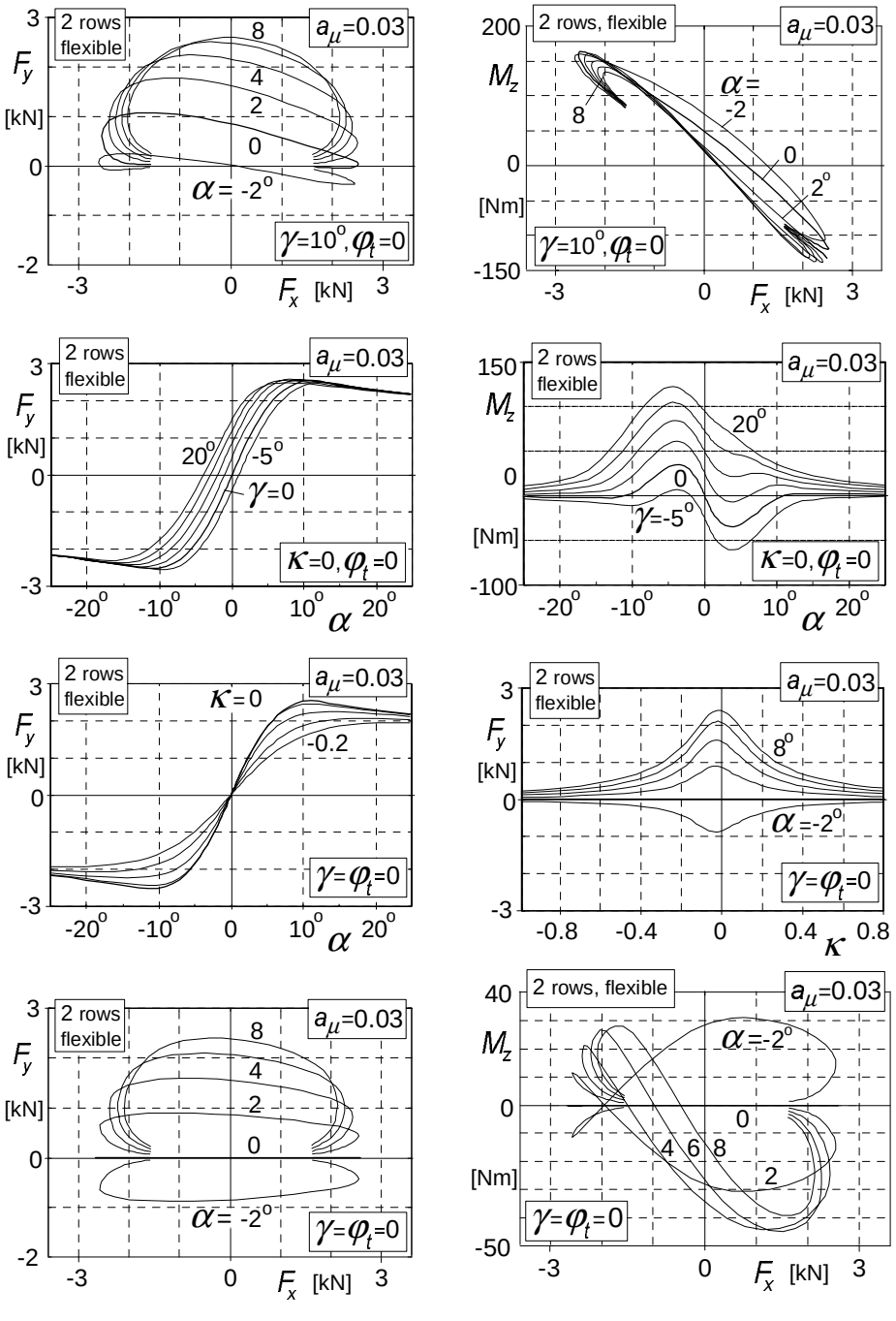

Fig. 3.35c. Characteristics computed with tread simulation model.

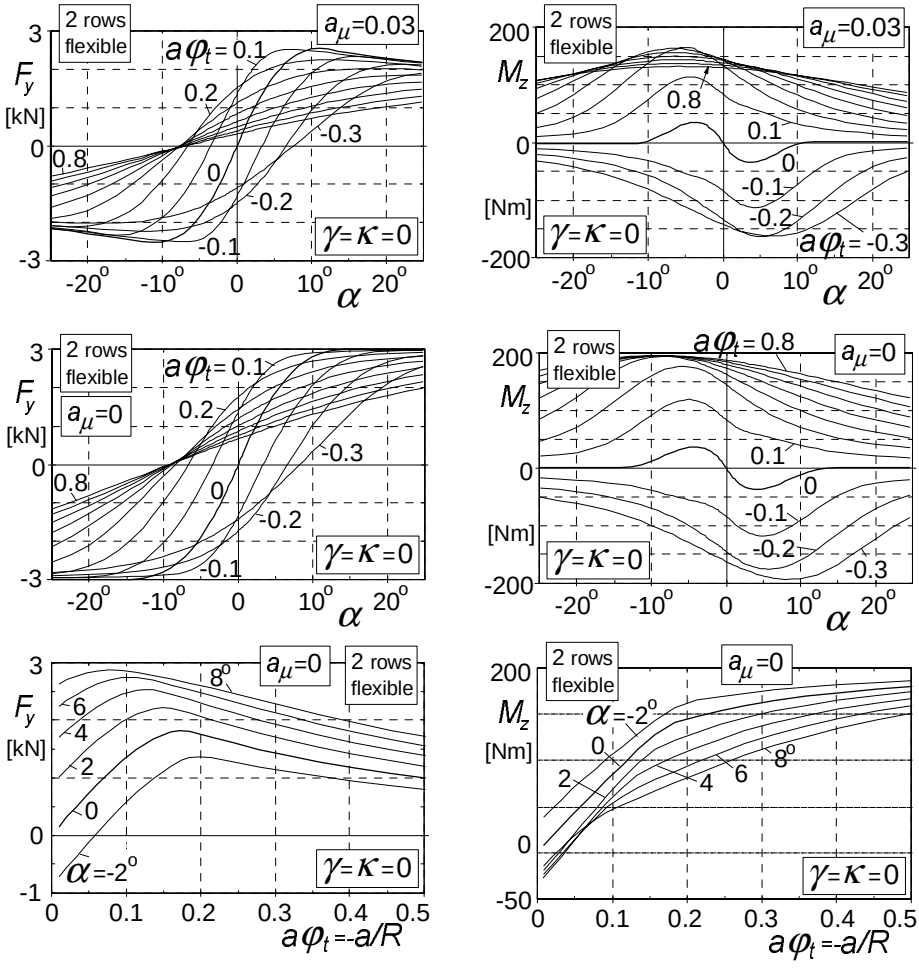

Fig. 3.35d. Characteristicscomputed with tread simulation model.

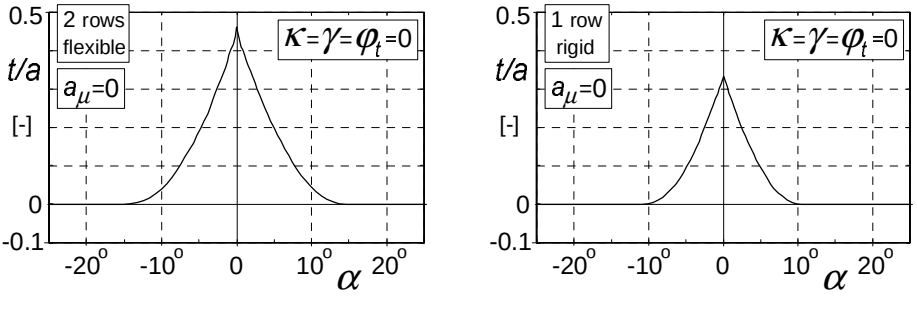

Fig. 3.36. Pneumatic trail variation as computed with tread simulation model.

The two diagrams in the second row demonstrate the effects of tread width, carcass flexibility and friction decay with velocity on the side force and moment versus slip angle characteristics for a series of camber angles. The plots may be compared with those of Figs.3.28. The lower half of Fig.3.35c refers to the case without camber and may be compared with the plots of the upper half of Fig.3.35b that does not include the effects of tread width.

Figure 3.35d presents the force and moment characteristics for a series of levels of turn slip including large values of spin corresponding to a radius of curvature equal to $a/0.8$. The figures of the second row refer to the case of constant friction ($a_\mu = 0$) and may be compared with Figs.3.31,32. An interesting effect of tread width is the further decrease of the side force at higher levels of turn slip due to longitudinal slip that occurs on both sides of the contact patch which consumes a lot of the available frictional forces. Of course, the aligning torque is now considerably larger. The third row of diagrams represent the spin force and moment characteristics at various levels of side slip. In Fig.3.37 the pure spin characteristics have been drawn for the model with a rigid carcass provided with one row of tread elements (same as Fig.3.25) and with two rows computed with the tread simulation model. Comparison clearly shows the considerable reduction of the peak side force and the much larger level of the aligning torque caused by the finite tread width. The influence of carcass flexibility appears to be very small both for the force and for the moment.

These results indicate that the single row theory developed in Section 3.2 also

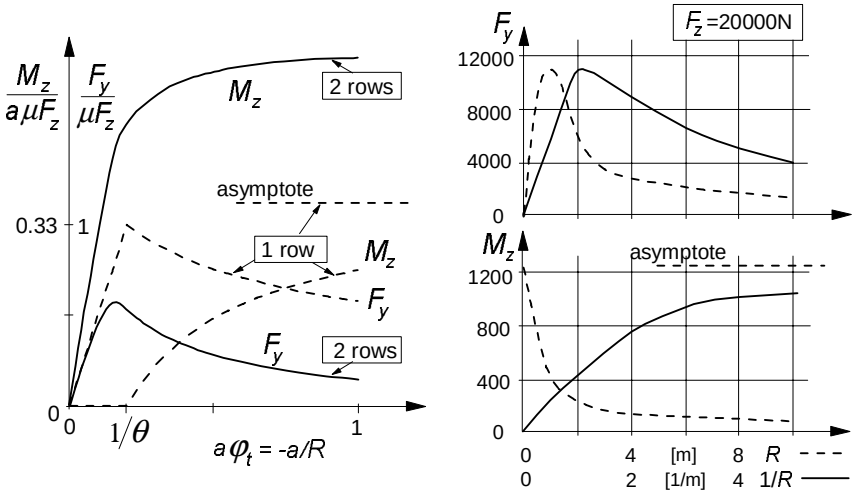

Fig. 3.37. Pure turn slip characteristics according to the model (left, rigid carcass with one or two rows of elements) and results from experiments with a bias ply truck tyre (right, 9.00-20 eHD, p_i = 5.5 bar, V = 1-3 km/h on dry road, from Freudenstein, 1961). Model paramaters: $\theta = 5$, $a_\mu = 0$, $b_{\text{row}} = 0.5\,a$.

for high spin in combination with side slip has only limited practical significance. The influence of small spin, i.e. camber, on the side force versus slip angle characteristic as calculated with the aid of the simple single row, rigid carcass brush model may be considered as reasonable.

Freudenstein (1961) has conducted side slip and turning experiments with a bias-ply truck tyre on a dry road surface. The side slip measurement results of this tyre were already depicted in Fig.3.6. In the right hand diagram of Fig.3.37 the results from the turning experiments have been presented. As abscissa, both the path radius and the path curvature have been used. Obviously, the calculated two-row model characteristics show good qualitative agreement with the experimental curves. For the values $a = 0.1$m, $\mu F_z = 20000$N and $\theta = 8$ a very reasonable also quantitative correspondance for both the force and the moment characteristics of Fig.3.37 can be obtained. Freudenstein suggests the following formula for the peak moment generated at pure turning at wheel speed $V = 0$.

$$|M_{z,\max}| = M_{z\varphi\infty} \approx \frac{3}{8}\mu F_z (a + \frac{2}{3} b) \tag{3.117}$$

As Freudenstein did not give the camber characteristics of the truck tyres on which the turning behaviour was measured, we are not able to compare the responses to camber and turning. According to Hadekel (1952), for aircraft tyres the lateral force due to turning is about four times higher than the camber force at equal values of spin. From experiments performed by Higuchi (1997) a factor of about three can be deduced for a radial ply car tyre, cf. Chap.7 discussion above Fig.7.11. This supports the theory of the reduced curvature of the peripheral line of the cambered tyre pressed on a frictionless surface due to the high lateral bending stiffness of the tread band, as illustrated in Fig.2.10, and the associated coefficient ε_γ in Eq.(3.55).

The program *TreadSim* also provides information on the distribution of contact forces and deflections of belt and tread elements. Some examples of the deformation pattern have been depicted in the Figs.3.38 and 39. In Fig.3.38 the deflections of the single row brush model have been depicted and in addition of the model with carcass lateral, yaw and bending compliance. As indicated, the scale of the drawing has been chosen larger in lateral direction. In the middle two diagrams the influence of camber and of turning on the deflections at side and brake slip has been shown. Turning was considered with an exceptionally small turn radius R equal to a which is half the contact length. One may note the central section where adhesion occurs. The latter situation also occurs with the middle row of tread elements of the three row brush model depicted in Fig.3.39. In this drawing the scales are the same. Clearly, the tyre generates longitudinal deflections of the outer rows of elements that contributes to the torque.

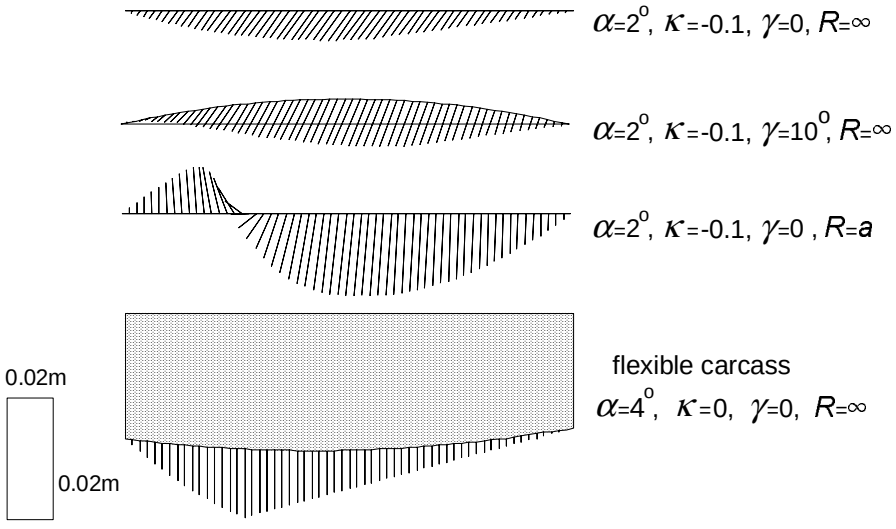

Fig. 3.38. Examples of deflection patterns at various combinations of slip for the single row model with rigid and flexible carcass.

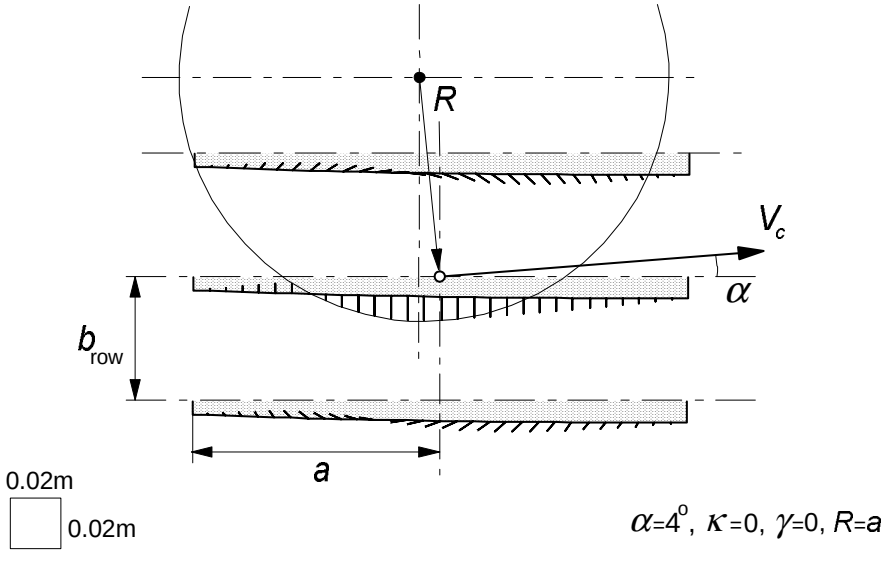

Fig. 3.39. Deflections of the tread elements and of the belt for the three row model at side slip and turning.

3.4. Application: Braking up to Wheel Lock

When the vehicle is being braked forcefully and a possible downward slope does not compensate for the reduction in speed of travel, the situation can no longer be considered as steady state. The influence of the rate of change of the longitudinal speed and of the effect of combined slip on the lateral stability may no longer be neglected. Instead of using the two first-order differential equations (1.42) for the lateral and yaw motions we must now consider the complete set including the equation for the longitudinal motion which is also of the first order.

Because of the complexity involved, the influence of the height of the centre of gravity on the vehicle motion will be disregarded. With a finite height, fore and aft but also lateral load transfer would occur, the latter causing unequal braking forces on the left and right locked wheels that gives rise to a stabilising torque counteracting the effect of the fore and aft load transfer.

The steer angle is kept equal to zero. This two-wheel, single track, rigid vehicle with zero c.g. height has been depicted in Fig.3.40 where the wheel on axle 2 is considered to be locked. For the three states we obtain the equations:

$$\begin{aligned} m(\dot{u} - vr) &= F_{x1} + F_{x2} \\ m(\dot{v} + ur) &= F_{y1} + F_{y2} \\ mk^2\dot{r} &= aF_{y1} - bF_{y2} \end{aligned} \tag{3.118}$$

with

$$\begin{aligned} \tan\alpha_1 &= -\frac{v + ar}{u} \\ \tan\alpha_2 &= -\frac{v - br}{u} \end{aligned} \tag{3.119}$$

and

$$\begin{aligned} F_{y1} &= F_{y1}(\alpha_1, \kappa_1, F_{z1}) \\ F_{y2} &= F_{y2}(\alpha_2, \kappa_2, F_{z2}) \end{aligned} \tag{3.120}$$

For a proper simulation of the motion, the slip ratio's κ_i should result from the wheel speeds of revolution Ω_i which would require additional degrees of freedom. For this occasion we will employ an alternative approach that involves the introduction of functions for the side force in which its direct dependence on the braking effort (or brake pressure) is included. This is possible when 'dry' friction is assumed to occur between tyre and road and the curves of the right-most

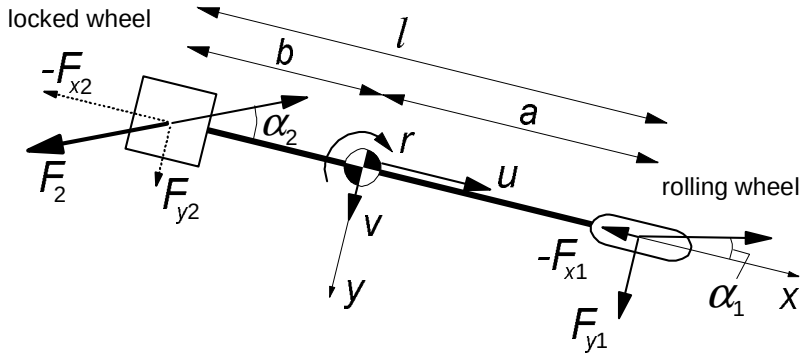

Fig.3.40. 'Bicycle' model with one wheel locked.

diagram of Fig.1.2 do not show inward endings and thus double valued functions are avoided. The characteristics of Fig.3.16 will be used for our analysis. In Fig3.41 the characteristics have been reproduced: one curve for the freely rolling wheel, another one for the wheel that is being braked with a braking effort corresponding to a brake force $B_1 = -F_{x1}$ at straight ahead rolling (α small) and finally for a wheel that is locked completely. The second curve shows that at higher slip angles a lower horizontal plateau is followed until the straight inclined line is reached where also this wheel gets locked (note that sinα has been used as abscissa which makes the relationship linear). A full discussion of this behaviour has been given in Subsection 3.2.3 in connection with the treatment of the tyre brush model.

As shown in Fig.3.40 we assume that the wheel on axle 2 is locked and that on axle 1 the wheel may be braked. The characteristics of Fig.3.41 apply. First, the situation near the undisturbed straight ahead motion will be studied. Linearisation with both slip angles assumed small yields for the horizontal wheel forces:

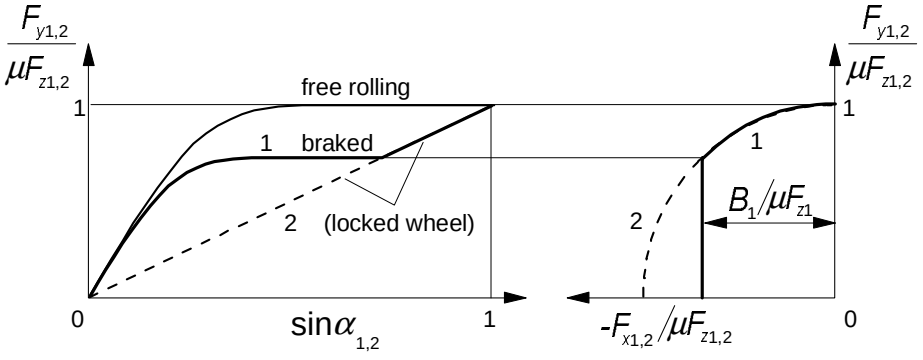

Fig.3.41. Tyre side force characteristics for freely rolling and braked wheels.

$$
\begin{aligned}
F_{x1} &= -B_1 \\
F_{y1} &= F_{y1}(\alpha_1, B_1) \rightarrow C_1(B_1)\alpha_1 \\
F_{x2} &= -\mu F_{z2}\cos\alpha_2 \rightarrow -\mu F_{z2} \\
F_{y2} &= \mu F_{z2}\sin\alpha_2 \rightarrow \mu F_{z2}\alpha_2 = C_2\alpha_2
\end{aligned}
\tag{3.121}
$$

For the locked wheel we have now an effective cornering stiffness:

$$
C_2 = \mu F_{z2} = \mu \frac{a}{l} mg \tag{3.122}
$$

As a result the Eqs.(118-120) reduce to:

$$
\begin{aligned}
m\dot{u} &= -B_1 - \mu F_{z2} \\
m\dot{v} + \frac{1}{|u|}(C_1 + C_2)v + \left\{m u + \frac{1}{|u|}(aC_1 - bC_2)\right\}r &= 0 \\
mk^2\dot{r} + \frac{1}{|u|}(a^2C_1 + b^2C_2)r + \frac{1}{|u|}(aC_1 - bC_2)v &= 0
\end{aligned}
\tag{3.123}
$$

Furthermore, we have introduced the absolute value of the forward speed u in the denominators to allow for the consideration of negative values of u while at the same time the sign of α remains unchanged (cf. the corresponding equations (1.46) for the non-driven or braked vehicle). Negative values of u correspond to the case of locked front wheels.

Elimination of the lateral velocity v from equations (3.123) yields:

$$
\begin{aligned}
m^2k^2u^2\ddot{r} + m\left\{-k^2B_1 + (a^2 + k^2)C_1 + b^2C_2\right\}|u|\dot{r} + \\
+ \left\{l^2C_1C_2 - mu|u|(aC_1 - bC_2)\right\}r = 0
\end{aligned}
\tag{3.124}
$$

When compared with Eq.(1.50), considering (1.48), it is noted that in the second coefficient of (3.124) the term k^2C_2 has disappeared and that $-k^2B_1$ has been added. This is due to the differentiation of u in the elimination process of v. We had originally in the second coefficient of (3.124) the term:

$$
mk^2\dot{u}\,\mathrm{sgn}(u) = -k^2\left(\mu\frac{a}{l}mg + B_1\right) = -k^2(C_2 + B_1) \tag{3.125}
$$

which explains the changes observed . In other respects, Eq.(3.124) is similar to the homogeneous version of Eq.(1.50). However, an important difference appears in the coefficients which are now dependent on the time because of the presence of the linearly with time decreasing speed u. We have the additional equation for u (by integration of the first of Eqs.(3.123)):

$$u = u_o - \frac{1}{m}\left(\mu\frac{a}{l}mg + B_1\right)\,\mathrm{sgn}(u)\cdot t \tag{3.126}$$

The exact solution of Eq.(3.124) can be found because of the fortunate fact that the equation can be reduced to the differential equation of Bessel the solution of which is known in tabular form. Before giving an example of such a complete solution we will analyse the motion just after the application of a slight disturbance which allows us to approximate the equation to one with constant parameters in which u is replaced by its initial value u_o. For this substitutive equation the solution can be found easily. We obtain:

$$r = D_1 e^{\lambda_1 t} + D_2 e^{\lambda_2 t} \tag{3.127}$$

with $D_{1,2}$ denoting the constants of integration (governed by the initial values of the state variables v and r) and $\lambda_{1,2}$ representing the eigenvalues, that is: the roots of the characteristic equation of the substitutive differential equation:

$$A\lambda^2 + B\lambda + (C - u_o|u_o|D) = 0 \tag{3.128}$$

Comparison with the coefficients of Eq.(3.124) reveals the expressions for the quantities A, B, C and D. Since, apparently, the first three are always positive and in the case considered C_2 is much smaller than C_1 which makes D also a positive quantity, we expect that the substitutive system can only become unstable because of a possibly negative third coefficient. Then, one of the roots (lets say λ_1) becomes positive (while remaining real). Obviously, this can only occur when u is positive which means: when the wheels of the rear axle are locked. Locked front wheels which occurs when in our system description $u<0$ will not destabilise the system but makes the vehicle unsteerable. This because of the fact that changing the steer angle of a locked wheel can not effect the orientation of its frictional force vector. The car with locked rear wheels corresponds in behaviour with the case of excessive oversteer while locked front wheels would give rise to extreme understeer. The critical speed for the case of locked rear wheels is derived by making the third coefficient of Eq.(3.128), or of Eq.(3.124), equal to zero. We find by using (3.122):

$$u_{crit} = \sqrt{\frac{\mu g l}{1 - \dfrac{\mu F_{z1}}{C_1}}} \tag{3.129}$$

From this expression it can be seen that when a rigid front tyre is considered (so that $C_1 \to \infty$) we obtain the simple form: $u_{crit}=\sqrt{(\mu g l)}$. The influence of an elastic front tyre is not very great as the front cornering stiffness may range from 6 to

30 times the tyre normal load. Considering a dry road with $\mu = 1$ we find a critical speed of about 20 km/h.

In view of this very low speed above which the vehicle with rear wheels locked becomes unstable and the fact that normally the speed will already be a lot larger than the critical speed when the brakes are being applied it is more useful to consider the degree of instability as a function of speed. We will adopt the root λ_1 to represent the degree of instability. Figure 3.42 illustrates the manner in which the roots vary with speed of travel. The diagram includes the case of front wheels locked ($u < 0$), where obviously the roots remain negative and become complex at higher speeds of travel (real part: dotted curve). As a practical indication for the degree of instability we may employ the height of the horizontal asymptote to which λ_1 tends when $u \to \infty$. For that we find:

$$\lambda_1\Big|_{u\to\infty} = \sqrt{\frac{g}{l}\cdot\frac{ab}{k^2}\cdot\left(\frac{C_1}{F_{z1}} - \mu\right)} \tag{3.130}$$

which shows that instability decreases when the front tyre cornering stiffness is lower and becomes more in balance with the here very low rear 'cornering stiffness' (3.122). It also becomes clear that when the front wheels are locked as well ($C_1 = \mu F_{z1}$) the degree of instability reduces to zero representing indifferent stability.

The complete solution of Eq.(3.124) can be found by applying the Lommel transformation of the Bessel differential equation and using the modified

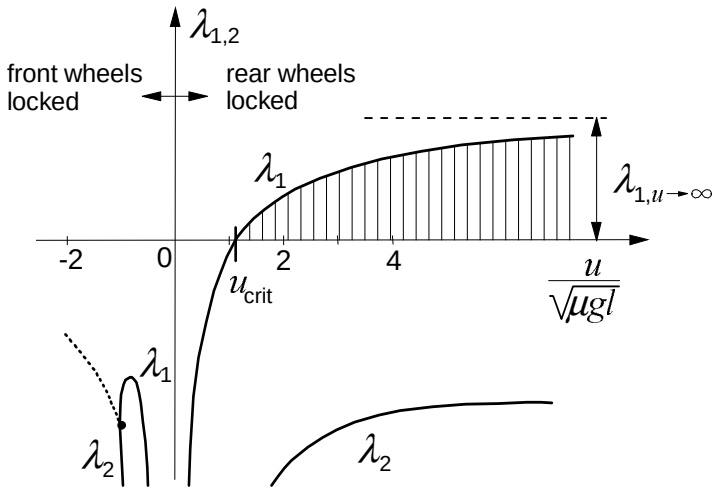

Fig. 3.42. Real (part of the) eigenvalues of the substitutive linear system with constant coefficients.

functions of Bessel in its solution. These functions are available in tabulated form and can be found in the book of Abramowitz and Stegun (1965, cf. Eq.9.1.53 for the transformed equation and p.377 for the solution).

In the paper of Koiter and Pacejka (1969) the exact solution has been given together with examples of the numerically computed solution for the complete non-linear system. For the special case with parameters $a = b = k$, $B_1 = 0$, $C_1/\mu F_z = 6$ the solution of the linear equation (3.124) is presented in Fig.3.43. The exact solution is compared with the approximate one (3.127) of the substitutive equation. The solution in the form of a stable and an unstable branch has been drawn in the (u, r) plane constituting the projection of the complete 3-dimensional trajectory in the (u, v, r) space. Along the u axis we may introduce the time axis considering the relationship (3.126). In the case considered the non-dimensional eigenvalues $\lambda_{1,2}\sqrt{(l/\mu g)}$ take the values 1.26 and -3.43 respectively. For the sake of comparison the initial values have been taken the same for both pairs of solutions. No visible difference can be detected between the two decaying stable branches. The 'unstable' branch of the exact solution, however, shows for greater values of time an increasing difference with the corresponding approximate exponential solution. At the start of the motion where the rear axle tends to break away the agreement is very good. It can be shown that when expanded in a series of powers of the time t the solutions are identical up to and including the third term (with t^2). This supports our choice of defining the degree of instability.

Along the vertical axis the yaw rate is plotted. After having attained a

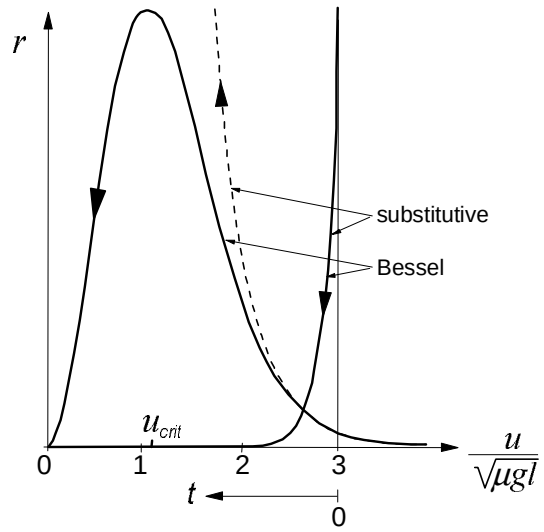

Fig. 3.43. Solutions of the exact and the approximated linear systems representing the variation of the yaw rate r with forward velocity u or with time t.

maximum, the yaw angle develops at a lesser rate until the motion reaches a complete stop. The area underneath the curves is proportional to the final angle of swing. This finite angle will linearly depend on the initial values of the variables r and v. Consequently, the final deviation with respect to the original rectilinear path can be kept within any chosen limit and, strictly speaking, the actual system is always stable.

Finally, the solutions for the non-linear system governed by the Eqs.(3.118, 119) and tyre characteristics according to Fig.3.41 have been established by numerical integration of the equations of motion. Now, the character of the motion may change with the level of the initial disturbance. In Figs.3.44 and

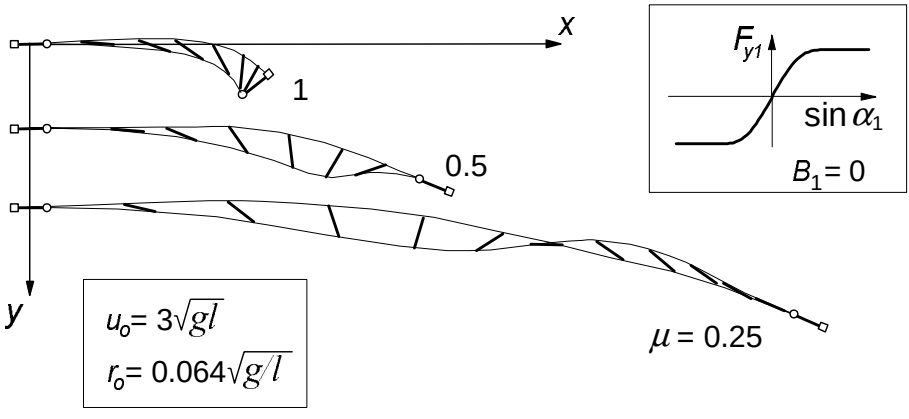

Fig. 3.44. Development of the vehicle motion after the rear wheels get locked while the front wheels remain rolling freely.

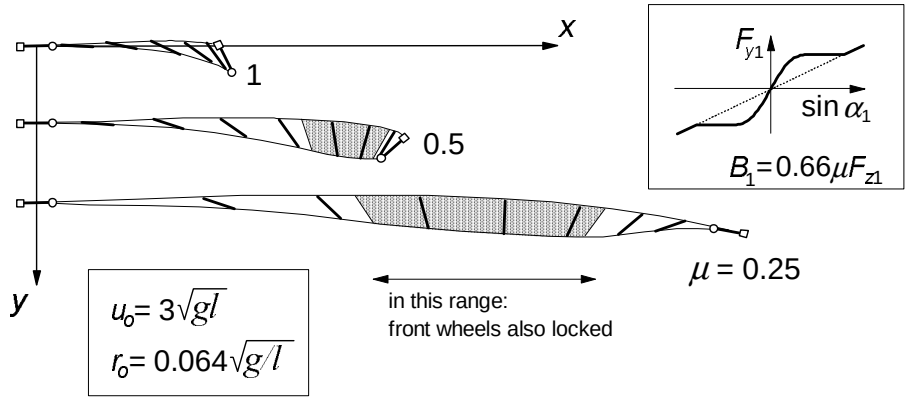

Fig.3.45. Development of the vehicle motion after the rear wheels get locked while also the front wheels are being braked.

3.45, the resulting motions for two cases have been depicted. The first, without braking the front wheels (Fig.3.44) and the second with also the front wheels being braked but at a lower effort to make sure that they roll at least initially. The initial speed of travel and disturbances have been kept the same for all cases but the coefficient of friction μ has been varied. At lower friction the time available to develop the angle of swing is larger and we see that an angle of more than 180 degrees may be reached. Then the locked wheels are moving at the front ($u<0$) and we have seen that that situation is stable while the motion can become oscillatory (cf. Fig.3.42). For the case of Fig.3.44 with $\mu = 0.25$ we indeed observe that a sign change occurs once for the yaw rate r. When the brakes are applied also at the front axle, the deceleration is larger and we have less time to come to a stop. Consequently, the final angles of Fig.3.45 are smaller than those reached in Fig.3.44. The shaded zones indicate the ranges where also the front wheels get locked. This obviously occurs when the slip angle of the initially rolling wheels 1 becomes sufficiently large and exceeds the value indicated in Fig.3.41 where the inclined straight line is reached. It has been found (not surprisingly) that the influence of raising the initial speed is qualitatively the same as the effect of reducing the coefficient of friction.

Chapter 4

SEMI-EMPIRICAL TYRE MODELS

4.1. Introduction

In the preceding chapter the theory of the tyre force and moment generating properties have been dealt with based on physical tyre models. The present chapter treats models that have been specifically designed to represent the tyre as a vehicle component in a vehicle simulation environment. The modelling approach is termed 'semi-empirical' because the models are based on measured data but may contain structures that find their origin in physical models like those treated in the preceding chapter. The mathematical descriptions are restricted to steady-state situations. The non-steady-state behaviour will be discussed in subsequent chapters.

In the past, several types of mathematical functions have been used to describe the cornering force characterisic. Exponential, arctangent, parabolic (up to its maximum) and hyperbolic tangent functions (difference of two) have been tried with more and less success. Often, only very crude approximations could be achieved. To improve the accuracy, tables of measured data points have been used together with interpolation schemes. Also, higher order polynomials were popular but proved not always suitable in terms of accuracy and the very large deviations that occur outside the ranges of slip covered by the original measurement data used in the fitting process. Mathematical representations of longitudinal force and aligning torque came later and only relatively recently the combined slip condition was included in the empirical description. The longitudinal slip ratio was introduced as an input variable instead of the braking or driving force which was common practice in the early days of vehicle dynamics analysis. This latter method, however, is still in use for certain applications.

In the following sections of this chapter, first, a relatively simple approach will be discussed that is based on the similarity concept and after that, in the remainder of the chapter, a detailed description will be given of the Magic Formula tyre model. The two model approaches belong to the second and first categories of Fig.2.11 respectively.

4.2. The Similarity Method

The method to be discussed in this section is based on the observation that the pure slip curves remain approximately similar in shape when the tyre runs at conditions that are different from the reference condition. The reference condition is defined here as the state where the tyre runs at its rated (nominal) load (F_{zo}), at camber equal to zero ($\gamma = 0$), at either free rolling ($\kappa = 0$) or at side slip equal to zero ($\alpha = 0$) and on a given road surface (μ_o). A similar shape means that the characteristic that belongs to the reference condition is regained by vertical and horizontal multiplications and shifting of the curve. The similarity method has been first used by Pacejka (1958) and later by Radt and Pacejka (1963). A demonstration that in practice similarity indeed approximately occurs is given by Radt and Milliken (1983), also see Milliken and Milliken (1995). The Figs.4.1 and 4.2 present the results when the force and moment as well as the slip angle have been normalised resulting in the non-dimensional quantities shown along the axes. The raw data have been processed to make the characteristics pass through the origin of the graph. The curve results from a Magic Formula fit. The parameters B', C', D' and E' for the non-dimensional

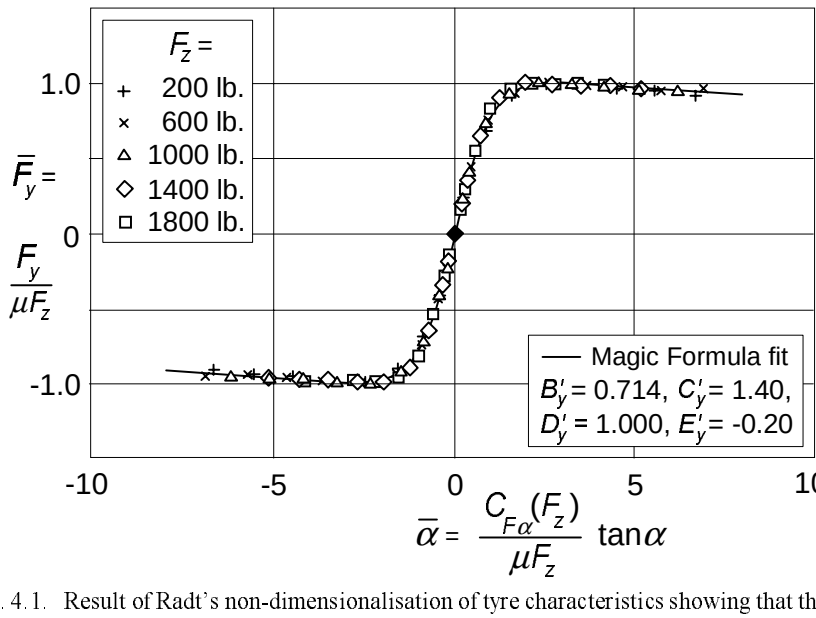

Fig. 4.1. Result of Radt's non-dimensionalisation of tyre characteristics showing that the tyre side force characteristics measured at different loads reduce to virtually the same curve when the force and the slip angle are normalized as indicated.

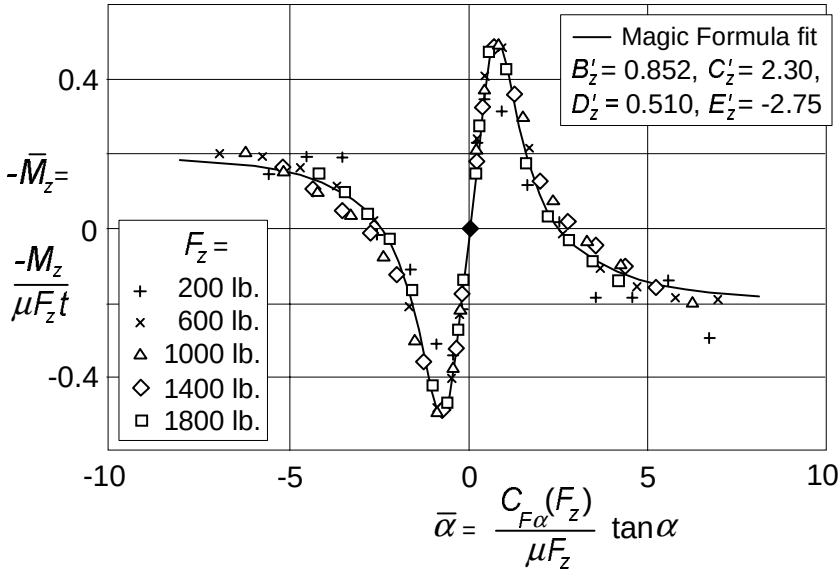

Fig. 4.2. Result of Radt's non-dimensionalisation of the tyre aligning torque characteristic after normalising the moment and the slip angle as indicated; t represents the pneumatic trail at vanishing slip angle.

side force (subscript $_y$) and for the non-dimensional moment (subscript $_z$) have been used in the non-dimensional version of the Magic Formula given in Eqs.(1.6) and similar for the moment. Later on, the formula will be introduced again, Eqs.(4.6,10).

The resulting model is through its simplicity relatively fast. It is capable to represent pure slip conditions rather well including the influence of a camber angle. The description of the situation at combined lateral and longitudinal slip is qualitatively satisfactory. Quantitatively, however, deviations may occur at higher levels of the combined two slip values.

4.2.1. Pure Slip Conditions

The functions representing the reference curves which are found at pure slip conditions are designated with the subscript $_o$. We have, for instance, the reference function $F_y = F_{yo}(\alpha)$ that represents the side force vs slip angle relationship at nominal load F_{zo}, with longitudinal slip and camber equal to zero and the friction level represented by μ_o. We may now try to change the condition to a situation at a different wheel load F_z. Two basic changes will occur with the characteristic: (1) a change in level of the curve where saturation of the side

force takes place (peak level) and (2) a change in slope at vanishing side slip ($\alpha = 0$). The first modification can be created by multiplying the characteristic both in vertical and horizontal direction with the ratio F_z / F_{zo}. The horizontal multiplication is needed to not disturb the original slope. We obtain for the new function:

$$F_y = \frac{F_z}{F_{zo}} F_{yo}(\alpha_{eq}) \tag{4.1}$$

with the equivalent slip angle:

$$\alpha_{eq} = \frac{F_{zo}}{F_z} \alpha \tag{4.2}$$

Because, obviously, the derivative of F_{yo} with respect to its argument α_{eq} at $\alpha_{eq} = 0$ is equal to the original cornering stiffness $C_{F\alpha o}$, we find for the derivative of F_y with respect to α the same value for the slope at $\alpha = 0$:

$$\frac{\partial F_y}{\partial \alpha} = \frac{F_z}{F_{zo}} \frac{\mathrm{d}F_{yo}}{\mathrm{d}\alpha_{eq}} \frac{\partial \alpha_{eq}}{\partial \alpha} = \frac{\mathrm{d}F_{yo}}{\mathrm{d}\alpha_{eq}} = C_{F\alpha o} \tag{4.3}$$

which proves that the slope at the origin of the characteristic is not affected by the successive multiplications. The second step in the manipulation of the

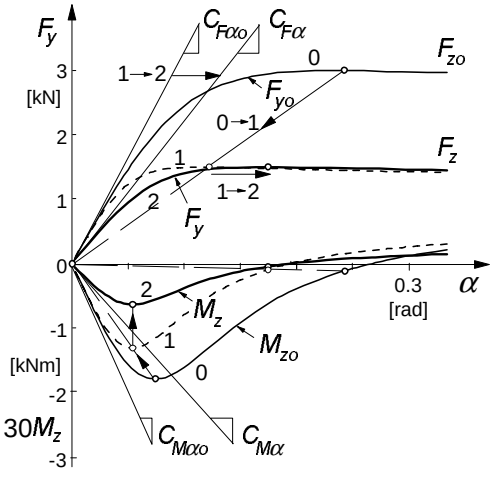

Fig.4.3. Using the similarity method to adapt F_y and M_z curves to a new level of load.

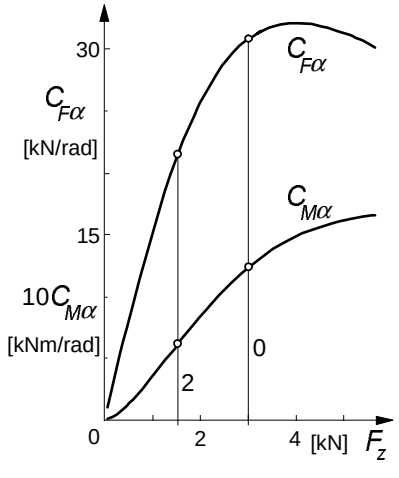

Fig.4.4. Cornering and aligning stiffness versus wheel load.

original curve is the adaptation of the slope. This is accomplished by a horizontal multiplication of the newly obtained characteristic. This is done by multiplying the argument with the ratio of the new and the original cornering stiffness. Consequently, the new argument reads:

$$\alpha_{eq} = \frac{C_{F\alpha}(F_z)}{C_{F\alpha o}} \frac{F_{zo}}{F_z} \alpha \tag{4.4}$$

Together with Eq.(4.1) we have the new formulation for the side force vs slip angle relationship at the new load F_z. In Fig.4.3 the two steps taken to obtain the new curve have been illustrated. Here, the nominal load F_{zo}= 3000N and the new load F_z= 1500N.

In the same figure the characteristic of the aligning torque has been adapted to the new condition. For this, we use the knowledge gained when working with the brush model (cf. Fig.3.4). More specifically, we will obey the rule that according to the theory, obviously, the point where the M_z curve reaches the α axis lies below the peak of the F_y curve. In Fig.3.4 this occurs at $\tan\alpha = 1/\theta_y$. This requirement means that the same equivalent slip angle (4.4) must be used as for the argument of the F_y function (4.1). Secondly, we will use information on the new value of the aligning stiffness $C_{M\alpha}$. The reference curve for M_{zo} that is used is more realistic then the theoretical curve of Fig.3.4. Typically, the moment changes its sign in the larger slip angle range where F_y reaches its peak.

With the same equivalent slip angle and the new aligning stiffness we obtain the expression for the new value of the aligning torque according to the similarity concept:

$$M_z = \frac{F_z}{F_{zo}} \frac{C_{M\alpha}(F_z)}{C_{M\alpha o}} \frac{C_{F\alpha o}}{C_{F\alpha}(F_z)} M_{zo}(\alpha_{eq}) \tag{4.5}$$

The first and third factors being the inverse of the multiplication factor used in (4.4), are needed to maintain the original slope. The second factor multiplies the intermediate M_z curve (1 in Fig.4.3) in vertical direction to adapt the slope to its new value (2) while not disturbing the α scale. It may be noted that the combined second and third factor equals the ratio of the new and the original values of the pneumatic trail t/t_o.

For the calculations connected with Fig.4.3 the reference characteristics for F_{yo}, M_{zo} and $C_{F\alpha}$ have been described by means of the Magic Formula type functions (cf. Eqs.(1.6)). For this occasion, the aligning stiffness is modelled as the product of a certain fraction of the contact length $2a$ and the cornering stiffness. The resulting characteristics for these four quantities as shown in Figs. 4.3 and 4.4 are realistic. The following formulae have been used:

Side force at nominal load F_{zo}

$$F_{yo} = D_{yo}\sin[C_y \arctan\{B_{yo}\alpha - E_y(B_{yo}\alpha - \arctan(B_{yo}\alpha))\}] \tag{4.6}$$

with stiffness factor

$$B_{yo} = C_{F\alpha o}/(C_y D_{yo}) \tag{4.7}$$

peak factor for the side force which in general is different from the one for the longitudinal force, consequently we introduce μ_{yo} beside μ_{xo}:

$$D_{yo} = \mu_{yo} F_{zo} \tag{4.8}$$

and cornering stiffness as function of wheel load F_z

$$C_{F\alpha} = c_1 c_2 F_{zo} \sin\left\{2\arctan\left(\frac{F_z}{c_2 F_{zo}}\right)\right\} \tag{4.9}$$

Aligning torque at nominal wheel load:

$$M_{zo} = D_{zo}\sin[C_z \arctan\{B_{zo}\alpha - E_z(B_{zo}\alpha - \arctan(B_{zo}\alpha))\}] \tag{4.10}$$

with stiffness factor

$$B_{zo} = -C_{M\alpha o}/(C_z D_{zo}) \tag{4.11}$$

peak factor (a_o representing half the contact length at nominal load)

$$D_{zo} = c_3 a_o D_{yo} \tag{4.12}$$

and aligning stiffness as function of wheel load F_z

$$C_{M\alpha} = tC_{F\alpha} = c_4 a C_{F\alpha} \tag{4.13}$$

where apparently the pneumatic trail $t = c_4 a$. Half the contact length a is assumed to be proportional with the square root of the wheel load

$$a = a_o\sqrt{F_z/F_{zo}} \tag{4.14}$$

The resulting approximation of the pneumatic trail turns out to be quite adequate and might be considered to be used in the set of Magic Formula Tyre model equations (4.E42) to be dealt with later on.

The values of parameters used for the calculations to be conducted have been listed in Table 4.1.

Table 4.1. Parameter values used in Section 4.2.

F_{zo}	3000 N	C_y	1.3	C_x	1.5	c_1	8	c_5	1	c_9	0.3
a_o	0.08 m	E_y	-1	E_x	-1	c_2	1.33	c_6	0.3	c_{10}	0
b	0.07 m	C_z	2.3	μ_{yo}	1	c_3	0.25	c_7	100	c_{11}	4
r_e	0.30 m	E_z	-2	μ_{xo}	1.26	c_4	0.5	c_8	15		

The next two items we will deal with is a change in friction coefficient from μ_{yo} to μ_y and the introduction of a camber angle γ. The first change can be handled by multiplying the curves in radial direction with factor μ_y/μ_{yo}. Together with the change in load we find:

$$F_y = \frac{\mu_y F_z}{\mu_{yo} F_{zo}} F_{yo}(\alpha_{eq}) \tag{4.15}$$

with

$$\alpha_{eq} = \frac{C_{F\alpha}(F_z)}{C_{F\alpha o}} \frac{\mu_{yo} F_{zo}}{\mu_y F_z} \alpha \tag{4.16}$$

The friction coefficient may be assumed to depend on the slip velocity V_s. To model the situation on wet roads a decaying function $\mu(V_s)$ may be employed, cf. e.g. Eq.(4.E23).

When considering the computed characteristics of Fig.3.35c (2nd row) for small camber angles a horizontal shift of the F_y curve may give a reasonable result. Then, the peak side force remains unchanged which is a reasonable assumption but not always supported by experimental evidence (where often but not always a slight increase in maximum side force is manifested) or by computations with a physical model with constant friction and finite contact width which show a slight decrease. For small angles, the camber thrust is approximated by the product of the camber stiffness and the camber angle: $F_{y\gamma}= C_{F\gamma}\gamma$. Consequently, the α shift should amount to

$$S_{Hy} = \frac{C_{F\gamma}(F_z)}{C_{F\alpha}(F_z)} \gamma \tag{4.17}$$

so that

$$\alpha^* = \alpha + S_{Hy} \tag{4.18}$$

which gives rise to α_{eq} (4.16) with α replaced by $\alpha^* = \alpha + S_{Hy}$.

For the representation of the aligning moment at the new conditions the situation is more complex. We observe from Fig.3.35c that for not too large slip angles the original curve M_{zo} tends to both shift sideways and upwards. If the same equivalent slip angle and thus the same horizontal shift (4.17) as for the force is employed, the moment would become zero where also the force curve crosses the α axis. A moment equal to $-C_{M\alpha}S_{Hy}$ would arise at $\alpha = 0$. However, the moment should become equal to $C_{M\gamma}\gamma$, with a positive camber moment stiffness $C_{M\gamma}$. This implies that an additional vertical shift is required equal to:

$$S_{Vz} = C_{M\gamma}(F_z)\gamma + C_{M\alpha}(F_z) S_{Hy} \tag{4.19}$$

This additional moment corresponds to the so-called residual torque M_{zr}, which

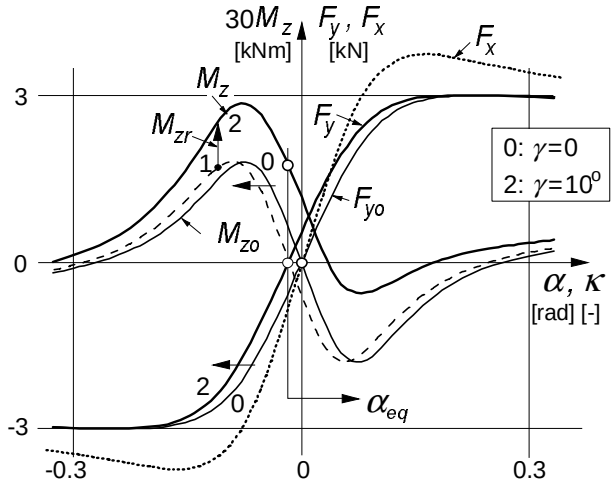

Fig. 4.5. Introduction of a camber angle in the side force and the aligning torque pure slip characteristics according to the similarity method. The longitudinal force pure slip characteristic. ($F_z = F_{zo} = 3000$N, $\mu_y = \mu_{yo} = 1$, $\mu_x = \mu_{xo} = 1.26$).

is the moment that remains when the side force becomes equal to zero. For larger values of the slip angle the additional moment should tend to zero as can be observed in Fig.3.35c. This may be easily accomplished by dividing (4.19) by a term like $1 + c_7\alpha^2$.

The dependencies of the camber stiffnesses on the vertical load may be assumed linear. We have:

$$C_{F\gamma} = c_5 F_z \ , \qquad C_{M\gamma} = c_6 \frac{b^2}{r_e} C_{F\kappa} \tag{4.20a}$$

where b denotes half the (assumedly constant) width of the contact patch, r_e the effective rolling radius and $C_{F\kappa}$ the longitudinal slip stiffness which is considered to be linearly increasing with load:

$$C_{F\kappa} = c_8 F_z \tag{4.20b}$$

In Fig.4.5 the different steps leading to the condition with a (small) camber angle have been demonstrated. First, the original curve (0) is moved to the left over a distance equal to the horizontal shift (4.17) yielding the intermediate curve (1). Then the residual torque is added: vertical shift (4.19), possibly made a function of slip angle by multiplying the shift with a decaying weighting function as suggested above. The load F_z and the friction coefficient μ_y have been kept equal to their reference values: 3000N and 1 respectively.

The longitudinal force at pure longitunal slip may be modelled in the same

way as we did for the side force. Equations similar to (4.6-8) hold for the reference function. An influence of camber on the longitudinal force, however, is assumed not to occur. In the same figure 4.5 the characteristic for F_x vs κ has been drawn. The values of the relevant additional parameters for the longitudinal force and the moment have been listed in Table 4.1.

We finally have the following similarity formulae for pure slip conditions (either at longitudinal or at lateral slip) for the longitudal force:

$$F_x = \frac{\mu_x F_z}{\mu_{xo} F_{zo}} F_{xo}(\kappa_{eq}) \tag{4.21}$$

with the equivalent longitudinal slip

$$\kappa_{eq} = \frac{C_{F\kappa}(F_z)}{C_{F\kappa o}} \frac{\mu_{xo} F_{zo}}{\mu_x F_z} \kappa \tag{4.22}$$

and for the side force:

$$F_y = \frac{\mu_y F_z}{\mu_{yo} F_{zo}} F_{yo}(\alpha_{eq}) \tag{4.23}$$

with the equivalent slip angle, containing the horizontal shift (4.17):

$$\alpha_{eq} = \frac{C_{F\alpha}(F_z)}{C_{F\alpha o}} \frac{\mu_{yo} F_{zo}}{\mu_y F_z} \left(\alpha + \frac{C_{F\gamma}(F_z)}{C_{F\alpha}(F_z)} \gamma \right) \tag{4.24}$$

and for the aligning torque:

$$M_z = \frac{\mu_y F_z}{\mu_{yo} F_{zo}} \frac{C_{M\alpha}(F_z)}{C_{M\alpha o}} \frac{C_{F\alpha o}}{C_{F\alpha}(F_z)} M_{zo}(\alpha_{eq}) + M_{zr} \tag{4.25}$$

with the residual torque corresponding to the vertical shift (4.19) provided with the reduction factor:

$$M_{zr} = \frac{C_{M\gamma}(F_z) + t(F_z)\, C_{F\gamma}(F_z)}{1 + c_7 \alpha^2} \gamma \tag{4.26}$$

4.2.2. Combined Slip Conditions

We will now address the problem of describing the situation at combined slip. The analysis of the brush model has gained considerable insight into the mechanisms that play a role and we will use the theoretical slip quantities $\sigma_{x,y}$ (3.34 or 32) and the magnitude σ (3.40) and we will adopt the concept similar to that of assessing the components of the resulting horizontal force according

to (3.49) and consider the pneumatic trail t as in (3.50) and include explicit contributions of F_x to the moment as indicated in (3.51). We have for the theoretical slip quantities with the α shift due to camber included:

$$\sigma_x = \frac{\kappa}{1+\kappa} \tag{4.27a}$$

$$\sigma_y^* = \frac{\tan\alpha^*}{1+\kappa} \tag{4.27b}$$

and

$$\sigma^* = \sqrt{\sigma_x^{\,2} + \sigma_y^{*\,2}} \tag{4.28}$$

with

$$\alpha^* = \alpha + \frac{C_{F\gamma}(F_z)}{C_{F\alpha}(F_z)}\gamma \tag{4.29}$$

In the ensuing theory we will make use of the theoretical slip quantities (4.27a,b), which does produce the slope in the constant α curves in the F_y vs F_x diagram at $F_x = 0$. It should be noted, however, that experience has shown that the use of practical slip quantities s_x and s_y^* (that is: κ and $\tan\alpha^*$ which may be obtained again by omitting the denominators in (4.27a,b)) may already give very good results as will be indicated later on in Fig.4.8. Note that when approaching wheel lock $\sigma_x \to \infty$. This calls for an artificial limitation by adding a small positive quantity to the denominator of (4.27a).

Because we are dealing with an in general non-isotropic tyre we have pure longitudinal and lateral slip characteristics that are not identical (cf. Fig.4.5). Still, we will take the lateral and longitudinal components but then of the respective pure slip characteristics F_{yo} and F_{xo}. If we want to use the theoretical slip quantities σ we must have available the pure slip characteristics with σ_x and σ_y as abscissa. This can be accomplished by fitting the original data after having computed the values of σ_x for each value of κ by using (4.27a) and similar for transforming α into $\tan\alpha$ and denote the resulting functions: $F_{xo}(\sigma_x)$, $F_{yo}(\sigma_y)$ and $M_{zo}(\sigma_y)$. Or, simpler, by replacing in the already available pure slip force and moment functions, expressed in terms of the practical slip quantities, the argument α (in radians) by $\tan\alpha$ (probably acceptable approximation) and κ by the expression given below (derived from Eq.(4.27a)).

$$\kappa = \frac{\sigma_x}{1-\sigma_x} \tag{4.30}$$

which would be successful if the F_x characteristic has been fitted for the whole range of positive (driving) and negative (braking) values of κ. Otherwise if only

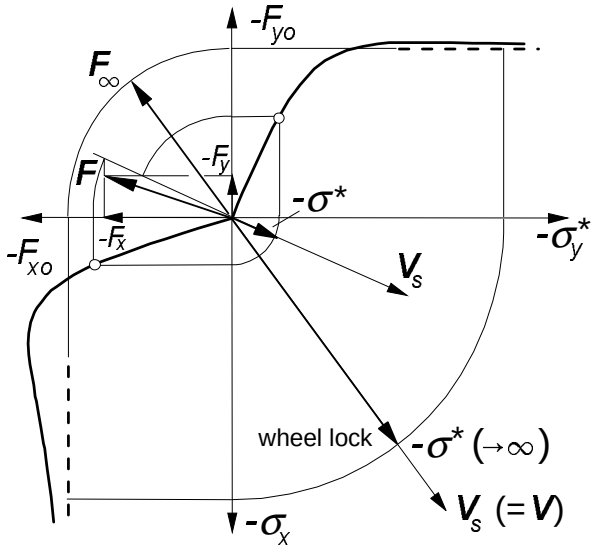

Fig.. 4.6. Construction of the resulting combined slip force from the pure slip characteristics according to Eqs.(4.31).

the braking side is available (κ and σ_x <0) and the driving side is modelled as the mirror image of the braking side one might better take:

$$\kappa = \frac{\sigma_x}{1 + |\sigma_x|} \tag{4.30a}$$

If the thus obtained function of F_x is plotted versus σ_x the resulting curve becomes symmetric. However, if then the abcsissa is transformed into κ by using (4.30) the resulting curve turns out to become asymmetric with the braking side identical to the characteristic we started out with. This asymmetry was already found to occur with the brush model discussed in Chapter 3.

Next, we should realise that through (4.18) camber has been accounted for and that, as a consequence, σ_y is to be replaced by σ_y^* defined by Eq.(4.27b). The resulting force and moment functions are denoted by $F_{xo}(\sigma_x)$, $F_{yo}(\sigma_y^*)$ and $M_{zo}(\sigma_y^*)$. As illustrated in Fig.4.6, the 'components' now become with σ^* denoting the magnitude of the theoretical slip vector (4.28):

$$F_x = \frac{\sigma_x}{\sigma^*} F_{xo}(\sigma^*) \ , \quad F_y = \frac{\sigma_y^*}{\sigma^*} F_{yo}(\sigma^*) \tag{4.31}$$

The figure shows how the force vector arises from the individual pure slip characteristics. At small slip, in general, the vector does not run opposite with respect to the slip speed vector V_s. At wheel lock, however, the force vector does

run opposite with respect to the slip speed vector because it is assumed here that the levels of the individual characteristics (asymptotes) are the same for the slip approaching infinity (in the Magic Formula we should have: $\mu_{yo}\sin(\frac{1}{2}\pi C_y) = \mu_{xo}\sin(\frac{1}{2}\pi C_x)$). At large slip the theory apparently fails to properly account for the contribution of the camber angle. At wheel lock one would expect the side force to become zero at vanishing slip angle. This will not exactly be the case in the model due to the equivalent theoretical side slip defined according to Eq.(4.27b) with α^* given by (4.18).

For the aligning torque we may define:

$$M_z = M_z' + M_{zr} - \frac{c_9 a_o}{F_{zo}} F_x F_y - c_{10} a_o F_x - c_{11} b \gamma F_x \tag{4.32}$$

with the first term directly attributable to the side force. This term can be written as:

$$M_z' = -t(\sigma^*) \cdot F_y \tag{4.33}$$

By considering (4.31) it turns out that (4.33) becomes:

$$M_z' = \frac{\sigma_y^*}{\sigma^*} M_{zo}'(\sigma^*) \tag{4.34}$$

The last three terms of Eq.(4.32) result from the moment exerted by the longitudinal force because of the moment arm that arises through the side force induced deflection, a possibly initial offset of the line of action and the sideways rolling of the tyre cross section due to camber. For the sake of simplicity these effects are assumed not to be influenced by the wheel load.

With the similarity expressions for the pure slip forces $F_{x,yo}$ and moment M_{zo}' we finally obtain the following formulae for combined slip conditions. For the longitudal force:

$$F_x = \frac{\sigma_x}{\sigma^*} \frac{\mu_x F_z}{\mu_{xo} F_{zo}} F_{xo}(\sigma_{eq}^x) \tag{4.35}$$

with the equivalent slip

$$\sigma_{eq}^x = \frac{C_{F\kappa}(F_z)}{C_{F\kappa o}} \frac{\mu_{xo} F_{zo}}{\mu_x F_z} \sigma^* \tag{4.36}$$

and for the side force:

$$F_y = \frac{\sigma_y^*}{\sigma^*} \frac{\mu_y F_z}{\mu_{yo} F_{zo}} F_{yo}(\sigma_{eq}^y) \tag{4.37}$$

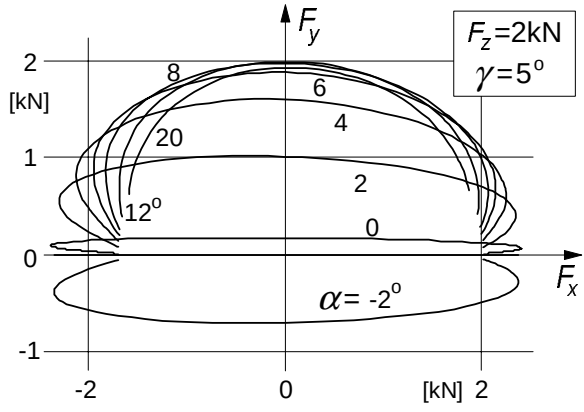

Fig. 4.7a. Cornering force versus longitudinal force at a new load and camber angle as computed with the similarity method.

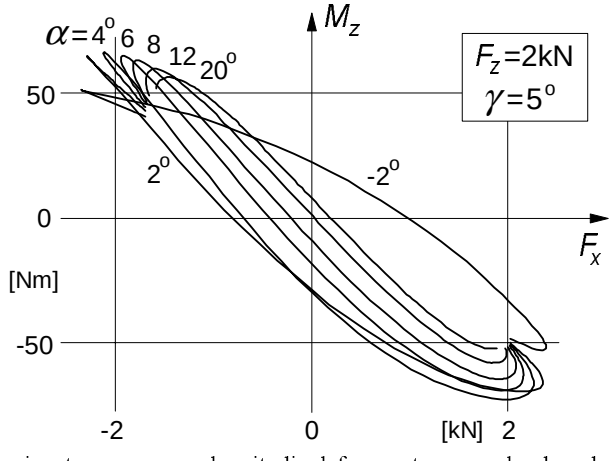

Fig. 4.7b. Aligning torque versus longitudinal force at a new load and camber angle as computed with the similarity method.

with the equivalent slip

$$\sigma_{eq}^{y} = \frac{C_{F\alpha}(F_z)}{C_{F\alpha o}} \frac{\mu_{yo} F_{zo}}{\mu_y F_z} \sigma^* \tag{4.38}$$

and for the aligning torque:

$$\begin{aligned} M_z = {} & \frac{\sigma_y^*}{\sigma^*} \frac{\mu_y F_z}{\mu_{yo} F_{zo}} \frac{C_{M\alpha}(F_z)}{C_{M\alpha o}} \frac{C_{F\alpha o}}{C_{F\alpha}(F_z)} M'_{zo}(\sigma_{eq}^{y}) + M_{zr} + \\ & - \frac{c_9 a_o}{F_{zo}} F_x F_y - c_{10} a_o F_x - c_{11} b \gamma F_x \end{aligned} \tag{4.39}$$

with the residual torque

$$M_{zr} = \frac{C_{M\gamma}(F_z) + t(F_z)\, C_{F\gamma}(F_z)}{1 + c_7(\sigma_{eq}^{y})^2}\gamma \tag{4.40}$$

On behalf of example calculations, the three additional non-dimensional parameters c_9, c_{10} and c_{11} have been given values listed in Table 4.1.

For the case of a load different from the reference value and the presence of a camber angle, the combined slip characteristics for the tyre side force and for the aligning torque have been assessed by using the above equations. The resulting diagrams with slip angle α used as parameter have been presented in the Figs.4.7a and b. Due to the use of the theoretical slip quantities (4.27a, 27b) we find that the curves of F_y show the slight slope near $F_x = 0$ also observed to occur with the physical brush model and sometimes more pronounced in experimentally assessed characteristics (Fig.3.18). The additional slope that arises when a camber angle is introduced (cf. Fig.3.35c, top) for which the torsional compliance is responsible does not appear. A special formulation would be needed to represent this effect. In the next section we will take care of this in connection with the Magic Formula tyre model.

It may be further remarked that the similarity model given by the equations (4.35-40) together with (4.27a,b), (4.28) and the reference pure slip functions does represent the actual tyre steady-state behaviour well in the following

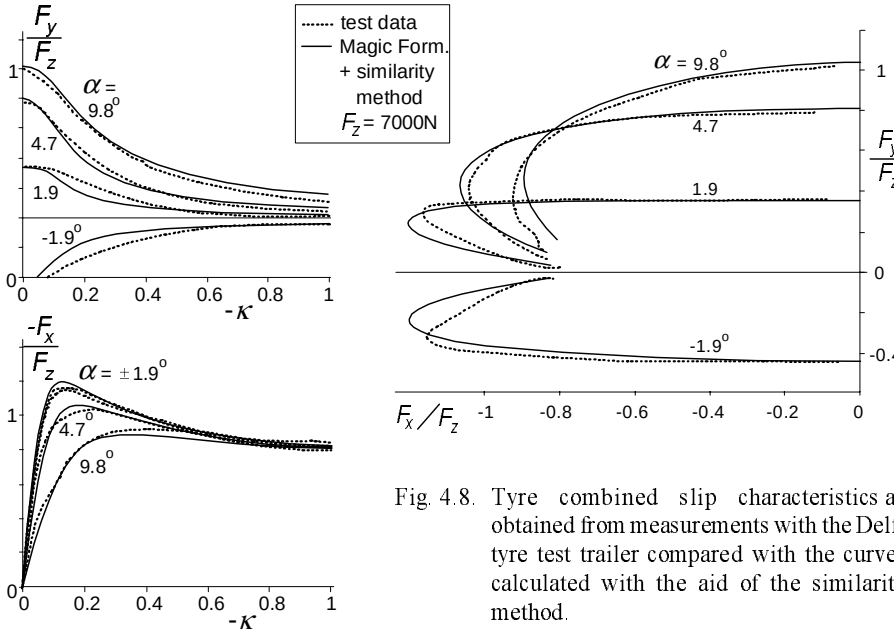

Fig. 4.8. Tyre combined slip characteristics as obtained from measurements with the Delft tyre test trailer compared with the curves calculated with the aid of the similarity method.

extreme cases: (1) in pure slip situations, (2) in the linearised combined slip situation (small α and κ) and (3) in the case of a locked wheel ($\gamma = 0$). As illustrated in Fig.4.6 the model correctly shows that when the wheel is locked, the resulting force acts in a direction opposite to the slip speed vector V_s if in the original reference pure slip curves the level of F_{xo} and of F_{yo} tend to the same level when both slip components approach infinity (governed by the parameters μ and C in the Magic Formula). Other combinations of slip may give rise to deviations with respect to measured characteristics. It is noted that when the terms for the aligning torque with parameters c_9, c_{10} and c_{11} are disregarded, the combined slip performance can be represented without the necessity to rely on combined slip measurement data.

A comparison with measured data is given in Fig.4.8. Here the similarity method is used where instead of the theoretical slip quantities the practical slip variables κ and $\tan\alpha$ have been employed. A relatively good agreement is achieved for this passenger car tyre in the combined slip situation.

4.2.2. Combined Slip Conditions with F_x as input variable

In more simple vehicle dynamics simulation studies with the wheel spin degree of freedom not included, one may prefer to use the longitudinal force F_x as input quantity instead of the longitudinal slip κ. This approach has been used, almost exclusively, in early vehicle dynamics research. However, for (quasi) steady-state cornering analysis, notably circuit simulation in the racing world, this option is still popular. An important limitation of using this method is the condition that the F_x vs κ characteristic (although not used) is supposed to show a positive slope over the entire range of longitudinal slip while at wheel lock $F_x = -\mu F_z$. Or,alternatively, we use only that part of the characteristic that lies in between the two peaks. This entails that the F_y vs F_x curves are single valued in the F_x range employed. Furthermore, it is assumed that the friction coefficient is the same for longitudinal and lateral directions and is denoted with μ.

The obvious main effect of the introduction of F_x on the side force is the lowering of the maximum side force that can be generated. For this to realise the right-hand expressions of Eqs.(4.23) and (4.25) are to be multiplied with the factor

$$\varphi_x = \frac{\sqrt{\mu^2 F_z^2 - F_x^2}}{\mu F_z} \tag{4.41}$$

while the expression (4.24) is to be divided by the same factor. The cornering

and aligning stiffnesses remain unaffected through this operation. These stiffnesses, however, do depend on the longitudinal force as becomes obvious from the curves of Fig.3.13 that belong to small side slip angles. The following functions may serve as a crude approximation of the actual relationships.

$$C_{F\alpha}(\mu,F_z,F_x) = \varphi_{x\alpha}\left\{C_{F\alpha}(F_z) - \tfrac{1}{2}\mu F_z\right\} + \tfrac{1}{2}(\mu F_z - F_x) \tag{4.42}$$

with

$$\varphi_{x\alpha} = \left\{1 - \left(\frac{F_x}{\mu F_z}\right)^n\right\}^{1/n} \tag{4.42a}$$

Depending on the user's desire one may choose for n a value in the range of 2 to 8 (more or less curved characteristic $C_{F\alpha}(F_x)$) . For the aligning stiffness we may use the formula:

$$C_{M\alpha}(\mu,F_z,F_x) = \varphi_x^2 C_{M\alpha}(F_z) \tag{4.43}$$

and similar for the camber stiffness:

$$C_{F\gamma}(\mu,F_z,F_x) = \varphi_x^2 C_{F\gamma}(F_z) \tag{4.44}$$

The camber moment stiffness may be disregarded. The load dependencies $C_{F,M\alpha}(F_z)$ and $C_{F\gamma}(F_z)$ of the freely rolling tyre already appeared in Eqs.(4.24, 25). It may be ascertained that the present model makes sure that the cornering stiffness vanishes when $F_x \to \mu F_z$ (wheel drive spin, $\kappa \to \infty$) while at $F_x = -\mu F_z$ (wheel lock, $\kappa = -1$) the side slip stiffness equals μF_z, which is correct. The functional relationships (4.21, 22) for F_x do not play a role anymore and the friction coefficient μ_y has been replaced by μ. The imposed longitudinal force should be kept within the boundaries $-\mu F_z \cos\alpha \le F_x \le \mu F_z$.

The resulting equations for the side force and the aligning torque with the longitudinal force serving as one of the input quantities now read:
For the side force:

$$F_y = \varphi_x \frac{\mu F_z}{\mu_o F_{zo}} F_{yo}(\alpha_{eq}) \tag{4.45}$$

with the equivalent slip angle

$$\alpha_{eq} = \frac{1}{\varphi_x} \frac{C_{F\alpha}(\mu,F_z,F_x)}{C_{F\alpha o}} \frac{\mu_o F_{zo}}{\mu F_z} \left(\alpha + \frac{C_{F\gamma}(\mu,F_z,F_x)}{C_{F\alpha}(\mu,F_z,F_x)}\gamma\right) \tag{4.46}$$

and for the aligning torque:

$$M_z = \varphi_x \frac{\mu F_z}{\mu_o F_{zo}} \frac{C_{M\alpha}(\mu,F_z,F_x)}{C_{M\alpha o}} \frac{C_{F\alpha o}}{C_{F\alpha}(\mu,F_z,F_x)} M_{zo}(\alpha_{eq}) + M_{zr} + \\ - \frac{c_9 a_o}{F_{zo}} F_x F_y - c_{10} a_o F_x - c_{11} b \gamma F_x \tag{4.47}$$

where the last terms have been taken from (4.39) and the residual torque reads:

$$M_{zr} = \varphi_x \frac{C_{M\gamma}(F_z) + t(F_z)\, C_{F\gamma}(F_z)}{1 + c_7 \alpha^2} \gamma \tag{4.48}$$

Exercise 4.1 given at the end of Section 4.3 addresses the problem of assessing the side force characteristics using the similarity technique with the longitudinal force considered as one of the input quantities.

In Section 4.3 the Magic Formula tyre model will be treated in detail. This complex model is considerably more accurate and will again employ the longitudinal slip κ as input variable.

4.3. The Magic Formula Tyre Model

A widely used semi-empirical tyre model to calculate steady-state tyre force and moment characteristics for use in vehicle dynamics studies is based on the so-called Magic Formula. The development of the model was started in the mid-eighties. In a cooperative effort TU-Delft and Volvo developed several versions (Bakker et al. 1987, 1989, Pacejka et al. 1993). In these models the combined slip situation was modelled from a physical view point. In 1993 Michelin (cf. Bayle et al. 1993) introduced a purely empirical method using Magic Formula based functions to describe the tyre horizontal force generation at combined slip. This approach was adopted by DVR (the Delft Vehicle Dynamics Research Center, a joint venture of TU-Delft and TNO- Delft). In the newer version of 'Delft Tyre' the original description of the aligning torque is altered to accommodate a relatively simple physically based combined slip extension. The pneumatic trail is introduced as a basis to calculate this moment about the vertical axis, cf. Pacejka (1996). A complete listing of the model is given in Section 4.3.2. In Section 4.3.3 the model is further extended by introducing formulae for the description of the situation at large camber and turn slip.

4.3.1. Model Description

The general form of the formula that holds for given values of vertical load and camber angle reads:

$$y = D\sin[C\arctan\{Bx - E(Bx - \arctan Bx)\}] \tag{4.49}$$

with

$$Y(X) = y(x) + S_V \tag{4.50}$$

$$x = X + S_H \tag{4.51}$$

where

Y: output variable F_x, F_y or possibly M_z

X: input variable $\tan\alpha$ or κ

and

B stiffness factor

C shape factor

D peak value

E curvature factor

S_H horizontal shift

S_V vertical shift

The Magic Formula *y(x)* typically produces a curve that passes through the origin $x = y = 0$, reaches a maximum and subsequently tends to a horizontal asymptote. For given values of the coefficients B, C, D and E the curve shows an anti-symmetric shape with respect to the origin. To allow the curve to have an offset with respect to the origin, two shifts S_H and S_V have been introduced. A new set of coordinates *Y(X)* arises as shown in Fig.4.9. The formula is capable

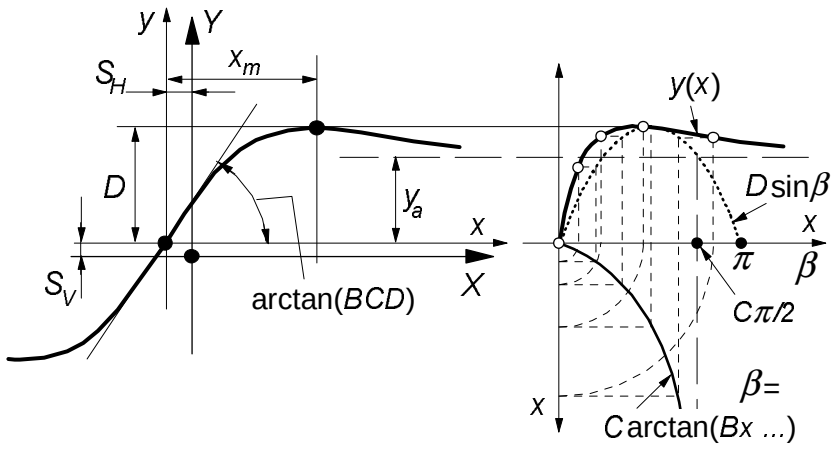

Fig. 4.9. Curve produced by the original sine version of the Magic Formula, Eqs.(4.49). The meaning of curve parameters have been indicated.

of producing characteristics that closely match measured curves for the side force F_y (and if desired also for the aligning torque M_z) and for the fore and aft force F_x as functions of their respective slip quantities: the slip angle α and the longitudinal slip κ with the effect of load F_z and camber angle γ included in the parameters.

Figure 4.9 illustrates the meaning of some of the factors by means of a typical side force characteristic. Obviously, coefficient D represents the peak value (with respect to the central x-axis and for $C \geq 1$) and the product BCD corresponds to the slope at the origin ($x = y = 0$). The shape factor C controls the limits of the range of the sine function appearing in formula (4.49) and thereby determines the shape of the resulting curve. The factor B is left to determine the slope at the origin and is called the stiffness factor. The factor E is introduced to control the curvature at the peak and at the same time the horizontal position of the peak.

From the heights of the peak and of the horizontal asymptote the shape factor C may be computed:

$$C = 1 \pm \left(1 - \frac{2}{\pi} \arcsin \frac{y_a}{D} \right) \tag{4.52}$$

From B and C and the location x_m of the peak the value of E may be assessed:

$$E = \frac{Bx_m - \tan\{\pi/(2C)\}}{Bx_m - \arctan(Bx_m)} \quad (\text{ if } C > 1) \tag{4.53}$$

The offsets S_H and S_V appear to occur when ply-steer and conicity effects and possibly the rolling resistance cause the F_y and F_x curves not to pass through the origin. Wheel camber may give rise to a considerable offset of the F_y vs α curves. Such a shift may be accompanied by a significant deviation from the pure anti-symmetric shape of the original curve (cf. Fig.3.35c,d). To accommodate such an asymmetry, the curvature factor E is made dependent of the sign of the abscissa (x).

$$E = E_o + \Delta E \cdot \text{sgn}(x) \tag{4.54}$$

Also the difference in shape that is expected to occur in the F_x vs κ characteristic between the driving and braking ranges can be taken care of. In Fig.4.10 the influence of the two shape factors C and E on the appearance of the curves have been demonstrated. The diagrams have been normalised by dividing y by D and multiplying x with CB making the curve peak level and initial slope independent of the parameters C and E.

In rather extreme cases, the sharpness that can be reached by means of the function given by Eq.(4.49) may not be sufficient. It turns out to be possible to considerably increase the sharpness of the curves by introducing an extra term

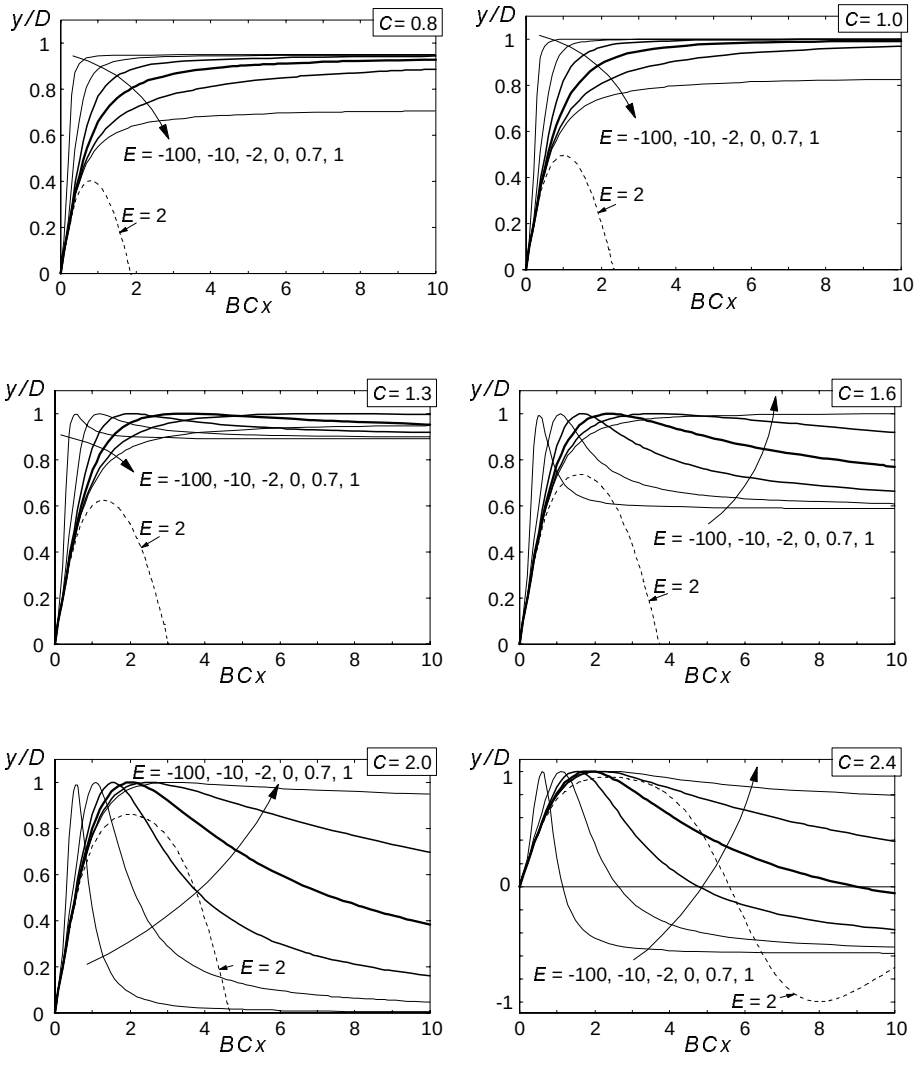

Fig. 4.10. The influence of the shape factors C and E on the appearance of the curve according to Eq.(4.49). Note that a value of $E > 1$ does not produce realistic curves with peak values $< D$.

in the argument of the arctan function. The modified function reads:

$$y = D \sin[C \arctan\{Bx - E(Bx - \arctan Bx) + H \arctan^7 Bx\}] \qquad (4.55)$$

Figure 4.11 demonstrates the effect of the new coefficient H. Too large values may give rise to an upward curvature of the curve near the origin as would also

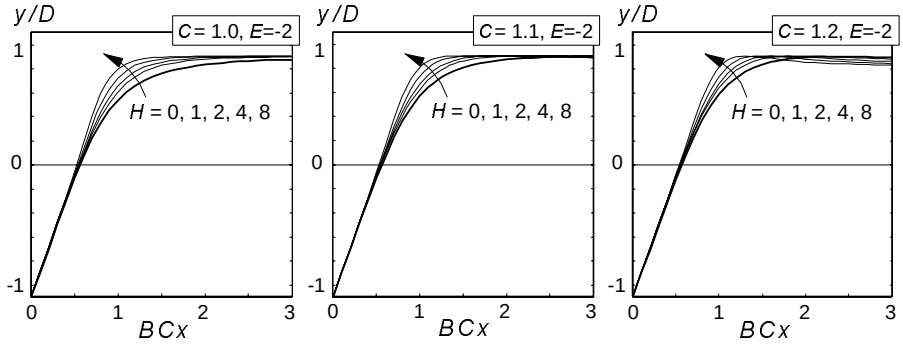

Fig. 4.11. Sharpness of curves near the peak may be increased by introducing additional term with additional sharpness factor H (according to Eq.(4.55)).

occur at large negative values of E (cf. the lower diagrams of Fig.4.10). In the ensuing text we will not use this additional coefficient H.

It may be furthermore of interest to note that the possibly awkward function arctan(x) may be replaced by the possibly faster and almost identical pseudo arctan function psatan(x) $= x(1+a|x|)/\{1+2(b|x|+ax^2)/\pi\}$ with $a = 1.1$ and $b = 1.6$.

The various factors are functions of normal load and wheel camber angle. Several parameters appear in these functions. A suitable regression technique is used to determine their values from measured data according to a quadratic algorithm for the best fit (cf. Oosten and Bakker, 1993). One of the important functional relationships is the variation of the cornering stiffness (almost exactly given by the product of the coefficients B_y, C_y and D_y of the side force function: $BCD_y = K_{y\alpha} = \partial F_y/\partial\alpha$ at $\tan\alpha = -S_H$) with F_z and γ.

$$BCD_y = p_1 \sin[2\arctan(F_z/p_2)]\cdot(1-p_3\gamma^2) \tag{4.56}$$

For zero camber, the cornering stiffness attains its maximum p_1 at $F_z = p_2$. In

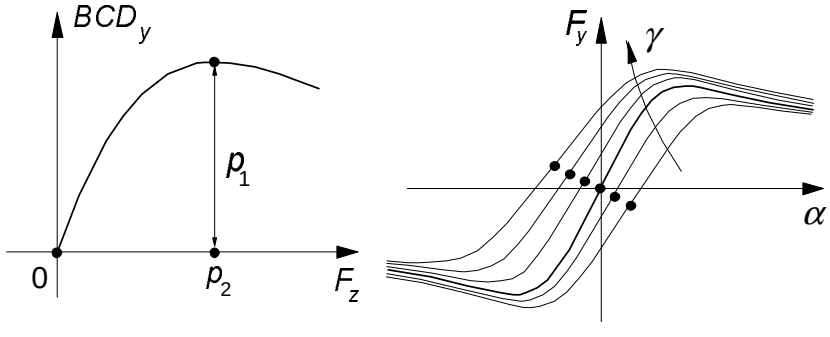

Fig. 4.12. Cornering stiffness versus vertical load and the influence of wheel camber, Eq. (4.56).

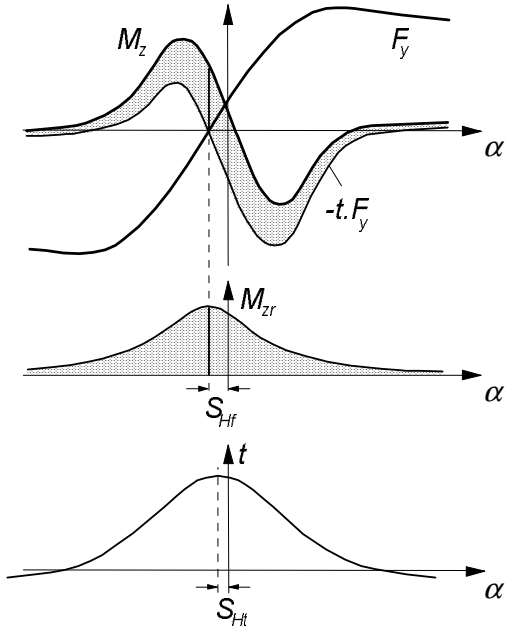

Fig. 4.13. The aligning torque characteristic composed of a part directly attributed to the side force and a part due the so-called residual torque (due to tyre conicity and camber).

Fig.4.12 the basic relationship has been depicted. Apparently, for a cambered wheel the cornering stiffness decreases with increasing $|\gamma|$. Note the difference in curvature left and right of the characteristics at larger values of the camber angle. To accomplish this, a split-E according to Eq.(4.54) has been employed. We refer to Section 4.3.2 for a complete listing of the formulae. Here, non-dimensional parameters have been introduced. For example, the parameters in (4.56) will become: $p_1 = F_{zo} p_{Ky1}$, $p_2 = F_{zo} p_{Ky2}$ and $p_3 = p_{Ky3}$, with F_{zo} denoting the nominal wheel load.

The aligning torque M_z can now be obtained by multiplying the side force F_y with the pneumatic trail t and adding the usually small (except with camber) residual torque M_{zr} (cf. Fig.4.13). We have:

$$M_z = -t \cdot F_y + M_{zr} \tag{4.57}$$

The pneumatic trail decays with increasing side slip and is described as follows:

$$t(\alpha_t) = D_t \cos[C_t \arctan\{B_t\alpha_t - E_t(B_t\alpha_t - \arctan(B_t\alpha_t))\}] \tag{4.58}$$

where

$$\alpha_t = \tan\alpha + S_{Ht} \tag{4.59}$$

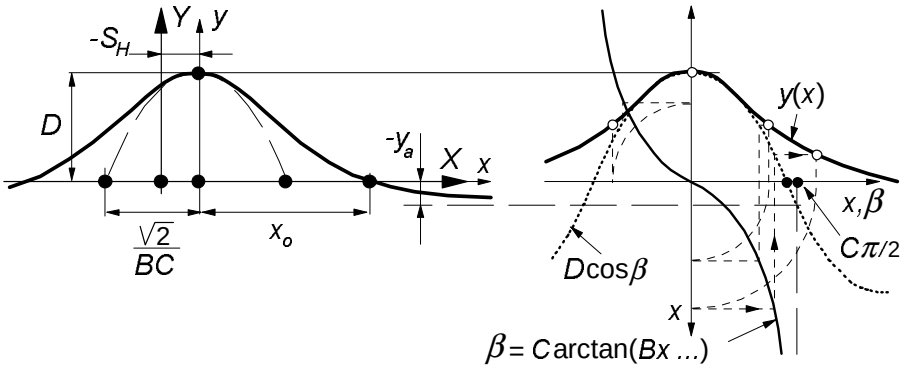

Fig. 4.14. Curve produced by the cosine version of the Magic Formula, Eq.(4.58). The meaning of curve parameters have been indicated.

The residual torque showing a similar decay:

$$M_{zr}(\alpha_r) = D_r \cos[\arctan(B_r \alpha_r)] \tag{4.60}$$

with

$$\alpha_r = \tan\alpha + S_{Hf} \tag{4.61}$$

It is seen that both parts of the moment are modelled using the Magic Formula, but instead of the sine function, the cosine function is employed. In that way a hill-shaped curve is produced. The peaks are shifted sideways.

The residual torque is assumed to attain its maximum D_r at the slip angle where the side force becomes equal to zero. This is accomplished through the horizontal shift S_{Hf}. The peak of the pneumatic trail occurs at $\tan\alpha = -S_{Ht}$. This formulation has proven to give very good agreement with measured curves. The advantage with respect to the earlier versions, where formula (4.49) is used for the aligning torque as well, is that we have now directly assessed the function for the pneumatic trail which is needed to handle the combined slip situation.

In Fig.4.14 the basic properties of the cosine based curve have been indicated (subscripts of factors have been deleted again). Again, D is the peak value, C is a shape factor determining the level y_a of the horizontal asymptote and now B influences the curvature at the peak (illustrated with the inserted parabola). Factor E modifies the shape at larger values of slip and governs the location x_o of the point where the curve intersects the x axis. The following formulae hold:

$$C = \frac{2}{\pi}\arccos\frac{y_a}{D} \tag{4.62}$$

$$E = \frac{Bx_o - \tan\{\pi/(2C)\}}{Bx_o - \arctan(Bx_o)} \quad (\text{ if } C > 1) \tag{4.63}$$

In case of the possible presence of large camber angles (motorcycles) it may be better to use in (4.57) the side force F_y that would arise at $\gamma=0$. Also, the side force function (4.49) and the cornering stiffness function (4.56) may be modified to better approximate large camber response for motorcycle tyres, cf. De Vries (1998a) and Sec.10.6 for a full listing of equations. We refer to Section 4.3.3 for the discussion of the model extension for larger camber and turn slip (path curvature) also applicable in case of combined slip with braking or driving forces.

In the paper of Pacejka and Bakker (1993) the tyre's response to combined slip was modelled by using physically based formulae. A newer more efficient way is purely empiric. This method was developed by Michelin and published by Bayle, Forissier and Lafon (1993). It describes the effect of combined slip on the lateral force and on the longitudinal force characteristics. Weighting functions G have been introduced which when multiplied with the original pure slip functions (4.49) produce the interaction effects of κ on F_y and of α on F_x. The weighting functions have a hill shape. They take the value one in the special case of pure slip (κ or α equal to zero). When, for example, at a given slip angle a from zero increasing brake slip is introduced, the relevant weighting function for F_y may first show a slight increase in magnitude (becoming larger than one) but will soon reach its peak after which a continuous decrease follows. The cosine version of the Magic Formula is used to represent the hill shaped function:

$$G = D\cos[C\arctan(Bx)] \tag{4.64}$$

Here, G is the resulting weighting factor and x is either κ or $\tan\alpha$ (possibly shifted). The coefficient D represents the peak value (slightly deviating from one if a horizontal shift of the hill occurs), C determines the height of the hill's base and B influences the sharpness of the hill. Coefficient B constitutes the main factor responsible for the shape of the weighting functions.

As an extension to the original function published by Bayle et al., the part with shape factor E will be added later on. This extension appears to improve the approximation, in particular at large levels of slip, especially in view of the strict condition that the weighting function G must remain positive for all slip conditions.

For the side force we get the following formulae:

$$F_y = G_{y\kappa}\cdot F_{yo} + S_{Vy\kappa} \tag{4.65}$$

with the weighting function now expressed such that it equals unity at $\kappa = 0$:

$$G_{y\kappa}=\frac{\cos[C_{y\kappa}\arctan(B_{y\kappa}\kappa_S)]}{\cos[C_{y\kappa}\arctan(B_{y\kappa}S_{Hy\kappa})]} \quad (>0) \tag{4.66}$$

where

$$\kappa_S = \kappa + S_{Hy\kappa} \tag{4.67}$$

and further the coefficients

$$B_{y\kappa} = r_{By1}\cos[\arctan\{r_{By2}(\tan\alpha - r_{By3})\}] \tag{4.68a}$$

$$C_{y\kappa} = r_{Cy1} \tag{4.68b}$$

$$S_{Hy\kappa} = r_{Hy1} + r_{Hy2}df_z \tag{4.68c}$$

$$S_{Vy\kappa} = D_{Vy\kappa}\sin[r_{Vy5}\arctan(r_{Vy6}\kappa)] \tag{4.69a}$$

$$D_{Vy\kappa} = \mu_y F_z \cdot (r_{Vy1} + r_{Vy2}df_z + r_{Vy3}\gamma)\cdot\cos[\arctan(r_{Vy4}\tan\alpha)] \tag{4.69b}$$

with df_z the notation for the non-dimensional increment of the vertical load with respect to the (adapted) nominal load, cf. next subsection 4.3.2, Eq.(4.E2). Figure 4.15 depicts the two weighting functions displayed both as functions of α and of κ and the resulting force characteristics (parameters according to Table 4.2 at end of Sec.4.3.3). Below, an explanation is given.

In Eq.(4.65) F_{yo} denotes the side force at pure side slip obtained from Eq.(4.49). The denominator of the weighting function (4.66) $G_{y\kappa}$ makes $G_{y\kappa} = 1$ at $\kappa = 0$. The horizontal shift $S_{Hy\kappa}$ of the weighting function accomplishes the slight increase that the side force experiences at moderate braking before the peak of $G_{y\kappa}$ is reached and the decay of F_y commences. This horizontal shift may be made dependent on the vertical load. $C_{y\kappa}$ controls the level of the horizontal asymptote. If $C_{y\kappa} = 1$ the weighting function (4.66) will approach zero when $\kappa \to \pm\infty$. This would be the correct value for $C_{y\kappa}$ if κ is expected to be used in the entire range from plus to minus infinity. If this is not intended then $C_{y\kappa}$ may be chosen different from one if $G_{y\kappa}$ is optimised with the restriction to remain positive. The factor $B_{y\kappa}$ influences the sharpness of the hill shaped weighting function. As indicated, the hill becomes more flat (wider) at larger slip angles. Then $B_{y\kappa}$ decreases according to (4.68a). When in an extreme situation α approaches 90°, that is when $V_{cx} \to 0$, $B_{y\kappa}$ will go to zero and, consequently, $G_{y\kappa}$ will remain equal to one unless κ goes to infinity which may easily be the case when at $V_{cx} \to 0$ the wheel speed of revolution Ω and thus the longitudinal slip velocity V_{sx} remains unequal to zero. The quantity $S_{Vy\kappa}$ is the vertical 'shift', which sometimes is referred to as the κ-induced ply-steer. At camber, due to the added asymmetry, the longitudinal force clearly produces a torque that creates a torsion angle comparable with a possibly already present ply-steer angle. This shift function varies with slip κ indicated in (4.69a).

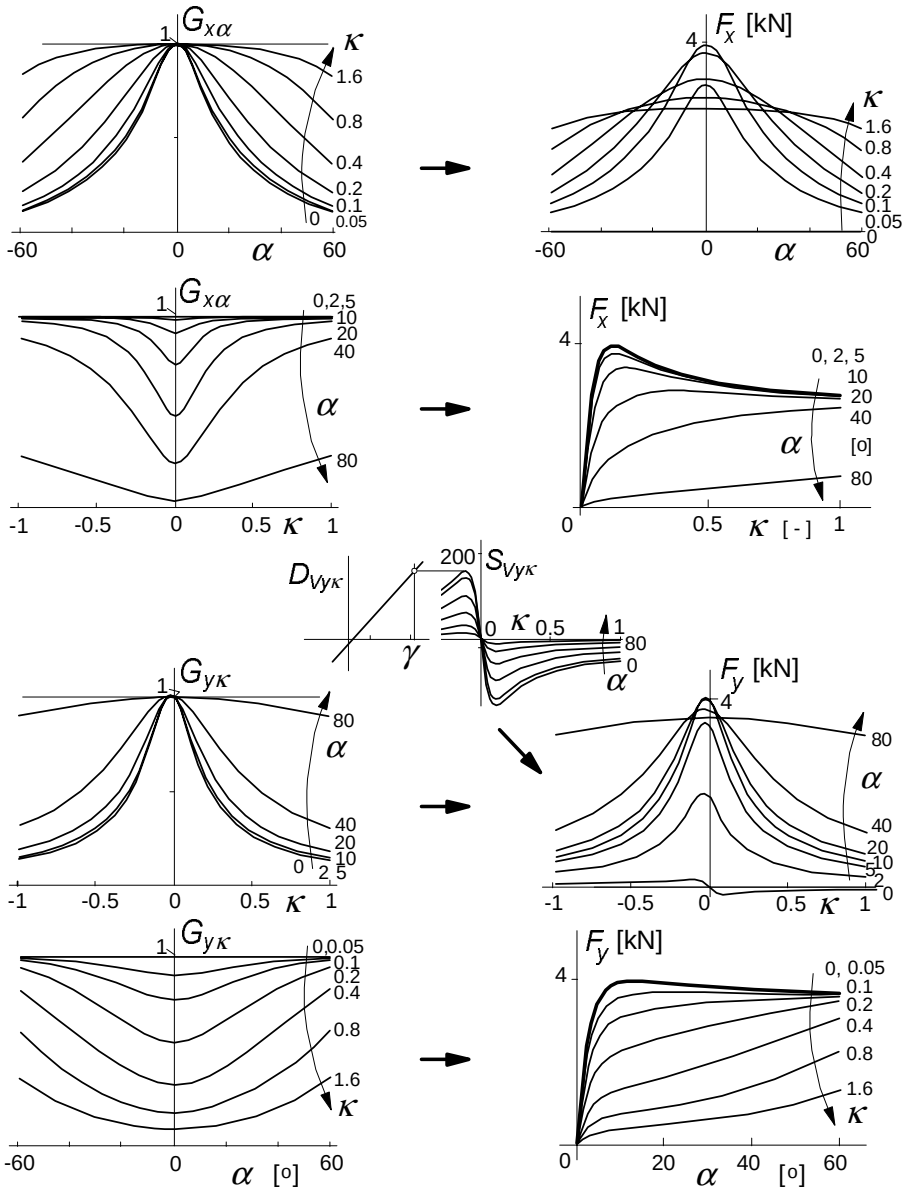

Fig. 4.15. Nature of weigthing functions and the resulting combined slip longitudinal and lateral forces, the latter also affected by the κ induced ply-steer 'vertical shift' $S_{V y\kappa}$.

As illustrated in Fig.4.15, its peak value $D_{Vy\kappa}$ depends on the camber angle γ and decays with increasing magnitude of the slip angle α. Figure 4.16 presents measured data together with the fitted curves as published by Bayle et al..

The combined slip relations for F_x are similar to what we have seen for the side force. However, a vertical shift function was not needed to be included. In Fig.4.17 a three-dimensional graph is shown indicating the variation of F_x and F_y with both α and κ. The initial *'S'* shape of the F_y vs κ curves (at small α) due to the vertical shift function is clearly visible.

For possible improvement of the general tendency of the model at larger levels of combined slip beyond the range of available test data one might include additional 'fabricated' data which are derived from similarity method results at larger values of the slip angle. Another possibility is the usage of the conditions at wheel lock where one might assume that the force and slip vector are co-linear. We then have for the ratio of the components:

$$\frac{F_x}{F_y} = \frac{V_{sx}}{V_{sy}} = \frac{\kappa}{\tan\alpha} = \frac{-1}{\tan\alpha} \tag{4.70}$$

or

$$F_x = F_{xo(\kappa=-1)} \cdot \cos\alpha = F_{xo(\kappa=-1)} \cdot \frac{V_{sx}}{V_s} \tag{4.71}$$

$$F_y = -F_{xo(\kappa=-1)} \cdot \sin\alpha = F_{xo(\kappa=-1)} \cdot \frac{V_{sy}}{V_s} \tag{4.72}$$

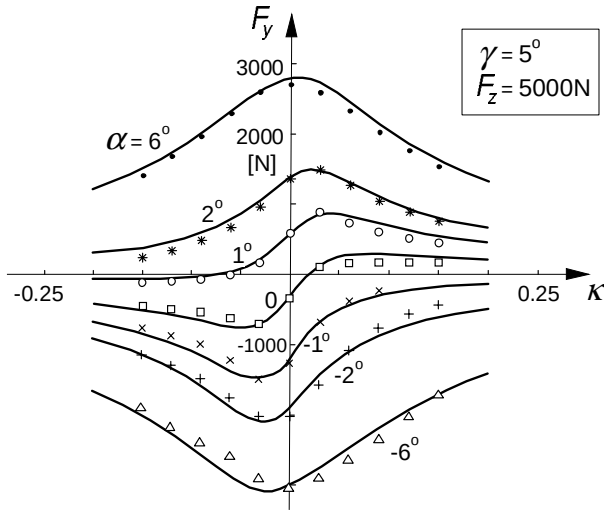

Fig. 4.16. The combined slip side force characteristics in the presence of a camber angle, Bayle et al. (1993).

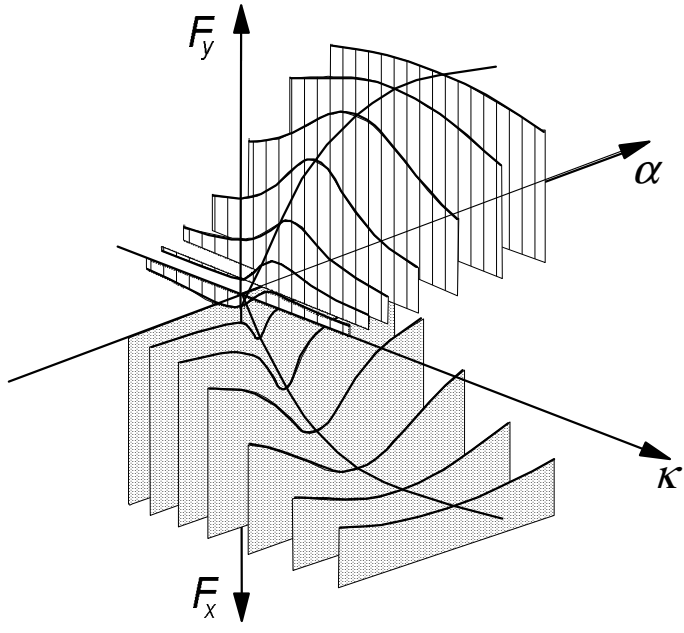

Fig. 4.17. Three-dimensional graph of combined slip force characteristics.

Regarding the aligning torque, physical insight is used to model the situation at combined slip. We write:

$$M_z = -t(\alpha_{t,eq}) \cdot F_y + M_{zr}(\alpha_{r,eq}) + s(F_y, \gamma) \cdot F_x \tag{4.73}$$

The arguments α_t and α_r (including a shift) appearing in the functions (4.59,61) for the pneumatic trail and residual torque at pure side slip are replaced by equivalent slip angles, as indicated by Eq.(4.74), incorporating the effect of κ on the composite slip.

$$\alpha_{t,eq} = \sqrt{\alpha_t^2 + \left(\frac{K_{x\kappa}}{K_{y\alpha}}\right)^2 \kappa^2} \cdot \mathrm{sgn}(\alpha_t) \tag{4.74}$$

and similar for $\alpha_{r,eq}$. To approximate the same effect on the degree of sliding in the contact patch as would occur with side slip, the longitudinal slip κ is multiplied with the ratio of the longitudinal and lateral slip stiffnesses.

Besides, an extra term is introduced in (4.73) to account for the fact that a moment arm s arises for F_x as a result of camber γ and lateral tyre deflection related to F_y. This extra term may give rise to a sign change of the aligning

torque in the range of braking as discussed before (cf. Fig.3.20).

The complete set of steady-state formulae has been listed in the subsequent section. Parameters p, q, r and s of the model are non-dimensional quantities. In addition, user scaling factors λ have been introduced. With that tool the effect of changing friction coefficient, cornering stiffness, camber stiffness etc. can be quickly investigated in a qualitative way without having the need to implement a completely new tyre data set. Scaling is done in such a way that realistic relationships are maintained. For instance, when changing the cornering stiffness and the friction coefficient in lateral direction (through $\lambda_{Ky\alpha}$ and $\lambda_{\mu y}$), the abscissa of the pneumatic trail characteristic is changed in a way equal to that of the side force characteristic and in accordance with the similarity method of Section 4.2.

4.3.2. Full Set of Equations

The Magic Formula model equations contain the non-dimensional model parameters p, q, r and s and, in addition, a set of scaling factors λ. Other parameters and variable quantities used in the equations are:

- g acceleration due to gravity,
- V_c magnitude of the velocity of the wheel contact centre C,
- $V_{cx,y}$ components of the velocity of the wheel contact centre C,
- $V_{sx,y}$ components of slip velocity V_s (of the point S) with $V_{sy} \approx V_{cy}$,
- V_r ($=R_e\Omega = V_{cx} - V_{sx}$) forward speed of rolling,
- V_o reference velocity ($=\sqrt{(gR_o)}$ or other specified value),
- R_o unloaded tyre radius ($=r_o$),
- R_e effective rolling radius ($=r_e$),
- Ω wheel speed of revolution
- ρ_z tyre radial deflection (>0 if compression),
- F_{zo} nominal (rated) load (≥ 0),
- F'_{zo} adapted nominal load

The effect of having a tyre with a different nominal load may be roughly approximated by using the scaling factor λ_{Fzo}

$$F'_{zo} = \lambda_{Fzo} F_{zo} \tag{4.E1}$$

Further, we introduce the normalized change in vertical load

$$df_z = \frac{F_z - F'_{zo}}{F'_{zo}} \tag{4.E2}$$

Instead of taking the slip angle α itself (in radians, from Eq.(2.12)) as input quantity one may in case of very large slip angles and possibly backwards

running of the wheel better use the tangent of the slip angle defined as the lateral slip:

$$\alpha^* = \tan\alpha \cdot \mathrm{sgn} V_{cx} = -\frac{V_{cy}}{|V_{cx}|} \tag{4.E3}$$

For the spin due to the camber angle we introduce

$$\gamma^* = \sin\gamma \tag{4.E4}$$

The longitudinal slip ratio is defined as follows:

$$\kappa = -\frac{V_{sx}}{|V_{cx}|} \tag{4.E5}$$

If the forward speed V_{cx} becomes or is equal to zero one might add a small quantity ε in the denominator of (4.E3, E5) to avoid singularity, or, when transient slip situations occur, one should use the transient slip quantities (or deformation gradients) $\tan\alpha'$ and κ' as defined and used in Chapters 7 and 8.

To avoid the occurrence of similar singularities in the ensuing equations due to e.g. zero velocity or zero vertical load, a small additional quantity ε (with same sign as its neighbouring main quantity) will be introduced in relevant denominators like in the next equation.

For the factor $\cos\alpha$ appearing in the equations for the aligning torque to properly handle the case of large slip angles and possibly backwards running ($V_{cx} < 0$) we have defined:

$$\cos'\alpha = \frac{V_{cx}}{V'_c} \tag{4.E6}$$

with

$$V'_c = V_c + \varepsilon_V \tag{4.E7}$$

where we may choose $\varepsilon_V = 0.1$.

For the normally encountered situations where turn slip may be neglected (path radius $R \to \infty$) and camber remains small, the factors ζ_i appearing in the equations, are to be set equal to unity:

$$\zeta_i = 1 \qquad (i = 0, 1, \ldots, 8)$$

In the following Section 4.3.3 where the influence of spin (turn slip and camber) is described in the extended Magic Formula model, the proper expressions will be given for these factors and additional equations will be introduced.

User Scaling Factors

The following set of scaling factors λ is available. The default value of these factors is set equal to one (except $\lambda_{\mu V}$ which equals zero if not used). We have:

pure slip

- λ_{Fzo} nominal (rated) load
- $\lambda_{\mu x,y}$ peak friction coefficient
- $\lambda_{\mu V}$ with slip speed V_s decaying friction
- $\lambda_{Kx\kappa}$ brake slip stiffness
- $\lambda_{Ky\alpha}$ cornering stiffness
- $\lambda_{Cx,y}$ shape factor
- $\lambda_{Ex,y}$ curvature factor
- $\lambda_{Hx,y}$ horizontal shift
- $\lambda_{Vx,y}$ vertical shift
- $\lambda_{Ky\gamma}$ camber force stiffness
- $\lambda_{Kz\gamma}$ camber torque stiffness
- λ_t pneumatic trail (effecting aligning torque stiffness)
- λ_{Mr} residual torque

combined slip

- $\lambda_{x\alpha}$ α influence on $F_x(\kappa)$
- $\lambda_{y\kappa}$ κ influence on $F_y(\alpha)$
- $\lambda_{Vy\kappa}$ κ induced 'ply-steer' F_y
- λ_s M_z moment arm of F_x

other

- λ_{Cz} radial tyre stiffness
- λ_{Mx} overturning couple stiffness
- λ_{My} rolling resistance moment

To change from a relatively high friction surface to a low friction surface the factors $\lambda_{\mu x}$ and $\lambda_{\mu y}$ may be given a value lower than unity. In addition, to reflect a slippery surface (wet) with friction decaying with increasing (slip) speed one may chose for $\lambda_{\mu V}$ a value larger than zero, e.g. Eqs.(4.E13,E23). The publications of Dijks (1974) and of Reimpell (1986) may be useful in this respect. Note, that the slip stiffnesses are not effected through these changes. A special degressive friction factor $\lambda'_{\mu x,y}$ is introduced to recognise the fact that vertical shifts of the force curves do vanish when $\mu \to 0$ but at a much slower rate.

$$\lambda'_{\mu x,y} = A_\mu \, \lambda_{\mu x,y} / \{1+(A_\mu - 1)\lambda_{\mu x,y}\} \qquad \text{(suggestion: } A_\mu = 10) \qquad (4.E8)$$

For the three forces and three moments acting from road to tyre and defined according to the diagram of Fig.2.3, the equations, first those for the condition

of pure slip (including camber) and subsequently those for the condition of combined slip, read:

Longitudinal Force (pure longitudinal slip)

$$F_{xo} = D_x \sin[C_x \arctan\{B_x\kappa_x - E_x(B_x\kappa_x - \arctan(B_x\kappa_x))\}] + S_{Vx} \tag{4.E9}$$

$$\kappa_x = \kappa + S_{Hx} \tag{4.E10}$$

$$C_x = p_{Cx1} \cdot \lambda_{Cx} \qquad (>0) \tag{4.E11}$$

$$D_x = \mu_x \cdot F_z \cdot \zeta_1 \qquad (>0) \tag{4.E12}$$

$$\mu_x = (p_{Dx1} + p_{Dx2} df_z) \cdot \lambda_{\mu x} / (1 + \lambda_{\mu V} V_s / V_o) \qquad (>0) \tag{4.E13}$$

$$E_x = (p_{Ex1} + p_{Ex2} df_z + p_{Ex3} df_z^2) \cdot \{1 - p_{Ex4} \operatorname{sgn}(\kappa_x)\} \cdot \lambda_{Ex} \qquad (\leq 1) \tag{4.E14}$$

$$K_{x\kappa} = F_z \cdot (p_{Kx1} + p_{Kx2} df_z) \cdot \exp(p_{Kx3} df_z) \cdot \lambda_{K\kappa\kappa}$$
$$(= B_x C_x D_x = \partial F_{xo} / \partial \kappa_x \quad \text{at } \kappa_x = 0) \quad (= C_{F\kappa}) \tag{4.E15}$$

$$B_x = K_{x\kappa} / (C_x D_x + \varepsilon_x) \tag{4.E16}$$

$$S_{Hx} = (p_{Hx1} + p_{Hx2} df_z) \cdot \lambda_{Hx} \tag{4.E17}$$

$$S_{Vx} = F_z \cdot (p_{Vx1} + p_{Vx2} df_z) \cdot \{|V_{cx}| / (\varepsilon_{Vx} + |V_{cx}|)\} \cdot \lambda_{Vx} \cdot \lambda'_{\mu x} \cdot \zeta_1 \tag{4.E18}$$

Lateral Force (pure side slip)

$$F_{yo} = D_y \sin[C_y \arctan\{B_y\alpha_y - E_y(B_y\alpha_y - \arctan(B_y\alpha_y))\}] + S_{Vy} \tag{4.E19}$$

$$\alpha_y = \alpha^* + S_{Hy} \tag{4.E20}$$

$$C_y = p_{Cy1} \cdot \lambda_{Cy} \qquad (>0) \tag{4.E21}$$

$$D_y = \mu_y \cdot F_z \cdot \zeta_2 \tag{4.E22}$$

$$\mu_y = (p_{Dy1} + p_{Dy2} df_z) \cdot (1 - p_{Dy3} \gamma^{*2}) \cdot \lambda_{\mu y} / (1 + \lambda_{\mu V} V_s / V_o) \qquad (>0) \tag{4.E23}$$

$$E_y = (p_{Ey1} + p_{Ey2} df_z) \cdot \{1 - (p_{Ey3} + p_{Ey4} \gamma^*) \operatorname{sgn}(\alpha_y)\} \cdot \lambda_{Ey} \qquad (\leq 1) \tag{4.E24}$$

$$K_{y\alpha o} = p_{Ky1} F'_{zo} \sin[2 \arctan\{F_z / (p_{Ky2} F'_{zo})\}] \cdot \lambda_{Ky\alpha}$$
$$(= B_y C_y D_y = \partial F_{yo} / \partial \alpha_y \text{ at } \alpha_y = \gamma = 0) \quad (= C_{F\alpha}) \tag{4.E25}$$

$$K_{y\alpha} = K_{y\alpha o} \cdot (1 - p_{Ky3} \gamma^{*2}) \cdot \zeta_3 \tag{4.E26}$$

$$B_y = K_{y\alpha}/(C_y D_y + \varepsilon_y) \tag{4.E27}$$

$$S_{Hy} = (p_{Hy1} + p_{Hy2}\, df_z)\cdot\lambda_{Hy} + p_{Hy3}\gamma^*\cdot\lambda_{Ky\gamma}\cdot\zeta_0 + \zeta_4 - 1 \tag{4.E28}$$

$$S_{Vy} = F_z\cdot\{(p_{Vy1} + p_{Vy2}\, df_z)\cdot\lambda_{Vy} + (p_{Vy3} + p_{Vy4}\, df_z)\gamma^*\cdot\lambda_{Ky\gamma}\}\cdot\lambda'_{\mu y}\cdot\zeta_2 \tag{4.E29}$$

$$K_{y\gamma o} = \{p_{Hy3}K_{y\alpha o} + F_z(p_{Vy3} + p_{Vy4}\, df_z)\}\,\lambda_{K y\gamma} \quad (= \sim \partial F_{yo}/\partial\gamma \text{ at } \alpha = \gamma = 0) \quad (= C_{F\gamma}) \tag{4.E30}$$

Aligning Torque (pure side slip)

$$M_{zo} = M'_{zo} + M_{zro} \tag{4.E31}$$

$$M'_{zo} = -t_o\cdot F_{yo} \tag{4.E32}$$

$$t_o = t(\alpha_t) = D_t\cos[C_t \arctan\{B_t\alpha_t - E_t(B_t\alpha_t - \arctan(B_t\alpha_t))\}]\cdot\cos'\alpha \tag{4.E33}$$

$$\alpha_t = \alpha^* + S_{Ht} \tag{4.E34}$$

$$S_{Ht} = q_{Hz1} + q_{Hz2}\, df_z + (q_{Hz3} + q_{Hz4}\, df_z)\gamma^* \tag{4.E35}$$

$$M_{zro} = M_{zr}(\alpha_r) = D_r\cos[C_r \arctan(B_r\alpha_r)] \tag{4.E36}$$

$$\alpha_r = \alpha^* + S_{Hf} \quad (= \alpha_f) \tag{4.E37}$$

$$S_{Hf} = S_{Hy} + S_{Vy}/K'_{y\alpha} \tag{4.E38}$$

$$K'_{y\alpha} = K_{y\alpha} + \varepsilon_K \tag{4.E39}$$

$$B_t = (q_{Bz1} + q_{Bz2}\, df_z + q_{Bz3}\, df_z^2)\cdot(1 + q_{Bz4}\gamma^* + q_{Bz5}|\gamma^*|)\cdot\lambda_{K y\alpha}/\lambda_{\mu y} \quad (>0) \tag{4.E40}$$

$$C_t = q_{Cz1} \quad (>0) \tag{4.E41}$$

$$D_{to} = F_z\cdot(R_o/F'_{zo})\cdot(q_{Dz1} + q_{Dz2}\, df_z)\cdot\lambda_t\cdot\operatorname{sgn} V_{cx} \tag{4.E42}$$

$$D_t = D_{to}\cdot(1 + q_{Dz3}\gamma^* + q_{Dz4}\gamma^{*2})\cdot\zeta_5 \tag{4.E43}$$

$$E_t = (q_{Ez1} + q_{Ez2}\, df_z + q_{Ez3}\, df_z^2)\cdot\left\{1 + (q_{Ez4} + q_{Ez5}\gamma^*)\frac{2}{\pi}\arctan(B_t C_t \alpha_t)\right\} \quad (\le 1) \tag{4.E44}$$

$$B_r = q_{Bz10} B_y C_y \tag{4.E45}$$

$$C_r = \zeta_7 \tag{4.E46}$$

$$D_r = F_z R_o\{(q_{Dz6} + q_{Dz7}\, df_z)\lambda_{Mr}\zeta_2 + (q_{Dz8} + q_{Dz9}\, df_z)\gamma^*\lambda_{Kz\gamma}\zeta_0\}\cos'\alpha\cdot\lambda_{\mu y}\operatorname{sgn} V_{cx} + \zeta_8 - 1 \tag{4.E47}$$

$$K_{z\alpha o} = D_{to} K_{y\alpha o} \quad (= \sim -\partial M_{zo}/\partial \alpha_y \text{ at } \alpha_y = \gamma = 0) \quad (= C_{M\alpha}) \tag{4.E48}$$

$$K_{z\gamma o} = F_z R_o (q_{Dz8} + q_{Dz9} df_z) \lambda_{Kz\gamma} - D_{to} K_{y\gamma o} \quad (= \sim \partial M_{zo}/\partial \gamma \text{ at } \alpha = \gamma = 0) \quad (= C_{M\gamma}) \tag{4.E49}$$

Longitudinal Force (combined slip)

$$F_x = G_{x\alpha} \cdot F_{xo} \tag{4.E50}$$

$$G_{x\alpha} = \cos[C_{x\alpha} \arctan\{B_{x\alpha}\alpha_S - E_{x\alpha}(B_{x\alpha}\alpha_S - \arctan(B_{x\alpha}\alpha_S))\}]/G_{x\alpha o} \quad (>0) \tag{4.E51}$$

$$G_{x\alpha o} = \cos[C_{x\alpha} \arctan\{B_{x\alpha}S_{Hx\alpha} - E_{x\alpha}(B_{x\alpha}S_{Hx\alpha} - \arctan(B_{x\alpha}S_{Hx\alpha}))\}] \tag{4.E52}$$

$$\alpha_S = \alpha^* + S_{Hx\alpha} \tag{4.E53}$$

$$B_{x\alpha} = r_{Bx1} \cos[\arctan(r_{Bx2}\kappa)] \cdot \lambda_{x\alpha} \quad (>0) \tag{4.E54}$$

$$C_{x\alpha} = r_{Cx1} \tag{4.E55}$$

$$E_{x\alpha} = r_{Ex1} + r_{Ex2} df_z \quad (\leq 1) \tag{4.E56}$$

$$S_{Hx\alpha} = r_{Hx1} \tag{4.E57}$$

Lateral Force (combined slip)

$$F_y = G_{y\kappa} \cdot F_{yo} + S_{Vy\kappa} \tag{4.E58}$$

$$G_{y\kappa} = \cos[C_{y\kappa} \arctan\{B_{y\kappa}\kappa_S - E_{y\kappa}(B_{y\kappa}\kappa_S - \arctan(B_{y\kappa}\kappa_S))\}]/G_{y\kappa o} \quad (>0) \tag{4.E59}$$

$$G_{y\kappa o} = \cos[C_{y\kappa} \arctan\{B_{y\kappa}S_{Hy\kappa} - E_{y\kappa}(B_{y\kappa}S_{Hy\kappa} - \arctan(B_{y\kappa}S_{Hy\kappa}))\}] \tag{4.E60}$$

$$\kappa_S = \kappa + S_{Hy\kappa} \tag{4.E61}$$

$$B_{y\kappa} = r_{By1} \cos[\arctan\{r_{By2}(\alpha^* - r_{By3})\}] \cdot \lambda_{y\kappa} \quad (>0) \tag{4.E62}$$

$$C_{y\kappa} = r_{Cy1} \tag{4.E63}$$

$$E_{y\kappa} = r_{Ey1} + r_{Ey2} df_z \quad (\leq 1) \tag{4.E64}$$

$$S_{Hy\kappa} = r_{Hy1} + r_{Hy2} df_z \tag{4.E65}$$

$$S_{Vy\kappa} = D_{Vy\kappa} \sin[r_{Vy5} \arctan(r_{Vy6}\kappa)] \tag{4.E66}$$

$$D_{Vy\kappa} = \mu_y F_z \cdot (r_{Vy1} + r_{Vy2} df_z + r_{Vy3}\gamma^*) \cdot \cos[\arctan(r_{Vy4}\alpha^*)] \cdot \zeta_2 \tag{4.E67}$$

Normal Load (see also Eq.(9.217))

$$F_z = p_{z1} \cdot (F'_{zo}/R_o) \cdot \max(\rho_z\,,\,0) \cdot \lambda_{Cz} \qquad (\geq 0)$$
$$(C_{Fz} = \partial F_z/\partial \rho_z = p_{z1}\lambda_{Cz} F'_{zo}/R_o) \tag{4.E68}$$

Overturning Couple (see also Sec.4.3.5)

$$M_x = F_z R_o \cdot (q_{sx1} - q_{sx2}\gamma^* + q_{sx3} F_y/F'_{zo}) \cdot \lambda_{Mx} \tag{4.E69}$$

Rolling Resistance Moment (see also Eqs.(9.236,230))

$$M_y = -F_z R_o \cdot \{q_{sy1} \arctan(V_r/V_o) + q_{sy2} F_x/F'_{zo}\} \cdot \lambda_{My} \tag{4.E70}$$

Aligning Torque (combined slip)

$$M_z = M'_z + M_{zr} + s \cdot F_x \tag{4.E71}$$

$$M'_z = -t \cdot F'_y \tag{4.E72}$$

$$t = t(\alpha_{t,eq}) = D_t \cos[C_t \arctan\{B_t \alpha_{t,eq} - E_t(B_t \alpha_{t,eq} - \arctan(B_t \alpha_{t,eq}))\}] \cdot \cos'\alpha \tag{4.E73}$$

$$F'_y = F_y - S_{Vy\kappa} \tag{4.E74}$$

$$M_{zr} = M_{zr}(\alpha_{r,eq}) = D_r \cos[C_r \arctan(B_r \alpha_{r,eq})] \tag{4.E75}$$

$$s = R_o \cdot \{s_{sz1} + s_{sz2}(F_y/F'_{zo}) + (s_{sz3} + s_{sz4} df_z)\gamma^*\} \cdot \lambda_s \tag{4.E76}$$

$$\alpha_{t,eq} = \sqrt{\alpha_t^2 + \left(\frac{K_{x\kappa}}{K'_{y\alpha}}\right)^2 \kappa^2} \cdot \mathrm{sgn}(\alpha_t) \tag{4.E77}$$

$$\alpha_{r,eq} = \sqrt{\alpha_r^2 + \left(\frac{K_{x\kappa}}{K'_{y\alpha}}\right)^2 \kappa^2} \cdot \mathrm{sgn}(\alpha_r) \tag{4.E78}$$

A set of parameter values have been listed in Appendix 3 for an example tyre in connection with the SWIFT tyre model to be dealt with in Chapter 9. Examples of computed characteristics compared with experimentally assessed curves for both pure slip and combined slip conditions are discussed in Section 4.3.6 of this chapter, cf. Figs.4.28-32. In the next section 4.3.3 the effect of having turn slip is modelled and some calculated characteristics have been presented for a set of hypothetical model parameters (Fig.4.19). Section 4.3.4 examines the possibility

to define the effects of conicity and ply-steer as responses to equivalent camber and slip angles. Section 4.3.5 gives a possibly better description than (4E.69) for the overturning couple of truck, car and racing tyres due to side slip and for the part due to camber that is illustrated for the case of a motorcycle tyre.

4.3.3. Extension of the Model for Turn Slip

The model described sofar contains the input slip quantities side slip, longitudinal slip and wheel camber. In the present section the turn slip or (in steady state) path curvature is added which completes the description of the steady state force and moment generation properties of the tyre.

Turn slip is one of the two components which together form the spin of the tyre, cf. Fig.3.22. The turn slip is defined here as:

$$\varphi_t = -\frac{\dot{\psi}}{V'_c} = -\frac{1}{R} \tag{4.75}$$

and the total tyre spin, cf. Eq.(3.55) :

$$\varphi = -\frac{1}{V'_c}\{\dot{\psi} - (1 - \varepsilon_\gamma)\Omega \sin\gamma\} \tag{4.76}$$

with the singularity protected velocity V'_c. Again, ε_γ denotes the camber reduction factor for the camber to become comparable with turn slip. For radial-ply car tyres this reduction factor ε_γ may become as high as ca. 0.7 (for some truck tyres even slightly over 1.0) while for a motorcycle tyre the factor is expected to be close to zero like with a homogeneous solid ball, cf. discussion below Eq. (3.117).

In the previous section the effect of camber was introduced. For the side force this resulted in a horizontal and a vertical shift of the F_y vs α curves, while for the aligning torque, besides the small effect of the shifted F_y curve, the residual torque M_{zr} was added in which a contribution of camber occurs. Furthermore, changes in shape appeared to occur which were represented by the introduction of γ in factors like μ_y, E_y, $K_{y\alpha}$, B_t, D_t etc. These changes may be attributed to changes in tyre cross section and contact pressure distribution resulting from the wheel inclination angle.

These shifts and shape changes will be retained in the model extension but will be expanded to cover the complete range of spin in combination with side slip and also longitudinal slip. The spin may change from zero to $\pm\infty$ when path curvature goes to infinity and, consequently, path radius to zero (when the velocity $V_c \to 0$). Weighting functions will again be introduced to gradually reduce peak side and longitudinal forces with increasing spin. Also, cornering stiffness

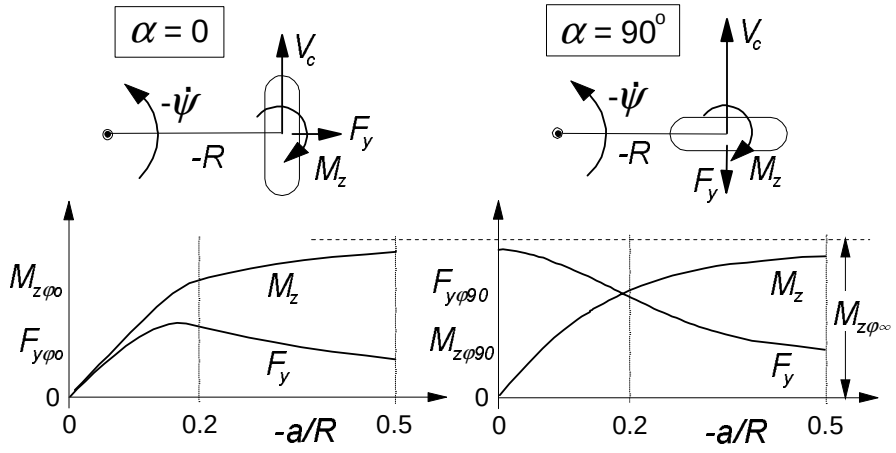

Fig. 4.18. Two basic spin force and moment diagrams.

and pneumatic trail will be subjected to such a reduction.

The theoretical findings which have been gained from the physical model of Section 3.3 presented in Fig.3.35d will be used as basis for the model development. Since these findings hold for only one value of the vertical load and zero longitudinal slip, the influence of load variations and longitudinal slip have been structured tentatively.

In Fig.4.18 for the two extreme cases of $\alpha = 0$ and $\alpha = 90°$ the courses of F_y and M_z vs $a\varphi_t = -a/R$ have been depicted. The pure spin side force characteristic shown in the left-hand diagram (at $\alpha = 0$), also indicated in the lower left diagram of Fig.3.35d, can be fabricated by sideways shifting of the side force curve belonging to zero spin (turn slip $\varphi_t = 0$ and $\gamma = 0$, upper or middle left diagram) while at the same time reducing its peak value D_y and its slope at the curve centre $K_{y\alpha}$. For this, we define the reduction functions to be substituted in the previous Eqs.(4.E22,26,29). The peak side force reduction factor:

$$\zeta_2 = \cos[\arctan\{B_{y\varphi}(R_o|\varphi_t| + p_{Dy\varphi 4}\sqrt{R_o|\varphi_t|})\}] \tag{4.77}$$

with sharpness factor:

$$B_{y\varphi} = p_{Dy\varphi 1}(1 + p_{Dy\varphi 2}df_z)\cos[\arctan(p_{Dy\varphi 3}\tan\alpha)] \tag{4.78}$$

and the slope reduction factor:

$$\zeta_3 = \cos[\arctan(p_{Ky\varphi 1}R_o^2\varphi_t^2)] \tag{4.79}$$

Herewith, the condition is satisfied that at $\varphi_t \to \infty$, where the wheel is steered about the vertical axis at a speed of travel equal to zero (that is: velocity of contact centre $V_c \to 0$ and path radius $R \to 0$, leading to $\zeta_2 = \zeta_3 = 0$), the side force

reduces to zero although a slip angle may theoretically still exist. Considering the upper or middle left diagram of Fig. 3.35d, it seems that the sideways shift saturates at larger values of spin. To model this phenomenon, which actually says that beyond a certain negative slip angle no spin is large enough to make the side force vanish, the sine version of the magic formula is used. We have:

$$S_{Hy\varphi}=D_{Hy\varphi}\sin[C_{Hy\varphi}\arctan\{B_{Hy\varphi}R_o\varphi-E_{Hy\varphi}(B_{Hy\varphi}R_o\varphi-\arctan(B_{Hy\varphi}R_o\varphi))\}] \tag{4.80}$$

The shape factor $C_{Hy\varphi}$ is expected to be equal or smaller than unity. To expression (4.80) is added the shift due to ply-steer and conicity. Finally, we subtract the horizontal displacement of the point of intersection of the side force vs slip angle curve which arises due to the vertical shift of the curve (which for now is thought to be solely attributed to the camber component of spin). This leads to a total horizontal shift:

$$S_{Hy} = (p_{Hy1} + p_{Hy2}\,df_z)\cdot\lambda_{Hy} + S_{Hy\varphi} - S_{Vy\gamma}/K'_{y\alpha} \tag{4.81}$$

in which the vertical shift due to γ reads:

$$S_{Vy\gamma} = F_z\cdot(p_{Vy3} + p_{Vy4}df_z)\gamma^*\cdot\zeta_2\cdot\lambda_{Ky\gamma}\cdot\lambda'_{\mu y} \tag{4.82}$$

cf. Eq.(4.E29). The quantity $K'_{y\alpha}$ is the singularity protected cornering stiffness defined by Eq.(4.E39). Through this manipulation, the camber/spin stiffness is solely attributed to the horizontal shift of the point of intersection $S_{Hy\varphi}$, cf. Eqs.(4.88,89). Apparently, the factors ζ in Eq.(4.E28) now read:

$$\zeta_0 = 0 \tag{4.83}$$

$$\zeta_4 = 1 + S_{Hy\varphi} - S_{Vy\gamma}/K'_{y\alpha} \tag{4.84}$$

The various factors appearing in (4.80) are defined as follows:

$$C_{Hy\varphi} = p_{Hy\varphi 1} \quad (>0) \tag{4.85}$$

$$D_{Hy\varphi} = (p_{Hy\varphi 2} + p_{Hy\varphi 3}df_z)\cdot\mathrm{sgn}(V_{cx}) \tag{4.86}$$

$$E_{Hy\varphi} = p_{Hy\varphi 4} \quad (\leq 1) \tag{4.87}$$

$$B_{Hy\varphi} = K_{yR\varphi o}/\{C_{Hy\varphi}D_{Hy\varphi}(K_{y\alpha o} + \varepsilon_K)\} \tag{4.88}$$

where the spin force stiffness $K_{yR\varphi o}$ is related to the camber stiffness $K_{y\gamma o}$ $(=C_{F\gamma})$ that is given by (4.E30):

$$K_{yR\varphi o}=K_{y\gamma o}/(1-\varepsilon_\gamma) \quad (=\partial F_{yo}/\partial R_o\varphi \text{ at } \alpha=\gamma=\varphi=0) \quad (=C_{F\varphi}/R_o) \tag{4.89}$$

for which we may define:

$$\varepsilon_\gamma = p_{\varepsilon\gamma\varphi 1}(1 + p_{\varepsilon\gamma\varphi 2}df_z) \tag{4.90}$$

Obviously, this parameter governs the difference of the response to camber with respect to that of turn slip.

For modelling the aligning torque, we will use as before the product of the side force and the pneumatic trail in the first term of Eqs.(4.E31,E71) while for the second term the residual torque will be expanded to represent large spin torque.

The middle right diagram of Fig.3.35d shows that at increasing turn slip the residual or spin torque increases while the moment due to side slip (clearly visible at $\varphi_t = 0$) diminishes. This decay is modelled by means of the weighting function ζ_5 multiplied with the pneumatic trail in Eq.(4.E43):

$$\zeta_5 = \cos[\arctan(q_{Dt\varphi 1} R_o \varphi)] \tag{4.91}$$

The second term of Eqs.(4.E31,E71), the residual torque, which in the present context may be better designated as the spin moment, is given by Eqs.(4.E36,75). Its peak value D_r has an initial value due to conicity that is expected to be taken over gradually by an increasing turn slip. In (4.E47) this is accomplished by the weighting function ζ_2 (4.77). The remaining terms will be replaced by the peak spin torque $D_{r\varphi}$. This means that the ζ's appearing in (4.E47) become besides according to (4.83):

$$\zeta_8 = 1 + D_{r\varphi} \tag{4.92}$$

As observed in the middle right diagram of Fig.3.35d, the peak torque (that will be assumed to occur at a slip angle $\alpha = -S_{Hf}$ where $F_y = 0$) grows with increasing spin and finally saturates. The magic formula describes this as follows:

$$D_{r\varphi} = D_{Dr\varphi} \sin[C_{Dr\varphi} \arctan\{B_{Dr\varphi} R_o \varphi - E_{Dr\varphi}(B_{Dr\varphi} R_o \varphi - \arctan(B_{Dr\varphi} R_o \varphi))\}] \tag{4.93}$$

Its maximum value (if $C_{Dr\varphi} \geq 1$) is $D_{Dr\varphi}$. The asymptotic level of the peak spin torque is reached at $\varphi \to \infty$ or $R \to 0$, and is denoted as $M_{z\varphi\infty}$. Consequently, with the shape factor $C_{Dr\varphi}$ the maximum value is expressed by:

$$D_{Dr\varphi} = M_{z\varphi\infty} / \sin(0.5\pi C_{Dr\varphi}) \tag{4.94}$$

where the moment $M_{z\varphi\infty}$ that occurs at vanishing wheel speed and at constant turning about the vertical axis is formulated as a function of the normal load:

$$M_{z\varphi\infty} = q_{Cr\varphi 1} \mu_y R_o F_z \sqrt{F_z / F'_{zo}} \cdot \lambda_{M\varphi} \quad (>0) \tag{4.95}$$

This expression may be compared with or replaced by expression (3.117) formulated by Freudenstein (1961). The shape factors in (4.93) are assumed to be given by constant parameters:

$$C_{Dr\varphi} = q_{Dr\varphi 1} \quad (>0) \tag{4.96}$$

$$E_{Dr\varphi} = q_{Dr\varphi 2} \quad (\leq 1) \tag{4.97}$$

while

$$B_{Dr\varphi} = K_{z\gamma ro} / \{(C_{Dr\varphi} D_{Dr\varphi} + \varepsilon_r)(1-\varepsilon_\gamma)\} \tag{4.98}$$

with $K_{z\gamma ro}$ assumed to depend on the normal load as follows:

$$K_{z\gamma ro} = F_z R_o (q_{Dz8} + q_{Dz9} df_z) \lambda_{Kz\gamma} \tag{4.99}$$

As has been indicated with Eq.(4.E49) we have now for the camber moment stiffness

$$K_{z\gamma o} = K_{z\gamma ro} - D_{to} K_{y\gamma o} \qquad (= C_{M\gamma}) \tag{4.100}$$

and consequently for the moment stiffness against spin:

$$K_{zR\varphi o} = K_{z\gamma o} / (1-\varepsilon_\gamma) \qquad (= C_{M\varphi} / R_o) \tag{4.101}$$

Now that the formulae for the peak of the spin torque $D_{r\varphi}$ has been developed, we must consider the remaining course of M_{zr} with the slip angle α. For this, Eq.(4.E36) is employed. According to the middle right diagram of Fig.3.35d the curves become flatter as the spin increases. Logically, for $\varphi \to \infty$ the moment should become independent of the slip angle. The sharpness is controlled by the factor B_r which we let gradually decrease to zero with increasing spin. For this, we introduce in Eq.(4.E45) the weighting function:

$$\zeta_6 = \cos[\arctan(q_{Br\varphi 1} R_o \varphi)] \tag{4.102}$$

The factor C_r controls the asymptotic level which corresponds to the torque at $\alpha = 90°$. In that situation the turn slip $\varphi = -\dot{\psi}/|V_{cy}| = 1/R$ which corresponds to the definition given by Eq.(4.76). The moment $M_{z\varphi 90}$ that is generated when the wheel moves at $\alpha = 90°$ increases with increasing curvature $1/R$ up to its maximum value that is attained at $R = 0$ and equals $M_{z\varphi\infty}$. We use the formula:

$$M_{z\varphi 90} = M_{z\varphi\infty} \cdot \frac{2}{\pi} \cdot \arctan(q_{Cr\varphi 2} R_o |\varphi|) \cdot G_{y\kappa}(\kappa) \tag{4.103}$$

with parameter $q_{Cr\varphi 2}$. This quantity may be difficult to assess experimentally; the value 0.1 is expected to be a reasonable estimate. (In any case, the argument of (4.104) should remain <1.) This moment at 90° is multiplied with the weighting function $G_{y\kappa}$ (4.E59) to account for the attenuation through the action of longitudinal slip.

We obtain for the factor $\zeta_7 = C_r$ in Eq.(4.E46) using (4.E36) with $|\alpha_r| \to \infty$:

$$\zeta_7 = \frac{2}{\pi} \cdot \arccos[M_{z\varphi 90} / (|D_{r\varphi}| + \varepsilon_r)] \tag{4.104}$$

Finally, we must take care of the weighting function ζ_1 which is introduced in the expressions (4.E12,18) for F_x to let the longitudinal force diminish with increasing spin. We define:

$$\zeta_1 = \cos[\arctan(B_{x\varphi} R_o \varphi)] \tag{4.105}$$

with

$$B_{x\varphi} = p_{Dx\varphi 1}(1 + p_{Dx\varphi 2} df_z)\cos[\arctan(p_{Dx\varphi 3}\kappa)] \tag{4.106}$$

With the factors ζ_0, ζ_1,.....ζ_8 determined and substituted in the equations (4.E9-78) the description of the steady-state force and moment generation has been completed. To show that the formulae produce qualitative correct results, a collection of computed curves have been presented in the diagrams of Fig.4.19. In Table 4.2 the values of the model parameters have been listed. The diagrams show that the formulae are perfectly capable to at least qualitatively approximate the curves that have been computed with the brush simulation model of Chapter 3 (cf. Fig.3.35). It has not been attempted to find a best fit for the parameters.

Table 4.2. Magic Formula hypothetical parameter values. Parameters that govern the influence of longitudinal slip and changes in vertical load have been given the tentative value zero.

$F_z = 3000$N $F_{zo} = 3000$N $R_o = 0.3$m $R_e = R_o$ ($a = 0.1$m)						
$p_{Cx1} = 1.65$	$p_{Dx1} = 1$	$p_{Dx2} = 0$	$p_{Ex1} = -0.5$	$p_{Ex2} = 0$	$p_{Ex3} = 0$	$p_{Ex4} = 0$
$p_{Kx1} = 12$	$p_{Kx2} = 10$	$p_{Kx3} = -0.6$	$p_{Hx1} = 0$	$p_{Hx2} = 0$	$p_{Vx1} = 0$	$p_{Vx2} = 0$
$p_{Cy1} = 1.3$	$p_{Dy1} = 1$	$p_{Dy2} = 0$	$p_{Dy3} = 0$			
$p_{Ey1} = -1$	$p_{Ey2} = 0$	$p_{Ey3} = 0$	$p_{Ey4} = 0$			
$p_{Ky1} = 10$	$p_{Ky2} = 1.5$	$p_{Ky3} = 0$	$p_{Hy1} = 0$	$p_{Hy2} = 0$	$p_{Hy3} = 0.25$	
$p_{Vy1} = 0$	$p_{Vy2} = 0$	$p_{Vy3} = 0.15$	$p_{Vy4} = 0$			
$q_{Bz1} = 6$	$q_{Bz2} = -4$	$q_{Bz3} = 0.6$	$q_{Bz4} = 0$	$q_{Bz5} = 0$	$q_{Bz9} = 0$	$q_{Bz10} = 0.7$
$q_{Cz1} = 1.05$	$q_{Dz1} = 0.12$	$q_{Dz2} = -0.03$	$q_{Dz3} = 0$	$q_{Dz4} = -1$	$q_{Dz6} = 0$	$q_{Dz7} = 0$
$q_{Dz8} = 0.6$	$q_{Dz9} = 0.2$	$q_{Ez1} = -10$	$q_{Ez2} = 0$	$q_{Ez3} = 0$	$q_{Ez4} = 0$	$q_{Ez5} = 0$
$q_{Hz1} = 0$	$q_{Hz2} = 0$	$q_{Hz3} = 0$	$q_{Hz4} = 0$			
$r_{Bx1} = 5$	$r_{Bx2} = 8$	$r_{Cx1} = 1$	$r_{Hx1} = 0$			
$r_{By1} = 7$	$r_{By2} = 2.5$	$r_{By3} = 0$	$r_{Cy1} = 1$	$r_{Hy1} = 0.02$		
$r_{Vy1} = 0$	$r_{Vy2} = 0$	$r_{Vy3} = -0.2$	$r_{Vy4} = 14$	$r_{Vy5} = 1.9$	$r_{Vy6} = 10$	
$s_{sz1} = 0$	$s_{sz2} = -0.1$	$s_{sz3} = -1.0$	$s_{sz4} = 0$			
$p_{Dx\varphi 1} = 0.4$	$p_{Dx\varphi 2,3} = 0$	$p_{Ky\varphi 1} = 1$	$p_{Dy\varphi 1} = 0.4$	$p_{Dy\varphi 2} = 0$	$p_{Dy\varphi 3,4} = 0$	
$p_{Hy\varphi 1} = 1$	$p_{Hy\varphi 2} = 0.15$	$p_{Hy\varphi 3} = 0$	$p_{Hy\varphi 4} = -4$	$p_{\varepsilon y\varphi 1} = 0$	$p_{\varepsilon y\varphi 2} = 0$	
$q_{Dt\varphi 1} = 10$	$q_{Cr\varphi 1} = 0.2$	$q_{Cr\varphi 2} = 0.1$	$q_{Br\varphi 1} = 0.1$	$q_{Dr\varphi 1} = 1$	$q_{Dr\varphi 2} = -1.5$	

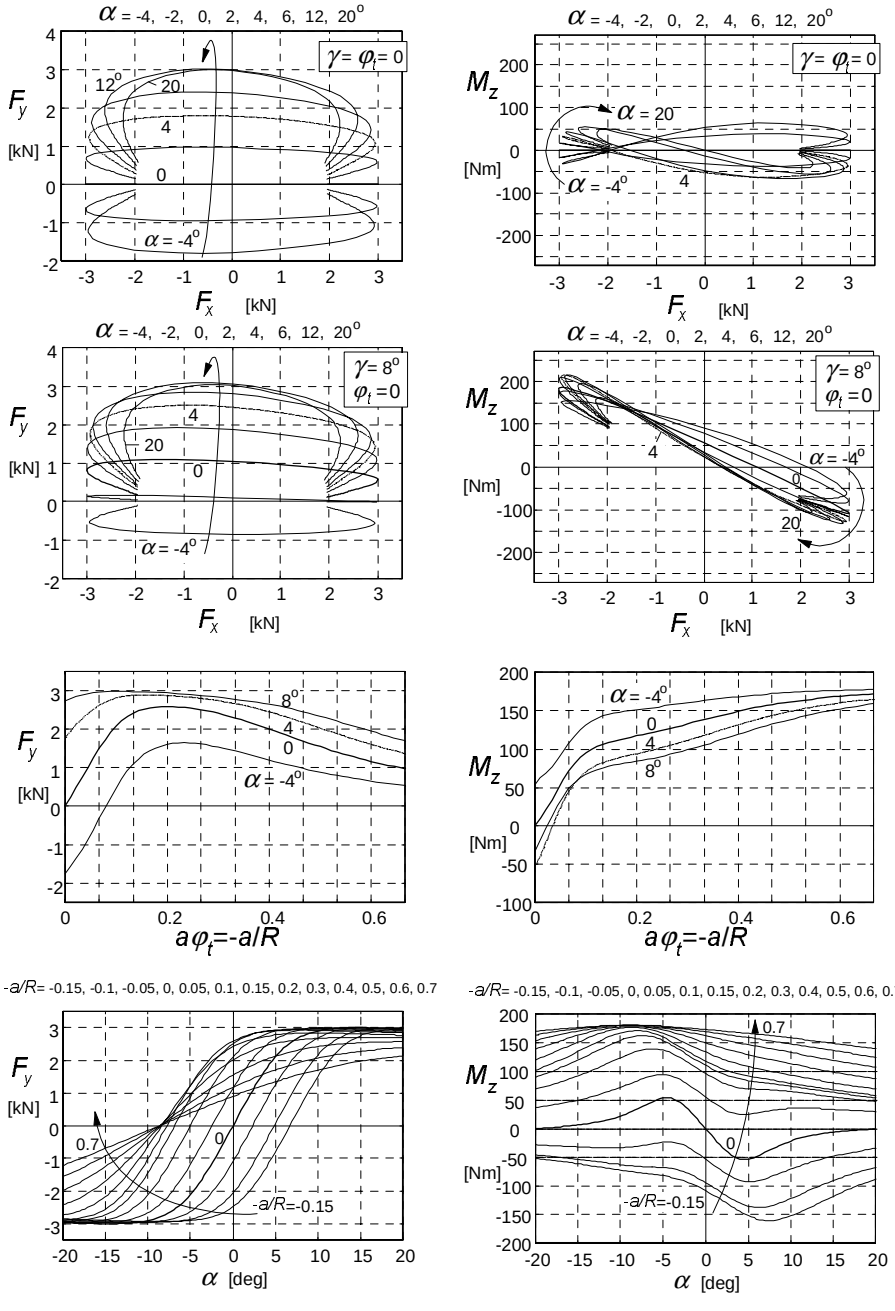

Fig. 4.19. Magic Formula results for steady-state response of forces $F_{x,y}$ and moment M_z to slip angle α, slip ratio κ, camber angle γ and path curvature $\varphi_t = -1/R$.

4.3.4. Ply-Steer and Conicity

In the formulae for the side force F_y and the aligning torque M_z, the vertical shift S_{Vy}, the horizontal shift S_{Hy} and the residual torque peak value D_r contain terms which produce the initial values of side force and aligning torque that occur at straight ahead running (at $\alpha = 0$). These initial values are known to be the result of conicity and ply-steer, which are connected with non-symmetry of the tyre construction. These two possible sources result in markedly different behaviour of the tyre when, at geometrically zero side slip, the tyre is rolled forwards or backwards. If we would have a tyre that exhibits ply-steer but no conicity the generated side force will point to the opposite direction when the wheel is changed from forward to backward rolling. This would also be the case when on a test rig the wheel moves at a small steer angle ψ and the road surface motion is changed from backward to forward. For that reason, ply-steer is sometimes referred to as pseudo side slip. If on the other hand the tyre would show pure conicity, the side force will remain pointing in the same direction when the wheel is rolled in the opposite direction. That behaviour is similar to that of a cambered wheel, which explains the term: pseudo camber. In Fig.4.20 for the different cases the diagrams for the side force variation resulting from yaw angle variations have been depicted. The curved or scewed foot prints of the tyre that due to non-symmetric construction of carcass and belt would arise on a zero friction surface explains the resulting characteristics. Definitions of conicity and ply-steer follow from the forces found at zero steer angle ψ.

The deformations of the tyre rolling on a friction surface resemble those that would occur with a tyre (free of conicity and ply-steer) that rolls at a small

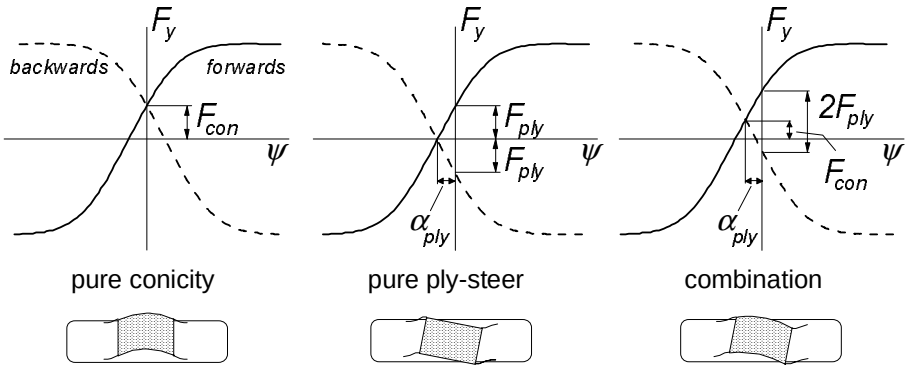

Fig. 4.20. Side force vs steer angle characteristics at forward and backward rolling showing the cases of pure conicity, pure ply-steer and a combination of both situations. Below, the associated foot prints on a frictionless surface have been depicted.

camber and side slip angle respectively. It is therefore tempting to assume that in these comparable cases the moment M_z and the force F_y respond at the same rate which would mean that the associated pneumatic trails are equal for ply-steer and side slip and for conicity and camber. The assumption is partly supported by an extensive experimental investigation of Lee (2000), which assessed a strong linear correlation between conicity and the difference between slip angles where F_y and M_z become equal to zero. In Fig.4.21 this difference is designated as δ_o. Lee found that at $\delta_o = 0$ conicity is almost zero. This means that for vanishing conicity the remaining ply-steer produces a moment that is approximately equal to minus the pneumatic trail for side slip times the side force. With the introduction of the (small) equivalent slip angle α_{ply} we have:

$$M_{ply} \approx -C_{M\alpha}\alpha_{ply} \text{ with } C_{M\alpha} = tC_{F\alpha} \tag{4.107}$$

and

$$F_{ply} \approx C_{F\alpha}\alpha_{ply} \tag{4.108}$$

Also according to Lee, the residual torque at zero side force, M_{zr0} in Fig.4.21, is strongly correlated with δ_o and thus with conicity. We find from the diagram:

$$M_{zr0} \approx C_{M\alpha}\delta_o \tag{4.109}$$

If we may further assume that for the conicity force and moment a similar correspondence with camber response exists we would have after introducing an equivalent camber angle γ_{con}:

$$M_{con} \approx C_{M\gamma}\gamma_{con} \text{ with } C_{M\gamma} = t_\gamma C_{F\gamma} \tag{4.110}$$

where t_γ (>0) represents the distance of the point of application of the resulting camber thrust in front of the contact centre (that is: negative trail). The conicity force becomes:

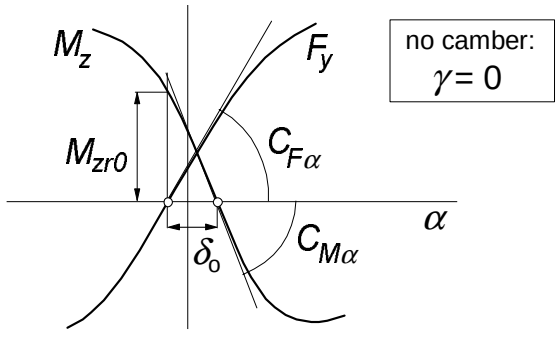

Fig. 4.21. The situation near zero slip angle, force and moment due to conicity and ply-steer.

$$F_{con} \approx C_{F\gamma}\gamma_{con} \tag{4.111}$$

With these assumptions it is possible to estimate the contributions of ply-steer and conicity in the initial values of side force and aligning torque (at $\alpha = \gamma = 0$) from a set of tyre parameters that belongs to one direction of rolling.

This enables the vehicle modeller to switch easily from the set of parameter values of the tyre model that runs on the left-hand wheels of a car to the set for the right-hand wheels. To accomplish this, the equivalent camber parts of the left-hand tyre model must be changed in sign for both the aligning moment and the side force to make the model suitable for the right-hand tyre. Also, it is then easy to omit e.g. all conicity contributions which were originally present in the tyre from which the parameters have been assessed through the fitting process.

To develop the theory, we will first consider the case of a tyre without ply-steer and conicity and study the situation when a camber angle is applied. This condition is reflected by the diagram of Fig.4.22. Considering the relations entered in this figure, we may write for the distance δ_γ

$$\delta_\gamma = \left(\frac{C_{M\gamma}}{C_{M\alpha}} + \frac{C_{F\gamma}}{C_{F\alpha}} \right) \gamma \tag{4.112}$$

and consequently we can find the camber angle γ from the distance δ_γ . In a similar fashion the conicity will be assessed in terms of the equivalent camber angle and after that, the part attributed to ply-steer can be determined and expressed in terms of the equivalent slip angle. Figure 4.23 illustrates the conversion to equivalent angles. We find similar to the inverse of (4.112)

$$\gamma_{con} = \frac{\delta_o}{\dfrac{C_{M\gamma}}{C_{M\alpha}} + \dfrac{C_{F\gamma}}{C_{F\alpha}}} \tag{4.113}$$

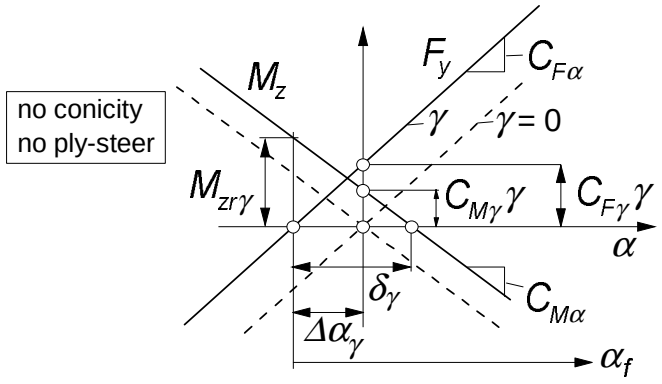

Fig. 4.22. Characteristics of a tyre without ply-steer or conicity near the origin at $\alpha = 0$, with and without camber.

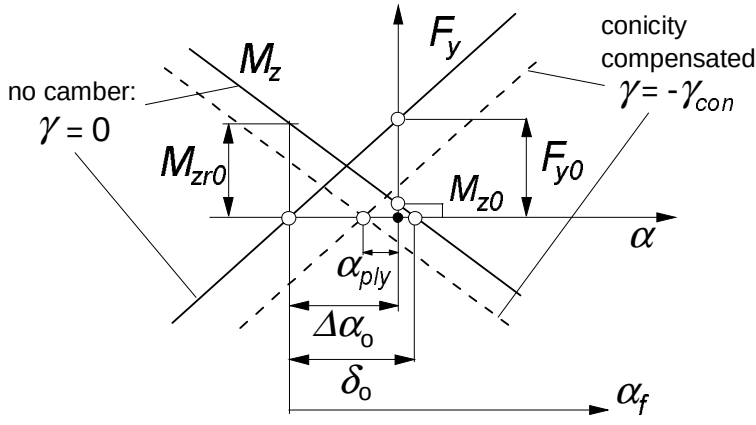

Fig. 4.23. Characteristics of a tyre with ply-steer and conicity showing conversion to equivalent camber and slip angle.

The equivalent slip angle can now be obtained from:

$$\alpha_{ply} = \left(\Delta\alpha_o - \frac{C_{F\gamma}}{C_{F\alpha}} \gamma_{con} \right) \operatorname{sgn} V_{cx} \tag{4.114}$$

The four slip and camber stiffnesses are available from Eqs.(4.E25,30,48,49). The sign of the forward velocity has been properly introduced.

The next thing we have to do is expressing δ_o and $\Delta\alpha_o$ in terms of the shifts and the initial residual torque as defined in Section 4.3.2. We obtain with (4.E38):

$$\Delta\alpha_o = S_{Hf} \tag{4.115}$$

and from (4.109) and Fig.4.23:

$$\delta_o = \frac{F_{y0}}{C_{F\alpha}} + \frac{M_{z0}}{C_{M\alpha}} = M_{zr0}/C_{M\alpha} \tag{4.116}$$

with $C_{M\alpha}$ according to Eq.(4.E48) and the initial residual torque from (4.E47):

$$M_{zr0} = D_{ro} = F_z R_o (q_{Dz6} + q_{Dz7} df_z) \cdot \lambda_{Mr} \tag{4.117}$$

Finally,the initial side force and torque are to be removed from the equations by putting the parameters p_{Hy1}, p_{Hy2}, p_{Vy1}, p_{Vy2}, q_{Dz6} and q_{Dz7} or the scaling factors λ_{Hy}, λ_{Vy} and λ_{Mr} equal to zero and by replacing in Eqs.(4.E20,37) the original side slip input variable $\alpha^* = \tan\alpha \cdot \operatorname{sgn} V_x$ by its effective value:

$$\alpha^*_{eff} = (\tan\alpha + \alpha_{ply}) \operatorname{sgn} V_x \tag{4.118}$$

and in Eqs.(4.E28,29,47) the original camber $\gamma^* = \sin\gamma$ by the effective total

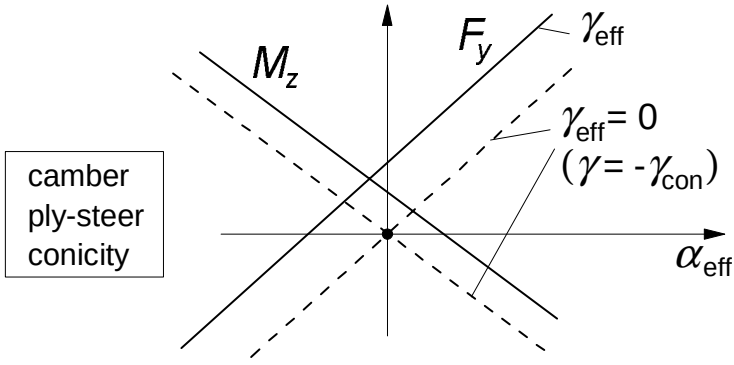

Fig. 4.24. The final diagram with effective side slip and camber variables.

camber:

$$\gamma^*_{eff} = \sin(\gamma + \gamma_{con}) \tag{4.119}$$

where it should be realised that both α_{ply} and γ_{con} are small quantities. The resulting diagram of Fig.4.24 shows characteristics that pass through the origin when the effective camber angle is equal to zero. For the tyre running on the other side of the vehicle the same model can be used but with γ_{con} in (4.119) changed in sign.

The theory above is based on considerations near the origin of the side force and aligning torque vs slip angle diagrams. The introduction of effective slip and camber angles may, however, give rise to slight changes in peak levels of the side force and probably also of the aligning torque. For the former, the situation may be repaired by moving the force characteristic in a direction parallel to the tangent at $F_y = 0$ resulting in an additional vertical shift:

$$\Delta S_{Vy} = F_z \cdot \{(p_{Vy1} + p_{Vy2}\, df_z) - (p_{Vy3} + p_{Vy4}\, df_z)\gamma_{eff}\} \tag{4.120}$$

and an associated additional horizontal shift:

$$\Delta S_{Hy} = -\Delta S_{Vy} / K'_{y\alpha} \tag{4.121}$$

Tyre Pull

If identical tyres would be fitted on the front axle of an automobile but with the conicity forces pointing in the same direction, and the vehicle moves along a straight line (that is: side forces are equal to zero) a steering torque must be applied that opposes the residual torques M_{zr0} generated by the front tyres (Fig.4.21). This is actually only approximately true because we may neglect the trails connected with ply-steer and conicity with respect to the vehicle wheel

base. (In reality we have a small couple acting on the car exerted by the equal but opposite side forces front and rear which counteract the small, mainly conicity, torques front and rear.) The phenomenon that a steer torque must be applied when moving straight ahead is called: tyre or vehicle pull. If the steering wheel would be released, the vehicle will deviate from its straight path.

If on the right-hand wheel a tyre is mounted that is identical with the left-hand tyre one would actually expect that the conicity forces are directed in opposite directions and neutralise each other (as will occur also with the moments). This is because of the observation that one might compare the condition on the right-hand side with an identical tyre rolling backwards with respect to condition of the left-hand tyre. In contrast, the ply-steer forces of the left and right tyres act in the same direction but are compensated by side forces that arise through a small slip angle of the whole vehicle.

If the ply-steer angles front and rear are not the same, a small steer angle of the front wheels equal to the difference of the ply-steer slip angles front and rear is required for the vehicle to run straight ahead. The whole vehicle will run at a slip angle equal to that of the rear wheels.

4.3.5. The Overturning Couple

The overturning couple is especially important to investigate the vehicle roll-over occurrence and the curving behaviour of a motorcycle. In moderate conditions Eq.(4.E69) may often be sufficient to model the overturning moment. In the present section we will study cases that require more elaborate modelling.

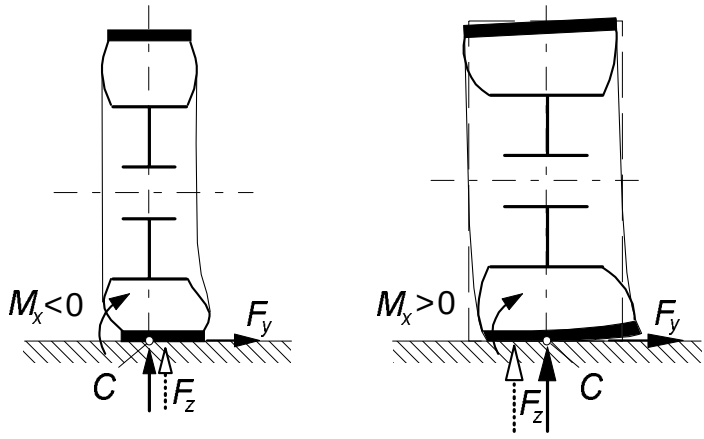

Fig. 4.25. Narrow and wide tyre subjected to side slip giving rise to an overturning couple that may be of a different sign.

Due to Side Slip

Experience with measuring truck tyres, racing tyres and passenger car tyres shows that a positive overturning couple arises especially at low vertical loads as a response to positive side slip (situation depicted in Fig.4.25) while camber remains zero. This is probably in contrast to the behaviour of narrow passenger car or motorcycle tyres where due to the lateral deflection connected with the side force F_y, the point of application of the resultant vertical force F_z moves in the direction of the side force and as a result generates a negative couple M_x. The observation that a tyre may show a positive moment is expected to be connected with the belt that is stiff in torsion in the contact zone. This high stiffness opposes the flattening of the belt to remain in contact with the road when the belt is tilted through the action of the side force. This will especially be true when the contact patch is short, that is: at low load. As a result, the resultant vertical force vector will move more towards the edge away from the side force which causes the contact pressure to become relatively high on that side of the contact patch thereby enabling the overturning couple to become positive. At higher loads the middle portion of the belt contact range will show less resistance to remain horizontal and the overturning couple may turn to the more common negative values. It is of importance to note that the positive overturning couple at low loads and the ensuing sign change is observed to occur when measurements are conducted on e.g. a flat plank or flat trac machine where the axle height is recorded accurately and in the processing stage proper account is given to the standard definition of the overturning couple, that is the moment about the line of intersection of wheel centre plane and ground plane. If the change in loaded radius is disregarded as is often done in past practice when measuring with over the road test vehicles the positive part and the connected sign change is not observed. Consequently, it is of crucial importance that the tyre test engineer and the vehicle dynamicist take care of employing, at least, the same definition for the overturning couple.

The phenomenon may in some way be connected with the negative camber stiffness that is observed to occur with some type of tyres also especially at low loads turning to positive at higher loads. The negative camber force generally changes to positve values when the camber angle becomes sufficiently large. At moderate loads this also appears to happen with the overturning couple changing from positive to negative values at larger slip angles, that is: at higher side forces. The overturning couple response to wheel camber is always negative as might be expected. Obviously, the associated camber moment stiffness to be defined as $C_{Mx\gamma} = -\partial M_x/\partial\gamma$ at zero camber is positive.

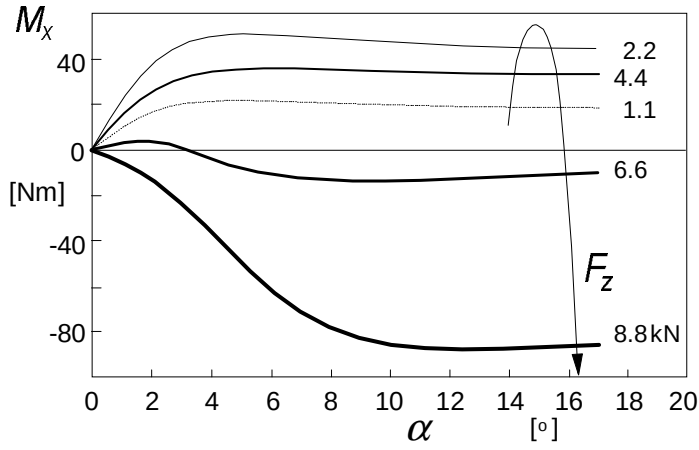

Fig. 4.26. Overturning couple calculated with formulae (4.122-124), cf. Fig.4.30 for similar measured characteristics.

To model such a sign changing situation, the overturning couple response to side slip of the wheel is taken as an example. We will use a formula that is established by adding two functions:

$$M_x = -F_z(y_1 + y_2) \tag{4.122}$$

with the two contributions to the moment arm:

$$y_1 = R_o q_{x1} \frac{F_y}{F_{zo}} \tag{4.123}$$

$$y_2 = -R_o q_{x2} \cos\{q_{x3} \arctan(q_{x4} F_z / F_{zo})^2\} \cdot \sin\{q_{x5} \arctan(q_{x6} F_y / F_{zo})\} \tag{4.124}$$

The first term y_1 increases with the side force. The second term y_2 grows, at least initially, with $-F_y$ and decays with vertical load F_z. For the parameter values listed in Table 4.3, also containing assumed parameters for the side force characteristic, Eqs.(4.E19-27), the overturning couple has been calculated. Figure 4.26 shows the resulting curves. The same tendencies have been found to occur both with truck tyres and passenger car tyres. For the latter, we may refer to the diagram given in Fig.4.30. The same figure, which has been reproduced from the dissertation of Van der Jagt (2000), contains the diagram showing the decrease of the loaded radius with slip angle. This information is needed to assess the moment about the longitudinal axis through the wheel centre. In Chapter 9 a formula is given which assumes that the decrease of the loaded radius is proportional to the squares of the lateral and the longitudinal deflection of the carcass, cf. Eq.(9.222). Experiments indicate that also the tyre vertical

stiffness is effected by horizontal tyre forces, cf. Reimpell (1986), Eq.(9.217).

Table 4.3. Parameter values for overturning couple computation, cf. Eqs.(4.120-122).

F_{zo} =4.4 kN	R_o = 0.3 m				
μ_y = 1	C_y = 1.4	E_y = -1	p_{Ky1} = 20	p_{Ky2} = 1.5	
q_{x1} = 0.042	q_{x2} = 0.56	q_{x3} = 0.955	q_{x4} = 2.35	q_{x5} = 1.25	q_{x6} = 0.46

Due to Camber

The second case to be dealt with concerns the motorcycle tyre. A special problem can be identified that concerns the possibly very large wheel inclination angle. Similar situations may be encountered with a car tyre when examining the roll over event or when the wheel runs over a locally steep transverse slope. In these cases, the geometry of the cross section of the tyre with its finite width becomes of importance and is largely responsible for the overturning couple that

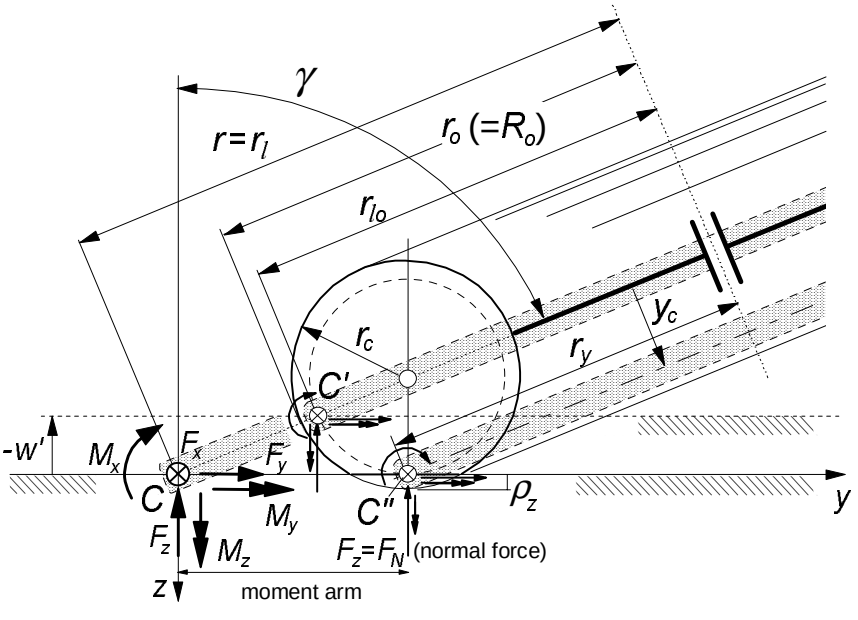

Fig. 4.27. The motorcycle wheel at very large camber angle γ. Two alternative approaches to define the contact centre C and the associated 'loaded radius' r_l and as a consequence the overturning couple M_x. Instead of the circle, the actual section contour may be taken.

arises as a result of the wheel inclination angle with respect to the road surface.

In Fig.4.27 the configuration at very large camber of a motorcycle wheel has been depicted. For simplicity, the tyre cross section has been assumed to be purely circular. Of course, if instead of relying on a possibly less precise measurement, the overturning couple is to be derived from a calculation where the location of the point of application of the normal force and its distance to the line of intersection (i.e. to point C) which is the moment arm, is of crucial importance, the actual measured cross section contour of the undeformed tyre, free radius versus distance to wheel centre plan $r_{yo}(y_{co})$, should be utilised. Note that at the point of contact with the not yet deformed tyre we have: $\mathrm{d}\, r_{yo}/\mathrm{d}\, y_{co} = -\tan\gamma$. As a consequence of the definition of the point of intersection or contact centre C which is located on the line of intersection of the wheel centre plane and the road plane, the loaded radius r_l which by definition is equal to the distance between wheel centre and contact centre, may become excessively large when the camber angle becomes large.

Although still perfectly correct, this standard definition may seem less attractive and one might want to choose for an alternative approach. Two possible alternatives have been indicated in Fig.4.27. The first one employs a value for the loaded radius r_l' that remains equal to the value that holds for the upright wheel: r_{lo} which is equal to the free radius r_o minus the normal deflection ρ_z. It should then be realised that a concurrent (slight) rise $-w'$ of the effective road plane may not be negligible. This method to acquire the overturning couple M_x' corresponds to the practical procedure often employed when measuring on the road where the actual height of the wheel centre above the road surface is not measured. The second alternative is possibly the physically most realistic one. It defines a contact centre C'' located above the lowest point of the undeformed tyre. A drawback is that an effective wheel plane has to be defined in the vehicle dynamic model that is shifted with respect to the wheel centre plane over a distance y_c.

It turns out that the overturning couples that would act about the three possible virtual contact centres defined above, become quite different from each other although the moment about the longitudinal axis through the wheel centre remains, of course, the same. We find successively if the resultant normal force is assumed to act along a line that passes through the lowest point of the (assumedly circular) tyre cross section and a through F_y with lateral compliance induced additional shift is disregarded:

1. *Standard definition, using C* (for general contour and for circle section):

$$r_l = r_{yo} + y_{co}\tan\gamma - \rho_z/\cos\gamma = r_o - r_c + (r_c - \rho_z)/\cos\gamma \tag{4.125}$$

$$M_x = -F_z(y_{co}/\cos\gamma - \rho_z\tan\gamma) = -F_z(r_c - \rho_z)\tan\gamma \tag{4.126}$$

2. *Practical definition, using C'*:

$$r_l' = r_{lo} = r_o - \rho_z \tag{4.127}$$

$$M_x' = -F_z(r_c - \rho_z)\sin\gamma + F_y w' \tag{4.128}$$

$$w' = -(r_c - \rho_z)(1 - \cos\gamma) \tag{4.129}$$

3. *Physically more realistic definition, using C"*:

$$r_l'' = r_y = r_o - r_c + (r_c - \rho_z)\cos\gamma \tag{4.130}$$

$$M_x'' = 0 \tag{4.131}$$

$$y_c = (r_c - \rho_z)\sin\gamma \tag{4.132}$$

The forces act in the points C, C' and C'' respectively.

The overturning couple M_x according to the standard definition (4.126) is directly responsible for the lean angle of the motorcycle in a steady turn to become larger than what would be expected according to the ratio of centrifugal force and vehicle weight. In the practical definition it would be the combination of M_x' and the effective road surface rise w' that causes the increase in roll angle, while with the third definition it would be due to the lateral shift y_c of the virtual wheel plane.

Irrespective of the definition employed, it must be clear how the measured data have been processed and converted from the wheel axle system of axes (where in general the forces are measured) to the road and line of intersection based axes system. An additional conversion may be necessary to suit the requirements of the vehicle dynamicist. It may be realised that with respect to the standard definition of the loaded radius r_l, Eq.(4.125), the effective rolling radius r_e follows a quite different course. Also at large camber angles r_e will remain close to the radius $r_l'' = r_y$ defined by (4.130) and shown in Fig.4.27.

To account for the effect of the lateral tyre deflection and through that the change in vertical pressure distribution, the part of M_x attributed to wheel camber and defined by one of the above or similar expressions, should be extended with the part of the overturning couple described by Eqs.(4.122-124) or, if appropriate, by a simpler version of that.

Note on the Aligning Torque at Large Camber

It may be of interest to be aware of another unexpected phenomenon that arises at large camber angles. One might make a mistake when deriving the aligning torque from the wheel axle oriented measured forces and moments. If these latter quantities are denoted with an additional subscript a the aligning torque is obtained from the moment equilibrium about the vertical axis as

follows (cf. Fig.4.27):

$$M_z = M_{za}\cos\gamma + M_{ya}\sin\gamma - F_{xa} r \sin\gamma \tag{4.133}$$

or alternatively from the moment equilibrium about the wheel radius:

$$M_z = M_y \tan\gamma + M_{za}/\cos\gamma \tag{4.134}$$

If the fact is not recognised that at camber a longitudinal force F_x is generated even at free rolling where M_{ya} is zero or very small, and consequently, F_{xa} is disregarded in Eq.(4.133), the calculated aligning torque is incorrect. In (4.134) the rolling resistance moment M_y may not be negligible for a cambered wheel running at a side slip angle. Then, the relatively stiff belt may be axially deformed in an asymmetric way. This may explain that experiments tend to indicate that the through camber generated F_x is virtually independent of the slip angle.

4.3.6. Comparison with Experimental Data for a Car and a Truck Tyre

In the figures 4.28,29 and 4.31,32 the computed and measured characteristics of a 195/65 R15 car tyre (on the road with Delft Tyre Test Trailer, averaged over two slip angle and brake pressure sweep cycles) and a 315/80 R22.5 truck tyre (on Calspan flat track test stand) have been presented. In general, it is observed that a good agreement between computed and measured curves can be achieved with the model. An exception is the attempt to (physically) describe the measured course of the aligning torque at braking. The diagrams concerned, in Figs.4.29 and 32, show a rather unpredictable variation of the moment while the brake pressure is increased until wheel lock is reached. This is assumedly due to the large direct contribution of the braking force times the moment arm. This distance between the line of action of F_x and the wheel centre plane is suspected to vary due to local road camber variations and possibly tyre non-uniformities while the tyre rolls.

Figure 4.30 presents the overturning couple and the loaded radius for a passenger car tyre as reported by Van der Jagt (2000) and measured with the Ford MTS Flat Trac III tyre testing facility. One may compare the measured characteristics with the calculated curves shown in Fig.4.26 obtained from Eqs. (4.122-124) with hypothetical (not optimized) parameter values (Table 4.3).

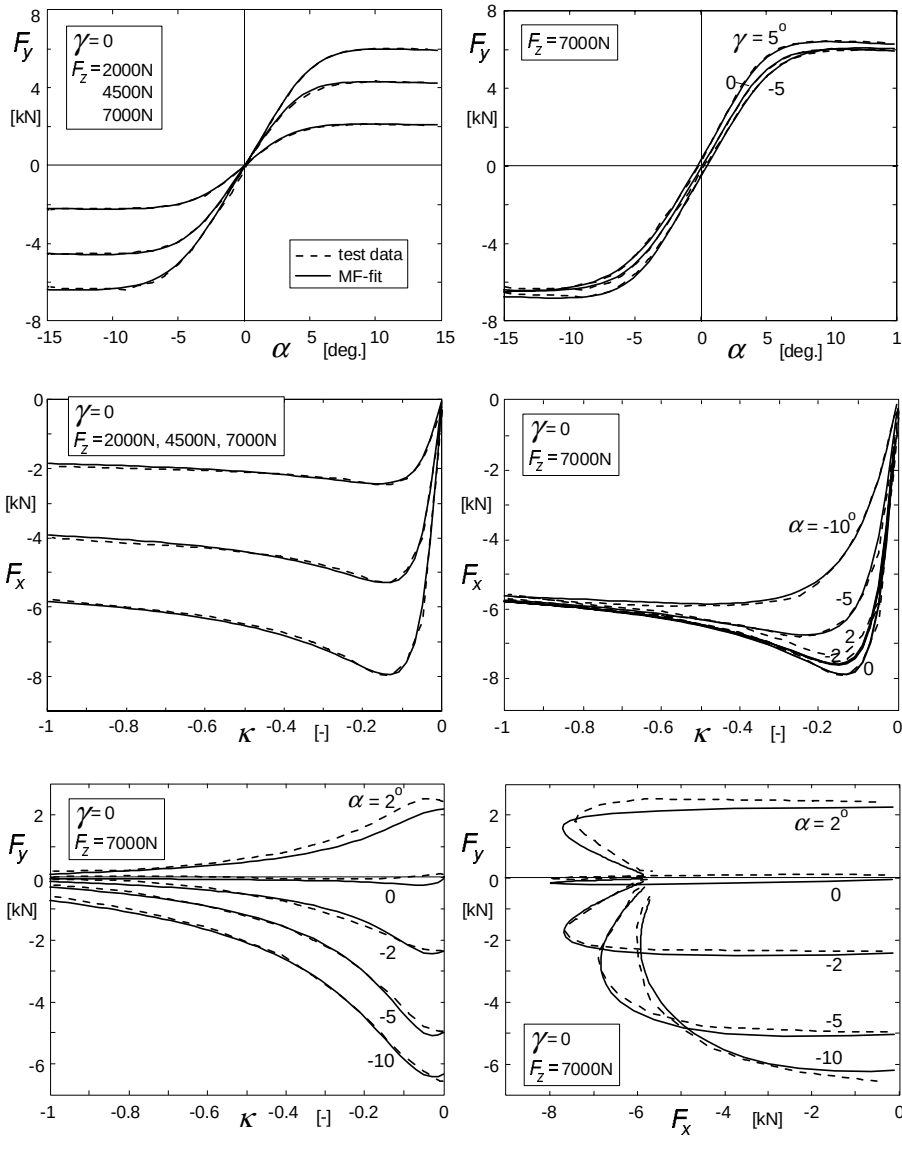

Fig. 4.28. Force characteristics of a 195/65 R15 car tyre. Magic Formula computed results compared with data from measurements (dotted curves) conducted with the Delft Tyre Test Trailer (2000).

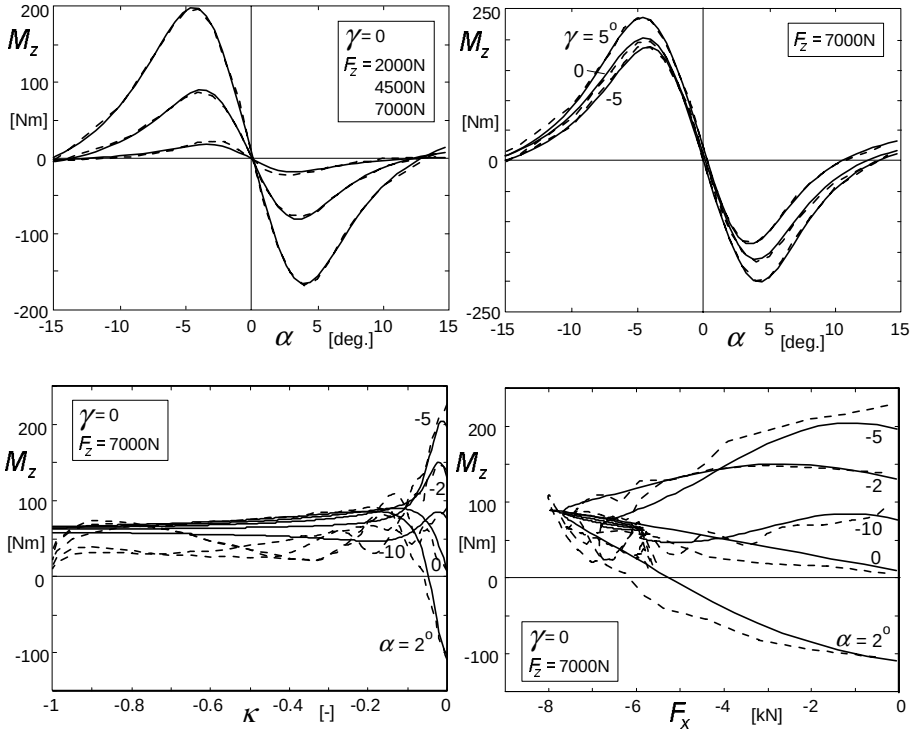

Fig. 4.29. Aligning torque characteristics of a 195/65 R15 car tyre. Magic Formula model computed results compared with data from measurements (dotted curves) conducted with the Delft Tyre Test Trailer (2000).

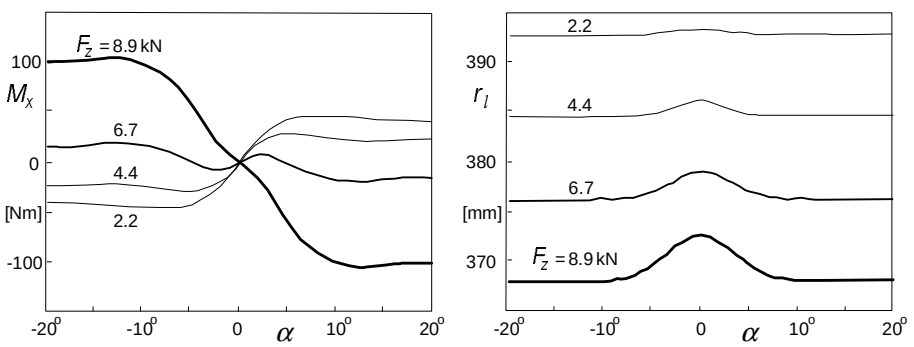

Fig. 4.30. Overturning couple and loaded radius of a passenger car tyre measured on Ford's MTS Flat-Trac III tyre testing machine (V.d. Jagt, 2000). Compare with Fig.4.26.

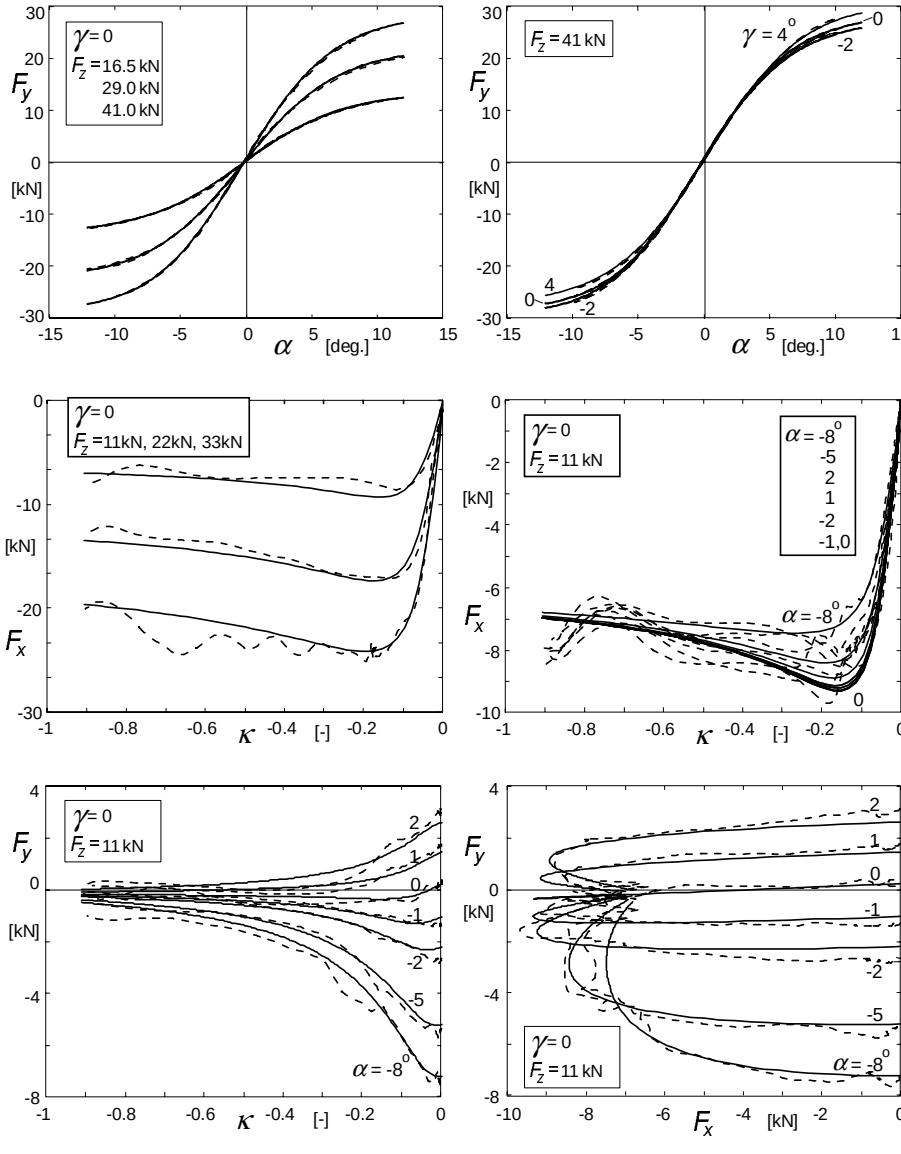

Fig. 4.31. Force characteristics of a 315/80 R22.5 truck tyre. Magic Formula computed results compared with data from measurements conducted with the Calspan flat track tyre test facility (2000) (dotted curves).

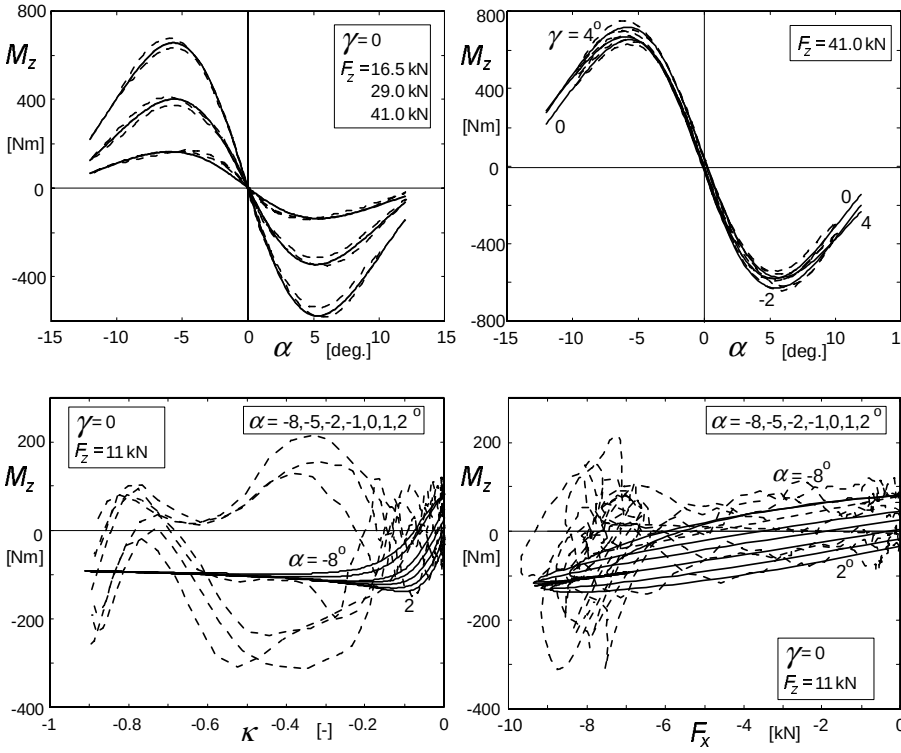

Fig. 4.32. Aligning torque characteristics of a 315/80 R22.5 truck tyre. Magic Formula computed results compared with data from measurements conducted with the Calspan flat track tyre test facility (2000) (dotted curves).

Exercise 4.1. Assessment of off-nominal tyre side force characteristics and combined slip characteristics with F_x as input quantity

Consider the diagrams of Fig.4.33. For the original (nominal) side force characteristic $F_{yo}(\alpha)$ and for the cornering stiffness vs wheel load characteristic $C_{F\alpha}(F_z)$, employ the formulae as given by Eqs.(4.6-4.9) using the data indicated in the figure. The variation of camber stiffness with wheel load $C_{F\gamma}(F_z)$ is assumed to be linear. To cover the combined slip situation use Eqs.(4.41-44) (note: $C_{F\alpha}$ is expressed in N/degree, convert this first into N/rad to get in line with Eq.(4.42)). In Eq.(4.42a) choose $n = 4$. In the nominal condition we have parameter values:

$$F_{zo} = 3000\text{N},\ \mu_o = 0.8,\ C_{F\alpha o} = 400\text{N/deg},\ C_{F\gamma o} = 50\text{N/deg}.$$

Use Eqs.(4.45, 46) and do the following:

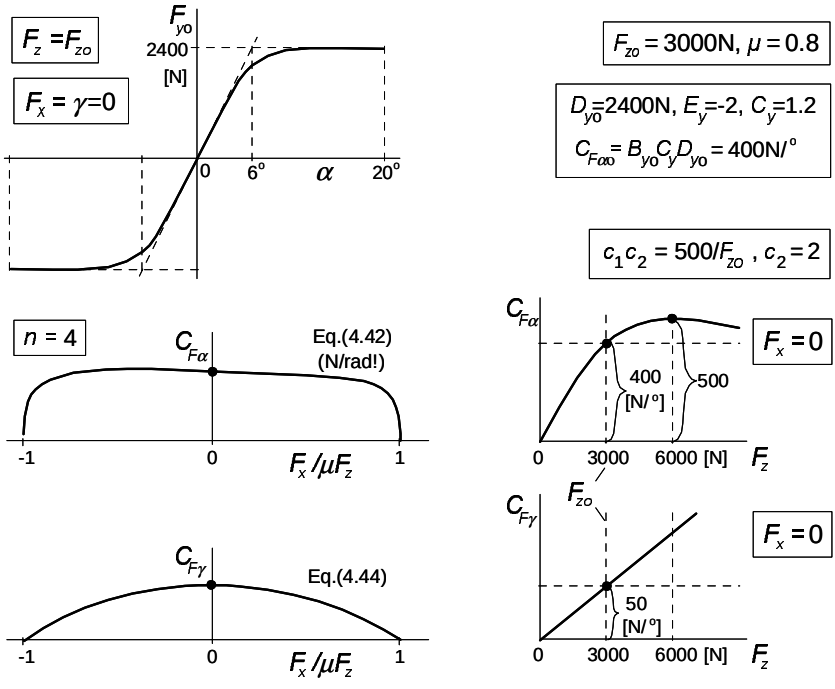

Fig. 4.33. On the assessment of off-nominal and combined slip tyre side force characteristics with longitudinal force as input quantity using the similarity method (Exercise 4.1).

1. Derive and plot the function $F_y(\alpha)$ for the following parameter values describing the tyre at a different condition:
   F_z= 4000N, μ = 0.9, γ = 4°, F_x= 2000N.
2. Plot the graph for $F_y(F_x)$ for the constant slip angles α = 2, 4, 6 and 8°at the condition $\mu = \mu_o$, $F_z = F_{zo}$ and γ = 0.

Exercise 4.2. Assessment of force and moment characteristics at pure and combined slip using the Magic Formula and the similarity method with κ as input

Given are the pure slip force and moment characteristics at nominal vertical load F_{zo} = 4000N and the cornering stiffness vs vertical load (cf. Figs.4.34a,b). The problems are formulated as follows:

1. Determine for the original curves, that is at the nominal load, the values of the coefficients B, C, D and E from the data indicated in the figures below. The vertical and horizontal shifts are disregarded. Use the formula (4.49) for the longitudinal force, the side force and also for the moment. Consider Fig.4.9 and use the formulae (4.52,53) and (4.56). Draw the resulting curves.

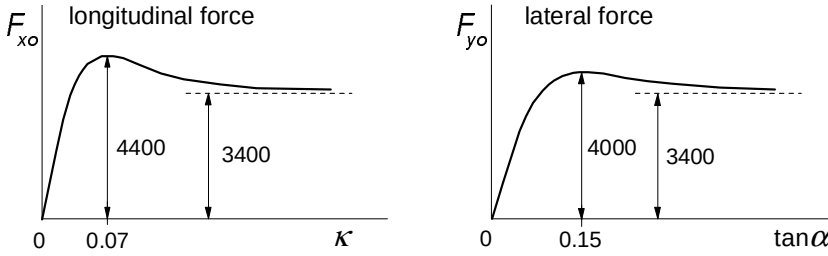

Fig.4.34a. Original tyre force characteristics at pure slip (Exercise 4.2).

μ_{xo}	= 1.1	μ_{yo}	= 1.0
$F_{x,peak}$	= 4400N	$F_{y,peak}$	= 4000N
F_{xa}	= 3400N	F_{ya}	= 3400N
κ_m	= 0.07	tanα_m	= 0.15
$C_{F\kappa o}$	= $C_{F\kappa}(4000)$	$C_{F\alpha o}$	= $C_{F\alpha}(4000)$

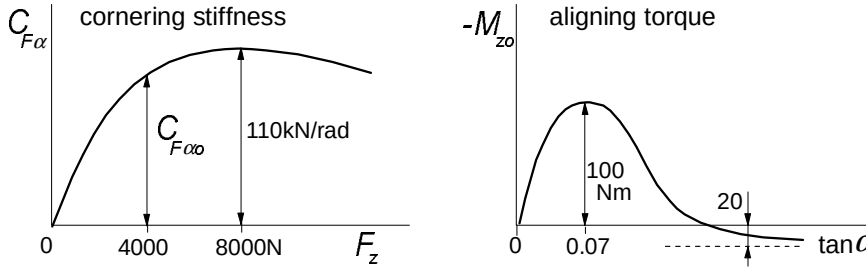

Fig.4.34b. Cornering stiffness and original moment characteristics (Exercise 4.2).

p_1	= 110kN/rad	$-M_{z,peak}$	= 100Nm
p_2	= 8000N	$-M_{za}$	= -20Nm
further:		tanα_m	= 0.07
$C_{F\kappa}(F_z)$	= $40F_z$ [N]	$C_{M\alpha o}$	= $C_{M\alpha}(4000)$
effective compliance parameter		$t(F_z)$	= $0.5\times10^{-5}F_z$ [m]
for M_z, Eq.(4.39):		$C_{M\alpha}(F_z)$	= $t.C_{F\alpha}(F_z)$ [Nm/rad]
c_9	= $2\times10^{-5}\,F_{zo}/a_o$	c_{10}	= 0

2. For F_z= 2000, 4000 and 6000N with μ_x= μ_{xo} and μ_y= μ_{yo} while γ= 0 compute and plot the curves for pure slip $F_x(\kappa)$, $F_y(\alpha)$ and $M_z(\alpha)$. Employ the similarity Eqs.(4.21-26).

3. For F_z = 6000N with μ_x= μ_{xo}, μ_y= μ_{yo} and γ= 0 compute and plot the combined slip curves $F_y(F_x)$ and $M_z(F_x)$ at two slip angles: α = 2° and 8°. The values of the longitudinal slip may range from κ = -1 to +1. Use Eqs.(4.27-29) and (4.35-40).

Chapter 5

NON-STEADY-STATE OUT-OF-PLANE STRING-BASED TYRE MODELS

5.1. Introduction

The transient and oscillatory dynamic behaviour of the tyre will be discussed in this and two ensuing chapters. The present chapter is devoted to the model development of the tyre as an integral component. The stretched string model is chosen as the basis for the physical description of the out-of-plane (anti-symmetric) behaviour. This model exhibits a finite contact length that allows the study of short path wavelength phenomena. The model is relatively simple in structure and integrates the carcass compliance and contact patch slip properties. For the moment response to yaw variations the finite width of the contact patch needs to be introduced which is accomplished by connecting to the string the brush model featuring only fore and aft tread element compliance. In the more advanced string model the added tread elements are allowed to also deflect sideways. The behaviour of this more complex model is expected to be more realistic. This becomes especially apparent in the treatment of the side force response to a constant slip angle when the wheel runs over an undulated road surface. The inertia of the tyre is of importance when running at higher speeds (gyroscopic couple) and when the frequency of lateral and yaw excitation can no longer be considered small. Several approximations of the kinematic and dynamic model will be discussed. In Chapter 6 the theory will be applied in the analysis of the wheel shimmy phenomenon. In Chapter 7 the model will be simplified to the single point contact model that restricts the application to longer wavelength situations but enables the extension of the application to longitudinal and combined transient slip situations. Chapter 9 treats the more complex model that includes an approximate representation of the effect of the finite contact length, the compliance of the carcass and the inertia of the belt. This more versatile model is able to consider both out-of-plane and in-plane tyre dynamic behaviour that can be extended to the non-linear slip range also at relatively short wavelengths. Moreover, rolling over road unevennesses is included.

5.2. Review of Earlier Research

In the theories describing the horizontal non-steady-state behaviour of tyres one can identify two trends of theoretical development. One group of authors assumes a bending stiffness of the carcass and the other bases its theory on the string concept.

In principle, the string theory is simpler than the beam theory, since with the string model the deflection of the foremost point alone determines the path of the tread for given wheel movements, whereas with the beam model the slope at the foremost point also has to be taken into account as an additional variable. The latter leads to an increase in order of the system by one.

Von Schlippe (1941) presented his well-known theory of the kinematics of a rolling tyre, and introduced the concept of the stretched string model. For the first time a finite contact length was considered. In the same paper Dietrich applied this theory to the shimmy problem. Later on, two papers of Von Schlippe and Dietrich (1942,43) were published in which the effect of the width of the contact area is also considered. Two rigidly connected coaxial wheels, both approximated by a one- dimensional string model, are considered. The strings and their elastic supports are also supposed to be elastic in the circumferential direction.

Segel(1966) derived the frequency response characteristics for the one-dimensional string model. These appear to be similar to response curves which arise in Saito's approximate theory for the beam model (1962). For the same string model Sharp and Jones (1980) developed a digital simulation technique which is capable of generating the exact response of the model. Earlier, Pacejka (1966) employed an analogue computer and tape recorder (as a memory device) for the simulation according to the excellent von Schlippe approximation in which the contact line is approximated by a straight line connecting the two end points.

Smiley (1958) gave a summary theory resembling the one-dimensional theory of von Schlippe (1941) He has correlated various known theories with several systematic approximations to his summary theory.

Pacejka (1966) derived the non-steady-state response of the string model of finite width provided with tread elements. The important gyroscopic effect due tyre inertia has been introduced and the non-linear behaviour of the tyre due to partial sliding has been discussed. Applications of the tyre theory to the shimmy motion of automobiles was presented. In Pacejka (1972) the effect of mass of the tyre has been investigated with the aid of an exact analysis of the behaviour of

a rolling stretched string tyre model provided with mass. This complicated and cumbersome theory not suitable for dynamic vehicle studies was then followed by an approximate more convenient theory (Pacejka, 1973a) taking into account the inertial forces only up to the first harmonic of its distribution along the tyre circumference. An outline of the theory together with experimental results will be given in the present chapter.

Rogers derived empirical differential equations (1971) which later were given a theoretical basis (1972). As a result of Rogers' research, shimmy response of tyres in the low frequency range (mass effect not included!) can be described satisfactorily up to rather high reduced frequencies (i.e. short wavelengths) by using simple second-order differential equations.

Sperling (1977) conducted an extensive comparative study of different kinematic models of rolling elastic wheels. Recently, Besselink (2000) investigated and compared a number of interesting earlier models (Von Schlippe, Moreland, Smiley, Rogers, Kluiters, Keldysh, Pacejka) in terms of frequency response functions and step responses to side slip, path curvature (turn slip) and yaw angle, and judged their performances also in connection with the shimmy phenomenon.

Sekula et al. (1976) derived transfer functions from random slip angle input test data in the range of 0.05 to 4.0 Hz. From this information cornering force responses were deduced for both radial and bias-ply tyres to slip angle step inputs. Ho and Hall (1973) conducted an impressive experimental investigation using relatively small aircraft tyres tested on a 120 inch research road wheel up to an oscillating yaw frequency of 3 Hz. A critical correlation study with theoretical results revealed that reasonable or good fit of the experimental frequency response plots can be achieved by using the theoretical functions (5.32,92,93) presented hereafter. It should be pointed out that in testing small scale tyres certain similarity rules, cf. Pacejka (1974), should be obeyed.

Full scale experimental tyre frequency response tests have been carried out by several researchers,e.g. by Meier-Dörnberg up to a yaw frequency of 20 Hz. Some of the latter investigations have been reported on by Strackerjan (1976). This researcher developed a dynamic tyre model based on a somewhat different modelling philosophy compared to the model described by Pacejka (1973) and discussed hereafter. Both types of models show good agreement with measured behaviour. The straightforward approach employed by Strackerjan is similar to the method followed in Chapter 9.

In 1977 Fritz reported on an extensive experimental investigation concerning the radial force and the lateral force and aligning torque response to vertical axle oscillations at different constant yaw (side slip) angles of the wheel. Also, the mean value of side-force and moment have been determined. Earlier, Metcalf

(1963) conducted small scale tyre experiments and Pacejka (1981) produced theoretical results in terms of mean cornering stiffness using a taught string tyre model provided with elastic tread elements. Laerman (1986) conducted extensive tests on both car and truck tyres and compared results with a theoretical model in terms of average side force and aligning torque and frequency response characteristics. The model includes tyre mass (based on Strackerjan, 1976) and allows sliding of tread elements with respect to the ground. Similar experiments on car tyres have been carried out by Takahashi et al. (1987). They developed a relatively simple mathematical model suitable for vehicle dynamics studies including cornering on uneven roads (cf. Chapter 8).

In 2000 Maurice published experimental data up to over 60Hz and a dynamic and short wavelength non-linear model development that will be dealt with in Chapter 9. The model is connected with the in-plane dynamic model of Zegelaar (1998, cf. Chapter 9) and forms a versatile combined slip model that works with the Magic Formula steady-state functions derived in Chapter 4.

Another aspect of tyre behaviour is the non-steady-state response to wheel camber variations. Segel and Wilson (1976) found for a specific motorcycle tyre that after a step change in camber angle about 20 percent of the ultimately attained side force responds instantaneously to this input. The remainder responds in a way similar to the response of the side force to a step change in slip angle although with a larger relaxation length. Higuchi (1997) conducted comprehensive research on the non-linear response to camber based on the string model and experimentally assessed responses to stepwise changes of the camber angle. In Chapter 7 the response to camber changes will be discussed.

The next section treats the essentials of the theory of anti-symmetric tyre non-steady-state and dynamic tyre behaviour on the basis of the stretched string model..

5.3. The Stretched String Model

The tyre model, depicted in Fig.5.1, consists of an (assumedly endless) string which is kept under a certain pretension by a uniform radial force distribution (comparable with inflation pressure in real tyres). In the axial direction the string is elastically supported with respect to the wheel-centre-plane but is prevented from moving in the circumferential direction. The string contacts the horizontal smooth road over a finite length. It is assumed that the remaining free portion of the string maintains its circular shape (in side view).

The model may be extended with a number of parallel strings keeping a constant mutual distance. As a result of this extension, a finite contact width

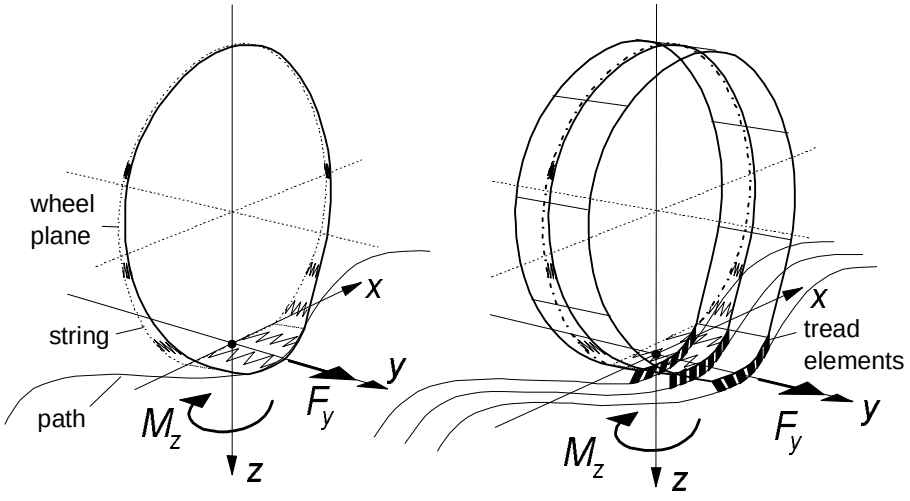

Fig. 5.1. Tyre model with single stretched string and model extended with more parallel strings provided with tread elements which are flexible in the longitudinal direction.

arises. The strings are thought to be provided with a large number of elastic tread elements which, for reasons of simplification, are assumed to be flexible in the circumferential direction only. From the above assumptions it follows that longitudinal deformations which arise at both sides of the wheel-centre-plane when the wheel axle is subjected to a yaw rate, are supposed to be taken up by the tread elements only.

For the theory to be linear, we must restrict ourselves to small lateral deformations and assume complete adhesion in the contact area. The wheel-centre-plane is subjected to motions in the lateral direction (lateral displacement $\bar{y}$) and about the axis normal to the road (yaw angle ψ). These motions constitute the input to the system. The excitation frequency is denoted by ω (= $2\pi n$). With V representing the assumed constant speed of travel we obtain for the spatial or path frequency $\omega_s = \omega / V$ and the wavelength of the path of contact points $\lambda = V/n = 2\pi/\omega_s$. The distance travelled becomes $s = Vt$.

Alternative input quantities may be considered which are not related to the position of the wheel with respect to the road but to its rate of change characterized by the slip angle $\alpha = \psi - \mathrm{d}\bar{y}/\mathrm{d}s$ and the path curvature or turn slip $\varphi = -\mathrm{d}\psi/\mathrm{d}s$. The force F_y and the moment M_z which act from the ground on the tyre in the y-direction and about the z-axis respectively form the response to the imposed wheel plane motion.

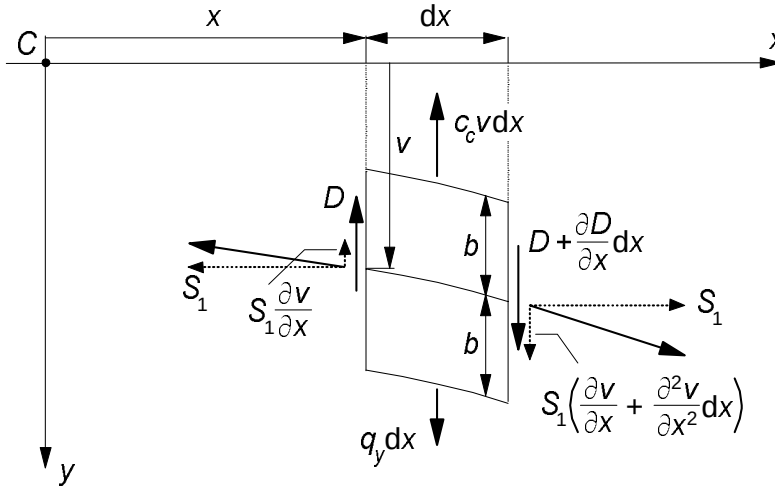

Fig. 5.2. Lateral equilibrium of deflected tread band element.

5.3.1. Model Development

To obtain an expression for the lateral deflection v of the string we consider the lateral equilibrium of an element of the tread band shown in Fig.5.2. The element is of full tread width and contains elements of the parallel strings with the rubber in between. In the lateral direction (y), the equilibrium of forces acting on the element of length dx and width $2b$ results in the following equation:

$$q_y \mathrm{d}x - c_c v \mathrm{d}x - D + D + \frac{\partial D}{\partial x}\mathrm{d}x - S_1 \frac{\partial v}{\partial x} + S_1\left(\frac{\partial v}{\partial x} + \frac{\partial^2 v}{\partial x^2}\mathrm{d}x\right) = 0 \quad (5.1)$$

where c_c denotes the lateral carcass stiffness per unit length, S_1 the circumferential (in the x-direction) component of the total tension force acting on the set of strings and D the shear force in the cross section of the tread band acting on the rubber matrix. The shear force is assumed to be a linear function of the shear angle according to formula:

$$D = S_2 \frac{\partial v}{\partial x} \quad (5.2)$$

With the introduction of the effective total tension $S = S_1 + S_2$ we deduce from Eq.(5.1):

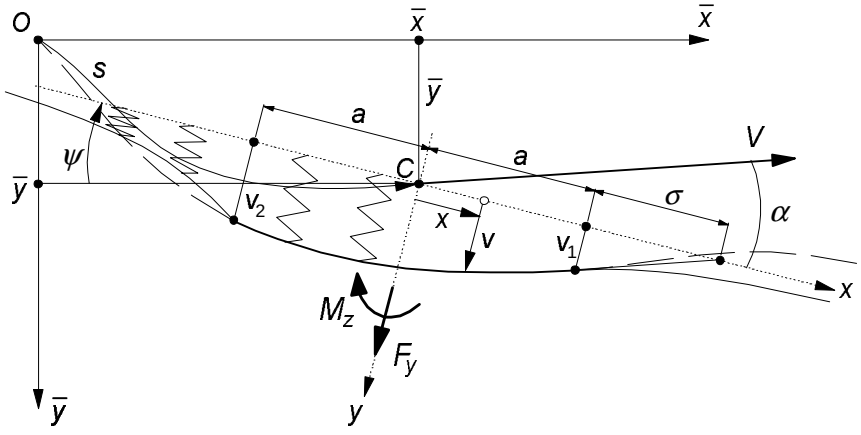

Fig. 5.3. Top-view of the single string model and its position with respect to the fixed frame.

$$S\frac{\partial^2 v}{\partial x^2} - c_c v = -q_y \tag{5.3}$$

In the part of the tyre not making contact with the road the contact pressure vanishes so that $q_y = 0$ and

$$S\frac{\partial^2 v}{\partial x^2} - c_c v = 0 \qquad \text{if} \quad |x| > a \tag{5.4}$$

The lateral behaviour of the model with several parallel strings and of the model with a single string will be identical if parameter S is the same. In Fig.5.3 a top-view of the single string model is depicted. The length σ, designated as the relaxation length has been indicated in the figure. The relaxation length equals:

$$\sigma = \sqrt{\frac{S}{c_c}} \tag{5.5}$$

With this quantity introduced Eq.(5.4) for the free portion of the string becomes:

$$\sigma^2\frac{\partial^2 v}{\partial x^2} - v = 0 \qquad \text{if} \quad |x| > a \tag{5.6}$$

If we consider the circumference of the tyre to be much longer than the contact length we may assume that the deflection v_2 at the trailing edge has a negligible effect on the deflection v_1 at the leading edge. The deflections of the free string near the contact region may then be considered to be the result of the deflections of the string at the leading edge and at the trailing edge respectively and not of

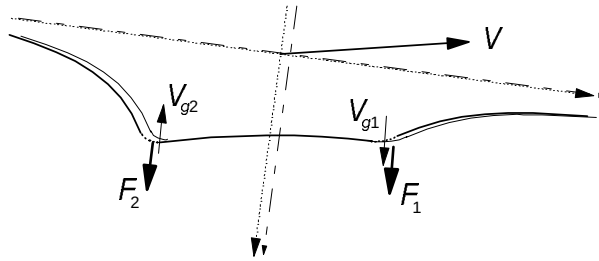

Fig. 5.4. Two successive positions of the string model. Vanishing regions of sliding at the leading and trailing edges and the compatibility of sliding speed V_g and frictional forces F required to maintain a possible kink which apparently can only exist at the trailing edge (2).

a combination of both. The deflections in these respective regions now read approximately:

$$v = C_1 e^{-x/\sigma} \quad \text{if} \quad x > a$$
$$v = C_2 e^{x/\sigma} \quad \text{if} \quad x < -a \tag{5.7}$$

which constitute the solution of Eq.(5.6) considering the simplifying boundary condition that for large $|x|$ the deflection tends to zero. At the edges $x = \pm a$ where $v = v_1$ and $v = v_2$ respectively we have for the slope:

$$\frac{\partial v}{\partial x} = -\frac{v_1}{\sigma} \quad \text{for} \quad x \downarrow a$$
$$\frac{\partial v}{\partial x} = \frac{v_2}{\sigma} \quad \text{for} \quad x \uparrow -a \tag{5.8}$$

Because we do not consider the possibility of sliding in the contact zone, a kink may show up in the shape of the deflected string at the transition points from the free range to the contact zone. It seems a logical assumption that through the rolling process the string forms a continuously varying slope around the leading edge while at the rear, because of the absence of bending stiffness, a discontinuity in slope may occur. An elegant proof of this statement follows by considering the observation that in vanishing regions of sliding at the transition points, cf. Fig.5.4, the directions of sliding speed of a point of the string with respect to the road and the friction force exerted by the road on the string that is needed to maintain a possible kink are compatible with each other at the trailing edge but incompatible at the leading edge. Therefore, it must be concluded that a kink may only arise at the trailing edge of the contact line. Consequently, the equation for the slope at the leading edge (first of (5.8)) can be rewritten as:

$$\frac{\partial v}{\partial x} = -\frac{v_1}{\sigma} \quad \text{if} \quad x \uparrow a,\ x = a,\ x \downarrow a \tag{5.9}$$

This equation constitutes an important relationship for the development of the ultimate expression for the deflection of the string as we will see a little later.

In Chapter 2 we have derived the general differential equations for the longitudinal and lateral sliding velocity of a rolling body which is subjected to lateral slip and spin. These equations (2.58,59) become if the sliding speed equals zero as is our assumption here:

$$\frac{\partial u}{\partial x} - \frac{\partial u}{\partial s} = y\varphi \tag{5.10}$$

$$\frac{\partial v}{\partial x} - \frac{\partial v}{\partial s} = -\alpha - x\varphi \tag{5.11}$$

In these equations s denotes the distance travelled by the wheel centre (or better: the contact centre) and x and y the coordinates the considered particle would have with respect to the moving axes system (C, x, y) in the horizontally undeformed state.

These partial differential equations will be solved by using Laplace transformation. The transforms will be written in capitals. The transformation will not be conducted with respect to time but with respect to the distance travelled $s = Vt$ where the speed V is assumed to be a constant. The Laplace transform of a variable quantity, generally indicated by q, is defined through:

$$L[q(s)] = Q(p) = \int_0^\infty e^{-ps} q(s)\,\mathrm{d}s \tag{5.12}$$

where p is the Laplace variable.

With initial conditions $u(x, 0) = v(x, 0) = 0$ at $s = 0$ we obtain from (5.10,11) the transformed equations:

$$\frac{\mathrm{d}U}{\mathrm{d}x} - pU = y\Phi \tag{5.13}$$

$$\frac{\mathrm{d}V}{\mathrm{d}x} - pV = -A - x\Phi \tag{5.14}$$

The solutions of these ordinary first-order differential equations read:

$$U = C_u e^{px} - \frac{1}{p} y\Phi \tag{5.15}$$

$$V = C_v e^{px} + \frac{1}{p} A + \frac{1}{p}\left(\frac{1}{p} + x\right)\Phi \tag{5.16}$$

In Eqs.(5.15,16) the coefficients C_u and C_v are constants of integration. They are functions of p and depend on the tyre construction, that is the structure of the

model. For our string model with tread elements which can be deformed in the longitudinal direction only, we have the boundary conditions at the leading edge $x = a$:

$$u = 0 \quad \text{or} \quad U = 0 \tag{5.17}$$

and

$$\frac{\partial v}{\partial x} = -\frac{v_1}{\sigma} \quad \text{or} \quad \frac{\mathrm{d}V}{\mathrm{d}x} = -\frac{V_1}{\sigma} \tag{5.18}$$

with the latter equations (5.18) corresponding to Eq.(5.9).

The constant C_u now obviously becomes:

$$C_u = \frac{1}{p} y \Phi e^{-pa} \tag{5.19}$$

For the determination of C_v we have to differentiate Eq.(5.16) with respect to x

$$\frac{\mathrm{d}V}{\mathrm{d}x} = C_v p e^{px} + \frac{1}{p}\Phi \tag{5.20}$$

With (5.18) we obtain

$$C_v = -\frac{1}{p}\left(\frac{1}{\sigma}V_1 + \frac{1}{p}\Phi\right)e^{-pa} \tag{5.21}$$

which with (5.16) yields for the deflection at the leading edge

$$V_1 = \frac{\sigma}{1 + \sigma p}(A + a\Phi) \tag{5.22}$$

and for the deflection in the contact zone

$$V = \frac{1}{p}\left\{-\frac{A + (\sigma + a + 1/p)\Phi}{1 + \sigma p} e^{p(x-a)} + A + \left(x + \frac{1}{p}\right)\Phi\right\} \tag{5.23}$$

The terms containing $e^{p(x-a)}$ point to a retardational behaviour, which corresponds to delay terms in the original expressions. Note that a memory effect exists due to the fact that the non-sliding contact points retain information about their location with respect to the inertial system of axes ($\bar{x}$, O, $\bar{y}$) as long they are in the contact zone.

Equation (5.22) transformed back yields the first-order differential equation for the deflection of the string at the leading edge:

$$\frac{\mathrm{d}v_1}{\mathrm{d}s} + \frac{1}{\sigma}v_1 = \alpha + a\varphi \qquad \left(= \psi - \frac{\mathrm{d}\bar{y}}{\mathrm{d}s} - a\frac{\mathrm{d}\psi}{\mathrm{d}s}\right) \tag{5.24}$$

This equation which is of fundamental importance for the transient behaviour of the tyre model (note the presence of the relaxation length σ in the left-hand

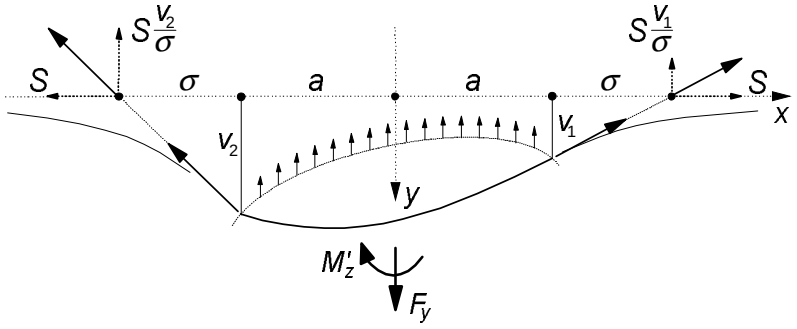

Fig. 5.5. Equilibrium of forces in the contact region.

member) might have been found more easily by considering a simple trailing wheel system with trail equal to σ and swivel axis located in the wheel plane a distance $\sigma + a$ in front of the wheel axis, cf. Fig.5.3. The equation may also be found immediately from Eq.(5.14) by taking $x = a$ and considering condition (5.9). Equation (5.16) may also be transformed back which produces the delay terms mentioned before. However, we prefer to maintain the expression in the transformed state since we would like to obtain the result, that is: the force and moment response, in the form of transfer functions.

The force and moment transfer functions

For the calculation of the lateral force F_y and the moment M_z' due to lateral deflections acting on the string two methods may be employed. According to the first method used by von Schlippe (1941) and by Segel (1966) the internal (lateral) forces acting on the string are integrated along the length of the string extending from minus infinity to plus infinity taking into account the circular shape of the string from side-view. The latter is important for the moment acting about the vertical axis. A correct result for the moment is obtained if not only the lateral forces acting on the string are taken into account but also the radial forces (the air pressure) which arise due to the string tension and which act along lines out of the centre-plane due to the lateral deflection of the string. Surprisingly, a simpler configuration where the string lies in horizontal plane (without considering the circular shape) appears to produce the same result. This is proven by considering the second method.

The second method which has been used by Temple (cf. Hadekel, 1952) is much simpler and leads to the same correct result. The equilibrium of only that portion of the string is considered which makes contact with the road surface. On this piece of string the internal lateral forces, the string tension force and the external forces, constituting the force F_y and the moment M_z' are acting (cf. Fig.5.5).

According to Temple's method we obtain for the lateral force:

$$F_y = c_c \int_{-a}^{a} v\,\mathrm{d}x + S(v_1 + v_2)/\sigma \tag{5.25}$$

and for the moment due to lateral deformations

$$M_z' = c_c \int_{-a}^{a} vx\,\mathrm{d}x + S(a+\sigma)(v_1 - v_2)/\sigma \tag{5.26}$$

with v_1 and v_2 denoting the deflections at $x = a$ and $-a$ respectively and $S = \sigma^2 c_c$ according to Eq.(5.5). For a first application of the theory we refer to exercise 5.1.

The moment M_z^* due to longitudinal deformations which in our model are performed by only the tread elements is derived from the deflection u distributed over the contact area. With c_{px}' denoting the longitudinal stiffness of the elements per unit area we obtain:

$$M_z^* = -c_{px}' \int_{-a}^{a} \int_{-b}^{b} u\,y\,\mathrm{d}x\,\mathrm{d}y \tag{5.27}$$

By adding up both contributions the total moment is formed

$$M_z = M_z' + M_z^* \tag{5.28}$$

The Laplace transforms of F_y, M_z' and M_z^* is now readily obtained using Eqs. (5.23) and (5.15) with (5.19) and the transformed versions of Eqs.(5.25),(5.26) and (5.27). In general the transformed responses may be written as

$$\begin{aligned} L\{F_y\} &= H_{F,\alpha} A + H_{F,\varphi} \Phi \\ &= H_{F,y} Y + H_{F,\psi} \Psi \end{aligned} \tag{5.29}$$

etc. The coefficients of the transformed input variables constitute the transfer functions. The formulae, for convenience written in vectorial form, for the responses to α, φ and ψ read (since $\alpha = -\mathrm{d}\bar{y}/\mathrm{d}s$ expressions for the response to $\bar{y}$ have been omitted):

$$\begin{aligned} \boldsymbol{H}_{F,(\alpha,\varphi,\psi)}(p) = \frac{c_c}{p}\Bigg[& 2(\sigma+a)\left(1, \frac{1}{p}, 0\right) + \\ & - \frac{1}{p}\left(1 + \frac{\sigma p - 1}{\sigma p + 1} e^{-2pa}\right)\left(1, \sigma + a + \frac{1}{p}, -(\sigma + a)p\right)\Bigg] \end{aligned} \tag{5.30}$$

$$\begin{aligned} \boldsymbol{H}_{M',(\alpha,\varphi,\psi)}(p) = \frac{c_c}{p}\Bigg[& 2a\left\{\sigma(\sigma+a) + \tfrac{1}{3}a^2\right\}(0, 1, -p) + \\ & - \frac{a(1+e^{-2pa}) + p\left\{\sigma(\sigma+a) - 1/p^2\right\}(1-e^{-2pa})}{(\sigma p + 1)p}\left(1, \sigma+a+\frac{1}{p}, -(\sigma+a)p\right)\Bigg] \end{aligned} \tag{5.31}$$

and furthermore

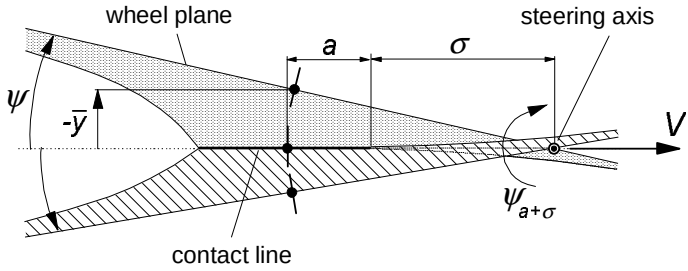

Fig.5.6. Steady-state response that occurs when swivelling about the $\sigma + a$ point.

$$\boldsymbol{H}_{M_z^*;(\alpha,\varphi,\psi)}(p) = \frac{\kappa^*}{ap}\left\{1 - \frac{1}{2ap}\left(1 - e^{-2pa}\right)\right\}(0, 1, -p) \tag{5.32}$$

in which the parameter

$$\kappa^* = \tfrac{4}{3}a^2 b^3 c'_{px} \tag{5.33}$$

has been introduced.

The transfer functions of the responses to $\bar{y}$ and ψ are obtained by considering the relations between the transformed quantities

$$\Phi = -p\Psi \tag{5.34}$$

$$A = \Psi - pY \tag{5.35}$$

and inserting these in (5.29). We find in general for the transfer function conversion:

$$H_y = -pH_\alpha \tag{5.36}$$

$$H_\psi = H_\alpha - pH_\varphi \tag{5.37}$$

By transforming back the expressions such as (5.23,29), the deflection, the force and the moment can be found as a function of distance travelled s for a given variation of α and φ or of $\bar{y}$ and ψ.

An interesting observation may be made when considering the situation depicted in Fig.5.6. Here a yaw oscillation of the wheel plane is considered around an imaginary vertical steering axis located at a distance $\sigma + a$ in front of the wheel centre. When yaw takes place about this partular point the contact line remains straight and positioned on the line along which the steering axis moves. Consequently, the response of the model to such a yaw motion is equal to the steady-state response. That is, for the force F_y and the moment M'_z, the transfer functions become equal to the cornering stiffness $C_{F\alpha}$ and minus the aligning stiffness $C_{M\alpha}$ respectively. As we realise that the angular motion about the $\sigma + a$

point is composed of the yaw angle ψ and the lateral displacement $\bar{y} = -(\sigma + a)\psi$ and furthermore that the response to $d\bar{y}/ds$ is equal to the response to $-\alpha$, we find, e.g., for the transfer function of F_y to ψ_{s+a}:

$$H_{F,\psi(\sigma+a)} = C_{F\alpha} = H_{F,\psi} + (\sigma + a)pH_{F,\alpha} \tag{5.38}$$

With the aid of (5.37) the fundamental relationship between the responses to α and φ can be assessed. We have in general:

$$H_{\varphi} = \frac{1}{p}\left(H_{\alpha} - H_{\psi ss}\right) + (\sigma + a)H_{\alpha} \tag{5.39}$$

where for the responses to F_y and M_z' we have the steady-state response functions denoted by $H_{\psi ss}$

$$H_{F,\psi(\sigma+a)} = H_{F,\psi ss} = C_{F\alpha} \tag{5.40}$$

and

$$H_{M',\psi(\sigma+a)} = H_{M',\psi ss} = -C_{M\alpha} \tag{5.41}$$

The important conclusion is that we may suffice with establishing a single pair of transfer functions, e.g. H_{α} for F_y and M_z', and derive from that the other functions by using the relations (5.36,37,39) together with (5.40,41). Since in practice the frequency response functions are often assessed experimentally by performing yaw oscillation tests we give below the conversion formulae to be derived from the transfer functions H_{ψ}. Later on, we will address the problem of first subtracting M_z^* from the measured total moment M_z to retrieve M_z' for which the conversion is valid.

$$H_{\alpha} = -\frac{1}{(\sigma+a)p}\left(H_{\psi} - H_{\psi ss}\right) \tag{5.42}$$

$$H_{\varphi} = \frac{1}{p}\left(H_{\alpha} - H_{\psi}\right) \tag{5.43}$$

$$H_{y} = -pH_{\alpha} \tag{5.44}$$

Strictly speaking, the above conversion formulae only hold exactly for our model. The actual tyre may behave differently especially regarding the effect of the moment M_z^* that in reality may slightly rotate the contact patch about the vertical axis and thus affects the slip angle seen by the contact patch. As a consequence the observation depicted in Fig.5.6 may not be entirely true for the real tyre.

In the following, first the step response functions will be assessed and after that the frequency response functions.

5.3.2. Step and Steady-State Response of the String Model

An important characteristic aspect of transient tyre behaviour is the response of the lateral force to a stepwise variation of the slip angle α. The initial condition at $s=0$ reads: $v(x)=0$; for $s>0$ the slip angle becomes $\alpha=\alpha_o$. From Eq. (5.23) we obtain for small slip angles by inverse transformation for the lateral deflection of the string in the contact region:

$$\frac{v}{\alpha_o} = a - x + \sigma\left\{1 - e^{-(s-a+x)/\sigma}\right\} \qquad \text{for} \quad x > a - s \tag{5.45}$$

while for the old points which are still on the straight contact line the simple expression holds:

$$\frac{v}{\alpha_o} = s \qquad \text{for} \quad x \le a - s \tag{5.46}$$

Expression (5.45) is composed of a part $(a - x)\alpha_o$ which is the lateral displacement of the wheel plane during the distance rolled $a - x$ and an exponential part. The point which at the instant s considered is located at coordinate x was the point at the leading edge when the wheel was rolled a distance a-x ago that is at s-a+x. At that instant we had a deflection at the leading edge $v_{1(s-a+x)}$. The new $v = v_{(s)}$ equals the old $v_1 = v_{1(s-a+x)}$ plus the subsequent lateral displacement of the wheel $(a-x)\alpha_o$. Obviously, the exponential part of (5.45) is the v_1 at the distance rolled s-a+x. This can easily be verified by solving Eq.(5.24) for v_1.

With (5.25), finally, the expression for the force can be calculated for the two intervals, with and without the old contact points

$$F_y = \Gamma_{F,\alpha}\alpha_o = c_c\{2(\sigma + a)s - \tfrac{1}{2}s^2\}\,\alpha_o \qquad \text{if } s \le 2a \tag{5.47}$$

$$F_y = \Gamma_{F,\alpha}\alpha_o = 2c_c\left\{(\sigma + a)^2 - \sigma^2 e^{-(s-2a)/\sigma}\right\}\alpha_o \qquad \text{if } s > 2a \tag{5.48}$$

For the aligning torque we obtain by using (5.26):

$$M_z' = \Gamma_{M',\alpha}\alpha_o = c_c\left\{\tfrac{1}{6}s^3 - \tfrac{1}{2}(\sigma + a)s^2\right\}\alpha_o \qquad \text{if } s \le 2a \tag{5.49}$$

$$M_z' = \Gamma_{M',\alpha}\alpha_o = -2c_c\left\{\tfrac{1}{3}a^3 + \sigma a(\sigma + a) - \sigma^2 a e^{-(s-2a)/\sigma}\right\}\alpha_o \quad \text{if } s > 2a \tag{5.50}$$

where the quantities $\Gamma(s)$ designate the unit step response functions. These functions correspond to the integral of the inverse Laplace transforms of the transfer functions (5.30,31) given above.

The graph of Fig.5.7 shows the resulting variation of F_y and M_z' vs travelled distance s. As has been indicated, the curves are composed of a parabola (of the

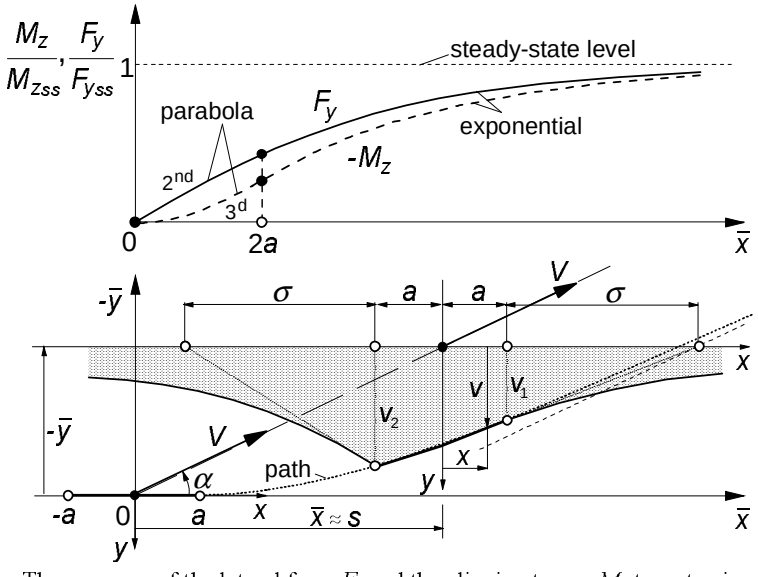

Fig.5.7. The response of the lateral force F_y and the aligning torque M_z to a step input of the slip angle α, calculated for a relaxation length $\sigma = 3a$.

second and third degree respectively) and an exponential function. The step responses have been presented as a ratio to their respective steady-state values.

The steady-state values of F_y and M_z' (or M_z) are directly obtained from (5.25) and (5.26) by considering the shape of the deflected string at steady-state side slip (Fig.5.8), i.e. a straight contact line at an angle α with the wheel plane and a deflection at the leading edge $v_1 = \sigma\alpha$ through which the condition to avoid a kink in the string at that point is obeyed, or from Eqs.(5.48,50) by letting s approach infinity. We have:

$$F_y = C_{F\alpha}\alpha \tag{5.51}$$

$$M_z = -C_{M\alpha}\alpha \tag{5.52}$$

with the cornering and aligning stiffnesses:

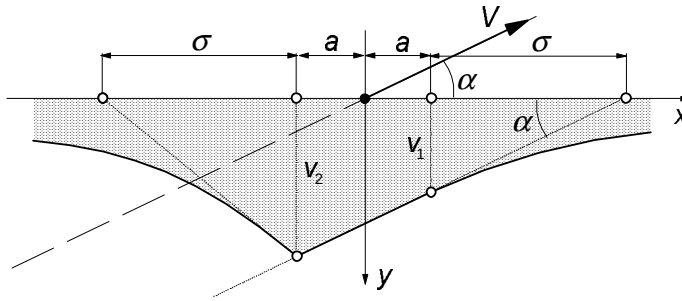

Fig. 5.8. Steady-state deflection of a side slipping string tyre model (complete adhesion).

$$C_{F\alpha} = 2c_c(\sigma + a)^2 \tag{5.53}$$

$$C_{M\alpha} = 2c_c a\{\sigma(\sigma + a) + \tfrac{1}{3}a^2\} \tag{5.54}$$

and the pneumatic trail:

$$t = \frac{C_{M\alpha}}{C_{F\alpha}} = \frac{a\{\sigma(\sigma + a) + \frac{1}{3}a^2\}}{(\sigma + a)^2} \tag{5.55}$$

The variation of these quantities and of the pneumatic trail $t = C_{M\alpha}/C_{F\alpha}$ and also of the relaxation length with wheel load F_z, the latter being assumed to vary proportionally with a^2, turns out to be quite unrealistic when compared with experimental evidence. A variation much closer to reality would be obtained if tread elements were attached to the string. For more details, also concerning the non-linear characteristics and the non-steady analysis of that enhanced but much more complicated model we refer to Section 5.4.3.

The unit step responses Γ to the other input variable φ and the associated variables $\bar{y}$ and ψ are of interest as well. They may be derived by inverse transformation and subsequent integration of the transfer functions (5.30, 31,36,37) or directly by considering the associated string deflections similar to (5.45,46) or from the unit step responses to the slip angle, corresponding to the coefficients of α_o shown in (5.47-50), by making use of the following relationships analogous to Eqs.(5.39,36,37):

$$\Gamma_\varphi = \int \left(\Gamma_\alpha - H_{\psi ss}\right) \mathrm{d}s + (\sigma + a)\,\Gamma_\alpha \tag{5.56}$$

$$\Gamma_y = -\frac{\mathrm{d}}{\mathrm{d}s}\Gamma_\alpha \tag{5.57}$$

$$\Gamma_\psi = \Gamma_\alpha - \frac{\mathrm{d}}{\mathrm{d}s}\Gamma_\varphi \tag{5.58}$$

Figure 5.9 illustrates the manner in which the deflection of the string model reacts to a step change of each of the four wheel motion variables (slip angle, lateral displacement of the wheel plane, turn slip and yaw angle). Figure 5.10 presents the associated responses of the side force and the aligning torque. The responses have been divided by either the ultimate steady-state value of the transient response or the initial value, if relevant. For the moment response to turn slip and lateral displacement both the initial and the final values vanish and a different reference value had to be chosen to make them non-dimensional. The various steady-state coefficients and the lateral and torsional stiffnesses read in

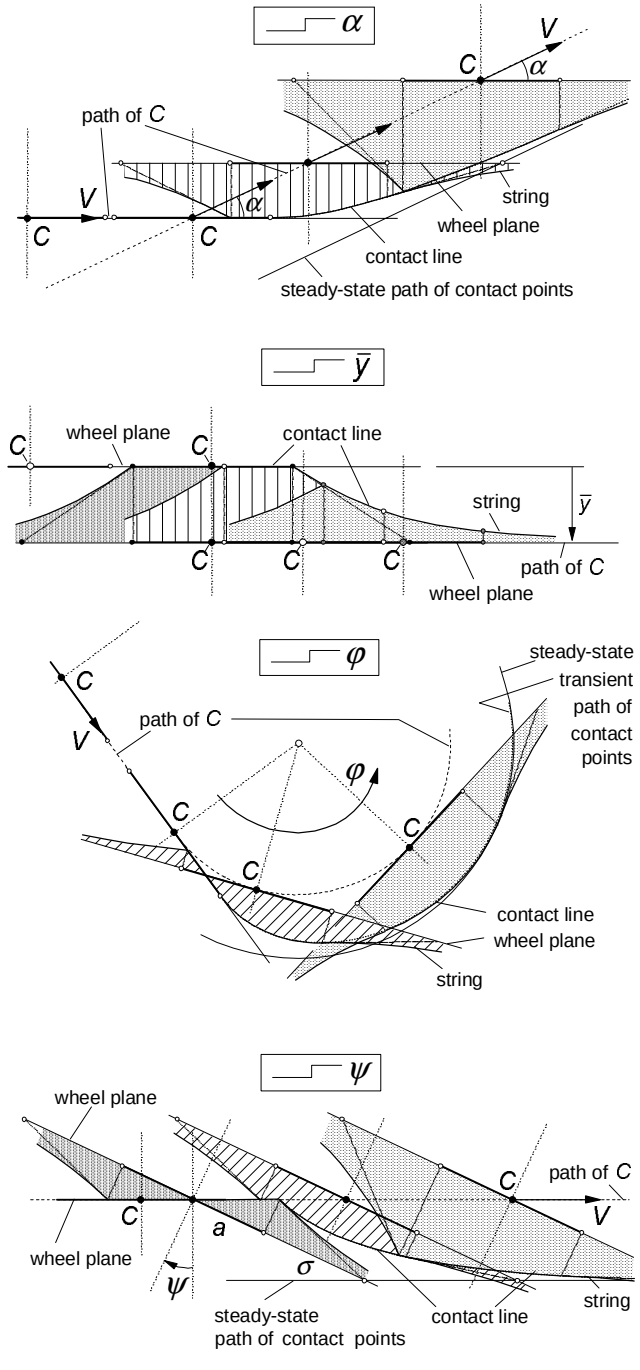

Fig. 5.9. Transient response of string deflection to step change in motion variables.

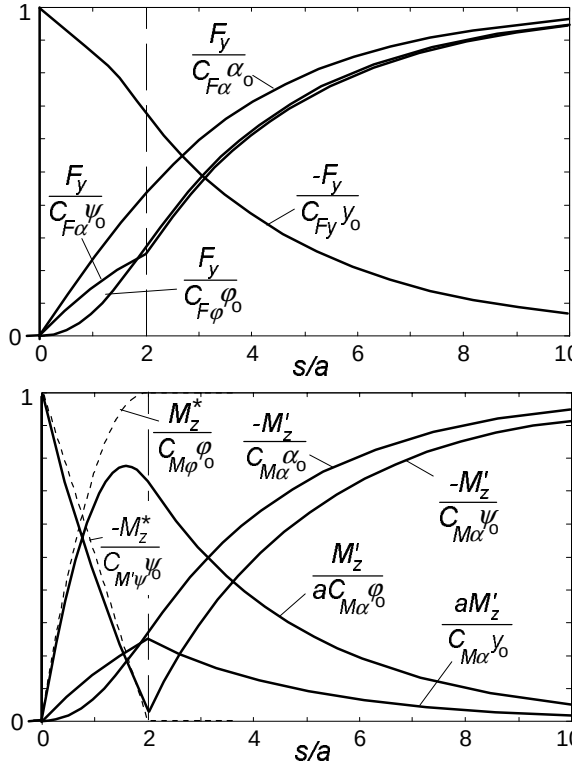

Fig. 5.10. Step response of side force F_y, aligning torque M_z' and tread width moment M_z^* to side slip α, lateral displacement $\dot{y}$, turn slip φ and yaw angle ψ. Computed for string model with deflection relaxation length $\sigma = 3a$.

terms of the model parameters:

Lateral stiffness of the standing tyre:

$$C_{Fy} = 2c_c(\sigma + a) \tag{5.59}$$

Cornering or lateral slip stiffness:

$$C_{F\alpha} = 2c_c(\sigma + a)^2 \tag{5.60}$$

Aligning stiffness

$$C_{M\alpha} = 2c_c a\{\sigma(\sigma + a) + \tfrac{1}{3}a^2\} \tag{5.61}$$

Torsional stiffness of (thin) standing tyre

$$C_{M'\psi} = 2c_c a\{\sigma(\sigma + a) + \tfrac{1}{3}a^2\} \tag{5.62}$$

Turn slip stiffness for the force

$$C_{F\varphi} = 2c_c a\{\sigma(\sigma + a) + \tfrac{1}{3}a^2\} \tag{5.63}$$

Note that the steady-state response of M_z' to φ equals zero. The responses to side slip have already been presented in Fig.5.7. It now appears that the response of the side force to turn slip φ is identical to the response of M_z' to α. This reciprocity property is also reflected by the equality of the slip stiffnesses given by (5.61,63). It furthermore appears that the responses of F_y to ψ and φ and of M_z' to α tend to approach the steady-state condition at the same rate. This will be supported by the later finding that the corresponding frequency responses at low frequencies (large wavelengths) are similar. The frequency responses at short wavelengths are mainly governed by the step response behaviour shortly after the step change has commenced. As appears from the graphs, at distances rolled smaller than the contact length large differences in transient behaviour occur. As expected, the initial responses of F_y to $\bar{y}$ and of M_z' to ψ are immediate and associated with the respective stiffnesses (5.59,62).

The response of the moment M_z^* due to tread width modelled with the brush model that deflects only in the longitudinal direction, may be derived by considering the Laplace transform of the longitudinal deflection u according to Eq.(5.15) with (5.19). Through inverse transformation or simply by inspection of the development of this deflection while the element moves through the contact range the following expressions are obtained:

$$\frac{u}{\varphi_o} = -(a - x)y \qquad \text{for} \quad x > a - s \tag{5.64}$$

$$\frac{u}{\varphi_o} = -ys \qquad \text{for} \quad x \le a - s \tag{5.65}$$

By using Eq.(5.27) the following expressions for the step response of M_z^* to φ result:

$$M_z^* = \Gamma_{M^*;\varphi}\varphi_o = \tfrac{4}{3}c'_{px}(as - \tfrac{1}{4}s^2)b^3\varphi_o \qquad \text{if } s \le 2a \tag{5.66a}$$

$$M_z^* = \Gamma_{M^*;\varphi}\varphi_o = \tfrac{4}{3}c'_{px}a^2b^3\varphi_o \qquad \text{if } s > 2a \tag{5.66b}$$

The graphical representation of these formulae is given in Fig.5.10. The slip and stiffness coefficients employed read:

Turn slip stiffness for the moment, cf. (5.66b):

$$C_{M\varphi} = \kappa^* = \tfrac{4}{3}c'_{px}a^2b^3 \tag{5.67}$$

Torsional stiffness of standing tyre due to tread width, cf. (5.32) with $p \to \infty$:

$$C_{M^*\psi} = \frac{1}{a}C_{M\varphi} = \tfrac{4}{3}c'_{px}ab^3 \tag{5.68}$$

Note that the steady-state response of M_z' to φ equals zero.

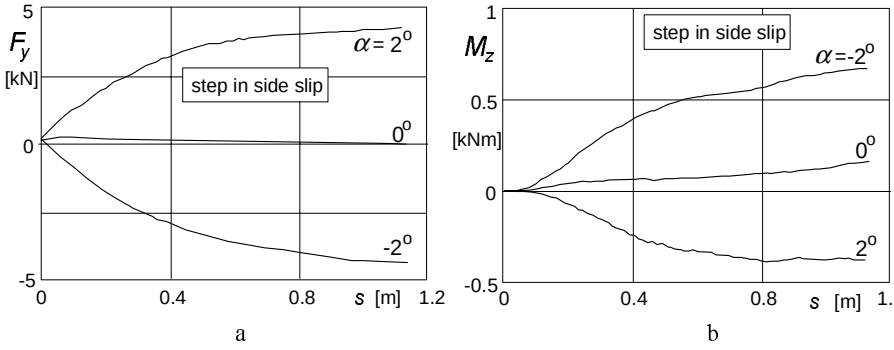

Fig. 5.11. Step response of side force F_y and aligning torque M_z to slip angle α as measured on an aircraft tyre with vertical load F_z = 35kN. (From Besselink, 2000; test data is provided by Michelin Aircraft Tire Corporation).

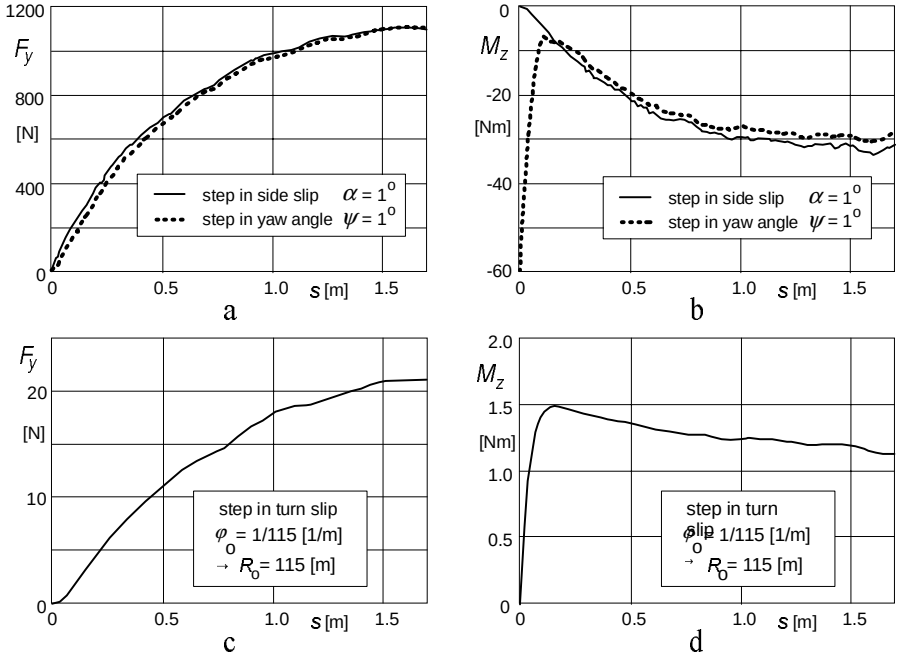

Fig.5.12. Step response of side force F_y and aligning torque M_z to slip angle α, yaw angle ψ and turn slip φ ($\alpha = 0$) as measured on a passenger car tyre at load F_z = 4kN. Tests were conducted on the flat plank machine of TU-Delft. Turn slip results have been obtained by integration of the response to turn slip impulse = step yaw angle, and division by $-R\psi$. (From Higuchi, 1997).

As a result of a step change in turn slip, longitudinal slip at both sides of the contact patch occur. The transient response extends only over a distance rolled equal to the contact length, at the end of which the steady-state response has been reached. As indicated in the graph the approach curve has a parabolic shape. The response to a step change in yaw angle is immediate (like that of M_z') after which a decline occurs which for M_z^* is linear (derivative of response to φ).

In Figs.5.11,12 experimentally obtained step responses have been presented. The diagrams show very well the exponential nature of the force response to side slip. Especially the aircraft tyre exhibits the 'delayed' response of the aligning torque to side slip as predicted by the theory (Fig.5.10). Figure 5.12 shows a similar delay in the responses of F_y to yaw and to turn slip also found in the theoretical results. The peculiar response of the moment to yaw and turn slip is clearly formed by the sum of the responses of M_z' and of M_z^*, although with a ratio that differs from the assumption adopted in Fig.5.10.

Graphs of step response functions may serve to compare the performance of different models and approximations with each other. This will be done in Section 5.4. First we will discuss the frequency response functions.

5.3.3. Frequency Response Functions of the String Model

The frequency response functions for the force and the moment constitute the response to sinusoidal motions of the wheel and can be easily obtained by replacing in the transfer functions (5.30,31,32) the Laplace variable p by $i\omega_s$. The path frequency ω_s (rad/m) is equal to $2\pi/\lambda$ where λ denotes the wavelength

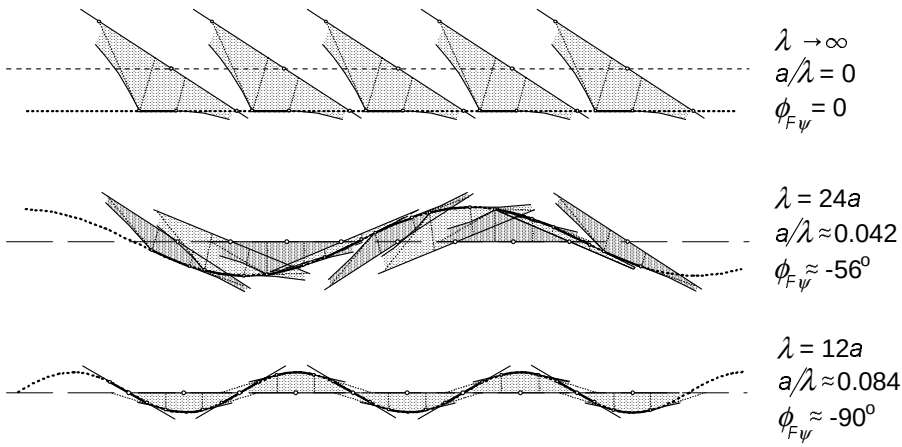

Fig. 5.13. The string model at steady-state side slip and subjected to yaw oscillations with two different wavelengths λ.

of the sinusoidal motion of the wheel. Figure 5.13 illustrates the manner in which the string deflection varies with travelled distance when the model is subjected to a yaw oscillation with different wavelengths.

The frequency response functions such as $H_{F,\psi}(i\omega_s)$ are the complex ratios of output, e.g. F_y, and input, e.g. ψ. In Figs.5.14,15 the various frequency response functions have been plotted as a function of the non-dimensional path frequency $a/\lambda = \frac{1}{2}\omega_s a/\pi$. The functions are represented by their absolute value $|H|$ and the phase angle ϕ of the output with respect to the input (if negative then output lags behind input), e.g.

$$H_{F,\psi} = |H_{F,\psi}|\, e^{i\phi_{F\psi}} = \frac{|F_y|}{|\psi|} e^{i\phi_{F\psi}} \tag{5.69}$$

If the variables are considered as real quantities one gets: $\alpha = |\alpha| \cos(\omega_s s)$ and for its response: $F_y = |F_y| \cos(\omega_s s + \phi)$. In the figure the absolute values have been made non-dimensional by showing the ratio to their values at $\omega_s = 0$, the steady-state condition. Three different ways of presentation have been used, each with its own advantage.

The force response to slip angle very much resembles a first-order system behaviour, as can be seen in the upper graph with a log-log scale. The cut-off frequency that is found by considering the steady-state response and the asymptotic behaviour at large path frequencies, appears to be equal to

$$\omega_{s,F\alpha,co} = \frac{1}{\sigma + a} \tag{5.70}$$

However, the phase lag at frequencies tending to zero is not equal to $\omega_s(\sigma + a)$, as one would expect for a first-order system, but somewhat smaller. Analysis reveals that the phase lag tends to:

$$-\phi_{F,\alpha} \rightarrow \sigma_{F\alpha}\omega_s \qquad \text{for } \omega_s \rightarrow 0 \tag{5.71}$$

with the relaxation length for the side force with respect to the slip angle

$$\sigma_{F\alpha} = \sigma + a - t \tag{5.72}$$

which with (5.55) becomes equal to $3.23a$ if $\sigma = 3a$. The phase lag does approach 90° for frequencies going to infinity. The first-order approximation with the same cut-off frequency has been added in the graph for comparison. The corresponding frequency response function reads:

$$H_{F,\alpha 1} = \frac{C_{F\alpha}}{1 + i\omega_s(\sigma + a)} \tag{5.73}$$

The frequency response of the force to yaw shows a wavy curve for the amplitude at higher frequencies (at wavelengths smaller than ca. two times the contact length). The decline of the peaks occurs according to the same asymptote

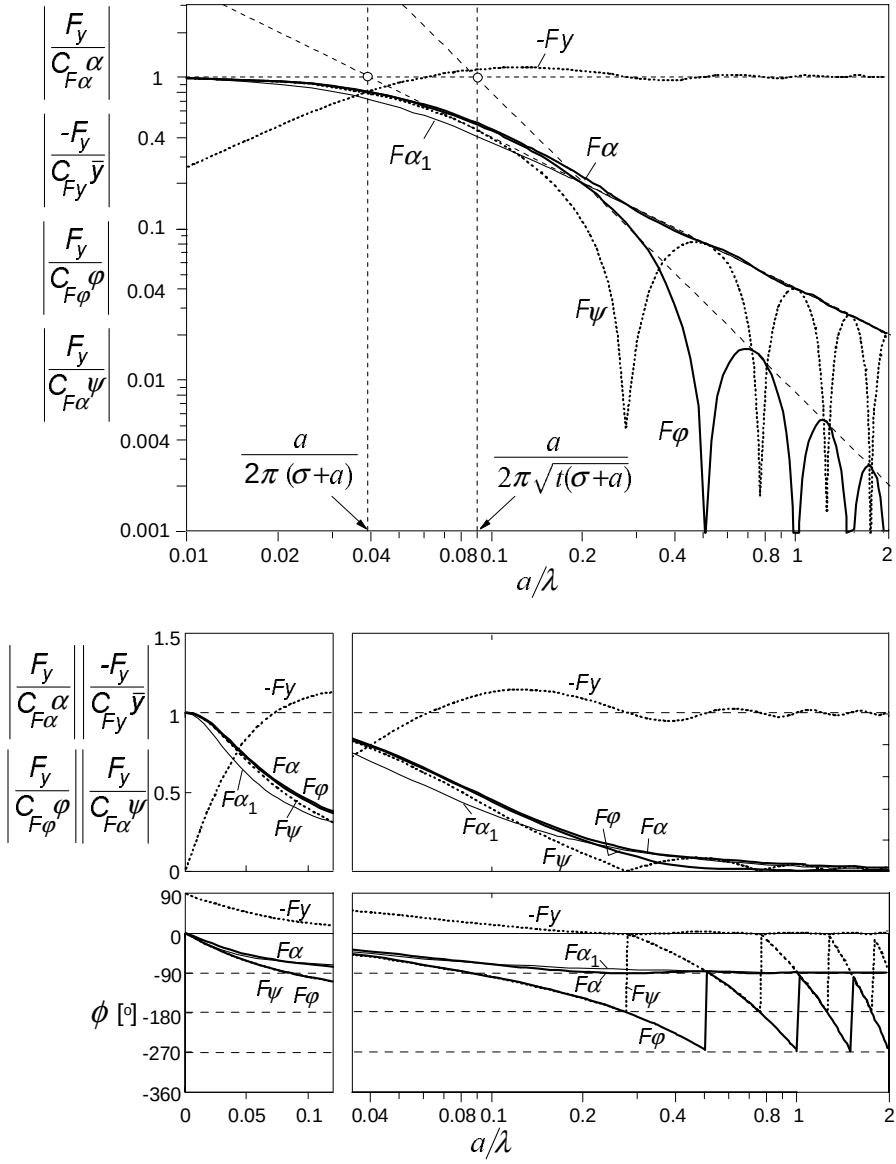

Fig. 5.14. String model frequency response functions for the side force with respect to various motion input variables. The non-dimensional path frequency is half the contact length divided by the wavelength of the motion: $a/\lambda = \omega_s/2\pi$. For the response to α a first-order approximation with the same cut-off frequency, $\omega_s = 1/(\sigma + a)$, has been added ($F\alpha_1$). Three ways of presentation have been used: log-log, lin-log and lin-lin. The model parameter $\sigma = 3a$, which leads to $t = 0.77a$.

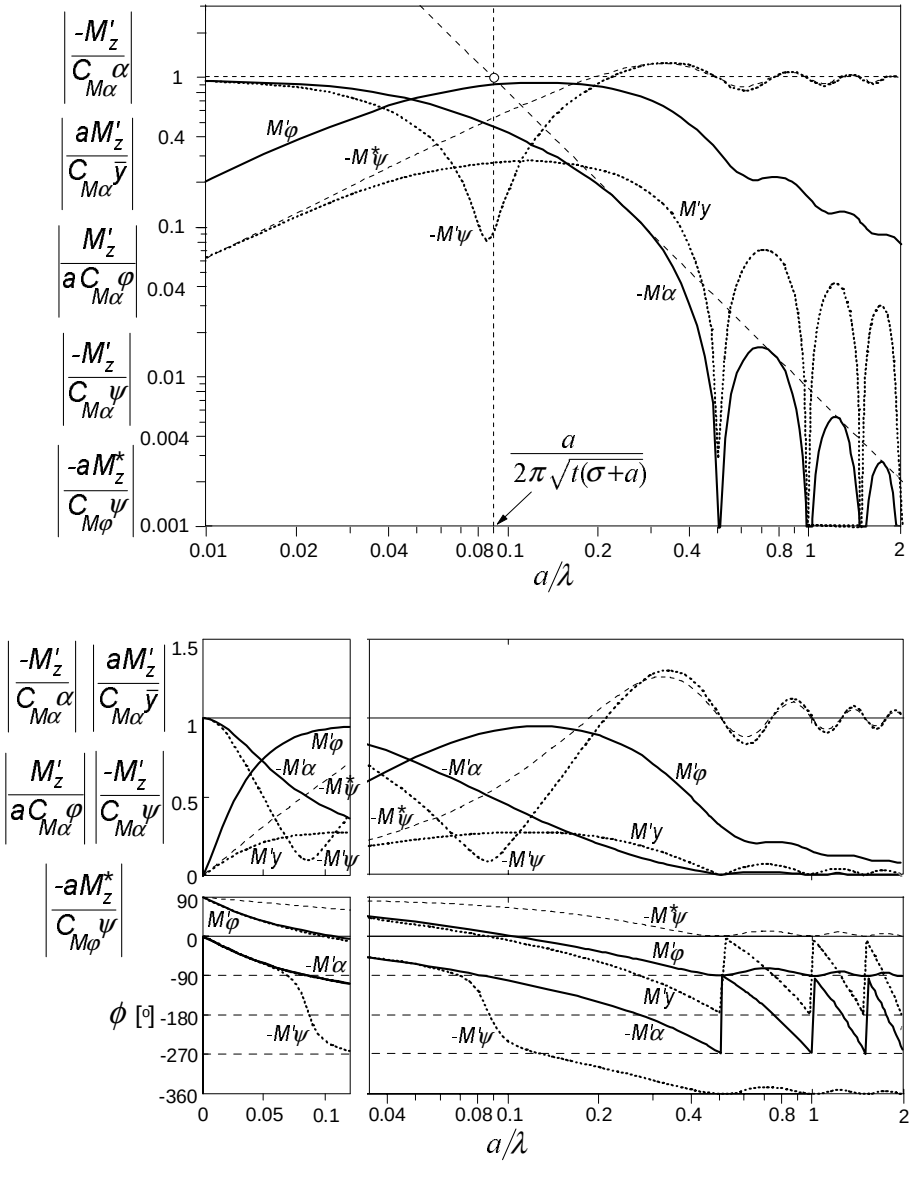

Fig. 5.15. String model frequency response functions for the aligning torque with respect to various motion input variables. Same conditions as in Fig.5.14. The response functions of the moment due to tread width M_z^* have been added.

as found for the slip angle response. Consequently, the same cut-off frequency applies.

$$\omega_{s,F\psi,co} = \frac{1}{\sigma + a} \tag{5.74}$$

When analysing the behaviour at small frequencies it appears that here the phase lag does tend to:

$$-\phi_{F,\psi} \rightarrow \sigma_{F\psi}\omega_s \qquad \text{for } \omega_s \rightarrow 0 \tag{5.75}$$

with the relaxation length for the side force with respect to the yaw angle:

$$\sigma_{F\psi} = \sigma + a \tag{5.76}$$

Further analysis reveals that when developing the frequency response function $H_{F,\psi}$ in a series up to the second degree in $i\omega_s$:

$$\begin{aligned} H_{F,\psi}(i\omega_s) &= C_{F\alpha}\{1 - \sigma_{F\psi}\, i\omega_s(1 - b_{F2}\, i\omega_s)\} + \ldots \\ &= C_{F\alpha}(1 - \sigma_{F\psi} b_{F2}\omega_s^2 - \sigma_{F\psi} i\omega_s) + \ldots \end{aligned} \tag{5.77}$$

and subsequently employing the fundamental relationship (5.42) between α and φ responses, the frequency response function $H_{F,\alpha}$ up to the first degree in $i\omega_s$ becomes:

$$H_{F,\alpha}(i\omega_s) = C_{F\alpha}(1 - \sigma_{F\alpha}\, i\omega_s) + \ldots = C_{F\alpha}(1 - b_{F2}\, i\omega_s) + \ldots \tag{5.78}$$

which shows that

$$\sigma_{F\alpha} = b_{F2} \tag{5.79}$$

which is an important result in view of assessing $\sigma_{F\alpha}$ from yaw oscillation measurement data and checking the correspondence with (5.72).

The aligning torque ($-M_z'$, Fig.5.15) shows a response to the slip angle which is closer to a second-order system with a phase lag tending to a variation around 180° and a 2:1 asymptotic slope of the amplitude with a cut-off frequency equal to:

$$\omega_{s,M\alpha,co} = \frac{1}{\sqrt{t(\sigma + a)}} \tag{5.80}$$

where t denotes the pneumatic trail, cf. (5.55). Again, the response of F_y to φ turns out to be the same as the response of $-M_z'$ to α. As the graph of Fig.5.15 shows, the amplitude of M_z' as a response to yaw oscillations ψ exhibits a clear dip at (with parameter $\sigma = 3a$) a wavelength $\lambda = \sim 12a$. This condition corresponds to the situation depicted in Fig.5.13 (third case) and is referred to as the meandering phenomenon or as kinematic shimmy which occurs in practice when the wheel is allowed to swivel freely about the vertical axis through the wheel centre and the system is slowly moved forwards. The nearly symmetric string

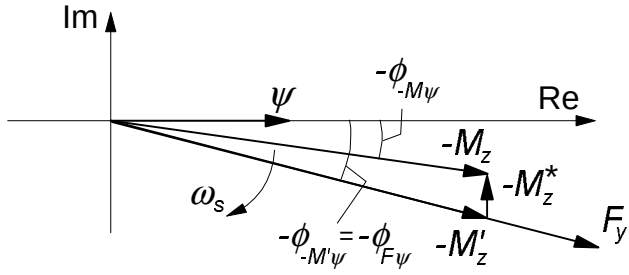

Fig.5.16. Complex representation of side force and moment response to yaw oscillations ψ.

deformation explains why the amplitude of the aligning torque almost vanishes at this wavelength. At higher frequencies the amplitude remains finite and approaches at $\omega_s \to \infty$ the same value as it had at $\omega_s = 0$ that is: $-M_z' = C_{M\alpha}\psi = C_{M'\psi}\psi$. The phase angle approaches -360°. It is interesting that analysis at frequencies approaching zero shows that the phase lag both for the response of $-M_z'$ to α and to ψ (and thus also for F_y to φ) approach the value $\omega_s(\sigma+a)$ that also appeared to be true for the response of F_y to ψ. So we have:

$$\sigma_{M'\psi} = \sigma_{M\alpha} = \sigma_{F\varphi} = \sigma_{F\psi} = \sigma + a \tag{5.81}$$

Expressions equivalent to (5.70,72,74,79,80,81) appear to hold for the enhanced model with tread elements attached to the string, cf. Section 5.4.3.

The torque due to tread width $-M_z^*$ shows a response to yaw angle ψ that increases in amplitude with path frequency and starts out with a phase lead of 90° with respect to ψ. At low frequencies the moment acts like the torque of a viscous rotary damper with damping rate inversely proportional with the speed of travel V. We find with Eq.(5.67):

$$M_z^* = -\frac{1}{V}\kappa^*\dot{\psi} \qquad \text{for } \omega_s \to 0 \tag{5.82}$$

At high frequencies $\omega_s \to \infty$, that is at vanishing wavelength $\lambda \to 0$ where the tyre is standing still, the tyre acts like a torsional spring and the moment $-M_z^*$ approaches $C_{M^*\psi}\psi = C_{M\varphi}/a$, cf. (5.68). The cut-off frequency appears to become:

$$\omega_{s,M^*\varphi,co} = \frac{1}{a} \tag{5.83}$$

The total moment about the vertical axis is obtained by adding the components due to lateral and longitudinal deformations:

$$M_z = M_z' + M_z^* \tag{5.84}$$

For the standing tyre one finds from a yaw test the total torsional stiffness $C_{M\psi}$ which relates to the aligning stiffness and the stiffness due to tread width as follows:

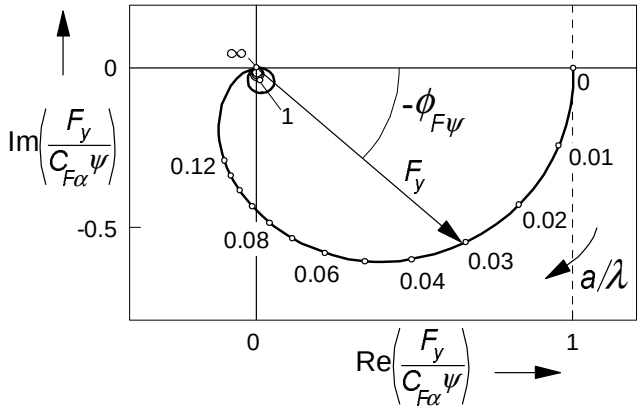

Fig.5.17. Nyquist plot of the non-dimensional frequency response function of the side force F_y with respect to the wheel yaw angle ψ. Parameter: $\sigma = 3a$.

$$C_{M\psi} = \frac{1}{a} C_{M\varphi} + C_{M\alpha} \tag{5.85}$$

Obviously, this relationship offers a possibility to assess the turn slip stiffness for the moment $C_{M\varphi}$.

Due to the action of M_z^* the phase lag of $-M_z$ will be reduced. This appears to be important for the stabilisation of wheel shimmy oscillations (cf. Chapter 6). The total moment and its components can best be presented in a Nyquist plot where the moment components and the resulting total moment appear as vectors in a polar diagram. Figure 5.16 depicts the vector diagram at a low value of the path frequency ω_s.

By considering the various phase angles at low frequencies we may be able to extract the moment response due to tread width from the total (measured) response and find the response of the moment for a 'thin' tyre. Since at low frequencies the moment vector $-M_z^*$ tends to point upwards we find while considering (5.75,81) and (5.82):

$$|M_z^*| = |M_z|(\sigma_{F\psi}\omega_s + \phi_{-M\psi}) = \kappa^*\omega_s|\psi| \tag{5.86}$$

With known $\sigma_{F\psi}$ and $\phi_{-M\psi}$ to be determined from the measurement at low frequency, the moment turn slip stiffness $C_{M\varphi} = \kappa^*$ may be assessed in this way.

In the diagrams of Figs.5.17,18 the non-dimensional frequency response functions $H_{F,\psi}(i\omega_s)/C_{F\alpha}$ and $-H_{M,\psi}(i\omega_s)/C_{M\alpha}$ with its components $-H_{M,\psi}(i\omega_s)/C_{M\alpha}$ and $-H_{M^*,\psi}(i\omega_s)/C_{M\alpha}$ have been presented as a function of the non-dimensional path frequency a/λ. The parameter values are $\sigma = 3a$ and $C_{M\varphi} = aC_{M\alpha}$.

The diagram of Fig.5.17 clearly shows the increase in phase lag and decrease of the amplitude of F_y with decreasing wavelength λ. The wavy behaviour and

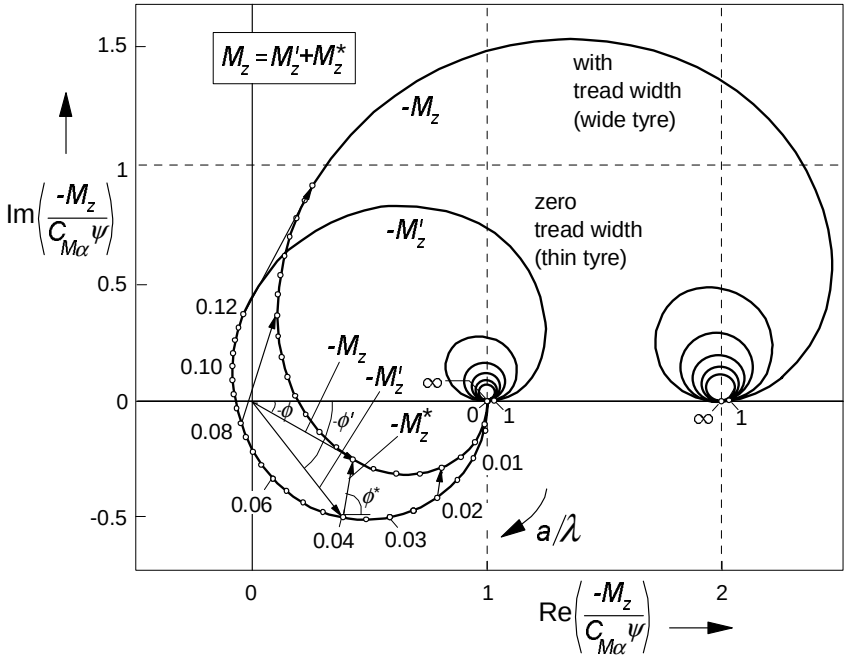

Fig.5.18. Nyquist plot of the non-dimensional frequency response function of the aligning moment M_z with respect to the wheel yaw angle ψ. The contributing components M_z' due to lateral deformations and M_z^* due to tread width and associated longitudinal deformations. Parameters: $\sigma = 3a$ and $C_{M\varphi} = aC_{M\alpha}$.

the associated jumps from 180° to 0 of the phase angle displayed in Fig.5.14 become clear when viewing the loops that appear to occur when the wavelength becomes smaller than about two times the contact length.

The aligning torque vector, Fig.5.18, for the 'thin' tyre turns over 360° before from a wavelength of about the contact length the loops begin to show up. At about $\lambda = 12a$ the curve gets closest to the origin. This corresponds to the frequency where the dip occurs in Fig.5.15 and is illustrated as the last case of Fig.5.13.

For values of κ^* sufficiently large the total moment curve does not circle around the origin anymore. The curve stretches more to the right and ends where the wheel does not roll anymore and the tyre acts as a torsional spring with stiffness expressed by (5.85). In reality, the tyre will exhibit some damping due to hysterisis. That will result in an end point located somewhat above the horizontal axis.

The calculated behaviour of the linear tyre model has unmistakeable points of agreement with results found experimentally at low values of the yaw frequency. At higher frequencies and higher speeds of rolling the influence of the

tyre inertia and especially the gyroscopic couple due to tyre lateral deformation rates is no longer negligible. In Section 5.5 and Chapter 9 these matters will be addressed.

Exercise 5.1. String model at steady turn slip

Consider the single stretched string tyre model running along a circular path with radius R anti-clockwise ($\varphi = 1/R$) and without side slip ($\alpha = 0$) as depicted in Fig.5.19.

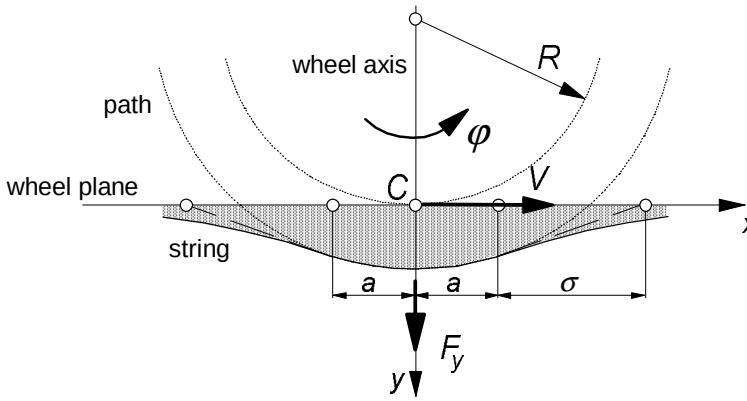

Fig. 5.19. The string tyre model in steady turning state.

Derive the expression for the lateral force F_y acting upon the model under these steady-state circumstances. First find the expression for the lateral deflection $v(x)$ using Eq.(2.61) which leads to a quadratic approximation of the contact line. Then use Eq.(5.25) for the calculation of the side force.

Now consider in addition some side slip and determine the value of α required to neutralize the side force generated by the path curvature $1/R$. Make a sketch of the resulting string deformation and wheel-plane orientation with respect to the circular path for the following values of radius and relaxation length: $R = 6a$ and $\sigma = 2a$.

5.4. Approximations and Other Models

In the present section, approximations to the exact theory will be treated to make the theory more accessible to applications. Subsection 5.4.2 discusses a number of other models known in the literature. After that in Subsection 5.4.3 a more complex model showing tread elements flexible also in the lateral direction will be treated to provide a reference model that is closer in performance to the real tyre.

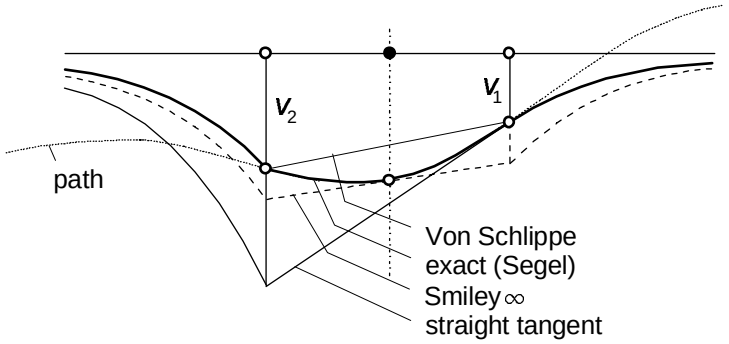

Fig. 5.20. Several approximative shapes of the contact line of the string model.

5.4.1. Approximate Models

In the literature, several simpler models have been proposed. Not all of these are based on the string model but many do. Figure 5.20 depicts a number of approximated contact lines as proposed by several authors. The most well known and accurate approximation is that of Von Schlippe (1941) who approximated the contact line by forming a straight connection between the leading and trailing edges of the exact contact line. Kluiters (1969) gave a further approximation by introducing a Padé filter to approximately determine the location of the trailing edge. Smiley (1957) proposes an alternative approximation by considering a straight contact line that touches the exact contact line in its centre in a more or less approximate way. Pacejka (1966) considered a linear or quadratic approximation of the contact line touching the exact one at the leading edge; the first and simplest approximation is referred to as the straight tangent approximation. A further simplification, completely disregarding the influence of the length of the contact line, results in the first-order approximation referred to as the point contact approximation.

In the sequal we will discuss Von Schlippe's and Smiley's second-order approximation as well as the straight tangent and point contact approximations. The performance of these models will be shown in comparison with the exact 'bare' string model and with the enhanced model with laterally compliant tread elements. Figures 5.21-27 gives the results in terms of step response, frequency response Bode plots and Nyquist diagrams.

For some of the other approximate models (Rogers 1972, Kluiters 1969, Keldysh 1945 and Moreland 1954) only the governing equations will be provided with some comments on their behaviour. For more information we refer to the original publications or to the extensive comparitive study of Besselink (2000).

The simplest models: straight tangent and point contact, can easily be extended into the non-linear regime. In Chapter 6 this will be demonstrated for the straight tangent model in connection with the non-linear analysis of the shimmy phenomenon. In Chapter 7 the non-linear single point contact model will be fully exploited. These models only show an acceptable accuracy for wheel oscillations at wavelengths which are relatively large with respect to the contact length. Chapter 9 is especially devoted to the development of a model that can operate at smaller wavelengths and non-linear (combined slip) conditions which requires the inclusion of the effect of the length of the contact zone.

Von Schlippe's straight connection model

This model which shows results that can hardly be distinguished from the exact ones, only requires the string deflections at the leading and trailing edges v_1 and v_2. We find for the Laplace transforms of these deflections as derived from the expressions (5.22,23) in vectorial form:

$$\boldsymbol{H}_{v1,(\alpha,\varphi,\psi)}(p) = \frac{\sigma}{1+\sigma p}(1, a, 1-ap) \tag{5.87}$$

$$\boldsymbol{H}_{v2,(\alpha,\varphi,\psi)}(p) = -\frac{1}{p}\frac{e^{-2ap}}{1+\sigma p}\left(1, \sigma+a+\frac{1}{p}, -(\sigma+a)p\right) + \frac{1}{p}\left(1, -a+\frac{1}{p}, ap\right) \tag{5.88}$$

where the exponential function refers to the retardation effect over a distance equal to the contact length. The transfer functions to the alternative set of input variables (v, ψ) may be obtained by using the conversion formulae (5.36,37).

The responses to a step change in slip angle become, cf. (5.45,46):

$$v_1(s) = \Gamma_{v1,\alpha}\alpha_o = \sigma\left(1 - e^{-s/\sigma}\right)\alpha_o \tag{5.89}$$

$$v_2(s) = \Gamma_{v2,\alpha}\alpha_o = s\,\alpha_o \qquad \text{if} \quad s \le 2a \tag{5.90}$$

$$v_2(s) = \Gamma_{v2,\alpha}\alpha_o = \left[2a + \sigma\left\{1 - e^{-(s-2a)/\sigma}\right\}\right]\alpha_o \qquad \text{if} \quad s > 2a \tag{5.91}$$

responses to step changes of other input variables may be determined by using the conversion formulae (5.56-58).

The side force and the aligning torque are obtained as follows:

$$F_y = c_c(\sigma+a)(v_1+v_2) = \tfrac{1}{2}C_{F\alpha}\frac{v_1+v_2}{\sigma+a} \tag{5.92}$$

$$M_z' = c_c\left\{\sigma(\sigma+a)+\tfrac{1}{3}a^2\right\}(v_1-v_2) = \tfrac{1}{2}C_{M\alpha}\frac{v_1-v_2}{a} \tag{5.93}$$

The first equation shows that the force is obtained by multiplying the average

lateral deflection with the lateral stiffness, cf. (5.59) with (5.60), and the moment by multiplying the slope of the connection line with the torsional stiffness of the 'thin' tyre (5.62) or (5.61). It may be noted that due to the adopted straight contact line, the turn slip stiffness for the force becomes slightly less than the exact one (5.63):

$$C_{F\varphi} = 2c_c a\sigma(\sigma + a) \tag{5.94}$$

The various diagrams show that only in some particular cases a (small) difference between 'exact' and 'Von Schlippe' can be observed. The model can be easily used in vehicle simulation studies by remembering the $(\bar{x},\bar{y})$ coordinates of the leading edge with respect to the global axis system (cf. Fig.5.3) and use these coordinates again after the wheel is rolled a distance $2a$ further when the trailing edge has assumed this location.

Smiley's and Roger's approximations

Assuming in Fig.5.3 that the wheel moves along the $\bar{x}$ axis with only small deviations in the lateral direction and in yaw, the lateral coordinate $\bar{y}_1$ of the leading edge follows from Eq.(5.24). After realising that

$$\bar{y}_1 = \bar{y} + a\psi + v_1 \tag{5.95}$$

the differential equation for $\bar{y}$ becomes:

$$\sigma \frac{\mathrm{d}\bar{y}_1}{\mathrm{d}s} + \bar{y}_1 = \bar{y} + (\sigma + a)\psi \tag{5.96}$$

The problem Smiley has addressed is the assessment of the location of the centre of the contact line. The lateral coordinate $\bar{y}_0$ of this point may be approximated by using a Taylor series. Starting out from the position of the centre contact point, the slope and the curvature etc. of the path of contact points, the relationship between the lateral coordinate of the foremost contact point and that of the centre point can be written as follows:

$$\bar{y}_1 = \bar{y}_0 + a\frac{\mathrm{d}\bar{y}_0}{\mathrm{d}s} + \frac{a^2}{2!}\frac{\mathrm{d}^2\bar{y}_0}{\mathrm{d}s^2} + \ldots. \tag{5.97}$$

Its derivative becomes:

$$\frac{\mathrm{d}\bar{y}_1}{\mathrm{d}s} = \frac{\mathrm{d}\bar{y}_0}{\mathrm{d}s} + a\frac{\mathrm{d}^2\bar{y}_0}{\mathrm{d}s^2} + \frac{a^2}{2!}\frac{\mathrm{d}^3\bar{y}_0}{\mathrm{d}s^3} + \ldots. \tag{5.98}$$

After substitution of these series in Eq.(5.96) the following generic formula is obtained:

$$\sum_{i=1}^{n} \frac{(n\sigma + a)\,a^{n-1}}{n!} \frac{\mathrm{d}^n \bar{y}_0}{\mathrm{d}\,s^n} + \bar{y}_0 = \bar{y} + (\sigma + a)\psi \tag{5.99}$$

The side force and the aligning torque can be found by multiplying the lateral deflection $v_0 = \bar{y}_0 - \bar{y}$ and the torsion angle $\beta = \mathrm{d}\bar{y}_0/\mathrm{d}s - \psi$ with the respective stiffnesses C_{Fy} and $C_{M'\psi}$, cf. Eqs.(5.59,62). We obtain:

$$F_y = C_{Fy}(\bar{y}_0 - \bar{y}) \tag{5.100}$$

$$M'_z = -C_{M'\psi}\left(\frac{\mathrm{d}\bar{y}_0}{\mathrm{d}\,s} - \psi\right) \tag{5.101}$$

Using the conversion formulae (5.36,37) the transfer functions with respect to α and φ can be obtained. For the order n of (5.99) equal to 2, the model becomes of the second order and one finds the following transfer functions in vector form:

$$\boldsymbol{H}_{F,(\alpha,\varphi,\psi)}(p) = C_{Fy} \frac{\left(a(\sigma + ½a)p + \sigma + a\,,\; a(\sigma + ½a)\,,\; \sigma + a\right)}{a(\sigma + ½a)p^2 + (\sigma + a)p + 1} \tag{5.102}$$

and

$$\boldsymbol{H}_{M',(\alpha,\varphi,\psi)}(p) = -C_{M'\psi} \frac{\left(1\,,\; -a(\sigma + ½a)p\,,\; a(\sigma + ½a)p^2 + 1\right)}{a(\sigma + ½a)p^2 + (\sigma + a)p + 1} \tag{5.103}$$

It may be noted that the side force turn slip stiffness for this approximate model is somewhat larger than according to the exact expression. We have for Smiley's model:

$$C_{F\varphi} = 2c_c a(\sigma + ½a)(\sigma + a) \tag{5.104}$$

The step responses of Fig.5.21 show reasonable to very good correspondence for the different inputs. Also the frequency response functions, shown in Fig.5.23, indicate that the accuracy of this relatively simple Smiley2 approximation is quite good. The dip in the M'_z response to ψ is well represented and is located at the 'meandering' path frequency (zero of (5.103)) $a\omega_s = 2\pi a/\lambda = \sqrt{\{a/(\sigma + ½a)\}}$. The approximation may be considered to be acceptable for wavelengths larger than about 4 times the contact length ($a/\lambda = 0.125$). In his publication, Smiley recommends to use the order $n = 3$.

The initial empirically assessed formulae of Rogers (1972) are almost the same as the functions (5.102,103); the terms ½a do not appear in his expressions but in the numerator of the moment response to turn slip (second element of 5.103) the empirically assessed term $-\varepsilon$ is added. Also a connection with Kluiters' approximation appears to exist.

Kluiters' approximation

Kluiters (1969) (cf. Besselink, 2000) adopted a Padé filter to approximate the position of the trailing edge. The transfer function of y_2 with respect to y_1 reads if the order of the filter is taken equal to 2:

$$\boldsymbol{H}_{y2,y1}(p) = \frac{\frac{1}{3}a^2p^2 - ap + 1}{\frac{1}{3}a^2p^2 + ap + 1} \tag{5.105}$$

With

$$\bar{y}_1 = \bar{y} + a\psi + v_1 \tag{5.106}$$

$$v_2 = \bar{y}_2 - \bar{y} + a\psi \tag{5.107}$$

we obtain with (5.87):

$$\boldsymbol{H}_{v2,(\alpha,\varphi,\psi)}(p) = -\frac{1}{p}\frac{\frac{1}{3}a^2p^2 - ap + 1}{(\sigma p+1)(\frac{1}{3}a^2p^2+ap+1)}\left(1, \sigma+a+\frac{1}{p}, -(\sigma+a)p\right) + \\ + \frac{1}{p}\left(1, -a+\frac{1}{p}, ap\right) \tag{5.108}$$

The deflection at the foremost point is, of course, governed by transfer function (5.87). The correspondence of this third-order model with Von Schlippe's model is very good for wavelengths larger than about 1.5 times the contact length The accuracy is better than even Smiley's third-order approach. It turns out that when a first-order Padé filter is used the formulae of Rogers without ε arise.

Straight tangent approximation

For this very simple approximation the contact line is solely governed by the deflection v_1 at the leading edge. The approximated shape of the deflected string corresponds to the steady-state deflection depicted in Fig.5.8 with deflection angle $\alpha' = v_1/\sigma$. The side force and aligning torque are found by multiplying the deflection angle with the cornering stiffness and the aligning stiffness respectively.

Using (5.87) we obtain for the transfer functions:

$$\boldsymbol{H}_{F,(\alpha,\varphi,\psi)}(p) = C_{F\alpha}\frac{1}{1+\sigma p}(1, a, 1-ap) \tag{5.109}$$

$$\boldsymbol{H}_{M',(\alpha,\varphi,\psi)}(p) = -C_{M\alpha}\frac{1}{1+\sigma p}(1, a, 1-ap) \tag{5.110}$$

The step responses equal the respective slip stiffnesses multiplied with the responses of v_1/σ according to (5.89). As expected, the accuracy becomes much less and from the frequency response functions we may conclude that acceptable

agreement is attained when the path frequency is limited to about $a/\lambda = 0.04$ or a wavelength larger than about 12 times the contact length. The response of the aligning torque to path curvature appears to be far off when compared with the exact responses. Since this particular response is the least important in realistic situations the straight tangent model may still be acceptable. In the analysis of the shimmy phenomenon this will be demonstrated to be true for speeds of travel which are not too low (where the wavelength becomes too short).

Figures 5.24,25 clearly show that at least up to $a/\lambda = 0.04$ the phase lag closely follows the exact variation with frequency. The amplitude, however, is too large, especially for the moment. A combination with a fictive M_z^* (first-order approximation, see further on) with properly chosen parameter $\kappa^* = C_{M\varphi}$ may help to reduce the amplitude of the moment to a more acceptable level also for non-dimensional path frequencies higher than 0.04. Figure 5.27 shows a considerable improvement if we would chose $C_{M\varphi} = 0.6C_{M\alpha}$.

Differential equation (5.125), to be shown later on, governs the straight tangent approximation. Because we have a deflection shape equal to that occurring at steady-state side slip motion the extension of the model to non-linear large slip conditions is easy to establish. We may employ the steady-state characteristics, e.g. Magic Formulae, and obtain:

$$F_y = F_y(\alpha') \ , \quad M_z = M_z(\alpha') \tag{5.111}$$

with the deflection angle

$$\alpha' = \frac{v_1}{\sigma} \tag{5.112}$$

The amplitude of the self-excited shimmy oscillation appears to become limited due to the non-linear, degressive, characteristics of the side force and the aligning torque versus slip angle.

Single point contact model

This simplest approximation disregards the influence of the length of the contact line. The lateral deflection at the contact centre at steady-state side slip should be taken equal to that of the exact model. This requires a model relaxation length σ_0 equal to the sum of the string deflection relaxation length σ and half the contact length a. The corresponding transfer function for the deflection v_0 become:

$$\boldsymbol{H}_{v0,(\alpha,\varphi,\psi)}(p) = \frac{\sigma_0}{1 + \sigma_0 p}(1, 0, 1) \tag{5.113}$$

with

$$\sigma_0 = \sigma + a \tag{5.114}$$

Apparently, the response to turn slip vanishes. A deflection angle may still be defined: $\alpha' = v_0/\sigma_0$. As a result, response functions for the force and the moment are obtained:

$$\boldsymbol{H}_{F,(\alpha,\varphi,\psi)}(p) = C_{F\alpha}\frac{1}{1+\sigma_0 p}(1,0,1) \tag{5.115}$$

$$\boldsymbol{H}_{M',(\alpha,\varphi,\psi)}(p) = -C_{M\alpha}\frac{1}{1+\sigma_0 p}(1,0,1) \tag{5.116}$$

This function corresponds to the frequency response function (5.73) that holds for a first-order system with the same cut-off frequency as the one for the exact model. With relaxation length $\sigma_0 = \sigma + a$ the model produces a correct phase lag for the response to yaw oscillations at large wavelengths as was already assessed before, cf. (5.81). Except for the moment response to yaw, the amplitudes appear to become somewhat too small in the probably acceptable wavelength range $\lambda >$ ca. $24a$. In the Nyquist plot of Fig.5.25 the curve for the moment response coincides with that of Smiley's approximation (not the frequency marks!). The response of the side force to turn slip may be artificially introduced by putting an 'a' instead of the '0' in the input vector of (5.115). This would, however, require an additional first-order differential equation for the side force.

Differential equation (5.130) governs the single point contact model.

Approximations of tread width moment response

The transfer function (5.32) for M_z^* may be simplified by following the approach of Von Schlippe but now for the longitudinal deflections, that is: by assuming a linear interpolation of the longitudinal deflection u between the exact deflections at the leading and trailing edges. As the deflection at the first point is equal to zero, the linear interpolation would lead to an average deflection equal to half the deflection at the rear most point u_2. The corresponding transfer function becomes:

$$\boldsymbol{H}_{M^*,(\alpha,\varphi,\psi)}(p) = \frac{\kappa^*}{2ap}\left(1 - e^{-2pa}\right)(0,1,-p) \tag{5.117}$$

Figures (5.22,26) show the performance of this linear interpolation model together with the exact response and other approximated model responses. The approach may be used in connection with the Von Schlippe lateral deflection approximation where the location of the contact point at the leading edge is remembered over a distance rolled equal to the contact length when this information is used to calculate the deflection at the rear edge.

Expansion of the exact response function (5.32) in a series of powers of p yields when limiting to the second power (for the response to ψ):

$$\boldsymbol{H}_{M^*_z(\alpha,\varphi,\psi)}(p) = \kappa^* \left(1 - \tfrac{2}{3}ap\right)(0, 1, -p) \tag{5.118}$$

where $\kappa^* = C_{M\varphi}$. The first-order (only first term in 5.118) and the second-order (both terms) approximations show responses as presented in the figures. The first-order response has been indicated in combination with the straight tangent response for M'_z in Fig.5.27. The vectors for $-M^*_z$ point upwards (vertically). The case of $C_{M\varphi} = 0.6\, aC_{M\alpha}$ generates a response which improves on the straight tangent bare string response. Especially compared with the enhanced model provided with tread elements the agreement is satisfactory. To model the foot print, Chapter 9 uses a first-order differential equation with the relaxation length equal to a. This corresponds to the cut-off frequency of the exact model (5.83).

Differential equations

From the various approximate transfer functions the governing differential equations can be easily established by replacing the Laplace variable p with the differentiation operator $\mathrm{d}/\mathrm{d}s$. This is not the case with the exact and the Von Schlippe transfer functions since these are of infinite order. We may expand these functions in series of powers of p and truncate at a certain power, after which p is replaced by $\mathrm{d}/\mathrm{d}s$. Truncation after the first degree of the series expansion of the exact functions (5.30,31,32) yields the differential equations written in terms of input variables α and φ (t denoting the pneumatic trail):

$$\sigma\frac{\mathrm{d}F_y}{\mathrm{d}s} + F_y = C_{F\alpha}\alpha + C_{F\varphi}\varphi - C_{F\alpha}(a-t)\frac{\mathrm{d}\alpha}{\mathrm{d}s} - C_{F\varphi}a\frac{\mathrm{d}\varphi}{\mathrm{d}s} + \cdots \tag{5.119}$$

$$\begin{aligned}\sigma\frac{\mathrm{d}M'_z}{\mathrm{d}s} + M'_z = {} & -C_{M\alpha}\alpha + aC_{M\alpha}\frac{\mathrm{d}\alpha}{\mathrm{d}s} + \\ & + a\left\{\left(\sigma + \tfrac{1}{3}a\right)C_{M\alpha} + \tfrac{1}{15}a\left(C_{M\alpha} - a\sigma C_{Fy}\right)\right\}\frac{\mathrm{d}\varphi}{\mathrm{d}s} + \cdots\end{aligned} \tag{5.120}$$

with coefficients according to (5.55,59-63). When using the conversion formulae (5.34,35), equations in terms of input variables $\bar{y}$ and ψ are obtained:

$$\sigma\frac{\mathrm{d}F_y}{\mathrm{d}s} + F_y = C_{F\alpha}\left(\psi - \frac{\mathrm{d}\bar{y}}{\mathrm{d}s} - a\frac{\mathrm{d}\psi}{\mathrm{d}s} + (a-t)\frac{\mathrm{d}^2\bar{y}}{\mathrm{d}s^2}\right) + \cdots \tag{5.121}$$

$$\sigma\frac{\mathrm{d}M'_z}{\mathrm{d}s} + M'_z = -C_{M\alpha}\left(\psi - \frac{\mathrm{d}\bar{y}}{\mathrm{d}s} - a\frac{\mathrm{d}\psi}{\mathrm{d}s} + a\frac{\mathrm{d}^2\bar{y}}{\mathrm{d}s^2}\right) + \cdots \tag{5.122}$$

From Eq.(5.118) we, finally, obtain the differential equations for M^*_z:

$$M_z^* = C_{M\varphi}\left(\varphi - \tfrac{2}{3}a\frac{\mathrm{d}\varphi}{\mathrm{d}s}\right) + \cdots \tag{5.123}$$

or in terms of the yaw angle:

$$M_z^* = -C_{M\varphi}\left(\frac{\mathrm{d}\psi}{\mathrm{d}s} - \tfrac{2}{3}a\frac{\mathrm{d}^2\psi}{\mathrm{d}s^2}\right) + \cdots \tag{5.124}$$

The straight tangent approximation remains when the last term of the right-hand member of both Eqs.(5.121,122) is omitted. The same result is obtained when the single first-order differential equation (5.24) is used in combination with the deflection angle α' (5.112) and the cornering and aligning stiffnesses. We have the following set of equations for the straight tangent approximation:

$$\frac{\mathrm{d}v_1}{\mathrm{d}s} + \frac{1}{\sigma}v_1 = \psi - \frac{\mathrm{d}\bar{y}}{\mathrm{d}s} - a\frac{\mathrm{d}\psi}{\mathrm{d}s} \qquad (= \alpha + a\varphi) \tag{5.125}$$

$$\alpha' = \frac{v_1}{\sigma} \tag{5.126}$$

$$F_y = C_{F\alpha}\alpha' \ , \quad M_z = -C_{M\alpha}\alpha' \tag{5.127}$$

or in case of larger slip angles:

$$F_y = F_y(\alpha') \ , \quad M_z = M_z(\alpha') \tag{5.128}$$

The set may be used in combination with the first-order version of (5.24):

$$M_z^* = -C_{M\varphi}\frac{\mathrm{d}\psi}{\mathrm{d}s} \qquad (= C_{M\varphi}\varphi) \tag{5.129}$$

or in the non-linear case φ may be used as input in the steady-state model description extended with turn slip (cf. Section 4.3.3).

The single point contact model with transfer functions (5.115,116) is governed by the single first-order differential equation:

$$\frac{\mathrm{d}v_0}{\mathrm{d}s} + \frac{1}{\sigma_0}v_0 = \psi - \frac{\mathrm{d}\bar{y}}{\mathrm{d}s} \qquad (= \alpha) \tag{5.130}$$

with the relaxation length

$$\sigma_0 = \sigma + a = \frac{C_{F\alpha}}{C_{Fy}} \tag{5.131}$$

The 'transient' slip angle

$$\alpha' = \frac{v_0}{\sigma_0} \tag{5.132}$$

completes the description together with Eqs.(5.127 or 128).

By considering only terms up to the first degree in p of the (transformed) equations (5.119-122) the following individual first-order differential equations can be defined which hold exactly for $\lambda \to \infty$ ($p \to 0$), if use is made of the notation for the individual relaxation lengths (5.72) and (5.81):

$$\sigma_{F\alpha}\frac{\mathrm{d}F_y}{\mathrm{d}s} + F_y = C_{F\alpha}\alpha \tag{5.134}$$

$$\sigma_{M\alpha}\frac{\mathrm{d}M'_z}{\mathrm{d}s} + M'_z = -C_{M\alpha}\alpha \tag{5.135}$$

$$\sigma_{F\varphi}\frac{\mathrm{d}F_y}{\mathrm{d}s} + F_y = C_{F\varphi}\varphi \tag{5.136}$$

and in terms of the alternative set of inputs:

$$\sigma_{F\alpha}\frac{\mathrm{d}F_y}{\mathrm{d}s} + F_y = -C_{F\alpha}\frac{\mathrm{d}\bar{y}}{\mathrm{d}s} \tag{5.137}$$

$$\sigma_{M\alpha}\frac{\mathrm{d}M'_z}{\mathrm{d}s} + M'_z = C_{M\alpha}\frac{\mathrm{d}\bar{y}}{\mathrm{d}s} \tag{5.138}$$

$$\sigma_{F\psi}\frac{\mathrm{d}F_y}{\mathrm{d}s} + F_y = C_{F\alpha}\psi \tag{5.139}$$

$$\sigma_{M'\psi}\frac{\mathrm{d}M'_z}{\mathrm{d}s} + M'_z = -C_{M\alpha}\psi \tag{5.140}$$

where the respective individual relaxation lengths read (according to the exact bare string model):

$$\sigma_{F\alpha} = \sigma + a - t \tag{5.72}$$

$$\sigma_{M'\psi} = \sigma_{M\alpha} = \sigma_{F\varphi} = \sigma_{F\psi} = \sigma + a \tag{5.81}$$

If also the relaxation length for F_y with respect to α is taken equal to $\sigma_0 = \sigma + a$ the, with respect to turn slip improved, single contact point approximation arises.

Table 5.1 presents the values of the individual relaxation lengths as defined by Eqs.(5.71,75, etc.) and assessed numerically for the various models discussed above, with $\sigma = 3a$. For the corresponding enhanced model with tread elements we refer to Section 5.4.3. For all models $\sigma_{F\psi} = C_{F\alpha}/C_{Fy}$ has been kept the same.

In practical cases shimmy occurs at path frequencies below the meandering frequency, even below about half this value. This corresponds to a practical upper limit of $a/\lambda = 0.04$ or for the wavelength λ a lower limit of ca. 12.5 times the contact length ($25a$). It turns out that in this practical range the agreement between the various models is good or reasonable.

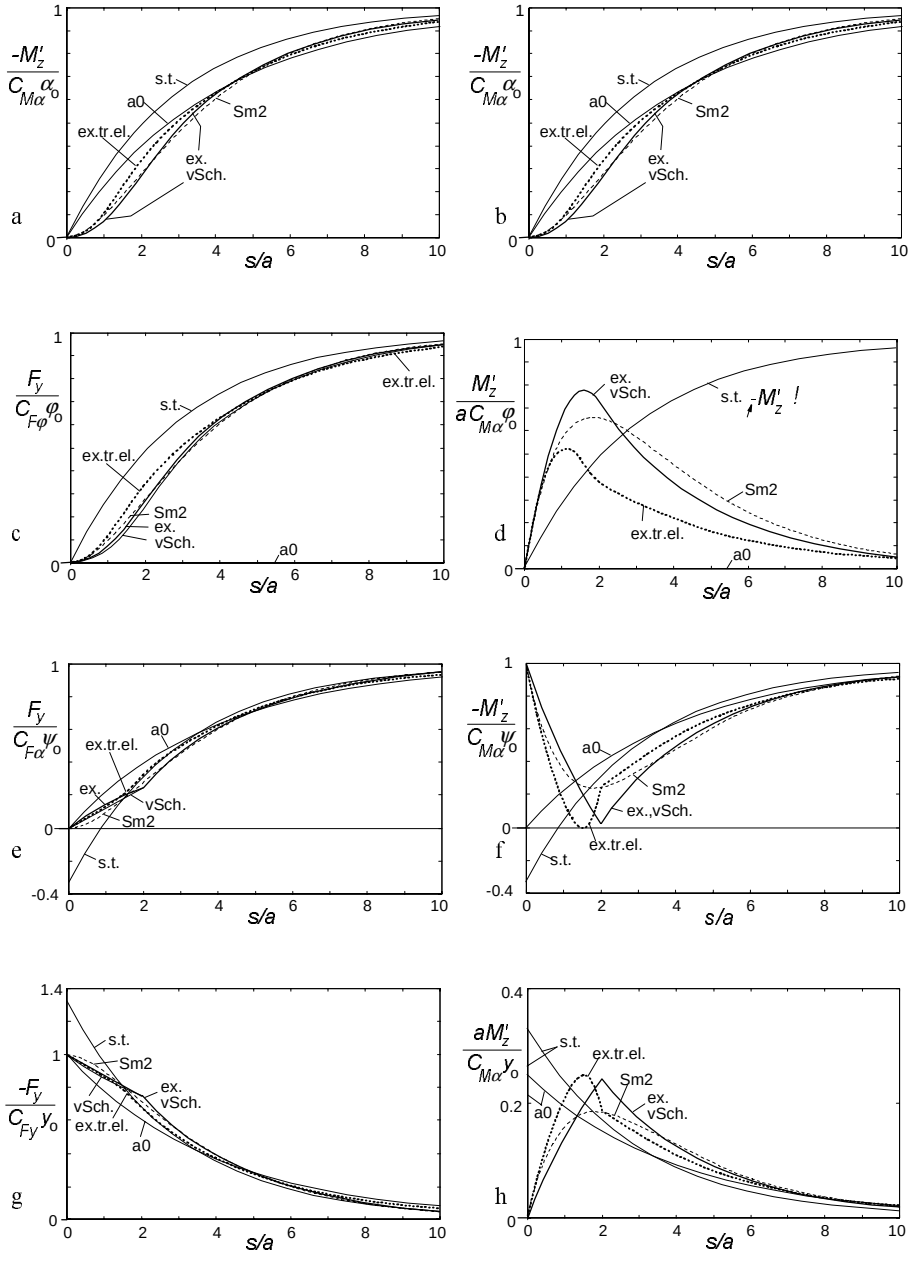

Fig. 5.21. Step responses of side force and aligning torque to several inputs for exact and approximate models:
ex.: exact 'bare' string model; vSch.: Von Schlippe; Sm2: Smiley second order; s.t.: straight tangent; a0: point contact; ex.tr.el.: exact with tread elements.

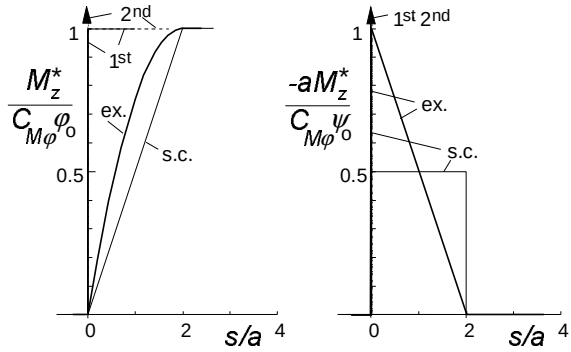

Fig. 5.22. Step response of the moment due to tread width to turn slip (path curvature) and yaw angle for exact and approximations:
ex.: exact (brush model); s.c.: straight connection (linear interpolation);
2nd : second-order approximation; 1st : first-order approximation.

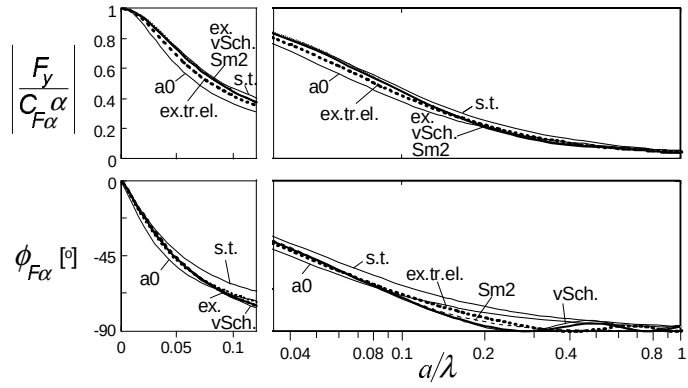

a

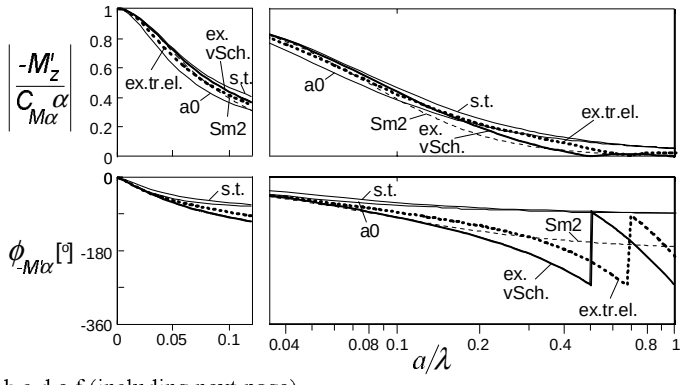

b

Fig. 5.23 a,b,c,d,e,f (including next page).
Frequency response functions of side force and aligning torque to several inputs for exact and approximate models:
ex.: exact 'bare' string model; vSch.: Von Schlippe; Sm2: Smiley second order; s.t.: straight tangent; a0: point contact; ex.tr.el.: exact with tread elements.

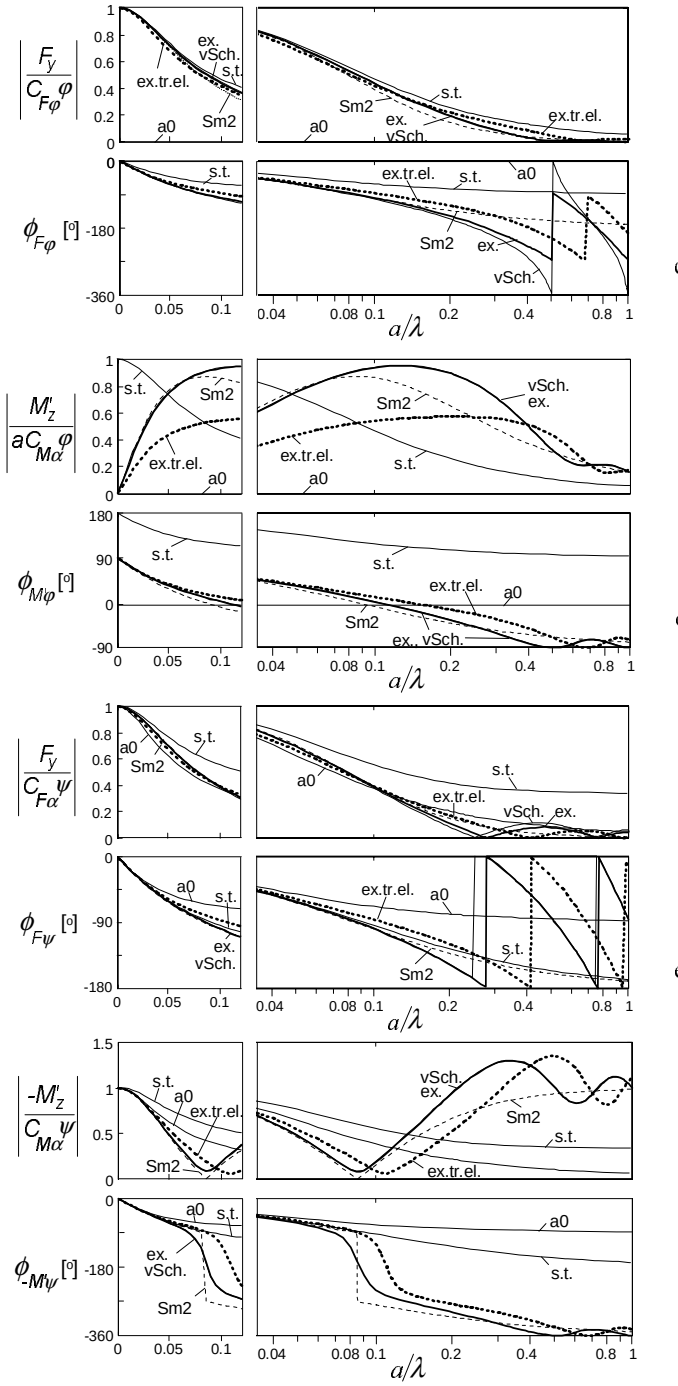
$\left|\frac{F_y}{C_{F\varphi}\varphi}\right|$
$\phi_{F\varphi}$ [°]
$\left|\frac{M'_z}{aC_{M\alpha}\varphi}\right|$
$\phi_{M\varphi}$ [°]
$\left|\frac{F_y}{C_{F\alpha}\psi}\right|$
$\phi_{F\psi}$ [°]
$\left|\frac{-M'_z}{C_{M\alpha}\psi}\right|$
$\phi_{-M'\psi}$ [°]
a/λ
ex.
vSch.
s.t.
ex.tr.el.
a0
Sm2
c
d
e
f

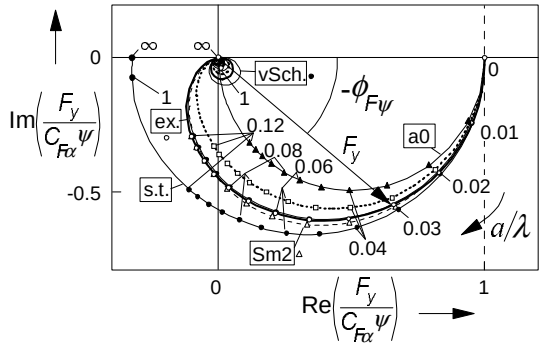

Fig.5.23 cont'd.

Fig.5.24. Nyquist plot of the frequency response function of the side force F_y with respect to the wheel yaw angle ψ. Parameter: $\sigma = 3a$.

ex.: exact 'bare' string model;
vSch.: Von Schlippe;
Sm2: Smiley second order;
s.t.: straight tangent;
a0: point contact;
ex.tr.el.: exact with tread elmnts.

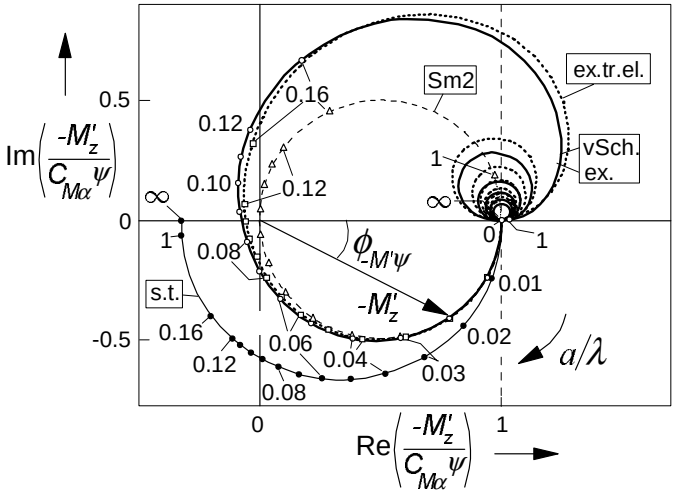

Fig.5.25. Nyquist plot of the frequency response function of the aligning torque $-M'_z$ with respect to the wheel yaw angle ψ. Curve a0 is hided by Sm2. Same conditions as in Fig.5.24.

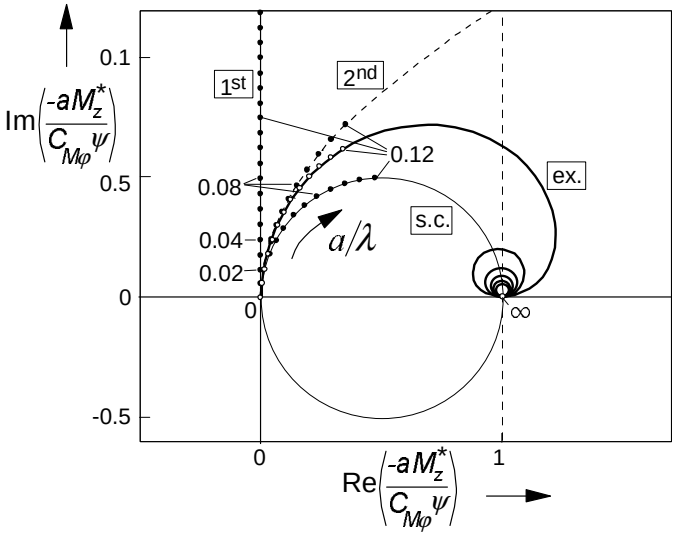

Fig.5.26. Nyquist plot of the frequency response function of the torque due to tread width $-M''_z$ with respect to the wheel yaw angle ψ.

ex.: exact (brush);
s.c.: straight connection (linear interpolation);
2nd : second-order app.;
1st : first-order approx.

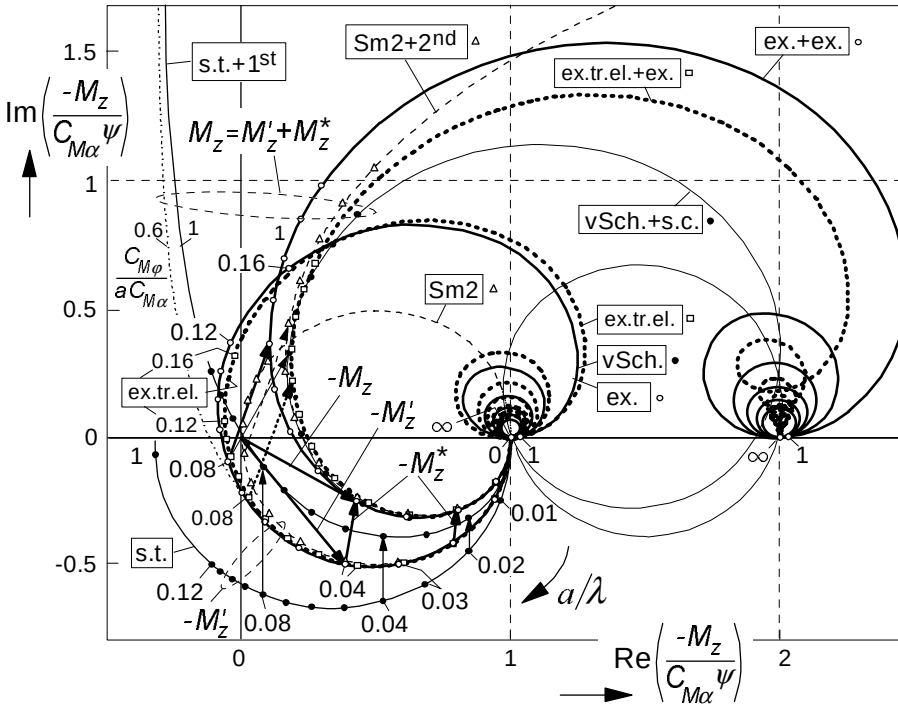

Fig.5.27. Nyquist plot of the non-dimensional frequency response function of the aligning moment M_z with respect to the wheel yaw angle ψ. Contributing components M_z' due to lateral deformations and M_z^* due to tread width and associated longitudinal deformations. Parameters: $\sigma = 3a$ and $C_{M\varphi} = aC_{M\alpha}$. Exact and approximate models: ex.: exact 'bare' string model; vSch.: Von Schlippe; Sm2: Smiley second order; s.t.: straight tangent; a0: point contact (hidden by Sm2); ex.tr.el.: exact w. tr.elmts. ex.: exact (brush); s.c.: straight connection (linear interpolation); 2nd : second-order approximation; 1st : first-order approx. (also $C_{M\varphi} = 0.6\,aC_{M\alpha}$).

Table 5.1. Individual relaxation lengths for the various models, defined for $\omega_s \to 0$.

	exact	vSchl.	Smiley2	str.tang.	$a=0$	ex.tr.el.
$\sigma_{F\alpha}/a$	3.23	3.25	3.12	3.00	4.00	3.51
$\sigma_{M\alpha}/a$	4.00	4.00	4.00	3.00	4.00	4.00
$\sigma_{F\varphi}/a$	4.00	4.11	4.00	3.00	--	4.00
$\sigma_{F\psi}/a$	4.00	4.00	4.00	4.00	4.00	4.00
$\sigma_{M'\psi}/a$	4.00	4.00	4.00	4.00	4.00	4.00

5.4.2. Other Models

Two more models will be briefly discussed. These are the models of Keldysh, cf. Goncharenko (1981) and Besselink (2000), and of Moreland (1954). The models are not based on the stretched string concept. They feature two degrees of freedom: the lateral deflection and the torsion deflection, and disregard the finite length of the contact zone. The single point or straight tangent approximations of the string model have a single degree of freedom where the lateral and the angular deflection at the leading edge are linked through an algebraic relationship. The additional degree of freedom of Keldysh's and Moreland's single point models with a non-holonomic constraint (first-order differential equation) raises the order of the description from one to two.

Keldysh's model

This model is known to be used in the Russian aircraft industry and was published in 1945. Goncharenko employed the model for his research in shimmy of landing gears. In addition to lateral and torsional stiffnesses, damping has been included between contact patch and rim. The side force and aligning torque become expressed in terms of lateral deflection v and torsion angle β:

$$F_y = k_y \dot{v} + c_y v \tag{5.141}$$

$$M_z = k_\psi \dot{\beta} + c_\psi \beta \tag{5.142}$$

With the assumption of full adhesion the following relation must hold regarding the direction of the path of the contact point of the rolling tyre:

$$\psi + \beta = \frac{\mathrm{d}(v + \bar{y})}{\mathrm{d}s} \tag{5.143}$$

Regarding the path curvature a linear equation is introduced:

$$\frac{\mathrm{d}(\psi + \beta)}{\mathrm{d}s} = -q_\alpha v - q_\beta \beta + q_\gamma \gamma \tag{5.144}$$

Interesting is that Keldysh did take into account the wheel camber angle γ as an additional input variable. The transfer functions with respect to α, φ, ψ and γ become:

$$\boldsymbol{H}_{F,(\alpha,\varphi,\psi,\gamma)}(p) = (c_y + k_y V p)\,\frac{\left(p + q_\beta\,,\ 1\,,\ q_\beta\,,\ q_\gamma\right)}{p^2 + q_\beta p + q_\alpha} \tag{5.145}$$

and

$$\boldsymbol{H}_{M,(\alpha,\varphi,\psi)}(p) = -(c_\psi + k_\psi V p)\,\frac{\left(q_\alpha,\ -p,\ p^2 + q_\alpha,\ -q_\gamma p\right)}{p^2 + q_\beta p + q_\alpha} \tag{5.146}$$

Surprisingly, it turns out that these transfer functions (except the one with respect to γ) correspond to the functions of Rogers (with ε=0) (Eqs.5.102,103 with ½a omitted) if, as Besselink indicated, the following equivalence conditions hold:

$$q_\alpha = \frac{1}{a\sigma}\ ,\quad q_\beta = \frac{a+\sigma}{a\sigma}\ ,\quad c_y = C_{Fy} = \frac{C_{F\alpha}}{a+\sigma}\ ,\quad c_\psi = C_{M'\psi} = C_{M\alpha} \tag{5.147}$$

Furthermore, comparison with the Von Schlippe approximation at steady state, shows that:

$$q_\beta = \frac{C_{F\alpha}}{C_{F\varphi}}\ ,\quad q_\gamma = \frac{C_{F\gamma}}{C_{F\varphi}} \tag{5.148}$$

where, as before, $C_{F\gamma}$ designates the camber force stiffness.

Moreland's model

This model, first published in 1954 in the paper "The story of shimmy", used to be a popular tool in the U.S. for the analysis of aircraft shimmy. The structure is similar to that of Keldysh's model. The differences are that: the damping coefficient k_ψ is omitted and more important: turn slip and camber are not considered and instead of equation (5.144) the following relation is used:

$$\frac{\mathrm{d}\beta}{\mathrm{d}t} = -\frac{1}{\tau}\left(\frac{F_y}{C_{F\alpha}} + \beta\right) \tag{5.149}$$

The transfer functions with respect to the slip angle that were established read:

$$\boldsymbol{H}_{F,\alpha}(p) = C_{F\alpha}\,\frac{k_y \tau V^2 p^2 + (k_y + c_y\tau)\,Vp + c_y}{C_{F\alpha}\tau V p^2 + (k_y V + C_{F\alpha})p + c_y} \tag{5.150}$$

$$\boldsymbol{H}_{M,\alpha}(p) = -C_{M\alpha}\,\frac{k_y V p + c_y}{C_{F\alpha}\tau V p^2 + (k_y V + C_{F\alpha})p + c_y} \tag{5.151}$$

The fact that we are dealing here with a *time* constant τ gave rise to criticism and caused difficulties in attempts to fit experimental data. To make the model pure path dependent τ should be made inversely proportional with speed V; this in addition to omitting the damping coefficient k_y. It may be observed that when

considering the relations (5.147) the substitution for τ

$$\tau = \frac{a\sigma}{(a+\sigma)V} \tag{5.152}$$

leads to a transfer functions with respect to α that is identical to the corresponding functions established by Keldysh and Rogers.

5.4.3. Enhanced String Model with Tread Elements

Although the string model with its simplicity and essential features served us well in gathering insight and establishing proper mathematical descriptions and useful approximations, the string model shows a behaviour that in several views differs considerably from the properties of the real tyre. The relaxation length σ for the tyre deflection does not change with vertical load, and thus the relaxation length for the side force to yaw $\sigma_{F\psi} = \sigma + a$ does not vary sufficiently and does not approach zero when $F_z \to 0$ as would occur with the real tyre. The same discrepancy holds for the cornering stiffness. The pneumatic trail of the string model is often too large. When considering larger values of slip, that is, when sliding is allowed to occur in the contact zone, the calculated steady-state characteristics for the bare string model do not appear adequate as they exhibit a kink at the slip angle where the force has reached its maximum and the moment becomes equal to zero where full sliding commences. Also, when at side slip the lateral force distribution along the contact line is analysed it appears that a discontinuity occurs at the point of transition from adhesion to sliding. This is caused by the fact that in the range of adhesion the contact line (that is: the string) is straight and the external frictional forces are equal to the internal elastic forces and remain relatively small. From the transition point onwards the string slides over the ground and the side forces are governed by the vertical force distribution and the friction coefficient. Here the contact line gets curved to let the string tension force S contribute to the transmission of the ground forces to the tyre. Finally, it can be easily assessed that the relaxation length of the bare string model does not change with increasing slip angle as is observed to occur in practice. These reasons lead to the desire to develop a model that shows a better behaviour and when too complex may serve as a reference for understanding and for the development of simpler models. In the sequel we will briefly discuss the development of the string model provided with elastic tread elements; for more information, cf. Pacejka (1966, 1981). The results concerning this model's transient and oscillatory out-of-plane behaviour have already been included in the various graphs of the preceding section.

Steady-state characteristics

Figure 5.28 depicts the structure of the model. The total deflection v is made up of the lateral deflection of the string (the carcass) v_c and the lateral deflection of the tread element v_p. Associated stiffnesses of carcass and tread elements are c_c and c_p both per unit length and the latter integrated over the tread width $2b$. The string effective tension force is S, cf. Section 5.3.1. The following model constants are introduced:

$$\sigma = \sqrt{\frac{S}{c_c}}\,, \quad \sigma_c = \sqrt{\frac{S}{c_c+c_p}}\,, \quad \varepsilon = \frac{\sigma_c}{\sigma} = \sqrt{\frac{c_c}{c_c+c_p}} \tag{5.153}$$

A parabolic vertical pressure distribution is assumed according to Eq.(3.4). At the trailing edge a sliding range starts to built up when side slip increases. Also at the leading edge sliding may occur when the tread element stiffness is relatively large. The bare string model does show a relatively short sliding range that grows and ultimately meets the rear sliding range at increasing side slip. We will assume that the tread element stiffness is sufficiently small to disregard front sliding.

The total deflection v at steady-state side slip in the range $x_t<x<a$ where the tips of the elements adhere to the ground, follows the differential equation (5.11) with $\varphi = 0$:

$$\frac{\mathrm{d}v}{\mathrm{d}s} = -\alpha \qquad \text{if} \quad x_t < x \le a \tag{5.154}$$

The deflection of the string outside the contact range is governed by the differential equation:

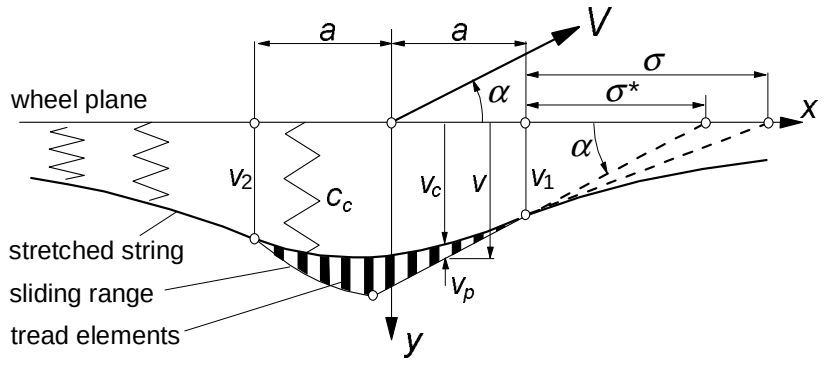

Fig. 5.28. Enhanced string model provided with tread elements.

$$\sigma^2 \frac{\mathrm{d}^2 v_c}{\mathrm{d}x^2} - v_c = 0 \qquad \text{if} \quad |x| > a \tag{5.155}$$

And in the contact zone:

$$\sigma_c^2 \frac{\mathrm{d}^2 v_c}{\mathrm{d}x^2} - v_c = -(1-\varepsilon^2)\, v \qquad \text{if} \quad |x| \le a \tag{5.156}$$

To solve for the coordinate of the transition point x_t and the five constants of integration in the solutions of Eq.(5.154) and of Eq.(5.156) for the two zones: adhesion and sliding, we need six boundary conditions. These concern zero tread element deflection at the leading edge and continuity of deflection and slope of the string and continuity of the element deflection at the transition point. The conditions read:

$$x = a: \qquad v_c = v \ (= v_1) \ , \quad \frac{\mathrm{d}v_c}{\mathrm{d}x} = -\frac{v_c}{\sigma} \tag{5.157}$$

$$x = x_t: \qquad \lim_{x \uparrow x_t} \left(\frac{\mathrm{d}v_c}{\mathrm{d}x} , \ v_c , \ v \right) = \lim_{x \downarrow x_t} \left(\frac{\mathrm{d}v_c}{\mathrm{d}x} , \ v_c , \ v \right) \tag{5.158}$$

$$x = -a: \qquad \frac{\mathrm{d}v_c}{\mathrm{d}x} = \frac{v_c}{\sigma} \tag{5.159}$$

Once expressions for the deflection $v_p = v - v_c$ and the transition point x_t have been established, the force and moment can be assessed by integration along the contact length of q_y over the sliding range and of $c_p v_p$ over the adhesion range. The resulting formulae can be found in the original publication. We will restrict ourselves here with showing the characteristics for the values $\sigma = 3.75a$ and $c_p / c_c = 55$. Figure 5.29 depicts the deflected model at a number of slip angles. In Fig.5.30 the force and moment characteristics have been presented with along the abscissa the quantity $\theta_c \alpha$. The composite model parameter θ_c is defined as:

$$\theta_c = \frac{2}{3} \frac{c_c a^2}{\mu F_z} \tag{5.160}$$

For transient tyre analysis the relaxation length for the leading edge: σ for the bare string model and σ^* for the model with tread elements here defined as the distance between leading edge and the point of intersection of wheel plane and elongation of the straight contact line (Figs.5.8,28,29) is of importance. We have:

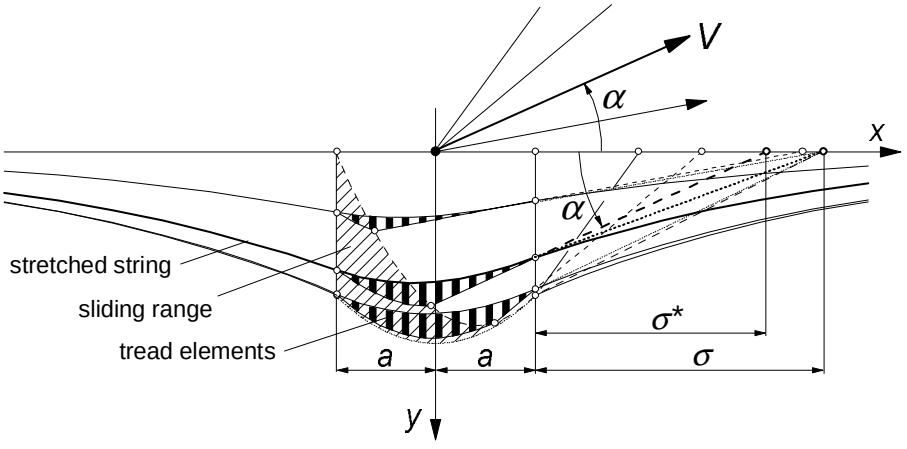

Fig. 5.29. The enhanced string tyre model at increasing slip angles showing growing sliding range and decreasing 'intersection' length σ^*.

$$\sigma^* = \frac{v_1}{\alpha} \tag{5.161}$$

The variation of this 'intersection length' σ^* with slip angle has been plotted as well. The parameters have been chosen such that at $\alpha = 0$ we have $\sigma^* = 3a$.

The diagram also contains the curve for the pneumatic trail $t = -M_z/F_y$. At $\alpha = 0$ the value of the pneumatic trail becomes $t = 0.49a$ which is much more in accordance with experimental findings than what we had with the bare string

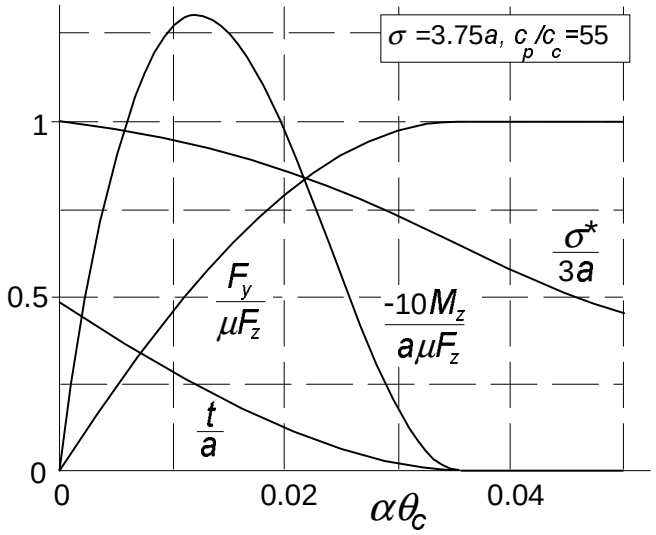

Fig.5.30. Steady-state side slip characteristics of the string model with tread elements.

model. The value $0.49a$ also supports the magnitude that had been found for the relaxation length for the force to side slip $\sigma_{F\alpha}=\sigma^{*}+a\text{-}t=3.51a$ as indicated in Table 5.1, cf. Eq.(5.72) .

Expressions for the slip stiffnesses, the pneumatic trail and the relaxation length and their relationship with vertical load will be presented in the subsequent subsection, where the linear model is discussed.

Non-steady-state behaviour at vanishing sliding range (linear analysis)

We will restrict ourselves to the derivation of the response to the slip angle α and use conversion formula (5.39), with σ replaced by σ^{*} (5.171) to obtain the response functions to turn slip φ and (5.36,37) for the responses to y and ψ. For the total deflection v, or transformed: V, Eqs.(5.11,14) and thus (5.16) hold in general.With A representing the transformed α we get:

$$V = C_v e^{px} + \frac{1}{p}A = \left(C_A e^{px} + 1\right)\frac{1}{p}A \tag{5.162}$$

With the Laplace transformed version of Eq.(5.156) the differential equation for V_c is obtained:

$$\sigma_c^2 \frac{\mathrm{d}^2 V_c}{\mathrm{d}x^2} - V_c = -\left(1-\varepsilon^2\right)\left(C_A e^{px} + 1\right)\frac{1}{p}A \tag{5.163}$$

with solution:

$$V_c = \left\{C_+ e^{(a-x)/\sigma_c} - C_- e^{-(a-x)/\sigma_c} + \left(1-\varepsilon^2\right)\left(\frac{C_A e^{px}}{1-\sigma_c^2 p^2} + 1\right)\right\}\frac{1}{p}A \tag{5.164}$$

The three integration constants can be determined by using the boundary conditions at the leading and trailing edges (5.157,159):

$$C_\pm = \tfrac{1}{2}\varepsilon(1\pm\varepsilon)\left(\frac{1+\sigma p}{1\pm\sigma_c p}C_A e^{pa} + 1\right) \tag{5.165}$$

$$C_A = -\frac{2+B_+ + B_-}{B} \tag{5.166}$$

with

$$B = (1+\sigma p)\left(\frac{B_+}{1+\sigma_c p} + \frac{B_-}{1-\sigma_c p}\right)e^{pa} + 2\frac{1-\sigma p}{1-\sigma_c^2 p^2}e^{-pa} \tag{5.167}$$

$$B_\pm = \frac{1\pm\varepsilon}{1\mp\varepsilon}e^{\pm 2\frac{a}{\sigma_c}} \tag{5.168}$$

Integration of $V_p = V - V_c$ times the stiffness c_p over the contact length yields the transformed expressions for the force F_y and, after multiplication with x, the moment M'_z. The following formulae are obtained for their transfer functions to the slip angle α.

$$H_{F,\alpha}(p) = c_p\varepsilon\frac{1}{p}\left\{2\varepsilon a + \frac{1-\sigma^2p^2}{1-\sigma_c^2p^2}\,\frac{e^{pa}-e^{-pa}}{p}\varepsilon C_A + \right.$$
$$\left. + \sigma\left(1-e^{2a/\sigma_c}\right)C_+ + \sigma\left(1-e^{-2a/\sigma_c}\right)C_-\right\} \tag{5.169}$$

$$H_{M',\alpha}(p) = c_p\varepsilon\frac{1}{p}\left[\frac{1-\sigma^2p^2}{1-\sigma_c^2p^2}\left(a\frac{e^{pa}+e^{-pa}}{p} - \frac{e^{pa}-e^{-pa}}{p^2}\right)\varepsilon C_A + \right.$$
$$+ \sigma\left\{a\left(1+e^{2a/\sigma_c}\right) + \sigma_c\left(1-e^{2a/\sigma_c}\right)\right\}C_+ + \tag{5.170}$$
$$\left. + \sigma\left\{a\left(1+e^{-2a/\sigma_c}\right) - \sigma_c\left(1-e^{-2a/\sigma_c}\right)\right\}C_-\right]$$

By letting $p \to 0$ in the expressions for $\sigma^* = V_1/A$ (5.162, $x = a$)and the transfer functions (5.169,170), the relaxation length and the slip stiffnesses may be assessed. We find:

$$\sigma^* = \frac{\sigma\left\{(1+\varepsilon)e^{2a/\sigma_c} + (1-\varepsilon)e^{-2a/\sigma_c} - 2\right\} - 4a}{\frac{1+\varepsilon}{1-\varepsilon}e^{2a/\sigma_c} + \frac{1-\varepsilon}{1+\varepsilon}e^{-2a/\sigma_c} + 2} \tag{5.171}$$

$$C_{F\alpha} = 2c_p\varepsilon^2\left[a(\sigma^* + a) + \right.$$
$$-\tfrac{1}{4}\sigma\sigma^*\left\{(1+\varepsilon)e^{2a/\sigma_c} + (1-\varepsilon)e^{-2a/\sigma_c} - 2\right\} + \tag{5.172}$$
$$\left. + \tfrac{1}{4}\sigma^2(1-\varepsilon^2)\left(e^{2a/\sigma_c} + e^{-2a/\sigma_c} - 2\right)\right]$$

$$C_{M\alpha} = 2c_p\varepsilon^2\left[\tfrac{1}{3}a^3 + \right.$$
$$-\tfrac{1}{4}\sigma\left\{\sigma^*(1+\varepsilon) - \sigma(1-\varepsilon^2)\right\}\left\{a\left(1+e^{2a/\sigma_c}\right) + \sigma_c\left(1-e^{2a/\sigma_c}\right)\right\} + \tag{5.173}$$
$$\left. -\tfrac{1}{4}\sigma\left\{\sigma^*(1-\varepsilon) - \sigma(1-\varepsilon^2)\right\}\left\{a\left(1+e^{-2a/\sigma_c}\right) - \sigma_c\left(1-e^{-2a/\sigma_c}\right)\right\}\right]$$

$$C_{F\varphi} = C_{M\alpha} \tag{5.174}$$

and the pneumatic trail:

$$t = \frac{C_{M\alpha}}{C_{F\alpha}} \tag{5.175}$$

It is of interest to examine how these quantities vary with vertical load F_z. For this purpose, we assume that the contact length varies with the square root of the radial tyre compression and that the load is a linear function of the compression. Then we find that, if at the nominal or static load F_{zo} half the contact length is denoted with a_o, the F_z vs a relationship is described by:

$$\frac{a}{a_o} = \sqrt{\frac{F_z}{F_{zo}}} \tag{5.176}$$

This introduced in the above expressions yields the characteristics shown in the diagram of Fig.5.31. The various non-dimensional quantities have been presented both for the bare string model and for the enhanced model. As has been expected, we now see that the relaxation length for the force and moment responses to yaw, σ^*+a, vanishes when the load goes to zero. The pneumatic trail's ratio to half the contact length is a lot more realistic when the tread elements are added. The same holds for the cornering and aligning stiffnesses shown in Fig.5.32. With the enhanced model the curves both start at the origin and exhibit a realistic shape. The feature, usually exhibited by passenger car tyres, that the cornering stiffness bends downwards after it has reached the peak (cf. Fig.1.3) may be attributed to the reduced lateral stiffness of the tyre cross section at higher vertical compression, cf. Pacejka (1981, p.729 or 1971, p.698) for an analytical formula.

The frequency response functions for the enhanced model are presented in Figs.5.33 and 5.34. They may be compared with the plots of Figs.5.14 and 5.15 which hold for the bare string model. The model parameters are again: $\sigma=3.75a$, c_p/c_c = 55. An important result of the analysis is that expressions (5.70,72,74,79,80, 81) for relaxation lengths and cut-off frequencies are the same for the bare string model and the enhanced model if in these expressions σ is replaced by σ^* defined by (5.171).

For comparison, the plots for the step responses and for the frequency response functions have been presented in the Figs.5.21-27 together with results of other models. Also Table 5.1 (below Fig.5.27) contains data computed with the new model. The general course of the curves is similar. Important differences with respect to the bare string model are the considerable shift of the cut-off frequency of the M_z' response to α and similarly of F_y to φ and together with these: the meandering frequency where the dip of the M_z' response to ψ occurs The reduction of the pneumatic trail t is responsable for the increase of the cut-off frequency.

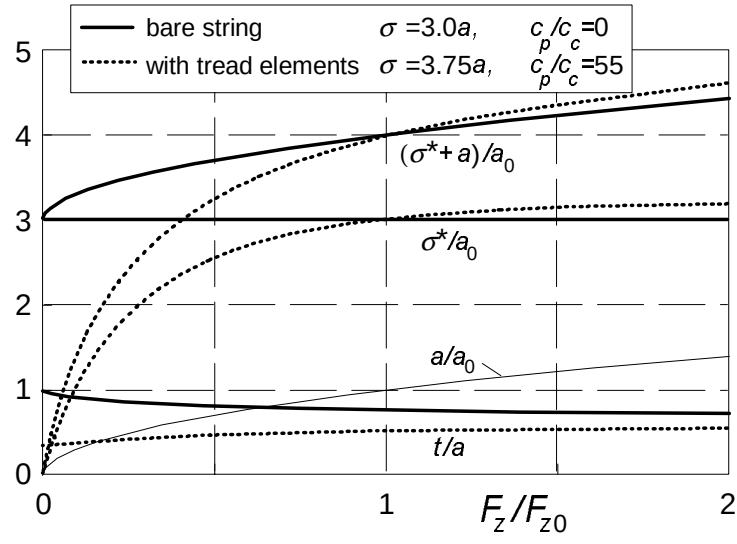

Fig.5.31. The variation of the relaxation length and half the contact length as a ratio to the static value of the latter and the ratio of the pneumatic trail to half the contact length with normalised vertical load both for the bare string model and for the model with tread elements.

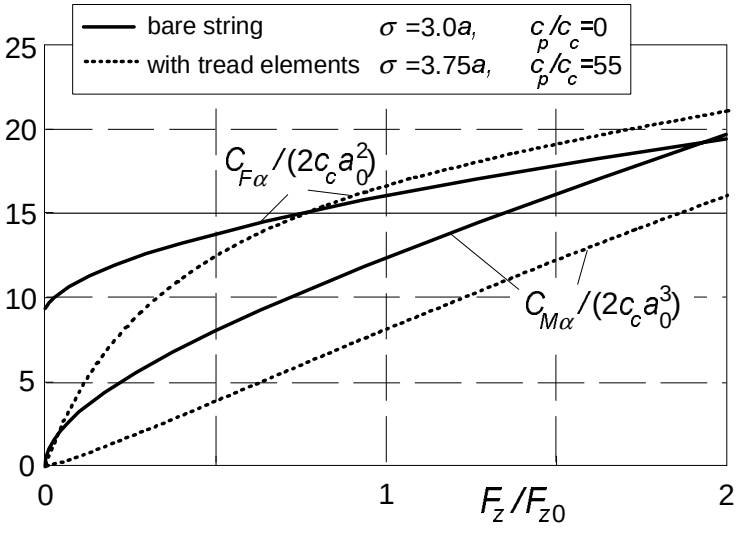

Fig.5.32. The variation of non-dimensionalised cornering and aligning stiffnesses with normalised vertical load both for the bare string model and the model with tread elements.

Experimental results assessed on a 2.5m diameter steel drum have been presented in Fig.5.35. The responses are depicted in the Nyquist diagram (cf. Figs.5.17,18) as a ratio to their values assessed at steady-state side slip. Two light truck tyres have been tested at a vertical load of F_z = 10kN. Both tyres possess the same cross-ply construction but exhibit a different tread design. The original tyre shows a block tread design (central rib with transverse blocks, oval foot print), which is relatively weak in the longitudinal direction at the sides of the contact patch. The modified tyre is provided with circumferential ribs (three ribs, almost rectangular foot print) making the tread relatively stiff in the longitudinal direction. As expected, the ribbed tyre generates more resistance against turning which is reflected by a larger moment due to tread width M_z^* and consequently a considerably smaller phase lag of the resulting self-aligning torque $-M_z$. The side force does not appear to be much affected at least in the larger wavelength range. In Table 5.2 parameters estimated from the measurements have been listed. The intersection length or deflection relaxation length σ^* was determined from the formula:

$$\sigma^* = \frac{C_{F\alpha}}{C_{Fy}} - a \tag{5.177}$$

When considering the relation $a/\lambda = an/V$ with $V_{km/h} = 3.6 V_{m/s}$ the value for the non-dimensional path frequency at V=10 km/h and an excitation frequency of 1Hz becomes a/λ=0.0414 which roughly corresponds with that indicated on the thin tyre model curve of Fig.5.18.

Table 5.2. Parameters for two 9.00-16 tyres with different tread patterns.

	blocks	ribs		blocks	ribs
r_o	0.5m	0.5m	F_z	10 kN	10 kN
a	0.115m	0.08m	$C_{F\alpha}$	64 kN/rad	53 kN/rad
b	0.092m	0.10m	$C_{M\alpha}$	3.9 kNm/rad	3.5 kNm/rad
t	0.53a	0.82a	C_{Fy}	165 kN/m	175kN/m
σ^*	2.4a	2.8a	κ^*	0.25 $C_{M\alpha}a$	1.0 $C_{M\alpha}a$

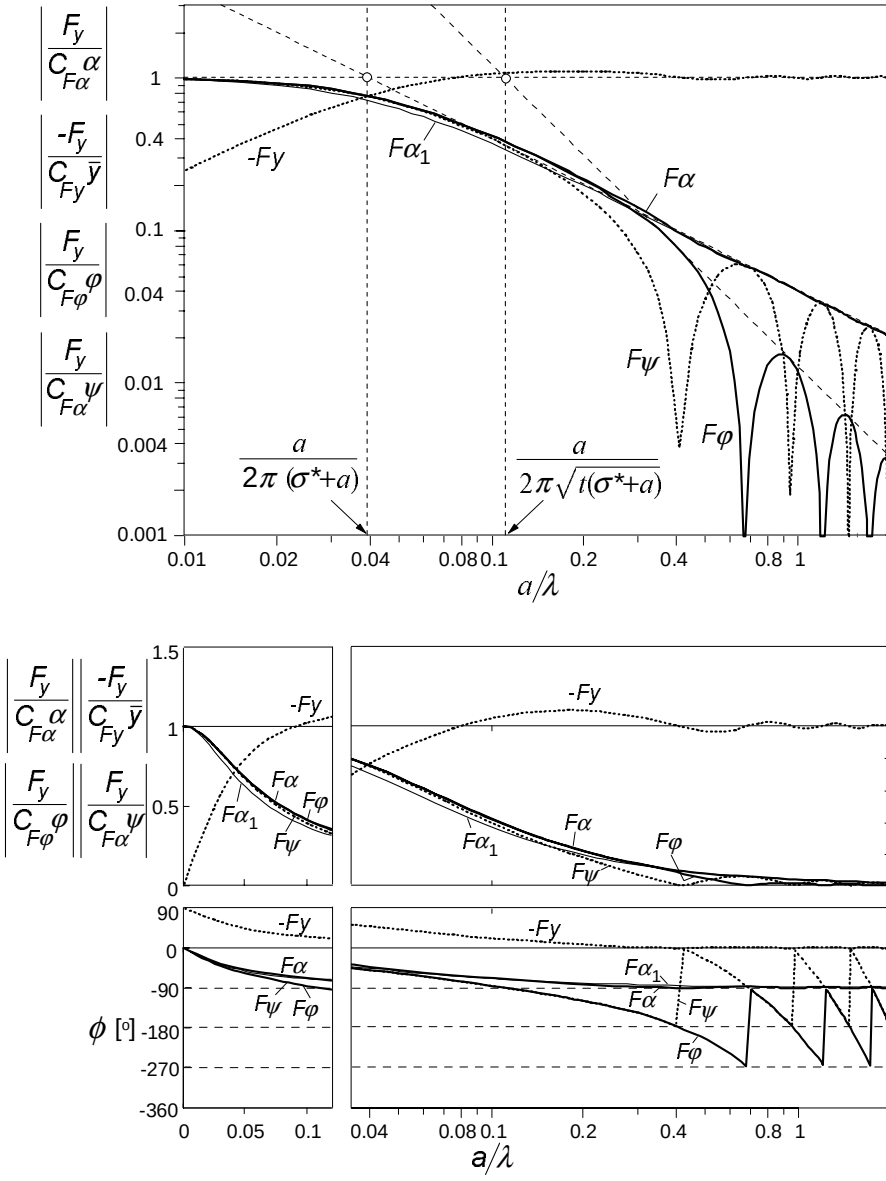

Fig. 5.33. Frequency response functions of the string model with tread elements for the side force with respect to various motion input variables. For the response to α a first-order approximation with the same cut-off frequency, $\omega_s = 1/(\sigma^* + a)$, has been added ($F\alpha_1$). Three ways of presentation have been used: log-log, lin-log and lin-lin. The model parameters are: $\sigma = 3.75a$, $c_p/c_c = 55$ which leads to $\sigma^* = 3a$, $t = 0.49a$.

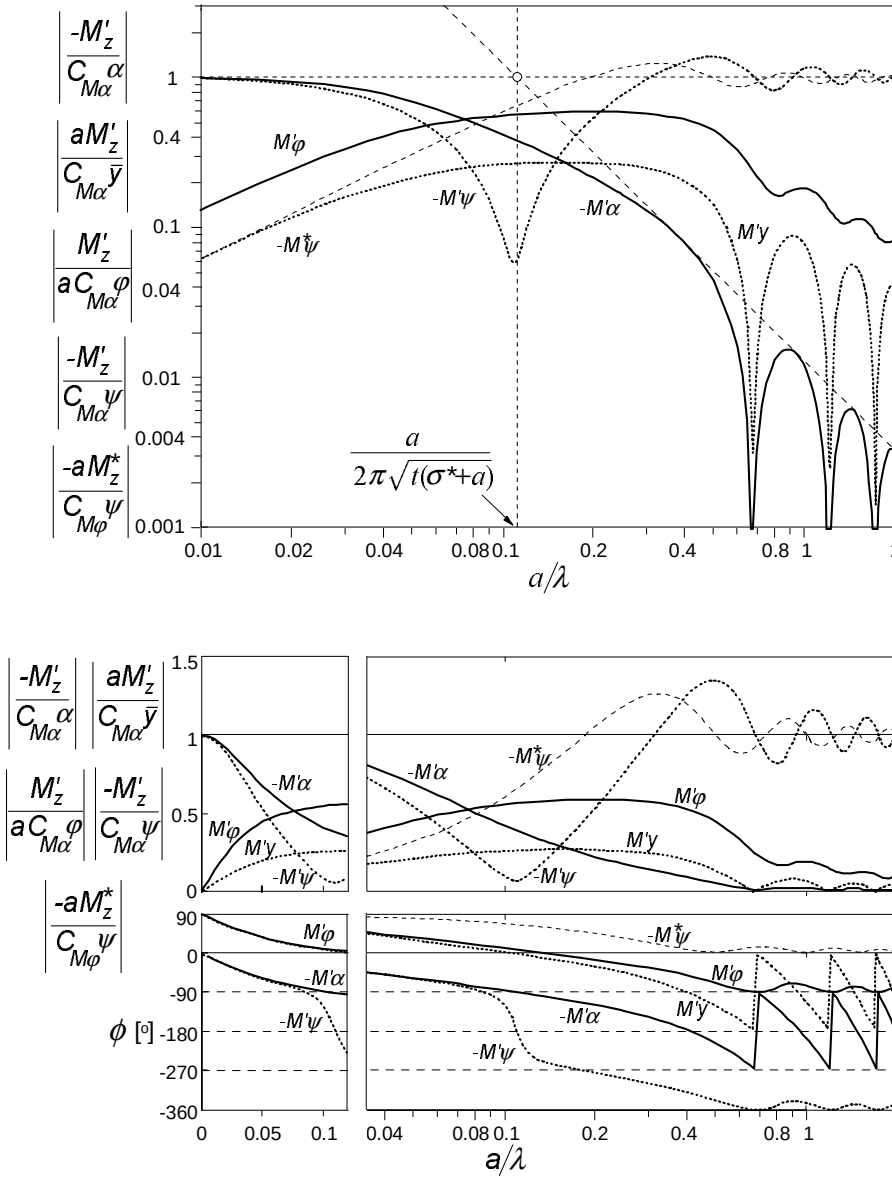

Fig. 5.34. Frequency response functions of string model with tread elements for the aligning torque with respect to various motion input variables. Same conditions as in Fig.5.33. The response functions of the moment due to tread width M_z^* have been added.

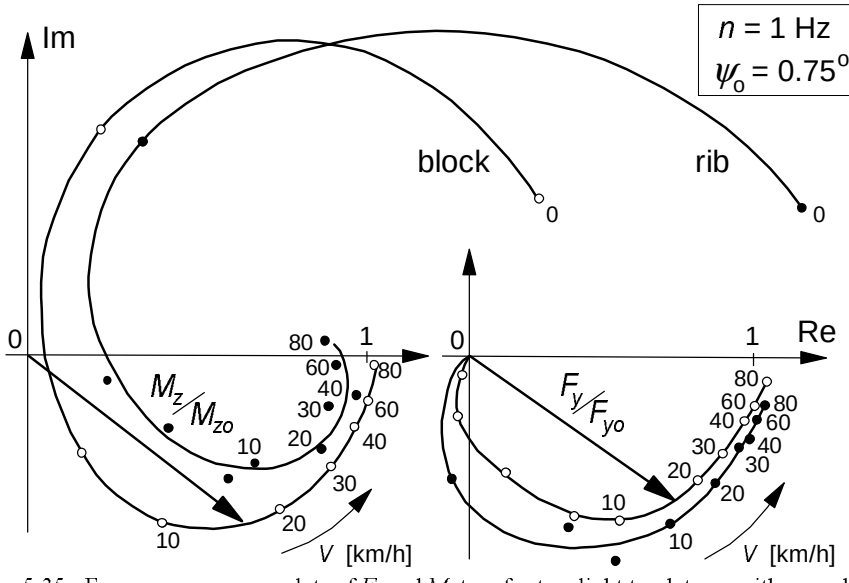

Fig. 5.35. Frequency response plots of F_y and M_z to ψ for two light truck tyres with same bias ply carcass but different tread patterns. Measurements were performed on a 2.5m drum at a vertical load of 10kN, a yaw amplitude of 0.75° at a frequency n=1Hz.

5.5. Tyre Inertia Effects

It has been found experimentally that higher frequencies and greater speeds of travel bring about an increasingly important deviation of the response with respect to the kinematic representation with dynamic influences disregarded.

Figure 5.36 presents an example of response curves obtained experimentally. The response curves for the moment M_z and the side force F_y to the yaw angle ψ have been shown as a function of the speed of travel V for fixed values of the excitation frequency n of the imposed yaw oscillation. The force and moment outputs are given as a ratio to their steady-state values (at $\omega_s = \omega = 0$) indicated by the subscript o.

We observe that for higher frequencies the curves of the moment response appear to shift upwards. The force response curves, on the other hand, show an increase in amplitude while the phase lag remains approximately unchanged for constant wavelength $\lambda = V/n$.

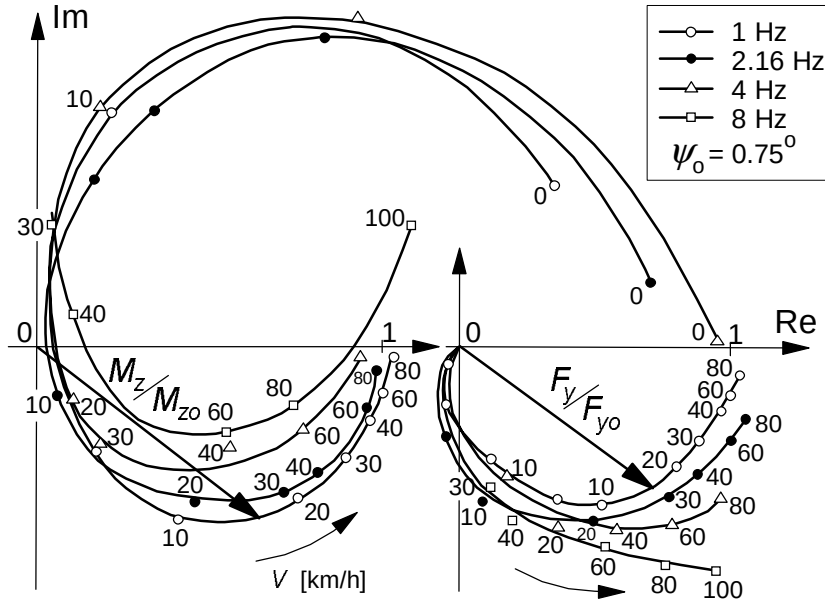

Fig. 5.36. Frequency response plots of F_y and M_z to ψ for light truck tyre with block tread pattern. Measurements were performed on a 2.5m drum at a vertical load of 10kN, a yaw amplitude of 0.75° and at four different time frequencies.

5.5.1. First Approximation of Dynamic Influence (Gyroscopic Couple)

In the low frequency range, n<10Hz, the aligning torque appears to be affected most by the inertia of the tyre. A simple addition to the kinematic model may approximately describe the dynamic changes in the response of the moment. In this theory the gyroscopic couple due to the lateral deformation rate of the lower portion of the tyre has been introduced as the only dynamic influence. It is assumed here that the dynamic forces have a negligible effect on the distortion of the tyre.

The gyroscopic couple about the vertical axis is proportional to the wheel rotational speed and the time rate of change of the tilt (camber) distortion of the tyre, cf. Fig.5.37. Since this distortion is connected with the lateral deflection of the lower part of the tyre and the side force F_y is proportional to this deflection, we have for the gyroscopic couple:

$$M_{zgyr} = C_{gyr} V \frac{\mathrm{d}F_y}{\mathrm{d}t} \tag{5.178}$$

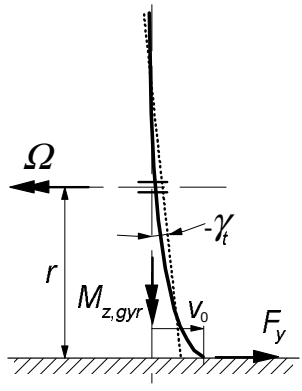

Fig. 5.37. The average tilt angle of the peripheral line of the deflected tyre.

in which t denotes the time. The tyre constant C_{gyr} is proportional to the tyre mass m_t and inversely proportional to the lateral stiffness C_{Fy} of the standing tyre. We have with the non-dimensional quantity c_{gyr} introduced:

$$C_{gyr} = c_{gyr} \frac{m_t}{C_{Fy}} \tag{5.179}$$

The total moment which acts upon the wheel is now composed of the moment due to lateral tyre deformation M_z' and that due to longitudinal anti-symmetric tread deformations M_z^* and finally the gyroscopic couple $M_{z,gyr}$:

$$M_z = M_z' + M_z^* + M_{z,gyr} \tag{5.180}$$

With this simple addition to the enhanced stretched string tyre model (provided with tread elements distributed over the assumedly rectangular contact area) calculations have been performed. Figure 5.38 shows the Nyquist plot of the responses with along the curves $\omega_s a = 2\pi n a/V = 2\pi a/\lambda$. It should be noted that the vector of the gyroscopic couple is directed perpendicularly to the vector of the lateral force. For the range of frequencies considered, the simple approximate dynamic extension theory gives a good representation of the effect on the moment response curves. However, the theory does not account for the dynamic changes in the force response.

5.5.2. Second Approximation of Dynamic Influence (First Harmonic)

More complex theories as developed by Pacejka (1973) and by Strackerjan (1976) and more recently by Maurice (2000), cf. Chapter 9, yield better results also with respect to the force response and extends to higher frequencies covering

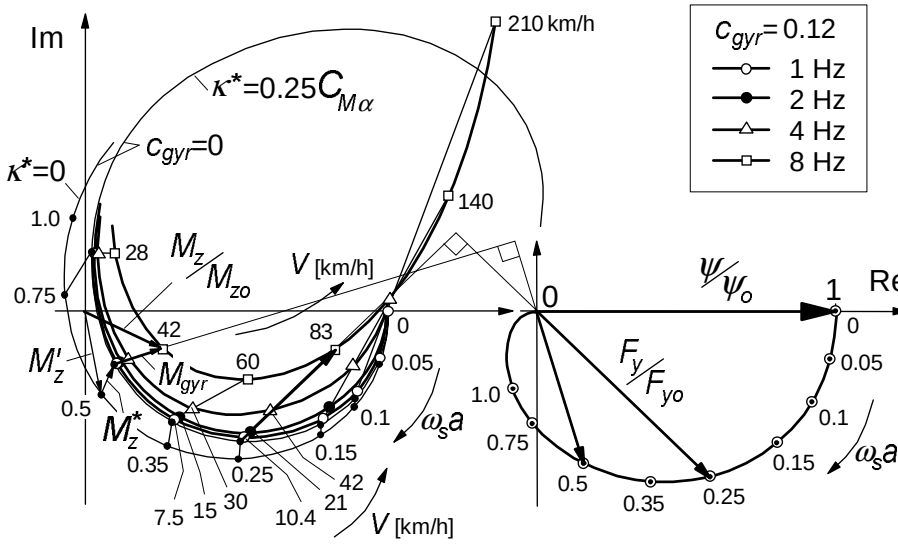

Fig.5.38. The influence of the frequency of the yaw oscillation on the dynamic response according to the simple approximate model extension using the gyroscopic couple due to the lateral tyre deflection time rate of change.

the first natural frequencies of the out-of-plane tyre dynamic behaviour. In these theories the tyre circular belt is considered to move not only about a longitudinal axis but also about a vertical axis and in the lateral direction. The belt rotation about the vertical axis gives rise to a gyroscopic couple about the longitudinal axis which on its turn results in a change in slip angle which influences F_y (and also M_z).

The interesting feature of the approach followed in the first reference mentioned above is that the kinematic theory and response equations as treated in Sections 5.3 and 5.4. with tyre inertia equal to zero can be employed. The kinematic part of the model will be considered to be subjected to a different, effective, set of input motion variables. Instead of taking the motion of the actual wheel-plane defined by $\bar{y}$ and ψ (or α and φ), an effective input is introduced that is defined as the lateral and the yaw motion of the line of intersection of the 'dynamic' belt plane and the road surface ($\bar{y}_e$, ψ_e). Figure 5.39 depicts the situation. The dynamic belt plane is defined as the virtual centre plane of the belt of the tyre that is displaced with respect to the rim through the action of lateral inertial forces only. These inertial forces distributed along the circumference of the belt are approximated in such a way that only the forces resulting from the zeroth and first modes of vibration are taken into account, that is: as if the belt would remain circular. Harmonics of second and higher order are neglected in

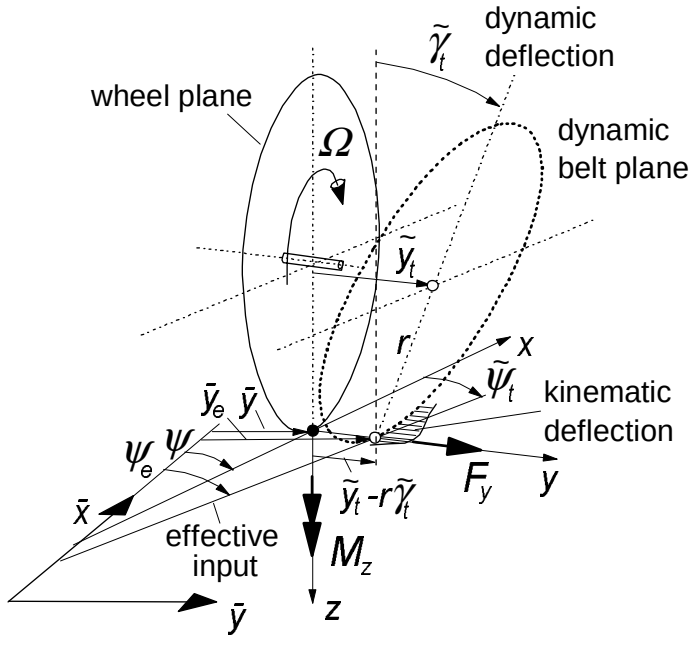

Fig. 5.39. 'Dynamic' average plane deflection of belt and associated effective input.

the dynamic part of the model. We have for the approximate dynamic lateral, camber and yaw deflections respectively:

$$\tilde{y}_t = -m_t(\ddot{\bar{y}} + \ddot{y}_t)/C_y$$

$$\tilde{\gamma}_t = -\{I_t\ddot{\gamma}_t + I_{tp}\Omega(\dot{\psi} + \dot{\psi}_t)\}/C_\gamma \tag{5.181}$$

$$\tilde{\psi}_t = -\{I_t(\ddot{\psi} + \ddot{\psi}_t) - I_{tp}\Omega\dot{\gamma}_t\}/C_\psi$$

with the total tyre deflections composed of dynamic and static parts (the latter resulting from external ground forces):

$$y_t = \tilde{y}_t + F_y/C_y$$

$$\gamma_t = \tilde{\gamma}_t - F_y r/C_\gamma \tag{5.182}$$

$$\psi_t = \tilde{\psi}_t + M_z'/C_\psi$$

and stiffnesses of the whole belt with respect to the rim C_y, C_γ and C_ψ. Furthermore the equations contain effective tyre inertia parameters m_t, I_t and

polar moment of inertia I_{tp}. The effective inputs to the kinematic model are defined by:

$$\bar{y}_e = \bar{y} + \tilde{y}_t - r\tilde{\gamma}_t$$
$$\psi_e = \psi + \tilde{\psi}_t \tag{5.183}$$

With the aid of these equations plus the kinematic tyre equations (e.g. Von Schlippe's approximate equations (5.87,88,92,93) with (5.36,37) and (5.32) for M_z^* with inputs ($\bar{y}$, ψ) replaced by effective inputs ($\bar{y}_e$, ψ_e)) the frequency response functions of the ground force F_y and moment $M_z = M_z' + M_z^*$ with respect to the actual inputs ($\bar{y}$, ψ) may be readily established.

For applications in vibratory problems associated with wheel suspension and steering systems, it is of greater interest to know the response of the equivalent force and moment that would act on the assumedly rigid wheel with tyre inertia included at the contact centre. The equivalent force and moment are obtained as follows:

$$F_{y,eq} = F_y - m_t\ddot{y}_t$$
$$M_{z,eq} = M_z' + M_z^* - I_t\ddot{\psi}_t + I_{tp}\Omega\dot{\gamma}_t \tag{5.184}$$

This result should correspond to the force and moment measured in the wheel hub, $F_{y,hub}$ and $M_{z,hub}$, after these have been corrected for the inertial force and moment acting on the assumedly rigid wheel plus tyre (inertia between load cells and ground surface). With inertia parameters of wheel plus tyre we find for this correction:

$$F_{y,eq} = F_{y,hub} + m_{wt}\ddot{\bar{y}}$$
$$M_{z,eq} = M_{z,hub} + I_{wt}\ddot{\psi} \tag{5.185}$$

When lifted from the ground, the equivalent ground to tyre forces vanish if the frequency of excitation is not too high (low with respect to the first natural frequency of the tyre).

For the set of parameter values measured on a radial ply steel-belted tyre listed in Table 5.3, the amplitude and phase of the equivalent moment as a response to yaw angle have been computed and are presented in Fig.5.40 as a function of the excitation frequency $n = \omega/2\pi$. Experimentally obtained curves up to a maximum of 8 Hz (on 2.5m drum) have been added. The phase lag that occurs in the lower frequency range is largely responsible for the creation of self-

Table 5.3. Parameters for car tyre model with dynamic belt extension (2nd approximation).

Bias-ply tyre				Radial-ply steel belted			
a	0.066 m	$C_\psi = C_\gamma$	29 Nm	a	0.063 m	$C_\psi = C_\gamma$	18.1 Nm
σ	0.230 m	C_y	270 kN/m	σ	0.377 m	C_y	360 kN/m
r	0.324 m	m_t	4.5 kg	r	0.322 m	m_t	5.7 kg
$C_{F\alpha}$	35.5 kN	I_t	0.235 kgm^2	$C_{F\alpha}$	49.0 kN	I_t	0.295 kgm^2
$C_{M\alpha}$	1.22 kNm	I_{tp}	0.47 kgm^2	$C_{M\alpha}$	1.4 kNm	I_{tp}	0.59 kgm^2
κ^*	80 Nm^2	(m_{tyre} = 8.9 kg)		κ^*	104 Nm^2	(m_{tyre} = 8.5 kg)	

excited wheel shimmy. The influence of tyre inertia is evident: the phase lag changes into phase lead at higher values of speed (similar as in Fig.5.38). In contrast to the dynamic response depicted in Fig.5.41 the kinematic model response (without the inclusion of tyre inertia) would produce the same response at equal wavelengths, $\lambda = V/n$, irrespective of the value of the speed of travel V.

The resonance frequencies, which at speeds close to zero approach a value somewhat larger than the natural frequency of the free non-rotating tyre, n_{oo}, appear to separate at increasing speed. Vibration experiments performed on a free tyre (not contacting the road) for the purpose of obtaining the values of certain tyre parameters, gave a clear indication that a considerable reduction of the lowest resonance frequency arises when the wheel is rotated around the wheel spin axis at higher speeds of revolution.

Nyquist plots for the $M_{z,eq}$ and $F_{y,eq}$ responses to ψ have been presented in Figs. 5.42 and 5.43. Both for the bias-ply and for the radial steel-belted tyre of Fig.5.40 theoretical and experimental results are shown. Parameters are according to Table 5.3. For each of the curves the excitation frequency remains constant while the speed varies along the curve.

An increase in frequency tends to raise the moment curves while the force response curves appear to expand with the phase angle at given wavelength remaining not much changed. The typical differences between the two types of tyres, notably in the shape of the upwards ends of the moment curves where the speed assumes high values, are well represented in the theoretical diagrams.

We may conclude, that the simple first approximation appears to give a considerable improvement for the moment response in the lower frequency range while for the force response and the higher frequency excitations the inclusion of the dynamics of the belt up to the first modes of vibration is required.

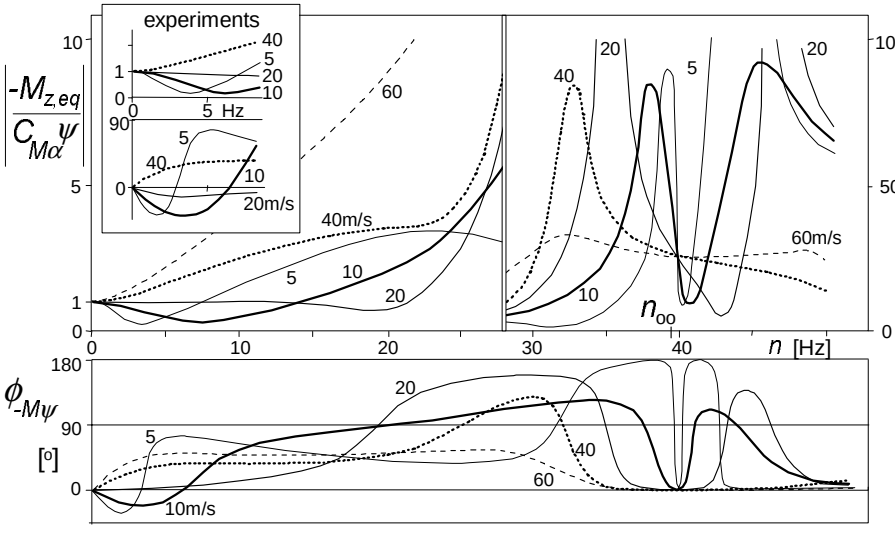

Fig. 5.40. Amplitude and phase response of equivalent aligning torque (as if acting from ground on rigid wheel-tyre) to yaw angle as a function of time frequency of excitation [Hz] computed using Von Schlippe approximation and exact M_z^* extended with dynamic theory according to second approximation with dynamic belt. Model parameters are listed in Table 5.3 (radial steel belted tyre). Curves hold for given speed of travel V [m/s]. Experimental results are given up to a frequency of 8 Hz. The yaw natural frequency of the free non-rotating tyre with fixed wheel spindle is n_{oo}.

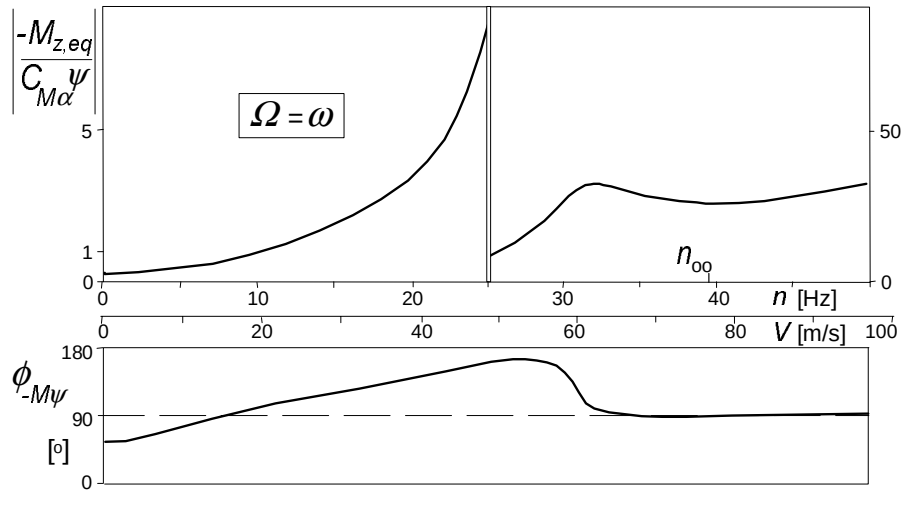

Fig. 5.41. Amplitude and phase response as a function of frequency with the frequency of excitation equal to that of wheel revolution.

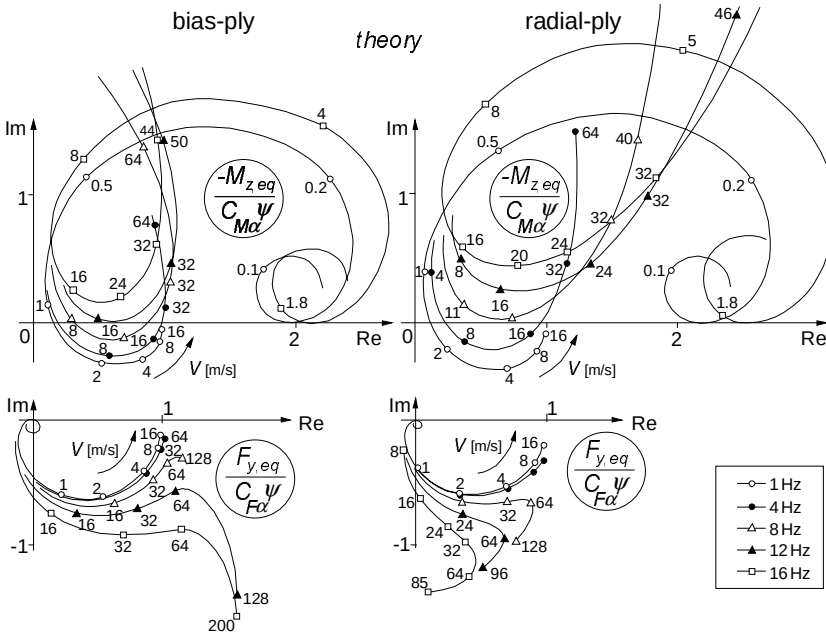

Fig. 5.42. Theoretical frequency response Nyquist plots of side force and aligning torque to yaw angle for different time frequencies. Same conditions as in Fig.5.40.

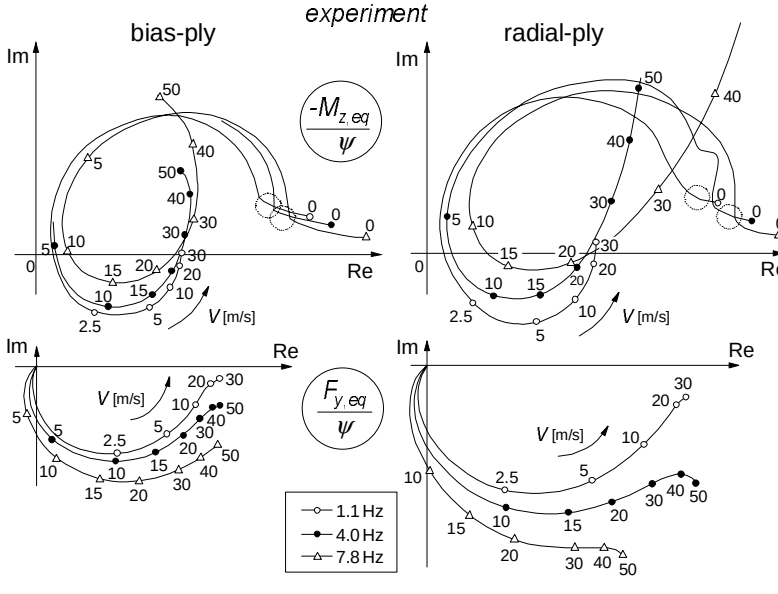

Fig. 5.43. Experimental frequency response Nyquist plots of side force and aligning torque to yaw oscillations for a radial and a bias-ply car tyre measured on a 2.5m drum.

Since we have here a dynamic model extension that allows the use of existing kinematic (mass less) models we have been able to investigate the effect of tyre inertia on these models. However, for the sake of simplicity these models have been restricted to a linear description allowing straightforward frequency response analysis. Extension into the non-linear regime in the time domain is cumbersome for models including a finite contact length (retardation) effect, (although an approximate non-linear Von Schlippe model may be established by attaching non-linear springs to the wheel plane at the leading and trailing edges the tips of which follow the path as if we had full adhesion) but also because in the dynamic extension, Eqs.(5.181-183), the function $F_y = F_y(\alpha')$ would be needed in an inverse form.

To further develop mathematical models that can be used under conditions that include short wavelengths, higher frequencies and large (combined) slip a different route appears to be more promising. The adopted principle is: separate modelling of the flexible belt with carcass and the contact patch with its transient slip properties. The theory of the non-steady state rolling and slipping properties of the brush model helps in this modelling effort. In Chapter 9 this advanced model will be discussed.

For less demanding cases (large wavelength, low frequency) the straight tangent or single point contact models may be employed. Such models may be used in combination with the approximate dynamic extension that accounts for the gyroscope couple due to the lateral deflection velocity. Furthermore, these simple models can be easily adapted to cover large slip non-linear behaviour, cf. Eqs.(5.125,126,128) or (5.130, 131,132) and Eq.(5.178) with F_y replaced by $C_{Fy}v_0$. Chapter 7 is devoted to the treatment of the very useful and relatively simple, possibly non-linear, single contact point transient slip models. With that single point contact model the problem of cornering (and braking) on undulated road surfaces can be made more accessible for vehicle simulation studies. First, we will address this difficult subject in the subsequent section using exact string models with and without tread elements which shows the deeper cause of the associated loss in cornering power.

5.6. Side Force Response to Time-Varying Load

In studies by Metcalf (1963), Pacejka (1971) and more recently by Laermann (1985) and by Takahashi (1987) and Pacejka (1992) it was found that the average value of the side force generated by a constant slip angle is reduced as a result of a periodical change of the vertical load. This reduction may be considerable and appears to depend on the amplitude of the vertical load variation as a ratio to the static load, on the wavelength of the motion, the speed of travel and on the magnitude of the slip angle. In Chapter 7 a more practical approach based on the single contact point model (that means: for accuracy limited to relatively large wavelengths) is adopted to model the non-steady-state behaviour at varying vertical load including high levels of slip. To lay the basis for that theory we will employ the advanced string model with tread elements that was developed in Section 5.4.3 for the case of a constant vertical load. The presence of tread elements turns out to be crucial to properly model the loss of side force when cornering on an undulated road surface. As in Section 5.4.3, only small slip angles will be considered allowing the theory to remain linear. First, we will develop the model based on the advanced string model with tread elements. Then, to simplify the model description, an adapted bare string model will be introduced and used in the further calculations.

5.6.1. String Model with Tread Elements Subjected to Load Variations

Figure 5.44 shows the tyre model in two successive positions while the wheel moves at a constant (small) slip angle over an undulated road surface which causes the contact length to vary with distance travelled s. When the contact centre C is moved a distance Δs, the following changes occur simultaneously: lateral shift of the wheel plane, forward rolling and change in contact length. These changes influence the position of the leading and trailing edges of the string. The $\bar{x}$ coordinates of these points are:

$$\begin{aligned} \bar{x}_1 &= s + a \\ \bar{x}_2 &= s - a \end{aligned} \tag{5.186}$$

the changes of which become:

$$\begin{aligned} \Delta\bar{x}_1 &= \Delta s + \Delta a \\ \Delta\bar{x}_2 &= \Delta s - \Delta a \end{aligned} \tag{5.187}$$

The changes in front and rear lateral string deflections $v_{c1,2}$ are composed of

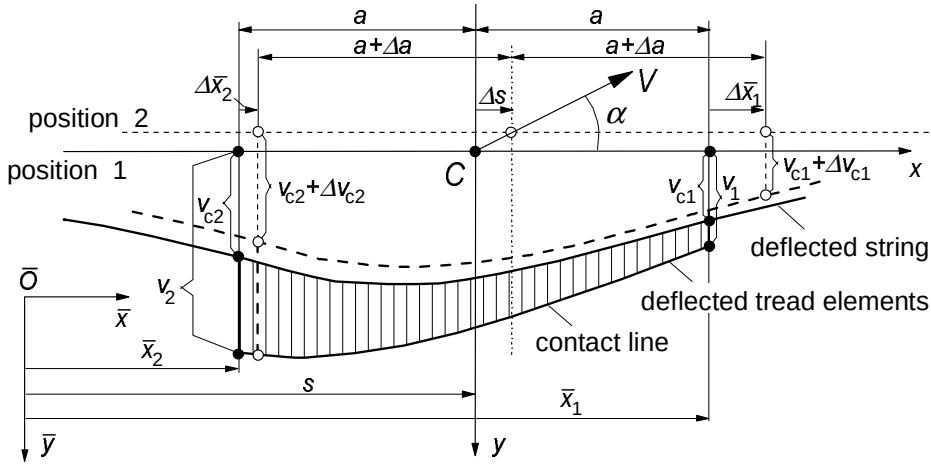

Fig. 5.44. Two successive positions of tyre model with varying contact length at constant slip angle α (sliding not considered).

various contributions. For the increment of the deflection at the leading edge Δv_{c1} we obtain:

1. due to lateral wheel displacement $\alpha\Delta s$:

$$\Delta v_{c1} = A(a)\cdot\alpha\Delta s \tag{5.188a}$$

2. due to loss of contact at the trailing edge ($\Delta\bar{x}_2 > 0$):

$$\Delta v_{c1} = -B(a)\frac{v_2 - v_{c2}}{\sigma_c}\Delta\bar{x}_2 \tag{5.188b}$$

3. due to loss of contact at the leading edge ($\Delta\bar{x}_1 < 0$):

$$\Delta v_{c1} = -B^*(a)\frac{v_1 - v_{c1}}{\sigma_c}\Delta\bar{x}_1 \tag{5.188c}$$

4. due to longitudinal displacement of leading edge ($\Delta\bar{x}_1$):

$$\Delta v_{c1} = -\frac{v_{c1}}{\sigma}\Delta\bar{x}_1 \tag{5.188d}$$

Similar expressions are obtained for the contributions to the change of the lateral deflection at the rear Δv_{c2}. The contact length dependent coefficients appearing in the equations are:

$$A(a) = \left\{-2\varepsilon + (1+\varepsilon)e^{2a/\sigma_c} - (1-\varepsilon)e^{-2a/\sigma_c}\right\}/P(a) \tag{5.189}$$

$$B(a) = 2/P(a) \tag{5.190}$$

$$B^*(a) = \left\{(1+\varepsilon)e^{2a/\sigma_c} + (1-\varepsilon)e^{-2a/\sigma_c}\right\}/P(a) \tag{5.191}$$

$$P(a) = \frac{1+\varepsilon}{1-\varepsilon}e^{2a/\sigma_c} - \frac{1-\varepsilon}{1+\varepsilon}e^{-2a/\sigma_c} \tag{5.192}$$

They are derived from solutions of the differential equations for the shape of the string deflection Eqs.(5.155-156). For the parameters employed we refer to the Eqs.(5.153). From the increments (5.187,188) the following differential equations are established for the unknown string deflections v_{c1} and v_{c2}:

$$\begin{aligned}\frac{\mathrm{d}v_{c1}}{\mathrm{d}s} = &-\left(1+\frac{\mathrm{d}a}{\mathrm{d}s}\right)\frac{v_{c1}}{\sigma} - B(a)\left(1-\frac{\mathrm{d}a}{\mathrm{d}s}\right)\frac{v_2 - v_{c2}}{\sigma_c} + \\ &+ B^*(a)\left(1+\frac{\mathrm{d}a}{\mathrm{d}s}\right)\frac{v_1 - v_{c1}}{\sigma_c} + A(a)\alpha\end{aligned} \tag{5.193}$$

$$\begin{aligned}\frac{\mathrm{d}v_{c2}}{\mathrm{d}s} = &\left(1-\frac{\mathrm{d}a}{\mathrm{d}s}\right)\frac{v_{c2}}{\sigma} + B(a)\left(1+\frac{\mathrm{d}a}{\mathrm{d}s}\right)\frac{v_1 - v_{c1}}{\sigma_c} + \\ &- B^*(a)\left(1-\frac{\mathrm{d}a}{\mathrm{d}s}\right)\frac{v_2 - v_{c2}}{\sigma_c} + A(a)\alpha\end{aligned} \tag{5.194}$$

The two remaining unknowns v_1 and v_2 representing the total lateral deflections and consequently the distances between wheel plane and contact line at the leading and trailing edges, are found by considering the following. In the rolling process of a side slipping tyre with a continuously changing contact length, in general, three intervals can be distinguished during the interval of the loadingcycle where contact with the road exists. In Fig.5.45 the load variation together with the corresponding variation of the contact length $2a$ of a side slipping tyre that periodically jumps from the road has been shown in the road plane $(\bar{x},\bar{y})$ for the interval that contact exists. Immediately after the first point touches the road, the contact line grows in two directions (interval I). This growth continues until the second interval II is reached, where growth of contact takes place only at the front, and at the rear loss of contact occurs. Finally, in the third interval III, loss of contact at both ends takes place until the tyre leaves the road. When the tyre does not leave the road, an additional interval II occurs before interval I is reached again and the cycle starts anew. In less severe cases, intervals I and III may not occur. We then have the relatively simple situation of continuous growth of contact at the front and loss of contact at the rear.

The unknowns v_1 and v_2, and the $\bar{y}$ coordinate of the contact points in the $(\bar{x},\bar{y})$

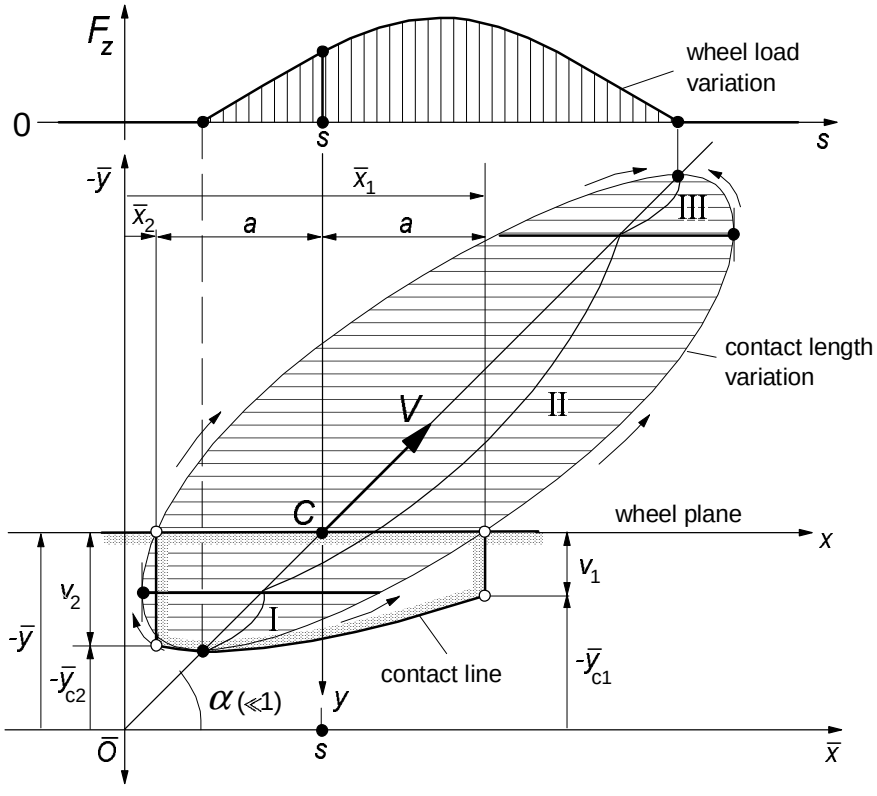

Fig. 5.45. On the development of the contact line of the tyre model with tread elements that periodically loses contact with the road.

plane are obtained as follows (cf. Fig.5.45):

Interval I: $\dot{\bar{x}}_1 > 0, \quad \dot{\bar{x}}_2 < 0 \quad \left(\dfrac{\mathrm{d}a}{\mathrm{d}s} > 1\right)$

$$v_1 = v_{c1}, \quad v_2 = v_{c2}$$
$$-\bar{y}_{c1} = s\alpha - v_{c1}, \quad -\bar{y}_{c2} = s\alpha - v_{c2} \tag{5.195a}$$

Interval II: $\dot{\bar{x}}_1 > 0, \quad \dot{\bar{x}}_2 > 0 \quad \left(-1 < \dfrac{\mathrm{d}a}{\mathrm{d}s} < 1\right)$

$$v_1 = v_{c1}, \quad v_2 = s\alpha + \bar{y}_{c2}$$
$$-\bar{y}_{c1} = s\alpha - v_{c1} \tag{5.195b}$$

Interval III: $\dot{\bar{x}}_1 < 0, \quad \dot{\bar{x}}_2 > 0 \quad \left(\dfrac{\mathrm{d}a}{\mathrm{d}s} < -1\right)$

$$v_1 = s\alpha + \bar{y}_{c1}, \quad v_2 = s\alpha + \bar{y}_{c2} \tag{5.195c}$$

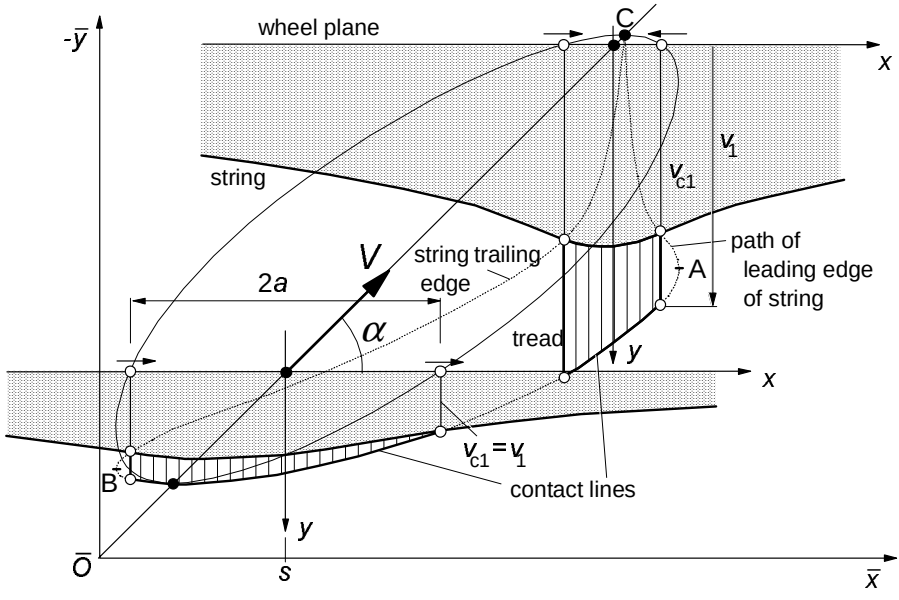

Fig. 5.46. The deflected tyre model in two positions during the interval of contact with the road

By means of numerical integration, Eqs.(5.193,94) have been solved with the aid of the equations (5.195) and the expressions (5.189-192) for the case formulated below in which the vertical tyre deflection ρ has been given a periodic variation with amplitude $\hat{\rho}$ greater than the static deflection ρ_o, so that periodic loss of contact between tyre and road occurs. The static situation will be indicated with subscript o. The tyre radius is denoted with r. The vertical deflection and the contact length are governed by the equations:

$$\rho = \rho_o - \hat{\rho}\sin\omega_s s \tag{5.196}$$

$$a^2 = 2r\rho - \rho^2 \tag{5.197}$$

The numerical values of the parameters of the system under consideration are:

$$a_o = 0.25r,\ (\rho_o = 0.03175r),\ \hat{\rho} = 0.1r,\ \omega_s = \pi/(4a_o),\ (\lambda = 8a_o)$$

$$\sigma = 3a_o,\ \varepsilon = 0.25,\ (\sigma_c = 0.75a_o,\ c_p = 15c_c) \tag{5.198}$$

In Fig.5.46 the calculated variation of contact length 2a (oval curve), the path of the contact points (lower curve AB) and the course of the points of the string at the leading and trailing edge (AC and BC) have been indicated. Two positions of the tyre have been depicted, one in interval II and the other in interval III.

It is necessary that the calculations in the numerical integration process be

carried out with great accuracy. A small error gives rise to a rapid build up of deviations from the correct course. In the case considered above, the integration time is limited and accurate results can be obtained. In cases, however, where continuous contact between tyre and road exists, a long integration time is needed before a steady state situation is attained, which is due to the fact that the exact initial conditions of a periodic loading cycle are not known. For this sort of situation, the exact method described above is difficult to apply due to strong drift of v_{c2} in particular.

For further investigation of the effect of a time varying load we will turn to an approximate method based on the string model without tread elements.

5.6.2. Adapted Bare String Model

The use of this model is much simpler since the deflections at both edges are independent of each other. Drift does not occur in the calculation process. In Fig.5.47 the deflected model has been shown in interval II. For the three intervals the following sets of equations apply:

growth of contact at leading edge:

$$\dot{\bar{x}}_1 > 0 \quad \left(\frac{\mathrm{d}a}{\mathrm{d}s} > -1\right) \tag{5.199a}$$

$$\frac{\mathrm{d}v_1}{\mathrm{d}s} = \alpha - \left(1 + \frac{\mathrm{d}a}{\mathrm{d}s}\right)\frac{v_1}{\sigma} \tag{5.199b}$$

$$\bar{x}_1 = s + a \tag{5.199c}$$

$$\bar{y}_{c1} = -s\alpha + v_1 \tag{5.199d}$$

growth of contact at trailing edge:

$$\dot{\bar{x}}_2 < 0 \quad \left(\frac{\mathrm{d}a}{\mathrm{d}s} > 1\right) \tag{5.200a}$$

$$\frac{\mathrm{d}v_2}{\mathrm{d}s} = \alpha - \left(1 - \frac{\mathrm{d}a}{\mathrm{d}s}\right)\frac{v_2}{\sigma} \tag{5.200b}$$

$$\bar{x}_2 = s - a \tag{5.200c}$$

$$\bar{y}_{c2} = -s\alpha + v_2 \tag{5.200d}$$

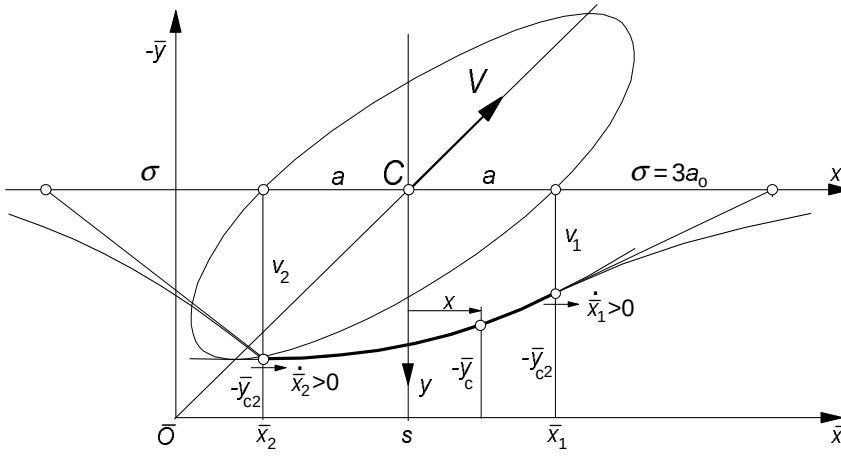

Fig. 5.47. On the development of the contact line of the bare string model.

loss of contact at leading edge:

$$\dot{\bar{x}}_1 < 0 \quad \left(\frac{\mathrm{d}a}{\mathrm{d}s} < -1\right) \tag{5.201a}$$

$$\bar{y}_{c1} = \bar{y}_c(\bar{x} = s + a) \tag{5.201b}$$

$$v_1 = s\alpha + \bar{y}_{c1} \tag{5.201c}$$

loss of contact at trailing edge:

$$\dot{\bar{x}}_2 > 0 \quad \left(\frac{\mathrm{d}a}{\mathrm{d}s} < 1\right) \tag{5.202a}$$

$$\bar{y}_{c2} = \bar{y}_c(\bar{x} = s - a) \tag{5.202b}$$

$$v_2 = s\alpha + \bar{y}_{c2} \tag{5.202c}$$

Solutions of the above equations show considerable differences from the results obtained using the more advanced model with tread elements. The most important difference is the fact that with the simple model the lateral force does not gradually drop to zero as the tyre leaves the ground.

In order to get better agreement, we will introduce a non-constant relaxation length $\sigma = \sigma^*(a)$ that is a function of the contact length $2a$ and thus of the vertical load. We take σ^* equal to the relaxation length of the more advanced model according to Eq.(5.171). Figure 5.48 presents the variation of relaxation length and contact length as a function of the vertical load as calculated for the current parameter values (5.198).

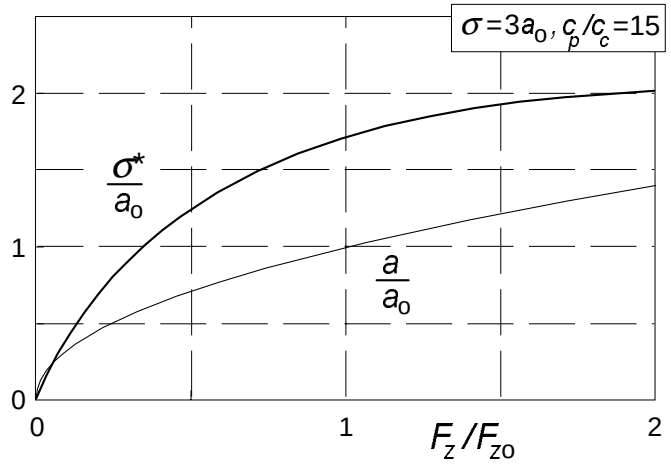

Fig. 5.48. The calculated variation of half the contact length and the relaxation length as a ratio to the static half contact length versus the vertical load ratio for the model with tread elements using Eq.(5.171).

In Fig.5.49 a comparison is made between the results of the three models: without tread elements, with tread elements (exact) and according to the approximation with varying $\sigma=\sigma^*(a)$. The calculations have been carried out for the parameter values (5.198). The approximate path of contact points shows good agreement with the path for the exact model with tread elements. When the tread elements are omitted we have the bare string model for which the path becomes wider and the lateral deflections greater.

5.6.3. The Force and Moment Response

The lateral force F_y and the moment M_z which act on the tyre can be assessed with good approximation through the following simplified formulae. In their derivations we have replaced the contact line by the straight line connecting the beginning and end points of the contact line (Von Schlippe's approach). For the model with tread rubber elements we obtain:

$$F_y = \frac{2c_c c_p}{c_c + c_p}\{a + \sigma A(a)\}\, v_0 \tag{5.203}$$

$$M_z = -\frac{2c_c c_p a}{c_c + c_p}\{\tfrac{1}{3}a^2 + \sigma(\sigma + a)C(a)\}\, \alpha_0 \tag{5.204}$$

and for the model without tread elements:

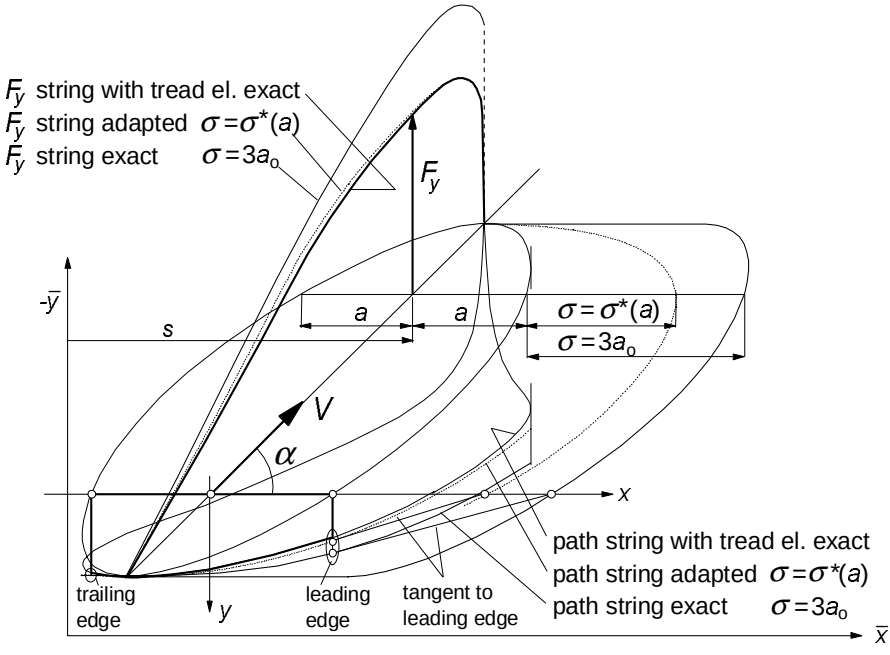

Fig. 5.49. Paths of contact points and variations of the side force according to three models.

$$F_y = 2c_c(a+\sigma)\,v_0 \tag{5.205}$$

$$M_z = -2c_c a\{\tfrac{1}{3}a^2+\sigma(\sigma+a)\}\,\alpha_0 \tag{5.206}$$

In these expressions the following quantities have been introduced:

$$v_0 = \tfrac{1}{2}(v_1+v_2), \quad \alpha_0 = \tfrac{1}{2}(v_1-v_2)/a \tag{5.207}$$

and

$$C(a) = A(a) - \frac{\sigma}{a}\varepsilon B^*(a) + \left(2+\frac{\sigma}{a}\right)\varepsilon B(a) \tag{5.208}$$

in which A, B and B^* are given by expressions (5.189-192).

For the sake of completeness the formulae for the moment have been added. However, we will restrict ourselves to the discussion of the variation of the force. For the three models considered, the variation of the cornering force has been shown in the same Fig.5.49. As expected, the approximate and exact theories drop to zero at the point of lift-off, whereas the force acting on the simple string model remains finite, at least under the here assumed condition of no sliding. The correspondence between exact and approximate solutions of the path and of the side force are satisfactory, and we will henceforth use the approximate method

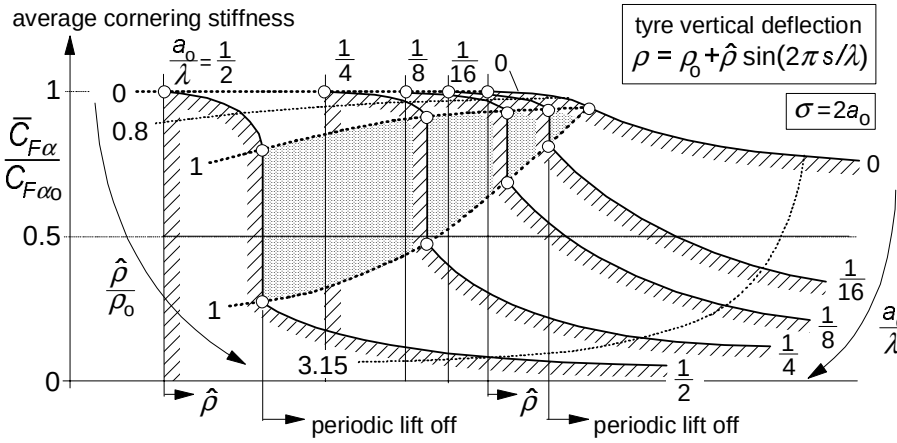

Fig. 5.50. Computed variation of average cornering stiffness with amplitude of the vertical tyre deflection, ρ, and path frequency, $1/\lambda$, for the bare string model.

according to the adapted bare string model for the investigation of the model with tread elements.

For a series of amplitudes $\hat{\rho}$ and wavelengths λ, the variation of the cornering force, or rather of the cornering stiffness, has been calculated. Since during loss of contact the vertical load remains zero, the period of the total loading cycle must become longer in order to keep the average vertical load unchanged. This change in period has been taken into account in the calculation of the average side force or cornering stiffness $\bar{C}_{F\alpha}$.

Figures 5.50 and 5.51 show the final result of this investigation, viz. the

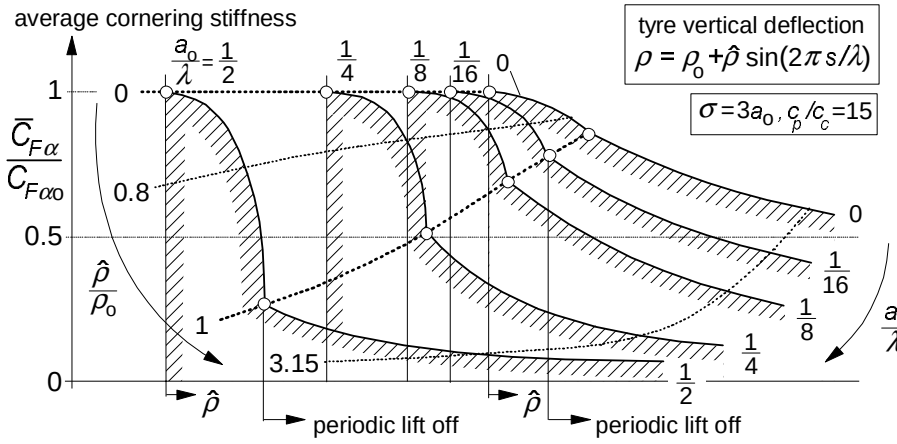

Fig. 5.51. Computed variation of average cornering stiffness with amplitude of the vertical tyre deflection (ρ) and path frequency ($1/\lambda$) using the adapted bare string model that approximates the string model with tread elements.

cornering stiffness averaged over one complete loading cycle as a function of the vertical deflection amplitude $\hat{\rho}$ and the path wavelength λ for both models with and without tread elements, that is: with the adapted bare string model and with the original bare string model. With the parameter values $\sigma = 3a_o$ and $c_p = 15c_c$ the relaxation length of the more advanced model with tread elements at the static load becomes $\sigma_o^* = 1.7a_o$. For the model without tread rubber the relaxation length has been taken equal to $\sigma = 2a_o$.

The figures clearly illustrate the unfavourable effect of increasing the amplitude $\hat{\rho}$ and the path frequency (decreasing the wavelength λ). The curve at zero path frequency is purely due to the non-linear variation of the cornering stiffness $C_{F\alpha}$ versus vertical load F_z shown in Fig.5.32 (cf. Fig.1.3 and discussion on the effect of load transfer in Chapter 1, Fig.1.7) and reflects the 'static' drop in average cornering stiffness. A pronounced difference between the response of both types of models is the sudden drop in average cornering stiffness that shows up in the curves of the bare string model when the frequency is larger than zero and the deflection amplitude reaches the value of the static deflection. This is in contrast to the gradual variation in average cornering stiffness which is observed to occur with the more advanced model, and no doubt also with the real tyre. Furthermore, the more advanced model with tread elements, already shows a noticeable decrease in average cornering stiffness before the tyre starts to periodically leave the ground. The 'dynamic' drop is represented by the dotted curves along which the path frequency changes and the deflection amplitude remains the same. The very low level to which the average stiffness is reduced, once loss of contact occurs, is of the same order of magnitude for both tyre models.

Chapter 6

THEORY OF THE WHEEL SHIMMY PHENOMENON

6.1. Introduction

As an application of the theory developed in the previous chapter we will study the self-excited oscillatory motion of a wheel about (an almost) vertical steering axis. This type of unstable motion is usually designated as the wheel shimmy oscillation. Shimmy is a violent and possibly dangerous vibration that may occur with front wheels of an automobile and with aircraft landing gears. Wobble of the front wheel of a motorcycle is an oscillatory unstable mode similar to shimmy. This steering vibration will be discussed in Chapter 10.

To investigate the shimmy phenomenon, the boundary of stability is established for system models of different degrees of complexity and we will examine the effect of employing different tyre models. The linear stability analysis is extended to non-linear systems which enables us to determine the limit of the shimmy amplitude (limit-cycle) and the magnitude of initial disturbance or unbalance to initiate the self-excited oscillation. Much of the contents of the present chapter is based on the work of Von Schlippe and Dietrich (1941), Pacejka (1966,81) and Besselink (2000).

Fromm, cf. Becker, Fromm and Maruhn (1931) is one of the first investigators who developed a theory for the shimmy motion of automobiles. Besides his advanced theoretical work, as a result of which the gyroscopic coupling between the angular motions about the longitudinal axis and about the steering axis was found to be the main factor causing shimmy, he has carried out and described, together with his co-workers Becker and Maruhn, some tests on a system with a rigid front axle. Also Den Hartog (1940) and Rocard (1949) have treated this 'gyroscopic' shimmy for systems with live axles. The phenomenon was experimentally examined by Olley (1947).

Another kind of shimmy is closely related to tyre and suspension lateral compliance and has been observed to occur with aircraft landing gears and automobiles equipped with independent front wheel suspensions. Many of the authors mentioned in connection with the development of non-steady-state out-

of-plane tyre models in Chapter 5 have used their model in connection with the analysis of the shimmy problem.

6.2. The Simple Trailing Wheel System with Yaw Degree of Freedom

First, the simplest system that can generate shimmy will be discussed. Consider the trailing wheel system depicted in Fig.6.1. The vertical swivel axis moves along the $\bar{x}$ axis with speed V. The motion variable is the yaw angle ψ of the wheel plane about the swivel axis. This axis intersects the road plane at a distance e (mechanical trail or caster length) in front of the contact centre. The system is provided with a rotation damper with viscous damping coefficient k and possibly with a torsional spring with stiffness c_ψ. The moment of inertia about the swivel axis is denoted with I. This quantity varies with caster length e. However, we may consider a constant value of I if caster is accomplished by inclining the swivel axis about the wheel spin axis. If the caster angle remains relatively small, the camber angle that arises through steering may be neglected and the equations assuming a vertical axis will hold with good approximation.

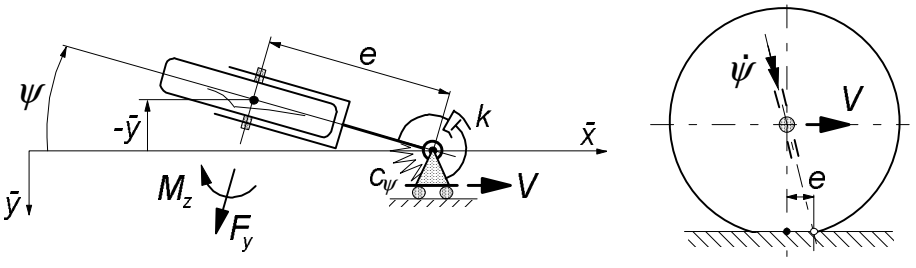

Fig. 6.1. Simple trailing wheel system that is capable of showing shimmy. Two ways of realising the mechanical caster length e of the contact centre with respect to the steering axis (king-pin) have been indicated.

The tyre will be considered massless and the contact line is approximated by a straight line tangent to the actual contact line at the leading edge (straight tangent approximation) for which the Eqs.(5.125-127) hold or by a single point, Eqs.(130-132), with and without the effect of tread width. The results will be compared with those obtained when using the almost exact Von Schlippe tyre model. We have the equations:

$$I\ddot{\psi} + k\dot{\psi} + c_{\psi}\psi = -F_y e + M_z \tag{6.1}$$

$$F_y = C_{F\alpha}\alpha' \tag{6.2}$$

$$M_z = M_z' + M_z^* \tag{6.3}$$

$$M_z' = -C_{M\alpha}\alpha' \tag{6.4}$$

$$M_z^* = -\kappa^* \frac{\mathrm{d}\psi}{\mathrm{d}s} \tag{6.5}$$

$$\alpha' = \frac{v_1}{\sigma} \tag{6.6}$$

$$\frac{\mathrm{d}v_1}{\mathrm{d}s} + \frac{v_1}{\sigma} = \psi - a\frac{\mathrm{d}\psi}{\mathrm{d}s} - \frac{\mathrm{d}\bar{y}}{\mathrm{d}s} \tag{6.7}$$

$$s = \bar{x} = Vt \tag{6.8}$$

$$\bar{y} = -e\psi \tag{6.9}$$

where $a=0$ when the single contact point tyre model is considered. To reduce the number of governing system parameters we will introduce the following non-dimensional quantities with the reference length a_o representing the actual or the nominal half contact length:

$$\underline{a} = \frac{a}{a_o},\ \underline{s} = \frac{s}{a_o},\ \underline{e} = \frac{e}{a_o},\ \underline{t} = \frac{C_{M\alpha}}{a_o C_{F\alpha}},\ \underline{\sigma} = \frac{\sigma}{a_o},\ \underline{v}_1 = \frac{v_1}{a_o},\ \underline{\omega}_s = \omega_s a_o$$

$$\underline{V} = V\sqrt{\frac{I}{C_{F\alpha}a_o^3}},\ \underline{\kappa}^* = \frac{\kappa^*}{C_{F\alpha}a_o^2} = \frac{\kappa^*\underline{t}}{C_{M\alpha}a_o},\ \underline{k} = \frac{k}{\sqrt{IC_{F\alpha}a_o}},\ \underline{c}_{\psi} = \frac{c_{\psi}}{C_{F\alpha}a_o} \tag{6.10}$$

which includes the non-dimensional pneumatic trail $\underline{t} = t/a_o$. After elimination of the time and all the variables except ψ and v_1 in Eqs.(6.1-9) and using the conversions (6.10) we obtain the non-dimensional differential equations:

$$\begin{aligned} &\underline{V}^2\frac{\mathrm{d}^2\psi}{\mathrm{d}\underline{s}^2} + (\underline{k}\underline{V} + \underline{\kappa}^*)\frac{\mathrm{d}\psi}{\mathrm{d}\underline{s}} + \underline{c}_{\psi}\psi + (\underline{e} + \underline{t})\frac{\underline{v}_1}{\underline{\sigma}} = 0 \\ &\frac{\mathrm{d}\underline{v}_1}{\mathrm{d}\underline{s}} + \frac{\underline{v}_1}{\underline{\sigma}} = (\underline{e} - \underline{a})\frac{\mathrm{d}\psi}{\mathrm{d}\underline{s}} + \psi \end{aligned} \tag{6.11}$$

The system is linear and of the third order. It is assumed that the tyre deflection relaxation length $\sigma = 3a$ or non-dimensionally: $\underline{\sigma} = 3$. In case of the single contact point tyre model $\underline{a}$ must be taken equal to zero and σ must be given the value of $\sigma + a = 4a$. In the non-dimensional notation $\underline{\sigma}$ takes the value of $\underline{\sigma} + \underline{a} = \underline{\sigma} + 1 = 4$. For the pneumatic trail we assume $t = 0.5a$ or $\underline{t} = 0.5$.

The characteristic equation of system (6.11) becomes:

$$\begin{vmatrix} \underline{V}^2 p^2 + (\underline{k}\underline{V} + \underline{\kappa}^*)p + \underline{c}_\psi & \underline{e} + \underline{t} \\ (\underline{e} - \underline{a})p + 1 & -(\underline{\sigma} p + 1) \end{vmatrix} = 0 \tag{6.12}$$

or

$$\begin{aligned} &\underline{\sigma}\underline{V}^2 p^3 + \{\underline{V}^2 + \underline{\sigma}(\underline{k}\underline{V} + \underline{\kappa}^*)\}p^2 + \\ &\quad + \{\underline{k}\underline{V} + \underline{\kappa}^* + \underline{\sigma}\underline{c}_\psi + (\underline{e} + \underline{t})(\underline{e} - \underline{a})\}p + \underline{e} + \underline{t} + \underline{c}_\psi = 0 \end{aligned} \tag{6.13}$$

In general we may write:

$$a_0 p^3 + a_1 p^2 + a_2 p + a_3 = 0 \tag{6.14}$$

According to the criterium of Hurwitz the conditions for stability of the motion of the third-order system read:

- all coefficients a_i of the characteristic equation must be positive:

$$a_0 > 0\,,\ a_1 > 0\,,\ a_2 > 0\,,\ a_3 > 0 \tag{6.15}$$

- the Hurwitz determinants H_{n-1}, H_{n-3} etc. must be positive, which yields for the third order ($n = 3$) system:

$$H_2 = \begin{vmatrix} a_1 & a_0 \\ a_3 & a_2 \end{vmatrix} > 0 \tag{6.16}$$

The first two coefficients of Eq.(6.13) are always positive. For the remaining coefficients the conditions for stability become:

$$a_2 = \underline{k}\underline{V} + \underline{\kappa}^* + \underline{\sigma}\underline{c}_\psi + (\underline{e} + \underline{t})(\underline{e} - \underline{a}) > 0 \tag{6.17}$$

$$a_3 = \underline{e} + \underline{t} + \underline{c}_\psi > 0 \tag{6.18}$$

while according to (6.16):

$$H_2 = a_2\{\underline{V}^2 + \underline{\sigma}(\underline{k}\underline{V} + \underline{\kappa}^*)\} - \underline{\sigma}\underline{V}^2(\underline{e} + \underline{t} + \underline{c}_\psi) > 0 \tag{6.19}$$

It can be easily seen that, if the last two conditions are satisfied, the first one is satisfied automatically. If the condition $a_n = a_3 > 0$ is the first to be violated then the motion turns into a monotonous unstable motion (divergent instability that is: without oscillations). Consequently, if $\underline{e} < -(\underline{t} + \underline{c}_\psi)$ meaning that the steering axis lies a distance $-e$ behind the contact centre that is larger than $t + c_\psi/C_{F\alpha}$, the wheel swings around over 180 degrees to the new stable situation. If $H_{n-1} = H_2$ is the first to become negative, the motion becomes oscillatorily unstable. The boundaries of the two unstable areas are: $a_3 = 0$ and $H_2 = 0$.

In the case of vanishing damping ($k = \kappa^* = 0$) condition (6.19) reduces to:

$$(\underline{e} + \underline{t})(\underline{e} - \underline{a} - \underline{\sigma}) > 0 \tag{6.20}$$

Apparently, in the ($\underline{e}$, $\underline{V}$) parameter plane the boundaries of (6.19) reduce to two parallel lines at $\underline{e} = \underline{\sigma} + \underline{a}$ and $\underline{e} = -\underline{t}$. When the caster lies in between these two values the yaw angle performs an oscillation with exponentially increasing amplitude at any speed of travel. Apparently, when the damping is zero, the speed and the torsional stiffness do not influence the extent of the unstable area. They will, however, change the degree of instability and the natural frequency (eigenvalues).

If we have damping, the limit situation may be considered where the speed V tends to zero. The condition for stability then becomes:

$$\underline{\kappa}^* + \underline{\sigma}\underline{c}_\psi + (\underline{e} + \underline{t})(\underline{e} - \underline{a}) > 0 \tag{6.21}$$

which shows that the values for $\underline{e}$ become complex if $\underline{\sigma}\underline{c}_\psi + \underline{\kappa}^* > \frac{1}{4}(\underline{t} - \underline{a})^2 + \underline{t}\,\underline{a}$. This implies that in that case the unstable area becomes detached from the $\underline{e}$ axis.

In Fig.6.2 the unstable areas have been shown for different values of the viscous steer damping $\underline{k}$ and with steer stiffness $\underline{c}_\psi = 0$. Damping reduces the size of the unstable area and pushes the extreme right-hand edge to lower values of speed. The curves resulting from the application of the straight tangent and the single contact point tyre model approximations have been displayed together with the shaded curves representing the boundaries according to the almost exact Von Schlippe approximation. For a more detailed study of the situation at small values of $\underline{V}$ (<ca. 2) where at very low damping alternative stable and unstable ranges appear to arise when the exact theory is applied, we refer to Stepan (1997).

Appreciable deviations appear to occur at low values of speed $\underline{V}$ where the path frequency $\underline{\omega}_s$ is relatively high and thus the wavelength λ relatively short. This is in accordance with findings in Fig.5.23-27 where the frequency response

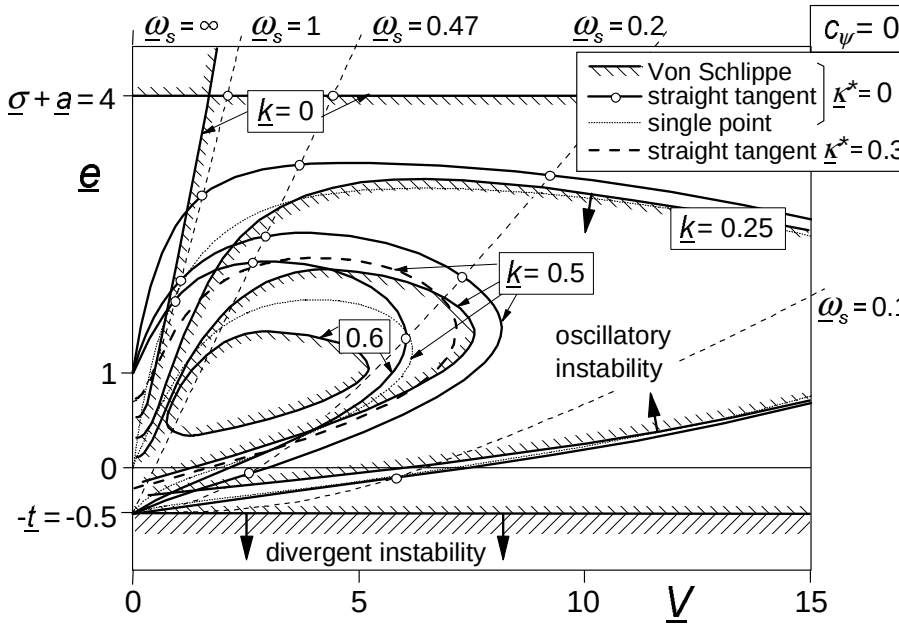

Fig. 6.2. Areas of instability for the trailing wheel system of Fig.6.1 without steer stiffness at different levels of viscous steer damping. Consequences of using different tyre models can be observed.

functions according to various approximations have been compared. The straight tangent approximation shows a tendency to predict a shimmy instability that is somewhat too strong. On the other hand, the single point contact model turns out to be too stable: for $\underline{k} = 0.6$ the unstable area vanishes all together. When employing the straight tangent approximation we at least appear to be on the safe side. For the case $\underline{k} = 0.5$ a curve has been added in Fig.6.2 to show the effect of artificially introducing a proper value of $\underline{\kappa}^*$ to improve the performance of the straight tangent model. The value $\kappa^* = C_{M\varphi} = 0.6aC_{M\alpha}$ that corresponds to $\underline{\kappa}^* = 0.3$ indeed produces a better result. This is in accordance with the curve added in the Nyquist diagram of Fig.5.27 for $C_{M\varphi} = 0.6\,aC_{M\alpha}$ that shows an improved aligning torque frequency response.

The non-dimensional path frequencies shown in the figure occur on the boundaries computed for the system with straight tangent approximation. Here the motion shows an undamped oscillation. Then, the solution of (6.13) contains a pair of purely imaginary roots. By replacing p by $i\underline{\omega}_s$ in the characteristic equation and then separating the imaginary and the real terms we get two equations which can be reduced to one by eliminating the total damping coefficient $\underline{k}\ \underline{V} + \underline{\kappa}^*$. The resulting relationship between $\underline{V}$ and $\underline{e}$ has been shown for a

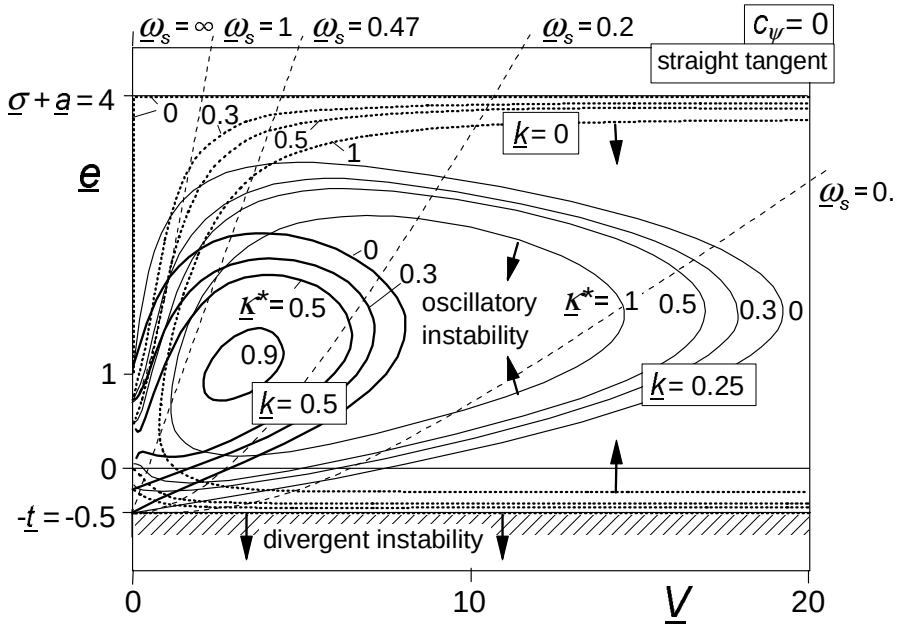

Fig. 6.3. Areas of instability for the trailing wheel system of Fig.6.1 without steer stiffness. Influence of tread width damping at different levels of viscous steer damping.

number of values of $\underline{\omega}_s$. At path frequency $\underline{\omega}_s = 1/\sqrt{\{\underline{\sigma}(1+\underline{t})\}} = 0.47$ a special case arises where the frequency curve reduces to a straight line originating from $(0,-\underline{t})$. By using one of the two equations, an expression for the non-dimensional path frequency may be obtained:

$$\underline{\omega}_s^2 = \frac{a_3}{a_1} = \frac{\underline{e} + \underline{t} + \underline{c}_\psi}{\underline{V}^2 + \underline{\sigma}\,(\underline{k}\underline{V} + \underline{\kappa}^*)} \tag{6.22}$$

Figure 6.3 presents the diagram indicating the influence of damping due to tread width κ^*. This type of damping is especially effective at low speed. This is understandable because we have seen that the equivalent viscous damping coefficient decreases inversely proportionally with the forward velocity. The boundaries now have a chance to become closed at the left-hand side, cf. Eq.(6.21).

As Fig.6.4 depicts, the steer torsional stiffness reduces the unstable shimmy area in size especially when sufficient damping is provided. At vanishing damping, the area of oscillatory instability appears to remain limited by the horizontal lines obtained from (6.20). The area of divergent instability is reduced through the restoring action of the torsional spring about the steering axis. Its

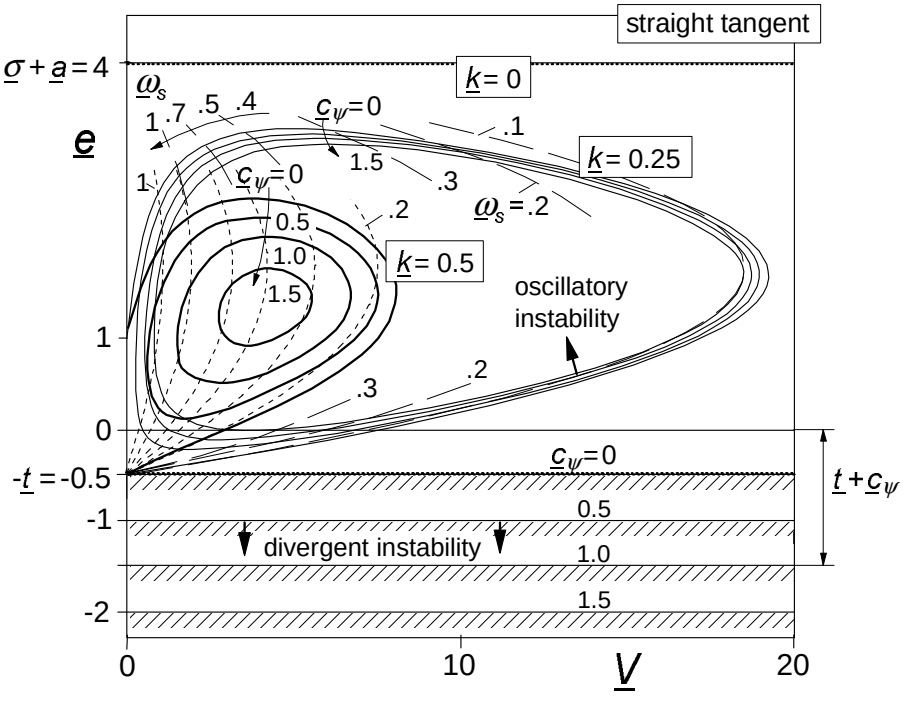

Fig. 6.4. Influence of steer stiffness c_ψ on shimmy instability and on divergent instability at different levels of steer damping without tread width damping.

upper boundary shifts downwards according to the negative trail $-\underline{e} = \underline{t} + \underline{c}_\psi$.

The influence of tyre inertia has not been indicated in the diagrams. As may be expected from the diagram of Fig.5.38, that shows that the phase lag of the moment response is reduced through the action of the gyroscopic couple $M_{z,gyr}$ especially at higher speeds, the area becomes limited at the right-hand side even in the absence of damping. Exercise 6.1 given below addresses this problem.

If the moment of inertia about the steering axis can not be considered as a constant but rather as a function of the trail e, e.g. replace I by $I_z + me^2$, then, considering the non-dimensionalisation defined by (6.10), the curves of the various diagrams must be reinterpreted: at a constant $\underline{k}$ the actual damping coefficient k is not a constant along the curve but increases with increasing $\underline{e}$ while at a given $\underline{V}$ the actual speed V deminishes at increasing $\underline{e}$.

Example

Consider the system with parameters:

$a = a_o = 0.14$ m, $\underline{t} = 0.5$, $\underline{\sigma} = 3$, $\underline{e} = 0$,
$I = 5.4$ kgm^2 , $C_{F\alpha} = 70000$ N/rad, $\underline{\kappa}^* = 0.25\,\underline{t} = 0.125$.

Speed of travel:

$$\underline{V} = V\sqrt{\frac{I}{C_{F\alpha}a^3}} \rightarrow V = 6\,\underline{V} \quad [\text{m/s}] = 21\,\underline{V} \quad [\text{km/h}]$$

Shimmy wavelength:

$\underline{\omega}_s = a\omega_s \rightarrow \omega_s = 7.14\,\underline{\omega}_s$ [rad/m]
$\lambda = 2\pi/\omega_s = 0.88/\underline{\omega}_s$ [m]

so that at

$\underline{\omega}_s = 0.3 \rightarrow \lambda = 2.9\text{m} = 21\,a$

and at

$\underline{\omega}_s = 0.1 \rightarrow \lambda = 8.8\text{m} = 63\,a$

Shimmy frequency:

$\omega = \omega_s V$ [rad/s]
$n = V/\lambda = \omega/(2\pi)$ [Hz]

at $\underline{V} = 5.6$ we have V=33 m/s and according to the stability graph of Fig.6.3 ($\underline{c}_\psi$=0) we have at this speed and caster $e = 0$ a non-dimensional path frequency $\underline{\omega}_s \approx 0.12$ so that $\omega_s \approx 0.85$ rad/m, $\lambda \approx 7.3$m, $\omega \approx 28$ rad/s and $n \approx 4.5$ Hz. This would be the case at the boundary of stability where $\underline{k} \approx 0.25$ with $\underline{\kappa}^* = 0.3$. At about the same point in the diagram of Fig.6.4 we would have with a non-dimensional steer stiffness $\underline{c}_\psi = 1$ and damping coefficient $\underline{k} = 0.25$ a non-dimensional path frequency $\underline{\omega}_s \approx 0.2$ which yields $\omega_s \approx 1.4$ rad/m, a wavelength $\lambda \approx 4.4$m and a frequency $n \approx 7.5$ Hz.

Exercise 6.1. Influence of the tyre mass on the stability boundary

Consider the wheel system of Fig.6.1. Derive the stability conditions for this system with the inclusion of the effect of tyre inertia approximated by the introduction of $M_{z,gyr}$ (5.178). In non-dimensional form the gyroscopic couple becomes

$$\underline{M}_{z,gyr} = \frac{M_{z,gyr}}{C_{F\alpha}a} = -\underline{C}_{gyr}\underline{V}^2\frac{\mathrm{d}\underline{F}_y}{\mathrm{d}\underline{s}} \tag{6.23}$$

with

$$\underline{C}_{gyr} = C_{gyr}\frac{aC_{F\alpha}}{I} = c_{gyr}\frac{m_t}{C_{Fy}}\frac{aC_{F\alpha}}{I} = c_{gyr}\frac{m_t}{I}a(\sigma + a) \tag{6.24}$$

cf. Eqs.(5.59,60) and (5.179).

Determine how the stability boundaries for the system without damping ($\kappa^* = k = c_\psi = 0$) are changed due to the inclusion of the gyroscopic couple. Consider the following parameter values

$$\underline{t} = 0.5, \quad \underline{\sigma} = 3, \quad \underline{C}_{gyr} = 0.04$$

Draw in the ($\underline{e}$, $\underline{V}$) diagram the boundaries for $C_{gyr} = 0$ and sketch the new stability boundary by calculating at least the boundary values for $\underline{V}$ at $\underline{e} = -\underline{t}$, $\underline{e} = 0$ and $\underline{e} = 1$ and moreover the boundary on the $\underline{e}$-axis. Indicate where the system is stable.

6.3. Systems with Yaw and Lateral Degrees of Freedom

The additional degree of freedom that allows the king-pin to move sideways, leads to a system which is of the fifth order. Figure 6.5 depicts the system with lateral compliance of the wheel suspension possibly associated with a torsional (camber) compliance with (virtual) axis of rotation assumed to be located at a height h above the ground (right-hand diagram). The inertia of the system (m, I_z) may be represented by two point masses m_A and m_B and a residual moment of inertia I^* about the vertical axis. The two mass points are connected by a massless rod with length e, and are located on the wheel axis and the steer axis respectively. Lateral damping will not be considered.

The following set of equations hold for the dynamics of the system of Fig.6.5 assuming a vertical steering axis and adopting the straight tangent tyre model, Eq.(5.125-127,6.7):

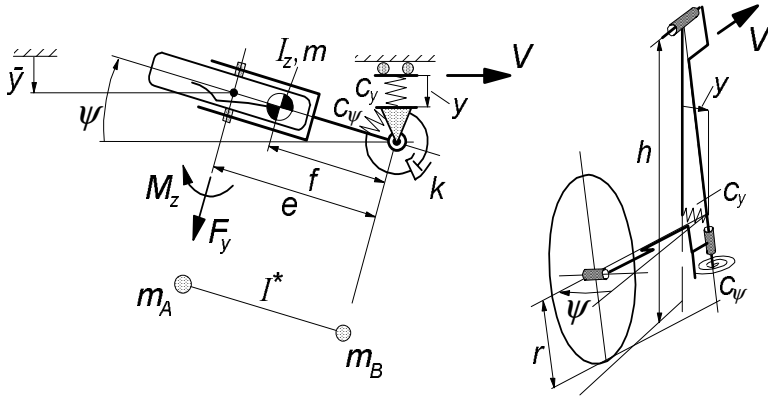

Fig. 6.5. Lateral compliance introduced in the system.

$$-m_A(e\ddot{\psi}-\ddot{y}) + m_B\ddot{y} + c_y y = F_y \tag{6.25}$$

$$m_A e(e\ddot{\psi}-\ddot{y}) + I^*\ddot{\psi} + k\dot{\psi} + c_\psi \psi = -F_y e + M_z \tag{6.26}$$

$$F_y = C_{F\alpha}\alpha' \tag{6.2}$$

$$M_z = M_z' + M_z^* \tag{6.3}$$

$$M_z' = -C_{M\alpha}\alpha' \tag{6.4}$$

$$M_z^* = -\kappa^* \frac{\mathrm{d}\psi}{\mathrm{d}s} \tag{6.5}$$

$$\alpha' = \frac{v_1}{\sigma} \tag{6.6}$$

$$\frac{\mathrm{d}v_1}{\mathrm{d}s} + \frac{v_1}{\sigma} = \alpha - a\frac{\mathrm{d}\psi}{\mathrm{d}s} \tag{6.27}$$

$$s = \bar{x} = Vt \tag{6.8}$$

where the slip angle α is obtained from:

$$\alpha = \psi - \frac{1}{V}(\dot{y} - e\dot{\psi}) \tag{6.28}$$

Before further studying the fifth-order system let us try to reduce the system to a lower order while retaining the lateral compliance.

Yaw and lateral degrees of freedom with rigid wheel/tyre (third order)

It can be shown that the lateral compliance of the wheel suspension has an effect that is similar to the effect of tyre lateral compliance. The basic effect of lateral compliance of the suspension may be isolated by considering the wheel and tyre as a rigid disc. As a result, a non-holonomic constraint equation arises that reduces the order of the system to three. Through this first-order differential equation the condition that the wheel is unable to perform lateral slip is obeyed. We obtain the constraint equation from (6.28) with wheel slip angle α forced to be equal to zero:

$$\alpha = \psi - \frac{1}{V}(\dot{y} - e\dot{\psi}) = 0 \tag{6.29}$$

In addition, we assume that for the rigid disc the aligning torque and the contact length vanish:

$$M_z = 0 \ , \quad a = 0 \tag{6.30}$$

After elimination of F_y from the Eqs.(6.25,26) and expressing $\dot{y}$ in terms of ψ and its derivative we find a third-order differential equation. Its characteristic equation with variable s in [rad/s] reads:

$$(I^* + m_B e^2)s^3 + (k + m_B eV)s^2 + (c_\psi + c_y e^2)s + c_y eV = 0 \tag{6.31}$$

The trivial condition against (divergent) instability that results from the last term of (6.31) which must remain positive becomes:

$$e > 0 \tag{6.32}$$

The condition for stability $H_2 > 0$, cf. (6.16), reads:

$$(k + m_B eV)(c_\psi + c_y e^2) > (I^* + m_B e^2)c_y eV \tag{6.33}$$

For the undamped case ($k=0$) this reduces to the simple condition for stability, if $e>0$:

$$m_B c_\psi > I^* c_y \tag{6.34}$$

Apparently, a negative residual moment of inertia ($I^* < 0$) will ensure stability. When f defines the location of the centre of gravity behind the steer axis and i^* denotes the radius of inertia of the combination (m_A, m_B, I^*) or only of the steerable part, a negative residual moment of inertia would occur if $i^{*2} < f(e-f)$. For such a system, an increase of the lateral stiffness strengthens the stability.

If on the other hand $I^* > 0$ a sufficiently large steer stiffness is needed to stabilise the system. It is surprising is that a larger lateral stiffness may then cause the system to become unstable again.

The conclusion that the freely swivelling wheel system (that is: $c_\psi = k = 0$) is stable if the residual moment of inertia $I^* < 0$ entails that when caster is realised by inclining the steering axis backwards (Fig.6.1 right-hand diagram) we have the situation that $m_A = 0$ so that $I^* = I$ which is always positive. Consequently, for such a freely swivelling system equipped with a rigid thin tyre the motion is always oscillatorily unstable.

The fifth-order system

The gyroscopic coupling terms that arise due to the angular camber velocity of the wheel system about the longitudinal axis located at a height h above the ground will be added to the Eqs.(6.25,26). For this, the coefficient β_{gyr} is introduced:

$$\beta_{gyr} = \frac{I_p}{mrh} \tag{6.35}$$

where I_p denotes the polar moment of inertia of the wheel. Furthermore the ratio

of distances with respect to the camber torsion centre is introduced:

$$\zeta_h = \frac{h}{h-r} \tag{6.36}$$

Moreover, to fully account for the effects of the angular displacement about the longitudinal axis, that also arises when steering around an inclined king-pin (to provide caster), one may include the camber force in Eq.(6.2), and the small (negative) stiffness effects resulting from the lateral shift of the normal force F_z. Because of the fact that these effects are relatively small and appear to partly compensate each other we will neglect the extra terms.

The differential equations that result when returning to the set I_z and m that replaces the equivalent set m_A, m_B and I^*, and eliminating all variables except y, ψ and α' read:

$$m(\ddot{y} - f\ddot{\psi}) + k_y\dot{y} + c_y y - m\beta_{gyr}V\dot{\psi} = \zeta_h C_{F\alpha}\alpha' \tag{6.37}$$

$$I_z\ddot{\psi} + (k + \kappa^*/V)\dot{\psi} + c_\psi\psi + m\beta_{gyr}V\dot{y} + fk_y\dot{y} + fc_y y = -C_{F\alpha}(e + t - f)\alpha' \tag{6.38}$$

$$\sigma\dot{\alpha}' + V\alpha' = -\zeta_h\dot{y} + (e - a)\dot{\psi} + V\psi \tag{6.39}$$

In the equations the lateral suspension damping, k_y, has been included. In the further analysis this quantity will be left out of consideration. To study the pure gyroscopic coupling effect, the ratio ζ_h will be taken equal to unity which would represent the case that the centre of gravity and the lateral spring are located at ground level. For the special case that the centre of gravity lies on the (inclined) steer axis, distance $f = 0$, the system description is considerably simplified. Our analysis will mainly be limited to this configuration. Besselink (2000) has carried out an elaborate study on the system of Fig.6.5 with the mass centre located behind the (vertical) steering axis ($f > 0$), even behind the wheel centre ($f > e$). For the complete results of this for aircraft shimmy important analysis we refer to the original publication. One typical result, however, where $f = e$ will be discussed here.

The complete set of non-dimensional quantities, extended and slightly changed with respect to the set defined by Eqs.(6.10), reads:

$$\underline{a} = \frac{a}{a_o},\ \underline{e} = \frac{e}{a_o},\ \underline{f} = \frac{f}{a_o},\ \underline{t} = \frac{C_{M\alpha}}{a_o C_{F\alpha}},\ \underline{\sigma} = \frac{\sigma}{a_o},\ \underline{i}_z = \frac{i_z}{a_o},\ \underline{y} = \frac{y}{a_o},\ \underline{\omega}_s = \omega_s a_o,$$

$$\underline{\kappa}^* = \frac{\kappa^*}{C_{F\alpha}a_o^2} = \frac{\kappa^*\underline{t}}{C_{M\alpha}a_o},\ \underline{k} = \frac{k}{\sqrt{I_z C_{F\alpha}a_o}},\ \underline{c}_\psi = \frac{c_\psi}{C_{F\alpha}a_o},\ \underline{c}_y = \frac{c_y a_o}{C_{F\alpha}},$$

$$\underline{m} = \frac{m a_o^2}{I_z} = \frac{1}{\underline{i}_z^2}\,,\quad \underline{V} = V\sqrt{\frac{I_z}{C_{F\alpha} a_o^3}}\,,\quad \underline{\omega} = \omega\sqrt{\frac{I_z}{C_{F\alpha} a_o}}\,,\quad \underline{s} = s\sqrt{\frac{I_z}{C_{F\alpha} a_o}} \tag{6.40}$$

Here, $\underline{s}$ denotes the non-dimensional Laplace variable. The non-dimensional differential equations follow easily from the original equations (6.37-39). For the stability analysis we need the characteristic equation which reads in non-dimensional form:

$$\underline{a}_0 \underline{s}^5 + \underline{a}_1 \underline{s}^4 + \underline{a}_2 \underline{s}^3 + \underline{a}_3 \underline{s}^2 + \underline{a}_4 \underline{s} + \underline{a}_5 = 0 \tag{6.41}$$

The coefficients of (6.41) with $f = k_y = 0$ are:

$$\begin{aligned}
\underline{a}_0 &= \underline{m}\underline{\sigma} \\
\underline{a}_1 &= \underline{m}\underline{V} + \underline{m}\underline{\sigma}\,(\underline{k} + \underline{\kappa}^*/\underline{V}) \\
\underline{a}_2 &= \underline{m}\underline{\sigma}\underline{c}_\psi + \underline{\sigma}\underline{c}_y + \zeta_h + \underline{m}\,(\underline{e} + \underline{t})(\underline{e} - \underline{a}) + \underline{\sigma}(\underline{m}\beta_{gyr} V)^2 + \underline{m}\,(\underline{k} + \underline{\kappa}^*/\underline{V})\underline{V} \\
\underline{a}_3 &= \underline{m}\underline{c}_\psi\underline{V} + \underline{c}_y\underline{V} + \underline{m}\,(\underline{e}+\underline{t})\underline{V} + (\zeta_h + \underline{\sigma}\underline{c}_y)(\underline{k} + \underline{\kappa}^*/\underline{V}) + \\
&\quad - (\underline{a} + \zeta_h \underline{t} - \underline{m}\beta_{gyr}\underline{V}^2)\underline{m}\beta_{gyr}\underline{V} \\
\underline{a}_4 &= (\underline{\sigma}\underline{c}_y + \zeta_h)\underline{c}_\psi + (\underline{e} + \underline{t})(\underline{e} - \underline{a})\underline{c}_y + \underline{m}\beta_{gyr} V^2 + \underline{c}_y(\underline{k} + \underline{\kappa}^*/\underline{V})\underline{V} \\
\underline{a}_5 &= \underline{c}_y(\underline{c}_\psi + \underline{e} + \underline{t})\underline{V}
\end{aligned} \tag{6.42}$$

The influence of a number of non-dimensional parameters will be investigated by changing their values. The other parameters will be kept fixed. The values of the fixed set of parameters are:

$$\underline{a} = 1\,,\ \underline{\sigma} = 3\,,\ \underline{t} = 0.5\,,\ \underline{m} = 0.5\,,\ \zeta_h = 1 \tag{6.43}$$

For the fifth-order system the Hurwitz conditions for stability read:

- all coefficients $\underline{a}_i$ of the characteristic equation must be positive:

$$\underline{a}_0 > 0\,,\ \underline{a}_1 > 0\,,\ \underline{a}_2 > 0\,,\ \underline{a}_3 > 0\,,\ \underline{a}_4 > 0\,,\ \underline{a}_5 > 0 \tag{6.44}$$

- the Hurwitz determinants $H_{n\text{-}3}$ and $H_{n\text{-}1}$ must be positive, which yields:

$$\underline{H}_2 = \begin{vmatrix} \underline{a}_1 & \underline{a}_0 \\ \underline{a}_3 & \underline{a}_2 \end{vmatrix} > 0\,,\quad \underline{H}_4 = \begin{vmatrix} \underline{a}_1 & \underline{a}_0 & 0 & 0 \\ \underline{a}_3 & \underline{a}_2 & \underline{a}_1 & \underline{a}_0 \\ \underline{a}_5 & \underline{a}_4 & \underline{a}_3 & \underline{a}_2 \\ 0 & 0 & \underline{a}_5 & \underline{a}_4 \end{vmatrix} > 0 \tag{6.45}$$

It turns out that for the case without damping and gyroscopic coupling terms ($k=\kappa^*=\beta_{gyr}=0$), a relatively simple set of analytical expressions can be derived for the conditions of stability. It can be proven that when $\underline{a}_5>0$, $\underline{H}_2>0$, $\underline{H}_4>0$ the other conditions are satisfied as well. Consequently, the governing conditions for stability of the system without damping and gyroscopic coupling read:

$$\frac{\underline{a}_5}{\underline{c}_y \underline{V}} = (\underline{c}_\psi + \underline{e} + \underline{t}) > 0 \tag{6.46}$$

$$\frac{\underline{H}_2}{\underline{m}^2 \underline{V}} = (\underline{e} + \underline{t})(\underline{e} - \underline{a} - \underline{\sigma}) + \frac{1}{\underline{m}} > 0 \tag{6.47}$$

$$\frac{\underline{H}_4}{\underline{m}^3 \underline{V}^2} = (\underline{e} + \underline{t})\left(\underline{c}_\psi - \frac{\underline{c}_y}{\underline{m}}\right)\left\{\left(\underline{c}_\psi - \frac{\underline{c}_y}{\underline{m}}\right)(\underline{e} - \underline{a} - \underline{\sigma}) + \frac{\underline{H}_2}{\underline{m}^2 \underline{V}}\right\} > 0 \tag{6.48}$$

We may ascertain that for the special case of a rigid wheel where $C_{F\alpha} \to \infty$ and $\underline{a}$, $\underline{\sigma}$, $\underline{t} \to 0$ the condition (6.46) corresponds with (6.32) and the condition

$$\underline{c}_\psi - \frac{\underline{c}_y}{\underline{m}} > 0 \tag{6.49}$$

that results from (6.48) corresponds with condition (6.34) if we realise that in the configuration studied here we have: $m_A=0$ and $I^*=I_z$.

For the case with an elastic tyre with stability conditions (6.46-48) we will present stability diagrams and show the effects of changing the stiffnesses. In addition, but then necessarily starting out from Eqs.(6.42,44,45), the influence of the steer and tread damping and that of the gyroscopic coupling terms will be assessed.

First, let us consider the system with lateral suspension compliance but without steer torsional stiffness, $c_\psi=0$, that is: a freely swivelling wheel possibly damped (governed by the combined coefficient $k+\kappa^*/V$) and subjected to the action of the gyroscopic couple (that arises when the lateral deflection is connected with camber distortion as governed by a non-zero coefficient β_{gyr}). From the above conditions it can be shown that for the simple system without damping and camber compliance stability may be achieved only at the academic case of large caster $e>a+\sigma$ when the lateral stiffness of the wheel suspension is sufficiently large:

$$\underline{c}_y > \underline{m}(\underline{e} + \underline{t}) + \frac{1}{\underline{e} - \underline{a} - \underline{\sigma}} \quad \text{while} \quad \underline{e} > \underline{a} + \underline{\sigma} \tag{6.50}$$

The minimum stiffness where stability may occur is:

$$\underline{c}_{y,crit} = \underline{m}(\underline{a} + \underline{\sigma} + \underline{t} + 2\underline{i}_z) \tag{6.51}$$

with i_z representing the radius of inertia:

$$\underline{i}_z^2 = \frac{1}{\underline{m}} = \frac{I_z}{ma^2} \tag{6.52}$$

The value of the caster length e_c where stability commences (at $\underline{c}_{y,crit}$) is:

$$\underline{e}_c = \underline{a} + \underline{\sigma} + \underline{i}_z \tag{6.53}$$

Consequently, it may be concluded that with respect to the third-order system of Fig.6.2 the introduction of lateral suspension compliance shifts the upper boundary of the area of instability to values of caster length e larger than $a+\sigma$. At the same time a new area of instability emerges from above. When the lateral stiffness becomes lower than the critical value (6.51) the stable area vanishes altogether at $e = e_c$.

The case with steer and tread damping shows ranges of stability that vary with speed of travel V. In Fig.6.6 areas of instability have been depicted for different values of the lateral stiffness. The upper left inset illustrates the case without damping. At vanishing lateral stiffness a narrow range of stability appears to remain in the negative trail range with a magnitude smaller than the pneumatic trail $\underline{t}$.

When a finite height h of the longitudinal torsion axis is considered, parameter β_{gyr} defined by (6.35) obtains a value larger than zero. For $\beta_{gyr}=0.2$ the diagram of Fig.6.7 arises. An important phenomenon appears to occur that is essential for this two degree of freedom system (not counting the 'half' degree of freedom stemming from the flexible tyre). A new area of instability appears to show up at higher values of speed. The area increases in size when the lateral (camber) stiffness decreases. At the same time the original area of oscillatory instability shrinks and ultimately vanishes. Around zero caster stable motions appear to become possible for all values of speed when a (near) optimum lateral stiffness is chosen. The high speed shimmy mode exhibits a considerably higher frequency than the one occurring in the lower speed range of instability. This is illustrated by the non-dimensional frequencies indicated for the case $\underline{c}_y=2$ at $\underline{e}=0.5$. The corresponding non-dimensional wavelength $\underline{\lambda}=\lambda/a$ is obtained by using the formula: $\underline{\lambda} = 2\pi\underline{V}/\underline{\omega}$. In Table 6.1 the non-dimensional frequencies $\underline{\omega}$, wavelengths $\underline{\lambda}$, and path frequencies $1/\underline{\lambda} = a/\lambda$ have been presented as computed for the four different values of non-dimensional velocities where the transition from stable to unstable or visa versa occurs. Also, the mode of vibration is quite different for this 'gyroscopic' shimmy exhibiting a considerably larger lateral motion amplitude of the wheel contact centre with respect to the yaw angle

amplitude than in the original 'lateral (tyre) compliance' shimmy mode. To illustrate this, the table shows the ratio of amplitudes of the lateral displacement $\bar{y}$ of the contact centre (cf. Fig.6.5) and the yaw angle multiplied with half the contact length: $a\psi$. For the two lower values of speed the lateral displacement appears to lag behind the yaw angle with about 135° while for the two higher speeds the phase lag amounts to about 90°.

Table 6.1. Non-dimensional frequencies, wavelengths and ratio of amplitudes of lateral displacement $\bar{y}$ at contact centre and yaw angle ψ times half contact length a for speeds at stability boundaries as indicated in Fig.6.7 at trail $\underline{e} = 0.5$.

$\underline{V} = 1.24$	$\underline{\omega} = 0.50$	$\underline{\lambda} = 15.5$	$1/\underline{\lambda} = a/\lambda = 0.065$	$\lvert \bar{y}/a\psi \rvert = 0.45$
4.45	0.84	33.3	0.030	0.14
9.60	2.40	25.2	0.040	2.51
28.50	4.50	39.8	0.025	1.64

Figure 6.8 depicts the special case of vanishing damping for a number of values of the lateral stiffness. At caster near or equal to zero limited ranges of speed with stable motions appear to occur. These speed ranges correspond with the stable ranges in between the unstable areas of Fig.6.7 (if applicable). For the indicated points A and B and for a number of neighbouring points the eigenvalues and eigenvectors have been assessed and shown in Figs.6.22,23 in Section 6.4.1 where the energy flow is studied.

The system will now be provided with torsional steer stiffness c_ψ. For the undamped case the conditions (6.46-6.48) hold to ensure stability. It can be observed that except for the condition (6.46) $\underline{c}_\psi$ appears in combination with $\underline{c}_y$ in the factor $\underline{c}_\psi - \underline{c}_y/\underline{m}$. We may introduce an effective yaw stiffness and an effective lateral stiffness:

$$\underline{c}_\psi^* = \underline{c}_\psi - \frac{\underline{c}_y}{\underline{m}} \qquad \text{and} \qquad \underline{c}_y^* = \underline{c}_y - \underline{m}\,\underline{c}_\psi \tag{6.54}$$

and establish a single diagram for the ranges of stability for the two effective stiffnesses as presented in Fig.6.10. The way in which the boundaries are formed may be clarified by the diagram of Fig.6.9. The parabola represents the variation of the second Hurwitz determinant H_2 divided by $\underline{m}^2\underline{V}$, cf. Eq.(6.47), as a function of the caster length $\underline{e}$. This same term also appears in the expression for the fourth Hurwitz determinant H_4 according to (6.48). For both cases $\underline{c}_\psi^* > 0$ and $\underline{c}_y^* > 0$ the straight line originating from the point $(\underline{\sigma} + \underline{a}, 0)$ at a slope $\underline{c}_\psi^*$ and $\underline{c}_y^*/\underline{m}$ respectively have been depicted. The points of intersection with the parabola

correspond to values of $\underline{e}$ where $H_4=0$. Depending on the signs of factor $\underline{e}+\underline{t}$ and of H_2 and a_5 the ranges of stability can be found. Five typical cases A-E have been indicated. They correspond to similar cases indicated in Fig.6.10. Case D at small negative $\underline{e}$ lies inside the small stable triangle of Fig.6.10. Here $\underline{c}_\psi^*>0$, $\underline{e}+\underline{t}>0$ and $H_2/\underline{m}^2\underline{V}>\underline{c}_\psi^*(\underline{\sigma}+\underline{a}-\underline{e})$. Case C shows a range of $\underline{e}$ where $H_4>0$ but at the same time $H_2<0$ so that instability prevails. For larger negative values of the caster stability arises because $\underline{e}+\underline{t}$ changes sign while a_5 remains positive. Also for larger values of $\underline{c}_\psi^*$ a stable area appears to show up for $\underline{e}<-\underline{t}$. For cases like D and E stability occurs for large values of the mechanical trail $\underline{e}$ (not very realistic for our present assumption that $f=0$ which means: c.g. on (inclined) steering axis). In a similar large range of $\underline{e}$ stability occurs for large effective lateral stiffness, e.g. case A. This case has already been referred to previously when discussing the situation without steer stiffness, cf. Fig.6.6 upper left inset, Eq.(6.50). Case B shows instability for all values of $\underline{e}$. As has been indicated in Fig.6.10, we can establish the abscissa $\underline{c}_\psi$ by shifting the vertical axis to the left over a distance $\underline{c}_y/\underline{m}$. At the left of the shifted axis the steer stiffness must be considered equal to zero so that $\underline{c}_y^*=\underline{c}_y$. The stability boundary $a_5=0$ shifts to the left together with the $\underline{c}_\psi=0$ axis.

In Fig.6.11 the diagram of Fig.6.10 is repeated but only for the version with $\underline{c}_\psi$ as abscissa and for one fixed value of $\underline{c}_y$. Figures 6.12 and 13 clearly show the influence of damping. The stable areas increase in size, while the unstable area tends to split itself into two parts, the higher stiffness part of which ($\underline{c}_\psi>\sim\underline{c}_y/\underline{m}$) appears to vanish at sufficient damping. Also in the low yaw stiffness range the instability is suppressed especially in the lower range of speed. For a caster length close to zero it appears possible to achieve stability through adapting the steer stiffness (making it a bit larger than $\underline{c}_y/\underline{m}$, cf. Case D of Fig.6.10) and/or by supplying sufficient damping.

The more complex situation where gyroscopic coupling is included has been considered in Figs.6.14-16. For vanishing steer stiffness, $\underline{c}_\psi\to 0$, the situation of Figs.6.8,7 is reached again. In Fig.6.14 where the damping is zero, the curve at low speed resembles the graph of Fig.6.11. As was observed to occur in the zero yaw stiffness case, we see that in the lower yaw stiffness range ($\underline{c}_\psi<\sim\underline{c}_y/\underline{m}$) an optimum value of the speed appears to exist where the unstable $\underline{e}$ range becomes smallest or vanishes altogether (at sufficient damping). In the higher stiffness range increasing the speed promotes shimmy except in the negative $\underline{e}$ range where the opposite may occur. In this same range of yaw stiffness an increase of the stiffness appears to lower the tendency to shimmy.

Besselink (2000) has analysed the more general and for aircraft landing gears more realistic configuration where the centre of gravity of the swivelling part is located behind the steering axis. Notably, the case where $f=e$ and the peculiar

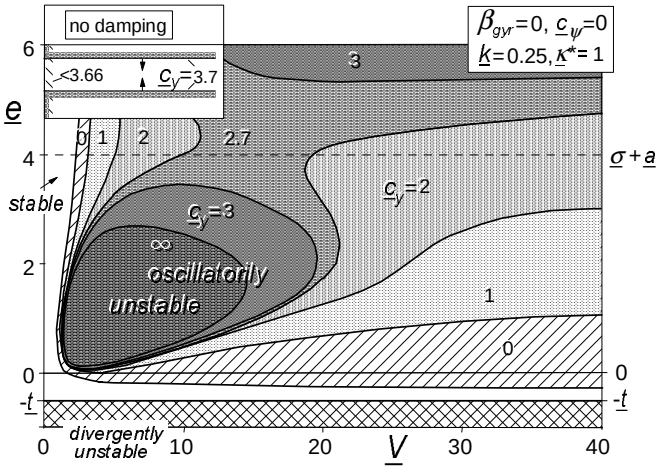

Fig. 6.6. Influence of lateral suspension compliance with non-dimensional stiffness c_y on stability. Gyroscopic couple and steer stiffness not regarded.
Non-dimensional parameters: f = 0, m = 0.5, t = 0.5, σ = 3.

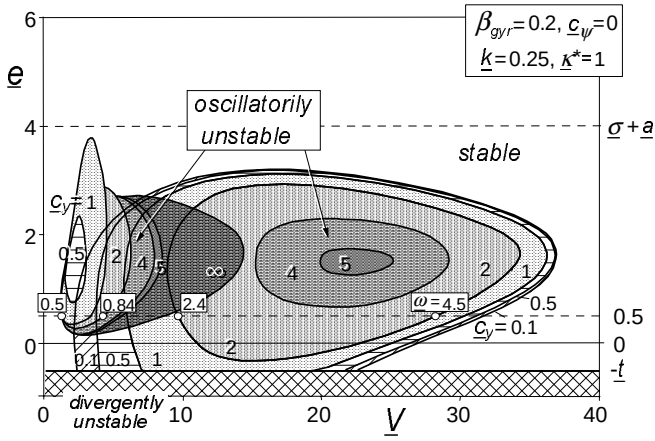

Fig. 6.7. Influence of lateral (camber) suspension compliance with gyroscopic coupling. Steer stiffness is equal to zero.
At increasing compliance 1/ c_y a new area of oscillatory instability shows up while the original area shrinks.
Frequencies have been indicated for the case c_y=2 at e = 0.5.

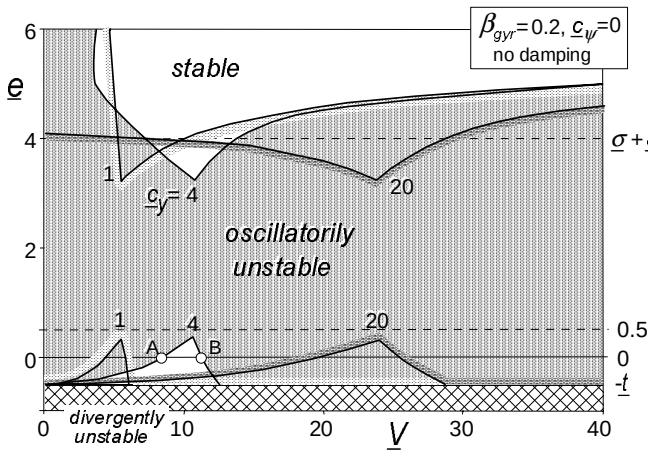

Fig. 6.8. Influence of lateral (camber) suspension compliance with gyroscopic coupling. Steer stiffness is equal to zero. Steer and tread damping equal to zero.
Eigenvalues and eigenvectors of points A and B are analysed in Figs.6.22,23.

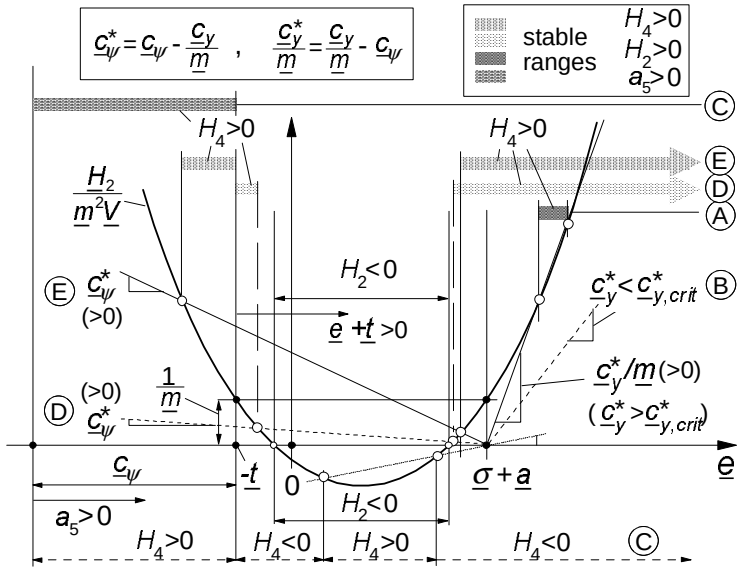

Fig. 6.9. Establishing the ranges of stability using the conditions (6.46-48) which hold for the fifth-order system without damping and gyroscopic coupling. The cases A-E correspond to those indicated in the stability diagram of Fig.6.10.

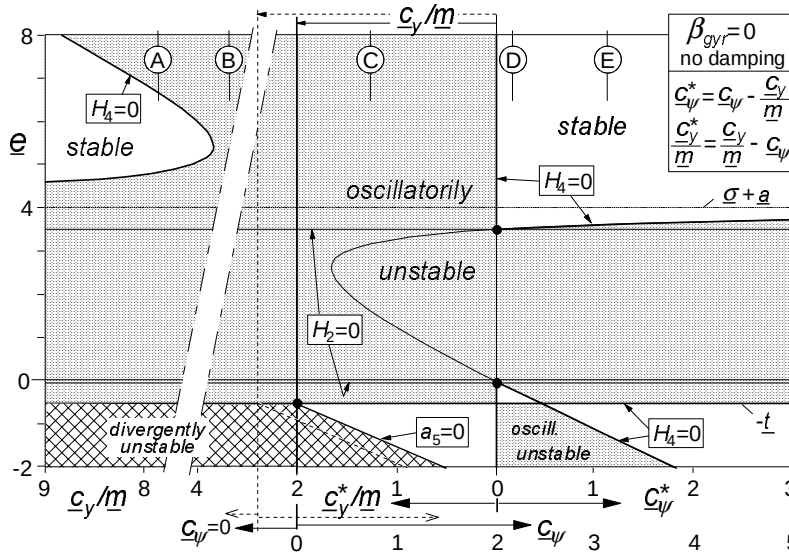

Fig. 6.10. Basic stability diagram according to conditions (6.46-48) for the fifth-order system without damping and gyroscopic coupling. The cases A-E correspond to those indicated in the stability diagram of Fig.6.9. The diagram hold in general, the case with $\underline{c}_y/\underline{m}$=2 is an example, note: $\underline{m}$ = 0.5.

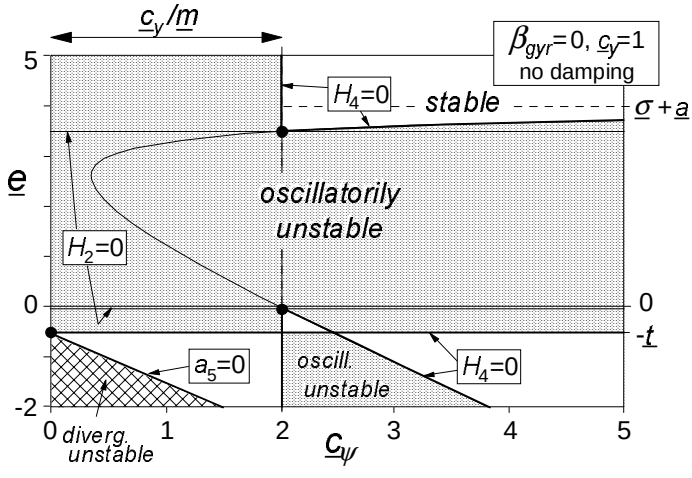

Fig. 6.11. Stability diagram according to Fig.6.10 with steer stiffness along abscissa, at a fixed value of the lateral stiffness, without damping or gyroscopic coupling.

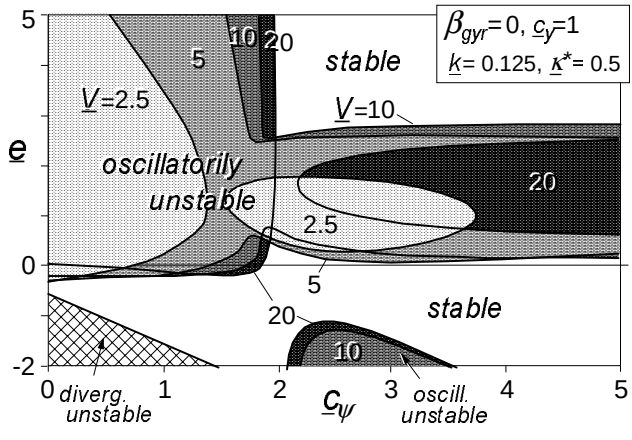

Fig. 6.12. Same as Fig.6.11 but with some damping. Areas of instability at different levels of speed.

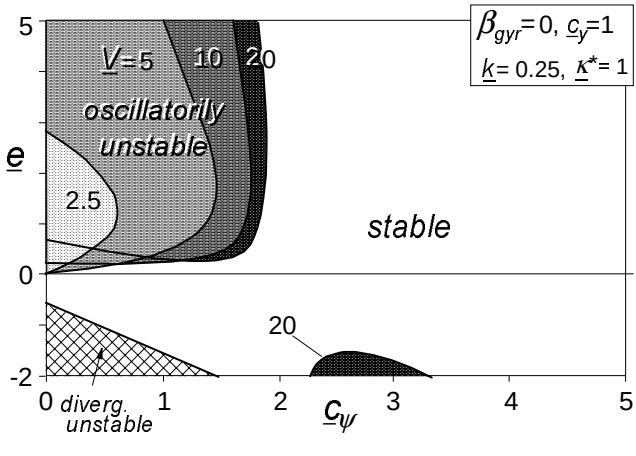

Fig. 6.13. Same as Fig.6.12 but with more damping.

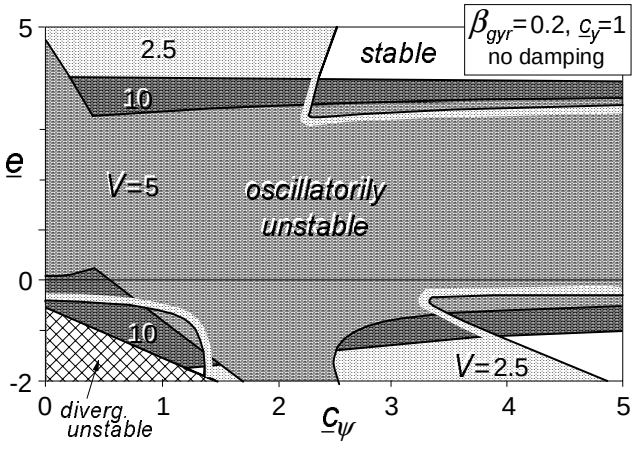

Fig. 6.14. Diagram for the case of Fig.6.11 but with gyroscopic coupling. Areas of instability at different levels of speed.

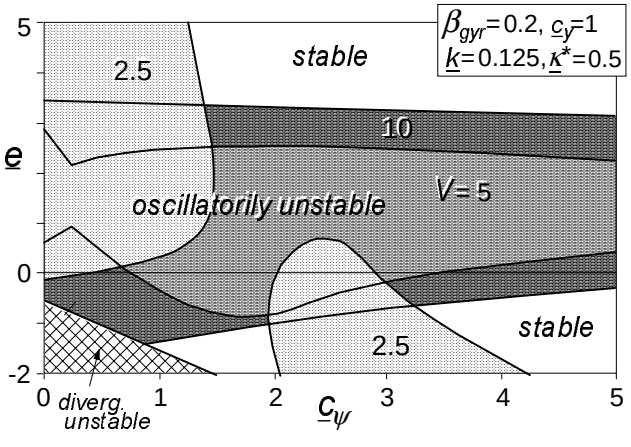

Fig. 6.15. Same as Fig. 6.14 but with some damping

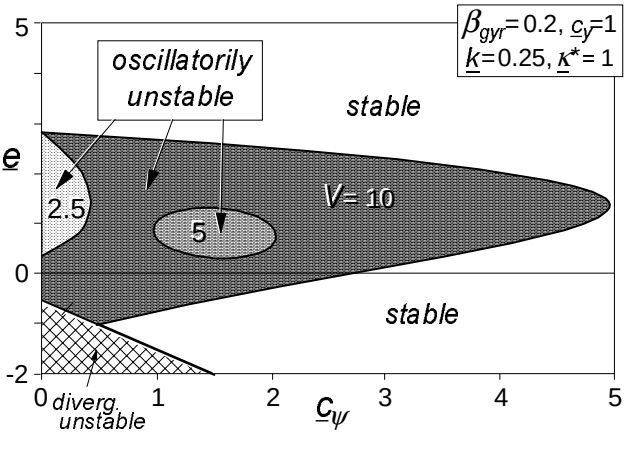

Fig. 6.16. Same as Fig. 6.15 but with more damping

case with $f > e$ which may be benificial to suppress shimmy. For the configuration that $f = e$ and damping and gyroscopic coupling are disregarded, the following conditions for stability hold:

$$a_5 > 0: \quad \underline{c}_{\psi} > \underline{c}_{\psi 1} = -(\underline{e} + \underline{t}) \tag{6.55}$$

$$H_2 > 0: \quad \underline{i}_z^2 = \frac{1}{\underline{m}} > (\underline{\sigma} + \underline{a})\underline{t} \tag{6.56}$$

$$H_4 > 0: \quad \min(\underline{c}_{\psi 2}, \underline{c}_{\psi 3}) < \underline{c}_{\psi} < \max(\underline{c}_{\psi 2}, \underline{c}_{\psi 3}) \tag{6.57}$$

with the two parabolic functions of $\underline{e}$:

$$\underline{c}_{\psi 2} = \frac{1 - \underline{e}\,\underline{c}_y}{\underline{m}(\underline{\sigma} + \underline{a})} + \frac{\underline{c}_y}{\underline{m}} + \underline{c}_y \underline{e}(\underline{\sigma} + \underline{a}) - \underline{c}_y \underline{e}^2 - \underline{t} \tag{6.58}$$

$$\underline{c}_{\psi 3} = \frac{\underline{c}_y(\underline{e} + \underline{t})(1 - \underline{e}\,\underline{m}\,\underline{t})}{\underline{m}\,\underline{t}} \tag{6.59}$$

Figure 6.17 depicts the boundaries of stability according to the above functions. The ordinates of two characteristic points have already been given in the figure. For the three other points we have the $\underline{e}$ values:

$$\underline{e}_1 = -\frac{\underline{i}_z^2}{\underline{\sigma} + \underline{a}} \tag{6.60}$$

$$\underline{e}_2 = \frac{\underline{t}}{\underline{c}_y(\underline{\sigma} + \underline{a} + \underline{t})} \tag{6.61}$$

$$\underline{e}_3 = \frac{\underline{i}_z^2}{\underline{t}} \tag{6.62}$$

The appearance of the stability diagram is quite different with respect to that of Fig.6.11 where $f = 0$. Still, an area of instability exists in between the levels of the trail: $-t < e < \sigma + a$. Like in the $f = 0$ case (clearly visible in Fig.6.12) we have two different ranges of instability: area 1 and area 2 where different modes of unstable oscillations occur. In the range of the caster length $-t < e < \sigma + a$ these areas correspond to the lower and the higher yaw stiffness regions.

For the points A and B which lie on the boundaries of the lower and the higher stiffness instability areas respectively, the modes of vibration have been analysed. The conditions for stability (6.55-57) of the undamped system without gyro's are independent of the speed. When changing the speed of travel the

damping of the mode that is just on a boundary of instability remains equal to zero. The other mode shows a positive damping which changes with speed as does the frequency of this stable mode. In the Figures 6.18 and 6.19 (from Besselink, 2000) the damping, frequency, amplitude ratio and phase lead of the lateral displacement of the contact centre $\bar{y}$ with respect to the yaw angle ψ have been presented for the two modes of vibration; in Fig.6.18 for case A and in Fig.6.19 for case B of Fig.6.17. Using a reference tyre radius r_{ref} the quantities y^* and V^* have been defined as follows: $y^* = y/r_{ref}$ [-], $V^* = V/r_{ref}$ [1/sec]. From the graphs can be observed that the lower yaw stiffness case A shows a mode on the verge of instability (mode 1) that has a lower frequency and a larger amplitude ratio $|y^*/\psi|$ than mode 2 in case B. Evidently case B exhibits a more pronounced yaw oscillation whereas the motion performed by mode 1 of case A comes closer to a lateral translational oscillation. The next section discusses the mode shapes of these periodic motions in relation with the energy flow into the unstable system.

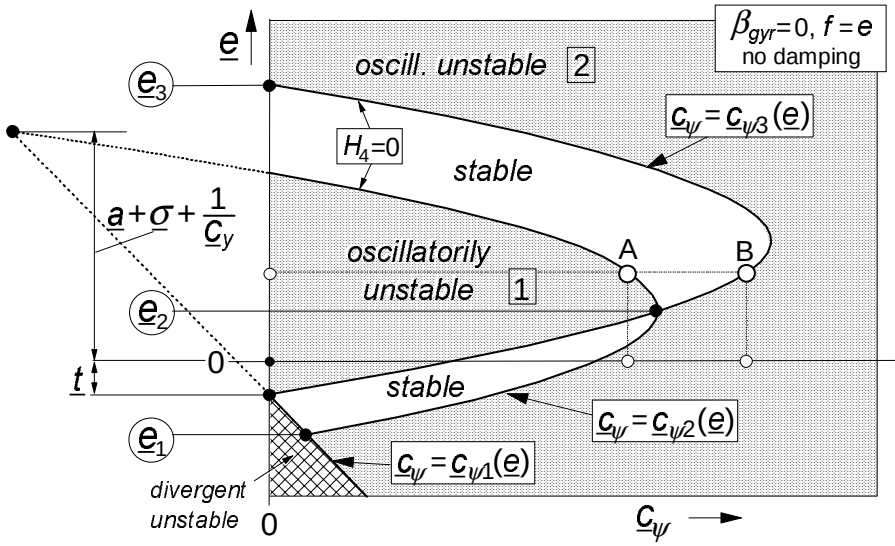

Fig. 6.17. Basic stability diagram for the case $\underline{f} = \underline{e}$ (c.g. distance $\underline{e}$ behind steer axis). Steer and tread damping are equal to zero. Gyroscopic coupling is disregarded. The functions $c_{\psi i}(e)$ are defined by Eqs.(6.55,58,59). Eigenvalues and eigenvectors of points A and B are analysed in Fig.6.18,19. (From: Besselink 2000).

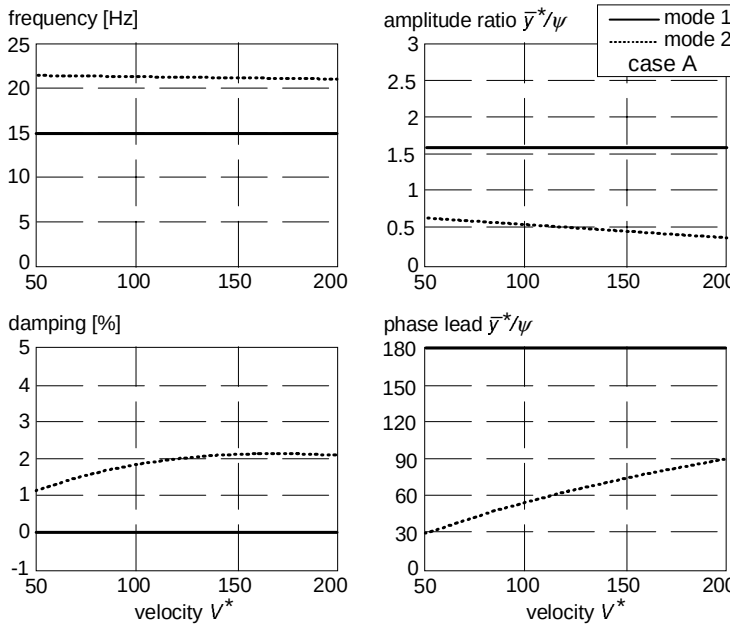

Fig. 6.18. Natural frequencies, damping and mode shapes for Case A of Fig.6.17.

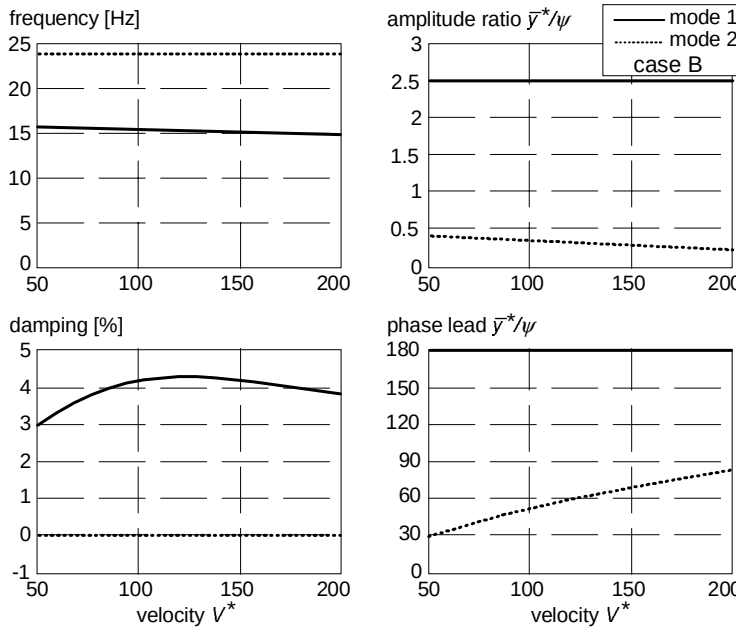

Fig. 6.19. Natural frequencies, damping and mode shapes for Case B of Fig.6.17.

Besselink has analysed the effects of changing a number of parameters of a realistic two-wheel, single axle main landing gear model configuration (of civil aircraft, also see Van der Valk 1993). Degrees of freedom represent: axle yaw angle, strutt lateral deflection, axle roll angle and tyre lateral deflection (straight tangent). This makes the total order of the system equal to seven. Important conclusions regarding the improvement of an existing system aiming at avoidance of shimmy have been drawn. Two mutually different configurations have been suggested as possible solutions to the problem, with the c.g. position f assumed to remain equal to the trail e.

- *large positive trail* ($e > 0$):

"An increase of the mechanical trail and a reduction of the lateral stiffness are required to improve stability at high forward velocity. Increasing the yaw stiffness will generally improve the shimmy stability of a gear with a positive mechanical trail provided that some structural damping is present. A limited reduction of the roll stiffness improves the stability at high forward velocities. The yaw moment of inertia should be kept as small as possible in case of a large positive mechanical trail".

- *small negative trail* ($e < 0$):

"For a landing gear with a negative trail an upper boundary exists for the yaw stiffness. The actual value of this stiffness may be quite low: for the baseline configuration the yaw stiffness would have to be reduced almost by a factor 3 to obtain a stable configuration with a negative trail. A relatively small increase in track width relaxes this requirement considerably. If the absolute value of the negative trail equals the pneumatic trail, there exists no lower limit for the yaw stiffness to maintain stability. The effect of increasing the lateral stiffness is quite similar to increasing the track width and improves the shimmy stability in case of negative trail".

In comparison with the baseline configuration the proposed modifications result in a major gain in stability. This illustrates that it may be possible to design a stable conventional landing gear, provided that the combination of parameter values is selected correctly.

For detailed information also on the results of simulations with a multi-body complex model in comparison with full scale experiments on a landing aircraft exhibiting shimmy we refer to the original work of Besselink (2000).

6.4. Shimmy and Energy Flow

To sustain the unstable shimmy oscillation, energy must be transmitted 'from the road to the wheel'. We realise that, ultimately, the power can only originate from the vehicle's propulsion system. The relation between unstable modes and the self-excitation energy generated through the road to tyre side force and aligning moment is discussed in detail in subsection 6.4.1. The transition of driving energy (or the vehicle forward motion kinetic energy) to self-excitation energy is analysed in subsection 6.4.2. Obviously, besides for the supply of self-excitation energy, the driving energy is needed to compensate for the energy that is dissipated through partial sliding in the contact patch.

6.4.1. Unstable Modes and the Energy Circle

To start out with the problem matter let us consider the simple trailing wheel system of Fig.6.1 with the yaw angle ψ representing the only degree of freedom of the wheel plane. If the mechanical trail is equal to zero it is only the aligning torque that exerts work when the wheel plane is rotated about the steering axis. If the yaw angle varies harmonically

$$\psi(s) = \psi_o \sin(\omega_s s) \tag{6.63}$$

the moment response becomes for small path frequency ω_s approximately:

$$M_z'(s) = -C_{M\alpha}\psi_o \sin(\omega_s s + \phi) \tag{6.64}$$

where the phase angle follows for instance from transfer functions (5.110) or (5.113) or Table 5.1 (below Fig.5.27):

$$\phi = \phi_{-M'\psi} = -\sigma_{M'\psi}\omega_s = -(\sigma + a)\omega_s \tag{6.65}$$

the negative value of which corresponds to the fact that the moment lags behind the yaw angle. The energy transmitted during one cycle can be found as follows ($\theta = \omega_s s$):

$$W = \int_{s=0}^{\lambda} M_z' \, \mathrm{d}\psi = C_{M\alpha}\psi_o^2 \int_0^{2\pi} \cos(\theta+\varphi)\sin\theta \, \mathrm{d}\theta = -\pi C_{M\alpha}\psi_o^2 \sin\phi \quad (>0) \tag{6.66}$$

Apparently, because of the negative phase angle the work done by the aligning torque is positive which means that energy is fed into the system. As a result, the undamped wheel system will show unstable oscillations which is in agreement with our earlier findings. It is of interest to note that in contrast to the above

result that holds for a tyre, a rotary viscous damper (with a positive phase angle of 90°) shows a negative energy flow which means that energy is being dissipated.

If we would consider a finite caster length e, more self-excitation will arise due to the contribution of the side force that also responds to the yaw angle with phase lag. At the same time, however, a part of F_y will now respond to the slip angle and, consequently, damps the oscillation. The slip angle arises as a result of the lateral slip speed which is equal to the yaw rate times the caster length. Finally, at $e = \sigma + a$ the moment and the side force are exactly in phase with the yaw angle (cf. situation depicted in Fig.5.6) and the stability boundary is reached. At $e = -t$ the moment about the steer axis vanishes if the simplified straight tangent or single contact point model is used. This also implies that the boundary of oscillatory instability is attained.

We will now turn to the much more complicated system with lateral compliance of the suspension included. The two components of the periodic oscillatory motion of the wheel that occurs on the boundary of (oscillatory) instability may be described as follows:

$$\bar{y}(t) = a_m \eta \sin(\theta + \xi) \tag{6.67}$$

$$\psi(t) = a_m \sin(\theta) \tag{6.68}$$

The quantity η represents the amplitude ratio, ξ indicates the phase lead of the lateral motion with respect to the yaw motion and θ equals ωt or $\omega_s s$. The energy W that flows from the road to the wheel during one cycle is equal to the work executed by the side force and the aligning torque that act on the moving wheel plane. Hence, we have:

$$W = \int_0^{2\pi} \left(F_y \frac{\mathrm{d}\bar{y}}{\mathrm{d}\theta} + M_z' \frac{\mathrm{d}\psi}{\mathrm{d}\theta} \right) \mathrm{d}\theta \tag{6.69}$$

When $W > 0$ energy flows into the system and if the system is considered to be undamped ($k = \kappa^* = 0$) the conclusion must be that the motion is unstable. Ultimately, the energy must originate from the power delivered by the vehicle propulsion system. How this transfer of energy is effectuated will be treated in the next section.

To calculate the work done, the force and moment are to be expressed in terms of the wheel motion variables (6.67,68). For this, a tyre model is needed and we will follow the theory developed by Besselink (2000) and take the straight tangent approximation of the stretched string model, which is governed by the Eqs.(6.2,4,6,7). For the periodic response of the transient slip angle α' to the input motion (6.67,68) the following expression is obtained:

$$\alpha'(\theta) = \frac{a_m}{1+\sigma^2\omega_s^2}\Big\{-(\sigma+a)\,\omega_s\cos(\theta) - \eta\omega_s\cos(\theta+\xi) + \\ + (1-a\sigma\omega_s^2)\sin(\theta) - \eta\sigma\omega_s^2\sin(\theta+\xi)\Big\} \tag{6.70}$$

With the expressions (6.2,4) for the force and the moment the integral (6.69) becomes:

$$W = \frac{\pi a_m^2 C_{F\alpha}\omega_s}{1+\sigma^2\omega_s^2}\left\{-\eta^2 + (\sigma+a)t + (t-a-\sigma)\eta\cos\xi - \left(\frac{1}{\omega_s} - (a+t)\sigma\omega_s\right)\eta\sin\xi\right\} \tag{6.71}$$

On the boundary of stability $W = 0$ and for a given path frequency ω_s or wavelength $\lambda = 2\pi/\omega_s$ a relationship between η and ξ results from (6.71). To establish the functional relationship it is helpful to switch to Cartesian coordinates:

$$x_p = \eta\cos\xi\ , \qquad y_p = \eta\sin\xi \tag{6.72}$$

The expression for the energy now reads:

$$W = -\frac{\pi a_m^2 C_{F\alpha}\omega_s}{1+\sigma^2\omega_s^2}\left\{x_p^2 + y_p^2 + (\sigma+a-t)x_p + \left(\frac{1}{\omega_s} - (a+t)\sigma\omega_s\right)y_p - (\sigma+a)t\right\} \tag{6.73}$$

Apparently, for a given value of W this represents the description of a circle. For $W = 0$ and after the introduction of the wavelength λ as parameter the function takes the form:

$$x_p^2 + y_p^2 + (\sigma+a-t)x_p + \left(\frac{\lambda}{2\pi} - (a+t)\sigma\frac{2\pi}{\lambda}\right)y_p - (\sigma+a)\,t = 0 \tag{6.74}$$

When the mode shape of the motion of the wheel plane defined by η and ξ or by x_p and y_p is such that (6.74) is satisfied, the motion finds itself on the boundary of stability. The centre of Besselink's energy circle is located at:

$$(x_{pc}, y_{pc}) = -\frac{1}{2}\left((\sigma+a-t),\ \left(\frac{\lambda}{2\pi} - (a+t)\sigma\frac{2\pi}{\lambda}\right)\right) \tag{6.75}$$

From (6.74) it can be ascertained that independent of λ the circles will always pass through the two points on the x_p axis: $x_p = -(\sigma+a)$ and $x_p = t$. We have now sufficient information to construct the circles with λ as parameter. In Fig.6.20 these circles have been depicted together with circles that arise when different tyre models are used. As expected, the circles for the more exact tyre models deviate more from those resulting from the straight tangent tyre model when the wavelength becomes smaller. That circles arise also for other massless models

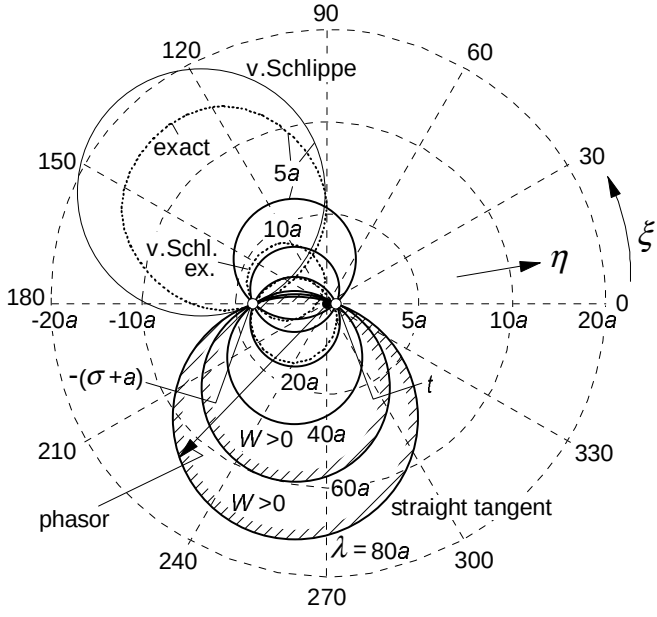

Fig. 6.20. Mode shape plot (amplitude ratio η, phase ξ) with Besselink's zero energy circles for different wavelengths and tyre model approximations, indicating mode shapes for which shimmy begins to show up (instability occurs if at a particular value of the motion wavelength λ the phasor end point gets inside the corresponding circle). At smaller wavelengths the circle belonging to the straight tangent approximation begins to appreciably deviate from the exact or Von Schlippe representation.

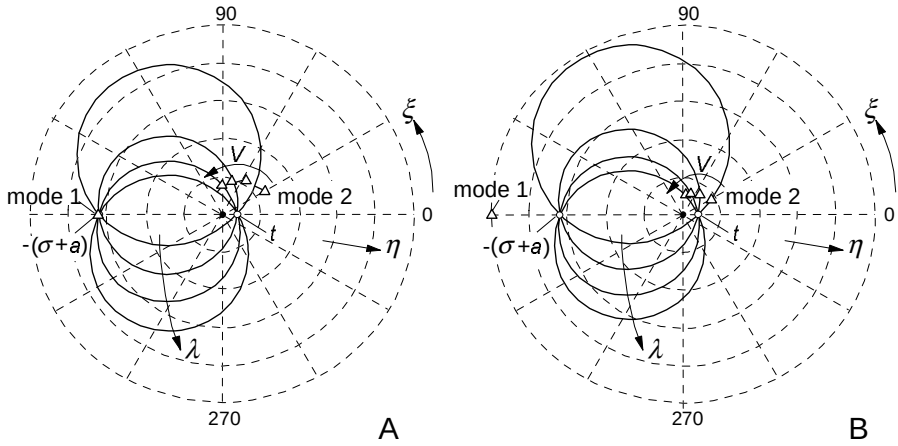

Fig. 6.21. Zero energy circles for the cases A and B of Fig.6.17 indicating the mode shape of mode 1 at the boundary of stability in case A and the same for mode 2 in case B.

of the tyre can be easily proven when considering the fact that at a given wavelength we have a certain amplitude and phase relationship of the force F_y and the moment M_z' with respect to the two input motion variables $\bar{y}$ and ψ. That the circles pass through the point $(-\sigma-a, 0)$ follows from the earlier finding that the response of all 'thin' tyre models when the wheel is swivelled around a vertical axis that is positioned a distantance $\sigma+a$ in front of the wheel axle (cf. Fig.5.6) are equal and correspond to the steady-state response.

When parameters of the system are changed and the mode shape is changed so that the end point of the phasor with length η and phase angle ξ moves from outside the circle to the inside, the system becomes oscillatory unstable. It becomes clear that depending on the wavelength a whole range of possible mode shapes of the wheel plane motion is susceptible to forming unstable shimmy oscillations.

As an example, the situation that arises with the cases A and B of Figs.6.17-19 have been depicted in Fig.6.21. In case A mode 1 is on the verge of becoming unstable. The mode shape corresponds to the motion indicated in Fig.5.6 and remains unchanged when the speed is varied. The circles, however, change in size and position when the speed is changed which correspond to a change in wavelength. Mode 2 appears to remain outside the circles indicating that this particular mode is stable. In case B mode 1 is stable and mode 2 sits on the boundary of stability. This is demonstrated in the right-hand diagram where the end point of the phasor of mode 2 remains located on the (changing) circles when the speed is changed.

As a second example we apply this theory to the configuration with $f=0$ with the gyroscopic coupling included. In Fig.6.8 the cases A and B have been indicated at a trail $e = 0$. Because of the gyroscopic action the condition for stability is speed dependent although damping is assumed equal to zero. This makes it possible to actually see that the zero energy circle is penetrated or exited when the speed is increased.

In Figs.6.22 and 23 the phasors (here considered as complex quantities) have been indicated for a number of values of the non-dimensional speed $\underline{V}$. The non-dimensional wavelength and eigenvalue of the mode considered change with speed as have been indicated in the respective diagrams. Cases A and B (with respectively mode 1 and 2 on the boundary of stability) have been marked. When the speed is increased from 6 to 14 two boundaries of stability (A and B) are passed in between which according to Fig.6.8 a stable range of speed exists. In Fig.6.22 we see that in accordance with this the phasor of mode 1 first lies inside the circle (belonging to $\underline{V} = 6$ with frequency $\underline{\omega} = 0.66$ and corresponding wavelength $\lambda = 57a$) then crosses the circle at $\underline{V}=9.05$ (A) and finally ends up

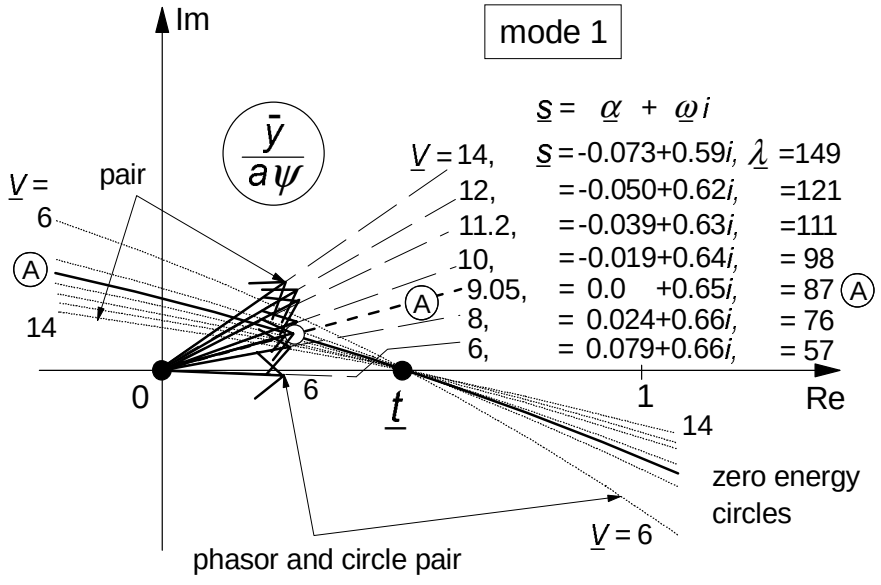

Fig. 6.22. System of Fig.6.8 with gyrocopic coupling making stability speed dependent. Circle segments and phasors of mode shapes of mode 1 for a series of speed values covering the range in which points A and B of Fig.6.8 are located. At increasing speed the phasor crosses the circle at $\underline{V} = 9.05$ into the stable domain.

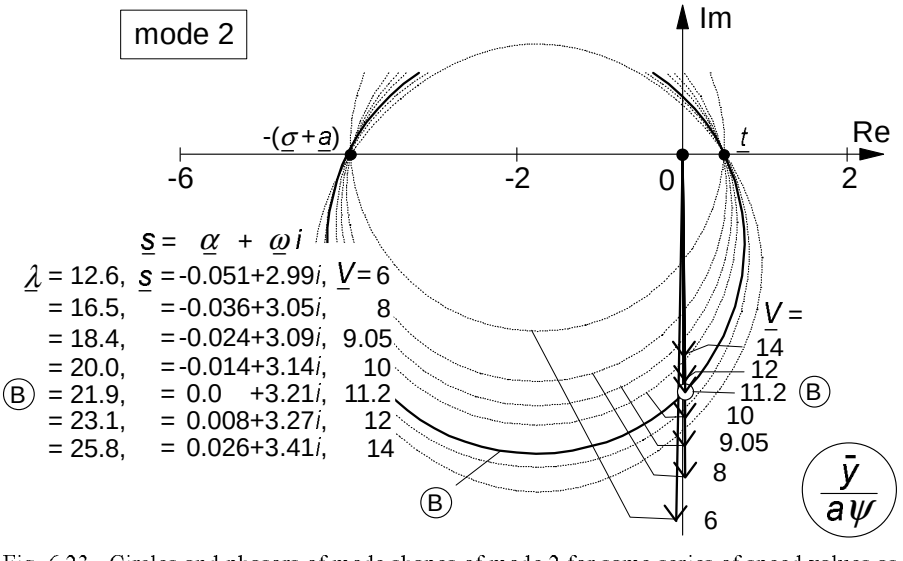

Fig. 6.23. Circles and phasors of mode shapes of mode 2 for same series of speed values as in Fig.6.22. At increasing speed the phasor crosses the circle at $\underline{V} = 11.2$ towards its inside which means: entering the unstable domain.

at a speed $\underline{V} = 14$ outside the circle meaning that this mode is now stable. At the same time, following mode 2 in Fig.6.23, we observe that first the mode point lies outside the circle at $\underline{V} = 6$ (now for the different frequency $\underline{\omega} = 2.99$ and wavelength $\lambda = 12.6a$), crosses the circle at $\underline{V} = 11.2$ (B) and moves to the inside of the circle into the unstable domain. From the eigenvalues $\underline{s}$ the change in damping and frequency can be observed. The mode shapes are quite different for the two modes. Mode 1 shows a relatively small lateral displacement $\bar{y}$ with respect to the yaw angle multiplied with half the contact length $a\psi$. At first $\bar{y}$ slightly lags behind ψ which turns into a lead at higher speeds. Mode 2 shows a higher frequency and smaller wavelength while $\bar{y}$ is relatively large and lags behind ψ.

Exercise 6.1. Zero energy circle applied to the simple trailing wheel system

Consider the third-order system of Fig.6.1 described by the Eqs.(6.1-9) but without damping: $\underline{k} = \underline{\kappa}^* = 0$. Establish the reduced expression for the work W from the general formula (6.69). Show that the stability condition $H_2 > 0$ corresponds to $W < 0$ which means that the mode shape point lies outside the zero energy circle.

6.4.2. Transformation of Forward Motion Energy into Shimmy Energy

The only source that is available to sustain the self-excited shimmy oscillations is the vehicle propulsion unit. The tyre side force has a longitudinal component that when integrated over one shimmy cycle must be responsible for an average drag force that is balanced by (a part of) the vehicle driving force.

In the previous section we have seen that the work done by the side force and the aligning torque is fed into the system to generate the shimmy oscillation. The link that apparently exists between self-excitation energy and driving energy will be examined in the present section. For this analysis dynamic effects may be left out of consideration. The wheel is considered to roll freely (without braking or driving torques).

During a short span of travelled distance ds of the wheel centre, the wheel plane moves sideways over a distance d$\bar{y}$ and rotates about the vertical axis over the increment of the yaw angle dψ. At the same time, the tyre lateral deflection is changed and, when sliding in the contact patch is considered, some elements will slide over the ground. Consequently, we expect that the supplied driving energy dE is equal to the sum of the changes of (self-) excitation energy dW, tyre potential energy dU and tyre dissipation energy dD.

In Fig.6.24 the tyre is shown in a deflected situation. We have the pulling force F_d acting in forward ($\bar{x}$) direction from vehicle to the wheel axle and

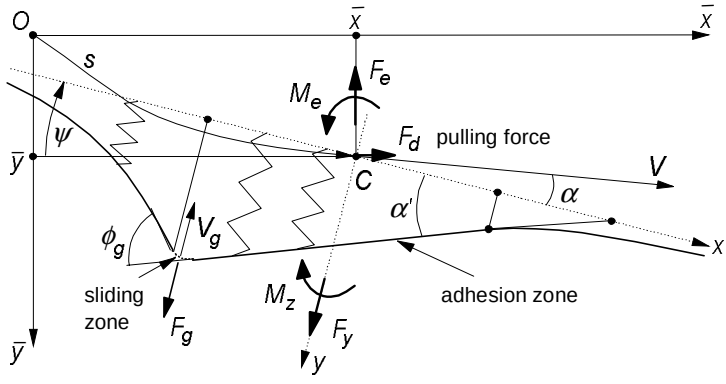

Fig. 6.24 . On the balance of driving, self-excitation and dissipation energy.

furthermore the lateral force F_e and yaw moment M_e from rim to tyre. These forces and moment are in equilibrium with the side force F_y and aligning torque M_z which act from road to tyre. A linear situation is considered with small angles and a vanishing length of the sliding zone. For the sake of simplicity, we consider an approximation of the contact line according to the straight tangent concept.

Energy is lost due to dissipation in the sliding zone at the trailing edge of the contact zone. To calculate the dissipated energy we need to know the frictional force and the sliding velocity distance. For the bare string model we have the concentrated force F_g that acts at the rear edge and that is needed to maintain the kink in the deformation of the string. This force is equal to the difference of the slopes of the string deflection just behind and in front of the rear edge times the string tension force $S = c_c\sigma^2$. For the straight tangent string deformation with transient slip angle or deformation gradient α', the slope difference is equal to $\phi_g = 2(\sigma+a)\alpha'/s$. The force becomes: $F_g = 2c_c\sigma(\sigma+a)\alpha'$. The average sliding speed V_g over the vanishing sliding range is equal to half the difference in slope of the string in front and just passed the kink times the forward speed V. This multiplied with the time needed to travel the distance ds gives the sliding distance s_g. We find for the associated dissipation energy:

$$\mathrm{d}D = F_g s_g = \frac{1}{2}F_g\varphi_g\,\mathrm{d}s = 2c_c\sigma(\sigma+a)\alpha'\frac{\sigma+a}{\sigma}\alpha'\,\mathrm{d}s = C_{F\alpha}\alpha'^2\,\mathrm{d}s = F_y\alpha'\,\mathrm{d}s \tag{6.76}$$

The same result appears to hold for the brush model. When considering the theory of Chapter 3, we find for small slip angle α' a length of the sliding zone at the trailing edge: $2a\theta\,\alpha'$ and a slope of the contact line in this short sliding zone with respect to the wheel plane $\beta_g = 1/\theta$. The average sliding speed becomes: $V_g = V(\beta_g+\alpha')$ which makes the sliding distance equal to $s_g = (\beta_g+\alpha')\mathrm{d}s$. The average side force acting in the sliding range appears to be: $F_g = C_{F\alpha}\theta\alpha'^2$. This results in the dissipated energy (considering that β_g is of finite magnitude

and thus much larger than α'):

$$\mathrm{d}D = F_g s_g = C_{F\alpha}\theta\alpha'^2\beta_g \mathrm{d}s = C_{F\alpha}\alpha'^2 \mathrm{d}s = F_y^2/C_{F\alpha}\mathrm{d}s = F_y\alpha'\mathrm{d}s \qquad (6.77)$$

which obviously is the same expression as found for the string model, Eq.(6.76).

At steady-state side slipping conditions with constant yaw angle $\psi=\alpha'=\alpha$ we obviously have a drag force $F_d=F_y\psi$. The dissipation energy after a distance travelled s equals $D=F_y^2/C_{F\alpha}s=F_y\alpha' s=F_y\psi s=F_d s$ which is a result that was to be expected.

The increment of the work W done by the side force and aligning torque acting on the sideways moving and yawing wheel plane (considered in the previous subsection) is:

$$\mathrm{d}W = F_e\mathrm{d}\bar{y} + M_e\mathrm{d}\psi = \left(F_y\frac{\mathrm{d}\bar{y}}{\mathrm{d}s} + M_z\frac{\mathrm{d}\psi}{\mathrm{d}s}\right)\mathrm{d}s \qquad (6.78)$$

The change in tyre deflection (note that the tyre almost completely adheres to the ground) arises through successively moving the wheel plane sideways over the distances $\mathrm{d}\bar{y}$ and $\psi\mathrm{d}s$ and rotating over the yaw angle $\mathrm{d}\psi$ and finally rolling forwards in the direction of the wheel plane over the distance $\mathrm{d}s$. These contributions correspond with the successive four terms in the expression for the change in potential energy:

$$\mathrm{d}U = F_y\left(-\frac{\mathrm{d}\bar{y}}{\mathrm{d}s} + \psi\right)\mathrm{d}s - M_z\frac{\mathrm{d}\psi}{\mathrm{d}s}\mathrm{d}s - F_y\alpha'\mathrm{d}s \qquad (6.79)$$

The increase in driving energy is:

$$\mathrm{d}E = F_y\psi\,\mathrm{d}s \qquad (6.80)$$

In total we must have the balance of energies:

$$\mathrm{d}E = \mathrm{d}W + \mathrm{d}U + \mathrm{d}D \qquad (6.81)$$

which after inspection indeed appears to be satisfied considering the expressions of the three energy components (6.76/77,78,79).

Integration over one cycle of the periodic oscillation will show that $U=0$ so that for the energy consumption over one cycle remains :

$$E = W + D \qquad (6.82)$$

At steady-state side slip with slip angle $\alpha=\psi$ the excitation energy $W=0$ and the driving energy becomes:

$$E = D = F_y^2/C_{F\alpha}s = F_y\psi s = F_d s \qquad (6.83)$$

The result presented through Eq.(6.81) demonstrates that the propulsion energy is partly used to compensate the energy lost by dissipation in the contact patch and partly to provide the energy to sustain the unstable shimmy oscillations.

6.5. Non-Linear Shimmy Oscillations

Non-linear shimmy behaviour may be investigated by using analytical and computer simulation methods. The present section first gives a brief description of the analytical method employed by Pacejka (1966) that is based on the theory of the harmonic balance of Krylov and Bogoljubov (1947). The procedure that is given by Magnus (1955) permits a relatively simple treatment of the oscillatory behaviour of weekly non-linear systems. Further on in the section results obtained through computer simulation will be discussed.

Due to the degressive nature of the tyre force and moment characteristics the system which was found to be oscillatory unstable near the undisturbed rectilinear motion (result of linear analysis) will increase in amplitude until a periodic motion is approached which is designated as the limit-cycle. The maximum value of the steer angle reached during this periodic motion is referred to as the limit-amplitude. For weakly non-linear systems this oscillation can be approximated by a harmonic motion. At the limit-cycle a balance is reached between the self-excitation energy and the dissipated energy.

In the analytical procedure an equivalent linear set of equations is established in which the coefficient of the term that replaces the original non-linear term is a function of the amplitude and the frequency of the oscillation. For example, the moment excerted by the tyre side force and the aligning torque about the steering axis: $f^*(\alpha') = F_y e - M_z$ may be replaced by the equivalent total aligning stiffness multiplied with the transient slip angle: $C^*\alpha'$. If dry friction is considered in the steering system, the frictional couple $m^*(\dot{\psi}) = K\,\mathrm{sgn}(\dot{\psi})$ may be replaced by the equivalent viscous damping couple $k^*\dot{\psi}$. The equivalent coefficients C^* and k^* are functions of the amplitudes of α' and $\dot{\psi}$ (or of $\omega\psi$) respectively. The functions are determined by considering a harmonic variation of α' and ψ and then taking the first harmonic of the Fourier series of the periodic response of the corresponding original non-linear terms.

We have with $\alpha' = \alpha'_o \sin\tau$ and $\psi = \psi_o \sin\theta$:

$$C^* = \frac{1}{\pi\alpha_o}\int_0^{2\pi} f^*(\alpha')\sin\tau\, d\tau \tag{6.84}$$

and

$$k^* = \frac{1}{\pi\omega\psi_o}\int_0^{2\pi} m^*(\dot{\psi})\cos\theta\, d\theta = \frac{4K}{\pi\omega\psi_o} \tag{6.85}$$

As expected, the function of the equivalent total aligning stiffness $C^*(\alpha'_o)$ starts for vanishing amplitude at the value $C_{F\alpha}e + C_{M\alpha}$ at a slope equal to zero and then

gradually decays to zero with the amplitude α_o' tending to infinity. The equivalent damping coefficient $k^*(\omega\psi_o)$ (6.85) appears to vary inversely proportionally with the steer angle amplitude, which means that it begins at very large damping levels and decreases sharply with increasing swivel amplitude according to a hyperbola. If clearance in the wheel bearing about the steer axis would be considered (in series with the steer damper) the matter becomes more complex and an equivalent steer stiffness c^* must be introduced. If the total angle of play is denoted by 2δ the equivalent coefficients k^* and c^* are found to be expressed by the functions:

$$k^* = \frac{4K}{\pi\omega\psi_o}\left(1 - \frac{\delta}{\psi_o}\right) \qquad (\psi_o > \delta) \tag{6.86}$$

and

$$c^* = \frac{4K}{\pi\psi_o}\sqrt{\frac{\delta}{\psi_o}\left(1 - \frac{\delta}{\psi_o}\right)} \qquad (\psi_o > \delta) \tag{6.87}$$

If $\psi_o < \delta$ the oscillation takes place inside the free space of the clearance and the equivalent damping and stiffness become equal to zero. Obviously, the clearance alleviates the initial strong damping effect of the dry friction.

If not all non-linearities are considered, we may, e.g., replace k^* by k and c^* by zero or c_ψ.

For the third-order system of Section 6.2 the non-linear version of Eqs.(6.11) is replaced by equivalent linear differential equations containing the coefficients C^*, c^* and k^*. The damping due to tread width is kept linear. The characteristic equation, which is similar to (6.13), becomes:

$$\begin{aligned} &\underline{\sigma}\,\underline{V}^2 p^3 + \{\underline{V}^2 + \underline{\sigma}(\underline{k}^*\underline{V} + \underline{\kappa}^*)\}p^2 + \\ &\quad + \{\underline{k}^*\underline{V} + \underline{\kappa}^* + \underline{\sigma}\underline{c}^* + \underline{C}^*(\underline{e} - \underline{a})\}p + \underline{C}^* + \underline{c}^* = 0 \end{aligned} \tag{6.88}$$

with non-dimensional quantities according to (6.10): C^*, c^* and k^* being treated like $C_{M\alpha}$, c_δ and k respectively. When the shimmy motion has been fully developed and the limit-cycle is attained, the solution of the equivalent linear system represents a harmonic oscillation with path frequency $\underline{\omega}_s$ and amplitudes α_o' and ψ_o. The amplitudes are obtained by using the condition that at this sustained oscillation the Hurwitz determinant $H_{n-1}=0$. Consequently we have for our third-order system at the limit-cycle: $H_2 = 0$. Hence, the equation that is essential for finding the magnitude of the limit-cycle reads:

$$\begin{aligned} &\{\underline{V}^2 + \underline{\sigma}(\underline{k}^*\underline{V} + \underline{\kappa}^*)\}\{\underline{k}^*\underline{V} + \underline{\kappa}^* + \underline{\sigma}\underline{c}^* + \underline{C}^*(\underline{e} - \underline{a})\} = \\ &\qquad = \underline{\sigma}\,\underline{V}^2(\underline{C}^* + \underline{c}^*) \end{aligned} \tag{6.89}$$

The frequency of the periodic oscillation that occurs when the relation (6.89) is

satisfied can easily be found when in (6.88) p is replaced by $i\underline{\omega}_s$. We obtain:

$$\underline{\omega}_s^2 = \frac{\underline{C}^* + \underline{c}^*}{\underline{V}^2 + \underline{\sigma}(\underline{k}^* \underline{V} + \underline{\kappa}^*)} \tag{6.90}$$

Moreover, we need the ratio of the amplitudes α_o' and ψ_o. From the second equation of (6.11), which is not changed in the linearisation process, we get with $\alpha' = v_1/\sigma$:

$$\frac{\alpha_o'}{\psi_o} = \sqrt{\frac{1 + (\underline{a} - \underline{e})^2 \underline{\omega}_s^2}{1 + \underline{\sigma}^2 \underline{\omega}_s^2}} \tag{6.91}$$

Equations (6.89-91) provide sufficient information to compute the amplitude and the frequency of the limit-cycle.

The stability of the limit-cycle of the weakly non-linear system may be assessed by taking the derivative of the Hurwitz determinant with respect to the amplitude. If $dH_2/d\psi_o > 0$ the limit-cycle is stable and attracts the trajectories, if negative, the limit-cycle is unstable and the oscillations deviate more and more from this periodic solution. In the original publication more information can be found on the analytic assessment of the solutions.

For the four different cases investigated, Fig.6.25 shows the basic motion properties. Figure 6.26 gives for the three non-linear cases the variation of the limit-amplitudes with damping parameter. The left-hand diagram shows that, with just non-linear tyre behaviour, in the range of the damping coefficient below the critical value as obtained in the linear analysis, the motion is unstable and the shimmy oscillation developes after a minute disturbance. The degressive shape of the tyre force and moment characteristics causes an increase in self-excitation energy that is less than the increase of the dissipation energy from the viscous damper. When the limit-amplitude is reached, the two energies become equal to each other. If through some external disturbance the amplitude has become larger than the limit-amplitude, the dissipation energy exceeds the self-excitation energy and the oscillation reduces in amplitude until the limit-cycle is reached again but now from the other side.

If dry friction is considered instead of the viscous damping we observe that the centre position is stable. In fact, the system may find its rest position away from the centre (at a small steer angle) if the dry frictional torque is sufficiently large. We now need a finite external disturbance (runnung over an asymmetric obstacle) to overcome the dry friction. If that has happened, the motion developes itself further and the stable limit-cycle is reached. If the initial conditions are chosen correctly we may spend a while near the unstable limit-cyle before either

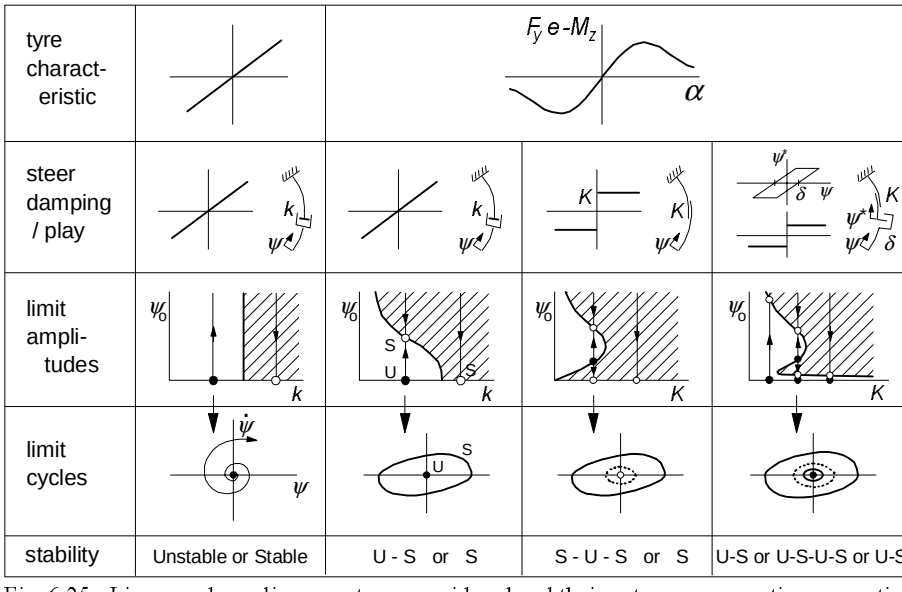

Fig. 6.25. Linear and non-linear systems considered and their automomous motion properties in terms of stability and possible limit-cycles.

the rest position or the large stable limit-cycle is approached. Figure 6.27 shows for this case the solutions in the three-dimensional state space. The unstable limit-cycle appears to lie on a tube shaped surface which is here the separatrix in the solution space. We see that when the initial conditions are taken outside the tube, the stable limit-cycle is reached. When the starting condition is inside the tube, one of the indicated possible rest positions will be ultimately attained.

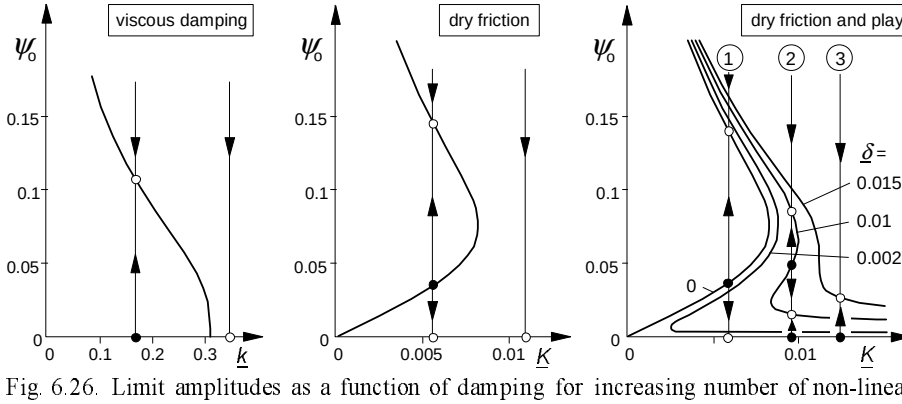

Fig. 6.26. Limit amplitudes as a function of damping for increasing number of non-linear elements: non-linear tyre, dry friction and play. ($\underline{V} = 6.66$, $\underline{\sigma} = 3$, $\underline{e} = 0$, $\underline{\kappa}'' = 0$).

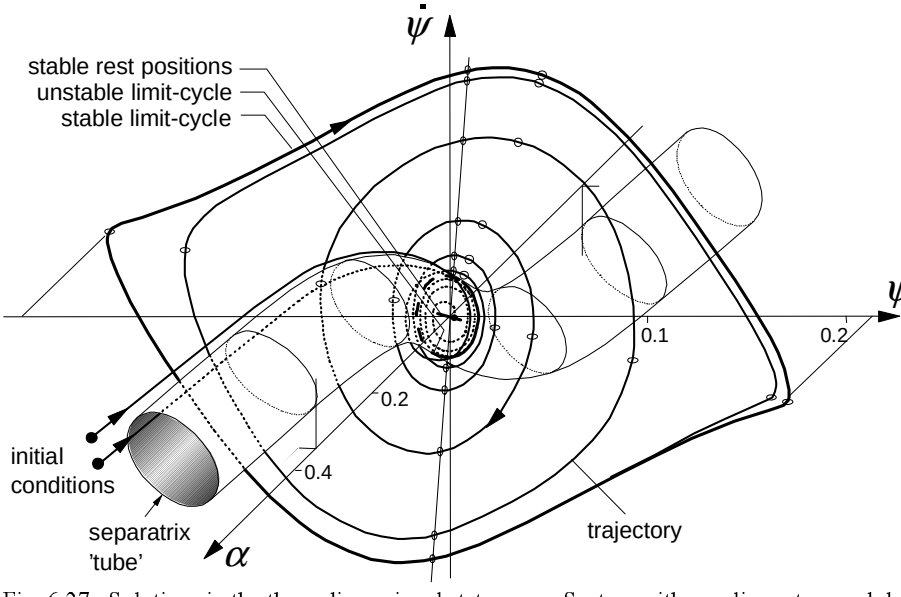

Fig. 6.27. Solutions in the three-dimensional state space. System with non-linear tyre and dry friction ($\underline{V} = 6.66$, $\underline{\sigma} = 3$, $\underline{e} = 0$, $\underline{\kappa}^* = \underline{k} = \underline{\delta} = 0$, $\underline{K} = 0.0035$). Line piece for possible rest positions, unstable and stable limit-cycle. Tube shaped separatrix separating space of trajectories leading to a rest position from the space of solution curves leading to the stable limit-cycle.

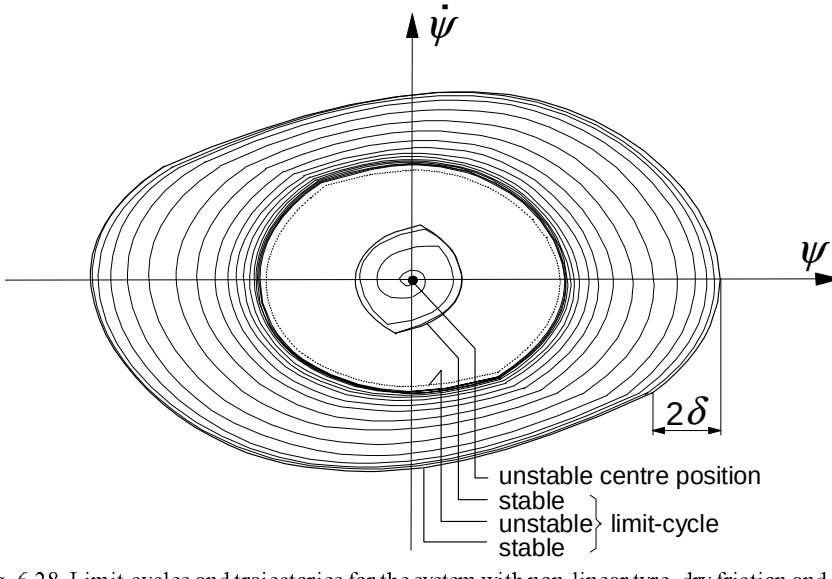

Fig. 6.28. Limit-cycles and trajectories for the system with non-linear tyre, dry friction and play in the wheel bearings. (Case 2 of Fig.6.26).

The introduction of play about the steering axis with δ being half the clearance space, appears indeed to be able to relax the action of the dry friction. For small play and enough dry friction (case 2 in Fig.6.26) the small stable limit-cycle is reached automatically. An additional disturbance may cause the motion to get over the 'nose' and reach the large stable limit-cycle. The plot of Fig.6.28 shows for this case the three limit-cycles and trajectories as projected on the ($\dot{\psi}$, ψ) plane. If the play is larger or the damping less, the large limit-cycle is reached without an external disturbance.

It is of interest to see how the limit-amplitudes ψ_o vary with the speed of travel V. Figure 6.29 depicts two cases: viscous damping and dry friction. The area inside which the amplitude increases due to instability may be designated as the area of self-excitation. The diagrams show the courses of the limit-amplitude for the two configurations with linear damping ($K = \delta = 0$) with unstable ranges of speed indicated in Fig.6.3. The right-hand diagram also gives the (smaller) area of self-excitation when dry friction is added. When the damping is linear, shimmy arises when the critical speed is exceeded. The amplitude grows as the vehicle speeds up. In the left-hand diagram, a maximum is reached beyond which the amplitude decreases and finally, at the higher boundary of stability, the oscillation dies out. With dry friction, the stable limit-cycle cannot be reached automatically. A sufficiently strong external disturbance may get the shimmy started.

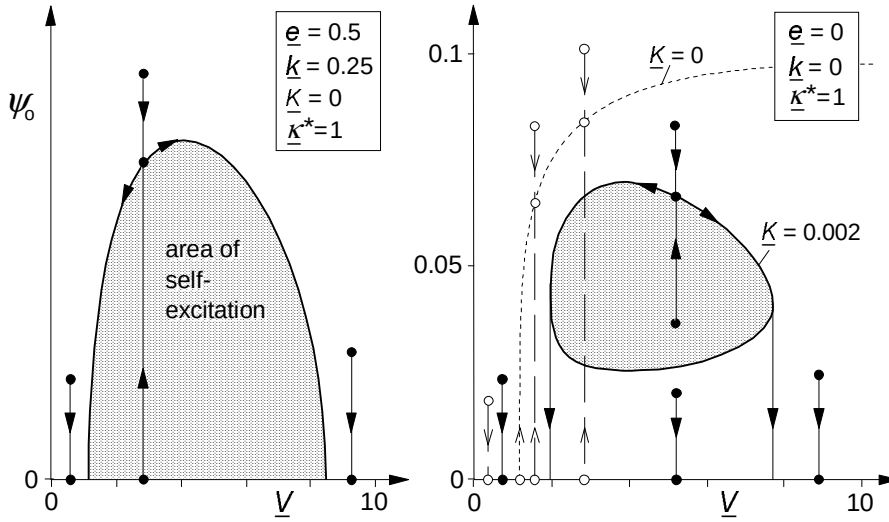

Fig. 6.29. Boundary of area of selfexcitation representing the course of limit-amplitudes of steer angle ψ as function of speed for system with non-linear tyre and viscous damping (left and right) and dry friction (right). ($\underline{\sigma}$ = 3, cf. Fig.6.3).

Another way of initiating the shimmy in the case of dry friction may be the application of wheel unbalance. Beyond a certain speed the imposed unbalance couple may have become large enough to overcome the dry friction. Then, when the forcing frequency is not too much apart from the shimmy natural frequency, the amplitude rises quickly and a state of synchronous motion may arise as depicted in Fig.6.30. In that state the system oscillates with a single frequency which corresponds to the wheel speed of revolution. When from that point onwards the vehicle speed is increased or decreased the synchronous oscillation may persist until the difference between the two frequencies becomes too large (or in other words: until the difference between free shimmy wavelength and wheel circumference is too great, that is: the system is detuned too much). Then, the unbalance torque is no longer able to drag the free shimmy motion along. The picture of the oscillation is now changed considerably. We have a motion with a beat character that consists of oscillations with two frequencies: one is the unbalance forcing frequency and the other will be close to the free shimmy frequency at the current speed. The shaded areas shown in the diagram indicate the speed ranges where these combination vibrations show up. The upper and lower boundaries of these areas represent the limits in between which the amplitude of the motion varies. When at decreasing speed the point at the vertical

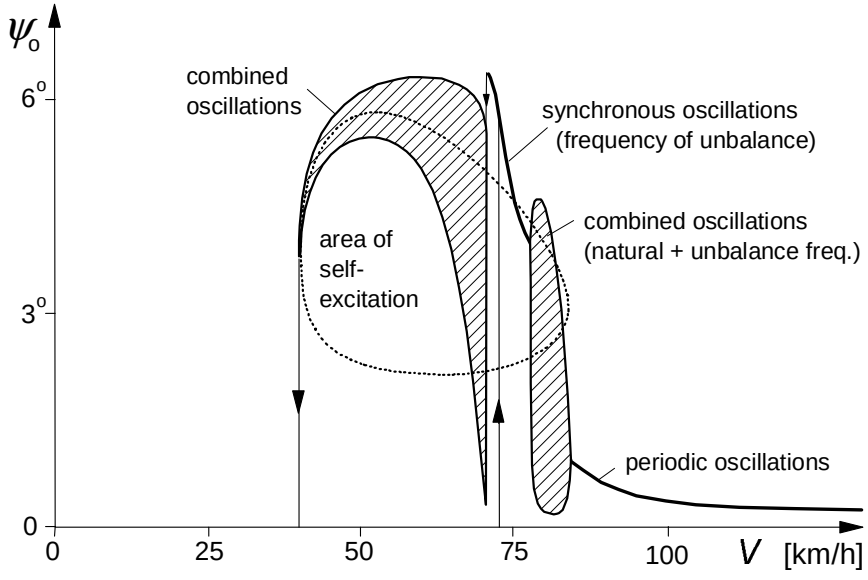

Fig. 6.30. The response of the tenth-order system, representing a light truck with non-linear tyre and dry friction, to wheel unbalance moment. The area of self-excitation of the autonomous system has been indicated. At nearly 75km/h violent shimmy develops. Then a range of speed with so-called synchronous oscillations occur. When the system is detuned too much, combined oscillations (beats) show up.

tangent to the area of self-excitation is reached the shimmy oscillation disappears. At increasing speed, the combination oscillations may pass to a forced vibration with a single frequency. This occurs when the degree of self-excitation has become too low. A similar phenomenon of synchronous motions and combined oscillations has been treated by Stoker (1950, p.166). He uses an approximate analytical method to investigate the second-order non-linear system of Van der Pol that is provided with a forcing member.

The diagram of Fig.6.30 represents the result of a computer simulation study with a relatively complex model of the 10th order. The model is developed to investigate the violent shimmy vibration generated by a light military truck equipped with independent trailing arm front wheel suspensions. For details we refer to the original publication, Pacejka (1966). The model features degrees of freedom represented by the following motion variables: lateral displacement and roll of the chassis, lateral and camber deflection of the suspension, steer angle of the front wheel (same left/right), rotation of the steering wheel and lateral tyre deflection. The degree of freedom of the steering wheel has been suppressed in the depicted case by clamping the steering system in the node that appears to occur in the free motion with the front wheels and the steering wheel moving in counter phase. The other lower frequency mode with front wheels and steering

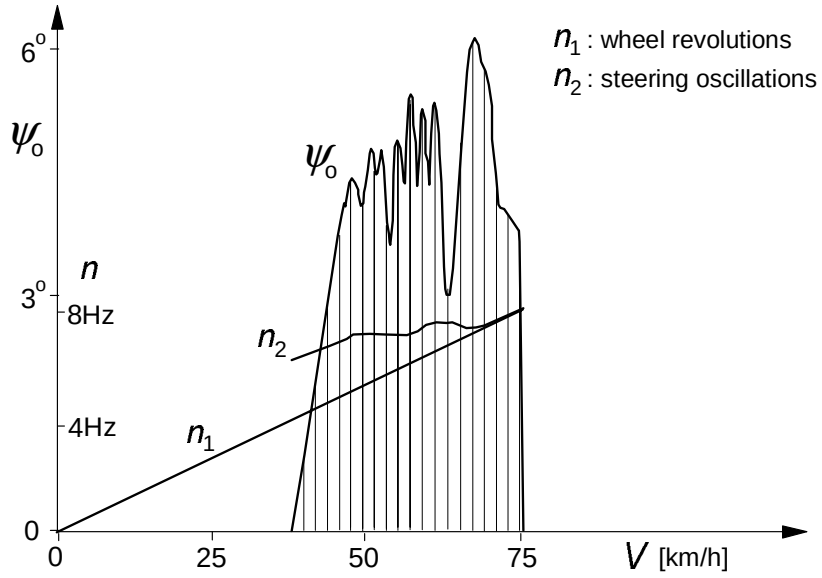

Fig. 6.31. Front wheel steer oscillation amplitude as a response to wheel unbalance as measured on a light truck. The speed is gradually reduced after violent shimmy was developed at ca. 75km/h. After a short range of speed exhibiting synchronous oscillations (single frequency), combined vibrations occur with two distinct frequencies.

wheel moving in phase occurs at lower values of speed and partly overlaps the range of the counter phase mode. It is expected that the in-phase mode is easily suppressed by loosely holding the steering wheel. This was more or less confirmed by experiments on a small mechanical wheel suspension/steering system model. The full scale truck only showed shimmy with counter oscillating front wheels and steering wheel.

Finally, Fig.6.31 presents the results of measurements performed on the truck moving over a landing strip. The front wheels were provided with unbalance weights. Shimmy appeared to start at a speed of ca. 75 km/h. Synchronous oscillations were seen to occur as can be concluded by considering the frequencies that appear to coincide in the small range of speed just below the speed of initiation of 75 km/h. Further downwards, the frequencies get separated and follow independent courses. This strengthens the impression that here the motion may be able to sustain itself. Afterwards, another test was conducted with only one wheel provided with an unbalance weight. The weight was attached to a cable that made it possible to remove the unbalance during the test run. After having the unbalance detached at the instant that the shimmy was fully developed, the shimmy remained to manifest itself with about the same intensity. This constituted the proof that we dealt with a self-sustained oscillation. The correspondence between the diagrams of Figs.6.30 and 31 is striking. Also the frequency of the autonomous vibration of the model (along the upper boundary of the area of self-excitation shown in Fig.6.30) was close to that according to the test results. The model frequency appears to vary from 6.1Hz at the low end of the speed (40-45 km/h) to 7Hz at the initiation velocity of 70-75km/h.

Chapter 7

SINGLE CONTACT POINT TRANSIENT TYRE MODELS

7.1. Introduction

For relatively low frequency and large wavelength transient and oscillatory vehicle motions, tyre inertia and the effect of the finite length of the contact patch may be neglected or taken care of in an approximative manner. In Chapter 5 a thorough treatment has been given of the out-of-plane stretched string tyre model together with a number of approximate models. One of these models did ignore the contact length. For the aligning torque the effect of tread width and the gyroscopic couple were introduced.

The present chapter deals with the further development of this type of model which in its simplest form has been and still is very popular in vehicle dynamics studies. Both in-plane and out-of-plane models will be discussed for small slip, linear and for large slip, non-linear conditions. The concept of the relaxation length is central in the model structure. The development of the single point contact models follows an essentially different and much simpler line compared with the theoretical approach on which the string model is based. Because of its simplicity it is possible to enhance the model to cover the full non-linear combined slip range including rolling from standstill or even change direction from forwards to backwards rolling. Camber and turn slip may be included.

With the linear and non-linear models, to be developed in this chapter, various vehicle dynamics problems may be approximately analysed such as the shimmy phenomenon (cf. curve for single point model in Fig.6.2), transient vehicle motions with oscillatory steer inputs, motion over undulated road surfaces at side slip and camber, steering vibrations induced by wheel imbalance and tyre out-of-roundness. In these studies the effect of tyre lag may be ascertained. In a number of applications to be treated in Chapter 8 we will address these problems (except wheel shimmy, which was the subject of Chapter 6).

7.2. Model Development

The model consists of a contact patch (point) that is suspended with respect to the wheel rim by a longitudinal (circumferential) and a lateral spring. These springs represent the compliance of the tyre carcass. The contact point may move (slip) with respect to the ground in lateral and longitudinal directions. Through this relative motion the side force, longitudinal force and aligning torque are generated. To determine these forces and moments, contact patch lateral slip (possibly including ply-steer) and longitudinal slip are defined. Camber contact line curvature, possibly including conicity and turn slip, is thought to exist which is represented by an effective total camber angle. These contact patch slip quantities may then be used as input in the steady-state tyre slip model, e.g. the Magic Formula, to calculate the transient force and moment variation that act upon the contact patch.

7.2.1. Linear Model

Figure 7.1 depicts the model in top view. At the instant considered, the wheel slip point S (attached to the wheel rim at a level near the road surface) and the contact point S' are defined to be located in the plane through the wheel axis and normal to the road. These points (which may be thought to lie on two parallel slip circles) move over the road surface with the wheel and contact patch slip velocities respectively. In the figure, the x and y components of the slip velocities

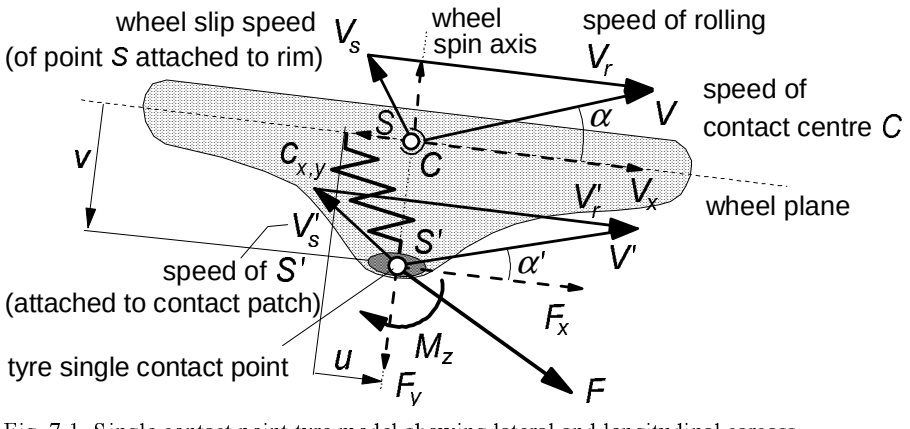

Fig. 7.1. Single contact point tyre model showing lateral and longitudinal carcass deflections, u and v. (Top view).

have been shown as negative quantities. The difference of the velocities cause the carcass springs to deflect. Consequently, the time rates of change of the longitudinal and lateral deflections u and v read:

$$\frac{\mathrm{d}u}{\mathrm{d}t} = -\left(V_{sx} - V'_{sx}\right) \tag{7.1}$$

and

$$\frac{\mathrm{d}v}{\mathrm{d}t} = -\left(V_{sy} - V'_{sy}\right) \tag{7.2}$$

If we assume small values of slip we may write for the side force acting from road to contact patch with $C_{F\alpha}$ denoting the cornering or side slip stiffness:

$$F_y = C_{F\alpha}\alpha' = -C_{F\alpha}\frac{V'_{sy}}{|V_x|} \tag{7.3}$$

It is assumed here that the difference between the wheel centre longitudinal velocity V_x and the longitudinal velocity V_{cx} of the contact centre is negligible.

$$V_{cx} \approx V_x \tag{7.4}$$

Consequently, we may employ V_x in the present chapter. With the lateral tyre stiffness at road level C_{Fy} we have for the elastic internal force that balances the side slip force:

$$F_y = C_{Fy}v \tag{7.5}$$

and we can write for Eq.(7.2) with (7.3,5) after having introduced the relaxation length for side slip σ_α:

$$\sigma_\alpha = \frac{C_{F\alpha}}{C_{Fy}} \tag{7.6}$$

the differential equation for the lateral deflection due to side slip v_α (later on we will also have a lateral deflection due to camber):

$$\frac{\mathrm{d}v_\alpha}{\mathrm{d}t} + \frac{1}{\sigma_\alpha}|V_x|v_\alpha = |V_x|\alpha = -V_{sy} \tag{7.7}$$

Where α is the wheel slip angle: $\alpha \approx -V_{sy}/|V_x|$. The side force is obtained by multiplying v_α with C_{Fy}.

In a similar way we can deal with the longitudinal force response. With the longitudinal tyre stiffness C_{Fx} at road level and the longitudinal slip stiffness $C_{F\kappa}$ we obtain for the relaxation length σ_κ:

$$\sigma_\kappa = \frac{C_{F\kappa}}{C_{Fx}} \tag{7.8}$$

and we can derive with Eq.(7.1) the differential equation for the fore and aft deflection u

$$\frac{\mathrm{d}u}{\mathrm{d}t} + \frac{1}{\sigma_\kappa}|V_x|u = |V_x|\kappa = -V_{sx} \tag{7.9}$$

with κ the longitudinal wheel slip ratio: $\kappa \approx -V_{sx}/|V_x|$. The longitudinal force may be obtained by multiplying u with the stiffness C_{Fx}.

Next, we consider wheel camber as input. For a suddenly applied camber angle γ (about the line of intersection at ground level!), we assume that a contact line curvature and thus the camber thrust $C_{F\gamma}\gamma$ is immediately felt at the contact patch. As a reaction, a contact patch side slip angle α' is developed that builts up the lateral carcass deflection $v=v_\gamma$. Again Eq.(7.5) applies. The side force that acts on the wheel now becomes:

$$F_y = C_{Fy}v_\gamma = C_{F\gamma}\gamma + C_{F\alpha}\alpha' \tag{7.10}$$

With wheel side slip kept equal to zero, $V_{sy}=0$, and $V'_{sy}=-|V_x|\alpha'$ Eq.(7.2) can be written in the form:

$$\frac{\mathrm{d}v_\gamma}{\mathrm{d}t} + \frac{1}{\sigma_\alpha}|V_x|v_\gamma = \frac{C_{F\gamma}}{C_{F\alpha}}|V_x|\gamma \tag{7.11}$$

This equation shows that according to this simple model the camber force relaxation length σ_γ is equal to the relaxation length for side slip σ_α. This theoretical result is substantiated by careful step response experiments, performed by Higuchi (1997) on a flat plank test rig (cf. Sec.7.2.3).

A similar equation results for the total spin φ including turn slip and camber:

$$\frac{\mathrm{d}v_\varphi}{\mathrm{d}t} + \frac{1}{\sigma_\alpha}|V_x|v_\varphi = \frac{C_{F\varphi}}{C_{F\alpha}}|V_x|\varphi \tag{7.12}$$

with according to Eq.(4.76):

$$\varphi = -\frac{1}{V_x}\{\dot{\psi} - (1-\varepsilon_\gamma)\Omega\sin\gamma\} \tag{7.13}$$

that shows that the turn slip velocity $\dot{\psi}$ can be converted into an equivalent camber angle.

The forces and moment are obtained from the deflections u and v by first assessing the transient slip quantities α', κ' and γ' and from these with the slip stiffnesses the forces and moment.

According to the adopted steady-state model, Eq.(4.E71), the moment response to camber (and turn slip) is the sum of the residual torque, M_{zr}, assumedly mainly due to finite tread width, and $-t_\alpha F_y$, assumedly caused by camber induced side slip, cf. discussion later on (below Eq.(7.40)). A first-order

approximation for the response of M_{zr} with the short relaxation length equal to half the contact length a may be employed. This, however, will be saved for Chapter 9 where short wavelengths responses are considered. Here we suffice with the assumption that the moment due to tread width responds instantaneously to camber and turn slip.

For the linear, small slip condition we find:

$$\alpha' \approx \tan\alpha' = \frac{v_\alpha}{\sigma_\alpha}, \qquad F_{y\alpha} = C_{F\alpha}\alpha', \qquad M_{z\alpha} = -C_{M\alpha}\alpha' = -t_\alpha F_{y\alpha} \tag{7.14}$$

$$\kappa' = \frac{u}{\sigma_\kappa}, \qquad F_x = C_{F\kappa}\kappa' \tag{7.15}$$

$$\gamma' = \frac{C_{F\alpha}}{C_{F\gamma}}\frac{v_\gamma}{\sigma_\alpha}, \qquad F_{y\gamma} = C_{F\gamma}\gamma', \qquad M_{zr\gamma} = (C_{M\gamma} + t_\alpha C_{F\gamma})\gamma \tag{7.16}$$

and similar for φ. The pneumatic trail due to side slip is denoted here with t_α. The total aligning torque becomes (cf. Eq.(4.E71) and Fig.4.21):

$$M_z = -t_\alpha(F_{y\alpha} + F_{y\gamma}) + M_{zr\gamma} \tag{7.17}$$

In an alternative model, used for motorcycle dynamics studies, the terms with $t_\alpha C_{F\gamma}$ or $t_\alpha F_\gamma$ in (7.16,17) are omitted, cf. discussion below Eq.(7.40).

The equations (7.7,9,11) may be written in terms of the transient slip quantities. For example, we may express v_α in terms of α' by using the first equation of (7.14). Insertion in (7.7) gives:

$$\sigma_\alpha \frac{\mathrm{d}\alpha'}{\mathrm{d}t} + |V_x|\alpha' = |V_x|\alpha = -V_{sy} \tag{7.18}$$

If we recognise the fact that the relaxation length is a function of the vertical load and if the average slip angle is unequal to zero, an additional term shows up in the linearised equation (variation of α' and of $F_z(t)$ small!) which results from the differentiation of $v_\alpha = \sigma_\alpha\alpha'$ with respect to time. Then, Eq.(7.7) becomes:

$$\sigma_\alpha \frac{\mathrm{d}\alpha'}{\mathrm{d}t} + \left(|V_x| + \frac{\mathrm{d}\sigma_\alpha}{\mathrm{d}F_z}\frac{\mathrm{d}F_z}{\mathrm{d}t}\right)\alpha' = |V_x|\alpha = -V_{sy} \tag{7.19}$$

Obviously, when using Eq.(7.18) a response to a variation of the vertical load can not be expected. If the load varies, Eq.(7.18) is inadequate and the original equation (7.7) should be used or the corresponding equation (7.19).

With (7.5) equation (7.7) may be written directly in terms of F_y. If we may consider the carcass lateral stiffness C_{Fy} virtually independent of the wheel load F_z we obtain by using Eq.(7.6) :

$$\sigma_\alpha \frac{\mathrm{d}F_y}{\mathrm{d}t} + |V_x|F_y = |V_x|F_{yss} \tag{7.20}$$

Since we have the same relaxation length for both the responses to side slip and

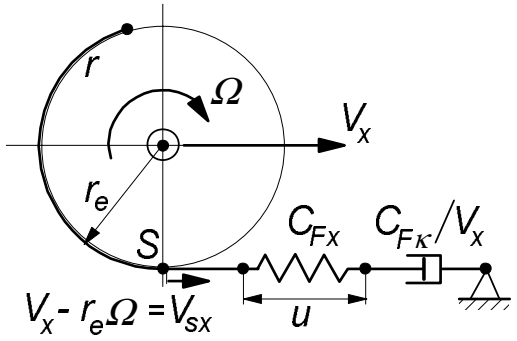

Fig. 7.2. Mechanical model of transient tangential tyre behaviour.

camber, this equation appears to hold for the combined linear response to the inputs α and γ or φ. In the right-hand member F_{yss} denotes the steady-state (instantaneous) response to these inputs and possibly a changing vertical load at a given slip condition. Multiplication with the pneumatic trail produces the moment $-M_z'$ (if $\gamma = \varphi = 0$). A similar differential equation may be written for the F_x response to κ.

The equations (7.7,9) have been written in the form (V_x not in denominator and $V_{sx,y}$ used as right-hand member) that makes them applicable for simulations of stopping and starting from zero speed occurrences. At speed $V_x = 0$ Eq.(7.9) turns into an integrator: $u = -\int V_{sx} dt$. With Eq.(7.15) the longitudinal force becomes: $F_x = C_{F\kappa}\kappa' = C_{F\kappa}\, u/\sigma_\kappa$ which with (7.8) is equal to: $C_{Fx}\, u$. This is the correct expression for the tyre that at standstill acts like a longitudinal or tangential spring. When the wheel starts rolling, the tyre gradually changes into a damper with rate: $C_{F\kappa}/|V_x|$. Figure 7.2 depicts a corresponding mechanical model with spring and damper in series. It shows that at low speed the damper becomes very stiff and the spring dominates. At higher forward velocities the spring becomes relatively stiff and the damper part dominates the behaviour of the tyre. A similar model may be drawn for the transient lateral behaviour. It may be noted that the equation (7.20) is not suited for moving near or at $V_x = 0$. In Section 8.6 the use of the transient models for the response to lateral and longitudinal wheel slip speed at and near zero speed will be demonstrated.

Apparently, Eq.(7.12) with (7.13) fails to describe the response to variations in wheel yaw angle ψ at vanishing speed. Then, the lateral deflection becomes $v_\varphi = -(C_{F\varphi}/C_{F\alpha})\int d\psi$. With $\varphi' = (C_{F\alpha}/C_{F\varphi})v_\varphi/\sigma_\alpha$ we have $\varphi' = -\psi/\sigma_\alpha$ indicating an instantaneous response of F_y which, however, should remain zero! We refer to Chapter 9, Section 9.2.1, Eq.(9.56 etc.), that suggests a further developed model that can handle this situation correctly. Consequently, it must be concluded that the present transient model cannot be employed to simulate parking manoeuvres unless F_y is suppressed artificially in the lower speed range.

7.2.2. Semi-Non-Linear Model

For the extension of the linear theory to cover the non-linear range of the slip characteristics, it may be tempting to employ Eq.(7.20) and use the instantaneous non-linear force response as input in the differential equation. The input steady-state side force is calculated, e.g. with the Magic Formula, using the current wheel slip angle α. This method, however, may lead to incorrect results as due to the phase lag in side force response, the current (varying) wheel load may not correspond to the calculated magnitude attained by the side force. In limit conditions the tyre may then be predicted to be still in adhesion while in reality full sliding occurs. A better approach is the utilisation of the original equation (7.7) and calculate the side force afterwards by using the resulting transient slip angle α' as input in the Magic Formula.

In general, we have the three equations (7.7,9,11) and possibly (7.12) and the first equations of (7.14-17) producing α', κ' and γ' or φ' which are used as input in the non-linear force and moment functions (γ or φ directly in the expressions for M_r), e.g. the equations of the Magic Formula tyre model (Chapter 4).

$$F_x = F_x(\kappa', \alpha', F_z) \tag{7.21}$$

$$F_y = F_y(\alpha', \gamma', \kappa', F_z) \tag{7.22}$$

$$M_z' = -t_\alpha F_y \tag{7.23}$$

$$M_{zr} = M_{zr}(\gamma, \alpha', \kappa', F_z) \tag{7.24}$$

$$M_z = M_z' + M_{zr} + s \cdot F_x \tag{4.E71}$$

where if required, γ may be replaced by φ as the spin argument.

This non-linear model is straightforward and is often used in transient or low frequency vehicle motion simulation applications. Starting from zero speed or stopping to standstill is possible. However, as has been mentioned before, at V_x equal or close to zero the equations (7.7,9) act as integrators of the slip speed components $V_{sx,y}$, which may give rise to possibly very large deflections. The limitation of these deflections may be accomplished by making the derivatives of the deflections u and v equal to zero, if (1) the forward wheel velocity has become very small ($<V_{low}$) and (2) the deflections take values larger than physically possible. This can be seen to correspond with the combined equivalent side slip value exceeding the level α_{sl} where the peak horizontal force occurs. Approximately, we may adopt the following limiting algorithm with the equivalent slip angle according to Eq.(4.E78):

if: $|\alpha'_{r,eq}| > \alpha_{sl}$ and $|V_x| < V_{low}$

then: if: $(V_{sx} + |V_x|u/\sigma_\kappa)u < 0$: $\dot{u} = 0$ else: Eq.(7.9) applies

if: $(V_{sy} + |V_x|v/\sigma_\alpha)v < 0$: $\dot{v} = 0$ else: Eq.(7.7) applies

else: Eqs.(7.7,9) apply (7.25)

with roughly:

$$\alpha_{sl} = 3D_y/C_{F\alpha}$$

Experience in applying the model has indicated that starting from standstill gives rise to oscillations which are practically undamped. Damping increases when speed is built up. To artificially introduce some damping at very low speed, which with the actual tyre is established through material damping, one might employ the following expression for the transient slip κ' , as suggested by Besselink, instead of Eq.(7.15):

$$\kappa' = \left(\frac{u}{\sigma_\kappa} - \frac{k_{Vlow}}{C_{F\kappa}} V_{sx} \right) \tag{7.26}$$

The damping coefficient k_{Vlow} should be gradually suppressed to zero when the speed of travel V_x approaches a selected low value V_{low}. Beyond that value the model should operate as usual. In Chapter 8, Sec.8.6 an application will be given. A similar equation may be employed for the lateral transient slip.

Another extreme situation is the condition at wheel lock. At steady state Eq.(7.9) reduces to:

$$\frac{1}{\sigma_\kappa}|V_x|u = -V_x \tag{7.27}$$

which indicates that the deflection u according to the semi-linear theory becomes as large as the relaxation length σ_κ. Avoiding the deflections from becoming too large, which is of importance at e.g. repetitive braking, calls for an enhanced non-linear model. Another shortcoming of the model that is to be tackled concerns the experimentally observed property of the tyre that its relaxation length depends on the level of slip. At higher levels of side slip, the tyre shows a quicker response to additional changes in side slip. This indicates that the relaxation lengths decrease with increasing slip.

7.2.3. Fully Non-Linear Model

Figure 5.29, repeated here as Fig.7.3 shows the deflected string model provided with tread elements at various levels of steady-state side slip. Clearly, this model predicts that the 'intersection' length σ^* decreases with increasing α that is: when

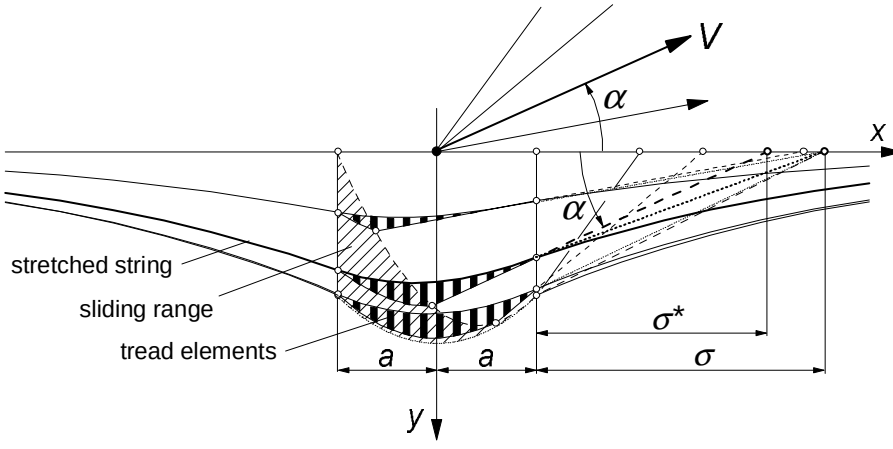

Fig. 7.3. The string tyre model with tread elements at increasing slip angles showing growing sliding range and decreasing 'intersection' length σ^*.

the sliding range grows. In the single point contact model we may introduce a similar reduction of the corresponding length. The intersection length σ_α^* is defined here as the ratio of the lateral deflection v_α and the transient lateral slip $\tan\alpha$:

$$\sigma_\alpha^* = \frac{v_\alpha}{\tan\alpha'} \tag{7.28}$$

In Eq.(7.7) the relaxation length σ is replaced by σ^* and we get:

$$\frac{\mathrm{d}\,v_\alpha}{\mathrm{d}\,t} + \frac{1}{\sigma_\alpha^*}|V_x|\,v_\alpha = |V_x|\tan\alpha = -V_{sy} \tag{7.29}$$

with apparently:

$$\sigma_\alpha^* = \frac{1}{C_{Fy}}\frac{F_y}{\tan\alpha'} = \frac{\sigma_{\alpha o}}{C_{F\alpha}}\frac{F_y}{\tan\alpha'} \approx \frac{\sigma_{\alpha o}}{C_{F\alpha}}\frac{|F_y'| + C_{F\alpha}\varepsilon_F}{|\tan\alpha_f'| + \varepsilon_F} \tag{7.30}$$

with the initial relaxation length (at $\alpha' = 0$):

$$\sigma_{\alpha o} = \frac{C_{F\alpha}}{C_{Fy}} \tag{7.31}$$

to which σ_α^* approaches when $\alpha' \to 0$. To avoid singularity, one may use the last expression of (7.30) with small ε_F and add to α' the shift $\Delta\alpha$ to arrive at α_f' as indicated in Fig.4.22. Figure 7.4 presents the characteristic of the intersection length together with the side force characteristic from which it is derived. Also in the equation for the camber deflection response (7.11) the relaxation length σ_α

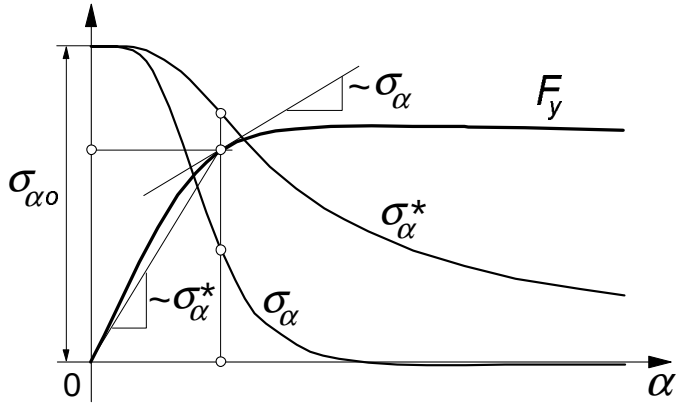

Fig. 7.4. Characteristics of tyre side force, 'intersection length' σ_α^* and relaxation length σ_α.

is replaced by σ_α^*.

A more direct way to write Eq.(7.29) is yielded by eliminating σ_α^* with the use of Eq.(7.28):

$$\frac{\mathrm{d}v_\alpha}{\mathrm{d}t} + |V_x|\tan\alpha' = |V_x|\tan\alpha = -V_{sy} \tag{7.32}$$

The transient slip angle α' is obtained from the deflection v_α by using the inverse possibly adapted $F_y'(\alpha')$ characteristic, cf. Higuchi (1997):

$$v_\alpha = \frac{F_y'(\alpha')}{C_{Fy}} \tag{7.33}$$

To avoid double valued solutions a for this purpose adapted characteristic for $F_y'(\alpha')$ in (7.30) or (7.33) may be required showing a positive slope in the slip range of interest. The value for α' or for σ_α^* when Eq.(7.29) is used, is obtained through iterations or by using information from the previous time step, cf. Higuchi(1997), Pacejka(1992), Takahashi(1996). The ultimate value of the force F_y is finally obtained from Eq.(7.22) by using the computed $\tan\alpha'$ $(= v_\alpha/\sigma_\alpha^*)$.

Writing the equation (7.32) entirely in terms of the transient slip angle by using (7.5) with $v = v_\alpha$ and remembering that $F_y = F_y(\alpha', F_z)$ directly yields:

$$\frac{1}{C_{Fy}}\frac{\partial F_y}{\partial \tan\alpha'}\frac{\mathrm{d}\tan\alpha'}{\mathrm{d}t} + |V_x|\tan\alpha' = -V_{sy} - \frac{1}{C_{Fy}}\frac{\partial F_y}{\partial F_z}\frac{\mathrm{d}F_z}{\mathrm{d}t} \tag{7.34}$$

The additional input $\mathrm{d}F_z/\mathrm{d}t$ requires information of the slope $\partial F_y/\partial F_z$ at given values of the slip angle. If the vertical load remains constant the last term vanishes and we have the often used equation of the restricted fully non-linear model:

$$\sigma_\alpha \frac{\mathrm{d}\tan\alpha'}{\mathrm{d}t} + |V_x|\tan\alpha' = -V_{sy} \tag{7.35}$$

with

$$\sigma_\alpha = \frac{1}{C_{Fy}} \frac{\partial F_y}{\partial \tan\alpha'} \tag{7.36}$$

If we consider an average slip angle α_o and a small variation $\tilde{\alpha}$ of $\tan\alpha$ and the corresponding lateral slip velocities, Eq.(7.35) becomes after having subtracted the average part:

$$\sigma_\alpha \frac{\mathrm{d}\tilde{\alpha}'}{\mathrm{d}t} + |V_x|\tilde{\alpha}' = -\tilde{V}_{sy} \tag{7.37}$$

which indicates that the structure of (7.35) is retained and that σ_α (7.36) represents the actual relaxation length of the linearised system at a given load and slip angle. Its characteristic has been depicted in Fig.7.4 as well. Obviously, the relaxation length is associated with the slope of the side force characteristic. It also shows that the relaxation length becomes negative beyond the peak of the side force characteristic which makes the solution of (7.35) but also of the original equation (7.29) or (7.32) unstable if the point of operation lies in that range of side slip. We may, however, limit σ_α downwards to avoid both instability and excessive computation time: $\sigma_\alpha = \max(\sigma_\alpha, \sigma_{\min})$. The transient response of the variation of the force proceeds in proportion with the variation of $\tilde{\alpha}'$ as $\tilde{F}_y = (\partial F_y/\partial\tan\alpha)\tilde{\alpha}'$.

When the Eq.(7.35) is used, an algebraic loop does not occur as is the case when Eq.(7.29) is employed. The relaxation length σ_α can be directly determined from the already available $\tan\alpha'$. However, since the last term of (7.34) has been omitted equation (7.35) has become insensitive to F_z variations.

Similar functions and differential equations can be derived for the transient response to longitudinal slip. We obtain for the distance factors:

$$\sigma_\kappa^* = \frac{1}{C_{Fx}} \frac{F_x}{\kappa'} = \frac{\sigma_{\kappa o}}{C_{F\kappa}} \frac{F_x}{\kappa'} \approx \frac{\sigma_{\kappa o}}{C_{F\kappa}} \frac{|F_x| + C_{F\kappa}\varepsilon_F}{|\kappa'| + \varepsilon_F} \tag{7.38}$$

and

$$\sigma_\kappa = \frac{1}{C_{Fx}} \frac{\partial F_x}{\partial \kappa'} \tag{7.39}$$

It is of interest to note that the extreme case of wheel lock can now be handled correctly. As we have seen below Eq.(7.27) the deflection then becomes equal to minus the relaxation length which according to the fully non-linear model becomes: $u = -\sigma_\kappa^*$. With (7.38) and $\kappa' = -1$ the deflection takes the value that

would actually occur at wheel lock: $u = F_x / C_{Fx}$.

The use of Eqs.(7.29,32) is attractive for simulation purposes because the solution contains the transient effect of changing vertical load. However, we may have computational difficulties to be reckoned with which may require some preparations. Using Eq.(7.35) proceeds in a straightforward manner if the derivative of the force vs slip characteristic is known beforehand. This requires some preparation and may become quite complex if the general combined slip situation is to be considered. Approximations using equivalent total slip according to Eq.(4.E78) may be realisable. A drawback, of course, is the fact that Eq.(7.35) does not respond to changes in F_z. In Chapter 9 this equation is used to handle the transient response of the tread deflections in the contact patch.

Figures 7.5-12 present results obtained by Higuchi (1997) for a passenger car 205/60R15 tyre tested on a flat plank machine (TU-Delft, cf. Fig.9.63). Figure 7.5 shows the response of the side force to step changes in slip angle at the nominal load of 4000N. The diagram clearly indicates the difference in behaviour at the different levels of side slip with a very rapid response occurring at $\alpha = 10°$. The fully non-linear model according to Eqs.(7.32) or (7.29) or as in this case, with constant vertical load, Eq.(7.35), in conjunction with Eqs.(7.22,23) gives satisfactory agreement. The measured response curves have been corrected for the side force variation that arises already at zero slip angle. The test is performed by loading the tyre after the slip angle (steer angle) has been applied. Subsequently, the plank is moved. The aligning torque behaves in a similar manner although a little initial delay in response occurs as correctly predicted by the string model and shown in Fig.5.12. At larger slip angles (beyond the level where the M_z peak occurs) the aligning torque first shows a peak in the response after which the moment decays to its steady-state value. This behaviour is nicely followed by the model. Figure 7.6 shows the side force response to small increments in slip angle. The experiment is conducted by, after having stopped the plank motion, steering the wheel half a degree further and continue the forward motion. It was first ascertained that the response of the side force to a step steer input was hardly influenced by having first lifted the tyre from the road surface or not. Of course, the aligning moment response, in the latter case, is quite different because of initial torsion about the vertical axis. The resulting side force responses as depicted in Fig.7.6 have been compared with the exponential response of the side force increment as predicted by the solution of Eq.(7.37) with (7.36). Fitting with a least square procedure gave the relaxation length σ_α as presented in Fig.7.7. The resulting variation of σ_α with slip angle level is compared with the slope of the steady-state side force characteristic, both normalised making their values equal to unity at vanishing slip angle.

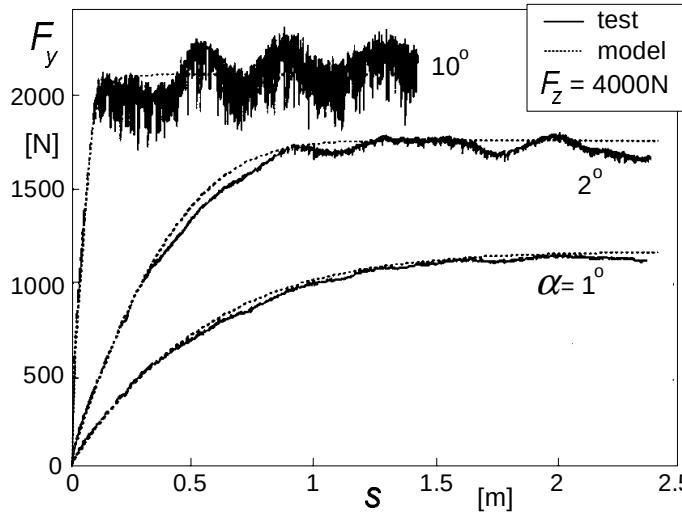

Fig. 7.5. Side force response to small and large step change in slip angle as assessed by flat plank experiments and computed with the model defined by Eqs.(7.32) or (7.29).

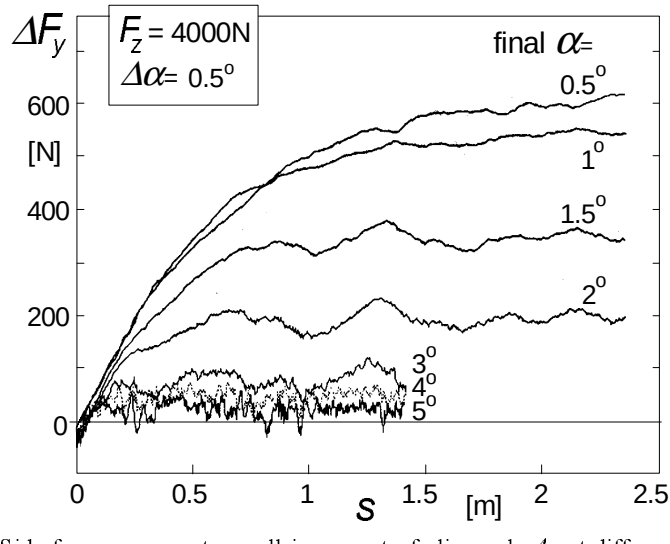

Fig. 7.6. Side force response to small increment of slip angle $\Delta\alpha$ at different levels of slip angle indicating the decrease of relaxation length at increasing slide slip level which is in agreement with expression (7.36).

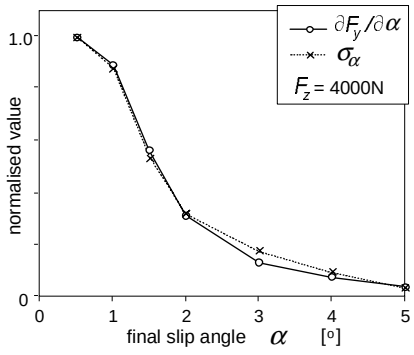

Fig. 7.7. Correspondence between F_y vs α slope and relaxation length σ_α as assessed by experiments.

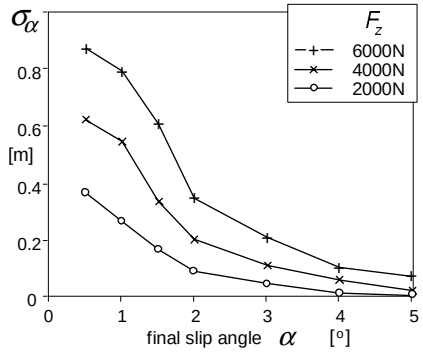

Fig. 7.8. Relaxation length measured at various wheel loads, decaying with increasing slip angle.

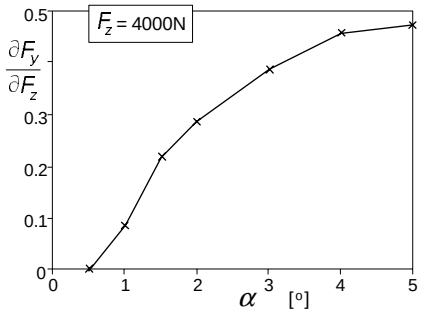

Fig. 7.9. The slope of F_y vs F_z as a function of slip angle, appearing in Eq.(7.34), as assessed by tests.

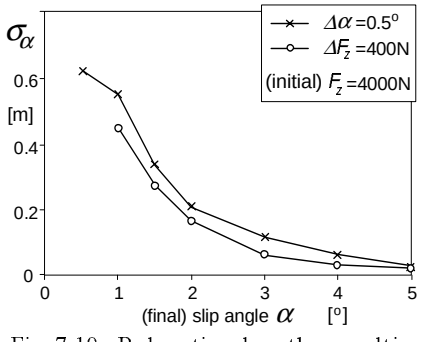

Fig. 7.10. Relaxation lengths resulting from small step changes in slip angle or wheel load, as function of slip angle level, Higuchi (1997).

The excellent agreement supports the theoretical findings. Additional experiments have been conducted by Higuchi investigating the response to small increments in vertical load at constant slip angle. As shown by Eq.(7.34) the partial derivative $\partial F_y/\partial F_z$ plays the role as input parameter. Figure 7.9 shows its variation with slip angle level. Figure 7.10 compares the resulting relaxation length values with those associated with changes in slip angle at constant load. Apparently, the relaxation length for slip angle change is larger than the one belonging to load change. However, due to the finite magnitude of the increments (0.5° and 400N respectively) the actual differences are expected to be smaller. In the diagram, the curve for $\Delta\alpha$ may be better shifted to the left over 0.25° while the curve for ΔF_z may be reduced a little in height using information from Fig.7.8 accounting for a decrease of the average load level of 200N.

Higuchi also investigated the responses to changes in camber angle, and to a limited extent also to the related turn slip. The change in camber was correctly established by rotating the road surface (the plank) about the line of intersection of wheel centre plane and plank surface (steer angle is kept equal to zero). The step response to turn slip φ_t=-1/R is obtained by integrating the response to a pulse change in turn slip, that is: load tyre, twist (ψ) and then roll in the new wheel plane direction, and multiply the result with 1/($R\psi$). The responses to camber and turn slip show quantitatively similar responses. The small initial delay of the response of the car tyre side force to camber and turn slip (cf. Fig.5.12,10) will effectively increase the relaxation length a little. Figures 7.11a and 7.11b show the responses of side force and moment to step changes in camber angle. The side force behaves in a manner similar to the response to side slip, Fig.7.5. Since we have a camber stiffness much smaller than the cornering stiffness, the camber force characteristic remains almost linear over a larger range of the camber angle (meaning: there is less sliding in the contact patch). Therefore, the difference in step responses remains relatively small. This is reflected by the diagram of Fig.7.12 showing the variation of the resulting relaxation length. Comparison with Fig.7.8 reveals that the relaxation lengths assessed for the responses to side slip (at small side slip) and camber have comparable magnitudes. This supports the theory of Eq.(7.11).

Comparison of the Figs.5.12 (lower left diagram) and 7.11a may reveal the quantitative difference in steady-state side force response to turn slip and camber angle. According to Eq.(3.55) the relationship between turn slip stiffness and camber stiffness will be: $C_{F\gamma}$= (1-ε_γ)$C_{F\varphi}/r_e$. With the tyre effective rolling radius equal to approximately 0.3m and the estimated steady-state levels reached in Figs.5.12 and 7.11a for R=115m and γ =10° respectively, we find for the reduction factor approximately: ε_γ=2/3.

The response of the aligning torque to camber is similar to the response to turn slip (cf. Fig.5.12). The moment quickly reaches a maximum after which a slower decay to the steady-state level occurs. The string model with tread width effect predicts the same for the response to turn slip as can be concluded by adding the curves for M_z' and M_z^* (response to φ, Fig.5.10) in an appropriate proportion. The model developed in the present chapter generates a similar response but through a different mechanism. Equation (4.E71) that for $F_x = 0$ takes the form:

$$M_z = M_z' + M_{zr} = -t_\alpha F_y + M_{zr} \tag{7.40}$$

is used after having computed the transient slip and camber angles α' and γ'.

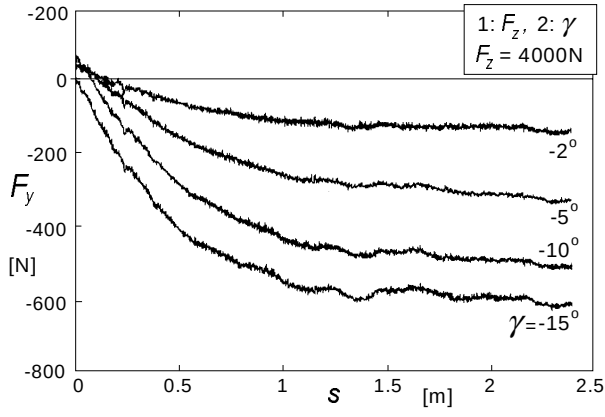

Fig. 7.11a. Side force response to step change in camber angle.

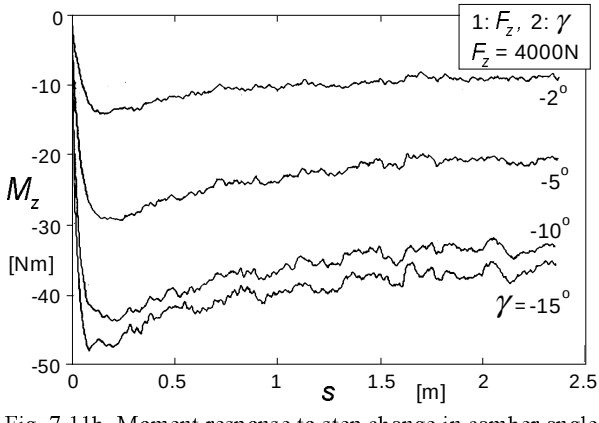

Fig. 7.11b. Moment response to step change in camber angle.

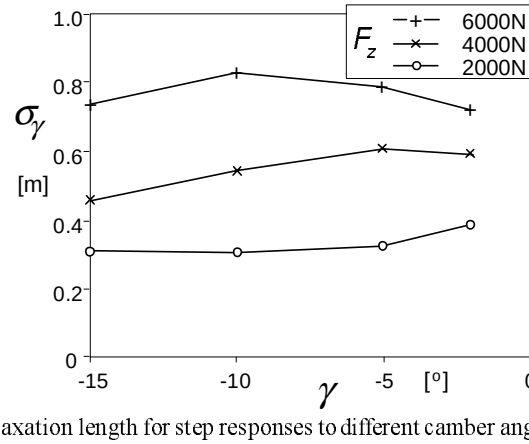

Fig. 7.12. Relaxation length for step responses to different camber angles (abscissa) at various wheel loads (camber after loading).

As can be seen in Fig.4.13 or 4.21, the aligning torque caused by camber at zero slip angle is attributed to the residual torque M_{zr} and to the counteracting moment equal to the aligning stiffness $C_{M\alpha}$ times $\Delta\alpha_\gamma$ which is the same as $-t_\alpha F_y$ at $\alpha = 0$. The residual torque responds quickly with a relatively short relaxation length (about equal to half the contact length) or as has been suggested above for the present model: instantaneously. As the side force responds slowly with relaxation length σ_α, and $-t_\alpha F_y$ is opposite in sign with respect to the residual torque, a similar response as depicted in Fig.7.11b will be developed by the model represented by Eq.(7.40). The mechanism behind this response is supported by the physical reasoning that the moment due to tread width, that responds relatively fast to changes in camber and turn slip, gives rise to a yaw torsion of the carcass/belt in the contact zone which acts as a slip angle. This side slip generates a side force that acts in the same direction as the camber force generated by the camber induced spin. In addition, an aligning moment is generated that acts in a sense opposite to that of the tread-width camber (spin) moment. Ideally, in Fig.4.21, the moment due to camber spin is equal to the residual torque M_{zr} while $-C_{M\alpha}\Delta\alpha_\gamma = t_\alpha F_y$ is equal to the moment due to the yaw torsion induced side slip. However, in reality, only a part of the camber force F_y results from camber spin induced side slip. It is expected that the above analysis is partly true. Perhaps even for an appreciable part. The remaining part that is responsible for the 'hump' in the moment response must then be due to the transient asymmetric lateral tyre deformation that vanishes when the steady-state condition is reached. Figure 5.9 depicts the nature of this transient deflection.

In an alternative model, used for motorcycle dynamics studies dealing with possibly large camber angles, the other extreme is used and the term $t_\alpha F_y$ is replaced by $t_\alpha F_{y\alpha}$, that is: with the side force attributed to the (transient) side slip angle alone (cf. Chapter 10).

7.2.4. Non-Lagging Part

The force response to camber change exhibits a peculiar feature. It turns out that directly after that the wheel is cambered, a side force is developed instantaneously. This, obviously, is caused by the non-symmetric distortion of the cross section of the lower part of the tyre. This initial 'non-lagging' side force shown in Fig.7.11a at a distance rolled $s = 0$ appears, in the case considered, to act in a direction opposite to the steady-state side force. Also equal directions turn out to occur as has been reported in the literature for a motorcycle tyre, cf. Segel and Wilson (1976). In these experiments the camber angle is applied after that the tyre is loaded. We may conduct an experiment where the free wheel is

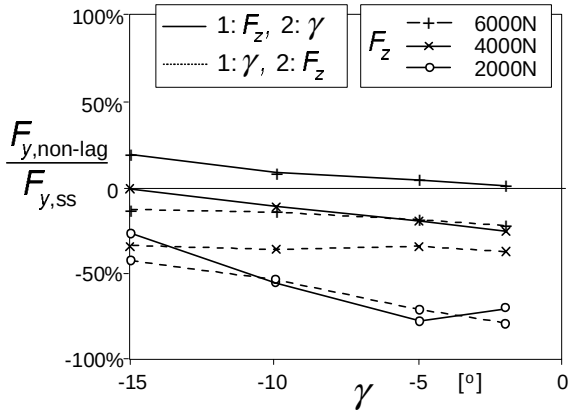

Fig. 7.13. Non-lagging part of side force response for the cases (1) applying camber after having loaded the tyre and (2) loading the tyre normal to the road after having cambered the wheel 'in the air'.

first cambered and then moved to the road in normal direction. This appears to result in a somewhat larger non-lagging part. Figure 7.13 gives the percentage of the non-lagging part with respect to the steady-state side force for different wheel loads and for the two considered ways of reaching the loaded and cambered condition before rolling has started. The higher loaded tyre appears to generate equally directed initial and steady-state side force responses to a change in camber angle.

To introduce this tyre property into the model we may define a non-lagging fraction ε_{NL}. The portion of the input camber angle γ_{NL} that gives rise to the non-lagging response is $\varepsilon_{NL}\gamma$. The remaining part $\gamma_L = (1 - \varepsilon_{NL})\gamma$ yields the lagged response. In the right-hand member of Eq.(7.11) γ must now be replaced by γ_L and the sum $\gamma' + \gamma_{NL}$ is to be used as input into Eq.(7.22), while the camber angle γ itself acts as the direct input into Eq.(7.24) for the residual torque (if we neglect the associated short relaxation length).

The following equations apply instead of Eq.(7.11):

$$\frac{\mathrm{d}v_\gamma}{\mathrm{d}t} + \frac{1}{\sigma_\alpha}|V_x|v_\gamma = (1-\varepsilon_{NL})\frac{C_{F\gamma}}{C_{F\alpha}}|V_x|\gamma \tag{7.41}$$

from which the transient camber angle is obtained

$$\gamma'_L = \frac{C_{F\alpha}}{C_{F\gamma}}\frac{v_\gamma}{\sigma_\alpha} \tag{7.42}$$

The non-lagging part is

$$\gamma_{NL} = \varepsilon_{NL}\gamma \tag{7.43}$$

so that the ultimate value for the input in Eq.(7.22) becomes:

$$\gamma' = \gamma'_L + \gamma_{NL} \tag{7.44}$$

For the linear case we would obtain for the camber force and moment responses:

$$F_{y\gamma} = C_{F\gamma}\gamma' \tag{7.45}$$

$$M_{z\gamma} = -t_\alpha C_{F\gamma}\gamma' + (C_{M\gamma} + t_\alpha C_{F\gamma})\gamma \tag{7.46}$$

For the fraction ε_{NL} we may take the ratio of the output side force as depicted in Fig.7.13 (at small camber). The non-lagging fraction is load dependent. This also holds for the non-lagging fraction that is found to occur when loading of the tyre (performed by moving the wheel in a direction perpendicular to the road surface) follows after that the free unloaded wheel has been tilted. When a vehicle moves over an undulated road surface the observed tyre properties regarding camber and side slip force response to wheel load variations will be of importance. In the following exercise and in Sec.8.2 this problem is addressed.

Exercise 7.1. Cambered wheel moving up and down.

Consider a wheel that runs at a constant camber angle at zero slip angle on a smooth road surface. The wheel axle is moved vertically as depicted in Fig.7.14. The forces are measured in the wheel hub.

1. Use Eqs.(7.41-45) and develop an expression for the side force response to a ramp change in vertical load defined as ($s = Vt$):

$$s < 0: \qquad F_z = F_{zo}$$
$$0 < s < s_r: \qquad F_z = F_{zo} + \Delta F_z s/s_r$$
$$s > s_r: \qquad F_z = F_{zo} + \Delta F_z$$

The camber angle and load variation are assumed to be relatively small and the equations can be kept linear with relaxation length $\sigma = \sigma_\alpha$ treated as a constant. We may simplify the equations to:

$$\sigma \frac{\mathrm{d}\tilde{v}}{\mathrm{d}s} + \tilde{v} = (1 - \varepsilon_{NL})c\frac{\tilde{F}_z}{F_{zo}}\gamma$$

$$\tilde{\gamma}'_L = b\frac{\tilde{v}}{\sigma}$$

where $c = C_{F\gamma o}/C_{F\gamma}$ and $b = C_{F\alpha o}/C_{F\gamma o}$. With

$$\gamma_{NL} = \varepsilon_{NL}\gamma$$

$$\gamma' = \gamma'_L + \gamma_{NL}$$

we have for the total side force:

$$F_y = C_{F\gamma}\gamma'$$

The change in side force becomes linearized:

$$\tilde{F}_y = C_{F\gamma o}\tilde{\gamma}'_L + \tilde{C}_{F\gamma}\gamma_{NL}$$

with

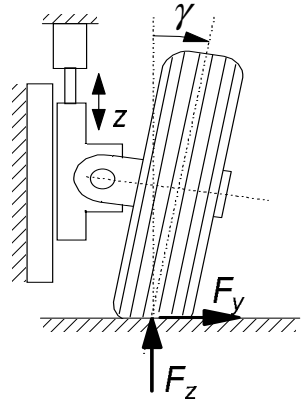

Fig. 7.14. Cambered wheel moved up and down (Exercise 7.1).

$$\tilde{C}_{F\gamma} = \frac{\tilde{F}_z}{F_{zo}} C_{F\gamma o}$$

and

$$\tilde{F}_z = F_z - F_{zo}$$

Take for the parameters the values:

$\sigma = 0.3$m, $b = 10$, $c = 0.03$m, $C_{F\gamma o} = 3000$N/rad,

$\gamma = 0.1$rad, $F_{zo} = 4000$N, $\Delta F_z = 500$N, $s_r = 1$m.

Draw a graph of the change in side force with travelled distance s for the three cases:

ε_{NL} =-0.4, 0, +0.4

Try to find a typical feature of the resulting variation of the course of the side force change that may enable you to assess the percentage non-lagging part ε_{NL} from a test result. Give the relevant formula.

2. Use the same set of equations and assume the increment in vertical load to change sinusoidally:

$$\tilde{F}_z = \Delta F_z \sin\omega_s s$$

Derive for a given constant camber angle the frequency response function

$$H_{Fy,Fz}(i\omega_s) = \frac{\tilde{F}_y(i\omega_s)}{\tilde{F}_z(i\omega_s)}$$

Plot the amplitude ratio and the phase lag versus path frequency ω_s for the same three values of ε_{NL}. Note typical feature of phase lag depending on sign of ε_{NL} from which the non-lagging percentage may be assessed. Derive the formula for the path frequency where phase lag either reaches a maximum or becomes 90 degrees.

7.2.5. The Gyroscopic Couple

In Chapter 5 the gyroscopic couple that arises as a result of the time rate of change of the average tyre tilt deflection angle has been introduced. This angle is considered to be proportional with the lateral tyre deflection v or the side force F_y. Equation (5.178) may be written in terms of the deflection with the use of (5.179):

$$M_{z,gyr} = c_{gyr} m_t r_e \Omega \frac{\mathrm{d}v}{\mathrm{d}t} \tag{7.47}$$

where at free rolling the wheel speed of revolution equals the forward velocity divided by the effective rolling radius of the tyre. In general, we have:

$$\Omega = \frac{V_x - V_{sx}}{r_e} \tag{7.48}$$

For a radial ply steel-belted car tyre the non-dimensional coefficient c_{gyr} has been estimated to take the value 0.5. The quantity m_t represents the mass of the tyre. Extending the expression (7.40) yields for the total aligning moment:

$$M_z = M_z' + M_{zr} + M_{z,gyr} \tag{7.49}$$

7.3. Enhanced Non-Linear Transient Tyre Model

A totally different approach to model the transient rolling properties of the tyre is based on the separation of contact patch slip properties and carcass compliance not through the use of relaxation lengths but by incorporating the carcass springs in the model explicitly. The contact patch is given some inertia to facilitate the computational process (computational causality). This has the drawback that a relatively high natural frequency is introduced, possibly making the computation slower. The method to be discussed, automatically accounts for the property that the lag in the response to wheel slip and load changes diminishes at higher levels of slip that in the previous section was realised by decreasing the relaxation length. This latter approach, however, appeared to possibly suffer from computational difficulties if the model has to also account for the transient response to wheel load variations. Also the response to combined slip was less easy to model. In developing the enhanced model, we should, however, try to maintain the nice feature of the relaxation length model to adequately handle the simulation at speeds near or equal to zero.

Figure 7.15 depicts the structure of the enhanced transient model. The contact patch can deflect in circumferential and lateral direction with respect to the lower part of the wheel rim. Only translations are allowed to ensure that the slip angle seen by the contact patch at steady state is equal to that of the wheel plane. To

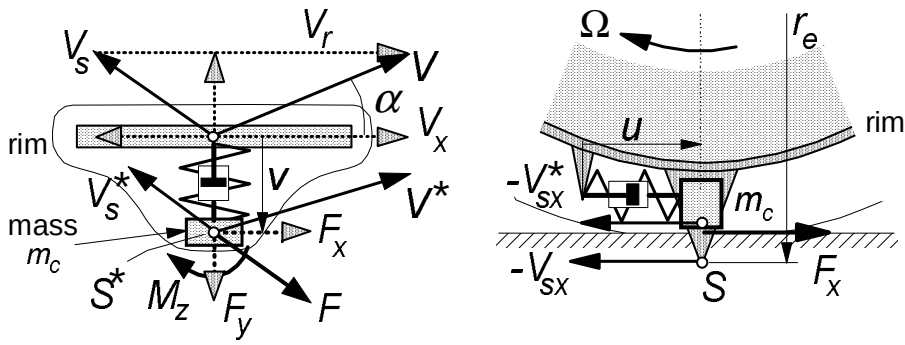

Fig. 7.15. Enhanced transient tyre model in top and side view showing carcass compliances and contact patch mass.

enable straightforward computations, a mass point is thought to be attached to the contact patch. That mass point coincides with point S^* the velocity of which constitutes the slip speed of the contact point. This slip velocity is used, together with the assumedly at the contact patch detected path curvature due to turn slip and the wheel camber, to compute the forces F_x, F_y and the moment M_z which act from road to contact patch. We may add a simple relaxation length model to enable computations near zero speed. The model was first employed by Van der Jagt et al.(1989) and later generalised by Pacejka and Besselink (1997). In Chapter 8 the model will be applied to investigate the effect of road undulations on the efficiency of anti-lock brake control.

With mass m_c and carcass stiffnesses $c_{cx,y}$ and damping ratios $k_{cx,y}$ introduced, the equations of motion for the contact patch mass point with longitudinal and lateral speed components $V^*_{sx,y}$ read:

$$m_c\dot{V}^*_{sx} + k_{cx}\dot{u} + c_{cx}u = F_x(\kappa',\alpha',F_z) \tag{7.50}$$

$$m_c\dot{V}^*_{sy} + k_{cy}\dot{v} + c_{cy}v = F_y(\alpha',\kappa',\gamma,F_z) - F_{y,NL} \tag{7.51}$$

The forces acting from ground to contact patch shown at the right-hand sides are computed from the steady-state formulae. The non-lagging camber force part $F_{y,NL}$ is assumed to act directly on the wheel rim. We may approximate the non-lagging force part by a linear relation with γ using the camber thrust stiffness $C_{F\gamma}$, the non-lagging fraction ε_{NL} (cf. Sec.7.2.4) and the weighting function $G_{y\kappa}$ (4.E59) to take care of the presence of a fore and aft force F_x:

$$F_{y,NL} = G_{y\kappa}\varepsilon_{NL}C_{F\gamma}\gamma \tag{7.52}$$

It should be noted that ε_{NL} changes with wheel load, cf. Fig.7.13.

To enable calculations near or at standstill we may add additional first-order differential equations with relaxation length σ_c. From these equations the transient slip quantities result which act as input in the steady-state slip force formulae. We have:

$$\sigma_c\frac{\mathrm{d}\alpha'}{\mathrm{d}t} + |V_x|\alpha' = -V^*_{sy} \tag{7.53}$$

$$\sigma_c\frac{\mathrm{d}\kappa'}{\mathrm{d}t} + |V_x|\kappa' = -V^*_{sx} \tag{7.54}$$

If needed, we may in the right-hand member of (7.51) replace argument γ with the transient spin slip φ' that results from an equation similar to (7.53):

$$\sigma_c\frac{\mathrm{d}\varphi'}{\mathrm{d}t} + |V_x|\varphi' = |V_x|\varphi \tag{7.55}$$

where in the right-hand member φ is to be replaced by the expression (7.13).

The contact relaxation length σ_c may be given a small but finite value, for instance equal to half the contact length, a_o, at nominal load that corresponds to our findings in Chapter 9. The equations (7.53-55) do not respond to load changes. For this, we rely on the effect of the carcass compliance which gives adequate results. Effectively, the resulting lateral compliance of the standing tyre is:

$$\frac{1}{C_{Fy}} = \frac{1}{c_{cy}} + \frac{\sigma_c}{C_{F\alpha}} \tag{7.56}$$

and the effective resulting tyre relaxation length (for side slip response):

$$\sigma_\alpha = \frac{C_{F\alpha}}{C_{Fy}} = \frac{C_{F\alpha}}{c_{cy}} + \sigma_c \tag{7.57}$$

This equation may, in fact, be employed to assess the lateral carcass stiffness at ground level c_{cy}. From the measured tyre relaxation length σ_α and cornering stiffness $C_{F\alpha}$ the lateral stiffness of the standing tyre C_{Fy} follows. By taking σ_c equal to half the contact length a the carcass lateral stiffness c_{cy} can be determined. The relaxation length for load variations remains equal to:

$$\sigma_{\alpha,Fz} = \frac{C_{F\alpha}}{c_{cy}} \tag{7.58}$$

which is a little smaller than σ_α. Although this results from practical modelling considerations, we may in fact come close to the measurement results of Fig.7.10.

If one is not interested to include the ability to simulate near or at zero forward speed, the contact relaxation length σ_c may be disregarded and taken equal to zero. In Chapter 9 the contact relaxation length σ_c forms an essential element in the model developed for short wavelength behaviour.

The deflection rates needed in Eqs.(7.50,51) are equal to the difference in slip velocities:

$$\dot{u} = V_{sx}^* - V_{sx} \tag{7.59}$$

$$\dot{v} = V_{sy}^* - V_{sy} \tag{7.60}$$

As has been mentioned before, the wheel slip velocity V_s with components $V_{sx,y}$ is defined as the horizontal velocity of the slip point S that is thought to be attached to the wheel rim a distance r_e, the effective rolling radius, below the wheel centre in the wheel centre plane.

$$V_{sx} = V_x - r_e\Omega \tag{7.61}$$

$$V_{sy} = V_y - r\dot{\gamma} \tag{7.62}$$

where $V_{x,y}$ denote the horizontal (parallel to road plane) components of the wheel centre velocity. In Eq.(7.62) the camber angle is assumed to be small and r_e is replaced by the loaded radius r.

The forces acting on the wheel rim, finally, become:

$$F_{xa} = k_{cx}\dot{u} + c_{cx}u \tag{7.63}$$

$$F_{ya} = k_{cy}\dot{v} + c_{cy}v + F_{y,NL} \tag{7.64}$$

The aligning torque becomes:

$$M'_z = -t_\alpha F_y \tag{7.65}$$

$$M_{zr} = M_{zr}(\gamma, \alpha', \kappa', F_z) \tag{7.66}$$

$$M_z = M'_z + M_{zr} + s \cdot F_x + M_{z,gyr} \tag{7.67}$$

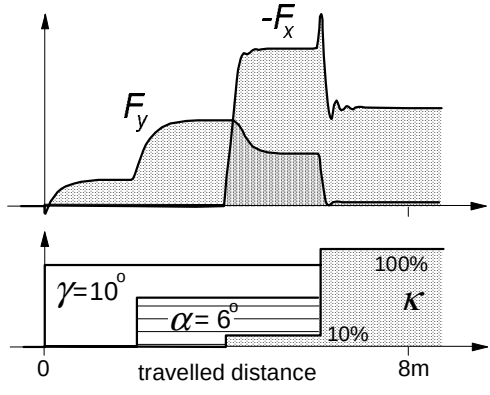

Fig. 7.16. Side force and brake force response to step changes in combined slip, computed with the enhanced transient tyre model of the present section.

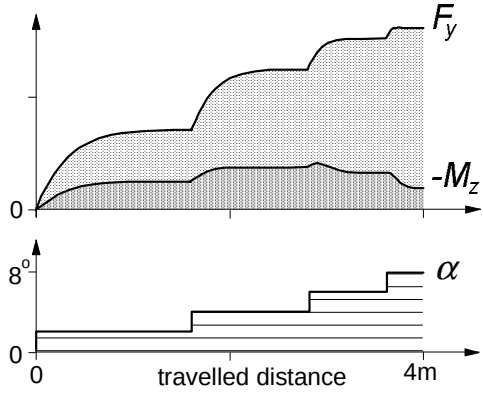

Fig. 7.17. Side force and aligning torque response to successive steps in side slip as computed with the transient fully non-linear model of Sec.7.2.4, Eq(7.29).

The last equation forms an extension of Eq.(4.E71) through the introduction of the gyroscopic couple that follows from Eq.(7.47).

To illustrate the performance of the model, the calculated side force response to successive step changes in camber angle, slip angle and brake slip has been presented in Fig.7.16. The contact patch relaxation length σ_c has not been used in this example. In Chapter 8 the model is applied in the problems of controlled braking on an uneven road and on starting from standstill where in the latter case σ_c is employed. The less demanding case of the response of side force and aligning torque to successive steps in pure side slip, shown in Fig.7.17, was calculated with the transient model of Section 7.2.3, Eq.(7.29). Very similar results are found when the enhanced model is used, that is: with the inclusion of the contact mass m_c.

Chapter 8

APPLICATIONS OF TRANSIENT TYRE MODELS

This chapter is devoted to the application of the single contact point transient tyre models as developed in the preceding chapter. The applications demonstrate the effect of the tyre relaxation length on vehicle dynamic behaviour.

8.1. Vehicle Response to Steer Angle Variations

In Chapter 1, Section 1.3.2 the dynamic response of the two-degree of freedom vehicle model depicted in Figs.1.9,11 to steer angle input has been analysed. As an extension to this model we will introduce tyres with lagged side force response. The system remains linear and we may use Eq.(7.18). The relaxation length will be denoted by σ. We have the new set of equations:

$$m(\dot{v} + Vr) = C_{F\alpha 1}\alpha_1' + C_{F\alpha 2}\alpha_2' \tag{8.1}$$

$$I\dot{r} = aC_{F\alpha 1}\alpha_1' - bC_{F\alpha 2}\alpha_2' \tag{8.2}$$

$$\frac{\sigma}{V}\dot{\alpha}_1' + \alpha_1' = \alpha_1 \tag{8.3}$$

$$\frac{\sigma}{V}\dot{\alpha}_2' + \alpha_2' = \alpha_2 \tag{8.4}$$

$$\alpha_1 = \delta - \frac{1}{V}(v + ar) \tag{8.5}$$

$$\alpha_2 = -\frac{1}{V}(v - br) \tag{8.6}$$

Figure 8.1 presents the computed frequency response functions, which hold for the extended system, for different values of the relaxation length. In Fig.8.2 the corresponding step response functions have been depicted. The diagrams show that the influence of the tyre lag on the vehicle motion is relatively small. At higher values of speed the effect diminishes and may become negligible. However, for closed loop vehicle control systems the additional phase lag caused by the relaxation lengths may significantly affect the performance.

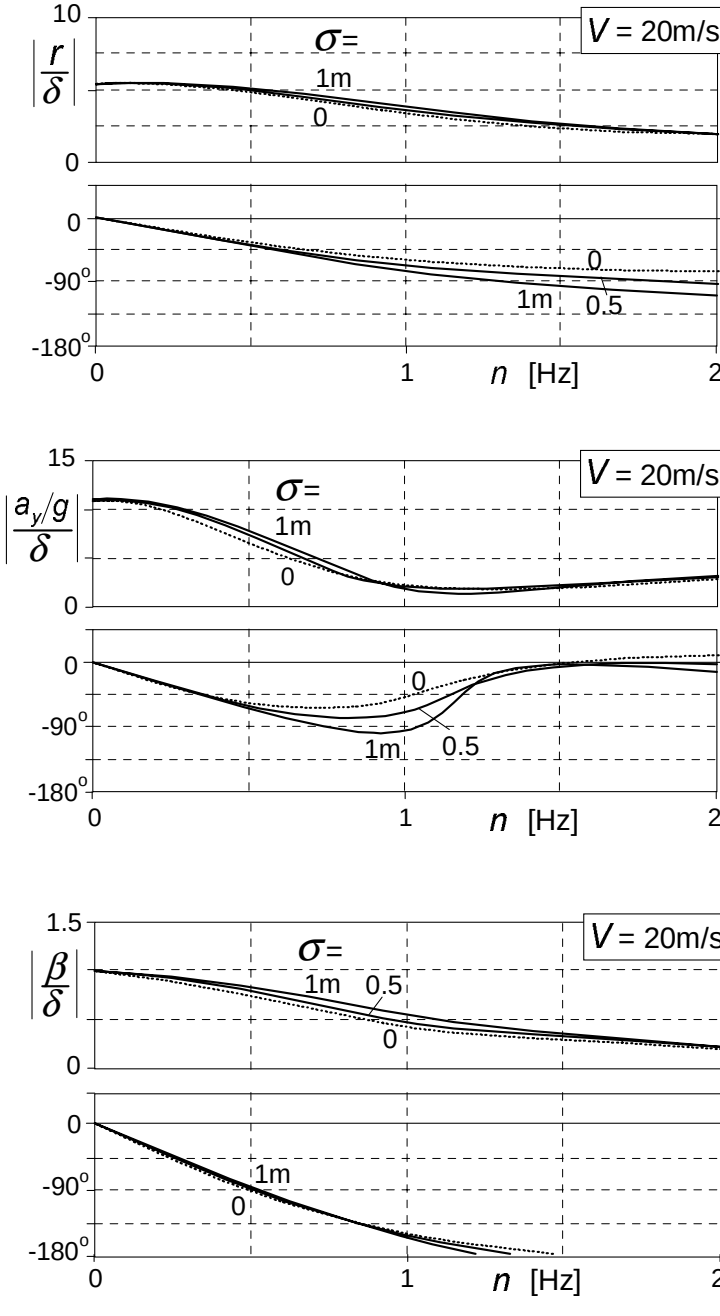

Fig. 8.1. Frequency response of yaw rate, lateral acceleration and side slip angle to steer angle of vehicle model featuring tyres with lagging side force response, cf. Fig. 1.15.

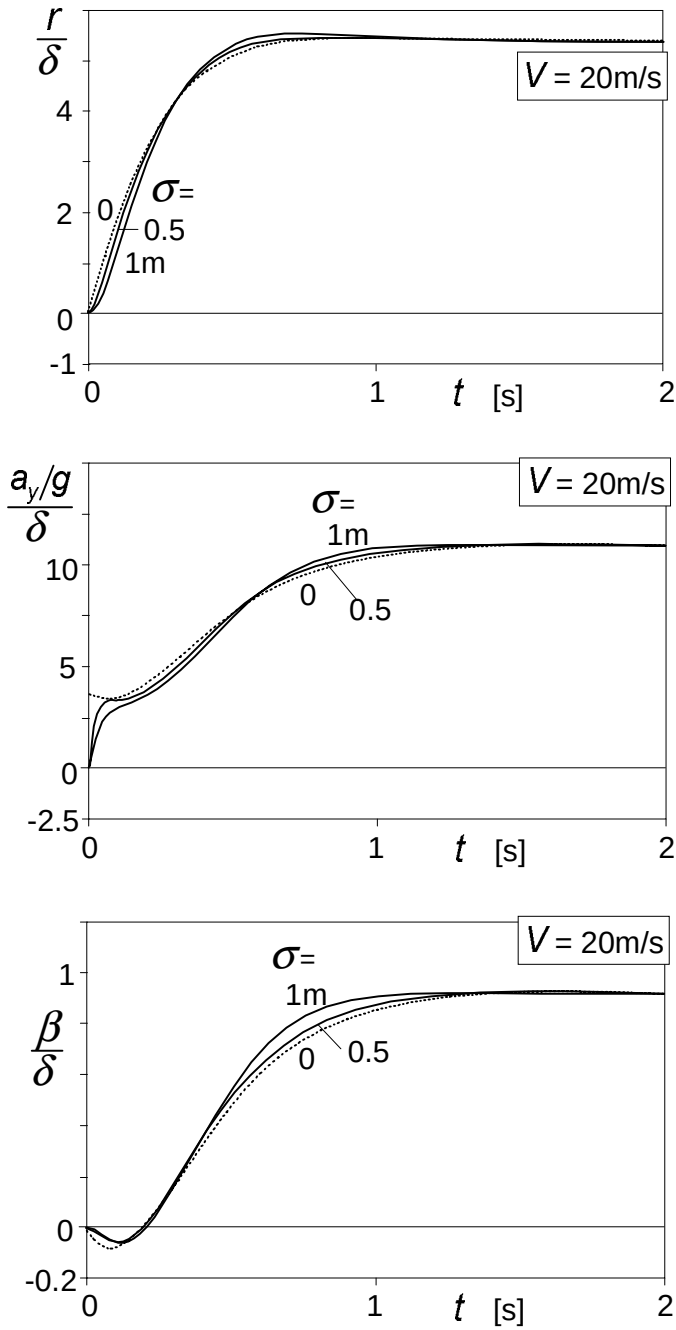

Fig. 8.2. Step response of yaw rate, lateral acceleration and vehicle side slip angle to steer angle of vehicle model featuring tyres with lagging side force response.

An interesting effect can be seen to occur near the start of the step response functions. With the relaxation length introduced, the responses appear to exhibit a more relaxed nature. The yaw rate response shows some initial lag.

8.2. Cornering on Undulated Roads

When a car runs along a circular path over an uneven road surface the wheels move up and down and may even jump from the road while still the centripetal forces are to be generated. Under these conditions, the wheels run at slip angles which may become considerably larger than on a smooth road. Consequently, on average, the cornering stiffness diminishes. This phenomenon was examined in Chapter 5, Section 5.6, where the stretched string model was found to be suitable to explain the decrease in cornering stiffness if the string relaxation length is made dependent on the varying wheel load to imitate the model provided with tread elements, cf. Fig.5.51.

These tyre models, however, are considered to be too complicated to be used in vehicle simulation studies. Instead, we will try the very simple transient tyre model as discussed in Sec.7.2.1 and compare the results with experimental findings. First, the small slip angle linear model will be considered. We use Eq.(7.20) which may be given the form:

$$\sigma \frac{\mathrm{d}F_y}{\mathrm{d}s} + F_y = F_{yss} = C_{F\alpha}\alpha \tag{8.7}$$

where s denotes the travelled distance and $\mathrm{d}s = V_x \mathrm{d}t$. The slip angle is assumed to be constant while the vertical load varies periodically.

$$F_z = F_{zo} + \Delta F_z = F_{zo} + \hat{F}_z \sin 2\pi \frac{s}{\lambda} \tag{8.8}$$

Essential is that both the cornering stiffness and the relaxation length vary with the vertical load:

$$C_{F\alpha} = C_{F\alpha}(F_z) \quad \text{and} \quad \sigma = \sigma(F_z) \tag{8.9}$$

Figure 8.3 illustrates the situation.

The loss in cornering power can be divided into the 'static' loss and the 'dynamic' loss. The static loss arises due to the curvature of the cornering stiffness versus wheel load characteristic. A similar loss has been experienced to occur as a result of lateral load transfer in the analysis of steady-state cornering of an automobile, cf. Fig.1.7. Figure 8.4 explains the situation at sinusoidally changing wheel load.

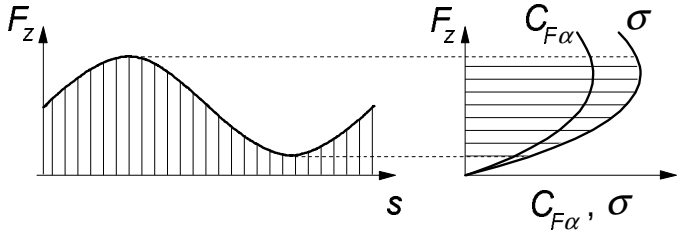

Fig. 8.3. Cornering stiffness and relaxation length varying with wheel load.

As will be shown in the analysis below, the dynamic loss appears to be attributed to the rate of change of the relaxation length with wheel load. This, of course, can only occur because of the fact that the cornering stiffness varies with wheel load since that rate of change forms the input in Eq.(8.7). Apparently, with both F_y and σ being dependent on F_z while α in the present analysis only affects F_y, the phenomenon is non-linear in F_z and linear in α.

If we assume a quadratic function for the $C_{F\alpha}$ vs F_z relationship with the curvature $bC_{F\alpha o}$

$$C_{Fa} = C_{Fao}(1 + a\Delta F_z - \tfrac{1}{2}b\Delta F_z^2) \tag{8.10}$$

the static loss can be simply found to become:

$$C_{F\alpha,stat.loss} = \tfrac{1}{4}b\hat{F}_z^{\,2}\,C_{F\alpha o} \tag{8.11}$$

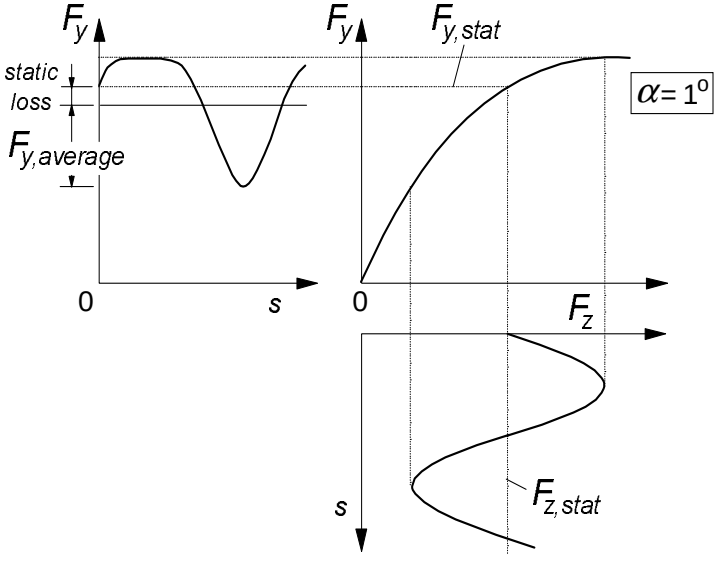

Fig. 8.4. The static loss in average side force due to the curved force vs load relationship.

The occurrence of the dynamic loss may be explained by assuming a linear variation of both the cornering stiffness and the relaxation length with load:

$$\sigma = cF_z \qquad C_{F\alpha} = eF_z \tag{8.12}$$

Equation (8.7) becomes herewith:

$$cF_z \frac{\mathrm{d}F_y}{\mathrm{d}s} + F_y = eF_z\alpha \tag{8.13}$$

or simplified:

$$z\frac{\mathrm{d}y}{\mathrm{d}s} + y = \beta z \tag{8.14}$$

with $z=cF_z$, $y=F_y$, $\beta=e\alpha/c$. Consider a truncated Fourier series approximation of the periodic solution:

$$y = y_o + y_{s1}\sin\omega_s s + y_{c1}\cos\omega_s s + y_{s2}\sin 2\omega_s s + \ldots \tag{8.15}$$

and its derivative:

$$\frac{\mathrm{d}y}{\mathrm{d}s} = y_{s1}\omega_s\cos\omega_s s - y_{c1}\omega_s\sin\omega_s s + 2y_{s2}\omega_s\cos 2\omega_s s - \ldots \tag{8.16}$$

while the input

$$z = z_o + \hat{z}\sin\omega_s s \quad \text{with} \quad \omega_s = \frac{2\pi}{\lambda} \tag{8.17}$$

Substitution of (8.15,16,17) in (8.14) and subsequently making the coefficients of corresponding terms in the left and right members equal to each other yields for the average output:

$$y_o = \beta z_o\left(1 - \frac{1}{2}\frac{\omega_s^2\hat{z}^2}{1+\omega_s^2 z_o^2}\right) \tag{8.18}$$

The average side force $F_{y,ave}$ expressed in terms of the original quantities now reads:

$$F_{y,ave} = C_{F\alpha o}\left(1 - \frac{1}{2}\frac{\omega_s^2 c^2\hat{F}_z^2}{1+\omega_s^2 c^2 F_{zo}^2}\right)\alpha \quad \text{with} \quad c = \frac{\mathrm{d}\sigma}{\mathrm{d}F_z} \tag{8.19}$$

For large F_z amplitudes and short wavelengths $\lambda=2\pi/\omega_s$ the formula shows that the dynamic loss approaches 50% of the side force generated on smooth roads. As we will see, this finding agrees very well with simulation and test results.

The aligning torque variation may be computed as well. In his study, Takahashi (1987) employed the equation based on the string concept and added the gyroscopic couple. We obtain according to Eqs.(5.135) and (5.178), the latter expression corresponding with (7.47):

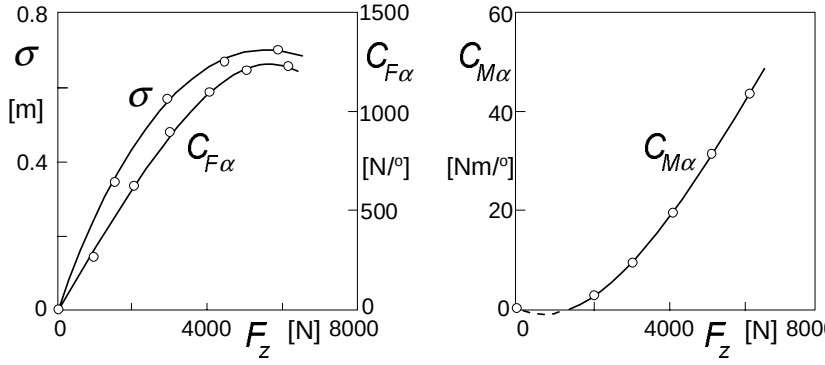

Fig. 8.5. Load dependency of tyre parameters according to measurements and third degree polynomial fits.

$$\sigma \frac{\mathrm{d}M_z'}{\mathrm{d}s} + M_z' = -C_{M\alpha}\alpha \tag{8.20}$$

and

$$M_{z,gyr} = C_{gyr} V^2 \frac{\mathrm{d}F_y}{\mathrm{d}s} \tag{8.21}$$

The total moment responding to the slip angle becomes:

$$M_z = M_z' + M_{z,gyr} \tag{8.22}$$

Experiments have been conducted to assess the relevant parameters of a 195/60R14-87H tyre at various values of the vertical load. The diagrams of Fig.8.5 present the characteristics for the relaxation length, the cornering stiffness and the aligning stiffness. The relaxation length was determined by curve fitting of the data obtained from a swept sine steering oscillation test at a speed of 30km/h in the frequency range of 0 to 2Hz. The gyroscopic coefficient C_{gyr} was assessed in a similar test but conducted at a speed of 170km/h. The resulting value turns out to be $C_{gyr} = 3.62\times10^{-5}$ s^2 that corresponds to the non-dimensional coefficient $c_{gyr} \approx 0.5$, cf. Eq.(5.179).

To assess the validity of the calculated force and moment response to load variations experiments have been carried out on a 2.5m drum with a special test rig at the Delft University of Technology. The wheel axle can be moved vertically while set at a given slip angle. The side force and moment measured at that slip angle have been corrected for the responses belonging to a slip angle equal to zero.

In Fig.8.6 in the left-hand diagrams the test results have been presented. The wheel axle is vertically oscillated with frequencies up to 8Hz and with an amplitude that corresponds to the ratio of amplitude and mean value of the wheel load equal to 0.9. The wheel runs at a constant small slip angle of one degree

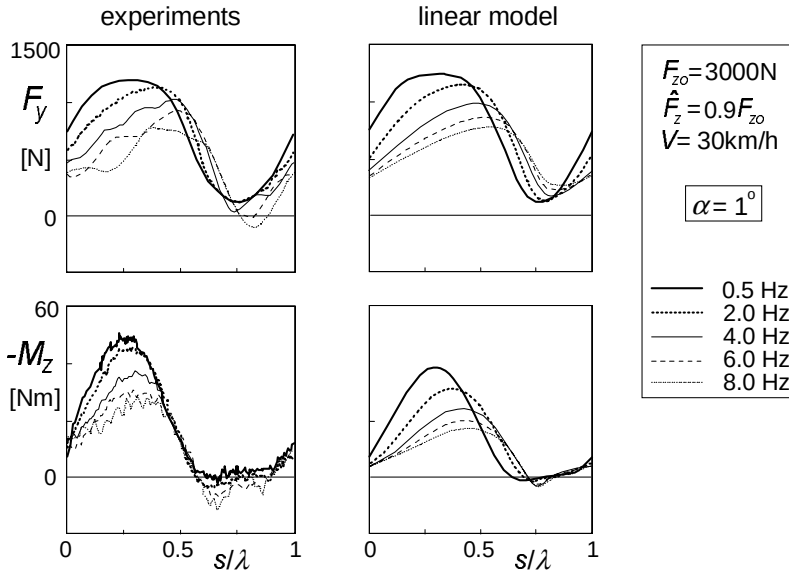

Fig. 8.6. Side force and aligning torque response to wheel load variation at a small slip angle.

with a speed of 30km/h. The response at the low frequency of 0.5Hz may be considered as quasi static and varies periodically, practically in phase with the axle motion. To enable a proper comparison at the different frequencies, the responses have been plotted against travelled distance divided by the current wavelength. The right-hand diagrams show the corresponding calculated responses. In view of the very simple set of equations that have been used, the agreement between test and model can be considered to be very good. Calculations conducted with the stretched string model of Section 5.6 were not much better. Only the moment responses turned out to be a little closer to the experimental findings. In the responses, two major features can be identified. First, we observe that the responses show some lag with respect to the input that grows with increasing frequency n which means: with decreasing wavelength λ. Second, and more important, we have the clear drop in average value of the side force which becomes larger at increasing frequency. After subtracting the static drop that occurs at the lowest frequency, the dynamic loss remains.

In Fig.8.7 the static and the dynamic parts of the decrease of the average side force as a ratio to the side force at zero vertical load amplitude, have been plotted versus frequency or wavelength for different input amplitude ratios. The model shows reasonable agreement with the experimental results. It has been found that the correspondence becomes a lot better when the speed is increased to 90km/h. Then, the wavelength is three times larger and a better performance of the model prevails. The curve of Fig.8.7 that holds for the amplitude ratio

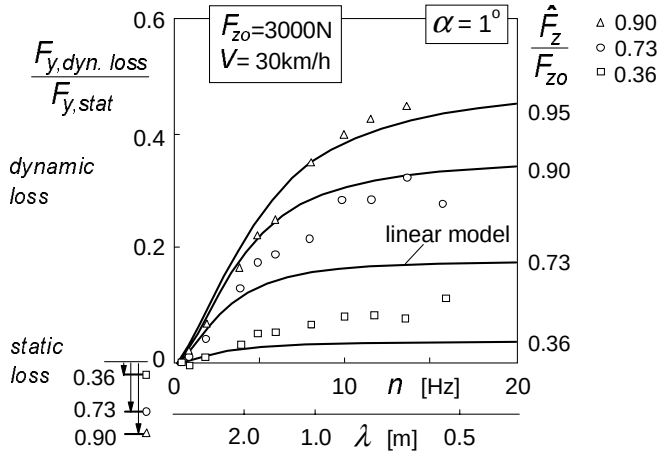

Fig. 8.7. Dynamic side force loss at a small slip angle for different load amplitude ratios.

0.95, where the tyre almost looses contact, appears to approach the value of ca. 0.5 when the frequency increases to large values. This indeed corresponds to the analytical result established by Eq.(8.19). On the other hand, the more advanced model of Section 5.6 predicts a possibly even larger reduction at the verge of periodic lift-off, cf. Fig.5.51 where the wavelength could be diminished to levels as small as the static contact length $2a_o$.

It may be obvious that an analogous model, Eq.(7.9) with $\kappa' = u/\sigma_\kappa$, can be used for the in-plane non-steady-state response to vertical load variations. Without special measures it is virtually impossible to maintain a certain level of the longitudinal slip κ at varying contact conditions. At a fixed braking torque, the average longitudinal braking force remains constant when the wheel keeps rolling. When the wheel runs over an uneven road surface and the wheel load changes continuously, the effect of the tyre lag is an increased average level of the longitudinal slip ratio. Applications of the single contact point in-plane transient model follow in Sections 8.3 and 8.5 where problems related with tyre out-of-roundness and braking on undulated roads are discussed.

The theory can be extended to larger values of slip if the non-linear model according to Eqs.(7.25,26) is employed. The equations may be used here in the form:

$$\sigma^* \frac{\mathrm{d}v}{\mathrm{d}s} + v = \sigma^* \alpha \tag{8.23}$$

with

$$\sigma^* = \frac{\sigma_o}{C_{F\alpha}} \frac{F_y}{\alpha'} \tag{8.24}$$

which quantity is a function of both the wheel load F_z and the transient slip angle or deformation gradient α'. It reduces to the relaxation length σ_o ($=\sigma$ at $\alpha'=0$) when α' tends to zero and F_y/α' to $C_{F\alpha}$. Obviously, offsets of the side force versus slip angle characteristic near the origin have been disregarded here. The transient slip angle follows from:

$$\alpha' = \frac{v}{\sigma^*} \tag{8.25}$$

The side force and moment are obtained by using the steady-state characteristics:

$$F_y = F_{y,ss}(\alpha', F_z) \tag{8.26}$$

$$M'_z = M'_{z,ss}(\alpha', F_z) \tag{8.27}$$

With the gyroscopic couple, cf. Eqs.(8.21), (7.5) and (5.179):

$$M_{z,gyr} = c_{gyr} m_t V^2 \frac{\mathrm{d}v}{\mathrm{d}s} \tag{8.28}$$

the total moment becomes:

$$M_z = M'_z + M_{z,gyr} \tag{8.29}$$

The steady-state characteristics as measured on the road at a number of wheel loads have been presented in Fig.8.8.

As has been noted in Sec.7.2.3 the assessment of σ^* requires some attention. In the investigation done by Takahashi (1992) and Higuchi (1997) the solution was obtained through iterations. Alternatively, we may use information from the previous time step to assess σ^*. When the load is rapidly lowered, violent vibrations may occasionally show up in the solution.

With this non-linear model, simulations have been done and experiments have been carried out for a slip angle equal to six degrees. Plots of the resulting

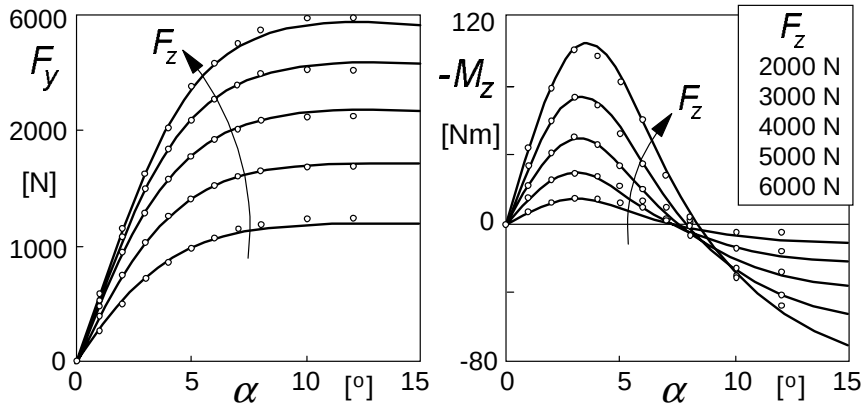

Fig. 8.8. Steady-state side force and aligning torque characteristics as measured on the road.

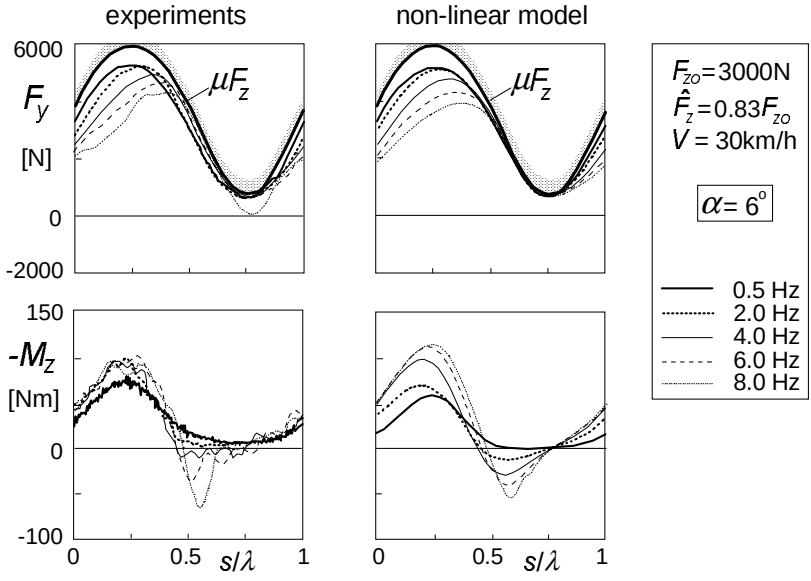

Fig. 8.9. Side force and aligning torque response to wheel load variation at a large slip angle.

responses are shown in Fig.8.9. The model appears to be successful in predicting the side force variation caused by the wheel load excitation at different frequencies. The load amplitude ratio of 0.83 gave rise to full sliding in certain intervals of the periodic motion. This can be seen to occur when the force signal touches the curve representing the maximally achievable side force μF_z. In this respect the model certainly performs well which cannot be said of the alternative

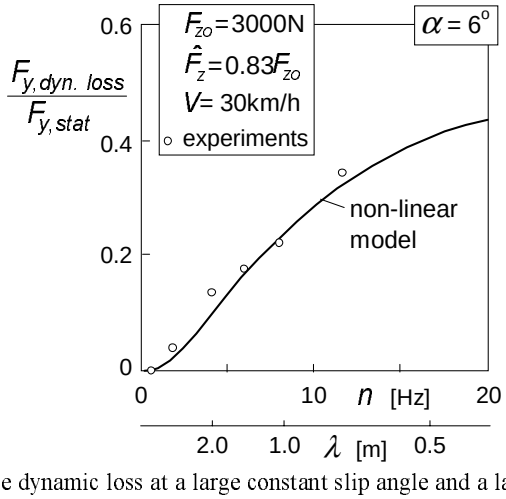

Fig. 8.10. The dynamic loss at a large constant slip angle and a large load amplitude ratio.

model governed by Eq.(7.20) with $F_{y,ss}$ calculated with Eq.(8.26) where α' is replaced by α. This model gives rise to a calculated force response that exceeds this physical limit when the load approaches its minimal value due the phase lag of the response. The dynamic loss of the average side force follows a tendency similar to what was found with the linear model at small slip angles. The result obtained at a constant slip angle of six degrees is shown in the diagram of Fig.8.10. The correspondence with the experimental outcome becomes even better than in the case of a slip angle equal to one degree, Fig.8.7.

Very similar results have been obtained with the more robust enhanced model of Section 7.3. The difference is that a small dynamic force acts on the little mass of the contact patch used in the model. This causes the ground force to be slightly different from the force felt at the wheel rim. It is, of course the ground force that cannot exceed the physical limit mentioned above.

8.3. Longitudinal Force Response to Tyre Non-Uniformity, Axle Motions and Road Unevenness

In this section the response of the axle forces F_x and F_z to in-plane axle motions (x, z), road waviness and tyre non-uniformities will be discussed. For a given tyre-wheel combination the response depends on rolling speed and frequency of excitation. This dependency, however, appears to be of much greater significance for the fore and aft force variation F_x than for the vertical load variation F_z.

The vertical force response has an elastic component and a component due to hysteresis. A similar mechanism is responsible for the generation of (at least an important portion of) the rolling resistance. The hysteresis (damping) part of the vertical load response appears to rapidly decrease to almost negligible levels at from zero increasing forward speed, cf. Pacejka (1981a) and Jianmin et al. (2001). We simplify the relationship between normal load F_z and radial tyre deflection ρ using the radial stiffness C_{Fz}:

$$F_z = C_{Fz}\rho \tag{8.30}$$

In Chapter 9 tyre inertia and other influences will be introduced to improve the relationship at higher frequencies and shorter wavelengths of road unevennesses.

A coupling between vertical deflection variation and longitudinal force appears to exist that is due to the resulting variation of the effective rolling

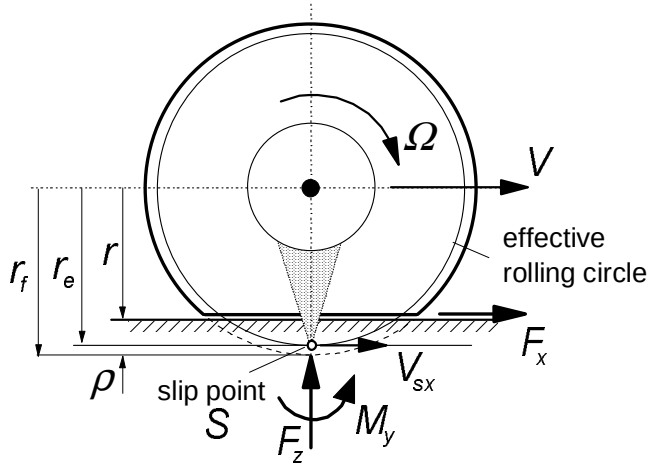

Fig. 8.11. The rolling wheel subjected to longitudinal slip (slip speed V_{sx})

radius of the tyre.

For the non-steady-state analysis we will employ the linear equation (7.9) that may take the form with $V = V_x$ (assumed positive):

$$\frac{\mathrm{d}u}{\mathrm{d}t} + \frac{1}{\sigma_\kappa} V u = V\kappa = -V_{sx} \tag{8.31}$$

The input is the longitudinal slip velocity that is defined as:

$$V_{sx} = V - r_e \Omega \tag{8.32}$$

Obviously, the effective rolling radius r_e plays here a crucial role.

8.3.1. Effective Rolling Radius Variations at Free Rolling

For a wheel with tyre that is uniform and rolls freely at constant speed over an even horizontal road surface, the tractive force required is due to rolling resistance alone. Under these conditions, the effective rolling radius r_e is defined to relate speed of rolling Ω with forward speed V:

$$V = r_e \Omega \tag{8.33}$$

The centre of rotation of the wheel body S lies a distance r_e below the wheel spin axis. As has been discussed in Chapter 1, by definition, this point which can be imagined to be attached to the wheel rim, is stationary at the instant considered if the wheel rolls freely (cf. Fig. 8.11 with slip speed $V_{sx} = 0$). In general, the effective rolling radius changes with tyre deflection ρ. We may write:

$$r_e = r_f - f(\rho) \tag{8.34}$$

with r_f denoting the free (undeformed) radius that may vary along the tyre circumference due to tyre non-uniformity. We have for the loaded radius:

$$r = r_f - \rho \tag{8.35}$$

Figure 8.12 shows variations of the effective rolling radius r_e and the loaded radius r as functions of wheel load F_z for two different tyres at different stages of wear and at different speeds as measured on a drum surface of 2.5m diameter. The from this diagram deduced reduction of the effective rolling radius $f(\rho)$ with respect to its theoretical original value r_f at zero wheel load ($\rho = 0$) has been presented in Fig.8.13. The influence of a change in tread depth has been shown. The slope η and the coefficient ε indicate the influence of changes in deflection

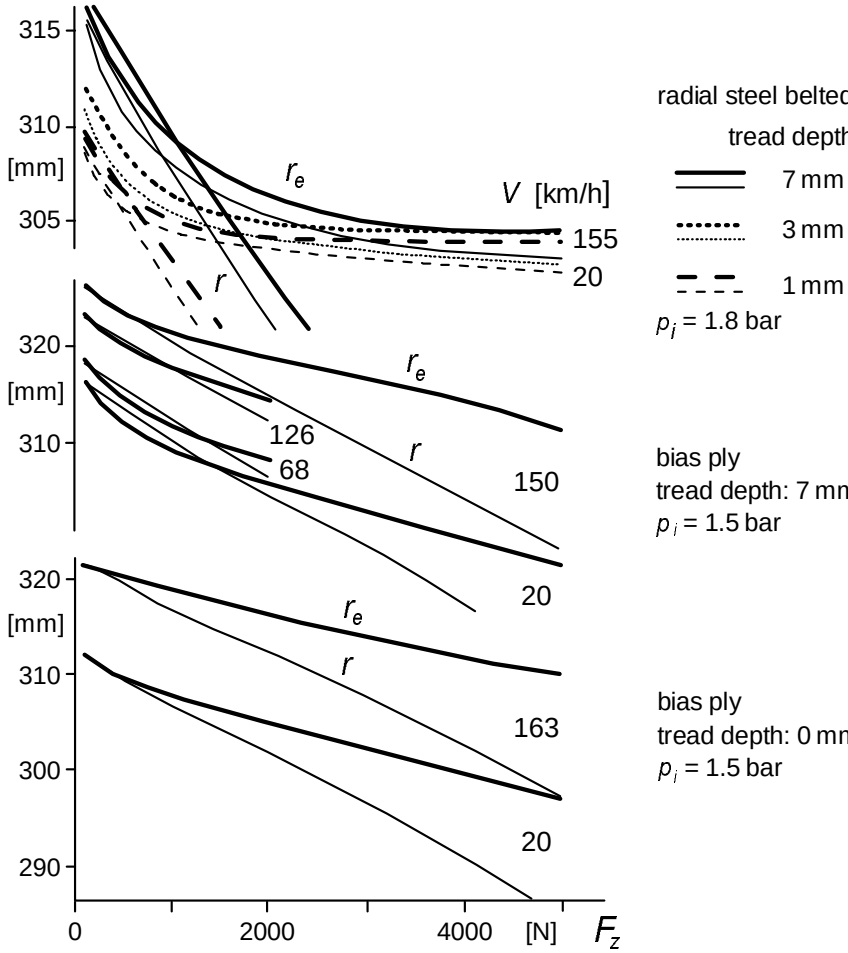

Fig. 8.12. Tyre effective rolling radius and loaded radius as a function of wheel load, measured on 2.5m drum at different speeds and for different tread depths and tyre design. Note the different scales for the radial and bias-ply tyre radii.

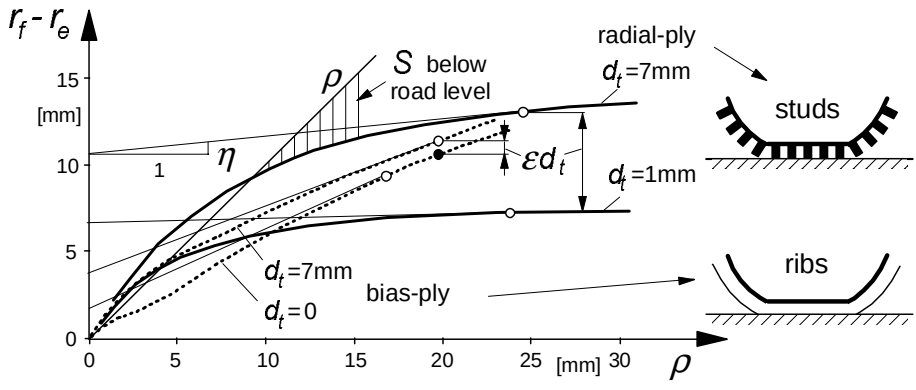

Fig. 8.13. Reduction of effective rolling radius r_e with respect to tyre free radius r_f due to tyre radial deflection ρ and tread depth change d_t. Situation at nominal load, F_{zo} = 3000N, has been indicated by circles.

and tread depth near the nominal load.

Figure 8.14 tries to explain the observation regarding the location of the slip point S. Possible locations have been indicated. At zero wheel load S lies at road level or a little lower (due to air and bearing resistance which slows the wheel down at the expence of some slip). A small wheel load causes a number of the originally radially directed tread elements to assume a vertical orientation. The rotation of these tread elements is lost which causes the effective radius to become smaller. Point S may then turn out to lie above road level! At higher loads we get the more commonly known situation of S located below road level. It has been assumed here that the belt with radius r_c is inextensible. Then, when the lower tread elements have a vertical orientation and translate backwards with respect to the wheel centre, the wheel will in one revolution cover a distance equal to the circumference of the belt. This means that the effective rolling radius equals the radius of the belt. When the tyre possesses a ribbed tread pattern, it

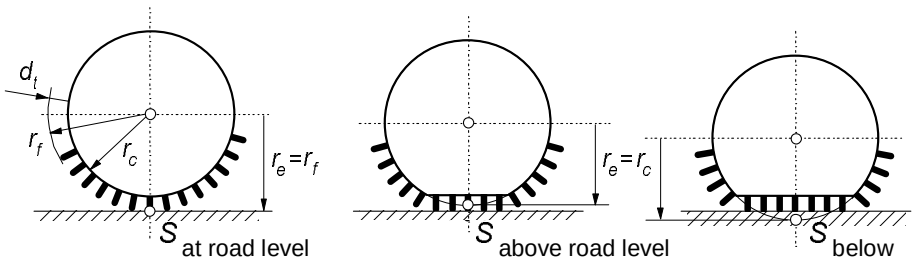

Fig. 8.14. Location of the centre of rotation, the slip point S, at three different radial deflections.

is expected that due to the greater coherence between rib elements in comparison to the independent studs of the radial-ply tyre, some rotation still occurs in the ribs in the contact zone which increases the effective radius and pushes point S earlier below the road surface. This theory seems to be supported by the curves of the new bias-ply tyre. The degree of effective incoherence ε is estimated for the radial-ply tyre to be equal to ca. 0.9 and for the bias-ply tyre equal to 0.2 at the rated load. Because we have plotted in Fig.8.13 the reduction of the effective radius with respect to the free unloaded radius: r_f-r_e, the decrease of r_e due the wearing off of the tread rubber is not shown directly. Only the indirect effect of tread wear is shown through the tread incoherence parameter ε. If due to the vertical tyre deflection the tread band is compressed and has decreased in circumference, the effective radius diminishes. This property which is more apparent to happen with the bias-ply tyre, is partly responsible for the slope of the curves shown at larger vertical deflections. This slope, denoted with η, is estimated to be equal to about 0.1 for the new radial-ply tyre with an almost inextensible belt and 0.4 for the new bias-ply tyre at their nominal load.

The analysis will be kept linear and we assume small deviations from the undisturbed condition. In the neighbourhood of this average state we write for the effective radius, the loaded radius and the radial deflection:

$$r_e = r_{e,o} + \tilde{r}_e \ , \quad r = r_o + \tilde{r} \ , \quad \rho = \rho_o + \tilde{\rho} \tag{8.36}$$

Small deviations from the undisturbed condition are indicated by a tilde. Variation of the free radius may occur along the circumference of the tyre. This kind of non-uniformity (out of roundness) is composed of two contributions. One is due to variations of the carcass radius r_c and the other due to variations of the tread thickness d_t. We have

$$\tilde{r}_f = \tilde{r}_c + \tilde{d}_t \tag{8.37}$$

The value of out of roundness is considered to be present at the moment considered along the radius pointing to the contact centre. The following linear relation between the effective radius variation and the imposed disturbance quantities is found to exist:

$$\tilde{r}_e = \tilde{r}_f - \varepsilon \tilde{d}_t - \eta\tilde{\rho} = \tilde{r}_c + (1 - \varepsilon)\tilde{d}_t - \eta\tilde{\rho} \tag{8.38}$$

The observation that a reduction in thickness of the tread rubber of a radial-ply tyre produces a decrease in effective rolling radius (at F_{zo}), amounting to only a small fraction of the reduction in tread depth is reflected by the factor (1-ε) in the right-hand expression of (8.38). The coupling coefficient η is relatively small for belted tyres. In contrast to bias-ply tyres the effective rolling radius of a belted tyre does not change very much with deflection once the initial tread thickness effect (at small contact lengths with tread elements still oriented

almost radially) has been overcome.

8.3.2. Computation of the Horizontal Longitudinal Force Response

The horizontal force response on undulated roads is composed of the following three contributions: the horizontal component of the normal load, the variation of the rolling resistance and the longitudinal force response to the variation of the wheel longitudinal slip. The horizontal in-plane force designated with X becomes with linearised variations, cf. Fig.8.15:

$$\begin{aligned} X &= X_o + \tilde{X} \\ &= -F_{ro} + \tilde{F}_x + F_{zo}\frac{\mathrm{d}w}{\mathrm{d}s} \\ &= -F_{ro} + \tilde{F}_r + \tilde{F}_\kappa + F_{zo}\frac{\mathrm{d}w}{\mathrm{d}s} \end{aligned} \tag{8.39}$$

with F_{ro} denoting the average rolling resistance force. For this occasion, it is assumed that the variation in rolling resistance force is directly transmitted to the tread through changes in vertical load. We write:

$$\tilde{F}_r = A_r \tilde{F}_z \tag{8.40}$$

where the variation of the vertical load results from variations in deflection and possibly from changes in radial stiffness along the tyre circumference:

$$\tilde{F}_z = C_{Fzo}\tilde{\rho} + \rho_o \tilde{C}_{Fz} \tag{8.41}$$

or expressed in terms of the variation in radial static deflection:

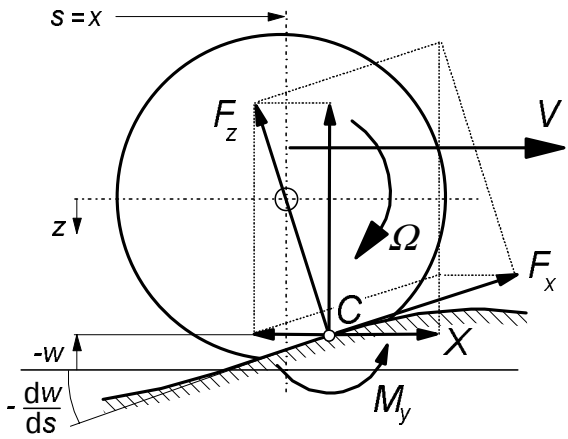

Fig. 8.15. In-plane excitation by road unevenness and by vertical and fore and aft axle motions.

$$\tilde{\rho}_s = -\rho_o \frac{\tilde{C}_{Fz}}{C_{Fzo}} \tag{8.42}$$

we may write:

$$\tilde{F}_z = C_{Fzo}(\tilde{\rho} - \tilde{\rho}_s) \tag{8.43}$$

The variation of the tangential slip force becomes with the transient longitudinal slipκ':

$$\tilde{F}_\kappa = C_{F\kappa}\kappa' = C_{F\kappa}\frac{u}{\sigma_\kappa} \tag{8.44}$$

where the tyre deflection u follows from Eq.(8.31). The longitudinal slip velocity appearing as input in (8.31) is governed by Eq.(8.32). With the variations in forward velocity, speed of revolution and effective rolling radius we find in linearised form:

$$V_{sx} = \tilde{V} - \Omega_o \tilde{r}_e - r_{eo}\tilde{\Omega} \tag{8.45}$$

The variation of the effective rolling radius follows from (8.38), where the deflection is a result of the combination of wheel vertical displacement, tyre out-of-roundness and road height changes:

$$\tilde{\rho} = z + \tilde{r}_c + \tilde{d}_t - w \tag{8.46}$$

The wheel angular velocity results from the dynamic equation:

$$I_w\dot{\Omega} = -rF_x - M_y \tag{8.47}$$

in which I_w denotes the wheel polar moment of inertia (including a large part of the tyre that vibrates along with the wheel rim if the frequency lies well below the in-plane first natural frequency, cf. Chap.9).

The moment M_y acts about the transverse axis through the contact centre C, Fig.8.15, and is composed of the part due to rolling resistance and a part due to excentricity of the tread band which constitutes the first harmonic of the tyre out-of-roundness. This latter part runs 90 degrees ahead in phase with respect to the loaded radius variation that is sensed at the contact centre. With subscript 1 referring to the first harmonic we have:

$$M_y = M_r + F_z\tilde{r}_{1,(\Omega t+\pi/2)} \tag{8.48}$$

The rolling resistance moment M_r is here supposed to be directly connected with the rolling resistance force F_r which is a simplifying assumption that has a negligible effect on the resulting responses. As a result, the rolling resistance components cancel out in the right-hand member of Eq.(8.47). This equation now reduces to:

$$I_w \dot{\Omega} = -r_o F_\kappa - F_{zo} \tilde{r}_{1,(\Omega t+\pi/2)} \tag{8.49}$$

Collection of the relevant equations (8.31,38,39,40,41,42,43,45) and elimination of all variables, except the input quantities:

$$\tilde{V}\,(=\dot{\tilde{x}}),\ z,\ w,\ \tilde{r}_c,\ \tilde{d}_t, \tilde{\rho}_s,\ \tilde{r}_1\ (= \text{first harmonic of } \tilde{r}_f = \tilde{r}_c + \tilde{d}_t) \tag{8.50}$$

and the output $\tilde{X}$ and, for now, also $\tilde{r}_e$ and $\tilde{\rho}$, yields the following Laplace transformed representation of the horizontal force variation with s designating the Laplace variable or $i\omega$:

$$\tilde{X} = C_{F\kappa} \frac{I_w \Omega_o s \cdot \tilde{r}_e - I_w s^2 \cdot \tilde{x} - F_{zo} r_o \exp(\tfrac{1}{2}\pi s/\Omega_o) \cdot \tilde{r}_1}{\sigma_\kappa I_w s^2 + I_w V_o s + C_{F\kappa} r_o^2} + \\ - A_r C_{Fz} \cdot (\tilde{\rho} - \tilde{\rho}_s) + F_{zo} s \cdot w / V_o \tag{8.51}$$

where with (8.38) and (8.46) we have the variations of effective radius and tyre deflection:

$$\tilde{r}_e = \eta(w - z) + (1 - \eta - \varepsilon)\tilde{d}_t + (1 - \eta)\tilde{r}_c \tag{8.52}$$

and

$$\tilde{\rho} = z + \tilde{r}_c + \tilde{d}_t - w \tag{8.53}$$

From this expression (8.51) of the combined response, the individual transfer functions or the frequency response functions to the various input quantities may be written explicitly. For the latter functions to obtain, we simply have to take the coefficients of one of the input variables (8.50) in (8.51), after (8.52) and (8.53) have been inserted in (8.51), and replace s by $i\omega$ or $i\Omega_o$ depending on the type of input variable.

Figure 8.16 presents both theoretical and experimental data, the latter being obtained from tests performed on a 2.5 m drum test stand provided with a specially designed rig (Pacejka, Van der Berg and Jillesma, 1977). The parameters of the tyres tested have been listed in Table 7.1. The response to z has been found by moving the axle up and down by means of a hydraulic actuator. The variation in carcass radius r_c has been achieved by mounting a reasonably uniform wheel and tyre with 2.5 mm eccentricity on the shaft and subsequently balancing the rotating system. In this test the axle was held fixed. The special arrangement resulted in a larger polar moment of inertia I_w (1.1 kgm^2). The response to d_t variations could be obtained by partly buffing off the tyre tread. On one side 5 mm less tread rubber remained with respect to the other side of the tyre. As a side effect, the average slip stiffness $C_{F\kappa}$ increased. The new value was estimated. All tyre parameters have been determined through special

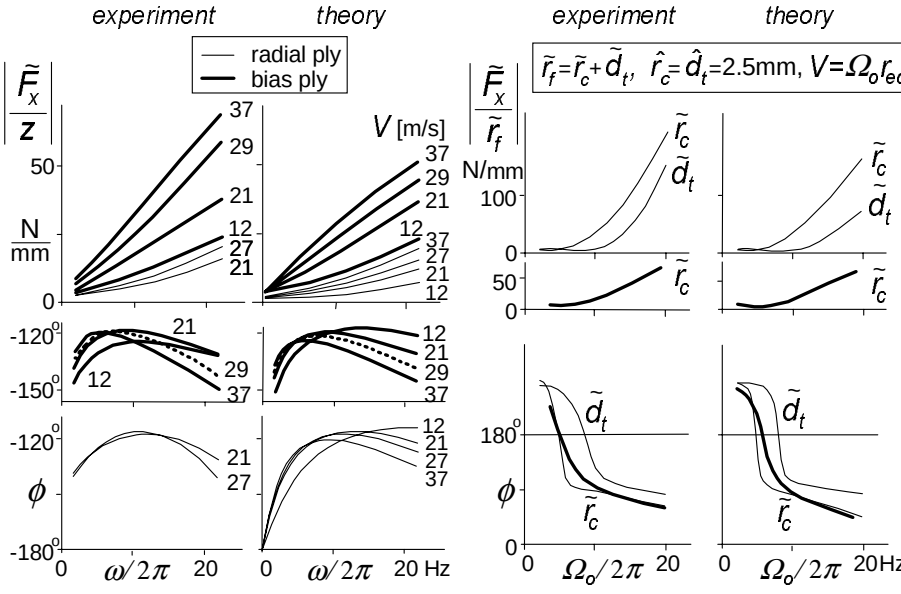

Fig. 8.16. Experimental and theoretical frequency response plots of the longitudinal force F_x to vertical axle oscillations z and to out-of-roundness (1st harmonic of variations in carcass radius r_c or in tread thickness d_t). Average vertical load F_{zo} = 3000N.

tests. Sometimes, slight changes of these values could result in a better match of the response data.

In general, a good correspondence with experimental results could be established. Also the phase relationship which is very sensitive to the structure of the model and changes in parameters, turns out to behave satisfactorily. A negative phase angle ϕ indicates that the response lags behind the input.

Table 8.1. Tyre in-plane parameter values for the radial and bias-ply tyres.

Radial steel-belted (p_i=1.8 bar, tread depth (at $\tilde{d}_t$=0)=6.5mm)
I_w = 0.8 (z) or 1.1 ($\tilde{r}_f$) kgm^2, r_{fo} = 0.315m, $r_o \approx$ 0.3m, η = 0.1, ε = 0.6 $\sigma_\kappa = C_{Fx}/C_{F\kappa}$, C_{Fx} = 565000N/m, $C_{F\kappa}$ = 80000N (500000N at $\hat{d}_t$= 2.5mm) F_{zo} = 3000N, F_{ro} = 25N, C_{Fz} = 133000 N/m, A_r = 0.0083
Bias-ply (p_i = 1.5 bar, tread depth = 6.5 mm)
I_w = 0.8 (z) or 1.1 ($\tilde{r}_f$) kgm^2, r_{fo} = 0.325m, $r_o \approx$ 0.3m, η = 0.4 $\sigma_\kappa = C_{Fx}/C_{F\kappa}$, C_{Fx} = 10^6 N/m, $C_{F\kappa}$ = 45000N F_{zo} = 3000N, F_{ro} = 60N, C_{Fz} = 190000N/m, A_r = 0.02

To explain these findings which turn out to be quite different for the two types of tyre, we shall now analyse the responses to vertical axle motions z and out-of-roundness $\tilde{r}_c$ (= $\tilde{r}_{c1}$ first harmonic) in greater detail.

8.3.3. Frequency Response to Vertical Axle Motions

After replacing in Eq.(8.51) the Laplace variable s by $i\omega$, with ω denoting the frequency of the excitation, we find for the response to vertical axle motions the following frequency response function with $X = F_x$:

$$\frac{\tilde{F}_x}{z} = -A_r C_{Fz} - \frac{\eta C_{F\kappa}}{r_o} \frac{2\zeta i\nu}{1 - \nu^2 + 2\zeta i\nu} \tag{8.54}$$

with the non-dimensional frequency:

$$\nu = \frac{\omega}{\omega_{\Omega o}} \tag{8.55}$$

and the speed dependent damping ratio:

$$\zeta = \frac{1}{2} \frac{I_w V}{C_{F\kappa} r_o^2} \omega_{\Omega o} = \frac{1}{2} \frac{V}{\sigma_\kappa \omega_{\Omega o}} \tag{8.56}$$

where the natural frequency of the tyre-wheel rotation with respect to the foot print has been introduced:

$$\omega_{\Omega o} = \sqrt{\frac{C_{Fx} r_o^2}{I_w}} = \sqrt{\frac{C_{F\kappa} r_o^2}{\sigma_\kappa I_w}} \tag{8.57}$$

An interesting observation is that an increase in slip stiffness or relaxation length decreases the non-dimensional damping coefficient ζ. A higher speed V, obviously, produces more damping.

For the extreme case, $\omega \to 0$, we find as expected only the contribution to rolling resistance:

$$\left.\frac{\tilde{F}_x}{z}\right)_{\omega \to 0} = -A_r C_{Fz} \tag{8.58}$$

If we neglect the small contribution from the rolling resistance, the first term of (8.54) vanishes. The magnitude of the remaining term reduces to a simple expression if the frequency is considered to be small with respect to the natural frequency:

$$\left|\frac{\tilde{F}_x}{z}\right|_{\omega \ll \omega_{\Omega o}} = 2\zeta \frac{\eta C_{F\kappa}}{r_o} v = \frac{\eta I_w}{r_o^3} V\omega = 2\pi \frac{\eta I_w}{r_o^3} V n \tag{8.59}$$

with V the speed of travel in m/s and n the frequency of the vertical axle motion in Hz. It is noted from Eq. (8.59) that the rise of the response in the lower frequency range with the frequency n and the speed V is in particular influenced by the magnitude of the factor η multiplied with the polar moment of inertia I_w. A small value of η, as with radial tyres, is favourable which is obviously caused by the fact that then the change of effective rolling radius with deflection is very small so that rotational accelerations and accompanying longitudinal forces are almost absent. The coefficient of Vn in (8.59) becomes for the radial-ply tyre: 18.6 and for the bias-ply tyre: 74.5. This would mean that if the wheel with bias-ply tyre that rolls at a speed of 10m/s, is oscillated vertically with an amplitude of 1mm at a frequency of 10Hz, the resulting longitudinal force gets an amplitude of 7.45N.

At higher frequencies it can be shown that the curves for the magnitude of expression (8.54) reach a common maximum (for all V) at $\omega = \omega_{\Omega o}$. The maximum response amplitude amounts to:

$$\left|\frac{\tilde{F}_x}{z}\right|_{\max} = \eta \frac{C_{F\kappa}}{r_o} + A_r C_{Fz} \tag{8.60}$$

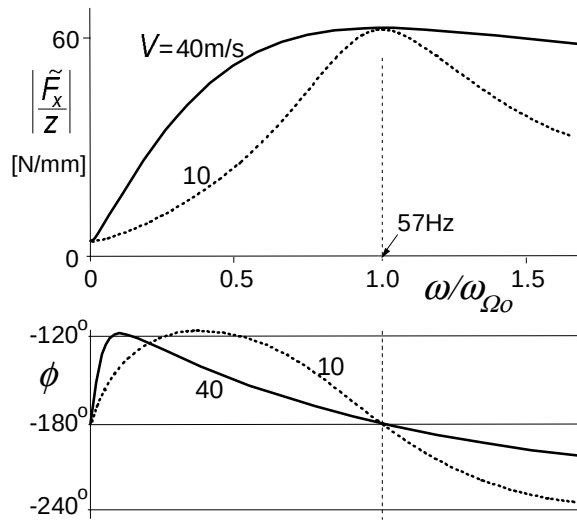

Fig. 8.17. Theoretical frequency response function of the longitudinal force F_x to vertical axle motions z for the bias-ply car tyre.

This maximum is determined again primarily by the effective rolling radius gradient η but now multiplied with slip stiffness C_{Fk}. For the radial tyre the maximum response becomes ca.28 N/mm at the natural frequency 43 Hz and for the bias-ply tyre this becomes ca.64N/mm at 57 Hz. Figure 8.17 shows both the amplitude and phase (lag) response calculated for the bias-ply tyre. Figure 8.16 has already indicated that for the radial tyre a much lower response is expected to occur.

8.3.4. Frequency Response to Radial Run-Out

From equation (8.51) we derive for the frequency response to radial (carcass) run-out considering only its first harmonic $\tilde{r}_f = \tilde{r}_1 = \tilde{r}_c$ with frequency equal to the wheel speed of revolution $\omega = \Omega$ (non-dimensional frequency $\nu = \Omega/\omega_{\Omega o}$):

$$\frac{\tilde{F}_x}{\tilde{r}_c} = -A_r C_{Fz} + i\,\frac{(1-\eta)\,C_{Fx}\nu^2 - F_{zo}/r_o}{1-\nu^2 + i\nu^2 r_o/\sigma_K} \tag{8.61}$$

This expression differs in two main respects from the one for the response to axle vertical motions (8.54). Firstly, we have now the factor 1-η instead of η and secondly, an additional term with F_{zo} shows up which is due to the excentricity, cf. Eq.(8.49). Figure 8.18 presents the response plots for the bias-ply tyre.

For speeds very low: $\Omega \to 0$ the expression reduces to:

$$\left.\frac{\tilde{F}_x}{\tilde{r}_c}\right)_{\omega\to 0} = -A_r C_{Fz} - i\,\frac{F_z}{r_o} \tag{8.62}$$

The amplitude ratio attains a minimum near

$$\nu = \sqrt{\frac{F_{zo}/r_o}{(1-\eta)\,C_{Fx}}} \tag{8.63}$$

which means for the radial tyre: near the frequency 0.14 $n_{\Omega o}$ and for the bias-ply tyre: near 0.13 $n_{\Omega o}$. With parameters corresponding to the experiment conducted (I_w = 1.1 kgm^2 resulting in natural frequencies of 36.5 and 48.5 Hz) we obtain for these frequencies: 5.1 and 6.3Hz respectively. The minimum value appears to become very close to $A_r C_{Fz}$ = 1100 and 3800N/m respectively. As can be seen in the upper right-hand diagram of Fig.8.16, the experimentally assessed curve also features such a dip in the low frequency range and the accompanying sharp decrease in phase lead. At the natural frequency $n_{\Omega o}$ (ν=1) the amplitude ratio comes close to its maximum value. This maximum is approximately equal to:

$$\left|\frac{\tilde{F}_x}{\tilde{r}_c}\right|_{\max} \approx -A_r C_{Fz} + (1-\eta)\,\frac{C_{Fk}}{r_o} - \frac{\sigma_K F_{zo}}{r_o^2} \tag{8.64}$$

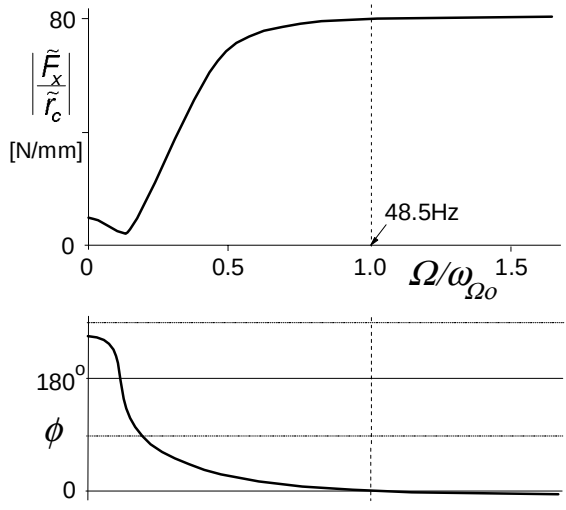

Fig. 8.18. Theoretical frequency response curve of longitudinal force to tyre out-of-roundness (1st harmonic) for the bias-ply car tyre. The speed of travel $V = r_c\Omega$.

The second term by far dominates this expression. The radial tyre attains 220 N/mm (at 36.5 Hz) and the bias-ply tyre 80 N/mm (at 48.5 Hz). Compared with the maximum longitudinal force response to vertical axle motions, Eq.(8.60), we note a much stronger sensitivity of the radial tyre to out-of-roundness (ca. 220 N/mm) than to vertical axle motions (ca. 28N/mm). This is due to the factor 1-η occurring in (8.64) which in (8.60) appears as η. For the bias-ply tyre with a much more compressible tread band, we have 80N/mm versus 64N/mm.

Exercise 8.1. Response to tyre stiffness variations

Derive from Eqs. (8.51) - (8.53) the frequency response function of F_x to the static deflection variation $\tilde{\rho}_s$, that is: to variations in radial tyre stiffness, for fixed axle height: $z = 0$. Then release the vertical axle motion and find the frequency response

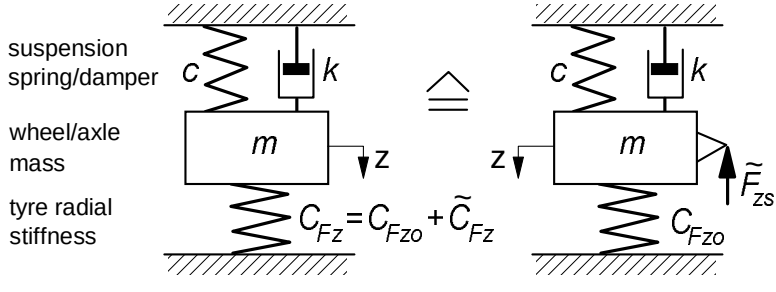

Fig. 8.19. Wheel suspension/mass system excited by tyre stiffness variations (Exercise 8.1).

function for z to $\tilde{\rho}_s$. Consider Fig.8.19 that represents the simplified axle/ wheel-suspension system. Small motions are considered so that only linear terms can be taken into account. Use the parameter values of the bias-ply tyre of Table 8.1 and furthermore the values for the mass, the suspension stiffness and the damping:

$$m = 50\,\text{kg}\,, \quad c = 40000\,\text{N/m}\,, \quad k = 2000\,\text{Ns/m}$$

Now find the total frequency response of F_x to $\tilde{\rho}_s$ for the released axle motion. It may be noted that the excitation by a variation of the radial stiffness is equivalent to the excitation by a vertical force:

$$\tilde{F}_{zs} = \rho_o \tilde{C}_{Fz} = -C_{Fzo}\tilde{\rho}_s$$

representing the variation of the 'static' tyre load at constant axle height while the tyre rolls.

Exercise 8.2. Self-excited wheel hop

Investigate the stability of the fourth-order system of Fig.8.20 using the Hurwitz criterium (cf. Eq.(1.118)). Employ Eqs.(8.31,38,45,46,47), assume M_y=0 and consider a flat road and a uniform tyre. Assess the range of the slope β of the wheel axle guidance surface where instability will occur for the undamped wheel suspension system. The effective rolling radius coupling coefficient η is the decisive parameter. Plot the stability boundary in the tanβ versus η diagram. Vary η between the values 0 and 1. Indicate the areas where stability prevails. Take the parameter values:

$$r_o = r_{eo} = 0.3\text{m}, \; \sigma_\kappa = C_{F\kappa}/C_{Fx} = 0.3\text{m}$$
$$C_{Fz} + c_z = C_{Fx} = 2\times10^5\,\text{N/m}$$
$$m = 30\,\text{kg}, \; I_w = 0.5mr_o^2\,\text{kgm}^2$$

That a moderate oscillatory instability may indeed show up with such a system has been demonstrated experimentally in professor S.K.Clark's laboratory at the University of Michigan in 1970.

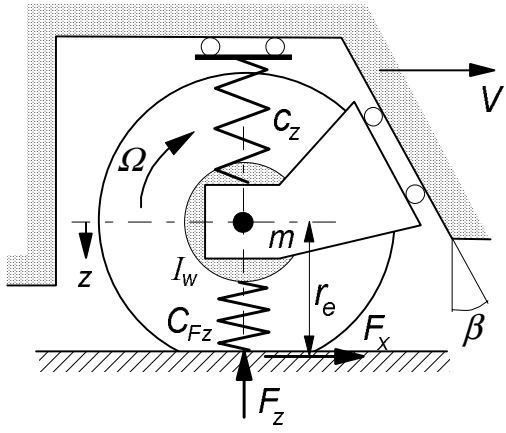

Fig. 8.20. On the possibly unstable wheel hop motion (Exercise 8.2).

8.4. Forced Steering Vibrations

A steering/suspension system of an automobile exhibits a rather complex configuration and possesses many degrees of freedom. A simplification is necessary to conduct a sensible analysis to gain insight into its general dynamic behaviour and into the influence of important parameters of the system. Investigation of the steering mode of vibration requires at least the steering degree of freedom of the front wheel, possibly extended with the rotation degree of freedom of the steering wheel. For the sake of simplicity, one degree of freedom may be suppressed by holding the steering spring clamped at the node of the natural mode of vibration. Furthermore, we will consider the influence of two more degrees of freedom: the vertical axle motion and the longitudinal deflection of the suspension with respect to the steadily moving vehicle mass. The picture of Fig.8.21 shows the lay-out of system. Due to the assumed orthogonality of the system (wheel axis, king-pin, road plane) the dynamically coupled horizontal motions (x,ψ) are not coupled with the vertical axle motion when small displacements are considered and tyre contact forces are disregarded.

First, we will examine the dynamics of the free system not touching the road. After that, the tyre is loaded and tyre transient models for the in-plane and out-of-plane behaviour are introduced and the systems response to wheel unbalance will be assessed and discussed.

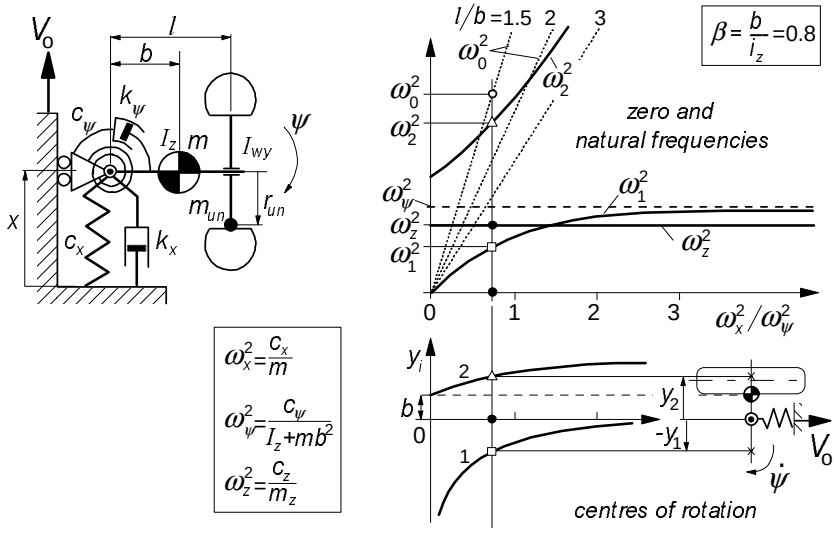

Fig. 8.21. Configuration of a simple steering/suspension system and the resulting natural frequencies and vibrational modes.

8.4.1. Dynamics of the Unloaded System Excited by Wheel Unbalance

The simple system depicted in Fig.8.21 possesses two horizontal degrees of freedom: the rotation about the vertical steering axis, ψ, and the fore and aft suspension deflection, x. The figure provides details about the geometry, stiffnesses, damping and inertia. The mass m represents the total mass of the horizontally moving parts. The length i_z denotes the radius of inertia: $i_z^2 = I_z/m$.

The wheel rim that revolves with a speed Ω is provided with an unbalance mass m_{un} (in the wheel centre plane at a radius r_{un}). The centrifugal force has a component in forward direction:

$$F_{un,x} = -m_{un} r_{un} \Omega^2 \sin \Omega t \tag{8.65}$$

The equations of motion of this fourth-order system read:

$$m\ddot{x} - mb\ddot{\psi} + k_x \dot{x} + c_x x = F_{un,x} \tag{8.66}$$

$$m(i_z^2 + b^2)\ddot{\psi} - mb\ddot{x} + k_\psi \dot{\psi} + c_\psi \psi = -lF_{un,x} \tag{8.67}$$

With damping disregarded, the magnitude of the frequency response function becomes:

$$\frac{\hat{\psi}}{m_{un} r_{un}} = \frac{l}{c_\psi} \frac{\Omega^2 \left\{ 1 - \left(\dfrac{\Omega}{\omega_0} \right)^2 \right\}}{\left\{ 1 - \left(\dfrac{\Omega}{\omega_1} \right)^2 \right\} \left\{ 1 - \left(\dfrac{\Omega}{\omega_2} \right)^2 \right\}} \tag{8.68}$$

in which we have the zero frequency:

$$\omega_0^2 = \frac{l}{l - b} \omega_x^2 \tag{8.69}$$

and the two natural frequencies:

$$\omega_{1,2}^2 = \tfrac{1}{2}(1 + \beta) \left\{ \left(\omega_x^2 + \omega_\psi^2 \right) \pm \left(\omega_x^2 - \omega_\psi^2 \right) \sqrt{1 + \frac{4\beta}{1 + \beta} \frac{\omega_x^2 \omega_\psi^2}{\left(\omega_x^2 - \omega_\psi^2 \right)^2}} \right\} \tag{8.70}$$

where we have introduced the 'uncoupled' natural frequencies:

$$\omega_x^2 = \frac{c_x}{m} \quad \text{and} \quad \omega_\psi^2 = \frac{c_\psi}{m(i_z^2 + b^2)} \tag{8.71}$$

and the coupling factor:

$$\beta = \frac{b^2}{i_z^2} \tag{8.72}$$

For the analysis, we are interested in the influence of the fore and aft compliance of the suspension. In the right-hand diagram of Fig.8.21 the two natural frequencies have been plotted as a function of the longitudinal natural frequency ratio (squared), which is proportional to the longitudinal stiffness c_x, together with the constant vertical natural frequency and the zero frequency for three different values of f/b. In addition, the location of the two centres of rotation according to the two modes of the undamped vibration have been indicated.

The two steer natural frequencies ω_1 and ω_2 increase with increasing longitudinal suspension stiffness. The lower natural frequency with a centre of rotation located at the inside of the king-pin, approaches the uncoupled natural frequency ω_ψ.

From (8.69) it is seen that a zero does not occur if the unbalance arm length l lies in the range $0<l<b$ which does not represent a usual configuration. For the normal situation with $b>0$ the zero frequency line may cross the second natural frequency curve if l is not too large. If the two frequencies coincide, the second resonance peak of the steer response to unbalance will be suppressed. In that case, the unbalance force line of action passes through the centre of rotation of the higher vibration mode.

It may be noted that the situation with contact between wheel and road can be simply modelled if the wheel is assumed to be rigid. The same equations apply with inertia parameters adapted according to the altered system with a point mass attached to the axle in the wheel plane. The point mass has the value I_w/r^2 where I_w denotes the wheel polar moment of inertia and r the wheel radius.

8.4.2. Dynamics of the Loaded System with Tyre Properties Included

In a more realistic model the in-plane and out-of-plane slip, compliance and inertia parameters should be taken into account. A possible important aspect is the interaction between vertical tyre deflection and longitudinal slip which may cause the appearance of a third resonance peak near the vertical natural frequency of the wheel system. The longitudinal carcass compliance gives rise to an additional natural frequency around 40 Hz of the wheel rotating against the foot print (cf. discussion in Section 8.3.3). Due to damping, originating from tangential slip of the tyre, a supercritical condition will arise beyond a certain forward velocity. This causes the additional natural frequency to disappear.

For the extended system with road contact, the following complete set of linear equations apply:

$$m(\ddot{x} + 2\zeta_x\omega_x\dot{x} + \omega_x^2 x) - mb\ddot{\psi} - F_x = F_{un,x} \tag{8.73}$$

$$m_z(\ddot{z} + 2\zeta_z\omega_z\dot{z} + \omega_z^2 z) = F_{un,z} \tag{8.74}$$

$$I_\psi(\ddot{\psi} + 2\zeta_\psi\omega_\psi\dot{\psi} + \omega_\psi^2\psi) - mb\ddot{x} + lF_x - M_z = -lF_{un,x} \tag{8.75}$$

$$I_w\dot{\Omega} + r_o F_x = 0 \tag{8.76}$$

$$\sigma_\kappa\dot{F}_x + V_o F_x = -C_{F\kappa}V_{sx} \tag{8.77}$$

$$\sigma_\alpha\dot{F}_y + V_o F_y = -C_{F\alpha}V_{sy} \tag{8.78}$$

$$V_{sx} = \dot{x} - l\dot{\psi} - r_o(\Omega - \Omega_o) + \Omega_o\eta z \tag{8.79}$$

$$V_{sy} = -V_o\psi \tag{8.80}$$

$$M_z = -t_\alpha F_y - \frac{1}{V_o}\kappa^*\dot{\psi} - C_{gyr}V_o\dot{F}_y \tag{8.81}$$

$$F_{un,x} = -m_{un}r_{un}\Omega_o^2\sin\Omega_o t \tag{8.82}$$

$$F_{un,z} = m_{un}r_{un}\Omega_o^2\cos\Omega_o t \tag{8.83}$$

$$V_o = r_o\Omega_o \tag{8.84}$$

Table 8.2. Parameter values of wheel suspension system and tyre considered.

m	30 kg	ω_z	70 rad/s	σ_κ	0.15 m	F_{zo}	3500N
m_z	40 kg	ω_ψ	85 rad/s	σ_α	0.3 m	C_{Fz}	160 kN/m
I_ψ	1.2 kgm^2	ζ_x	0.01	t_α	0.03 m	$C_{F\kappa}$	60 kN
I_w	0.8 kgm^2	ζ_z	0.06	κ^*	80 Nm^2	$C_{F\alpha}$	40 kN/rad
m_{un}	0.1 kg	ζ_ψ	0.08	C_{gyr}	2x10^{-5} s^2	η	0.4

The tyre side force differential equation (7.20) has been used and similar for the longitudinal force. The longitudinal slip speed follows from (8.45) with (8.52). Note that mechanical caster has not been considered so that the lateral slip speed is simply expressed by (8.80). The aligning torque is based on Eq.(7.49) with for M_{zr} the spin moment M_z^* according to Eq.(5.82) and the gyroscopic couple from Eqs.(7.47) or (5.178). The rolling resistance moment has been neglected in

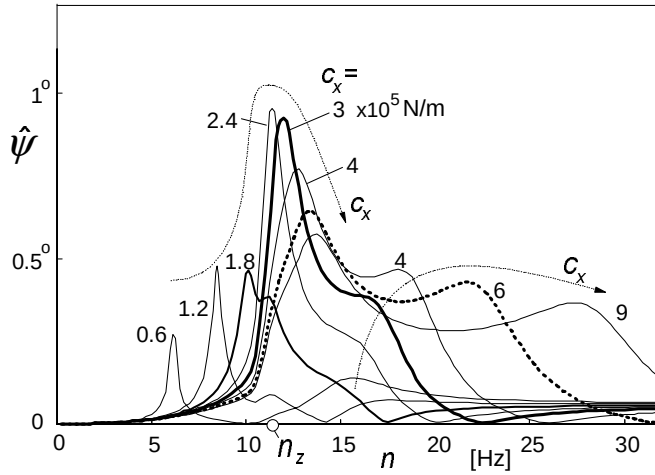

Fig. 8.22. Steer vibration amplitude due to wheel unbalance as a function of wheel frequency of revolution $n = \Omega_o/2\pi$ for various values of the longitudinal suspension stiffness.

(8.76) and the average effective rolling radius has been taken equal to the average axle height or loaded radius r_o (in reality r_e is usually slightly larger than r_o).

In Table 8.2 the set of parameter values used in the computations have been listed. The moment of inertia about the steering axis is denoted with I_ψ and equals $m(b^2+i_z^2)$. The amplitude of the steer angle that occurs as a response to a wheel unbalance mass of 0.1kg has been plotted as a function of the wheel speed of revolution in Fig.8.22. To examine the influence of the longitudinal suspension compliance a series of values of the longitudinal stiffness c_x has been

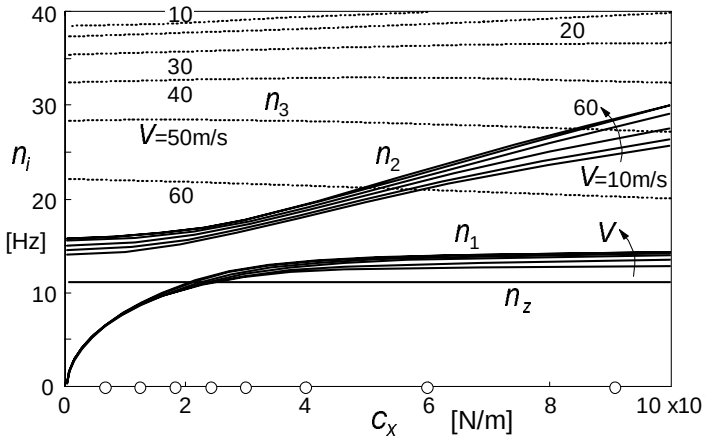

Fig. 8.23. Variation of the three natural frequencies with longitudinal suspension stiffness at different speeds together with the constant vertical natural frequency. The circles on the horizontal axis mark the stiffness cases of Fig.8.22.

considered. In Fig.8.23 these values have been indicated by marks on the stiffness axis. Clearly, in agreement with the variation of the natural frequencies assessed in this figure, the two resonance peaks move to higher frequencies when the stiffness is raised. A third resonance peak may show up belonging to the vertical natural frequency. This peak remains at the same frequency. It is of interest to observe that when the lowest steer natural frequency n_1 coincides with n_z the interaction between vertical and horizontal motions causes the peak to reach relatively high levels. As we have seen before, this interaction is brought about by the slope η indicated in Fig.8.13. The curves of the diagram of Fig.8.22 also exhibit the dip in the various curves that correspond with the zero's (ω_0) of Fig.8.23. The zero frequency closely follows the formula (8.69) of the free system. At the lowest stiffness the zero frequency n_0 almost coincides with the second natural frequency n_2 and suppresses the second peak.

It may be of interest to find out how the several tyre parameters affect the response characteristics of Fig.8.22. In Fig.8.24 the result of making these parameters equal to zero has been depicted for the stiffness case $c_x = 3\text{x}10^5$N/m. Neglecting the factor η (case 1) meaning that the effective rolling radius would not change with load, appears to have a considerable effect indicating that, with η, the vertical motion does amplify the steering oscillation. Omitting the gyroscopic tyre moment (2), while reinstating η, appears, as expected, to effectively decrease the steer damping. This is strengthened by additionally deleting the moment due to tread width (3). Omitting the relaxation lengths (4)

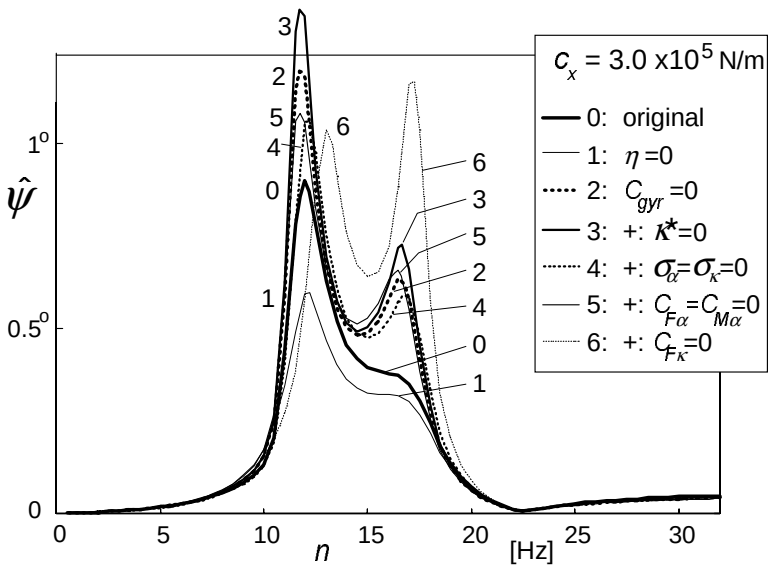

Fig. 8.24. Influence of various tyre parameters on the steer angle amplitude response curve.

lowers the peaks, thus removing the negative damping due to tyre compliance. Deleting, in addition, the side force and the aligning torque (5) raises the peaks again indicating that some energy is lost through the side slip. Disregarding the horizontal tyre forces altogether (6) brings us back to the (horizontally) free system treated in the previous subsection. As predicted by the analysis, two sharp resonance peaks arise as well as the dip at the zero frequency.

8.5. ABS Braking on Undulated Road

The aim of this section is to investigate the influence of dynamic effects due to vertical and longitudinal wheel vibrations excited by road irregularities upon the braking performance of the tyre and anti-lock braking system. These disturbing factors affect the angular velocity of the wheel and consequently may introduce disinformation in the signals transmitted to the ABS system upon which its proper functioning is based.

One may take the simple view that the primary function of the anti-lock device is to control the brake slip of the wheel to confine the wheel slip within a narrow range around the slip value at which the longitudinal tyre force peaks. In the same range it fortunately turns out that the lateral force that the tyre develops as a response to the wheel slip angle is usually sufficient to keep the vehicle stable and steerable.

In order to keep the treatment simple, we will restrict the vehicle motion to straight line braking and consider a quarter vehicle with wheel and axle that is suspended with respect to the vehicle body through a vertical and a longitudinal spring and damper. The analysis is based on the study of Van der Jagt et al.(1989).

8.5.1. In-Plane Model of Suspension and Wheel/Tyre Assembly

The vehicle is assumed to move along a straight line with speed V. The forward acceleration of the vehicle body is considered to be proportional with the longitudinal tyre force F_x. Vertical and horizontal vehicle body parasitic motions will be neglected with respect to those of the wheel axle. Consequently, the role of the wheel suspension is restricted to axle motion alone. These simplifications enable us to concentrate on the influence of the complex interactions between motions of the axle and the tyre upon the braking performance of the tyre. Figure 8.25 depicts the system to be studied. We have axle displacements x and z and a vertical road profile described by w and its slope dw/ds. To suit the limitations

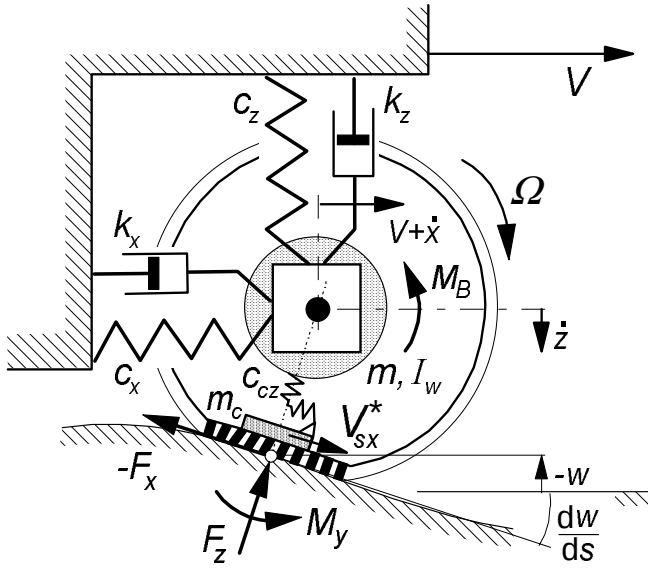

Fig, 8.25. System configuration for the study of controlled braking on undulated road surface.

of the tyre model employed, the wavelength λ of the road undulation is chosen relatively large. The wheel angular velocity is Ω and the braking torque is denoted with M_B. The unsprung mass and the polar moment of inertia of the wheel are lumped with a large part of those of the tyre and are denoted with m and I_w.

Through the tyre radial deflection the normal load is generated. Since we intend to consider possibly large slip forces, the analysis has to account for non-linear tyre characteristic properties. To adequately establish the fore and aft tyre contact force we will employ the enhanced transient tyre model discussed in Section 7.3. The contact relaxation length σ_c will be disregarded here. In the model, a contact patch mass m_c is introduced that can move with respect to the wheel rim in tangential direction, thereby producing the longitudinal carcass deflection u. The contact patch mass may develop a slip speed with respect to the road denoted by V^*_{sx}. The transient slip is defined by (V>0):

$$\kappa' = -\frac{V^*_{sx}}{V} \tag{8.85}$$

This longitudinal slip ratio is used as input in the steady-state longitudinal tyre characteristic. The internal tyre force that acts in the carcass and on the wheel axle will be designated as F_{xa} while the tangential contact force is denoted with F_x. According to the theory, this slip force is governed by the steady-state force vs slip relationship $F_{x,ss}(\kappa)$ which may be modelled with the Magic Formula.

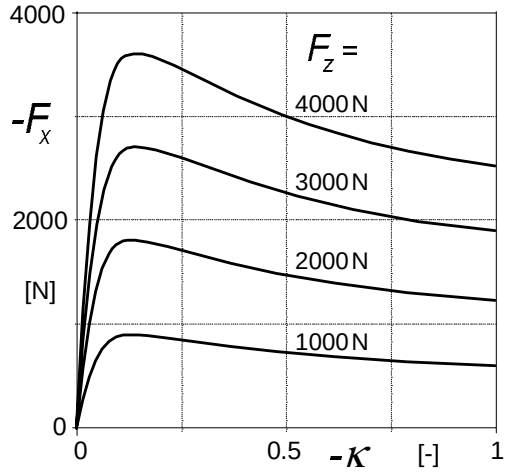

Fig. 8.26. Steady-state tyre brake force characteristics at different loads as computed with the aid of the Magic Formula and the similarity technique.

Since we have to consider the influence of a varying normal load, the relationship must contain the dependency on F_z. To handle this, the similarity method of Chapter 4 is used. We have the following equations:

$$F_{x,ss} = \frac{F_z}{F_{zo}} F_{xo}(\kappa_{eq}) \tag{8.86}$$

with argument

$$\kappa_{eq} = \frac{F_{zo}}{F_z} \frac{C_{F\kappa}(F_z)}{C_{F\kappa o}} \kappa' \tag{8.87}$$

The master characteristic $F_{xo}(\kappa)$ described by the Magic Formula holds at the reference load F_{zo} which is taken equal to the average load. Its argument κ is replaced by the equivalent slip value κ_{eq}. Also the longitudinal slip stiffness $C_{F\kappa o}$ is defined at the reference load. In Fig.8.26 the steady-state force characteristics have been presented for a set of vertical loads.

In-plane braking dynamics equations

The system has as input the road profile w and the brake torque M_B. The level w and the forward slope dw/ds are given as sinusoidal functions of the travelled distance s. To partly linearise the equations, the road forward slope is assumed to be small. The brake torque ultimately results from a control algorithm but may in the present analysis be considered as a given function of time.

The following equations apply for the wheel rotational dynamics, the horizontal and vertical axle motions and the tangential motion of the contact

patch mass:

$$I_w\dot{\Omega} + rF_{xa} + M_y = -M_B \tag{8.88}$$

$$m\ddot{x} + k_x\dot{x} + c_x x - F_{xa} - F_z\frac{\mathrm{d}w}{\mathrm{d}s} = 0 \tag{8.89}$$

$$m\ddot{z} + k_z\dot{z} + c_z z + F_z - F_{xa}\frac{\mathrm{d}w}{\mathrm{d}s} = 0 \tag{8.90}$$

$$m_c\dot{V}_{sx}^* + F_{xa} - F_x = 0 \tag{8.91}$$

with auxiliary equations for the tyre loaded radius

$$r = r_o - \rho \tag{8.92}$$

the radial deflection

$$\rho = z - w \tag{8.93}$$

the effective rolling radius

$$r_e = r_e(\rho) \tag{8.94}$$

the longitudinal carcass deflection rate

$$\dot{u} = V_{sx}^* - V_{sx} \tag{8.95}$$

the wheel slip velocity

$$V_{sx} = V + \dot{x} - r_e\Omega + \dot{z}\frac{\mathrm{d}w}{\mathrm{d}s} \tag{8.96}$$

and the transient slip

$$\kappa' = -\frac{V_{sx}^*}{V} \tag{8.97}$$

Moreover, the following constitutive relations are to be accounted for

$$F_z = F_z(\rho, u) \tag{8.98}$$

$$F_{xa} = F_{xa}(u, \dot{u}) \tag{8.99}$$

$$M_y = M_y(F_z, F_x) \tag{8.100}$$

$$F_x = F_{x,ss}(\kappa', F_z) \tag{8.101}$$

The function (8.101) is represented by Eqs.(8.86) and illustrated in Fig.8.26. The remaining constitutive relations are simplified to linear expressions.

Frequency response of wheel speed to road unevenness

As essential element of the analysis we will assess the response of the wheel angular velocity variation to road undulations at a given constant brake torque.

For this, the set of equations may be linearised around a given point of operation characterised by the average load F_{zo}, the constant brake torque M_{Bo} and the average slip ratio κ_o. We find for the constitutive relations:

$$\tilde{F}_z = c_{cz}(\tilde{\rho} + e_{zx}\tilde{u}) \tag{8.102}$$

$$\tilde{F}_{xa} = c_{cx}\tilde{u} + k_{cx}\dot{\tilde{u}} + e_{xz}\tilde{F}_z \tag{8.103}$$

$$\tilde{M}_y = A_r\tilde{F}_z + B_r\tilde{F}_{xa} \tag{8.104}$$

$$\tilde{F}_x = C_{xz}\tilde{F}_z + C_{x\kappa}\tilde{\kappa}' \tag{8.105}$$

where with the use of Eqs.(8.86.87)

$$C_{xz} = \frac{\partial F_{x,ss}}{\partial F_z} = \frac{F_{xo}}{F_{zo}} + \kappa_o\left(\frac{1}{C_{Fko}}\frac{\mathrm{d}C_{F\kappa}}{\mathrm{d}F_z} - \frac{1}{F_{zo}}\right)\frac{\mathrm{d}F_{xo}}{\mathrm{d}\kappa_{eq}} \tag{8.106}$$

and

$$C_{x\kappa} = \frac{\mathrm{d}F_{xo}}{\mathrm{d}\kappa_{eq}} \tag{8.107}$$

For the variation in effective rolling radius we have:

$$\tilde{r}_e = -\eta\tilde{\rho} \tag{8.108}$$

The linearised equations of motion are obtained from the Eqs.(8.88-91) by subtracting the average, steady-state values of the variable quantities and neglect products of small variations.

The frequency response of Ω to w has been calculated for different values of the longitudinal suspension stiffness c_x. The average condition is given by: the vehicle speed V_o=60 km/h, a vertical load F_{zo}=3000 N and a brake torque M_{Bo} = 300 Nm that corresponds to an average slip ratio κ_o = - 0.021. The road undulation amplitude $\hat{w}$=0.001 m,

Some of the tyre constitutive relations were determined directly from measurements while for some of the parameters values have been estimated. The small interaction parameters, η, e_{xz} and e_{zx}, and also the rolling resistance parameters A_r and B_r have been disregarded. Table 8.3 lists the parameter values used in the computations.

Table 8.3. Parameter values for wheel/tyre/suspension system.

I_w	0.95 kgm^2	c_x	100 kN/m	c_z	20kN/m	F_{zo}	3000 N
m	35 kg	k_x	2 kNs/m	k_z	2 kNs/m	r_o	0.29 m
m_c	1 kg	c_{cx}	10^3 kN/m	c_{cz}	170 kN/m	k_{cx}	0.8 kNs/m

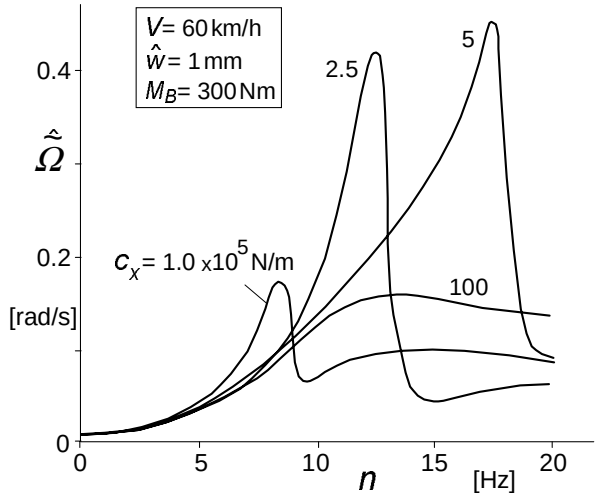

Fig. 8.27. Frequency response of amplitude of wheel spin fluctuations to road undulations w at a constant speed V and brake torque M_B and for different values of the longitudinal suspension stiffness c_x.

Figure 8.27 displays the amplitude of the wheel angular velocity variation as a function of the imposed frequency that is inversely proportional with the wavelength of the undulation. It is seen that the resonance peak height and the resonance frequency strongly depend on the fore and aft suspension stiffness.

8.5.2. Anti-Lock Braking Algorithm and Simulation

The actual control algorithms of ABS devices marketed by manufacturers can be quite complex and are proprietory items which incorporate several practical considerations. However, almost all algorithms make use of raw data pertaining to the angular speed and acceleration of the wheels. A detailed discussion of the various algorithms for predicting wheel motions and modulating the brake torque accordingly, has been given by Guntur (1975). The operational characteristic of a control algorithm used here for the purpose of illustration is shown in Fig.8.28. The salient features of the criteria used to increase or decrease applied brake torque (pressure) during a braking cycle depend critically upon both the momentary and treshold values of Ω and of $\dot{\Omega}$. It is assumed that the brake torque rate can be controlled at three different levels. Upon application of the brake the torque rises at a constant rate until point B is reached. After that the torque is reduced linearly until point C. The brake torque remains constant in the interval between points C and E. Compound criteria are considered at points A

and B for predicting when braking should be reduced to prevent the wheel from locking. Thus we have from the starting of brake application:

Increase of torque for $0 < t < t_B$ according to: $dM_B/dt = R_1$

The preliminary prediction time t_A is given by:

$$r_{eo}\dot{\Omega}(t_A) = Tg$$

where r_{eo} stands for the nominal effective rolling radius and T for a constant which sets the treshold for $\dot{\Omega}$.

From time t_B we have:

Decrease of torque for $t_B < t < t_C$ according to: $dM_B/dt = R_2$

The instant of prediction and action t_B is defined by:

$$r_{eo}\{\Omega(t_A) - \Omega(t_B)\} - Tg(t_B - t_A) = \Delta V_B$$

The time t_C marks the beginning of the constant torque phase CE, i.e.:

Constant torque for $t_C < t < t_E$: $dM_B/dt = 0$

Time t_C is found from:

$$\dot{\Omega}(t_C) = 0$$

Similarly, the criterion for increasing the torque at E:

Increase of torque for $t > t_E$ according to: $dM_B/dt = R_1$

is given by the compound reselection conditions generated at points D and E, with t_D and t_E being found from:

$$\ddot{\Omega}(t_D) = 0$$

and

$$r_{eo}[\{\Omega(t_D) - \Omega(t_E)\} + \dot{\Omega}(t_D)\cdot(t_E - t_D)] = \Delta V_E$$

For the simulation the following values have been used:

$T = -1$, $\Delta V_B = 0.1 r_{eo}\Omega(t_B)$ and $\Delta V_E = 1$ m/s

The brake torque rates have been set to:

$R_1 = -R_2 = 19000$ Nm/s

In order to simulate the braking manoeuvre of a quarter vehicle equipped with the anti-lock braking system, the deceleration of the vehicle is taken to be proportional to F_x. The results of the simulations performed are presented in Fig.8.29. The left-hand diagrams refer to the case of braking on an ideally flat road while the diagrams on the right-hand side depict the results obtained with the same system on a wavy road surface. For the purpose of simulation, the model was extended to include a hydraulic sub-system interposed between the brake pedal and the wheel cylinder. However, this extension is not essential to our discussion. In both cases the same hydraulic sub-system was used and the same control algorithm as the one discussed above was implemented.

The further parameters used in the simulation were:

Initial speed of the vehicle: 60 km/h, the road input with a wavelength of 0.83 m and an amplitude of 0.005 m.

The results of the simulation show that brake slip variations occur both on a flat as well as on undulated road surfaces. However, the very large variations of the transient slip value κ' in the latter case lead to a further deterioration of the braking performance. The average vehicle deceleration drops down from 7.1 m/s^2 to approximately 6 m/s^2. Although large fluctuations in the vertical tyre force are mainly responsible for this reduction, it is equally clear that severe perturbation occurring both in Ω and $\dot{\Omega}$ may be an additional source of misinformation for the anti-lock control algorithm. The important reduction in braking effectiveness resulting from vertical tyre force variations may be attributed to the term C_{cz} in the linearised constitutve relation (8.106) of the rolling and slipping tyre, and in particular to the contribution of the variation of the longitudinal slip stiffness with wheel load $dC_{F\kappa}/dF_z$. Both vertical and horizontal vibrations of the axle and the vertical load fluctuations on wavy roads appear to adversely influence the braking performance of the tyre as well as that of the anti-lock system.

In 1986, Tanguy made a preliminary study of such effects using a different control algorithm. He pointed out that wheel vibrations on uneven roads can pose serious problems of misinformation for the control logic of the anti-lock system. The results of the simulations discussed above and reported by Van der Jagt (1989) confirm Tanguy's findings.

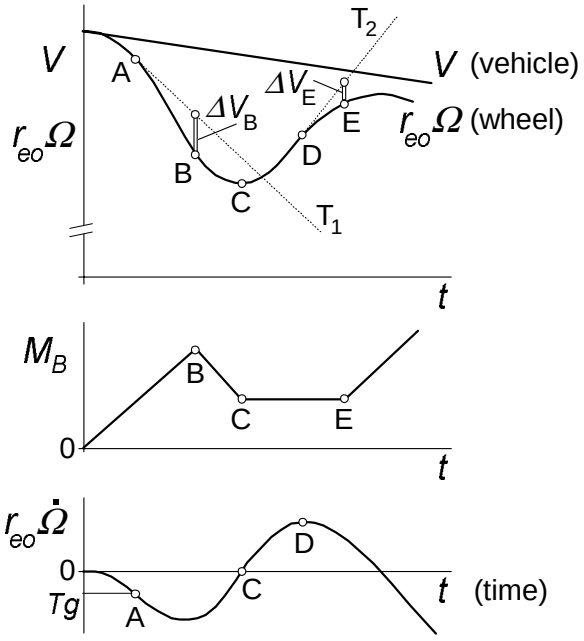

Fig. 8.28. Example of an ABS algorithm used to modulate the applied brake torque.

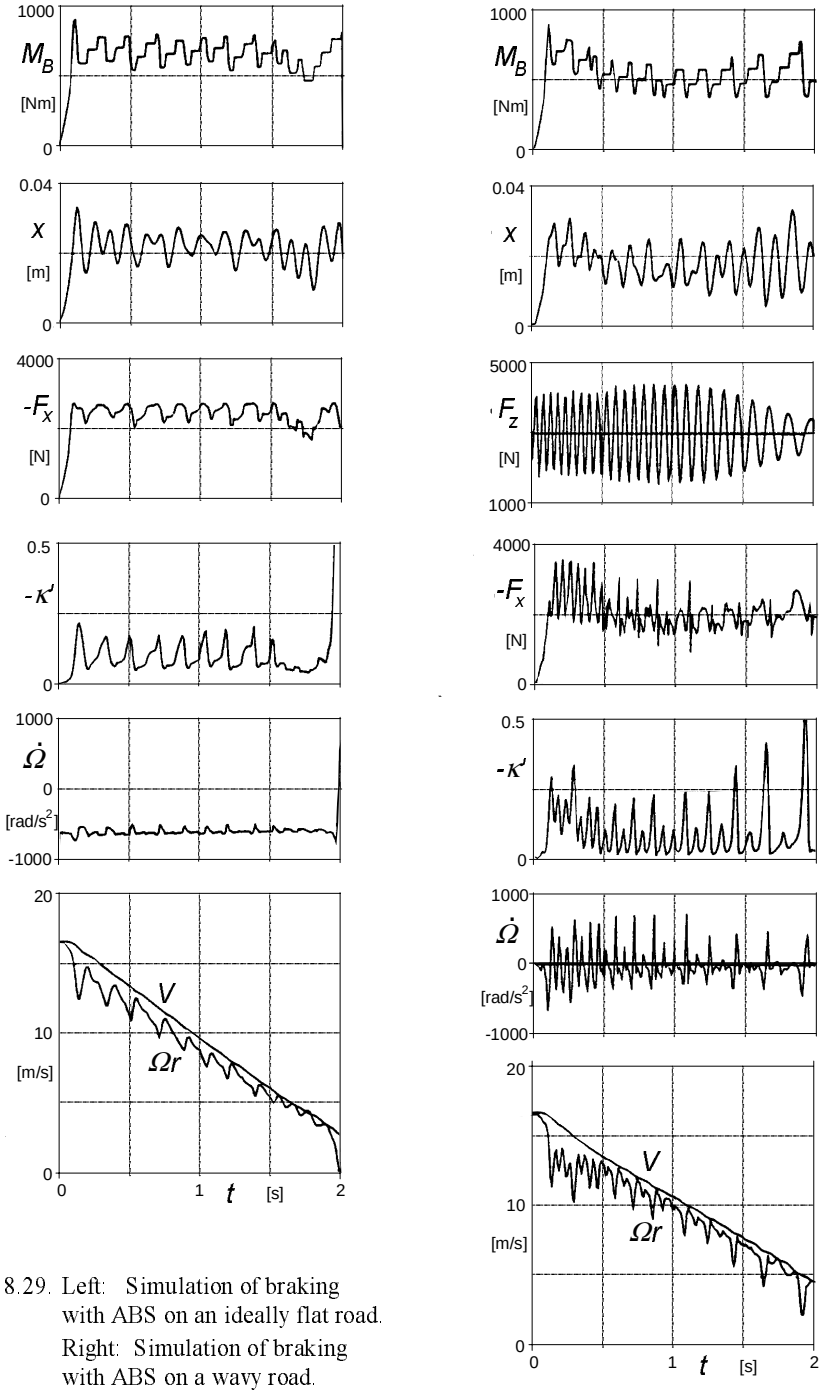

Fig. 8.29. Left: Simulation of braking with ABS on an ideally flat road.
Right: Simulation of braking with ABS on a wavy road.

8.6. Starting from Standstill

In this section the ability of the transient models to operate at and near zero speed conditions will be demonstrated. The four models treated in Secs.7.2.2, 7.2.3 and 7.3 will be employed in the simulation of the longitudinal motion of a quarter vehicle model on an upward slope of 5%, cf. Fig.8.30.

The following three different manoeuvres are considered:

1. Standing still on slope, stepwise application of drive torque and subsequently rolling at constant speed.
2. From standstill on slope: freely rolling backwards, then powerful propulsion followed by free rolling.
3. From standstill: rolling backwards, then braking to wheel lock, followed by free rolling again after which a short phase of drive torque is applied. Finally the quarter vehicle slows down on the slope.

The steady-state longitudinal force function of the transient longitudinal slip κ' is described by the formula:

$$F_x = D_x \sin[C_x \arctan\{B_x\kappa' - E_x(B_x\kappa' - \arctan(B_x\kappa'))\}] \tag{8.109}$$

For the successive transient tyre models the equations will be repeated below.

Semi non-linear transient model:
First-order differential equation for longitudinal tyre deflection u according to Eq.(7.9):

$$\frac{\mathrm{d}u}{\mathrm{d}t} + \frac{1}{\sigma_\kappa}|V_x|u = -V_{sx} \tag{8.110}$$

where σ_κ only depends on a possibly varying vertical load F_z. The transient slip

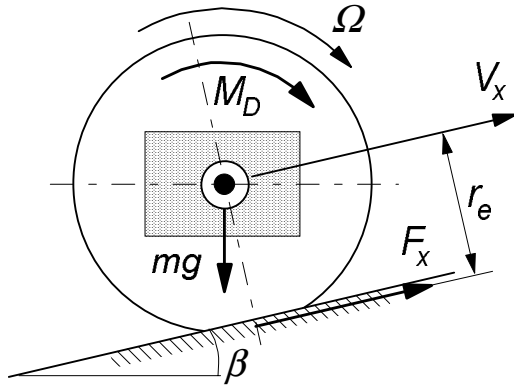

Fig. 8.30. On the problem of starting from standstill on a slope.

reads:

$$\kappa' = \frac{u}{\sigma_\kappa} \tag{8.111}$$

At low values of speed $|V_x| < V_{low}$ the deflection u may have to be restricted as was formulated in general by Eq.(7.25). For our present problem we have:

if: $|\kappa'| > A\kappa_{sl}$ and $|V_x| < V_{low}$ and $(V_{sx} + |V_x|u/\sigma_\kappa)u < 0$:

$$\frac{\mathrm{d}u}{\mathrm{d}t} = 0 \tag{8.112}$$

else:

$$\frac{\mathrm{d}u}{\mathrm{d}t} = -V_{sx} - \frac{1}{\sigma_\kappa}|V_x|u \tag{8.113}$$

The slip where the peak force occurs is roughly:

$$\kappa_{sl} = 3D_x/C_{F\kappa} \tag{8.114}$$

with the slip stiffness

$$C_{F\kappa} = B_x C_x D_x \tag{8.115}$$

For the factor A the value 1 is suggested but a higher value may improve the performance especially when the force characteristic exhibits a pronounced peak.

Fully non-linear transient model:
The same equations (8.110,111) hold but with σ_κ replaced by the κ' dependent and downwards limited quantity:

$$\sigma_\kappa^* = \max\left(\frac{\sigma_{\kappa o}}{C_{F\kappa}} \cdot \frac{|F_x| + C_{F\kappa}\varepsilon_F}{|\kappa'| + \varepsilon_F}\ ,\ \sigma_{\min}\right) \tag{8.116}$$

where $\sigma_{\kappa o}$ represents the value of the relaxation length at $\kappa' = 0$. We have the equation:

$$\frac{\mathrm{d}u}{\mathrm{d}t} + \frac{1}{\sigma_\kappa^*}|V_x|u = -V_{sx} \tag{8.117}$$

The transient slip now reads:

$$\kappa' = \frac{u}{\sigma_\kappa^*} \tag{8.118}$$

A deflection limitation is not necessary for this model. However, because of the algebraic loop that arises, the quantity (8.116) must be obtained from the previous time step.

Restricted fully non-linear model:
Analogous to Eq.(7.35) we have the equation for κ' :

$$\sigma_\kappa \frac{\mathrm{d}\kappa'}{\mathrm{d}t} + |V_x|\kappa' = -V_{sx} \tag{8.119}$$

with the κ' dependent relaxation length:

$$\sigma_\kappa = \frac{\sigma_{\kappa o}}{C_{F\kappa}} \frac{\partial F_x}{\partial \kappa'} \tag{8.120}$$

The model is not sensitive to wheel load variations which constitutes the restriction of the model. For the problem at hand this restriction is not relevant and the model can be used. The great advantage of the model is the fact that an algebraic loop does not occur. And again a u limitation is not needed. A straight forward simulation can be conducted. For the relation (8.120) the following approximate function is used:

$$\sigma_\kappa = \max\left[\sigma_{\kappa o}\left(1 - \frac{C_{F\kappa}}{3D_x}|\kappa'|\right), \sigma_{\min}\right] \tag{8.121}$$

where $\sigma_{\min}$ represents the minimum value of the relaxation length that is introduced to avoid numerical difficulties.

Enhanced non-linear transient model:
Following Sec.7.3 and Fig.7.15 we have for the differential equation for the longitudinal motion of the contact patch mass m_c:

$$m_c \dot{V}_{sx}^* + k_{cx}\dot{u} + c_{cx}u = F_x(\kappa') \tag{8.122}$$

where F_x denotes the contact force governed by Eq.(8.109).

The transient slip value is obtained from the differential equation (7.54):

$$\sigma_c \frac{\mathrm{d}\kappa'}{\mathrm{d}t} + |V_x|\kappa' = -V_{sx}^* \tag{8.123}$$

an equation similar to (8.119) but here with a constant (small) contact relaxation length. The longitudinal carcass stiffness c_{cx} in the contact zone should be found by satisfying the equation:

$$\sigma_{\kappa o} = \frac{C_{F\kappa}}{C_{Fx}} = \frac{C_{F\kappa}}{c_{cx}} + \sigma_c \tag{8.124}$$

The deflection rate needed in Eqs.(8.122) is equal to the difference in slip velocities of contact patch and wheel rim:

$$\dot{u} = V_{sx}^* - V_{sx} \tag{8.125}$$

The longitudinal force acting on the wheel rim results from:

$$F_{xa} = k_{cx}\dot{u} + c_{cx}u \tag{8.126}$$

Low speed additional damping:
At zero forward speed with each of the first three tyre models a virtually undamped vibration is expected to occur. An artificial damping may be introduced at low speed by replacing κ' in (8.109) by

$$\kappa' - \frac{k_{V,low}}{C_{F\kappa}} V_{sx} \tag{8.127}$$

which corresponds with the suggested Eq.(7.26). The gradual reduction to zero at $V_x = V_{low}$ is realised by using the formula:

$$\begin{aligned} k_{V,low} &= \tfrac{1}{2} k_{V,low0}\left\{1 + \cos\left(\pi \frac{|V_x|}{V_{low}}\right)\right\} && \text{if } |V_x| \le V_{low} \\ k_{V,low} &= 0 && \text{if } |V_x| > V_{low} \end{aligned} \tag{8.128}$$

Also with the enhanced model the additional damping will be introduced while k_{cx} is taken equal to zero to better compare the results.

Vehicle and wheel motion:
For the above tyre models the wheel slip speed follows from:

$$V_{sx} = V_x - r_e\Omega \tag{8.129}$$

The vehicle velocity and the wheel speed of revolution are governed by the differential equations:

$$m\dot{V}_x = F_{xa} - mg\tan\beta \tag{8.130}$$

$$I_w\dot{\Omega} = M_D - r_e F_{xa} \tag{8.131}$$

where r_e is the effective moment arm which turns out to correspond with experimental evidence, cf. Chap.9, Fig.9.34. For the first three models with contact patch mass not considered, we have:

$$F_{xa} = F_x \tag{8.132}$$

When at braking the wheel becomes locked we have: $\Omega = 0$.

Results:
The three different longitudinal manoeuvres listed above have been simulated with each of the four transient tyre models. In the Figs.8.31-34 some of the results have been presented. The parameter values have been listed in Table 8.4.

Figures 8.31 and 32 depict the process of standing still on a 5% upward slope (appropriate brake or drive torque), followed by a step drive torque input and subsequently rolling at constant speed (back to equilibrium drive torque).

Table 8.4. Parameter values.

m	600 kg	B_x	12.5	$\tan\beta$	0.05	$\sigma_{\kappa(o)}$	0.2 m
I_w	1 kgm^2	C_x	1.6	$k_{V,low0}$	770 Ns/m	$\sigma_{\min}$	0.02 m
g	9.81 m/s^2	D_x	3000 N	k_{cx}	0	σ_c	0.02 m
r_e	0.3 m	E_x	0	m_c	1 kg	ε_F	0.01

Tyre/wheel wind-up oscillations occur both at start and at end of step change in propulsion torque M_D. Results have been shown of the computations using the semi non-linear transient tyre model (Fig.8.31) and the enhanced model (Fig.8.32). Virtually the same results as depicted in Fig.8.32 have been achieved by using either the fully non-linear or the restricted non-linear transient tyre model. Only at low speed a frequency difference can be observed to occur when using the semi non-linear model.

Figure 8.33 shows the results of standing on the slope, then freely rolling backwards, subsequently applying a powerful propulsion, which is followed by free rolling. The tyre longitudinal force passes its peak and reaches the lower end of its characteristic which enables the wheel to spin up. Next, when the wheel slows down rapidly, the peak is passed again and a damped wheel/tyre wind-up oscillation occurs. Calculations have been performed using the enhanced transient tyre model of Sec.7.3 (with contact mass). The restricted fully non-linear tyre model, Eq.(7.35) not responding to load changes, turns out to yield almost equal results. The other two models and especially the semi non-linear model of Sec.7.2.3 (with σ constant), appear to perform less good under these demanding conditions (less F_x reduction in spin-up phase which avoids an equally rapid spinning up of the wheel). The low speed limit value V_{low} was increased to 5m/s to restrict the u deflection of the semi non-linear model over a larger speed range. The factor A was increased to 4 which improved the performance of this model. Omission of the limitation of the u deflection would lead to violent back and forth oscillations.

Finally, Fig.8.34 depicts the simulated manoeuvre: from standstill rolling backwards, then braking to wheel lock, which is followed by free rolling again after which a short phase of acceleration occurs; finally, the quarter vehicle slows down on the slope. During wheel lock the vehicle mass appears to vibrate longitudinally at low frequency with respect to the 'contact patch'. Calculations have been conducted with the simple semi non-linear transient tyre model. Practically equal results have been obtained when using one of the other three transient tyre models.

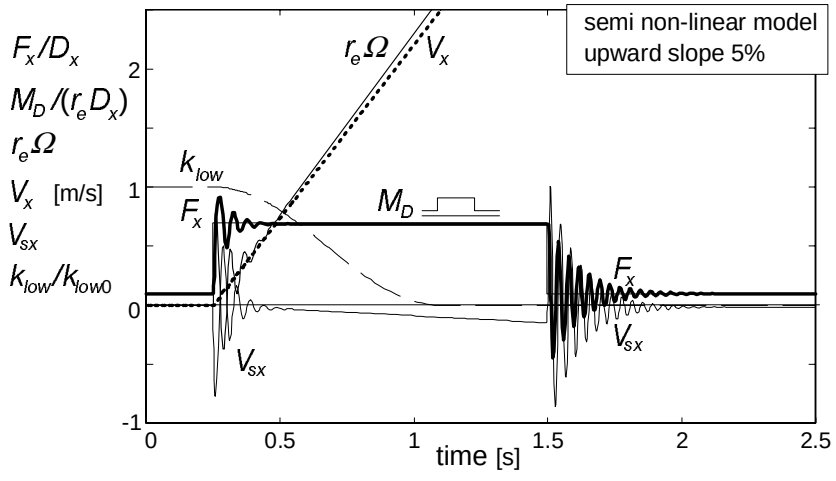

Fig. 8.31. Standing still on slope, acceleration and subsequently rolling at constant speed. Tyre/wheel wind-up oscillations occur both at start and at end of step change in propulsion torque M_D. Computations have been performed with the semi non-linear transient tyre model with constant relaxation length (V_{low} = 2.5m/s).

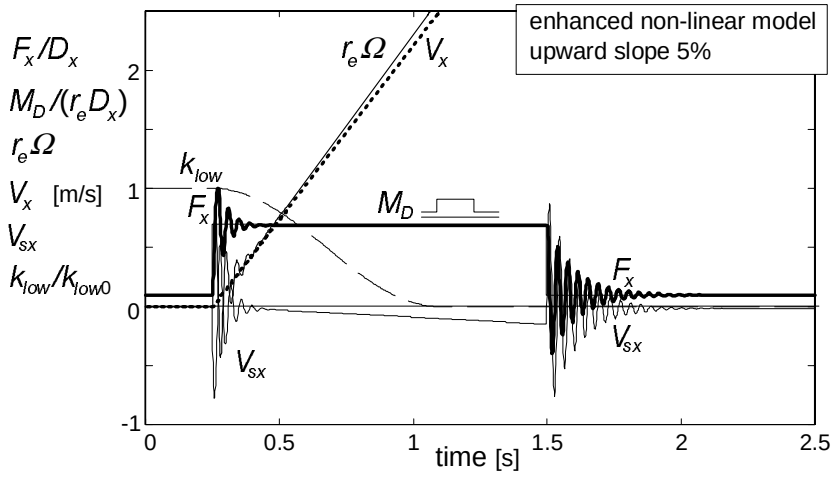

Fig. 8.32. Same simulation as in Fig.8.31 but now using the enhanced non-linear transient tyre model with carcass compliance (V_{low} = 2.5m/s). Only at low speed a frequency difference can be observed to occur. Very similar results are obtained with the fully non-linear transient models with changing relaxation length.

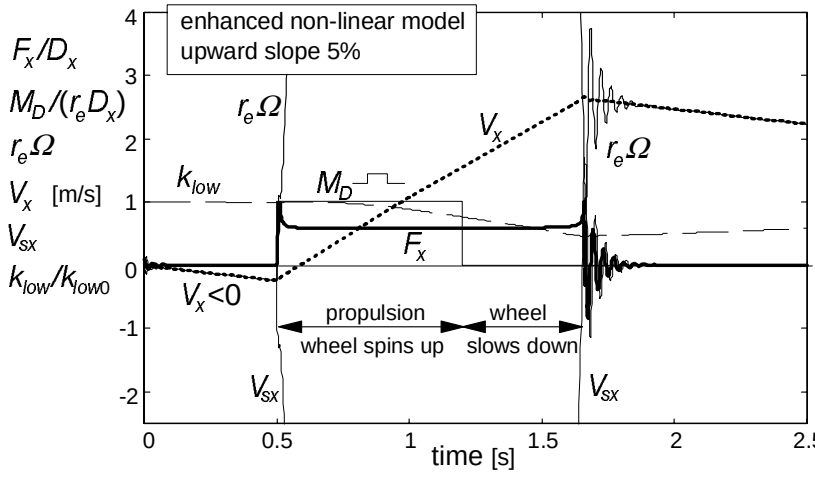

Fig. 8.33. From standstill on slope, freely rolling backwards, then powerful propulsion followed by free rolling. The tyre longitudinal force passes its peak and reaches the lower end of its characteristic which enables the wheel to spin up. Next, when the wheel slows down rapidly, the peak is reached again and a damped wheel/tyre wind-up oscillation occurs. Calculations using enhanced transient tyre model (V_{low} = 5m/s) which together with the restricted fully non-linear model turns out to perform best.

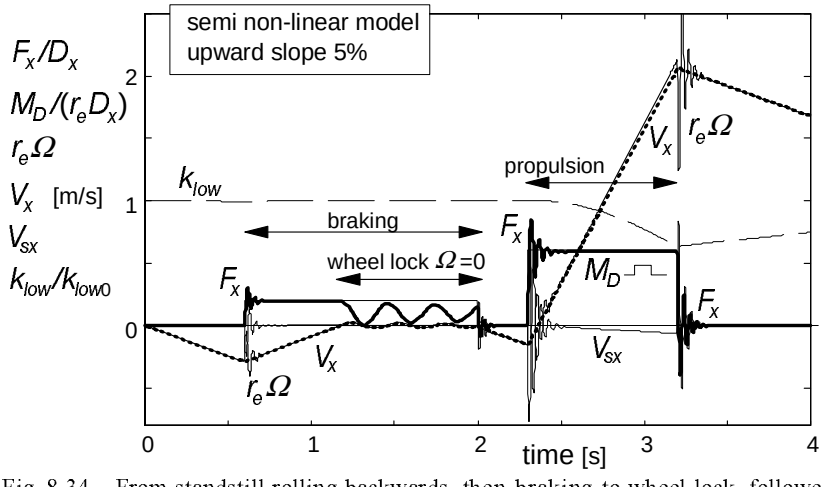

Fig. 8.34. From standstill rolling backwards, then braking to wheel lock, followed by free rolling again after which a short phase of acceleration occurs. Finally the quarter vehicle slows down on the slope. During wheel lock the vehicle vibrates at low frequency with respect to the 'contact patch'. Calculations with the simple semi non-linear transient tyre model. Practically same results are obtained when using one of the other three transient tyre models.

It may be concluded that the restricted fully non-linear model and the enhanced model with contact patch mass show excellent performance. It should be kept in mind that the restricted model does not react on wheel load variations. The semi non-linear model can be successfully used under less demanding conditions.

The next chapter deals with the development of a more versatile tyre model which can handle higher frequencies and shorter wavelengths. The enhanced model and the restricted fully non-linear transient tyre model will be used as the basis of this development.

Chapter 9

SHORT WAVELENGTH INTERMEDIATE FREQUENCY TYRE MODEL

9.1. Introduction

In Chapter 5 the stretched string model, possibly featuring tread elements and tyre inertia, was used to study the dynamic response of the side force and aligning torque to lateral, vertical and yaw motion variations of the wheel axle. These motions, however, had to be restricted in magnitude to allow the theory to remain linear. Several approximations were introduced to simplify the model description which made it possible to consider ranges of relatively large slip through a simple non-linear extension. The limitation, however, was that only relatively large wavelength phenomena (> ca. 1.5 m) could be investigated with these simplified models.

The present chapter describes a model that is able to cover situations where the wavelength is relatively short (>20 cm and possibly even shorter for modelling road obstacle enveloping properties and parking phenomena), the frequency is relatively high (< ca. 60 Hz) while the level of slip can be high. Situations in which combined slip occurs can be handled and the Magic Formula model can be used as the basis for the non-linear force and moment description. As a result, a continuous transition from time varying slip situations to steady-state conditions is realised. The original model development was restricted to the more important responses to variations of longitudinal and side slip. Also, the possibility to traverse distinct road irregularities (cleats) was included in the tyre model. The model is based on the work of Zegelaar (1998) and Maurice (2000) and is referred to as the *SWIFT* model (corresponding to the title of the present chapter). Subsequent developments of the model did make it possible to also include variations of camber and turn slip.

The crucial step that was taken to reach further than one can by using the string model is the separation of modelling the carcass and the contact patch. In this way a much more versatile model can be established that correctly describes slip properties at short wavelengths and at high levels of slip. The model achieved can be seen as a further development of the enhanced single contact

point model of Section 7.3, Fig.7.15. Five elements of the model structure can be distinguished: (1) The inertia of the belt that has been taken into account to properly describe the dynamics of the tyre. The restriction to frequencies of about 60Hz allows the belt to be considered as a rigid circular ring. (2) The so-called residual stiffnesses that has been introduced between contact patch and ring to ensure that the total static tyre stiffnesses in vertical, longitudinal, lateral and yaw directions are correct. The total tyre model compliance is made up of the carcass compliance, the residual compliance (in reality a part of the total carcass compliance) and the tread compliance. (3) The brush model that represents the contact patch featuring horizontal tread element compliance and partial sliding. On the basis of this model, the effects of the finite length and width of the footprint are approximately included. This element of the model is the most complex part and accomplishes the reduction of the allowed input wavelength to ca. 20cm. (4) Three effective inputs to enable the simulation of the tyre moving over an uneven road surface.The actual profile of the road is replaced by an effective set of three inputs: an effective height and slope of the road plane and an effective variation of the tyre effective rolling radius that accounts for the enveloping power of the tyre. The dynamic tyre slip and vibration model remains unchanged. (5) The Magic Formula tyre model to describe the non-linear slip force and moment properties. In Fig.9.1 the model structure has been depicted.

Similar more physically oriented models have been developed. A notable example is the BRIT model of Gipser. He employs a brush-ring model featuring tread elements distributed over a finite contact patch with realistic pressure

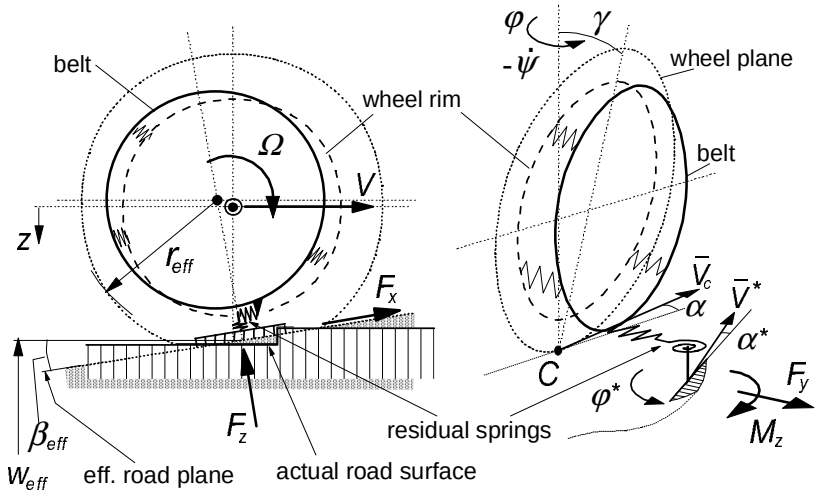

Fig. 9.1. General configuration of the SWIFT model featuring rigid belt ring, residual stiffnesses, contact patch slip model and effective road inputs.

distributions and demonstrates the use of the model with simulations of the tyre traversing a sinusoidal road surface also at a slip angle and at braking, cf. Gipser et al. (1997).

In the ensuing theoretical treatment, first, in Section 9.2, the slip model of the contact patch covering small wavelengths and large slip will be dealt with. Secondly, the model for the description of the dynamic behaviour of the rigid belt ring will be added, Sec.9.3. Thirdly, the feature of the model that takes care of running over uneven roads will be addressed, Sec.9.5. Full scale tyre test results will demonstrate the validity of the model.

9.2. The Contact Patch Slip Model

In this section, we will first represent the contact patch with tread elements by the brush model. Because of its relative complexity, the analytical model that describes the non-steady-state response to slip variations is approximated by a set of first-order differential equations. This contact model is tested by attaching the base line of the brush model to the wheel plane through a compliant carcass. For reasons of practical use, we finally introduce the Magic Formula to handle the non-linear behaviour of the model.

9.2.1. Brush Model Non-Steady-State Behaviour

The steady-state characteristics of the model have been discussed in Chapter 3. As a first step, we will derive the equations that govern the response of the forces and moment to small variations of the wheel slip with respect to a given level of wheel slip indicated with subscript $_o$.

Longitudinal Slip

For the case of pure longitudinal slip κ_{co} of the contact patch, the point of transition from adhesion to sliding is located according to Eq.(3.44) with (3.34,40) at a distance x_t from the contact centre:

$$x_t = a\left(\frac{2\theta|\kappa_{co}|}{1+\kappa_{co}} - 1\right) \tag{9.1}$$

The composite parameter θ has been defined in Chapter 3, Eq.(3.46). The length of the adhesion range $2am = a\text{-}x_t$ that begins at the leading edge is characterised by the fraction m that in the present chapter replaces the symbol λ to avoid

confusion with the notation for the wavelength. We have:

$$m = 1 - \theta \frac{|\kappa_{co}|}{1+\kappa_{co}} \quad \text{if} \quad \frac{|\kappa_{co}|}{1+\kappa_{co}} < \frac{1}{\theta} \quad \text{else} \quad m = 0 \tag{9.2}$$

An important observation is that at small variations of slip we may assume that only in the adhesion range changes in deflection occur.

For the development of the transient model we start out from the basic rolling contact differential equations (2.55,56). In the adhesion range we find for the longitudinal tread element deflection u_c in the case that only longitudinal slip is considered:

$$\frac{\partial \tilde{u}_c}{\partial t} - V_{rco} \frac{\partial \tilde{u}_c}{\partial x} = \tilde{V}_{sxc} = -V_{xco} \tilde{\kappa}_c \tag{9.3}$$

Where the tilde designates the variation with respect to the steady-state level. The average linear speed of rolling of the contact patch is equal to that of the wheel rim and reads:

$$V_{rco} = V_{ro} = V_x - V_{sxo} = V_x(1+\kappa_{co}) \tag{9.4}$$

The Fourier transform of the deflection becomes with U and K denoting the transformed quantities of u and κ respectively and ω_s the path frequency:

$$\tilde{U}_c = \frac{1}{i\omega_s}\left(1 - e^{-i\omega_s(a-x)V_x/V_{rco}}\right)\tilde{K}_c \tag{9.5}$$

Here, the boundary condition which says that the deflection vanishes at the leading edge is satisfied. By integrating over the range of adhesion and multiplying with the tread element stiffness c_p the frequency response function of the variation of F_x to the variation of κ_c is obtained. With the reduced frequency

$$\omega_s' = \frac{m\omega_s}{1+\kappa_{co}} \tag{9.6}$$

and the local derivative of F_x to κ_c

$$C_{F\kappa c} = \frac{2c_p m^2 a^2}{1+\kappa_{co}} \quad \text{if} \quad \frac{|\kappa_{co}|}{1+\kappa_{co}} < \frac{1}{\theta} \quad \text{else} \quad C_{F\kappa c} = 0 \tag{9.7}$$

the expression for the response function becomes when still adhesion occurs in the contact patch (first condition of (9.2)):

$$H_{F,\kappa c}(i\omega_s') = \frac{C_{F\kappa c}}{i\omega_s' a}\left\{1 - \frac{1}{2i\omega_s' a}\left(1 - e^{-2i\omega_s' a}\right)\right\} \tag{9.8}$$

In Fig.9.2 the resulting amplitude and phase characteristics have been shown

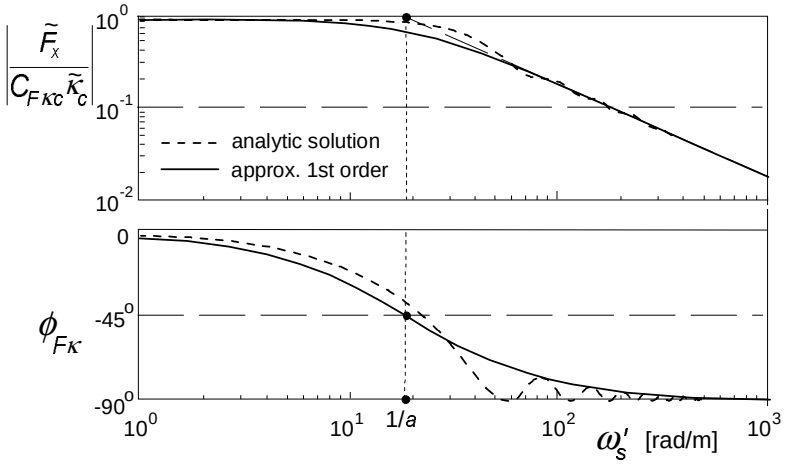

Fig. 9.2. Frequency response function of the longitudinal force variation to longitudinal slip variation of the brush model versus reduced path frequency according to the exact analytical solution and that of an approximate substitute first-order system at a given level of longitudinal slip.

together with those of an approximate first-order system. Especially the phase curve appears to exhibit a wavy pattern in the higher frequency range. These waves are considerably attenuated when the contact model is incorporated in a more complete tyre model including carcass compliance as will be shown below.

The first-order substitute model has a frequency response function that reads:

$$H_{F,\kappa c}(i\omega_s') = \frac{C_{F\kappa c}}{1 + i\omega_s' a} = \frac{C_{F\kappa c}}{1 + i\omega_s \sigma_c} \tag{9.9}$$

The approximation shows the same high frequency asymptote and steady-state level as the exact model. Apparently, the actual cut-off path frequency reads:

$$\omega_{s,c-o} = \frac{1 + \kappa_{co}}{m\,a} \tag{9.10}$$

that, obviously, reduces to $1/a$ when the average slip κ_{co} vanishes and as a consequence m (9.2) becomes equal to unity. When the average slip is chosen larger, the length of the adhesion range decreases and the cut-off frequency becomes higher. The relaxation length of the approximate contact model reads according to Eq.(9.9) with (9.6):

$$\sigma_c = \frac{m\,a}{1 + \kappa_{co}} \tag{9.11}$$

which reduces to zero when total sliding occurs.

The performance of the first-order system is reasonable but appears to

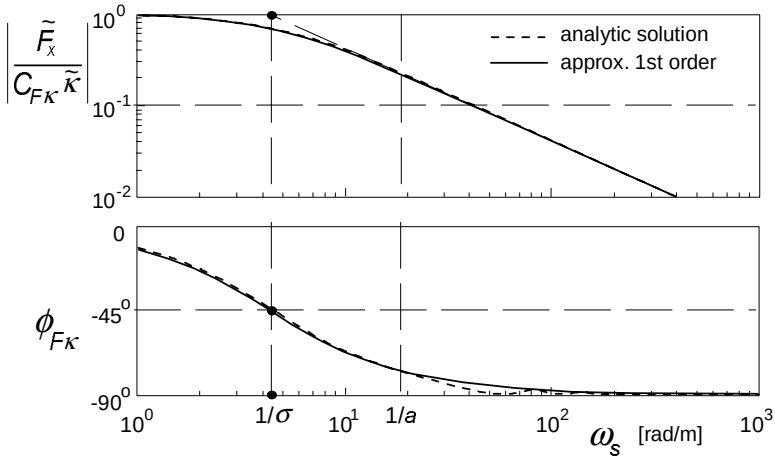

Fig. 9.3 . Frequency response function of the longitudinal force variation to longitudinal slip variation of the brush model attached to a flexible carcass versus path frequency according to the exact analytical solution and that of the approximate first-order system at zero longitudinal slip.

improve when the filtering action of the carcass compliance is taken into account. In that configuration we have the wheel slip velocity V_{sx} that acts as the input quantity. Adding the time rate of change of the carcass deflection produces the slip velocity of the brush model. The carcass deflection u equals (with fore and aft carcass stiffness c_x introduced):

$$u = \frac{F_x}{c_x} \tag{9.12}$$

The feed-back loop in the augmented system apparently contains a gain equal to $i\omega_s/c_x$. The resulting complete frequency response function reads:

$$H_{F,\kappa}(i\omega_s) = \frac{H_{F,\kappa c}(i\omega_s)}{1 + H_{F,\kappa c}(i\omega_s)\, i\omega_s/c_x} \tag{9.13}$$

When the approximate first-order system is employed for the contact model, the frequency response function for the complete model becomes using (9.13) with (9.9):

$$H_{F,\kappa}(i\omega_s) = \frac{C_{F\kappa c}}{1 + i\omega_s\sigma} \tag{9.14}$$

where the total relaxation length has been introduced which apparently reads:

$$\sigma = \sigma_c + \frac{C_{F\kappa c}}{c_x} = am + \frac{C_{F\kappa}}{c_x} \tag{9.15}$$

The local longitudinal slip stiffness of the contact patch is here equal to the local longitudinal slip stiffness of the complete model which obviously is due to the assumed inextensibility of the base line of the brush model. So we have at steady-state:

$$\frac{\partial F_x}{\partial \kappa} = C_{F\kappa} = C_{F\kappa c} \tag{9.16}$$

At vanishing slip we will add a subscript 0. When total sliding occurs, both σ_c and $C_{F\kappa}$ reduce to zero and the total relaxation length σ vanishes.

Figure 9.3 presents the frequency response function for the total model at vanishing slip, $\kappa_0 = 0$. It is noted that compared with the curves of Fig.9.2 the wavy pattern is considerably reduced. The approximate system performs very well. A wavelength of 20cm occurs at the path frequency ω_s = ca.30rad/m.

The differential equation that governs the transient slip response of the contact patch and through that the longitudinal force response, becomes for the approximate system:

$$\sigma_c \frac{\mathrm{d}\tilde{\kappa}_c'}{\mathrm{d}t} + |V_x|\tilde{\kappa}_c' = |V_x|\tilde{\kappa}_c = -\tilde{V}_{sxc} \tag{9.17}$$

The variation of the force becomes:

$$\tilde{F}_x = C_{F\kappa c}\tilde{\kappa}_c' \tag{9.18}$$

The structure of Eq.(9.17) corresponds with that of Eq.(7.37) of Chapter 7. The response, however, is insensitive to load variations but shows a nice behaviour. The transient response to load variations is sufficiently taken care of through the effect of carcass compliance. As a result, the relaxation length for the response to load variations becomes equal to $C_{F\kappa c}/c_x$ which is somewhat smaller than σ (9.15) that holds for the response to slip variations.

When the average steady-state relation for the longitudinal slip

$$|V_x|\kappa_{co} = -V_{sxco} \tag{9.19}$$

is added to Eq.(9.18) the equation for the total transient slip is obtained:

$$\sigma_c \frac{\mathrm{d}\kappa_c'}{\mathrm{d}t} + |V_x|\kappa_c' = |V_x|\kappa_c = -V_{sxc} \tag{9.20}$$

that completely corresponds to Eq.(7.54) of the enhanced non-linear transient tyre model. The transient slip κ_c' is subsequently used as input into the steady-state longitudinal force characteristic as will be explained later on and has already been indicated in Chap.7, Sec.7.3.

Lateral Slip

The lateral slip condition is more complex to handle because we have to deal with both the side force and the aligning torque. In addition, in the test condition, the carcass is allowed to not only deflect in lateral direction but also about the vertical axis. This is in accordance with the ultimate *SWIFT* configuration. The connected turn slip behaviour of the contact patch will be dealt with further on.

As with the longitudinal model development, first, the analytic response functions of the brush model will be assessed, in this case to side slip variations. Equation (2.56) gives rise to the following equation for the lateral tread deflection variations:

$$\frac{\partial \tilde{v}_c}{\partial t} - V_{rco}\frac{\partial \tilde{v}_c}{\partial x} = \tilde{V}_{syc} = -V_{xco}\tilde{\alpha}_c \tag{9.21}$$

Note that for the sake of simplifying in the present chapter the notation tanα is replaced by α, with or without subscript. Similar as for the longitudinal deflection we find for the Fourier transform V_c of the lateral deflection responding to slip angle variations, A_c denoting the brush model slip angle's transform (or actually of tanα_c):

$$\tilde{V}_c = \frac{1}{i\omega_s}\left(1 - e^{-i\omega_s(a-x)V_x/V_{rc0}}\right)\tilde{A}_c \tag{9.22}$$

Again, the responses to variations of the side slip only occur in the range of adhesion. The transition point from adhesion to sliding now occurs at:

$$x_t = a\left(2\theta|\alpha_{co}| - 1\right) \tag{9.23}$$

and the corresponding adhesion fraction becomes, cf. Eq.(3.8):

$$m = 1 - \theta|\alpha_{co}| \quad \text{if} \quad |\alpha_{co}| < \frac{1}{\theta} \quad \text{else} \quad m = 0 \tag{9.24}$$

As the slip angle of the contact patch remains small in the range where adhesion still occurs, cosα_{co} has been replaced by unity. By integration of the transformed deflection over the range of adhesion the frequency response functions of the force and the moment variations are established. They read at pure lateral slip ($V_{rc0} = V_x$) :

$$H_{F,\alpha c}(i\omega_s) = \frac{C_{F\alpha c}}{i\omega_s am}\left\{1 - \frac{1}{2i\omega_s am}\left(1 - e^{-2i\omega_s am}\right)\right\} \tag{9.25}$$

and

$$H_{M,\alpha c}(i\omega_s) = \frac{c_p}{i\omega_s}\left\{-\frac{1}{\omega_s^2}\left(1 - e^{-2i\omega_s am}\right) + \right.$$
$$\left. - \frac{a}{i\omega_s}\left(1 + (2m-1)e^{-2i\omega_s am}\right) + 2a^2 m(1-m)\right\} \tag{9.26}$$

The local slope of the steady-state side force characteristic of the brush model is given by:

$$C_{F\alpha c} = 2c_p m^2 a^2 \quad \text{if} \quad |\alpha_{co}| < \frac{1}{\theta} \quad \text{else} \quad C_{F\alpha c} = 0 \tag{9.27}$$

The normalised response function of the side force is identical to that of the longitudinal force if the factor $1+\kappa_{co}$ is omitted in (9.6). The approximate first-order description with response function

$$H_{F,\alpha c}(i\omega_s) = \frac{C_{F\alpha c}}{1 + i\omega_s \sigma_c} \tag{9.28}$$

where

$$\sigma_c = am \tag{9.29}$$

shows the same very good agreement with the exact result as assessed with the longitudinal force response. Similarly we have the differential equation for the variation of the transient side slip:

$$\sigma_c \frac{\mathrm{d}\tilde{\alpha}_c'}{\mathrm{d}t} + |V_x|\tilde{\alpha}_c' = |V_x|\tilde{\alpha}_c = -\tilde{V}_{syc} \tag{9.30}$$

The variation of the side force becomes:

$$\tilde{F}_y = C_{F\alpha c}\tilde{\alpha}_c' \tag{9.31}$$

After adding the steady-state equation

$$|V_x|\alpha_{co} = -V_{syco} \tag{9.32}$$

to Eq.(9.30), the equation for the total transient side slip is obtained:

$$\sigma_c \frac{\mathrm{d}\alpha_c'}{\mathrm{d}t} + |V_x|\alpha_c' = |V_x|\alpha_c = -V_{syc} \tag{9.33}$$

As before, the resulting α_c' is used as the input of the steady-state side force function.

We may follow the same procedure to assess the aligning torque equations as was done in Sec.7.3. The resulting first-order response, however, does not always agree with the analytically found tendency. The phase lag and the slope of the high frequency amplitude asymptote indicate that a second-order

behaviour prevails at zero average slip angle while at larger slip angles the response gradually changes into a first-order nature. Apparently, the mechanism is more complex and we should account for the transient response of the pneumatic trail. The variation of the aligning torque may be written as follows:

$$\tilde{M}_z = -t_{co}\tilde{F}_y - \tilde{t}_c F_{yo} \tag{9.34}$$

The analysis conducted by Maurice (2000) shows that the analytically assessed response function of the pneumatic trail variation to slip angle variations can be approximated by the first-order system (9.33) and a so-called phase leading network in series. The frequency response function of the latter reads:

$$H_p(i\omega_s) = C_{t\alpha c}\frac{1 + i\omega_s\sigma_1}{1 + i\omega_s\sigma_2} \tag{9.35}$$

The factor in this formula represents the local slope of pneumatic trail characteristic:

$$C_{t\alpha c} = \frac{\partial t_c}{\partial|\alpha_c|} \tag{9.36}$$

which, apparently, is a negative quantity. According to Maurice, adequate values for the parameters σ_1 and σ_2 can be obtained through the formulae:

$$\sigma_2 = \tfrac{1}{3}a(1 - \theta|\alpha_{co}|) \tag{9.37}$$

or alternatively:

$$\sigma_2 = t_c \tag{9.38}$$

and

$$\frac{\sigma_1}{\sigma_2} = \frac{1}{1 - m^2} \tag{9.39}$$

The block diagram of the current system governed by the equations (9.28,34,35) is presented in the upper diagram of Fig.9.4. The lower diagram shows an alternative structure of the same system, thereby displaying the extra moment ΔM_z which is governed by the ratio of parameters (9.39). This ratio tends to infinity when full adhesion occurs. Then, m=1 and α_{co}=0 as becomes clear from Eq.(9.24). The singularity involved has been circumvented by Maurice through the introduction of a function that limits the value of (9.39) around zero lateral slip, α_{co}=0. This, however, will slightly disturb the proper response at zero slip angle and thus degrades the linear analysis around zero slip. An alternative way of avoiding the singularity, which obviously is caused by the fact that we actually may have a moment without the simultaneous presence of a force, is the

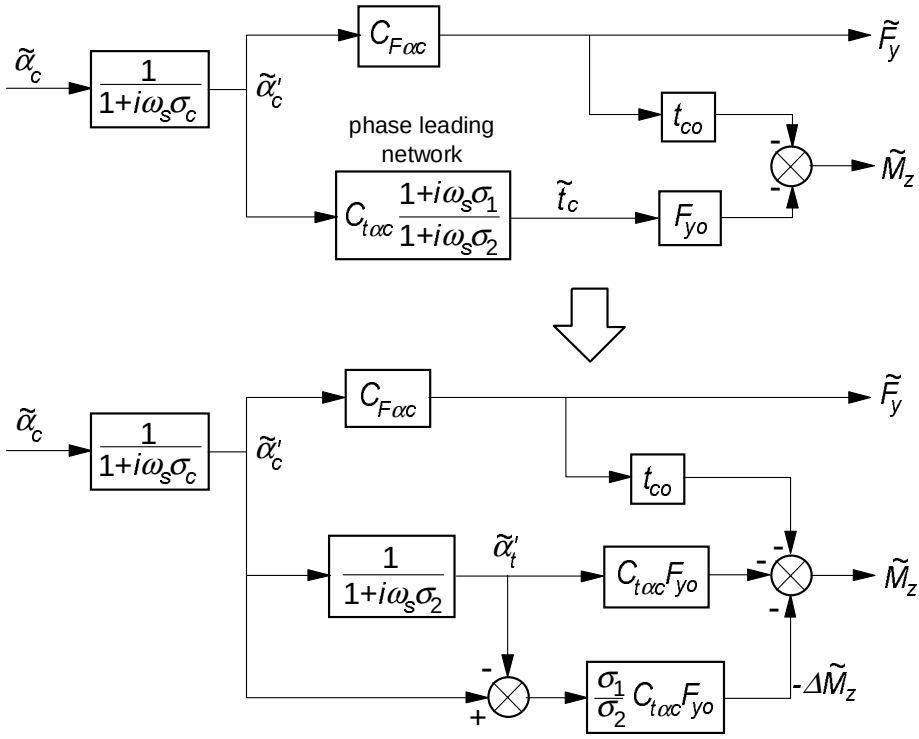

Fig. 9.4. Block diagram of the contact patch model to generate short wavelength transient responses of the side force and the aligning torque to small slip angle variations. The original upper diagram can be replaced by the lower diagram., thereby avoiding singularity at zero slip.

consideration of the extra transient moment ΔM_z. This moment is obtained by multiplication of the difference of the transient slip quantities for the force and for the pneumatic trail with three factors the combination of which may be designated with $C_{\Delta M}$:

$$C_{\Delta M} = -\frac{\sigma_1}{\sigma_2} C_{t\alpha c} F_{yo} \tag{9.40}$$

It turns out that now the singularity does not show up because both F_{yo} and $1/\sigma_1$ become zero at the same time. This indicates that indeed a moment may arise although at that instant of time the side force is zero. After writing out the factors in (9.40) by using expressions for the side force (3.11), the pneumatic trail (3.13) and further (9.36,39) while in (3.11) λ is replaced by m and $\theta_y \sigma_y$ by $\theta \alpha_{co} = z$ we find for $C_{\Delta M}$:

$$C_{\Delta M} = \frac{1}{3} a C_{F\alpha c0} \xi = C_{M\alpha c0} \xi \tag{9.41}$$

where $C_{M\alpha c0}$ denotes the aligning stiffness of the brush model at zero slip angle and the non-dimensional factor ξ is introduced:

$$\xi = \frac{(1-z)^2}{2-z}\left\{3 - \frac{(1-z)(1-2z/3)}{1-z+z^2/3}\right\} \quad \text{if } z<1 \quad \text{else} \quad \xi = 0 \tag{9.42}$$

with

$$z = \theta\,|\alpha_{co}| \tag{9.43}$$

Evaluation of (9.42) reveals that for $z < 1$ the factor ξ may possibly be approximated by

$$\xi \approx 1 - z \tag{9.44}$$

This approximation will be introduced later on when we will deal with the application of the Magic Formula.

The differential equations that apply for the contact patch model subjected to small side slip variations with respect to a given side slip level now read:

$$\sigma_c \frac{\mathrm{d}\tilde{\alpha}_c'}{\mathrm{d}t} + |V_x|\tilde{\alpha}_c' = |V_x|\tilde{\alpha}_c = -\tilde{V}_{syc} \tag{9.45}$$

$$\sigma_2 \frac{\mathrm{d}\tilde{\alpha}_t'}{\mathrm{d}t} + |V_x|\tilde{\alpha}_t' = |V_x|\tilde{\alpha}_c' \tag{9.46}$$

from which the variation of the force and moment result:

$$\tilde{F}_y = C_{F\alpha c}\tilde{\alpha}_c' \tag{9.47}$$

$$\tilde{M}_z = -t_{co}\tilde{F}_y - C_{t\alpha c}\tilde{\alpha}_t' F_{yo} + C_{\Delta M}(\tilde{\alpha}_c' - \tilde{\alpha}_t') \tag{9.48}$$

It is of importance to check the step responses to side slip starting from zero slip angle especially right after the start of the step change. Initially we have all variables equal to zero while the slip angle input has reached the new value α_{c0}. The various time derivatives become:

$$(t = 0: \quad \alpha_c = \alpha_{c0},\ \alpha_c' = \alpha_t' = 0,\ F_y = M_z = 0)$$

$$\frac{\mathrm{d}\alpha_c'}{\mathrm{d}t} = \frac{1}{\sigma_{c0}}|V_x|\alpha_{c0}\ , \quad \frac{\mathrm{d}\alpha_t'}{\mathrm{d}t} = 0 \tag{9.49}$$

$$\frac{\mathrm{d}F_y}{\mathrm{d}t} = \frac{|V_x|}{\sigma_{c0}} C_{F\alpha c0}\alpha_{c0}\ , \quad \frac{\mathrm{d}M_z}{\mathrm{d}t} = -t_{c0}\frac{\mathrm{d}F_y}{\mathrm{d}t} + C_{\Delta M0}\frac{\mathrm{d}\alpha_c'}{\mathrm{d}t} = 0$$

These results are correct. The last equation holds indeed because we have at

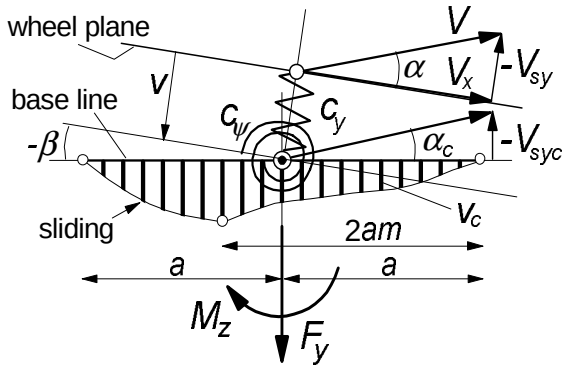

Fig. 9.5. The brush model attached to a carcass possessing lateral and torsional compliance.

vanishing slip angle according to Eq.(9.42): $\xi=1$ and consequently $C_{\Delta M}=t_{c0}C_{F\alpha c0}$ where $t_{c0}=a/3$. Evidently, the extra moment is responsible for the proper start of the course of the aligning torque showing zero slope. This property has been ascertained to occur both in reality and with models, cf. Figs.5.10 and 5.11. Also the response to a lateral wheel displacement $y = \int V_{sy}\mathrm{d}t$ at zero forward speed develops correctly. We find with Eq.(7.6) for the force: $F_y=-C_{Fy}y$ and for the moment: $M_z=0$.

The equations may now further be appraised by first introducing tyre carcass lateral and torsional compliance as depicted in Fig.9.5 and in the corresponding block diagram of Fig.9.6, and subsequently comparing the results with analytical solutions obtained by using Eqs.(9.25,26).

As a reference, the steady-state characteristics of the model have been presented in Fig.9.7. The diagram contains the curves for both the complete model and for the brush model alone. It is of interest to note the lower cornering stiffness due to the introduction of carcass compliance. The expression for the lower side slip stiffness can be found to read:

$$C_{F\alpha} = \frac{c_\psi}{c_\psi + C_{M\alpha c}} C_{F\alpha c} \tag{9.50}$$

The relaxation length of the complete model found from the cut-off frequency of the side force response function turns out to become:

$$\sigma = \frac{c_\psi}{c_\psi + C_{M\alpha c}}\left(am + \frac{C_{F\alpha c}}{c_y}\right) = \frac{c_\psi}{c_\psi + C_{M\alpha c}} am + \frac{C_{F\alpha}}{c_y} \tag{9.51}$$

The way the relaxation length changes with slip angle is depicted in the right-hand diagram of Fig.9.7. As one might expect, we find that this length multiplied with the increment in wheel slip angle is equal to the increase of the sum of carcass lateral deflection and the average deflection of the adhering tread

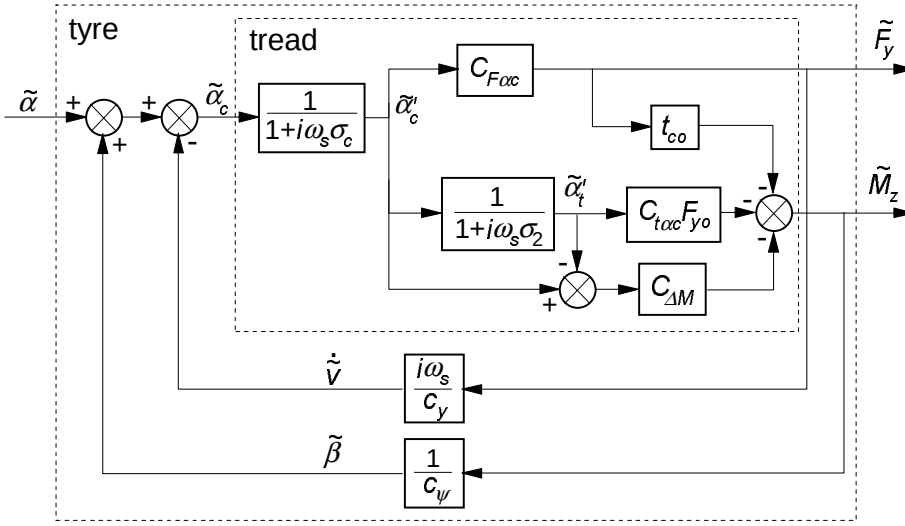

Fig. 9.6. Block diagram of the augmented system including carcass lateral and torsional compliance.

elements.

At three different levels of side slip, α_o=0, 0.08 and 0.16rad, the comparison of the simulation model with the analytical model has been conducted in terms of the path frequency response functions. Figure 9.8 shows the results. The general conclusion is that at least for wavelengths larger than 20cm the

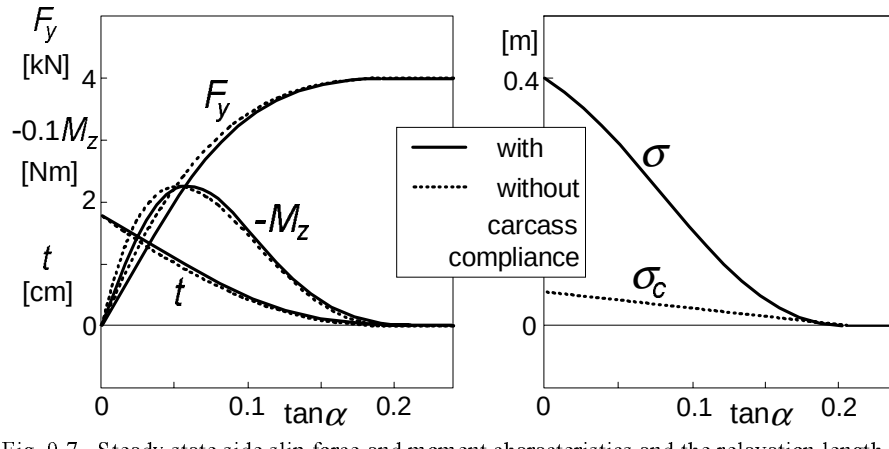

Fig. 9.7. Steady-state side slip force and moment characteristics and the relaxation length of the brush model (the contact patch) and of the model including the flexible carcass through which the brush model is attached to the wheel plane.

correspondence can be judged to be very good. The upper pair of diagramsthat refer to the side force response shows the sideways 'shift' of the phase lag curves which is caused by the drop in relaxation length with increasing average slip angle. The diagram for the aligning torque response clearly shows the transition from second to first-order behaviour when the average slip angle changes from zero to larger values.

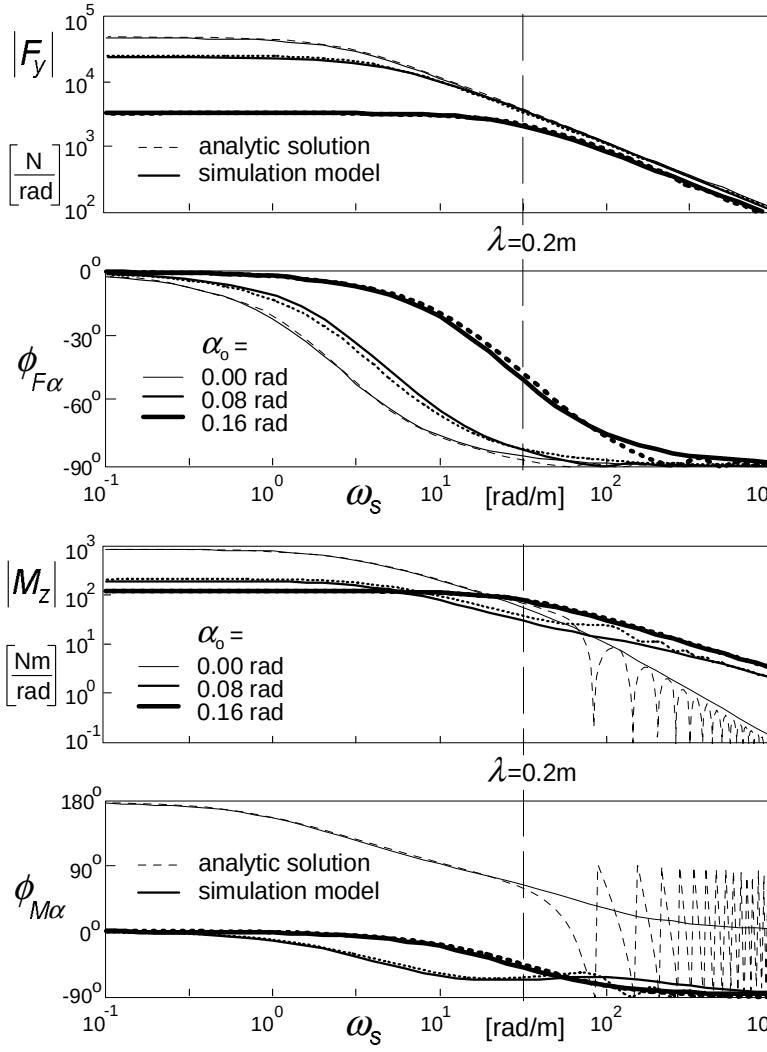

Fig. 9.8. Frequency response functions of linearised system including carcass flexibility at different average slip angle levels according to the analytical solution and to the approximate simulation model. The path frequency at a wavelength of the input wheel plane motion equal to 20cm has been indicated.

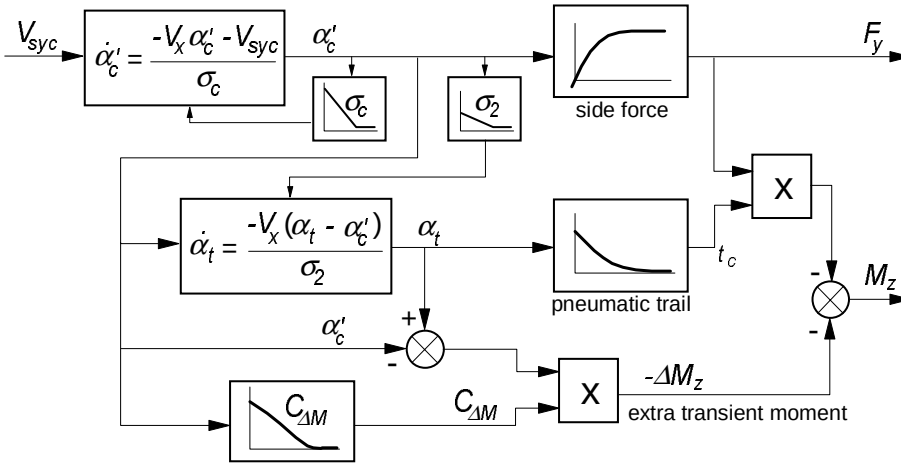

Fig. 9.9. Block diagram of the non-linear model of the contact patch (tread) also valid for larger slip angle variations.

The Eqs.(9.45-48) can be made applicable to the general case of large slip angle variations by adding to (9.45,46) the steady-state relations and by rewriting the Eqs.(9.47,48) in complete non-linear form so that, when considering a small variation, the linearised equations are recovered. We obtain for the transient slip quantities:

$$\sigma_c \frac{\mathrm{d}\alpha_c'}{\mathrm{d}t} + |V_x|\alpha_c' = |V_x|\alpha_c = -V_{syc} \tag{9.52}$$

$$\sigma_2 \frac{\mathrm{d}\alpha_t'}{\mathrm{d}t} + |V_x|\alpha_t' = |V_x|\alpha_c' \tag{9.53}$$

and for the force and moment:

$$F_y = F_y(\alpha_c') \tag{9.54}$$

$$M_z = -t_c(\alpha_t')F_y + C_{\Delta M}(\alpha_c' - \alpha_t') \tag{9.55}$$

The last term representing the extra moment is left in linearised form. This term may be replaced by the difference of two equal functions the derivative of which equals $C_{\Delta M}$, one with argument α_c' and the other with α_t'. Because of the fact that the difference of these two arguments remains small, the linearised version is expected to be sufficiently accurate. The block diagram of the non-linear system displayed in Fig.9.9 may further clarify the structure of the model.

To ensure that the above equations correctly describe the response to large slip angle variations, the simulation model results have been compared with the response of a physical model. That model features a finite number of tread

elements attached to a straight base line. The deflections of carcass and elements are computed at each time step in which the wheel is rolled further over a distance equal to the interval between two successive tread elements and is moved sideways according to the current value of the input slip angle. The actual model employed contains 20 elements. The parameter values used in both models have been listed in Table 9.1.

The slip angle variation is sinusoidal around a given average level. To cover a broad range of operation the computations have been conducted at three wavelengths: $\lambda = 0.2$, 1 and 5m, two average slip angle levels: $\alpha_o = 0$ and 0.08rad and one amplitude: $\hat{\alpha} = 0.08$rad.

Table 9.1. Parameter values used for brush model with flexible carcass.

vertical load	F_z	4000	N
friction coefficient	μ	1.0	-
half contact length	a	0.0535	m
longitudinal carcass stiffness	c_x	5.50×10^5	N/m
lateral carcass stiffness	c_y	1.25×10^5	N/m
torsional carcass stiffness	c_ψ	4000	Nm/rad
tread element stiffness /m	c_p	10^7	N/m^2
composite tyre parameter	θ	4.77	-

Figure 9.10 presents the results for the two models. The range of the abscissa has been chosen such that precisely two wavelengths are covered and the distance rolled is large enough to have a situation close to the periodic state. Again, the agreement is quite good and we may have confidence in the model. The bottom diagram presents the variation of the slip angle. The top pair of diagrams shows the responses at the relatively long wavelength of 5m so that a condition closer to steady state has been reached. From Fig.9.7 it can be seen that at the maximum α of 0.16 rad or almost 9° the aligning torque peak has been surpassed by far. This explains the two dips per wavelength. At a maximum of 0.08 rad the peak has just been surpassed.

The less deep dips occurring in the upper curves of diagrams *b* and *d* are delayed with respect to the slip angle when this has reached its minimum value equal to zero. At steady state, when $\lambda \to \infty$, the moment (and the force) would

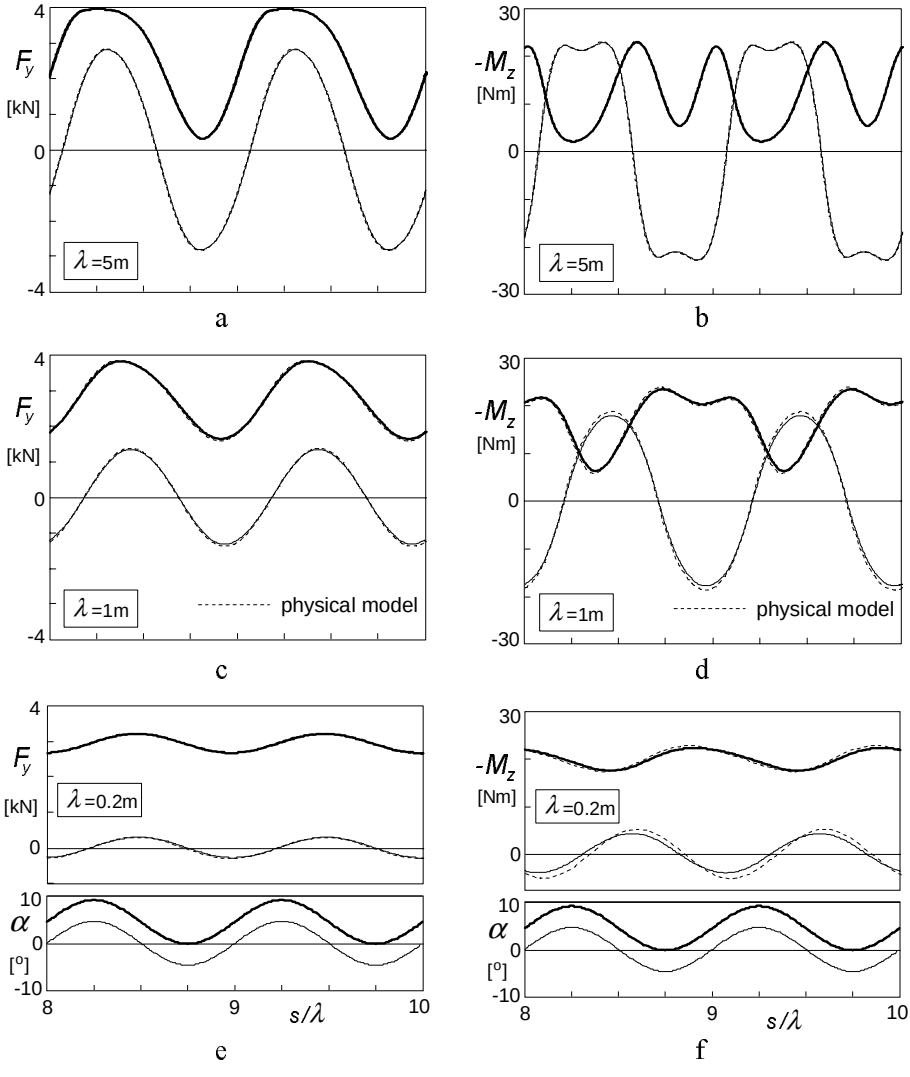

Fig.9.10. Side force and aligning torque responses of the non-linear brush simulation model with flexible carcass to sinusoidal slip angle input of the wheel plane with a slip angle amplitude of 0.08rad and average levels of 0 (thin curves) and 0.08rad (fat curves), compared with results of the physical model (broken curves).

have become equal to zero at that instant. The deeper dips belong to the maxima of the slip angle variation. The considerable reduction in amplitude of the response at the shorter wavelengths nicely agrees with the findings of Fig.9.8. The force responses correspond almost perfectly with the outcome of the physical model. Evidently, a similar correspondence is expected to occur with the

response of the longitudinal force to longitudinal slip variations.

Turn Slip

The last item to be studied in the development of the contact model is the response to variations in path curvature while the slip angle remains zero. We will not attempt to develop a background analytical model but take a more heuristic route. The results will be checked by comparing these with the computed responses of the physical model. The responses derived for the string model with tread elements as presented in Chapter 5, especially the step responses to φ as depicted in Fig.5.21c and d (ex.tr.el.) and Fig.5.10 may be helpful. We observe that the force response is similar to that of the aligning torque to a step change in slip angle. In both cases the slope at the start is zero. The further approach of the force to its steady-state level is assumed to occur according to the first-order equation with σ_c as relaxation length. The zero slope at the start may be modelled by subtracting a response curve that starts with the same slope but dies out after having reached its peak. Such a short term response may be obtained by taking the difference of two responses each leading to the same level but starting at different slopes the difference of which should correspond to the initial slope of the uncorrected force response curve. For simplicity we take for one of the two responses the uncorrected force response, so that $\sigma_{F1} = \sigma_c$. The relaxation length of the second response should then be equal to $\sigma_{F2} = \sigma_c/2$. The resulting equations for the force response to the turn slip velocity $\dot{\psi}_c$ read:

$$\sigma_c \frac{\mathrm{d}\varphi_c'}{\mathrm{d}t} + |V_x|\,\varphi_c' = -\dot{\psi}_c \tag{9.56}$$

$$\sigma_{F2} \frac{\mathrm{d}\varphi_{F2}'}{\mathrm{d}t} + |V_x|\,\varphi_{F2}' = -\dot{\psi}_c \tag{9.57}$$

The transient turn slip for the force finally becomes:

$$\varphi_F' = \varphi_c' - (\varphi_{F2}' - \varphi_{F1}') = 2\varphi_c' - \varphi_{F2}' \tag{9.58}$$

and the side force at pure path curvature is obtained from the non-linear steady-state response function:

$$F_y = F_y(\varphi_F') \tag{9.59}$$

For the range of turn slip $a|\varphi| < 1/\theta$ the relation remains linear and equals:

$$F_y = C_{F\varphi c0}\varphi_F' = C_{M\alpha c0}\varphi_F' = \frac{2}{3} c_p a^3 \varphi_F' \tag{9.60}$$

The moment response may be divided into the response due to the contact patch length that involves lateral tread deflections, and the response due to tread width

giving rise to longitudinal deflections. First, we will address the moment generated by the brush model with zero width. Figures 5.9,10 and 5.21indicate that we are dealing here with a response that after having reached a peak tends to zero. Again we may model this behaviour by subtracting two first-order responses. For this, we introduce two transient turn slip quantities φ_1' and φ_2' with respective relaxation lengths: $\sigma_{\varphi 1}$ and $\sigma_{\varphi 2}$. The two differential equations become:

$$\sigma_{\varphi 1}\frac{\mathrm{d}\varphi_1'}{\mathrm{d}t} + |V_x|\varphi_1' = -\dot{\psi}_c \tag{9.61}$$

$$\sigma_{\varphi 2}\frac{\mathrm{d}\varphi_2'}{\mathrm{d}t} + |V_x|\varphi_2' = -\dot{\psi}_c \tag{9.62}$$

At zero speed the response of the difference would become:

$$\varphi_1' - \varphi_2' = -\left(\frac{1}{\sigma_{\varphi 1}} - \frac{1}{\sigma_{\varphi 2}}\right)\psi_c \tag{9.63}$$

The deflection angle of the tread due to transient spin is defined as:

$$\alpha_M = -2a(\varphi_1' - \varphi_2') \tag{9.64}$$

which at zero speed becomes:

$$\alpha_M = 2a\left(\frac{1}{\sigma_{\varphi 1}} - \frac{1}{\sigma_{\varphi 2}}\right)\psi_c \tag{9.65}$$

The condition to be satisfied is that the deflection angle is equal to the yaw angle. Hence, we have:

$$\frac{1}{\sigma_{\varphi 1}} - \frac{1}{\sigma_{\varphi 2}} = \frac{1}{2a} \tag{9.66}$$

In the case of small angles we may write for the moment:

$$M_{z0} = -C_{M\alpha c0}\alpha_M \tag{9.67}$$

From Eqs.(9.61,62) it can be assessed that the initial slope of the response of the moment to a step change in spin $\varphi_c = -\dot{\psi}_c/V_x$ from zero to φ_{c0} turns out to be:

$$\frac{\mathrm{d}M_z}{\mathrm{d}s} = -2aC_{M\alpha c0}\left(\frac{1}{\sigma_{\varphi 1}} - \frac{1}{\sigma_{\varphi 2}}\right)\varphi_{c0} = -C_{M\alpha c0}\varphi_{c0} \tag{9.68}$$

For the second condition to assess the ratio's of the σ_φ's to half the contact length a, the best fit of the remaining course of the step response may serve.

When the angle of rotation ψ continuous to grow, the state of total sliding will be attained and the moment can be calculated to become:

$$M_{z\varphi\infty} = -\frac{3}{8}a\mu F_z \tag{9.69}$$

It has not been tried to derive the functional relationship between moment and increasing steer angle for the standing (non-rolling) brush model. The following non-linear function to describe the moment response in between the two extremes has been chosen:

$$M_z = -M_{z\varphi\infty}\sin\left\{\arctan\left(\frac{C_{M\alpha c0}}{M_{z\varphi\infty}}\varepsilon_\varphi\alpha_M\right)\right\} \tag{9.70}$$

The factor ε_φ has been introduced to have a parameter available to better approach the response shown by the physical model. The value 1.15 appeared to be appropriate. Similar to the relaxation length σ_c, Eqs.(9.29,24), the lengths $\sigma_{\varphi 1,2}$ are reduced in proportion with the magnitudes of transient turn slip quantities φ_1' and φ_2'.

For the evaluation of the model a comparison with the physical brush model has been executed. First, the flexible carcass is attached to the tread model, cf. Fig.9.5. To simulate this more complex situation, the approach of the enhanced transient model of Sec.7.3 has been adopted. The additional dynamic equations for the contact patch with mass m_c and moment of inertia I_c and carcass stiffnesses $c_{y,\psi}$ and damping coefficients $k_{y,\psi}$ read:

$$m_c(\dot{V}_{yc} + V_x\dot{\psi}_c) + k_y\dot{v} + c_y v = F_y \tag{9.71}$$

$$\dot{v} = V_{yc} - V_{sy} \tag{9.72}$$

$$I_c\ddot{\psi}_c + k_\psi\dot{\beta} + c_\psi\beta = M_z \tag{9.73}$$

$$\dot{\beta} = \dot{\psi}_c - \dot{\psi} \tag{9.74}$$

$$V_{syc} = V_{sy} + \dot{v} - V_x\beta \tag{9.75}$$

This extension of the model may, of course, also be used for the previously treated response to pure side slip. In fact, it is to be noted that the model for side slip, Eqs.(9.52-55), should be added to the spin model, Eqs.(9.61,62,64,70), to correctly account for their interaction in the complete model with carcass compliance included. In the physical model the brush model automatically responds to both the side slip and spin. When the wheel plane is subjected to only side slip, the spin of the base line of the tread model remains very small and may be neglected. On the other hand, when the wheel is being steered with wheel side slip remaining zero (path curvature), the base line does show non-negligible side slip especially at shorter wavelengths where the moment becomes considerable

and as a result the base line is yawed and thus induces side slip. This effect vanishes at steady-state turning. However, if we would add the effect of tread width, the spin torque also acts at steady state and thereby contributes largely to the side force response to spin of the complete model.

Due to the complexity that arises when adding tread width to the brush model,

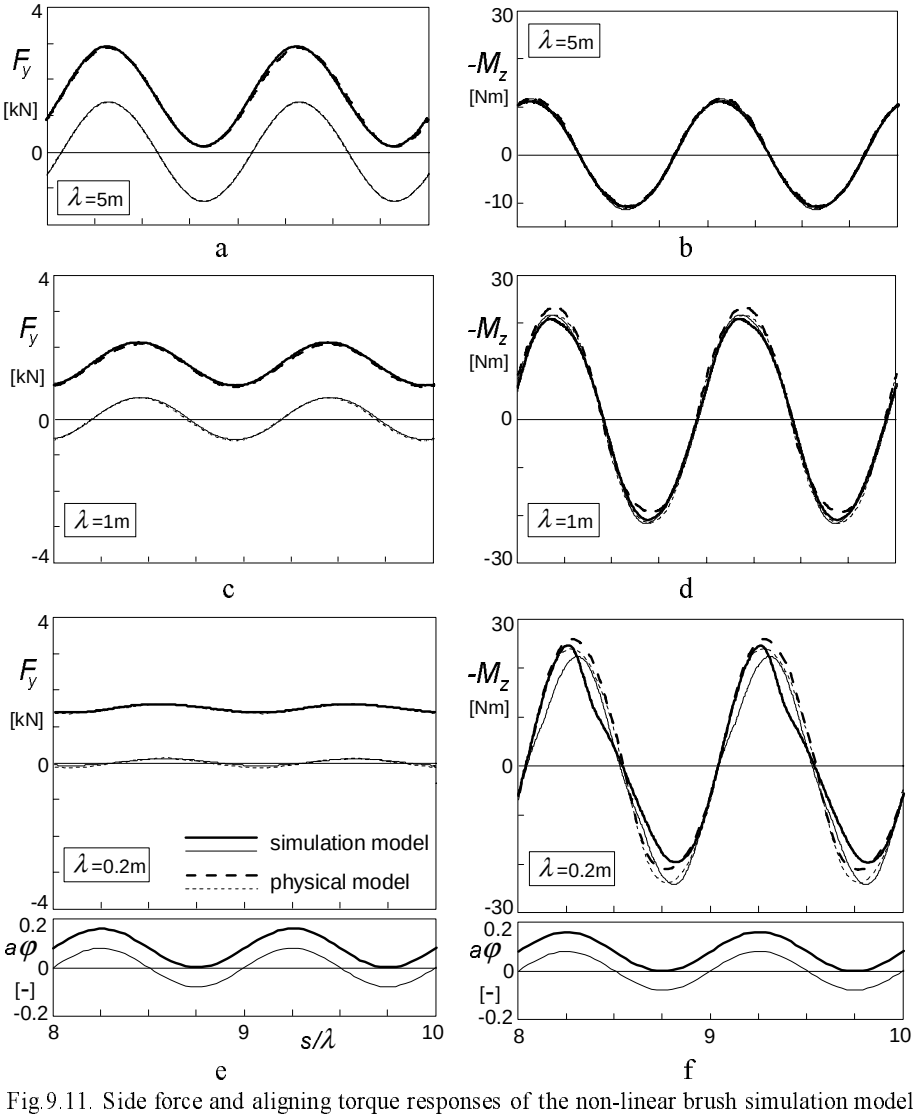

Fig.9.11. Side force and aligning torque responses of the non-linear brush simulation model with flexible carcass to sinusoidal path curvature variations (turn slip at $\alpha = 0$) of the wheel plane with an amplitude of $a\varphi$ of 0.08 and average levels of 0 (thin curves) and 0.08 (fat curves), compared with results of the physical model (broken curves).

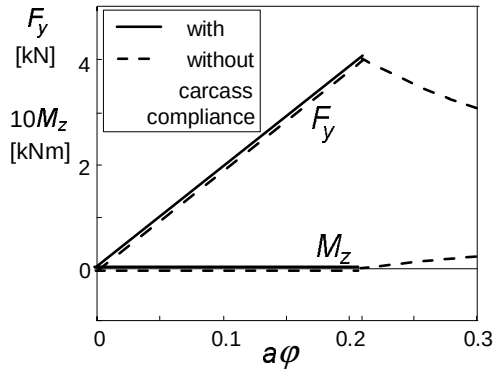

Fig. 9.12 . Steady-state turn slip force and moment characteristics of the brush model both with and without flexible carcass. The effect of tread width has not been included.

cf. Chap.3, it has been decided to consider this aspect when dealing with the ultimate model adapted to the use of the Magic Formula in the next section.

The diagrams of Fig.911 present the computed responses to varying turn slip. It is seen that the correspondence with the physical model is quite good. The deformation of the moment response curve occurring at shorter wavelengths is caused by the extra moment ΔM_z generated through the base line slip angle variation.

As a reference, the steady-state characteristics of the force and moment response to turn slip, as computed for the single row brush model with and without carcass compliance have been shown in Fig.9.12. Up to $a\varphi = 1/\theta$ the aligning torque remains zero which causes the characteristics for the cases without and with flexible carcass to become identical. The remaining course of the curves for the system including carcass compliance has not been computed as that part lies outside the range of evaluation.

Combined Slip

To cover the case of combined slip, also including longitudinal slip, the steady-state brush model characteristics are to be adapted as formulated in Chapter 3, Sec.3.2.3. In addition, the factor m that indicates the fraction of the contact length where adhesion occurs and is used to reduce the relaxation length σ_c is to be adapted by using the composite magnitude of slip of the contact patch:

$$\zeta_c' = \frac{\sqrt{\alpha_c'^2 + \kappa_c'^2}}{1 + \kappa_c'} \tag{9.76}$$

This expression holds because we have assumed that the brush model is isotropic. Using the magnitude of combined slip according to (9.76) the factor

m can be assessed:

$$m = 1 - \theta\zeta_c' \quad \text{if} \quad \zeta_c' < \frac{1}{\theta} \quad \text{else} \quad m = 0 \tag{9.77}$$

Maurice (2000) found excellent agreement with the physical model for the combined slip cases: $\alpha_o = 0.08$rad and $\hat{\alpha} = 0.08$rad and $\kappa_o = 0.06$ and $\hat{\kappa} = 0.06$ with a phase difference of 45° and wavelengths of 0.2, 1 and 5m.

Adding turn slip will influence the combined slip response further. The next section approaches this matter in a pragmatic way.

9.2.2. The Model Adapted to the Use of the Magic Formula

Now that we have treated all ingredients of the force and moment short wavelength responses to longitudinal, lateral and turn slip and have developed the structure of the contact model, we may carry on and show the performance of the model adapted to the use of the Magic Formula the parameters of which may have been assessed through full scale steady-state tyre measurements. The model includes the effect of tread width.

To simplify the matter, we will here consider a simplified set of formulae for the steady-state responses, the complete version of which have been listed in Chapter 4, Secs.4.3.2 and 4.3.3. Only the case of combined side slip and turn slip will be considered. Adding braking or driving, however, will not pose any problems.

A first problem that is encountered is the fact that in the model developed above where the contact patch is represented by the brush model, the steady-state characteristics employed belong the brush model and not to the total model including carcass. In Fig.9.7 the calculated total model characteristics can be seen together with those of the contact patch alone.

One obvious solution is to model the contact patch characteristics with the Magic Formulae. These, however, will deviate from those assessed for the complete tyre because the contact patch 'sees' a slip angle that differs (is smaller) from that of the wheel plane. A set of adapted *MF* parameters may be established off-line for the contact patch or an iteration loop may be included to achieve the correct stead-state behaviour of the total model. A practical way has been found which employs a first-order feed-back loop with small time constant. Instead of introducing an additional first-order differential equation, the already present first-order equation for the transient side slip α' has been used. The diagram of Fig.9.13 illustrates the set-up. A similar approach is followed in Sec.9.3 to account for the camber angle of the belt being different from the

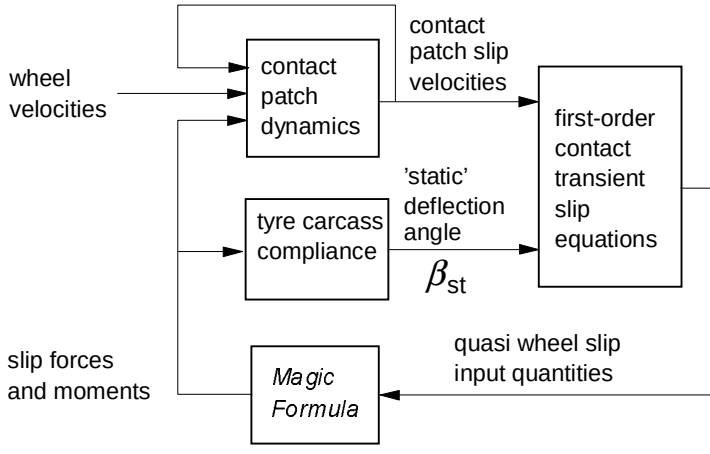

Fig. 9.13. Diagram explaining the model structure using the Magic Formula.

camber angle of the wheel plane.

The transient slip first-order differential equations listed below are identical to those derived in the previous section except for the first equation for the lateral transient slip:

transient slip equations for side slip, turn slip and camber

$$\sigma_c \frac{\mathrm{d}\alpha'}{\mathrm{d}t} + |V_x|\alpha' = -V_{syc} - |V_x|\beta_{st} \tag{9.78}$$

$$\sigma_2 \frac{\mathrm{d}\alpha'_t}{\mathrm{d}t} + |V_x|\alpha'_t = |V_x|\alpha' \tag{9.79}$$

$$\sigma_c \frac{\mathrm{d}\varphi'_c}{\mathrm{d}t} + |V_x|\,\varphi'_c = -\dot{\psi}_c \tag{9.80}$$

$$\sigma_{F2} \frac{\mathrm{d}\varphi'_{F2}}{\mathrm{d}t} + |V_x|\,\varphi'_{F2} = -\dot{\psi}_c \tag{9.81}$$

$$\sigma_{\varphi 1} \frac{\mathrm{d}\varphi'_1}{\mathrm{d}t} + |V_x|\,\varphi'_1 = -\dot{\psi}_c \tag{9.82}$$

$$\sigma_{\varphi 2} \frac{\mathrm{d}\varphi'_2}{\mathrm{d}t} + |V_x|\,\varphi'_2 = -\dot{\psi}_c \tag{9.83}$$

where in (9.78) the calculated deflection angle has been used:

$$\beta_{st} = M_z/c_\psi \tag{9.84}$$

composite transient slip quantities

$$\varphi'_F = \varphi'_c - \varphi'_{F2} \tag{9.85}$$

$$\varphi'_M = \varepsilon^*_\varphi \varphi'_c + \varepsilon_{\varphi 12}(\varphi'_1 - \varphi'_2) \tag{9.86}$$

dynamic contact patch equations

$$m_c(\dot{V}_{yc} + V_x\dot{\psi}_c) + k_y\dot{v} + c_y v = F_y \tag{9.87}$$

$$\dot{v} = V_{yc} - V_{sy} \tag{9.88}$$

$$I_c\ddot{\psi}_c + k_\psi\dot{\beta} + c_\psi\beta = M_z \tag{9.89}$$

$$\dot{\beta} = \dot{\psi}_c - \dot{\psi} \tag{9.90}$$

$$V_{syc} = V_{sy} + \dot{v} - V_x\beta \tag{9.91}$$

simplified side force and aligning torque Magic Formulae (*MF*)

$$F_y = D_y \sin\{C_y \arctan(B_y\alpha_y)\} \tag{9.92}$$

$$M_z = -tF_y + \Delta M_z + M_{zr} \tag{9.93}$$

$$C_y = p_{Cy1} \tag{9.94}$$

$$D_y = \mu F_z \cdot \zeta_2 \tag{9.95}$$

$$B_y = K_{y\alpha}/(C_y D_y) \tag{9.96}$$

$$K_{y\alpha} = C_{F\alpha 0} \cdot \zeta_3 \tag{9.97}$$

$$\alpha_y = \alpha' + S_{Hy} \tag{9.98}$$

$$S_{Hy} = D_{Hy\varphi} \sin\{C_{Hy\varphi} \arctan(B_{Hy\varphi} R_o \varphi'_F)\} \tag{9.99}$$

$$t = D_t \cos\{C_t \arctan(B_t\alpha_t)\} \tag{9.100}$$

$$\alpha_t = \alpha'_t + S_{Ht} \tag{9.101}$$

$$S_{Ht} = 0 \tag{9.102}$$

$$D_t = q_{Dz1} R_o \cdot \zeta_5 \tag{9.103}$$

$$D_{r\varphi} = D_{Dr\varphi} \sin\{C_{Dr\varphi} \arctan(B_{Dr\varphi} R_o \varphi'_M)\} \tag{9.104}$$

$$M_{zr} = M_{z\varphi} \approx D_{r\varphi} \tag{9.105}$$

$$\Delta M_z = C_{\Delta M}(\alpha' - \alpha'_t) \tag{9.106}$$

$$\zeta_2 = \cos\{\arctan(B_{y\varphi} R_o \varphi'_F)\} \tag{9.107}$$

$$\zeta_3 = \cos\{\arctan(p_{Ky\varphi} R_o^2 \varphi'^2_F)\} \tag{9.108}$$

$$\zeta_5 = \cos\{\arctan(q_{Dt\varphi 1} R_o \varphi'_F)\} \tag{9.109}$$

factors reduced with slip

$$C_{\Delta M} = C_{F\alpha 0} t_0 \cdot \max(1 - \theta\zeta', 0) \tag{9.110}$$

$$\sigma_c = a \cdot \max(1 - \theta\zeta', \varepsilon_{\lim}) \tag{9.111}$$

$$\sigma_2 = \frac{t_0}{a}\sigma_c \tag{9.112}$$

$$\sigma_{F2} = b_{F2}\sigma_c \tag{9.113}$$

$$\sigma_{\varphi 1} = b_{\varphi 1}\sigma_c \tag{9.114}$$

$$\sigma_{\varphi 2} = b_{\varphi 2}\sigma_c \tag{9.115}$$

with tyre composite parameter

$$\theta = \frac{C_{F\kappa 0}}{3\mu F_z} \tag{9.116}$$

and the total magnitude of equivalent side slip

$$\zeta' = \frac{1}{1+\kappa'}\sqrt{\left\{|\alpha'| + a\,\varepsilon_{\varphi 12}|\varphi_1' - \varphi_2'|\right\}^2 + \left(\frac{C_{F\kappa 0}}{C_{F\alpha 0}}\right)^2\left\{|\kappa'| + \tfrac{2}{3}b|\varphi_c'|\right\}^2} \tag{9.117}$$

where in the present application $\kappa' = 0$.

other parameter relations

$$\begin{aligned}
C_{F\alpha c0} &= C_{F\kappa c0} \\
t_{c0} &= q_{Dz1}R_o \\
C_{M\varphi^* c0} &= (2/3)^2 b^2 C_{F\kappa c0} \\
C_{M\alpha c0} &= t_{c0} C_{F\alpha c0} \\
C_{F\varphi c0} &= C_{M\alpha c0} \\
C_{M\varphi c0} &= C_{M\varphi^* c0} - t_{c0} C_{F\varphi c0} \\
t_0 &= t_{c0} \\
C_{F\alpha 0} &= C_{F\alpha c0}/(1 + t_0 C_{F\alpha c0}/c_\psi) \\
C_{M\alpha 0} &= t_0 C_{F\alpha 0} \\
C_y &= p_{Cy1} \\
B_t &= q_{Bz1} C_{F\alpha 0}/C_{F\alpha c0} \\
C_t &= q_{Cz1} \\
C_{F\varphi 0} &= C_{F\varphi c0} + C_{F\alpha c0} C_{M\varphi c0}/(c_\psi + C_{M\alpha c0}) \\
C_{M\varphi 0} &= C_{M\varphi c0} c_\psi/(c_\psi + C_{M\alpha c0})
\end{aligned}$$

$$\begin{aligned}
B_{y\varphi} &= p_{Dy\varphi 1} \\
C_{Hy\varphi} &= p_{Hy\varphi 1} \\
D_{Hy\varphi} &= p_{Hy\varphi 2} \\
B_{Hy\varphi} &= C_{F\varphi 0}/(R_o C_{Hy\varphi} D_{Hy\varphi} C_{F\alpha 0}) \\
C_{Dr\varphi} &= q_{Dr\varphi 1} \\
D_{Dr\varphi} &= M_{z\varphi\infty}/\sin(0.5\pi\, C_{Dr\varphi}) \\
K_{zR\varphi r0} &= (C_{M\varphi 0} + t_0 C_{F\varphi 0})/R_o \\
B_{Dr\varphi} &= K_{zR\varphi r0}/(C_{Dr\varphi} D_{Dr\varphi}) \\
M_{z\varphi\infty} &= q_{Cr\varphi 1} R_o \mu F_z \\
\\
k_{y\mathrm{crit}} &= 2\sqrt{(m_c c_y)} \\
k_{\psi\mathrm{crit}} &= 2\sqrt{(I_c c_\psi)} \\
k_y &= \zeta_k\, k_{y\mathrm{crit}} \\
k_\psi &= \zeta_k\, k_{\psi\mathrm{crit}}
\end{aligned} \tag{9.118}$$

Table 9.2. Parameter values for tyre model with Magic Formula including quantities introduced later on.

F_z	4000N	μ	1.0	p_{Cy1}	1.2	$p_{Ky\varphi 1}$	1.0
c_y	125×10^6 N/m	C_{Fkc0}	$15F_z$	q_{Bz1}	22	$p_{Hy\varphi 1}$	0.15
c_ψ	4×10^6 Nm/rad	a	0.0535 m	q_{Cz1}	1.192	$p_{Hy\varphi 2}$	1.0
m_c	0.5 kg	b	$0.9a$	q_{Dz1}	0.05	$q_{Cr\varphi 1}$	0.12
I_c	0.0005 kgm^2	R_o	0.3 m	$p_{Dy\varphi 1}$	0.4	$q_{Dr\varphi 1}$	1.0
ζ_k	0.1	ε_φ^*	1.0	$\varepsilon_{\varphi 12}$	4.0	$q_{Dt\varphi 1}$	10
b_{F2}	0.5	$b_{\varphi 1}$	0.5	$b_{\varphi 2}$	1/1.5		
$\varepsilon_{\lim}$	0.1	V_{low}	1 m/s	m_{qc}	400 kg	c_o	2.0

Steady-State, Step Response and Frequency Response Characteristics

To demonstrate the performance of the model a number typical characteristics will be presented. The hypothetical steady-state pure side slip and pure turn slip of the model are shown in Figs.9.14.

The step response graphs of Fig.9.15 show the proper shapes of the various curves, notably the initial horizontal tangent of the response curves of the side force to turn slip and of the moment to side slip, also shown in Fig.5.21 (no tread width). Also, the peak of the moment response curve to spin and the dip of the

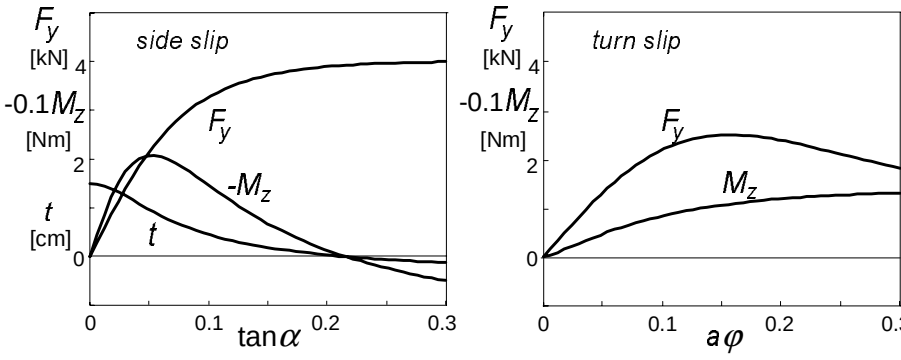

Fig. 9.14. Steady-state side slip and turn slip force and moment characteristics of the overall tyre model as defined by the Magic Formula. The effect of tread width has been included.

curve of the moment response to steer angle are exhibited as expected.

Figure 9.16 presents the frequency response functions of the linearised system at zero average side and turn slip with tread width effect included. The curves may be compared with those of the string model with tread elements, cf. Figs.5.23 (with zero tread width). In Fig. 9.17 the Nyquist plots of the moment response to steer angle have been depicted. The upper diagram shows the influence of tread width by changing the parameter $\varepsilon_{\varphi}^{*}$. If equal to zero the thin tyre is represented. The value 1 corresponds with the baseline configuration. The lower graph provides insight in the influence of the parameter $\varepsilon_{\varphi 12}$ that governs the magnitude of the effect of the transient yaw deflection angle α_M (9.64). The value 4 is used in the baseline configuration. When compared with the plots of Figs.5.27 and 5.35 it may be concluded that the model is capable of approaching the responses of more complex infinite order models and of actual tyres.

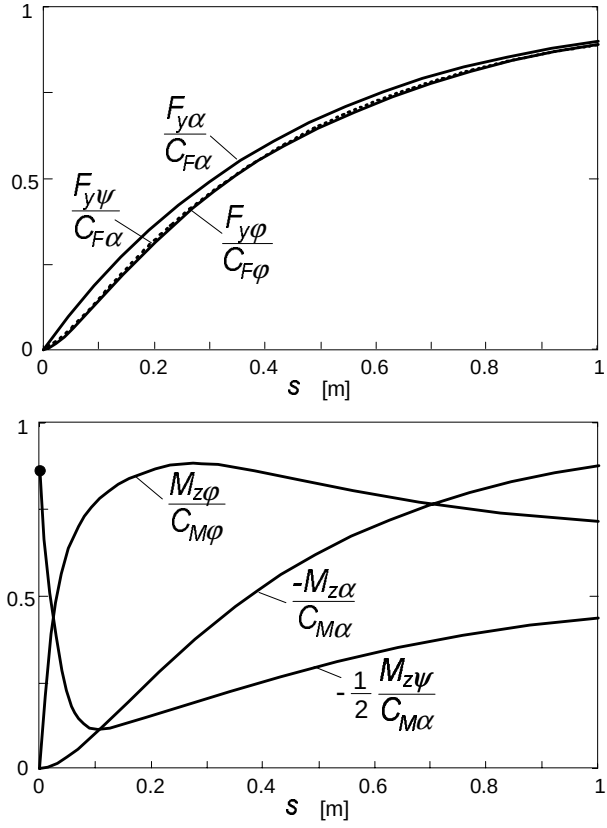

Fig. 9.15. Step response curves of the side force and of the aligning torque to side slip α, turn slip (path curvature) φ and steer angle ψ.

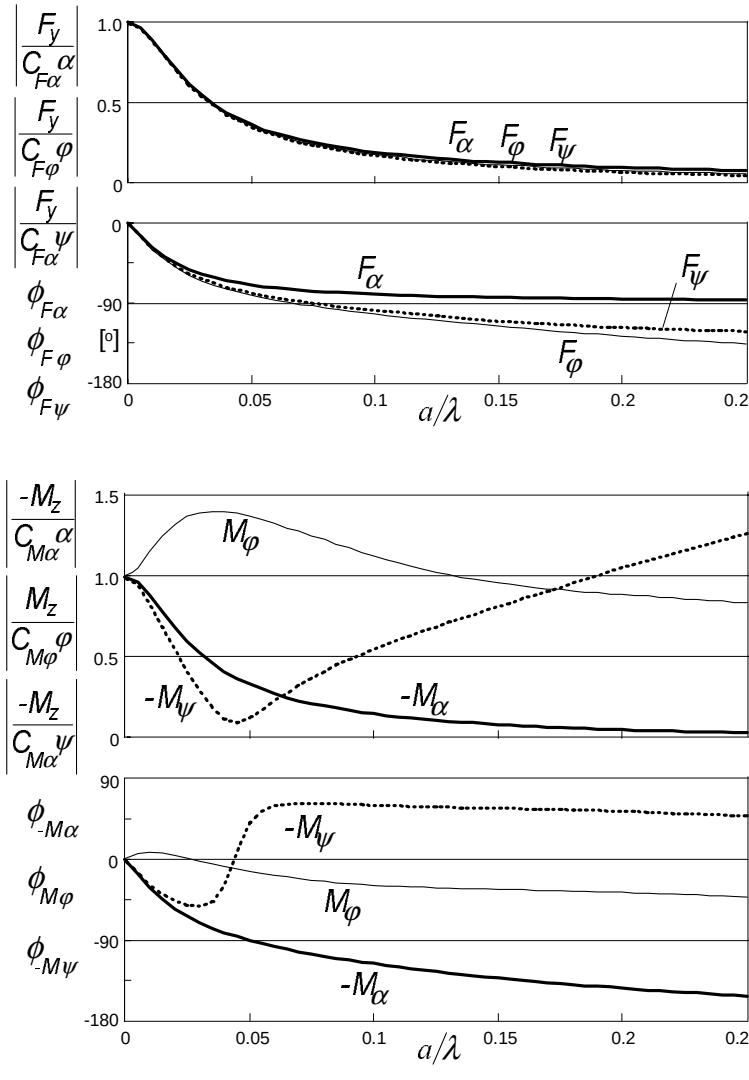

Fig. 9.16. Frequency response function of system with tread width. Curves for the force and moment responses to side slip α, turn slip (path curvature) φ and steer angle ψ have been indicated.

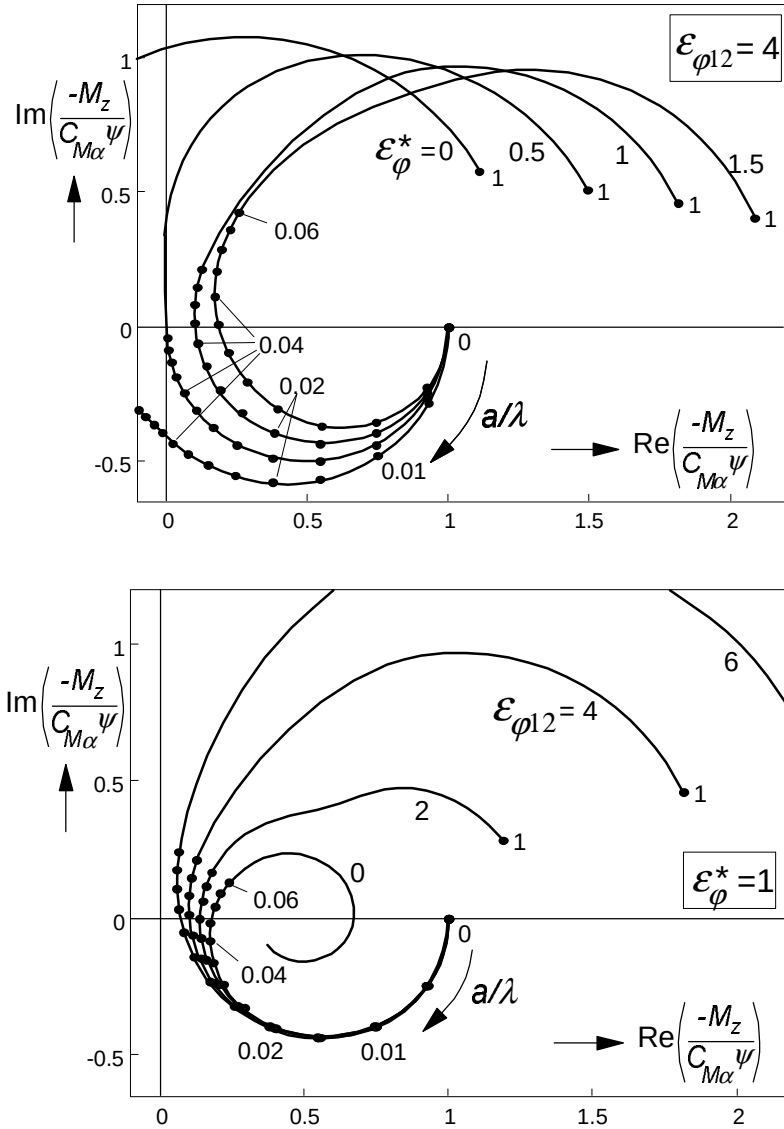

Fig. 9.17. Nyquist frequency response plots of the aligning torque to steer angle. Upper diagram: influence of tread width (4 is baseline value), lower diagram: influence of the transient yaw deflection response to turn slip (4 is baseline value).

Large Slip Angle and Turn Slip Response Simulations

The same sinusoidal manoeuvres has been simulated as was done before with the brush based contact model. The complete non-linear set of equations (9.78) to (9.118) have been used with parameters listed in Table 9.2.

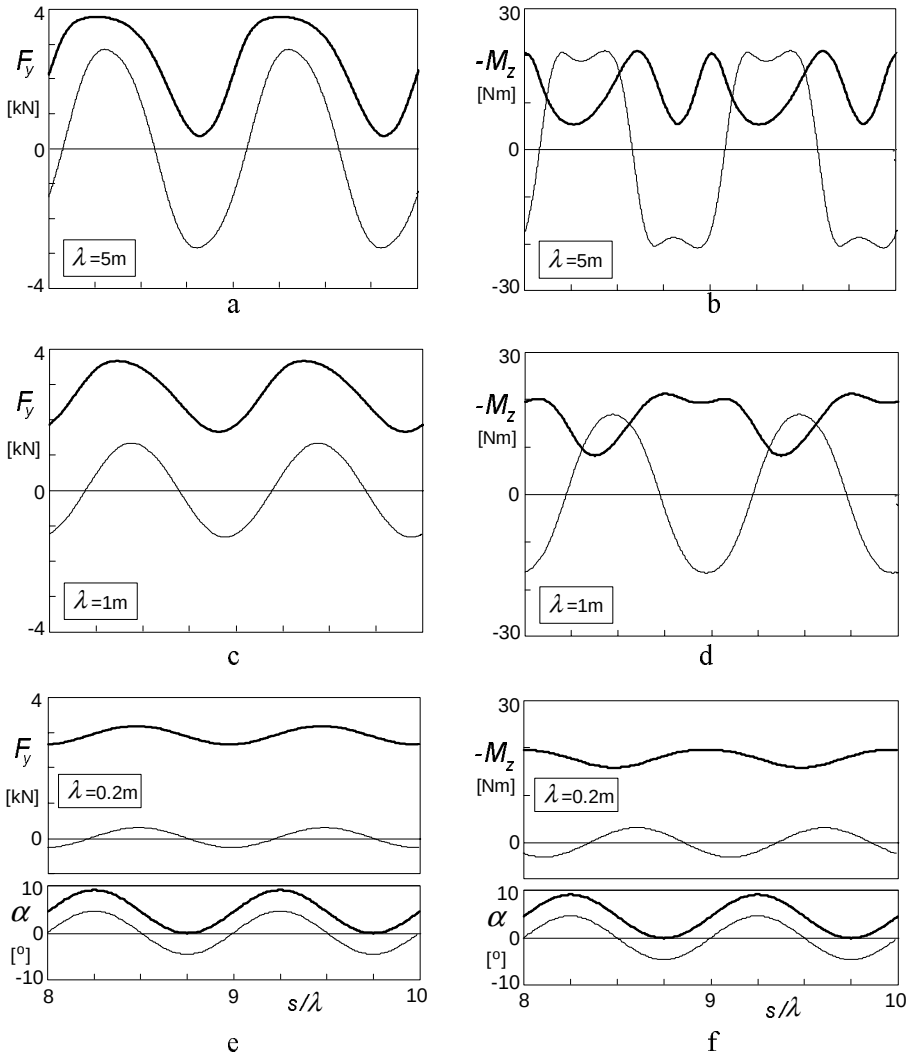

Fig. 9.18. Side force and aligning torque responses of the Magic Formula based simulation model with flexible carcass and finite tread width to sinusoidal slip angle input of the wheel plane with a slip angle amplitude of 0.08rad and average levels of 0 (thin curves) and 0.08rad (fat curves).

The slip angle variation is sinusoidal around average levels α_o = 0 and 0.08rad with one amplitude: $\hat{\alpha}$=0.08rad at three wavelengths: λ= 0.2, 1 and 5m. Similarly, the turn slip has two average levels: $a\varphi_o$ = 0 and 0.08 and one amplitude: $a\hat{\varphi}$=0.08, also at wavelengths: λ= 0.2, 1 and 5m.

The diagrams of Figs.9.18,19 present the results. We observe that the curves

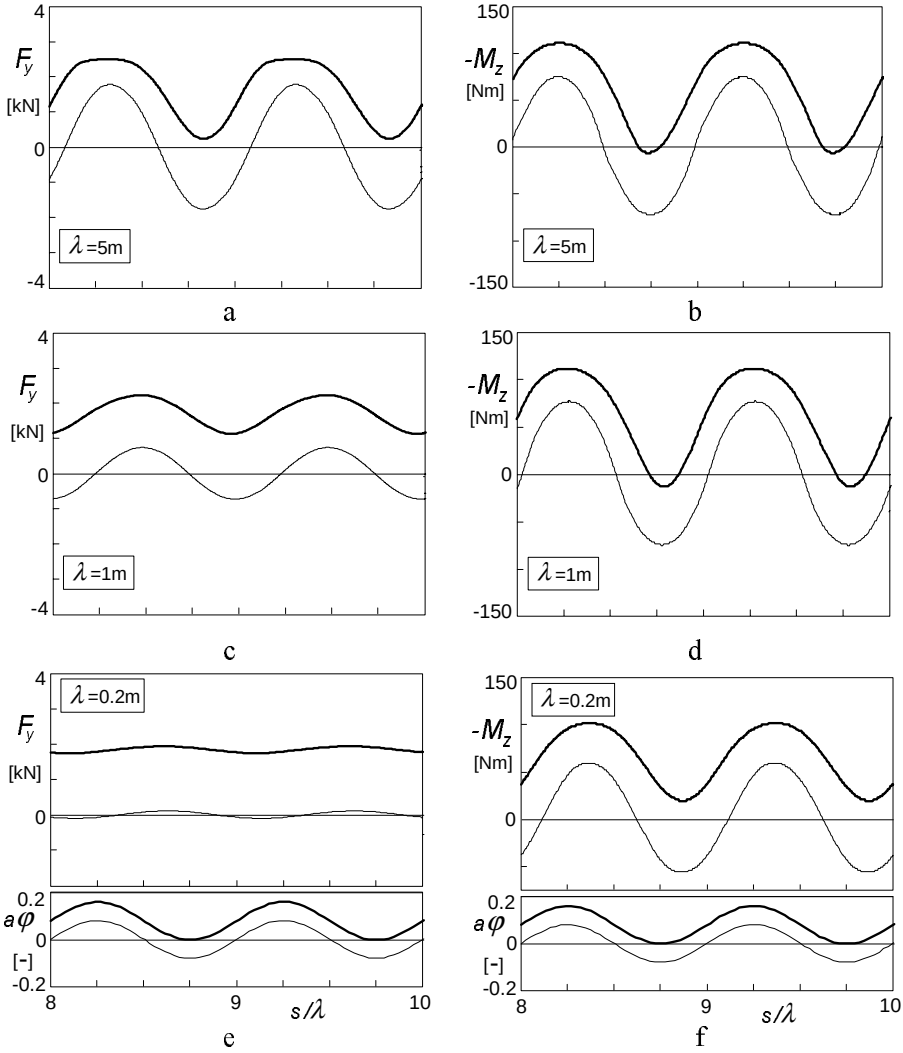

Fig. 9.19. Side force and aligning torque responses of the Magic Formula based simulation model with flexible carcass and finite tread width to sinusoidal path curvature variations (turn slip at α = 0) of the wheel plane with an amplitude of $a\varphi$ of 0.08 and average levels of 0 (thin curves) and 0.08 (fat curves).

are quite similar to those depicted in the Figs.9.10 and 11. Only, as expected, the moment response to turn slip is very much affected by the now introduced effect of the tyre tread width.

Maurice has conducted extensive experiments with a 205/60R15 91V tyre at 2.2 bar inflation pressure on a 2.5m drum test rig. The diagrams of Fig.9.20a present the computed results compared with experimental data for the case of pure side slip. The experiments have been carried out at very low speed to avoid inertia effects of the moving tyre. The wavelength ranges from 0.3 to 2.4m. The upper diagram refers to the case of zero average slip angle and 4° amplitude. The lower diagram shows the responses around an average slip angle of 4° which causes the curves to deviate considerably from the input sinusoidal shape. The curves clearly show that a shorter wavelength causes the response amplitude to

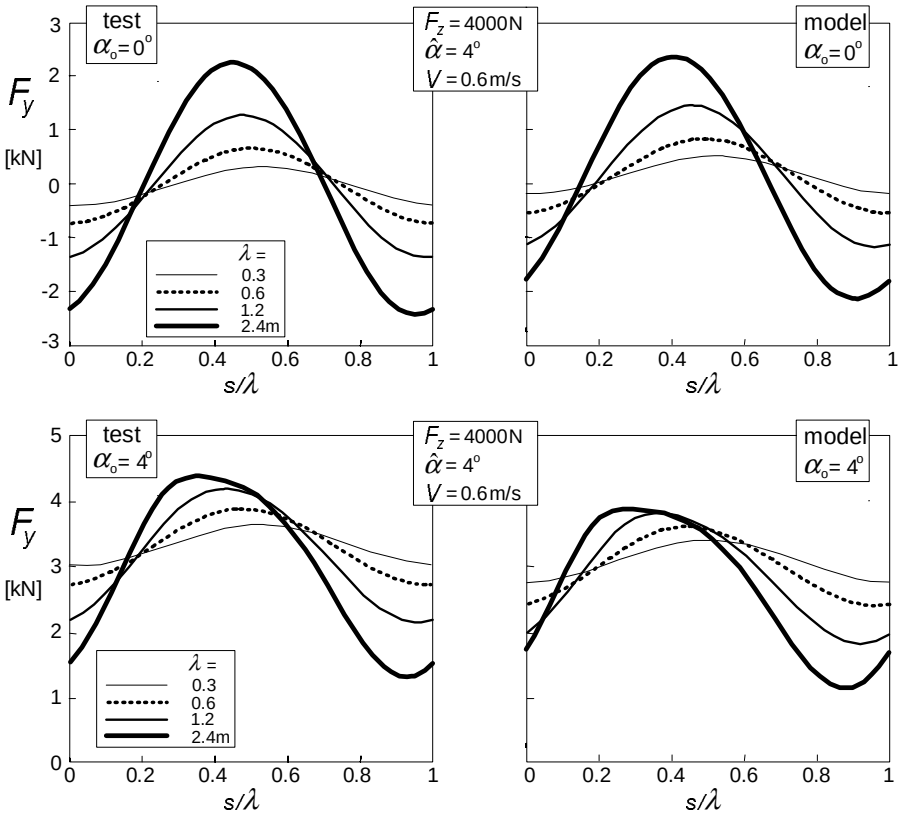

Fig. 9.20a. Comparison of theoretical model calculations and experimental results performed at 0.6 km/h on a 2.5 m drum (Maurice). The curves cover one wavelength of the periodic responses to sinusoidal slip angle variations. Force response to slip angle variations at two levels of side slip.

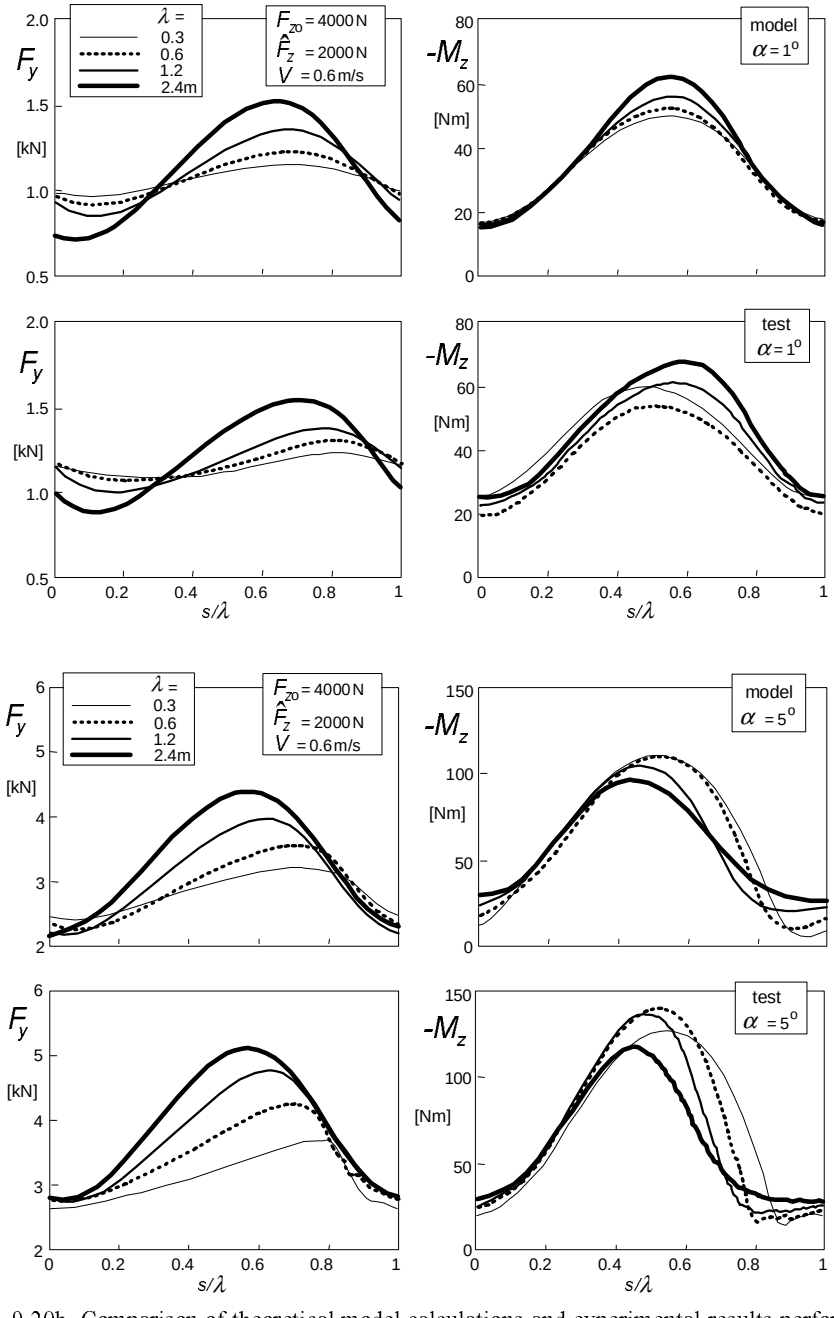

Fig. 9.20b. Comparison of theoretical model calculations and experimental results performed at 0.6 km/h on a 2.5 m drum (Maurice). The curves cover one wavelength of the periodic responses to sinusoidal load variations. Force and moment response to vertical load variations at two values of slip angle.

decrease and the phase lag to increase. It can also be observed that the responses occur more quickly at larger levels of slip which is due to the with slip sharply decreasing relaxation length. The magic formula was used to model the steady-state characteristics. The parameters were obtained from separate tests performed on the drum at the much higher speed of 60 km/h. The different conditions may explain the deviation in level of the calculated with respect to the measured responses.

Figure 9.20b present the comparison with the results of a second series of experiments at same conditions. Here, the vertical load is changed sinusoidally while the slip angle is kept at a small level and at a higher level. The results are similar to those discussed in Chapter 8, Fig.8.9. The moment response seems to be improved with the more complex tyre model.

The agreement of the computed results with experimental data is quite good. As has been reported by Maurice, also for the moment response a rather good agreement has been established. Since at the maximum slip angle of 8° the peak of the moment characteristic has been surpassed, the result becomes quite sensitive to small differences between actual and model steady-state characteristics of the aligning torque.

9.2.3. Parking Manoeuvres

Parking manoeuvres take place at very low or zero speed. The torque acting on the tyre at such conditions may become very large. The influence of the finite tread width is essential as the response to spin is now predominant. We might employ the equations developed above but then we should take care of the integration of the spin velocity to properly limit the built-up of the yaw transient slip. Similar problems arose when considering the problem of braking to stand-still or starting from stand-still, cf. Sec.8.6, Eqs.(8.112,113).

To achieve a much better agreement with experimental evidence, a different approach will be followed in the present application. It may be noted that an important characteristic is actually still missing. For the brush based model Eq.(9.70) was used. The equation governs the variation of the aligning torque M_z that arises when the non-rolling tyre is steered and the steer angle ψ is increased from zero to and beyond the state of full sliding. Ultimately, the torque reaches the magnitude that would also arise when the rolling tyre is subjected to a constant rate of turning $d\psi/dt$ (while the slip angle remains zero), at a forward speed V_x that decreases to zero. Then, the radius of turn R reduces to zero and thus the spin approaches infinity. Figure 9.21 illustrates the situation.

The missing characteristic will be modelled by using a for this purpose

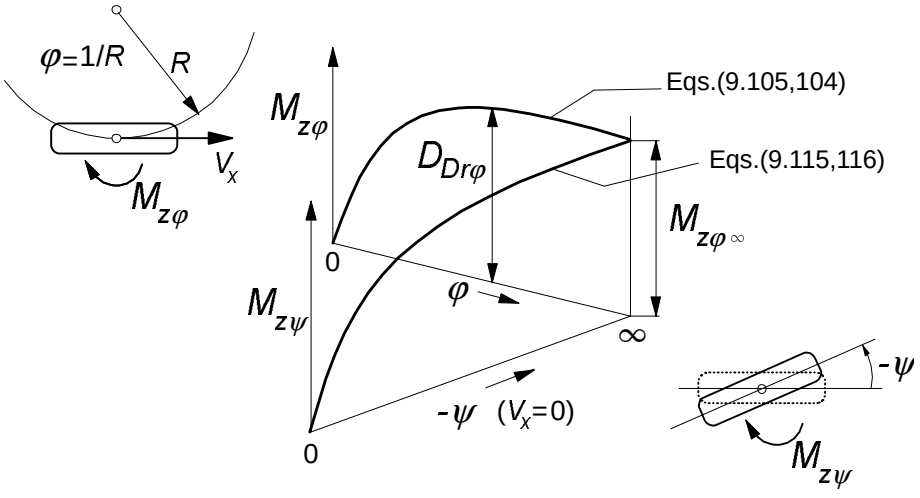

Fig. 9.21. Approaching the maximum torque at stand-still in two ways: 1. by decreasing the turn radius R to zero, 2. by increasing the steer angle $-\psi$ while standing still.

adequate model that has been developed by Van der Jagt (2000). In his dissertation a model study was discussed that is especially aimed at the generation of a proper moment response to steering at stand-still. First, the brush model was used to gain general insight into the phenomena that occur. Qualitatively good results have been obtained using this model, notably when a sinusoidal steer angle variation is imposed and the state of almost full sliding is attained periodically. For practical usage, a special type of model was developed of a nature completely different from the models used so far. Since this model appears to perform very well in the near zero speed range we have tried to incorporate Van der Jagt's model in the existing model structure. A gradual transition from the new type of model to the existing one when the speed approaches and surpasses a low speed threshold has been taken care of.

The principle of Van der Jagt's approach is that at a given rate of change of the steer input the growth rate of the tyre angular deflection decreases in proportion with a function of the remaining difference between the maximum achievable deflection and the current deflection. The torsional stiffness is assumed to be a constant and the resulting characteristic of the torque becomes similar to a first-order response function. The calculated moment gradually approaches its maximum value. When the direction of rotation of the wheel about the vertical axis is changed, the distance to the new, opposite, peak torque is large and, accordingly, the rate of reduction of the moment is large as well. It is this feature of the model that is attractive since a similar behaviour has been found to occur with the actual tyre subjected to an alternating left and right

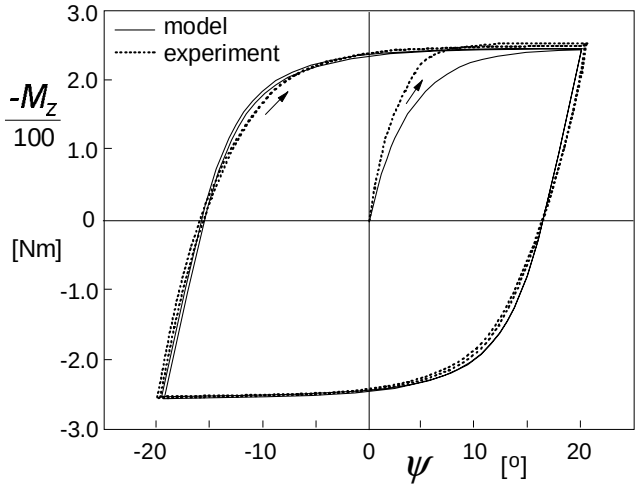

Fig. 9.22. Calculated and experimentally assessed variation of the moment versus steer angle for a non-rolling tyre pressed against a flat plate at a load $F_z = 4800$N.

sequence of turning. The equations that govern the moment generation at standstill are as follows:

$$\dot{\beta} = -\left(1 - p\left|\frac{M_{z\psi}}{M_{z\varphi\infty}}\right|^{c_o}\right)\dot{\psi} \tag{9.121}$$

$$M_{z\psi} = C_{M\psi}\beta \tag{9.122}$$

$$p = 0 \quad \text{if} \quad \operatorname{sgn}\beta \neq -\operatorname{sgn}\dot{\psi} \quad \text{else} \quad p = 1 \tag{9.123}$$

For the parameter value $c_o = 2$, Fig.9.22 presents the calculated variation of the torque versus the steer angle compared with experimentally obtained results as reported by Van der Jagt. The non-rolling tyre (size P205/65R15) is loaded to 4800N on a flat plate and subsequently steered at a rate of + and -1 deg./s. The correspondence is quite good perhaps except for the initial phase where the wheel starts to be steered from the condition where $M_z = 0$. To improve the model performance Van der Jagt suggests to use an exponent c_o the value of which depends on the last extreme of the deflection angle β. For possible further refinements of the model we refer to the original work.

When, instead of the new approach, the Magic Formula would be used with the integration limitation as suggested according to Eqs.(8.112,113), a sharp peak would arise in the curve where the direction of turning is changed. As a result, the moment decreases at a much slower rate than shown by the test result.

The problem is now how to integrate the new model feature in the original model structure. The transient slip quantity φ'_M, Eq.(9.86) may be recognised

to be proportional with the deflection angle. As can be seen from Eqs.(9.80,82,83,86) this quantity is obtained from integration of:

$$\dot{\bar{\varphi}}'_M = -\varepsilon^*_\varphi \frac{1}{\sigma_c}(\dot{\psi}_c + V_x\varphi'_c) - \varepsilon_{\varphi 12}\left\{\frac{1}{\sigma_{\varphi 1}}(\dot{\psi}_c + V_x\varphi'_1) - \frac{1}{\sigma_{\varphi 2}}(\dot{\psi}_c + V_x\varphi'_2)\right\} \quad (9.122)$$

In the new configuration, the integration is conducted at a gradually decreasing rate while approaching the maximum torque value. We have:

$$\varphi'_M = \int\left(1 - p\left|\frac{M_{z\varphi}}{M_{z\varphi\infty}}\right|^2\right)\dot{\bar{\varphi}}'_M \, \mathrm{d}t \quad (9.123)$$

where

$$p = 0 \quad \text{if} \quad \operatorname{sgn}\varphi'_M \neq \operatorname{sgn}\dot{\bar{\varphi}}'_M \quad \text{else} \quad p = w_{Vlow} \quad (9.124)$$

At zero speed $w_{Vlow} = 1$. The moment is calculated with the linear function:

$$M_{z\varphi} = D_{Dr\varphi}C_{Dr\varphi}B_{Dr\varphi}R_o\varphi'_M \quad (9.125)$$

For the standing tyre with speed V_x equal to zero the response to alternating steer angle variations will follow a course similar to that of Fig.9.22.

It is now desired to gradually change to the original equations when the tyre starts rolling. For this, the following speed window is used:

$$w_{Vlow} = \frac{1}{2}\left\{1 + \cos\left(\pi\frac{V_x}{V_{\text{low}}}\right)\right\} \quad \text{if} \quad |V_x| < V_{\text{low}} \quad \text{else} \quad w_{Vlow} = 0 \quad (9.126)$$

already appearing in Eq.(9.124). In addition, we need a downwards limited window factor to be used in (9.128):

$$w_{Vll} = \frac{w_{Vlow} + \varepsilon_{\text{lim}}}{1 + \varepsilon_{\text{lim}}} \quad (9.127)$$

with ε_{lim}, like in (9.111), representing a small positive quantity, say 0.1.

The adapted moment equation (9.105,104) is formulated as follows:

$$M_{z\varphi} = D_{Dr\varphi}\sin\left[\frac{1}{w_{Vll}}\arcsin\left\{w_{Vll}C_{Dr\varphi}\arctan\left(\frac{1}{w_{Vll}}\tan\left(w_{Vll}B_{Dr\varphi}R_o\varphi'_M\right)\right)\right\}\right] \quad (9.128)$$

which may be ascertained to reduce to the linear function (9.125) when w_{Vll} becomes equal to unity. When the speed exceeds the value V_{low} the equation gets very close to the original equation (9.104).

The adapted model will be applied now to the simulation of the motion of a rigid quarter car model with mass m_{qc} that, while a sinusoidal steering input is applied, starts rolling after 1.6sec. with a linearly increasing speed. The lateral

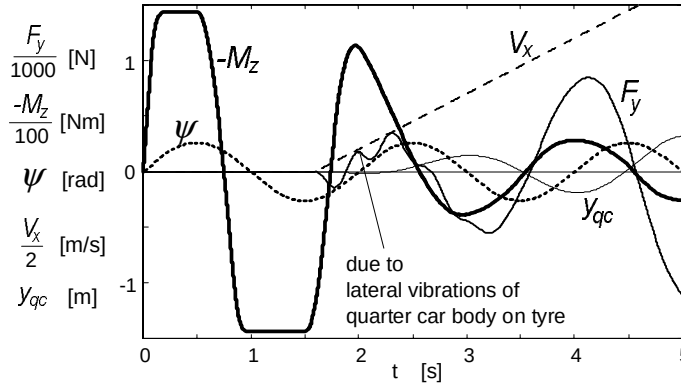

Fig. 9.23. Simulation results of a parking manoeuvre (car leaving the parking lot while steering sinusoidally).

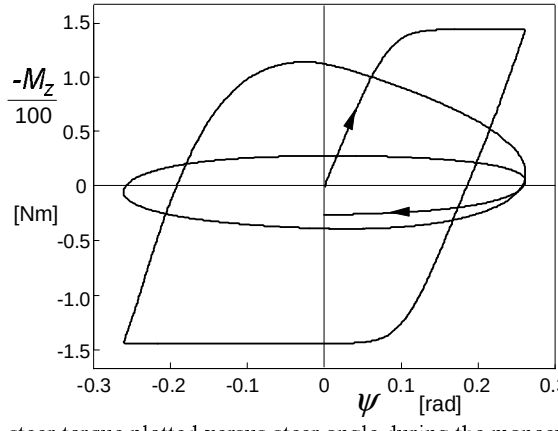

Fig. 9.24. The steer torque plotted versus steer angle during the manoeuvre of Fig.9.23.

acceleration of the quarter car axle results from the action of the side force that begins to develop after the wheel has started to roll:

$$\ddot{y}_{qc} = \frac{F_y}{m_{qc}} \tag{9.129}$$

The lateral wheel slip velocity is now not only a result of the yaw angle at a forward speed of the vehicle $\dot{x}_{qc}$ but also due to the lateral velocity of the wheel axle $\dot{y}_{qc}$. We have:

$$V_{sy} = -\dot{x}_{qc}\sin\psi + \dot{y}_{qc}\cos\psi \tag{9.130}$$

which serves as an input into the equations (9.88,91). The additional parameter values have been appended in Table 9.2.

Figure 9.23 shows the courses of variation of various quantities versus time. Simultaneously, in Fig.9.24, the moment is plotted versus steer angle. Several phenomena occur that deserves to be noted. The steer angle has an amplitude that is large enough to attain a level of the moment close to its maximum. The moment starts to decrease in magnitude as soon as the steer angle passes its peak value. The moment changes sign before the steer angle does the same. After 1.6 seconds the forward speed increases linearly with time and the side force starts to built up as a result of the slip angle that begins to develop. The car shows a lateral vibration in the low speed range as indicated by the fluctuations of the side force. Evidently, the quarter car vibrates against the lateral tyre stiffness. The moment amplitude decreases as the spin diminishes in amplitude due to the increasing speed. The side force amplitude increases because of the larger lateral oscillations of the quarter car mass induced by the increasing speed of travel at the constant steer input pattern with time. The loops shown in Fig.9.24 give a nice impression of the transition from the situation at stand-still to the condition at higher speeds. At stand-still the moment varies in accordance with the diagram of Fig.9.22.

It is important to note that for a more accurate study of responses to lateral and circumferential wheel displacements at or near forward speed equal to zero one might apply, instead of the abrupt integration limitation suggested earlier, Eqs.(8.112,113), the same structure of additional equations (9.122,124) and an adaptation such as applied in Eq.(9.128).

9.3. Tyre Dynamics

The contact patch model has been used above in connection with a flexible carcass. In the present section the inertia of the belt will be introduced. Since we restrict the application of the model to frequencies lower than ca. 60Hz the belt may be approximated as a rigid ring that is attached to the wheel rim through flexible side walls. To ensure that the total static tyre stiffness remains unchanged, residual springs have been introduced between contact patch and belt. In Fig.9.25 the structure of the model has been depicted. In this section, the response to camber variations will be taken into account.

9.3.1. Dynamic Equations

The wheel axle position is defined by the location of wheel centre (X,Y,Z) and

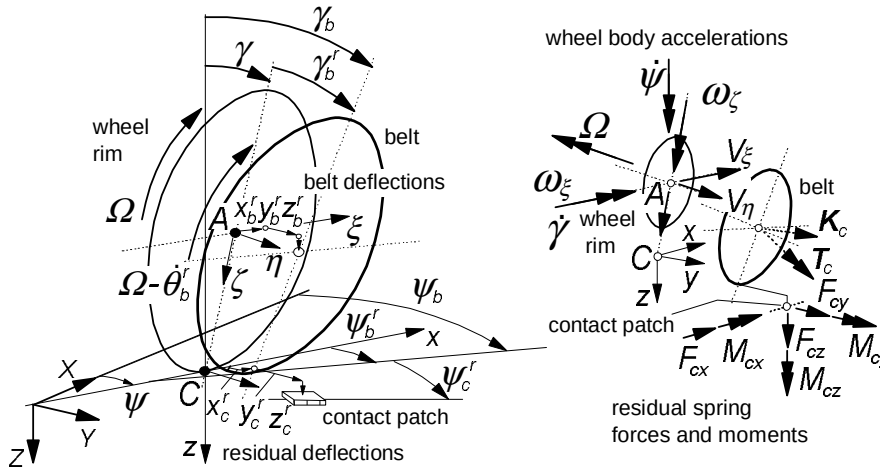

Fig. 9.25. Model structure featuring contact patch, residual compliance, rigid belt, carcass compliance and wheel rim.

orientation (γ,θ,ψ). The wheel speed of revolution is denoted by Ω. A moving axes system (C,x,y,z) has been defined of which the x axis points forwards and runs along the line of intersection of wheel plane and road plane. The y axis lies in the plane normal to the road plane and passing through the wheel spin axis. The z axis forms the normal to the road surface. The origin of the moving triad is the contact centre C. Another moving system of axes (A,ξ,η,ζ) is introduced of which the origin A is located in the wheel centre, the ξ axis is horizontal and the η axis runs along the wheel spindle axis. With respect to the wheel rim the belt shows relative displacements: $(x_b{}^r,y_b{}^r,z_b{}^r)$ and $(\gamma_b{}^r,\theta_b{}^r,\psi_b{}^r)$. The contact patch is displaced horizontally with respect to the belt corresponding to the deflections of the residual springs: $(x_c{}^r,y_c{}^r,z_c{}^r)$ and $\psi_c{}^r$. The superscript ^{r} designates a relative displacement; without the superscript we have the displacement with respect to the inertial system (X,Y,Z). All relative displacements are considered small and the dynamic equations may be linearised.

The wheel motion forms the input to the tyre system (possibly together with the road profile). From these, the wheel velocities V_ξ, V_η, V_ζ and ω_ξ, ω_η, ω_ζ (defined with respect to the axle triad (A,ξ,η,ζ)) or alternatively $\dot\gamma$, Ω, $\dot\psi$ (defined with respect to the moving contact triad (C,x,y,z)) and the camber angle γ and the radial tyre deflection ρ_z are available. The camber angle γ will be treated here as a small quantity.

The belt considered as a rigid circular body has a mass m_b and moments of inertia $I_{bx,y,z}$. The carcass (side walls) possesses stiffnesses $c_{bx,y,z}$ and damping coefficients $k_{bx,y,z}$. In the figure the force and moment vectors $\boldsymbol{K}_c$ and $\boldsymbol{T}_c$ defined to act from contact patch to and about the centre of the belt have been indicated.

Their components are defined with respect to the (A,ξ,η,ζ) triad. The first of the two sets of first-order differential equations for the six degrees of freedom reads:

dynamic belt equations

$$m_b(\dot{V}_{b\xi} - V_{b\eta}\omega_{b\zeta}) + k_{bx}\dot{x}_b^r + c_{bx}x_b^r + k_{bz}\Omega z_b^r = K_{c\xi} \tag{9.131}$$

$$m_b\dot{V}_{b\zeta} + k_{bz}\dot{z}_b^r + c_{bz}z_b^r - k_{bx}\Omega x_b^r = K_{c\zeta} \tag{9.132}$$

$$I_{by}\dot{\omega}_{b\eta} + k_{b\theta}\dot{\theta}_b^r + c_{b\theta}\theta_b^r = T_{c\eta} \tag{9.133}$$

$$m_b(\dot{V}_{b\eta} + V_{b\xi}\omega_{b\zeta}) + k_{by}\dot{y}_b^r + c_{by}y_b^r = K_{c\eta} \tag{9.134}$$

$$I_{bx}\dot{\omega}_{b\xi} + I_{by}\Omega\omega_{b\zeta} + k_{b\gamma}\dot{\gamma}_b^r + c_{b\gamma}\gamma_b^r + k_{b\psi}\Omega\psi_b^r = T_{c\xi} \tag{9.135}$$

$$I_{bz}\dot{\omega}_{b\zeta} - I_{by}\Omega\omega_{b\xi} + k_{b\psi}\dot{\psi}_b^r + c_{b\psi}\psi_b^r - k_{b\gamma}\Omega\gamma_b^r = T_{c\zeta} \tag{9.136}$$

Several coupling terms show up. These are due to the gyroscopic effect and due to the action of the rotating radial dampers with resulting coefficient $k_{bx} = k_{bz}$ and the lateral dampers with resulting angular damping coefficients $k_{b\psi} = k_{b\gamma}$. Figure 9.26 illustrates the mechanism that gives rise to the interaction terms. The example concerns the term $k_{bz}\Omega z_b^r$ in (9.131). The following relations between the two sets of wheel and axle angular velocities hold:

$$\omega_\xi = \dot{\gamma} \tag{9.137}$$

$$\omega_\eta = -\Omega + \dot{\psi}\sin\gamma \approx -\Omega + \dot{\psi}\gamma \tag{9.138}$$

$$\omega_\zeta = \dot{\psi}\cos\gamma \approx \dot{\psi} \tag{9.139}$$

For the relative displacements between belt and wheel rim we have the second set of six first-order differential equations:

$$\dot{x}_b^r = V_{b\xi} - V_\xi \tag{9.140}$$

$$\dot{y}_b^r = V_{b\eta} - V_\eta \tag{9.141}$$

$$\dot{z}_b^r = V_{b\zeta} - V_\zeta \tag{9.142}$$

and

$$\dot{\gamma}_b^r = \omega_{b\xi} - \dot{\gamma} \tag{9.143}$$

$$\dot{\theta}_b^r = \omega_{b\eta} + \Omega - \dot{\psi}(\gamma + \gamma_b^r) \tag{9.144}$$

$$\dot{\psi}_b^r = \omega_{b\zeta} - \dot{\psi} \tag{9.145}$$

The forces and moments appearing in the right-hand members of Eqs. (9.131-

136) can be expressed in terms of the forces acting in the residual springs that connect the contact patch with the belt. The residual spring deflections as defined in the model can be observed in greater detail in Fig.9.27. The directions of the residual spring forces and moments are defined to act parallel to the moving axes system (C,x,y,z) with the z axis normal to the road plane. Also, the vertical forces F_z are defined here, in contrast to the definition adopted in the remainder of this book, according to the consistent SAE convention. For the normal wheel load acting from road to tyre we introduce the positive quantity F_N. We have in case of a horizontal road plane with products of angles neglected and r_l denoting the loaded radius:

$$K_{c\xi} = F_{cx} \tag{9.146}$$

$$K_{c\zeta} = F_{cz} - \gamma F_{cy} \tag{9.147}$$

$$T_{c\eta} = r_l F_{cx} + M_{cy} \tag{9.148}$$

$$K_{c\eta} = F_{cy} + \gamma F_{cz} \tag{9.149}$$

$$T_{c\xi} = -r_l F_{cy} - (r_l \gamma_b - y_c^r) F_{cz} + M_{cx} \tag{9.150}$$

$$T_{c\zeta} = M_{cz} - y_c^r F_{cx} \tag{9.151}$$

Obviously, a proper axes transformation is to be performed if the road plane is not horizontal. As a result, transverse and forward slopes will affect the terms appearing in the right-hand members of Eqs.(9.146-151). It is left to the user to introduce these transformations.

The contact patch body is subjected to forces acting in the residual springs (subscript $_c$) and external forces acting from road surface to contact patch

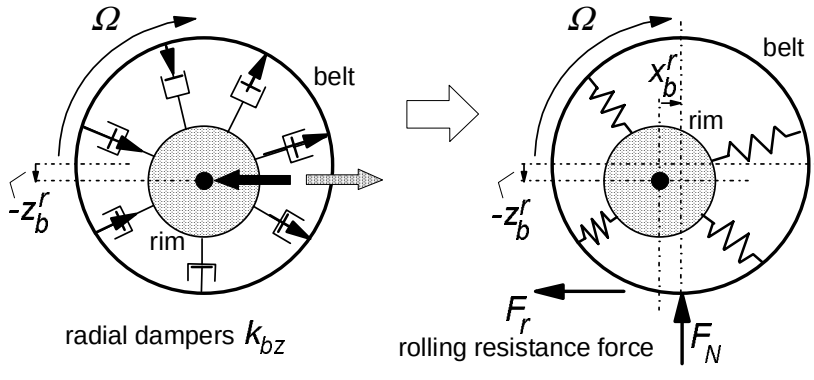

Fig. 9.26. The rotating radial dampers of the vertically deflected tyre gives rise to a resulting fore and aft force acting between belt and rim. The resulting longitudinal deflection produces a rolling resistance force F_r through the action of the normal load F_N.

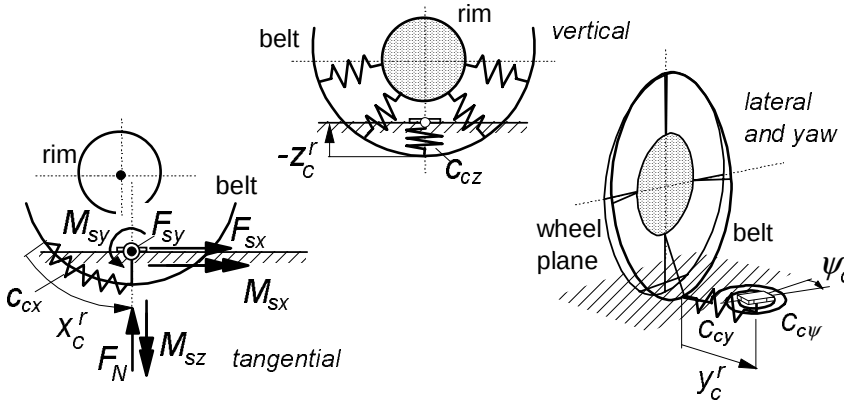

Fig. 9.27. Deflections of the residual springs attaching contact patch to belt.

(subscript $_s$). Figure 9.28 illustrates the situation. The second-order differential equations that govern the horizontal dynamics of the contact patch body read:

dynamic contact patch equations

$$m_c(\dot{V}_{cx} - V_{cy}\dot{\psi}_c) + k_{cx}\dot{x}_c^r + c_{cx}x_c^r = F_{sx} \tag{9.152}$$

$$m_c(\dot{V}_{cy} + V_{cx}\dot{\psi}_c) + k_{cy}\dot{y}_c^r + c_{cy}y_c^r = F_{sy} \tag{9.153}$$

$$I_c\ddot{\psi}_c + k_{c\psi}\dot{\psi}_c^r + c_{c\psi}\psi_c^r = M_{sz} \tag{9.154}$$

and in addition differential equations for the residual deflections:

$$\dot{x}_c^r = V_{cx} - V_{b\xi} + r_e(\Omega - \dot{\theta}_b^r) \tag{9.155}$$

$$\dot{y}_c^r = V_{cy} - V_{b\eta} + r_l(\dot{\gamma} + \dot{\gamma}_b^r) \tag{9.156}$$

$$\dot{\psi}_c^r = \dot{\psi}_c - \dot{\psi} - \dot{\psi}_b^r \tag{9.157}$$

Also here, in the right-hand members, a road slope will have an effect. An axes transformation is needed to properly introduce the belt velocities with respect to the location of the contact patch. From the deflections and deflection rates the residual spring and damper forces appearing in Eqs.(9.146-151) can be determined. We have:

$$F_{cx} = k_{cx}\dot{x}_c^r + c_{cx}x_c^r \tag{9.158}$$

$$F_{cy} = k_{cy}\dot{y}_c^r + c_{cy}y_c^r \tag{9.159}$$

$$M_{cz} = k_{c\psi}\dot{\psi}_c^r + c_{c\psi}\psi_c^r \tag{9.160}$$

while

$$M_{cx} = M_{sx} \tag{9.161}$$

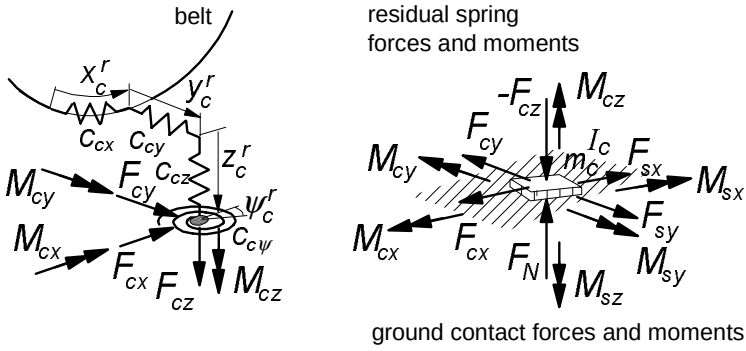

Fig. 9.28. Internal and external forces and moments acting on the contact patch body.

$$M_{cy} = M_{sy} \tag{9.162}$$

$$F_{cz} = F_{sz} \tag{9.163}$$

The contact forces and moments result from the contact slip model equations developed in the preceding section. The computed forces and moments have been defined according to the Magic Formula model which, at steady state, act with respect to the moving axes system (C,x,y,z). These forces and moments, here provided with subscript $_C$, are to be transformed to arrive at the set of forces and moments defined according to the system with lines of action shifted sideways over the calculated 'static' lateral displacement y_{st}^r of the contact patch with respect to the wheel plane. These corrected quantities correspond to the forces and moments provided with subscript $_s$ occurring in the Eqs.(9.152-154) and (9.161-163).

$$F_{sx} = F_{x,C} \tag{9.164}$$

$$F_{sy} = F_{y,C} \tag{9.165}$$

$$M_{sz} = M_{z,C} + y_{st}^r \cdot F_{x,C} \tag{9.166}$$

$$M_{sx} = M_{x,C} - y_{st}^r \cdot F_{z,C} \tag{9.167}$$

$$M_{sy} = M_{y,C} \tag{9.168}$$

$$F_{sz} = F_{z,C} \tag{9.169}$$

where the static lateral deflection is computed from the side force and the overall lateral compliance of the standing tyre at ground level:

$$y_{st}^r = \frac{F_{sy}}{C_{Fy}} = F_{sy}\left(\frac{1}{c_{cy}} + \frac{1}{c_{by}} + \frac{r_l^2}{c_{b\gamma}}\right) \tag{9.170}$$

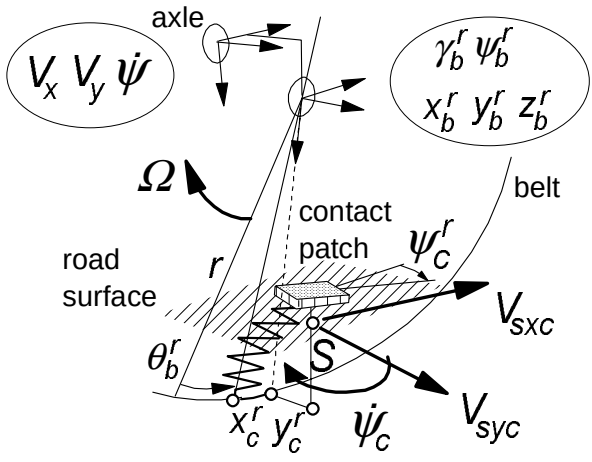

Fig. 9.29. Slip velocities of contact patch forming input to transient slip equations.

With the transient response variables computed with the aid of Eqs.(9.78-86) plus Eq.(9.20) the contact forces and moments may be found by using these variables as argument in the steady-state equations presented in Sections 4.3.2 and 4.3.3. We should, however, properly account for the response to a varying camber angle of the belt plane.

For this purpose, we introduce the tyre total spin velocity $\dot{\psi}_\gamma$, cf. Eq.(4.76) which has been corrected for the static belt camber deflection to enable the direct use of the relevant magic formulae (analogous to the use of β_{st} in Eq.(9.78)):

$$\dot{\psi}_\gamma = \dot{\psi}_c - (1-\varepsilon_\gamma)\Omega \sin(\gamma + \gamma_b^r - \gamma_{bst}^r) \tag{9.171}$$

with the 'static' belt deflection angle:

$$\gamma_{bst}^r = -r_l F_{sy} \frac{1}{c_{b\gamma}} \tag{9.172}$$

Further, we write instead of β_{st}:

$$\psi_{st}^r = M_{sz}\left(\frac{1}{c_{c\psi}} + \frac{1}{c_{b\psi}}\right) \tag{9.173}$$

The transient slip first-order differential equations are repeated below. They are identical to Eqs.(9.78-86) plus Eq.(9.20) except for the now added effect of the camber angle in the right-hand members. In (9.20) κ_c' may be replaced by κ' as at steady-state these are equal for contact patch and overall tyre model. The same holds for the spin variables φ_c' and φ'.

transient slip equations for longitudinal, side slip, turn slip and camber

$$\sigma_c \frac{\mathrm{d}\kappa'}{\mathrm{d}t} + |V_x|\kappa' = -V_{sxc} \tag{9.174}$$

$$\sigma_c \frac{\mathrm{d}\alpha'}{\mathrm{d}t} + |V_x|\alpha' = -V_{syc} - |V_x|\psi_{\mathrm{st}}^{r} \tag{9.175}$$

$$\sigma_2 \frac{\mathrm{d}\alpha_t'}{\mathrm{d}t} + |V_x|\alpha_t' = |V_x|\alpha_c' \tag{9.176}$$

$$\sigma_c \frac{\mathrm{d}\varphi'}{\mathrm{d}t} + |V_x|\,\varphi' = -\dot{\psi}_\gamma \tag{9.177}$$

$$\sigma_{F2} \frac{\mathrm{d}\varphi_{F2}'}{\mathrm{d}t} + |V_x|\,\varphi_{F2}' = -\dot{\psi}_\gamma \tag{9.178}$$

$$\sigma_{\varphi 1} \frac{\mathrm{d}\varphi_1'}{\mathrm{d}t} + |V_x|\,\varphi_1' = -\dot{\psi}_\gamma \tag{9.179}$$

$$\sigma_{\varphi 2} \frac{\mathrm{d}\varphi_2'}{\mathrm{d}t} + |V_x|\,\varphi_2' = -\dot{\psi}_\gamma \tag{9.180}$$

In addition, we need the composite transient slip quantities:

$$\varphi_F' = \varphi' - \varphi_{F2}' \tag{9.181}$$

$$\varphi_M' = \varepsilon_\varphi^* \varphi' + \varepsilon_{\varphi 12}(\varphi_1' - \varphi_2') \tag{9.182}$$

The slip variables employed in the magic formulae (*MF*) are replaced by the transient slip variables as indicated in the arguments of the following expressions:

output forces and moments

$$F_{x,C} = MF_{Fx}(\kappa', \alpha', \varphi_F', F_N) \tag{9.183}$$

$$F_{y,C} = MF_{Fy}(\kappa', \alpha', \varphi_F', \gamma, F_N) \tag{9.184}$$

$$M_{z,C} = -t_C F_{y,C} + M_{zr,C} + \Delta M_z \tag{9.185}$$

$$t_C = MF_t(\kappa', \alpha_t', \varphi_M', \gamma, F_N) \tag{9.186}$$

$$M_{zr,C} = MF_{Mzr}(\kappa', \alpha', \varphi_M', \gamma, F_N) \tag{9.187}$$

$$\Delta M_z = C_{\Delta M}(\alpha' - \alpha_t') \tag{9.188}$$

$$M_{x,C} = M_x \tag{9.189}$$

$$M_{y,C} = M_y \tag{9.190}$$

$$F_{z,C} = -F_N \tag{9.191}$$

Equation (9.188) has been added which is in agreement with the short wavelength transient slip theory, cf. Eqs.(9.106,110). The input to the transient slip equations (9.171,174-180) is constituted by the velocities of the contact patch, cf. Fig.9.29:

$$V_{sxc} = V_{cx} \tag{9.192}$$

$$V_{syc} = V_{cy} - V_x(\psi_b^r + \psi_c^r) \tag{9.193}$$

$$\dot{\psi}_c = \dot{\psi}_c \tag{9.194}$$

The overturning couple M_x can be modelled with the function (4.E69) where the F_y part may be replaced by the expression (4.122-124) with transient slip angle as argument, if the actual momentary loaded radius r_l (distance between points A and C) has been properly accounted for in the (steady-state) measurements and further processing. The wheel load F_N (=$|F_z|$) and the rolling resistance moment M_y depend on the radial deflection and on a number of other variables. The subsequent section provides information on the experimentally assessed functional relationships.

Finally we need to establish the output forces and moments that act from the tyre upon and about the wheel centre. These quantities are denoted with the symbols K and T and are provided with the subscript $_a$. The components are defined to act along and about the axes of the axle triad (A,ξ,η,ζ). We find:

$$K_{a\xi} = K_{b\xi} \tag{9.195}$$

$$K_{a\eta} = K_{b\eta} \tag{9.196}$$

$$K_{a\zeta} = K_{b\zeta} \tag{9.197}$$

$$T_{a\xi} = T_{b\xi} + y_b^r K_{b\zeta} - z_b^r K_{b\eta} \tag{9.198}$$

$$T_{a\eta} = T_{b\eta} + z_b^r K_{b\xi} - x_b^r K_{b\zeta} \tag{9.199}$$

$$T_{a\zeta} = T_{b\zeta} + x_b^r K_{b\eta} - y_b^r K_{b\xi} \tag{9.200}$$

where the forces and moments acting from belt centre to rim are retrieved from Eqs.(9.131-136):

$$K_{b\xi} = k_{bx}\dot{x}_b^r + c_{bx}x_b^r + k_{bz}\Omega z_b^r \tag{9.201}$$

$$K_{b\eta} = k_{by}\dot{y}_b^r + c_{by}y_b^r \tag{9.202}$$

$$K_{b\zeta} = k_{bz}\dot{z}_b^r + c_{bz}z_b^r - k_{bx}\Omega x_b^r \tag{9.203}$$

$$T_{b\xi} = k_{b\gamma}\dot{\gamma}_b^r + c_{b\gamma}\gamma_b^r + k_{b\psi}\Omega\psi_b^r \tag{9.204}$$

$$T_{b\eta} = k_{b\theta}\dot{\theta}_b^r + c_{b\theta}\theta_b^r \tag{9.205}$$

$$T_{b\zeta} = k_{b\psi}\dot{\psi}_b^r + c_{b\psi}\psi_b^r - k_{b\gamma}\Omega\gamma_b^r \tag{9.206}$$

Values of inertia parameters normalised with tyre mass m_o and reference moment of inertia $m_o r_o^2$ with r_o the unloaded tyre radius have been listed in App.3.

9.3.2. Constitutive Relations

In the study of Zegelaar (1998) important observations have been made regarding contact area dimensions, static and dynamic vertical stiffness and characteristics at different speeds of rolling, static longitudinal stiffness of the standing tyre, tyre radius growth with speed, rolling resistance, effective rolling radius and rolling resistance couple. Much of the results will be repeated below.

Dimensions of the Contact Area

Prints of the contact patch may be obtained by using ink or carbon paper. The shape appears to change from an oval shape at very low normal loads to a more rectangular shape at higher values of the load. An effective rectangular contact area may be defined with an area equal to that of the envelope of the actual print. The ratio of the width and length of the rectangle is taken equal to that of the actual contact area. The effective half length and half width are denoted as a and b. The dimensions depend on the normal load F_N ($=|F_z|$) and the following formulae have been found to give a good approximation:

$$a = (q_{a1}\sqrt{F_N/F_{No}} + q_{a2}F_N/F_{No})r_o \tag{9.207}$$

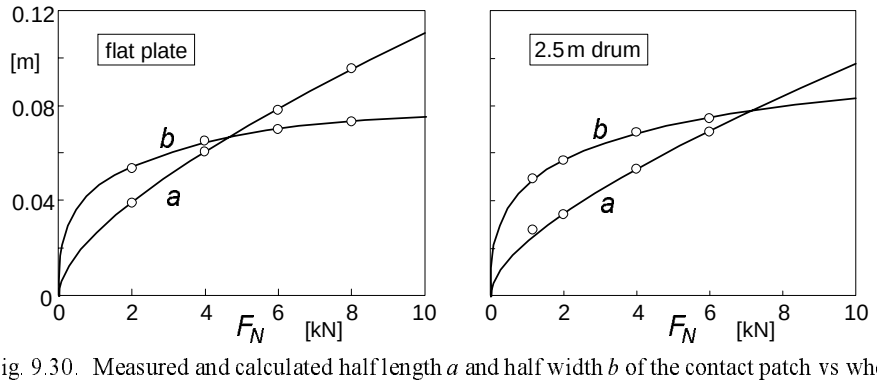

Fig. 9.30. Measured and calculated half length a and half width b of the contact patch vs wheel load, for the cases: loading on a flat plate and on a drum surface.

and

$$b = (q_{b1}\sqrt[3]{F_N/F_{No}} + q_{b2}F_N/F_{No})r_o \tag{9.208}$$

with r_o denoting the free tyre radius. Figure 9.30 presents the curves compared with the measured effective quantities for the tyre pressed on a flat surface and on a curved drum surface with 2.5m diameter. Obviously, the results are satisfactory. The dimensions of the tyre were again: 205/60R15 91V at 2.2 bar inflation pressure. The non-dimensional parameter values can be found in Table 9.3. In App.3.3 an alternative expression for a is presented based on the radial deflection ρ_z instead of on the normal load F_N. The resulting value is much less dependent on the possibly changed inflation pressure, cf. Fig.A3.1.

Table 9.3. Parameter values for contact patch dimensions (205/60R15 91V at 2.2 bar).

F_{No} (=$\|F_{zo}\|$) = 4000 N, r_o (= R_o) = 0.312 m, drum diameter = 2.5m			
$q_{a1,\text{flat}}$ = 0.140	$q_{a2,\text{flat}}$ = 0.053	$q_{b1,\text{flat}}$ = 0.240	$q_{b2,\text{flat}}$ = -0.037
$q_{a1,\text{drum}}$ = 0.120	$q_{a2,\text{drum}}$ = 0.050	$q_{b1,\text{drum}}$ = 0.247	$q_{b2,\text{drum}}$ = -0.027

The Sidewall Stiffnesses and Damping

The rigid ring model of the tyre freely rolling and loaded on the road shows three in plane modes of vibration: the vertical mode and two angular modes. One of these rotational modes vibrates in phase with rim angular vibration while the other moves in anti-phase. The natural frequencies have been estimated with the aid of experiments conducted on the drum test stand where the wheel, at fixed axle position, rolls over a short cleat or is excited by brake torque fluctuations, cf. Sec.9.3.3.

The experiments indicate that the natural frequencies lying in the range of 0-100Hz, decrease with velocity. Other researchers found the same tendency, notably Bruni, Cheli and Resta (1996). Since the sidewall stiffnesses are much larger than the residual stiffnesses it is decided to make the in-plane sidewall stiffnesses dependent on the speed of rolling. As to the out-of-plane vibrations, Maurice did not ascertain the necessity to make the lateral, yaw and camber stiffnesses speed dependent.

Zegelaar introduces a variable quantity Q_V that is a measure of the time rate of change of the loaded tyre deformation due to rolling. We have the non-dimensional quantity (V_o representing the reference velocity, cf. Sec.4.3.2):

$$Q_V = \frac{|\Omega|}{V_o}\sqrt{(x_b^r)^2 + (z_b^r)^2} \tag{9.209}$$

The following expressions for the sidewall stiffnesses have been found to be appropriate:

$$c_{bx} = c_{bx0}\left(1 - q_{bVx}\sqrt{Q_V}\right) \tag{9.210}$$

$$c_{bz} = c_{bz0}\left(1 - q_{bVz}\sqrt{Q_V}\right) \tag{9.211}$$

$$c_{b\theta} = c_{b\theta 0}\left(1 - q_{bV\theta}\sqrt{Q_V}\right) \tag{9.212}$$

The additional subscript $_0$ designates the situation of the loaded non-rotating tyre. The vertical and longitudinal stiffnesses have been assumed equal to each other. The parameters $q_{bVx,z,\theta}$ govern the speed dependency of the stiffnesses.

The sidewall damping coefficients $k_{bi} = k_{bx,y,z\gamma,\theta,\psi}$ are considered to be constant quantities. The interaction terms appearing in Eqs.(9.131-136) containing the coefficients $k_{bi}\Omega$ are omitted since these terms affect the rolling resistance and the aligning torque (also in steady state) and would make these speed dependent. The introduction of material damping being inversely proportional with frequency would be closer to reality. Further on, the rolling resistance will be introduced in an alternative, better controlled way.

For the constant stiffnesses non-dimensional parameters may be introduced. We define with F_{No}, r_o (=R_o) and m_o (the reference load, free tyre radius and tyre mass) the non-dimensional parameters q:

$$c_{bx0,y,z0} = q_{cbx,y,z}F_{No}/r_o \tag{9.213}$$

$$c_{b\gamma,\theta 0,\psi} = q_{cb\gamma,\theta,\psi}F_{No}r_o \tag{9.214}$$

$$k_{bx,y,z} = 2q_{kbx,y,z}\sqrt{m_o F_{No}/r_o} \tag{9.215}$$

$$k_{b\gamma,\theta,\psi} = 2q_{kb\gamma,\theta,\psi}\sqrt{m_o F_{No} r_o^3} \tag{9.216}$$

To provide more damping when the wheel speed gets close to zero, we may follow the theory of Chapter 7 and introduce $k_{V,low}$ as demonstrated in Chap.8, Eqs.(8.127,128) where the slip speed V_{sx} may be replaced V_{sxc}. In a similar way the residual stiffness and damping parameters c_c and k_c have been normalised.

The Normal Force

The spring with residual stiffness c_{cz} indicated in Fig.9.27 hides a structure that is a lot more complex than a spring with constant stiffness. Experiments reveal that the force deflection characteristics are non-linear: the force develops after contact has been made and increases slightly more than proportionally with the overall radial deflection ρ_z. Also, the tyre grows with speed due to the centrifugal action. Figure 9.31 illustrates both phenomena. Furthermore, it has been found useful to introduce F_x and F_y interaction terms in the vertical stiffness, cf.

Reimpell et al. (1986). The following formulae is proposed for the overall stiffness and growth functions:

$$F_N = |F_z| = \left\{1 + q_{V2}|\Omega|\frac{r_o}{V_o} - \left(q_{Fcx1}\frac{F_x}{F_{No}}\right)^2 - \left(q_{Fcy1}\frac{F_y}{F_{No}}\right)^2\right\}\left(q_{Fz1}\frac{\rho_z}{r_o} + q_{Fz2}\frac{\rho_z^2}{r_o^2}\right)F_{No} \tag{9.217}$$

with deflection:

$$\rho_z = r_o - r_l + \Delta r \tag{9.218}$$

and growth

$$\Delta r = q_{V1} r_o (\Omega r_o / V_o)^2 \tag{9.219}$$

Here, r_o denotes the radius of the free non-rotating tyre, r_l the loaded radius (axle height) and Δr the increase in free tyre radius due to wheel rotation velocity. The non-dimensional parameter q_{V1} governs the influence of tyre growth, q_{V2} the stiffness variation with speed, $q_{Fcx,y}$ the interaction with horizontal forces and $q_{Fz1,2}$ the stiffness and non-linearity of the force deflection characteristic at zero speed and horizontal forces. Appendix 3 presents the parameter values fitted to experimental data.

From the overall characteristics the properties of the residual spring are to be derived. An exact functional relationship may be established but it can be found that the residual radial spring characteristic can be approximated by the third degree polynomial function:

$$F_N = |F_z| = a_1\rho_{zr} + a_2\rho_{zr}^2 + a_3\rho_{zr}^3 \tag{9.220}$$

with the F_N related residual spring deflection (taking into account geometrical

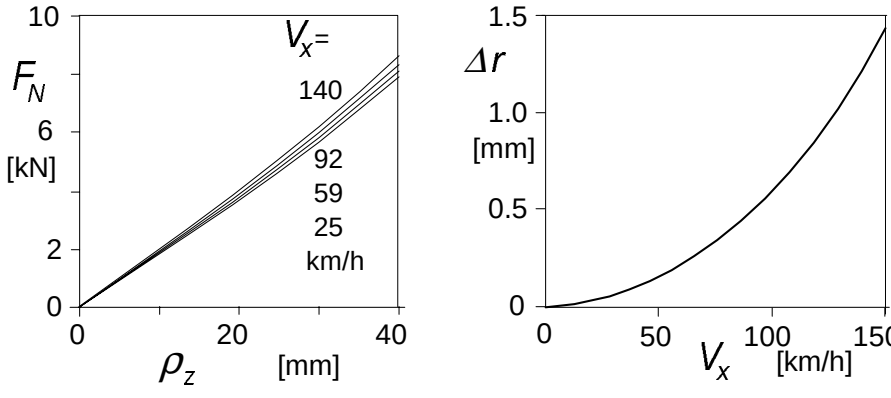

Fig. 9.31. Vertical load vs radial deflection characteristics at various forward velocities and tyre radius growth with speed.

interaction terms with horizontal deflections):

$$\rho_{zr} = z_b + \Delta r - q_{Fcx2}\rho_x^2/r_o - q_{Fcy2}\rho_y^2/r_o - w \tag{9.221}$$

Here, z_b is the vertical displacement of the centre of the belt ring (with respect to its location in the just touching unloaded and non-rotating condition on a flat horizontal road, $F_N = w = 0$), $\rho_{x,y}$ represent the longitudinal and lateral tyre contact deflections and w denotes the variation of the vertical position of the road plane at the contact centre with respect to its initial level. The actual loaded radius r_l reads with $r_o = R_o$ (cf. Fig.4.30 for measured evidence):

$$r_l = r_o + z_b^r + \Delta r - \rho_{zr} - (q_{Fcx2}\rho_x^2 + q_{Fcy2}\rho_y^2)/r_o \tag{9.222}$$

The coefficients appearing in (9.220) can be expressed in terms of sidewall stiffness c_{bz} and wheel speed of revolution Ω:

$$a_1 = \frac{c_{bz}A_1}{c_{bz} - A_1} \tag{9.223}$$

$$a_2 = \frac{c_{bz}^3 A_2}{(c_{bz} - A_1)^3} \tag{9.224}$$

$$a_3 = 2\frac{c_{bz}^4 A_2^2}{(c_{bz} - A_1)^5} \tag{9.225}$$

where

$$A_1 = q_{Fz1}(1 + q_{V2}|\Omega|r_o/V_o)F_{No}/r_o \tag{9.226}$$

$$A_2 = q_{Fz2}A_1/(q_{Fz1}r_o) \tag{9.227}$$

where the two non-dimensional parameters $q_{Fz1,2}$ of Eq.(9.217) appear. The horizontal tyre deflections at road surface level with respect to the wheel rim are:

$$\rho_x = x_b^r + r_o\theta_b^r + x_c^r \tag{9.228}$$

$$\rho_y = y_b^r - r_o\gamma_b^r + y_c^r \tag{9.229}$$

Appendix 3 provides the relevant parameter values for the passenger car tyre that has been tested.

Free Rolling Resistance

Experiments show that the rolling resistance force F_r (pointing backwards) is proportional to the tyre normal load F_N. A history on this subject can be found in the publication of Clark (1982). We have:

$$F_r = f_r F_N \tag{9.230}$$

The rolling resistance coefficient f_r depends on the forward speed and may be expressed in terms of powers of the speed, cf. Mitschke (1982):

$$f_r = q_{sy1} + q_{sy3}|V_x/V_o| + q_{sy4}(V_x/V_o)^4 \tag{9.231}$$

Parameter q_{sy1} governs the initial level of the rolling resistance force and typically lies in between 1 and 2 percent. Parameter q_{sy3} controls the slight slope of the resistance with speed. The last parameter q_{sy4} represents the sharp rise of the resistance that occurs after a relatively high critical speed is surpassed. Then, the so-called standing waves show up as a result of instability, cf. Pacejka (1981), or according to an alternative theory due to resonance, cf. Brockman and Braisted (1994). The formation of standing waves gives rise to large deflection variations and considerable energy loss. The phenomenon may result in failure of the tyre and poses an upper limit to the safe range of operation of the tyre.

Below, we will see that the rolling resistance will be introduced in the tyre model through the rolling resistance moment that is imposed on the tyre belt ring as an external torque about the y axis, cf. Eq.(9.236).

Effective Rolling Radius, Brake Lever Arm, Rolling Resistance Moment

In Chapter 8 the notion of the effective rolling radius has been introduced. Figure 8.12 shows the results of experiments of tyres running over a drum surface. In Subsection 8.3.1 the theory is restricted to a linearised representation of the variation of the effective rolling radius with radial defection. The complete non-linear variation versus normal load F_N may be described by the expression:

$$r_e = r_o + \Delta r - \left\{q_{re1}\rho_z + D_{re}\arctan\left(B_{re}\rho_z\right)\right\} \tag{9.232}$$

with

$$D_{re} = q_{re2}F_{No}/C_{Fz}$$
$$B_{re} = q_{re3}/D_{re} \tag{9.232a}$$

and the vertical stiffness of the standing tyre at nominal load F_{No} as derived from Eq.(9.217):

$$C_{Fz} = \frac{F_{No}}{r_o}\sqrt{q_{Fz1}^2 + 4q_{Fz2}} \tag{9.232b}$$

The longitudinal slip velocity is defined with r_e introduced as the slip radius, cf. e.g. Eq.(8.32). Note the slightly deviating formula in App.3, Eq.(A3.7).

In the present model with the belt ring and contact patch modelled as separate bodies, the longitudinal slip velocity V_{sxc} of the contact patch is used as input in the transient slip differential equation (9.174). In Eq.(9.192) with

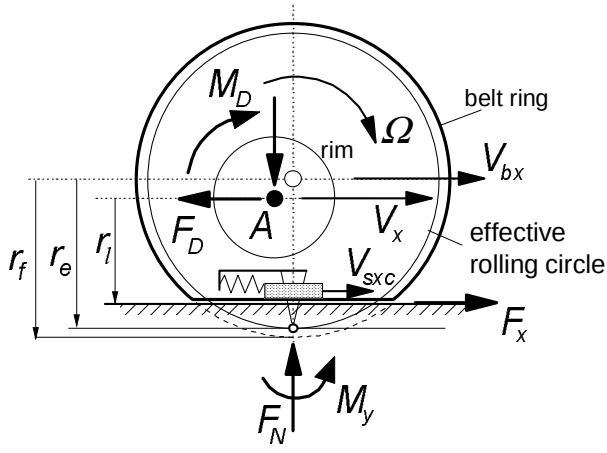

Fig. 9.32. The driven tyre-wheel combination with deflected belt and residual spring.

(9.155) the effective rolling radius r_e accomplishes the transmission of the rotational speed of the belt to the residual deflection rate of change. At steady-state condition, the deflection rates vanish and we have the following relation for the longitudinal slip speed:

$$V_{sxc} = V_x - r_e\Omega \tag{9.233}$$

We may consider the power balance of a wheel subjected to a propulsion torque M_D and a drag force F_D acting backwards on the wheel in its centre. Figure 9.32 depicts the situation. The connected power flow diagram is presented in Fig.9.33. The S represents a power source (the engine) and the R's are resistors where energy is dissipated. The balance of power requires that the equation holds:

$$M_D\Omega = F_D V_x + M_y\Omega - F_x V_{sxc} \tag{9.234}$$

or with (9.233):

$$M_D - M_y = F_x r_e \tag{9.235}$$

This suggests, at least for the model employed, that the moment arm equals the

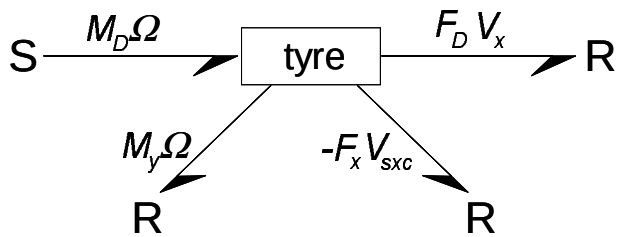

Fig. 9.33. Power flow diagram (bond graph) of driven tyre wheel combination in steady state.

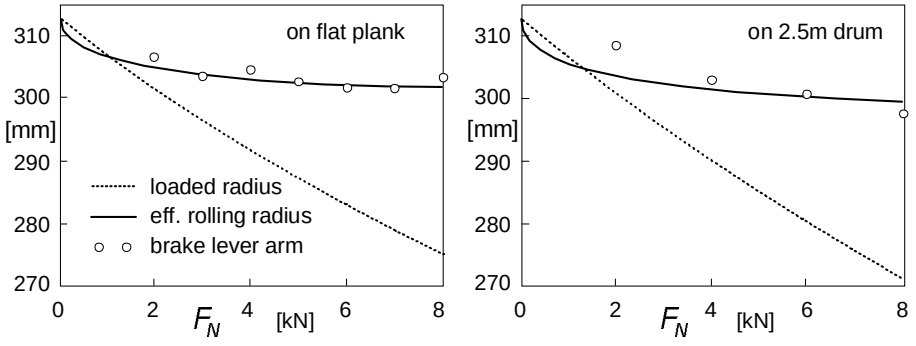

Fig. 9.34. Tyre radii as function of the normal load measured at zero or very low speed.

effective rolling radius (defined at zero driving or braking torque: free rolling). Consequently, the block named 'tyre' in the diagram of Fig.9.33 represents, when unfolding the bond graph, a junction structure containing a transformer with modulus r_e that transforms the angular speed into (a part of) the slip speed and, in opposite direction, the slip force into the drive torque.

Experiments have been carried out by Zegelaar on both the flat plank machine and the drum test stand to establish the effective rolling radius and the moment arm. In these tests a brake torque was applied to the wheel. The moment arm may be termed as the brake lever arm. The diagrams of Fig.9.34 have been obtained from tests performed at zero (brake lever arm) and very low speed of travel (effective rolling radius). Especially in case of the flat surface an excellent agreement has been found to occur. It is assumed that the growth of the effective rolling radius with speed is equal to that of the free tyre radius, cf. Eq.(9.219).

The diagrams of Fig.9.35 present the influence of speed on the two radii. The

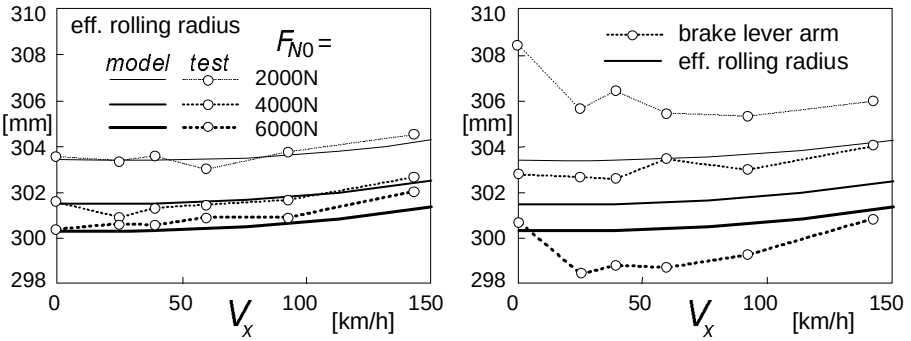

Fig. 9.35. Tyre radii measured on 2.5m drum as a function of the forward speed at three axle heights corresponding to the indicated initial loads. Average level and amplitude of brake torque are small.

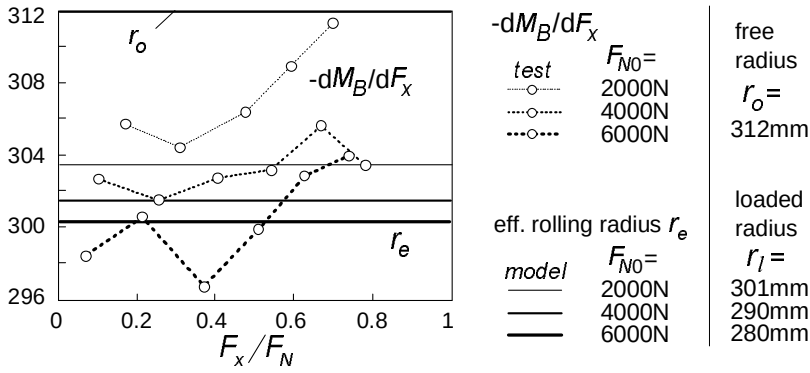

Fig. 9.36. Ratio of brake torque increment to brake force increment as function of level of brake force at a velocity of 25km/h and three different axle heights (loaded radii).

loaded radius has been kept fixed so that the vertical load rises when the speed is increased. Three different axle heights have been selected corresponding to the indicated initial vertical loads at zero speed F_{N0}. The left-hand diagram shows the degree of fit for the effective rolling radius. The right-hand diagram shows the correspondence with the brake lever arm. The tests from which the brake lever arm can be assessed have been conducted at low levels of the average and the standard deviation of the brake torque random input (120 and 22Nm respectively). The brake lever arm results from the longitudinal force response to the imposed brake torque variation at zero frequency. The influence of the average brake torque on the ratio of the torque amplitude and the force amplitude at zero frequency, $-dM_B/dF_x$, is given in Fig.9.36. This ratio does not appear to be a constant. Especially at low loads and relatively large braking forces large deviations arise from the value of the effective rolling radius. Obviously, due to its definition, the effective radius is not affected by the magnitude of the brake force.

With the effective radius adopted as the brake or driving torque moment arm the rolling resistance moment becomes (acting about *C-y* axis):

$$M_y = F_x(r_e - r_l) + F_r r_l \cdot \arctan(V_r/V_o) \tag{9.236}$$

which also contains the free rolling resistance moment $F_r r_l$ according to Eq.(9.230) and the arctan function to take care of a possible sign change of the wheel rolling speed.

In Appendix 3 a complete set of parameter values has been listed for both the *Magic Formula* model and the *SWIFT* model.

9.4. Dynamic Tyre Model Performance

A number of experiments has been conducted at the Delft University of Technology to assess the parameters of the dynamic model and to judge its performance. The steady-state side slip, longitudinal slip and camber force and moment characteristics have been typically assessed from over the road experiments with the Delft Tyre Test Trailer. For the model performance evaluation, steady-state characteristics have been used obtained from tests carried out on the drum with the strain gauge equipped measuring hub mounted in the measuring tower.

In Subsection 9.4.1 the dedicated dynamic test facilities will be described followed by Subsection 9.4.2 with the presentation of the model dynamic behaviour in comparison with experimental data. In Section 9.5 the model will be extended to include the description of running over road obstacles (cleats). The model development is followed by the presentation of experimental results compared with model behaviour.

9.4.1. Dedicated Dynamic Test Facilities

Dynamic Brake and Cleat Test Rig

Experiments have been conducted on the 2.5 m steel drum test stand provided with a specially designed rig equipped with a disc brake installation, cf. Fig.9.37. The wheel axle height can be adjusted to select the tyre initial load.

During the tests the axle position is held fixed and the wheel load rises with increasing speed. The wheel axle bearing attachments are equipped with piezo electric load cells. Steady-state or average force levels can not be measured with these force transducers. To provide an indication of the actual load increase with speed as measured on the measurement tower provided with a hub with strain gauges, Table 9.4 gives for a series of initial deflections (ρ_{z0} at zero speed) the values of the average vertical force derived from measurements at different speeds. The values have been obtained from Eqs.(9.217-219) after having fitted the parameters involved. The loads shown apply for the cases of nominal loads 2000, 4000, 6000N indicated in the graphs presented in the next section.

Much care has been taken to make the rig sufficiently rigid. This resulted in a lowest natural frequency just over 100 Hz which allows the use of test data up to ca. 60 Hz. In addition, to avoid force cross-talk, the brake shaft is connected

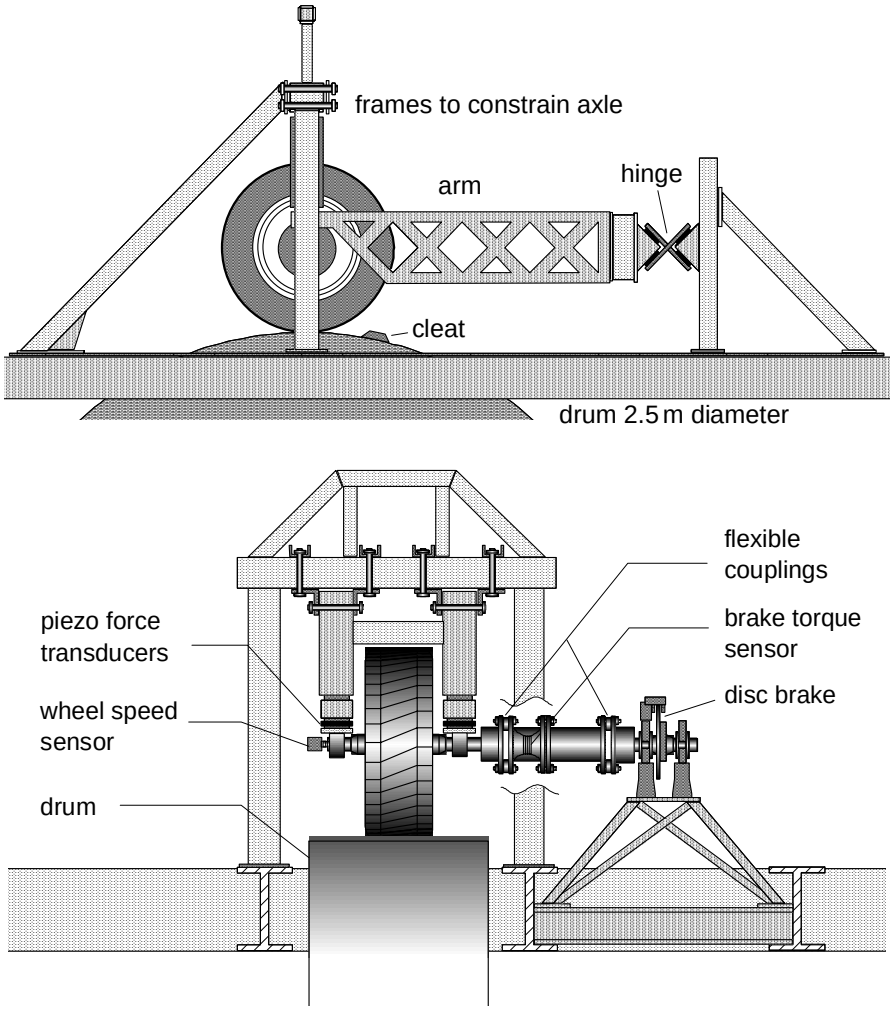

Fig. 9.37. Dynamic brake and cleat test facility in side and front view.

with the wheel shaft through an intermediate shaft equipped with two flexible couplings. These couplings are flexible in all directions except about the axis of rotation. This ensures that only the brake torque is transmitted to the wheel and that other parasitic forces and moments are largely suppressed. The brake torque is measured with strain gauges attached to the intermediate coupling shaft. A hydraulic servo system is used to control the brake pressure. The test facilities with numerous experimental and simulation results have been described in detail by Zegelaar (1998).

Table 9.4. Vertical load on 2.5m drum at constant axle height and increasing speed (tyre: 205/60R15 91V at 2.2 bar).

V_x [km/h]	initial vertical deflection ρ_{z0} [mm]			
0	0	11.90	22.57	32.33
	vertical load F_N [N] at constant axle height			
0	0	2115	4153	6133
25	7	2166	4246	6288
39	17	2202	4307	6352
59	40	2264	4404	6483
92	100	2388	4588	6727
143	249	2642	4939	7169

Pendulum and Yaw Oscillation Test Rigs

To assess the lateral and yaw tyre dynamic parameters two test rigs are used. One is the trailing arm 'pendulum' test stand with at one end a vertical hinge and at the other the steering head with piezo-electric measuring hub (Fig.9.38). At that point the arm is excited laterally up to ca. 25 Hz through a hydraulic actuator. The wheel load is adjusted by tilting the vertical hinge slightly forward. The arm length is 1.65m and the tyre is subjected to an almost purely lateral slip variation. The rig is useful to assess the overall relaxation length. The idea of the pendulum concept originates from Bandel et al. (1989). He designed and used an actual pendulum rig. The natural frequency of the freely swinging trailing arm with tyre rolling on the drum was taken to establish the tyre relaxation length σ. This quantity is the parameter of the first-order differential equation such as used in Chapter 7. Bandel found that σ increases with speed. However, when using a model with belt ring it turns out that the parameters can be kept constant, cf. De Vries (1998b). Consequently, tyre inertia, notably the gyroscopic couples, give rise to the speed dependency of the effective relaxation length.

Another rig was developed to investigate the response of the tyre subjected to yaw oscillations at frequencies up to ca. 65 Hz. The structure depicted in Fig.9.39 is light and very stiff. The two guiding members with flexible hinges intersect in the vertical virtual steering axis that is positioned in the wheel centre plane (centre point steering). A hydraulic actuator is mounted to generate the yaw vibration. The wheel axle is provided with a piezo-electric measuring hub. The tyre is loaded by adjusting the axle height above the drum surface. During

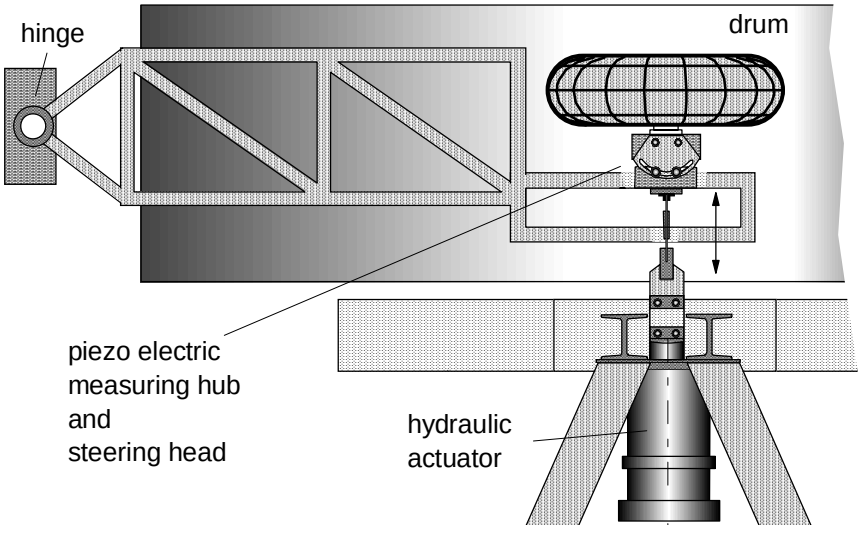

Fig. 9.38. The trailing arm 'pendulum' test rig exciting the tyre almost purely laterally. Frequencies up to ca. 25 Hz adequate for assessing the tyre relaxation length and gyroscopic coupling parameter.

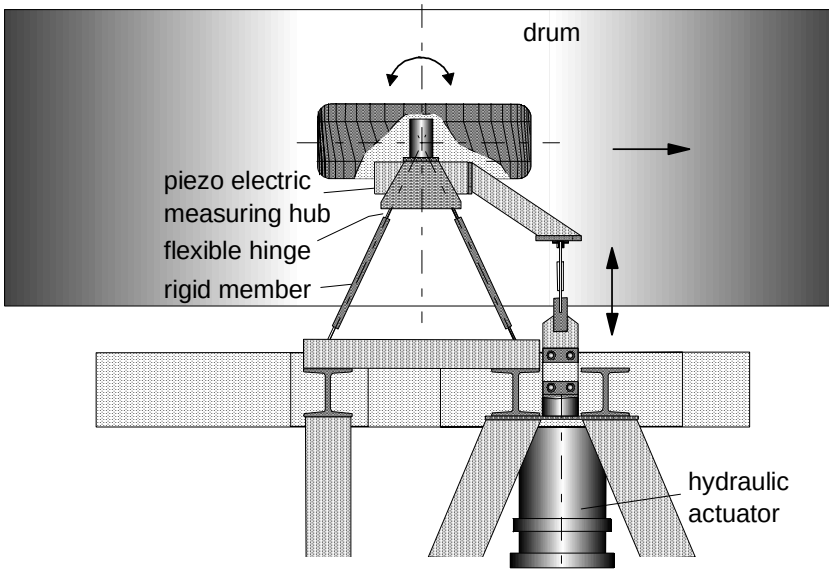

Fig. 9.39. The yaw oscillation test rig featuring centre point steering. Frequencies up to ca. 65 Hz enabling the assessment of tyre out-of-plane inertia and stiffness parameters including residual stiffnesses and rigid modes.

the test the loaded radius remains constant.

The measuring tower provided with a hydraulic vertical axle positioning installation is used to conduct pure braking and pure side slip tests as well as combined slip experiments at axle height oscillations and radial dynamic stiffness tests up to ca. 15 Hz.

A detailed description of the various side slip test facilities together with a full account on the numerous experiments conducted and the simulation results of the model have been given by Maurice (2000) and for motorcycle tyres by De Vries (1998a,b).

9.4.2. Dynamic Tyre Simulation and Experimental Results

In general, the values of the model parameters can estimated by minimizing the difference between measured and calculated frequency response functions (both amplitude and phase). In some cases (in particular the in-plane response) special aspects of the response functions had to be taken to successfully assist the parameter assessment. These aspects were: the position and width of resonance peaks (sidewall and residual stiffnesses and damping), the phase relationship in the low frequency range (overall relaxation length which it self is not a parameter!), the yaw response at zero speed (yaw residual stiffness). The residual damping ratios have been chosen equal to those of the sidewalls. Another help was the establishment of the inertia parameters of the relevant part of the tyre by cutting the tyre into pieces and considering the parameters of these parts. Rolling over a cleat might be used to estimate some of the parameters but the most accurate way is the identification through frequency response functions. These are obtained with the aid of the random brake test with brake torque (or the measured wheel speed) used as input, the yaw oscillation test and the vertical axle oscillation test.

Vibrational Modes

The vibrational modes of the tyre may be assessed through modal analysis of the tyre wheel system with axle fixed and tyre loaded or unloaded. When comparing these results with calculated modes using the parameter values assessed by means of the frequency response functions of the rolling tyre, it is found that the stiffnesses found from the dynamic rolling experiments are ca. 30% lower than those estimated from experimental modal analysis, cf. Zegelaar. These differences must be due to the different operational conditions and the larger amplitudes of the vibrations and higher temperatures that occur in the

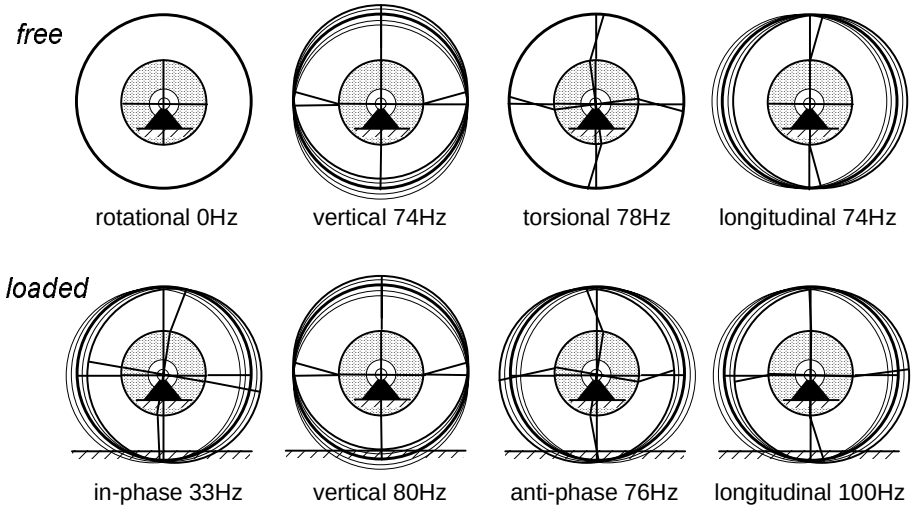

Fig. 9.39. Calculated in-plane vibrational modes of tyre/wheel system with axle fixed and tyre free or loaded on the drum surface with vertical load F_N = 4000N and at zero speed.

realistic rolling experiments.

The calculated vibrational rigid body modes at zero speed using the parameters as established from experiments carried out on the drum have been depicted in Figs.9.39 and 40.

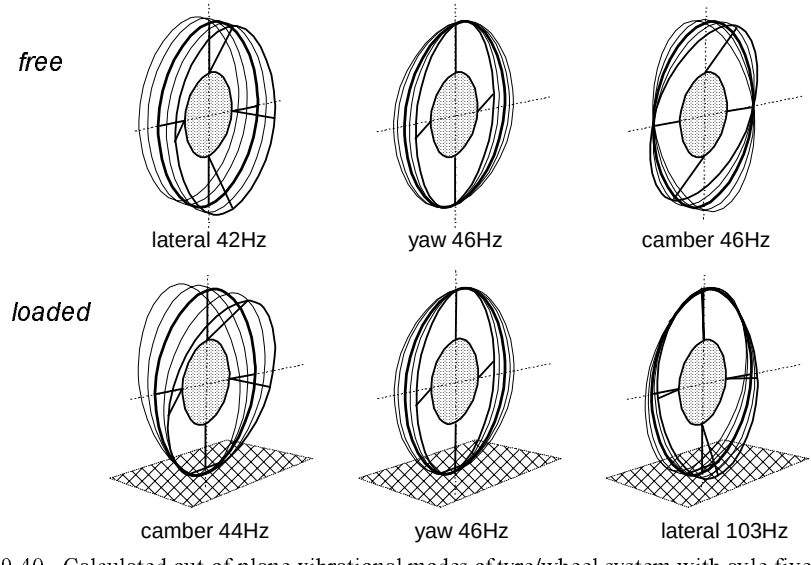

Fig. 9.40. Calculated out-of-plane vibrational modes of tyre/wheel system with axle fixed and tyre free or loaded on the drum surface with vertical load F_N = 4000N and zero speed.

We have four in-plane degrees of freedom of belt ring and wheel rim (two translational and two rotational) and three out-of-plane degrees of freedom (lateral, yaw and camber). As a consequence, we can distinguish four in-plane rigid modes and three out-of-plane rigid body modes. The mode shapes may change considerably when the tyre is making contact to the drum surface. The free rotation (0 Hz) mode changes into a mode with the belt and rim rotating in phase with respect to each other and the lateral and camber modes forming combinations: one low frequency mode with a low axis of camber oscillations and one high frequency mode with a rotation axis closer to top of the tyre and relatively large lateral deflections in the contact zone. The yaw mode in the loaded case should show a somewhat higher calculated natural frequency because in Maurice's model the spin response has not yet been included which means that the yaw stiffness of the tread elements is not taken into account.

The natural frequencies n and damping ratio ζ change with the speed of rolling. In Table 9.5 the values have been presented for the loaded tyre running at a velocity of 0 and 30 m/s. Especially the out-of-plane modes show considerable changes in frequency and damping. The camber and yaw mode natural frequencies which are identical in the unloaded zero speed case, exhibit a with speed growing mutual difference with the camber mode frequency becoming smaller and the yaw mode frequency larger.

Table 9.5. Natural frequencies and damping of vibrational modes of rigid ring tyre model calculated at a vertical load F_N = 4000N for two values of forward speed.

forward speed [m/s]	0	30	0	30
	n [Hz]		ζ [%]	
in-plane modes				
in-phase	33	30	0.10	0.25
vertical	80	75	0.05	0.05
anti-phase	76	71	0.05	0.05
longitudinal	100	129	0.77	0.35
out-of-plane modes				
camber	44	33	0.03	0.05
yaw	46	51	0.03	0.04
lateral	103	101	0.01	0.24

Frequency Response Functions

A typical example of measured and calculated in-plane frequency response functions has been depicted in Fig.9.41. Coherence functions show that the tests give sensible results up to ca. 80 Hz. Similar response functions have been obtained by Kobiki et al. (1990). The left-hand diagram of the figure represents the response function of the brake force to the imposed brake torque variation considered to be applied in the torque meter. The right-hand diagram shows the response of the force to wheel slip variations. The wheel slip is derived from the measured wheel and drum speeds.

The two peaks occurring in the left-hand diagram belong to the in-phase and the anti-phase modes. The single peak showing up in the right-hand diagram belongs to the mode that would arise if the rim is fixed also in rotation. The natural frequency lies in between the frequencies of the peaks in the left diagram. The natural freqencies contribute to assess the sidewall stiffnesses. From the right-hand diagram two quantities can be derived: the slip stiffness and the overall relaxation length. Through the latter, additional information is obtained to find the fore and aft residual stiffness. From careful interpretation of the frequency response functions assessed at different speeds, the sidewall stiffness dependence on the speed of rolling has been ascertained. Resulting calculated response functions at different loads and brake torque level gave satisfactory agreement with measured behaviour. We refer to the original work of Zegelaar (1998) for detailed information.

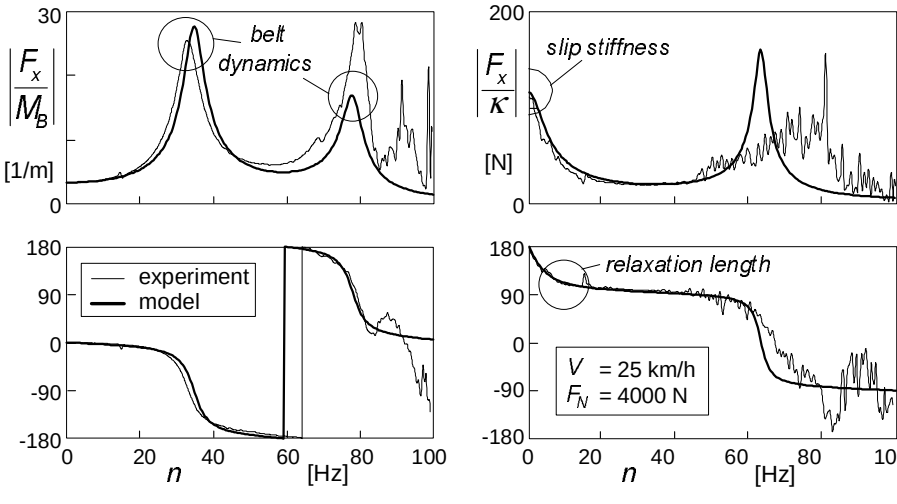

Fig. 9.41. Measured and calculated in-plane frequency response functions at an average braking force of 450N and assessed at a braking force standard deviation of 75N.

The out-of-plane frequency response functions of the side force and the aligning torque to yaw oscillations have been presented in Figs.9.42,43. The parameters have been assessed by minimising the difference between measured and calculated (complex) response functions. The correspondence achieved between measured and computed curves at different speeds, loads and side slip level is quite satisfactory, cf. Maurice (2000) for more details. To conduct a proper comparison, the measured data have been corrected for the inertia of the wheel and part of the tyre that moves with the wheel. The expected splitting up of the single peak at low velocity into two peaks, one belonging to the camber mode and the other to the yaw mode, and the growing difference of the two natural frequencies with increasing speed is clearly demonstrated. This phenomenon which is due to the gyroscopic action, has already been observed to occur with the stretched string model with inertia included approximately, cf. Fig.5.40. It is of importance to note that the theoretical results have been established by using the model that did not include the equations for the response to spin (9.177-180). Especially the aligning moment is sensitive to turn slip. The moment response curves to side slip and yaw of the massless tyre model as depicted in Fig.9.16 are quite different. The dip in the moment amplitude response curve to yaw oscillations occurring in the curve for M_ψ in Fig.9.16 does not appear in the curve for the response to side slip M_α. This dip also appears in the curves of Fig.5.40 where spin is included. It is surprising to see that a similar dip occurs in the Figs.9.42,43. The minimum arises here due to the tendency of the response to side slip to decrease and tend to zero at increasing path frequency while at the same time the moment amplitude increases due to tyre inertia when approaching the resonance peak. The dip in the measured curve of the upper right-hand diagram of Fig.9.42 at 25km/h is deeper than the one shown by the theoretical curve of the lower diagram. This may be due to the additional action of spin in the actual tyre. As demonstrated by both the theoretical and measured curves of Fig.9.43 the dip disappears altogether at larger average side slip.

The experiments conducted with the trailing arm 'pendulum' test rig where the tyre is subjected to almost pure side slip and the spin is very small, also show satisfactory correspondence with model behaviour (Maurice, 2000; also: De Vries, motorcycle tyres, 1998b). This also appears to hold for a limited number of conducted combined slip tests and the response to vertical axle motions at side slip and braking carried out with the measuring tower.

Apparently, the rigid ring model provided with the short wavelength transient slip model is very well capable of describing the dynamic tyre behaviour in the frequency range up to about 60 Hz. Furthermore, it may be concluded that the spin part is only necessary when dealing with short wavelength, especially low speed phenomena where tyre inertia is less important, such as with parking.

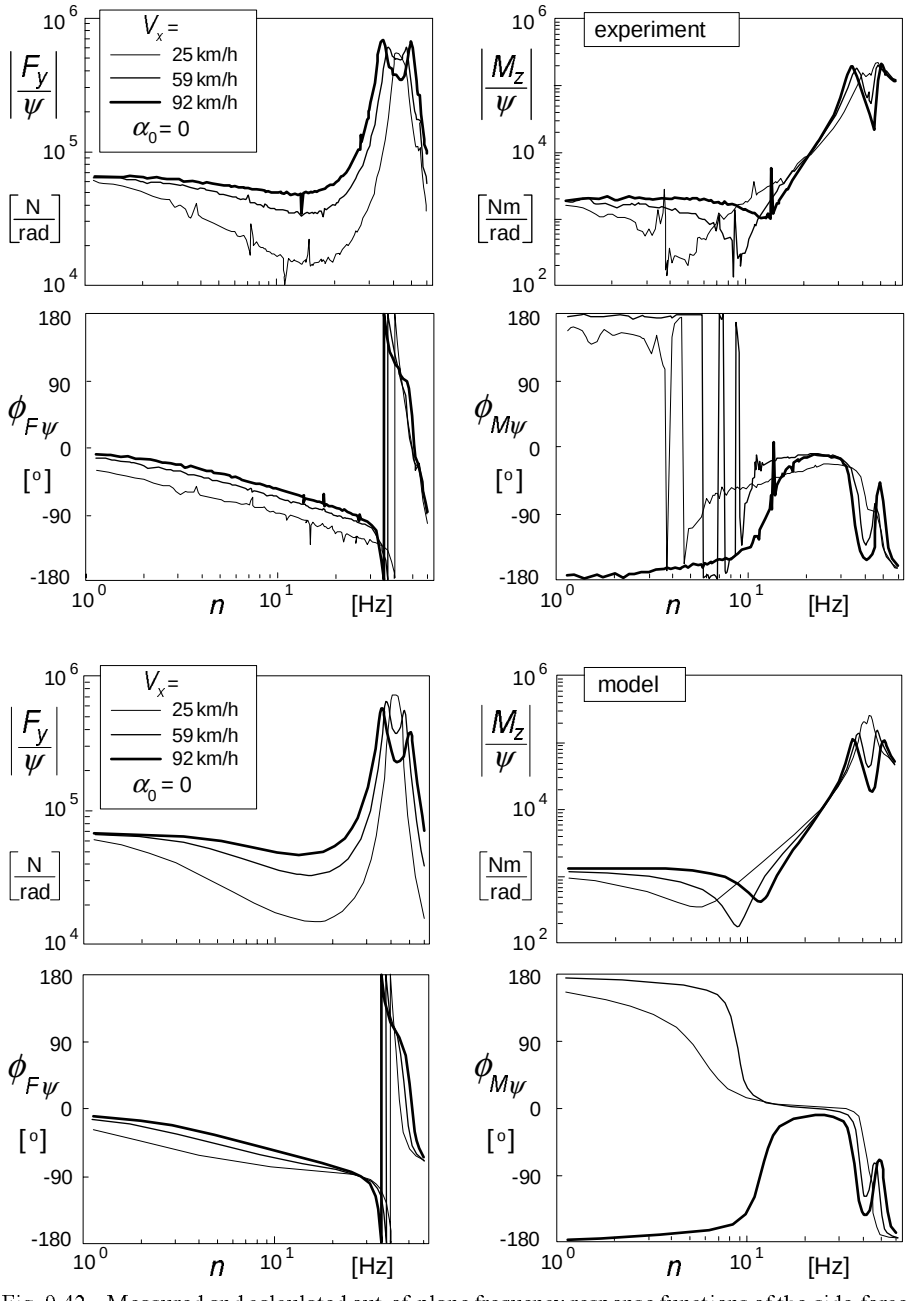

Fig. 9.42. Measured and calculated out-of-plane frequency response functions of the side force and aligning torque to steer angle variations at zero average slip angle for three values of forward speed and normal load F_N = 4000N.

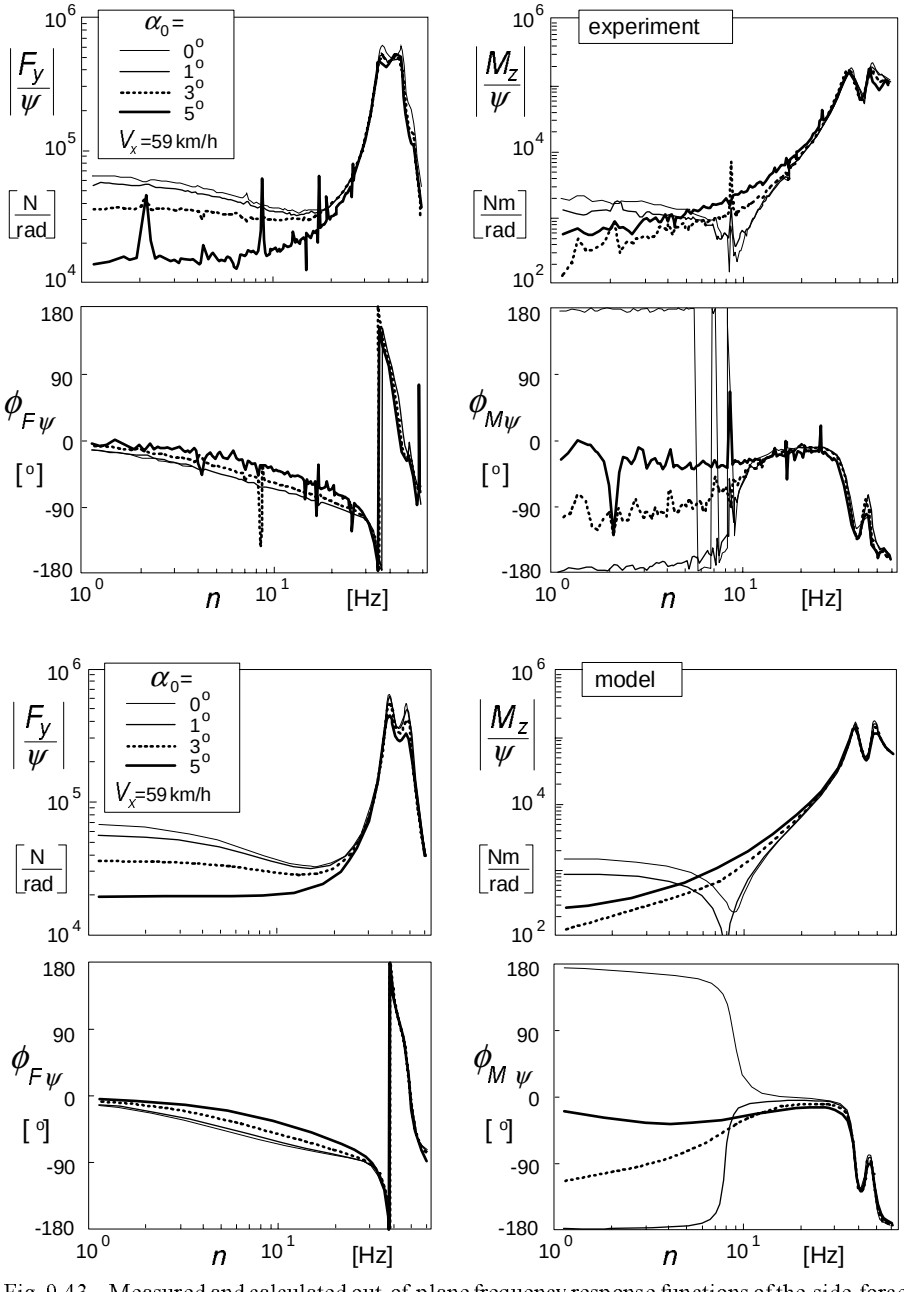

Fig. 9.43. Measured and calculated out-of-plane frequency response functions of the side force and aligning torque to steer angle variations at one value of speed and at four levels of average side slip and wheel load F_N = 4000N.

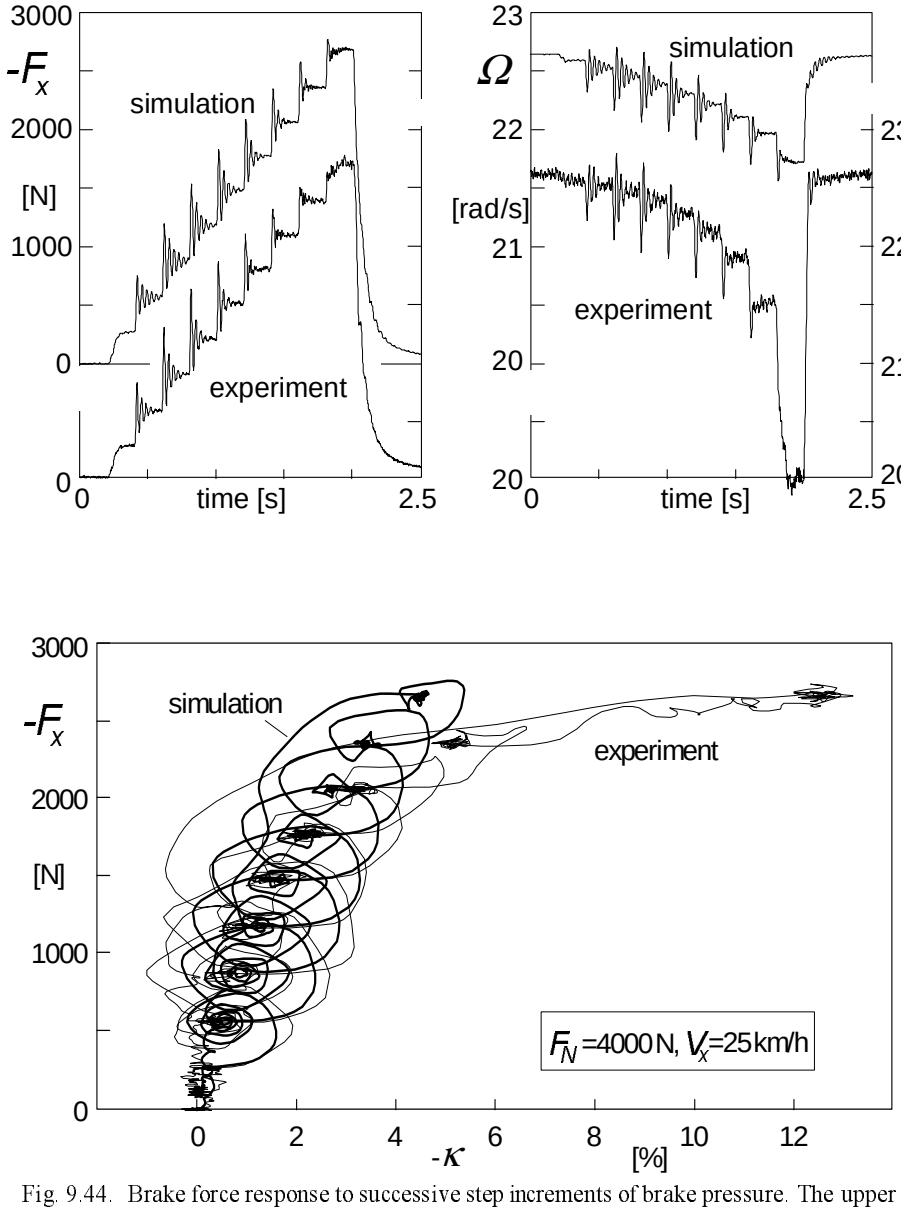

Fig. 9.44. Brake force response to successive step increments of brake pressure. The upper diagrams depict the variation of force and wheel speed of revolution with time. The lower figure shows the loops in the force versus wheel slip diagram. Apparently, the actual friction coefficient is lower than assumed in the model. (Zegelaar, 1998).

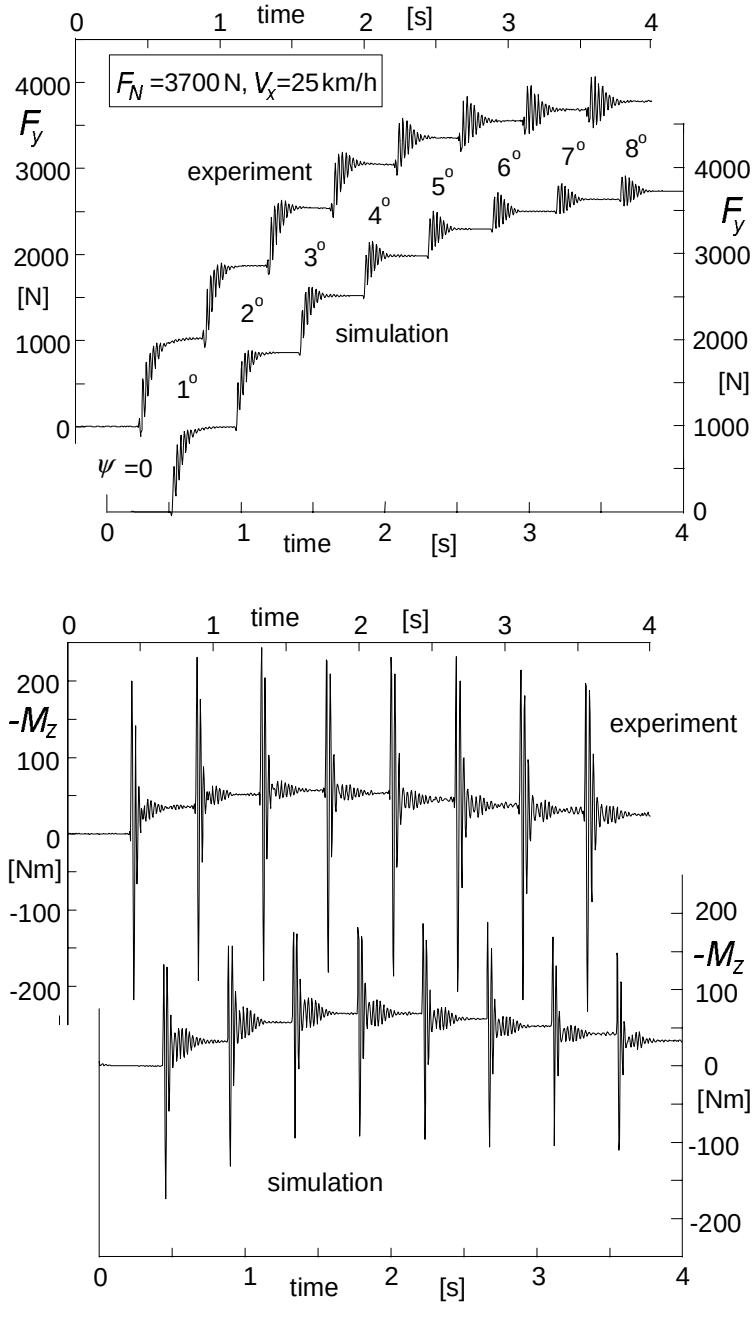

Fig. 9.45. Side force and aligning torque response to successive step changes in steer angle. (Maurice, 2000)

Time Domain Responses

To demonstrate the performance of the model, simulations and experiments have been carried out pertaining to successive stepwise increases in brake pressure and steer angle.

The response of the longitudinal force and the associated wheel speed has been presented in Fig.9.44. The lower diagram clearly depicts the oscillatory variation of the force versus slip ratio. The measured response shows a faster decay of the wheel velocity after the highest brake effort has been reached. Apparently, this is due to the friction coefficient being lower in the experiment than assumed in the model. Finally, the brake is released and the wheel spins up again. The oscillations (ca. 28Hz) correspond to the in-phase vibrational mode of the system with the brake disc/axle inertia included.

Figure 9.45 shows the responses to successive changes in steer angle for both the side force and the aligning torque at a given load and speed. The responses clearly show vibrations attributed to the yaw/camber mode with natural frequency of ca. 40Hz (cf. Fig.9.42, 25 km/h). Also, the decrease of the overall relaxation length at larger slip angle can be recognized.

9.5. Dynamic Tyre Response to Short Road Unevennesses

The actual road surface profile over which the tyre rolls may contain spectral components showing relatively short wavelengths. If the wavelength is smaller than two to three times the contact length a geometric filtering of the profile becomes necessary if the tyre model employed is assumed to contact the road in a single point. For the SWIFT model a special filter has been developed that takes care of the envelopment properties of the tyre and the variation in effective rolling radius that occurs when the tyre rolls over a short obstacle. The envelopment of an obstacle takes place in the contact zone. It is assumed that local dynamic effects can be neglected. The changing conditions that arise for the tyre when quasi-statically traversing an obstacle are measured and modelled and subsequently used as effective road plane inputs for the tyre model at higher speeds. The belt inertia takes care of the dynamic effects.

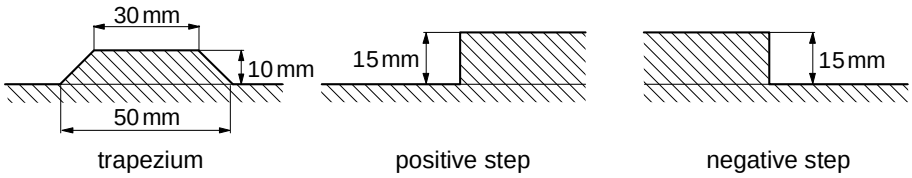

Fig. 9.46. Three typical obstacles used in Zegelaar's research.

9.5.1. Tyre Envelopment Properties

In the literature one finds numerous publications on tyre envelopment behaviour. We refer to the study of Zegelaar (1998) for an extensive list of references. A number of these will be mentioned here. Important experimental observations have been made by Gough (1963). He indicated that the tyre that is slowly rolled at constant velocity and axle height, over a cleat with length much smaller than the contact length, exhibits three distinct responses: (1) variations in the vertical force, (2) variations in the (horizontal) longitudinal force and (3) variations in the angular velocity of the wheel. Lippmann et al. (1965,67) studied the responses of both truck and passenger car tyres rolling over short sharp unevennesses like cleats and steps of several heights. From the experimental observations it has been concluded that an almost linear relationship exists between tyre force variation and step height. The superposition principle may therefore be employed to assess the response to an arbitrarily shaped unevenness by taking the sum of responses to a series of step changes in road surface height. These observations are expected to be approximately true if the obstacle height is not too large.

For three typical road unevennesses, depicted in Fig.9.46, Zegelaar has measured the responses of the tyre at three different constant axle heights. To avoid dynamic effects, the velocity of the drum on which the cleat is attached (Fig.9.37) was maintained at the very low level of 0.2 km/h.

Figure 9.47 presents the measured vertical load F_V, horizontal longitudinal force F_H and the from measurements derived effective rolling radius r_e. The latter quantity is obtained from the variation of the wheel rotation rate $\mathrm{d}\theta/\mathrm{d}s$ which is defined as: the difference of the incremental wheel angular displacement and the constant (undisturbed) incremental rotation, as a ratio to the increment of the travelled distance of the wheel axle. The following equations apply:

$$r_e = \frac{V_x}{\Omega}, \quad V_x = \frac{\mathrm{d}s}{\mathrm{d}t}, \quad \Omega = \Omega_o - \frac{\mathrm{d}\theta}{\mathrm{d}t}, \quad r_{eo} = \frac{V_x}{\Omega_o} \tag{9.237}$$

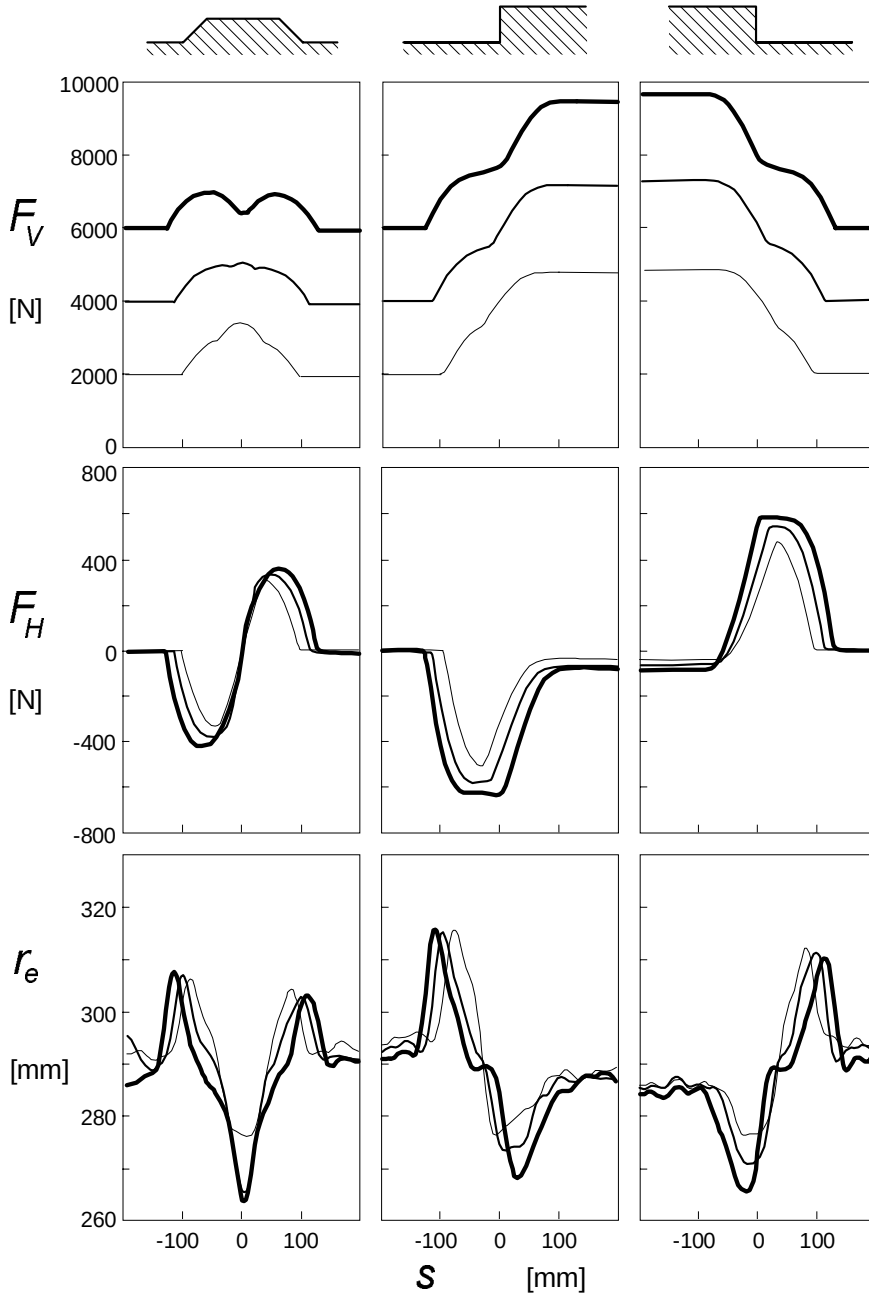

Fig. 9.47. Rolling over a trapezium cleat, an upward and a downward step (Fig.9.46) at very low speed and for three axle heights. Diagrams show measured variations of the vertical force F_V(upward +), the longitudinal horizontal force F_H (forward +) and the effective rolling radius r_e, Eq.(9.238). Tyre dimensions: 205/60R15).

and hence

$$r_e \approx r_{eo}\left(1 + r_{eo}\frac{\mathrm{d}\theta}{\mathrm{d}s}\right) \tag{9.238}$$

The peculiar shapes of the various response curves correspond very well with results found in the literature. Several tyre models have been used to simulate the experimental observations. Davis (1974) has developed a model featuring independent radial springs distributed along the circumference. By giving the individual springs a non-linear degressive characteristic the model is able to generate a vertical force response curve with the typical dip that shows up when running at relatively high initial loads. Badalamenti and Doyle (1988) developed a model also consisting of radial springs but now with additional interradial spring elements that connect the end points of adjacent radial springs in radial direction. When the deflections of neighbouring radial springs are not equal to each other, the interradial spring generates a radial 'shear force' that acts on the end points of the radial springs. Mousseau et al. (1994) and Oertel (1997) simulate the tyre rolling over a positive step by means of (different types of) finite element models. Zegelaar uses the flexible ring (belt) model of Gong (1993), that was developed with the aid of the modal expansion method, as a reference model in his research. The addition of tread elements with radial and tangential compliances to Gong's model did enable Zegelaar to employ the model for the study of traversing obstacles. Also this model shows responses very similar to the measured behaviour. Schmeitz (2001) employs the radial interradial model as a possible basis for the pragmatic model running over an arbitrary road surface.

9.5.2. The Effective Road Plane

To arrive at a geometrically filtered road profile description Bandel follows the idea of Davis and introduces the effective road plane. The effective plane height and slope variation may be established by conducting an experiment where the wheel is rolled at a very low velocity over an uneven road surface at constant axle height (above a horizontal reference plane) and the forces are measured, cf. Fig.9.48. It is argued that the resulting force (with the rolling resistance force omitted) that acts upon the wheel axle, is directed perpendicularly to the effective road plane. By dividing the variation of the measured vertical force, which is approximately equal to the vertical component of the normal force F_N, by the radial stiffness of the tyre, the effective road height variation, $-w$, is obtained. The effective slope is found by dividing the longitudinal horizontal force (after

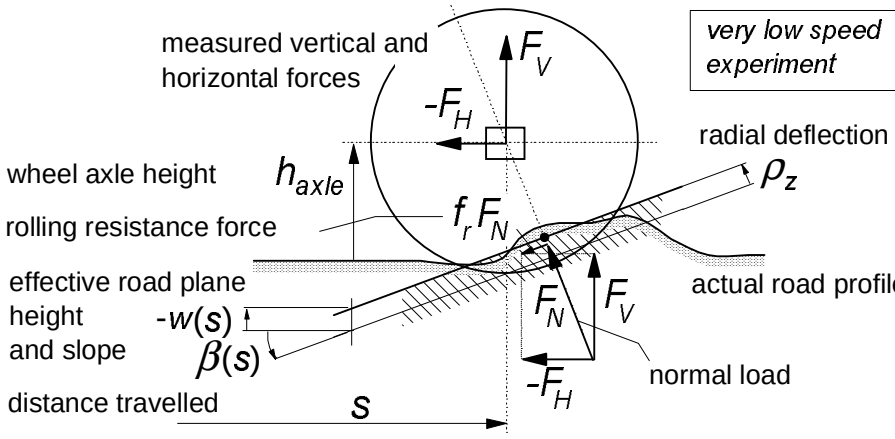

Fig. 9.48. The wheel rolled over a road irregularity at constant axle height to establish the effective road plane variation.

having subtracted the relatively small rolling resistance force) by the vertical force. Both effective quantities are functions of the longitudinal coordinate of the wheel centre s. The following formulae apply, cf. Eq.(9.230):

$$-w = \frac{\tilde{F}_V}{C_{Fz}} \approx \frac{\tilde{\rho}_z}{\cos\beta} = \frac{\tilde{F}_N}{C_{Fz}\cos\beta} \tag{9.239}$$

$$\tan\beta = -\frac{F_H + f_r F_N/\cos\beta}{F_V} \approx -\frac{F_H + f_r F_V}{F_V} \tag{9.240}$$

For the description of the effective road input the pragmatic modelling approach initiated by Bandel et al. (1988) and further developed by Zegelaar and extended by Schmeitz is most useful and will be discussed below. Bandel discovered that the function representing the response of the change in vertical force to a short rectangular obstacle, featuring the dip at high load and the nipple at low load, can be decomposed into two identical basic functions, which are each others mirror image. The basic functions are found to be approximately independent of the initial tyre vertical deflection, that is: independent of the axle height. To find the force response curve at a possibly different axle height, the basic force curves are shifted with respect to each other over a distance a bit less than the contact length and then added together. By dividing the result by the radial stiffness the effective road plane height variation is found.

Also for the measured longitudinal force variation a pair of basic force

functions can be assessed. Again, these are identical but the first must now be subtracted from the second and the result divided by the horizontal shift and the radial stiffness to find the variation of the slope of the effective road plane.

Zegelaar did experiments with the trapezium shaped cleat as indicated in Fig.9.46. He found basic curves which are practically symmetric in shape. Mirror imaging was not necessary and did certainly not apply for non-symmetric unevennesses such as the step. Also, the basic functions assessed for the vertical force appeared to be practically the same as the ones for the longitudinal force. These findings helped a lot to make the principle of the basic function easier and more widely applicable. One basic curve established from an experiment with a tyre rolling over a given road irregularity at a fixed constant axle position should be sufficient to serve as the source for assessing the equivalent road plane height

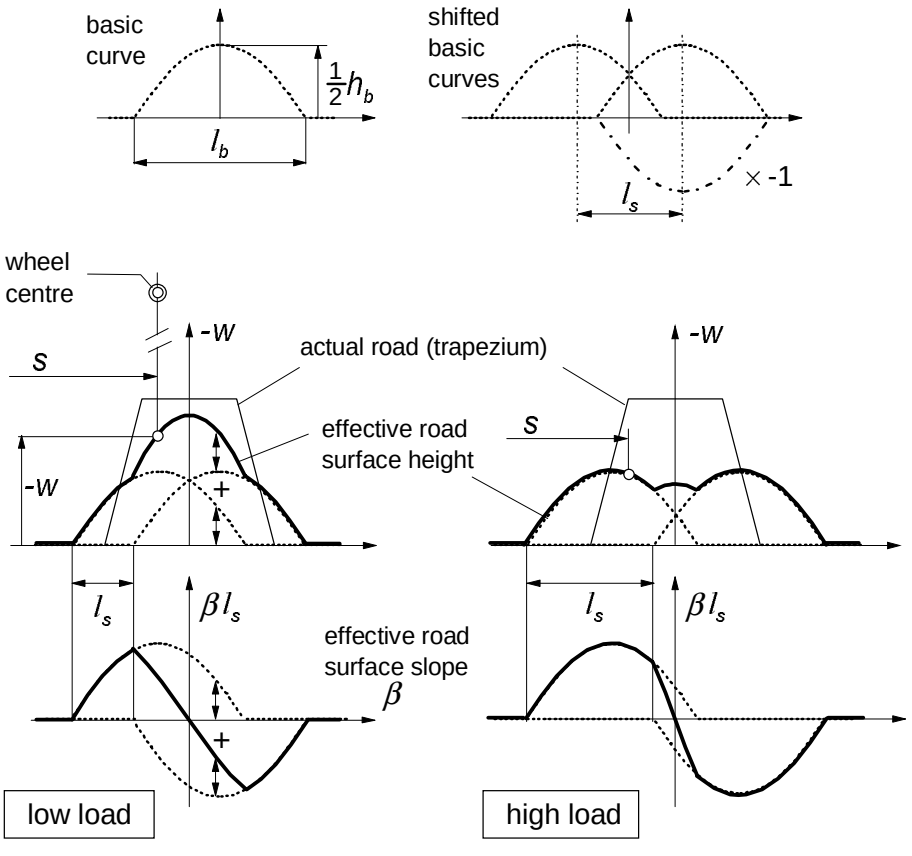

Fig. 9.49. The construction of the curves representing the effective height end effective slope of the local road plane from the basic function associated with the trapezium cleat.

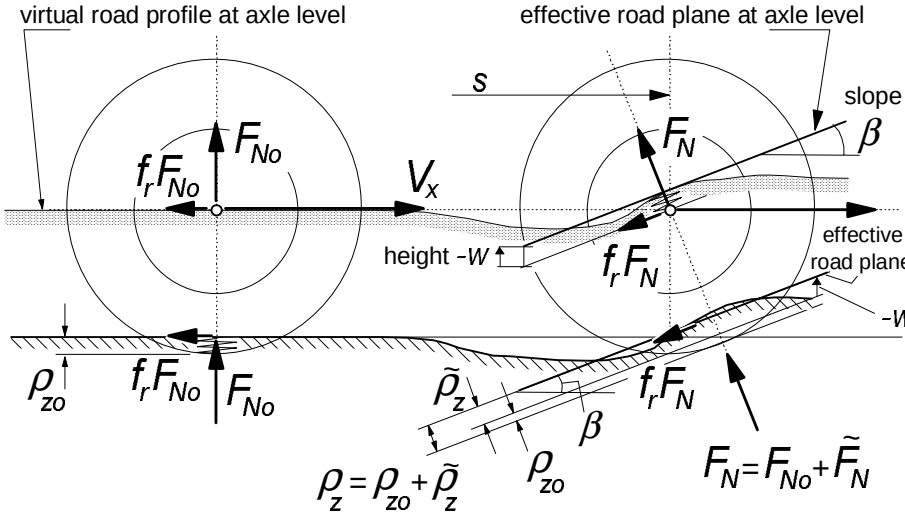

Fig. 9.50. The virtual road profile and effective road plane as sensed at wheel axle level.

and slope. These two equivalent quantities will later be completed with a third quantity: the effective rolling radius, to form the complete set of three effective inputs from road to tyre model.

Figure 9.49 demonstrates the use of the basic curve for the effective road plane height applicable for the tyre rolling over a short trapezoidal cleat at a constant axle height. The vertical scale has been exaggerated. The basic curve is approximated by a half sine wave. The base length of the curve is denoted with l_b, its height with $0.5h_b$ and the shift with l_s. The with travelled distance s varying values of w and β define the local effective wheel plane. Figure 9.50 clarifies the actual situation. At wheel position s the current effective road plane has been indicated. The virtual road profile defined as the path of the wheel centre that would occur at constant normal load has been drawn together with the actual road profile. The distance of the wheel centre location with respect to the virtual road profile corresponds to the increase of the actual radial tyre deflection. The distance of the wheel centre to the indicated effective road plane (translated to axle level with w and β regarded) is the increase in effective radial deflection which together with the initial deflection becomes equal to ρ_z.

The Two-Point Follower Technique

In Fig.9.51 an alternative technique is introduced using a single basic curve with full height h_b and a two-point follower. If the two points are moved along the basic curve the midpoint describes a curve that represents the characteristic

for the effective road height. The inclination angle of the follower corresponds to the slope of the effective road plane.

The response to a step change in road level may serve as a building block to compose the response to an arbitrary road unevenness. The corresponding basic function may be termed as the elementary basic function. The elementary basic curve may be represented by a quarter sine wave. For the steps given in Fig.9.46 the parameters of the basic curve have been determined by fitting the calculated force response to the vertical force variation measured for a series of axle heights (Fig.9.47).

Figure 9.52 shows the elementary basic curve for the upward step and the resulting effective road level and slope characteristics assessed by using the two-point follower technique. For the downward step the fitted basic function appears to come very close to the mirror image of the one determined for the upward step. The difference may very well be neglected. The parameters that control the size and position of the basic curve are the length l_b, the shift l_s and so-called offset l_f. The height h_b is equal to the step height. The offset is a new quantity that defines the position of the basic curve with respect to the step, cf. Fig.9.52.

A further important step is taken in the development of the assessment and use of basic functions. It is obvious that during the experiment that is performed at constant axle height, the normal load changes while rolling over an obstacle. The shift has been seen to change with axle height, that is: with a changed vertical load. The shift that corresponds to the length of the two-point follower has been found to be equal to a little less than the contact length. It seems therefore to be practical to adapt the strategy followed sofar. We will henceforth define the basic curve to hold for a constant vertical load which may be the tyre nominal load. The experiments are to be carried out at constant vertical load and at very low speed of travel. Schmeitz (2001) conducted such tests with the flat plank machine, cf. Sec.9.5.5. The effective road plane height variation follows directly from the experiment. Division of the vertical force by the radial stiffness is not needed anymore which relieves us from accounting of a possibly non-linear tyre compression characteristic, cf. Eq.(9.220). In addition, since the rolling resistance is now assumed to remain constant, it is no longer necessary to take account of the rolling resistance force when determining the effective slope, as was done in Eq.(9.240).

Zegelaar calculated the step response with the flexible ring model provided with tread elements and found good agreement with measured data. By fitting the quarter sine curve representing the basic function, parameter values have been assessed for a wide range of step heights. The results have been compared with the values calculated for a rigid wheel or zero normal load. Figure 9.53 illustrates the extreme case of the rigid wheel rolling over a step.

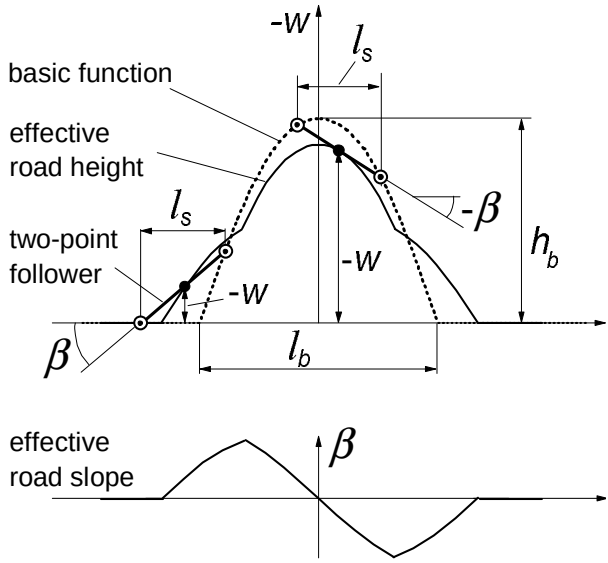

Fig. 9.51. Alternative method to determine the effective road height and slope using the basic curve with height h_b and the two-point follower with length equal to the shift l_s.

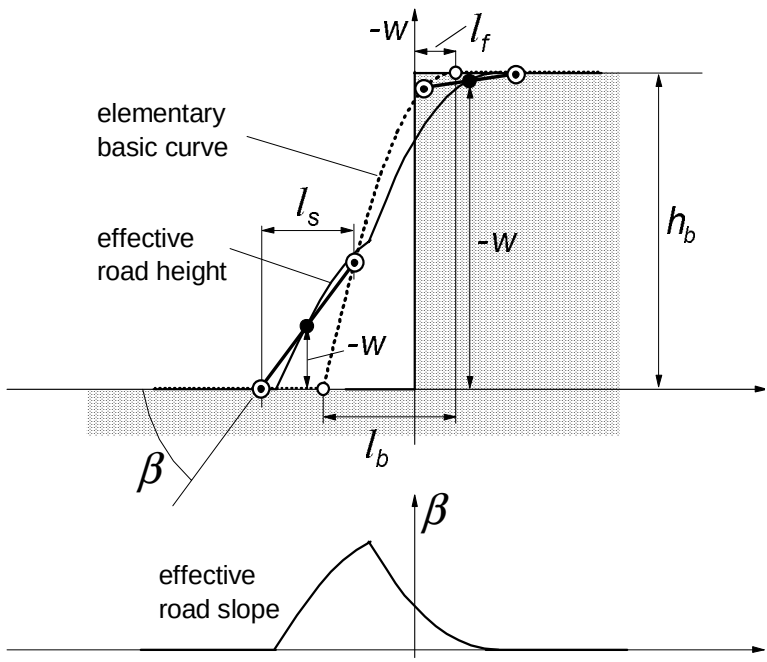

Fig. 9.52. The effective road response curves resulting from the (elementary) basic curve associated with the step change in road level by using the two-point follower concept.

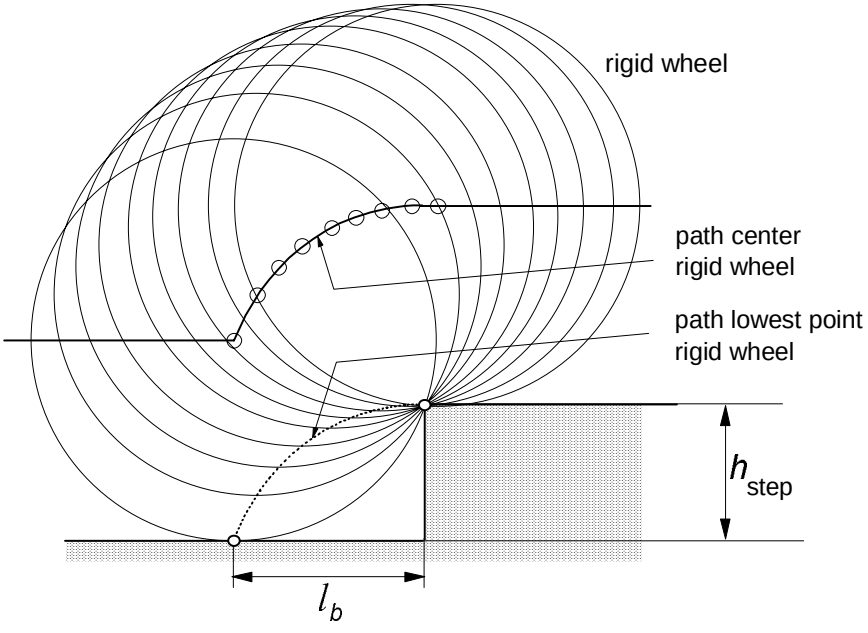

Fig. 9.53. The rigid wheel rolling over an upward step change in road level.

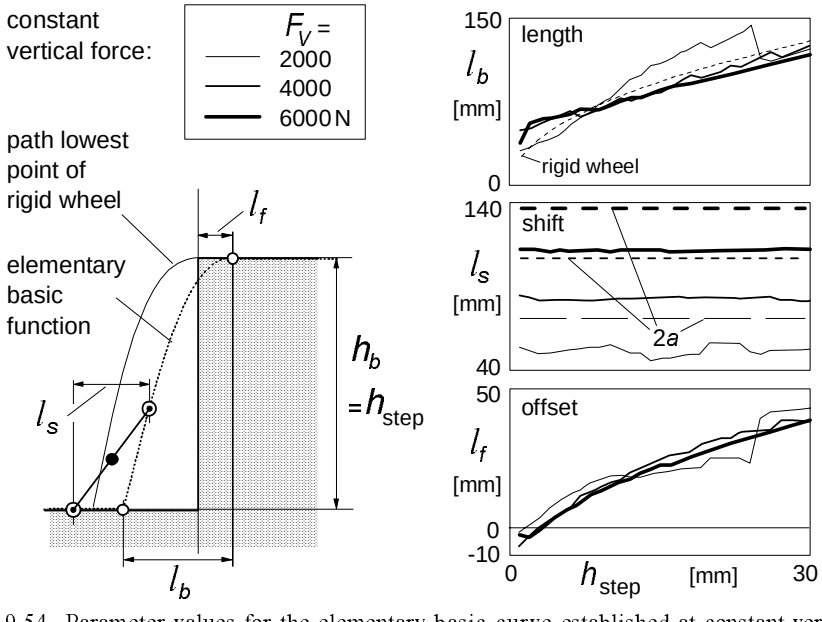

Fig. 9.54. Parameter values for the elementary basic curve established at constant vertical loads by computations using a flexible ring model with tread elements, Zegelaar (1998).

In Fig.9.54 Zegelaar's calculated results have been presented for a series of vertical loads F_V. The diagrams show that the basic curve length l_b and the offset l_f do change with step height h_{step} but are approximately independent of the vertical load F_V. The curve length may be estimated from the circle curve length, Fig.9.53:

$$l_b = \sqrt{r_o^2 - (r_o - h_{\text{step}})^2} \tag{9.241}$$

The horizontal shift l_s amounts to approximately 80% of the contact length $2a$. The offset may be approximated by a linear function becoming zero at vanishing step height.

The approach of employing basic curves to assess the effective road height and slope as inputs to the dynamic tyre model has been found adequate for the description of the response to single obstacles. Although, in principle, the method may be used also for a series of obstacles or for an arbitrary road surface profile with the elementary basic curve (that holds for a step unevenness) as building block, the rules that are to be followed may become rather cumbersome. For such a more general application the method developed by Schmeitz (2002) that is based on the so-called tandem egg technique is considered to be the best option.

The Tandem Egg Technique

Instead of using the basic profile and running over that with the two-point follower we may get a step closer to the actual tyre shape moving over the actual road surface profile. Schmeitz discovered that the principle of the circle moving over the surface (Fig.9.53) may be adopted but than with an ellipse instead of the

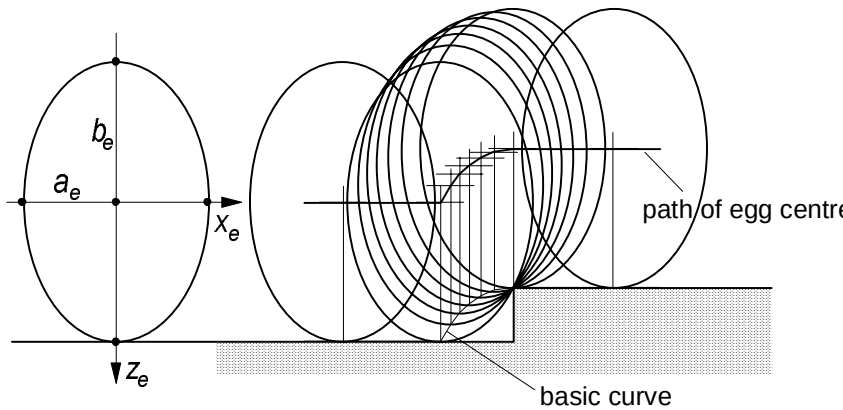

Fig. 9.55. 'Egg' moving over step road profile, producing basic curve.

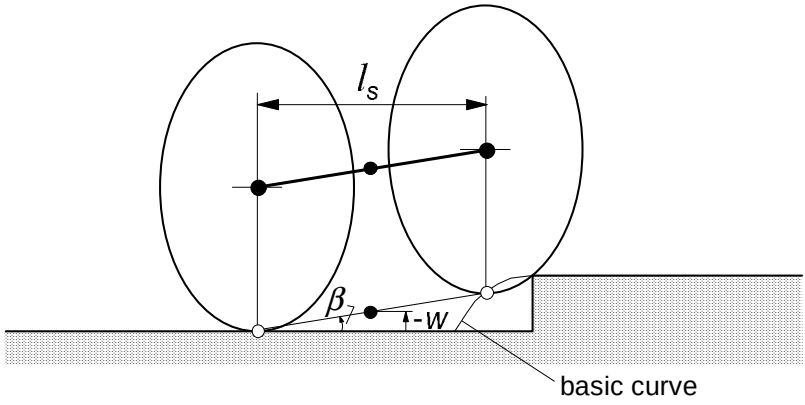

Fig. 9.56. The two-egg tandem configuration of Schmeitz, generating the effective road height and slope.

circle. The ellipse that takes the shape of a standing egg has a height approximately equal to that of the tyre but a curvature radius at the lowest point considerably smaller than that of the free tyre. In that way, the egg touches the step later than the circle. By choosing an optimal shape of the ellipse, the role of the offset l_f (that changes with step height) of the basic curve indicated in Fig.9.54 can be taken care of automatically. In Fig.9.55 the egg moving over a step has been illustrated. The dimensions of the egg are defined by the ellipse parameters. In terms of the coordinates x_e and z_e the ellipse equation reads:

$$\left(\frac{x_e}{a_e}\right)^{c_e} + \left(\frac{y_e}{b_e}\right)^{c_e} = 1 \tag{9.242}$$

The effective road height and slope can be assessed by using two eggs following each other at a distance equal to the shift length l_s. The change in height of the midpoint of the connecting line and the inclination of this line represent the effective road height and effective slope. Figure 9.56 illustrates this 'tandem egg' configuration. Fitting the tandem egg parameters follows from assessing the best approximation of low speed responses of a tyre running over steps of different heights at a number of constant vertical loads. Once the ellipse parameters have been established, the egg dimensions are not affected by step height or vertical load. It is not surprising that analysis shows that the shape of the lower part of the ellipse turns out to be practically identical to the contour of the tyre in side view just in front of the contact zone up to the height of the highest step considered in the fitting process. The tandem base length l_s does depend on the vertical load.

In a more efficient way of operation the basic curve or profile is assessed first, that is before the actual wheel rolls over the road section considered. This

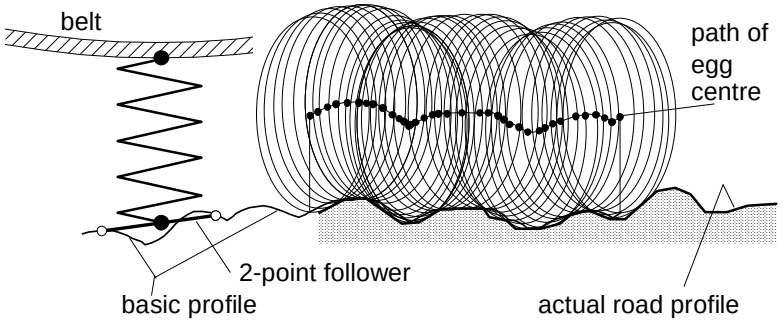

Fig. 9.57. The egg generating the basic road profile and three-point follower moving over it.

is achieved by sending one egg over a short section of the road ahead and having that determine the basic curve. The two-point follower is subsequently moved, concurrently with the actual wheel forward motion, over the basic profile, thereby generating the effective road inputs which are fed into the tyre model. Figure 9.57 illustrates the procedure. When traversing a single step it is, of course, more efficient to use an analytic expression for the basic curve based on Eq.(9.242).

9.5.4. The Effective Rolling Radius when Rolling over a Cleat

The third effective input is constituted by the effective rolling radius that changes when a road unevenness is traversed. In Fig.9.47 these variations have been shown in the lower diagrams. The curves have been derived from measurements by using the Eqs.(9.237,238).

In the effort to model the aspect of rolling over an obstacle it is important to realise that we have three elements that contribute to the variation of the rolling radius:

1. increment in normal load
2. the local slope
3. the local curvature

Figure 9.58 illustrates the matter. The first item has been dealt with before, cf. Sec.8.3.1, Fig.8.12, Eq.(8.38) and Eq.(9.232). According to the latter equation the effective radius is a function of vertical load and speed of rolling. In Fig.9.59 model considerations and the from experiments resulting graph have been repeated. For small variations in radial deflection we may employ the equation:

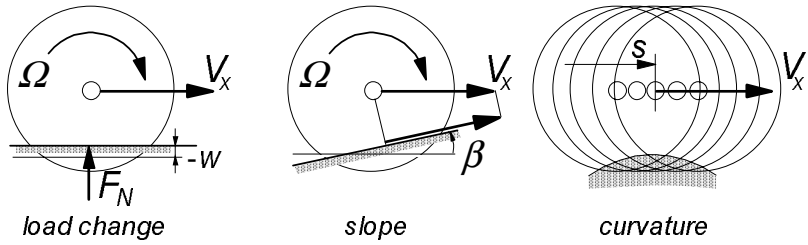

Fig. 9.58. Three contributions to the change in effective rolling radius.

$$\tilde{r}_{e\eta} = -\eta\tilde{\rho}_z \tag{9.243}$$

The second contribution accounts for the fact that at a slope the running speed parallel to the road surface is smaller than the forward, horizontal velocity. We have for the change in $r_e = V_x/\Omega$:

$$\tilde{r}_{e,\text{slope}} = r_{eo}(1-\cos\beta) \tag{9.244}$$

The third contribution comes from the road surface curvature. The analysis that attempts to model the relation between curvature and effective rolling radius is more difficult and requires special attention. Figure 9.60 unravels the process of rolling over a curved obstacle and indicates the connection with rolling over a drum surface with equal curvature. In contrast to the drum, the obstacle does not rotate. Consequently, to compare the process of rolling over a curved obstacle with that of rolling over a rotating drum surface, we must add the effect of the

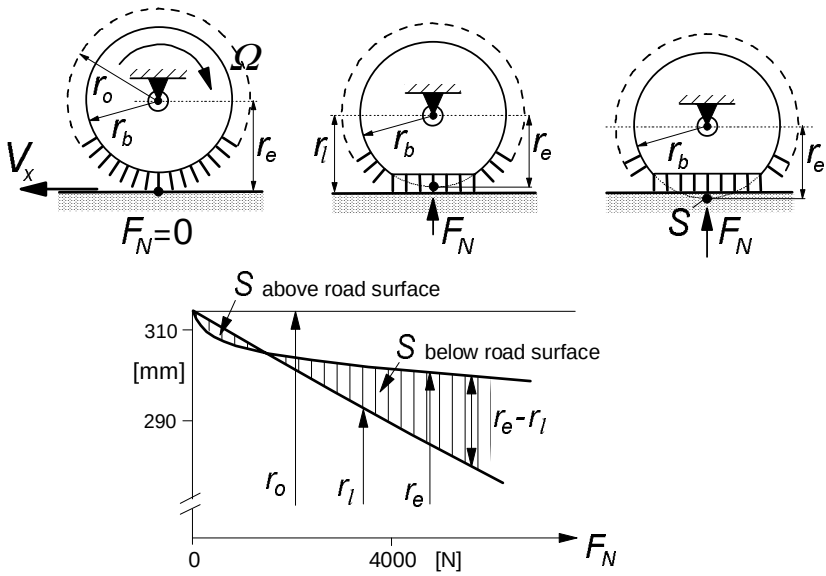

Fig. 9.59. The effective rolling radius varying with a change in normal load.

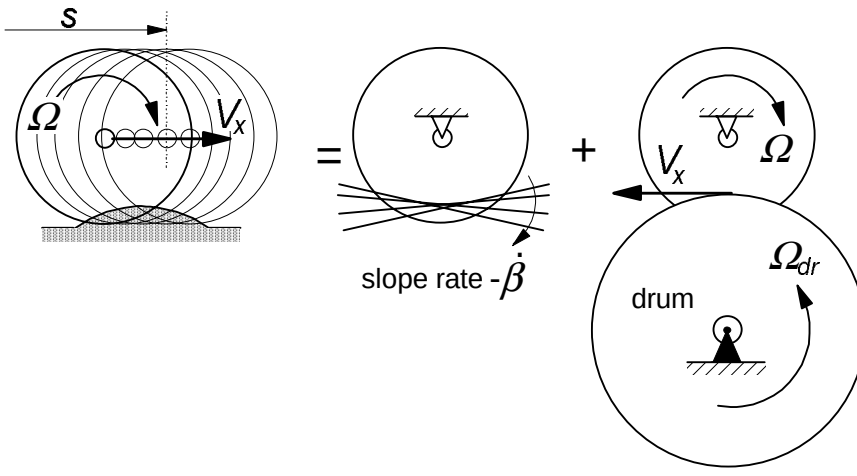

Fig. 9.60. Unravelling the process of rolling over a curved obstacle.

tyre supported by a counter rotating surface that does not move forwards. The left-hand diagram of Fig.9.61 depicts a possible test configuration with a plank that can be tilted about a transverse line in the contact surface. When being tilted, point S, that is attached to the wheel rim, must move along with the plank in longitudinal direction since the wheel slip is zero ($V_{sx} = 0$) as brake or drive torque is not applied. Consequently, the wheel rotates slightly and the following equation applies:

$$V_{sx} = -(r_{eo} - r_l)\frac{\mathrm{d}\beta}{\mathrm{d}t} - r_{eo}\tilde{\Omega} = 0 \tag{9.245}$$

The apparent variation in effective rolling radius derives from the equation:

$$\tilde{r}_e = \frac{V_x}{\Omega} - \frac{V_x}{\Omega_o} \approx -\frac{V_x}{\Omega_o^2}\tilde{\Omega} \tag{9.246}$$

so that we obtain for the contribution from the slope rate:

$$\tilde{r}_{e,\text{slope rate}} = \frac{r_{eo} - r_l}{\Omega_o}\frac{\mathrm{d}\beta}{\mathrm{d}t} \tag{9.247}$$

The relationship (9.245) has been confirmed to hold through elaborate experiments conducted by Zegelaar (1998) on the tilting plank of the Delft flat plank machine.

The other contribution that comes from the drum analogue is found by considering the simple model shown in the right-hand diagram of Fig.9.61. The tread elements with length d_t are assumed to stand perpendicularly on the drum

surface. The drum has a curvature with radius R_{dr}. The belt with radius r_b is considered inextensible. As a consequence we find the following relation between the wheel and drum velocities.

$$\Omega r_b = \Omega_{dr}(R_{dr} + d_t) = V_x\left(1 + \frac{d_t}{R_{dr}}\right) \tag{9.248}$$

and for the effective rolling radius for the tyre rolling freely over the drum surface:

$$r_{e,\text{drum}} = \frac{V_x}{\Omega} = \frac{r_b}{1 + d_t/R_{dr}} \tag{9.249}$$

For the model, the effective rolling radius of the tyre rolling over a flat surface is equal to the radius of the belt:

$$r_{eo} = r_b \tag{9.250}$$

Now, the tread depth is:

$$d_t = r_o - r_{eo} \tag{9.251}$$

Hence, the expression for the effective rolling radius on the drum can be rewritten as:

$$r_{e,\text{drum}} = \frac{r_{eo}}{1 + (r_o - r_{eo})/R_{dr}} \approx r_{eo}\left(1 - \frac{r_o - r_{eo}}{R_{dr}}\right) \tag{9.252}$$

The variation of the radius becomes:

$$\tilde{r}_{e,\text{drum}} = -(r_o - r_{eo})\frac{r_{eo}}{R_{dr}} \tag{9.253}$$

The drum radius is equal to the radius of curvature of the (effective) road surface

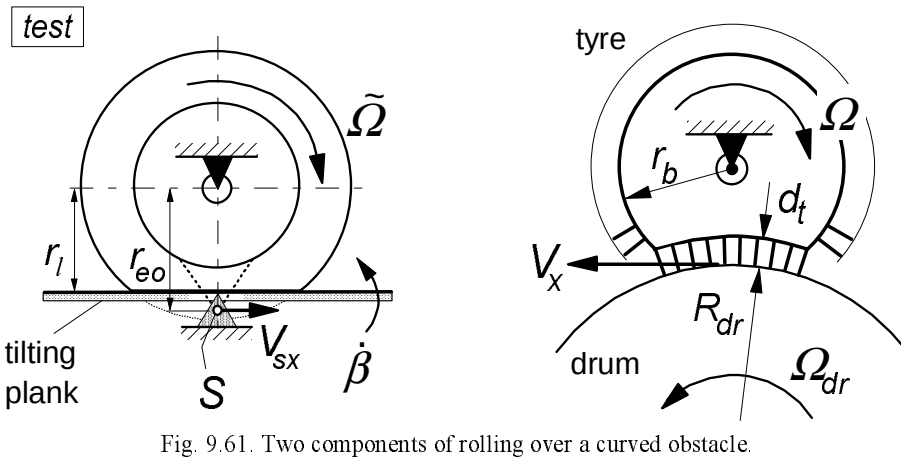

Fig. 9.61. Two components of rolling over a curved obstacle.

profile. This curvature corresponds to change in slope β with travelled distance s. Note that for the convex drum surface the β rate of change is negative. So, we have:

$$\frac{1}{R_{dr}} = -\frac{\mathrm{d}\beta}{\mathrm{d}s} \tag{9.254}$$

The slope rate of change may be written as:

$$\frac{\mathrm{d}\beta}{\mathrm{d}s} = \beta' = \frac{1}{V_x}\frac{\mathrm{d}\beta}{\mathrm{d}t} = \frac{1}{\Omega r_e}\frac{\mathrm{d}\beta}{\mathrm{d}t} \tag{9.255}$$

The drum contribution is now expressed as:

$$\tilde{r}_{e,\mathrm{drum}} = \frac{r_o - r_{eo}}{\Omega}\frac{\mathrm{d}\beta}{\mathrm{d}t} \tag{9.256}$$

Adding up the two contributions (9.247) and (9.256) yields the variation in effective rolling radius due to obstacle curvature:

$$\begin{aligned}\tilde{r}_{e,\mathrm{curvature}} &= \tilde{r}_{e,\mathrm{slope\ rate}} + \tilde{r}_{e,\mathrm{drum}} \\ &= \frac{r_o - r_l}{\Omega_o}\frac{\mathrm{d}\beta}{\mathrm{d}t} = \rho_z r_{eo}\frac{\mathrm{d}\beta}{\mathrm{d}s}\end{aligned} \tag{9.257}$$

where ρ_z is the radial compression of the tyre. By adding up all the contributions we finally obtain for the variation of the effective rolling radius with respect to the initial condition where $\beta = \mathrm{d}\beta/\mathrm{d}s = 0$ and $\rho_z = \rho_{zo}$:

$$\tilde{r}_e = -\eta\tilde{\rho}_z + r_{eo}(1 - \cos\beta) + \rho_z r_{eo}\frac{\mathrm{d}\beta}{\mathrm{d}s} \tag{9.258}$$

The last term constitutes by far the most important contribution to the effective rolling radius variation and thus to the wheel rotational acceleration that can only be brought about by a variation in the longitudinal force F_x. This force also often outweighs the part of the horizontal longitudinal force F_H that directly results from the slope it self, cf. (9.240).

The effective curvature $\mathrm{d}\beta/\mathrm{d}s$ may show abrupt changes at the beginning and end of the passage over an obstacle. To assess the curvature and at the same time smoothen the discontinuities of the response we may send β through a first-order filter and take the difference of input (β) and output. After division by the time constant which is taken inversely proportional with the speed of travel, and divide by the speed, the filtered curvature is obtained that vanishes at wavelengths approaching zero.

9.5.5. Simulations and Experimental Evidence

Zegelaar and Schmeitz have performed numerous experiments on the drum test stand (Fig.9.37) and the flat plank machine (Fig.9.62) and used the SWIFT with obstacle model to carry out the simulations. Figure 9.54 shows the obstacle parameter values for the quarter sine basic curve of Zegelaar. Table 9.6 gives the parameters used by Schmeitz which are based on the ellipse concept (tandem egg technique).

Table 9.6. Parameter values used for envelopment calculations. Tyre: 205/60R15, 2.2bar.

unloaded radius	r_o	0.310 m
effective rolling radius at F_N= 4000N	r_{eo}	0.305 m
slope effective rolling radius characteristic	η	0.3
vertical tyre stiffness at F_N= 4000N	C_{Fz}	220 N/mm
rolling resistance, cf. Eqs.(9.230,231)	q_{sy1}	0.01
half contact length, cf. Eq.(9.207)	a	cf. Table 9.3
half ellipse length /unloaded radius a_e/r_o	p_{ae}	1.0325
half ellipse height /unloaded radius b_e/r_o	p_{be}	1.0306
ellipse exponent c_e	p_{ce}	1.8230
shift length /contact length $l_s/2a$	p_{sh}	0.8773

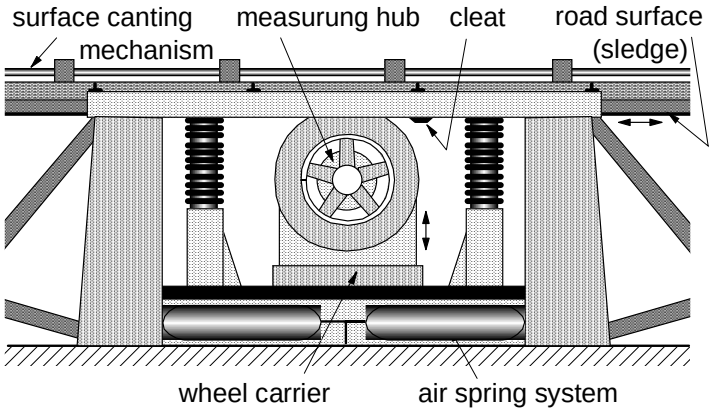

Fig. 9.62. The Delft flat plank machine with stroke of 7m and road canting system, cf. Fig..7.11.

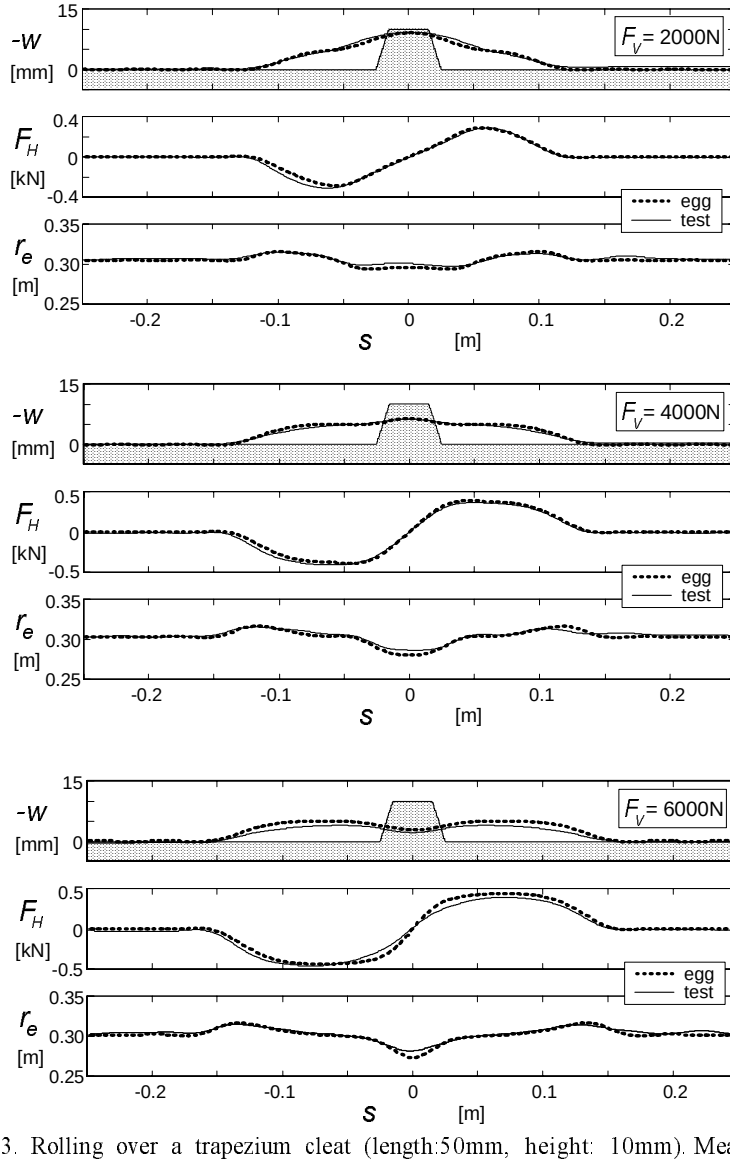

Fig. 9.63. Rolling over a trapezium cleat (length:50mm, height: 10mm). Measured and calculated variation of vertical axle displacement, horizontal longitudinal force and effective rolling radius at three different constant vertical loads. Measurements carried out on the Delft flat plank machine (very low speed) and calculations conducted with the use of the tandem egg technique (Fig.9.56) and Eq.(9.258). Tandem egg parameters according to Table 9.6.

The table shows that the height and length of the ellipse are slightly larger than the dimensions of the free tyre. It is the exponent that gives rise to the larger curvature of the ellipse near the ground.

Figure 9.63 presents the measured and calculated variations of the effective road plane height $-w$, the fore and aft force F_H and the effective rolling radius r_e with the vertical load kept constant while slowly rolling over the trapezium cleat. The effective road plane slope $\tan\beta$ follows from the ratio of the horizontal force variation and the vertical load. The calculations are based on the 2-egg tandem concept of Fig.9.56. The tandem is moved over the original road profile and the effective road plane height and slope are obtained. From the derivative of β the effective rolling radius is found by using Eq.(9.258) which also contains the two very small additional contributions. It is observed, that a good agreement between test and calculation results can be achieved. The use of the quarter sine basic curve function gives very similar results.

Figures 9.64-68 present the results of rolling over the same cleat at different speeds while the axle location is kept fixed. The responses of the vertical, fore and aft forces and the wheel angular speed have been indicated. In addition, the power spectra of these quantities have been shown. Especially at the higher loads the calculated responses appear to follow the measured characteristics quite well

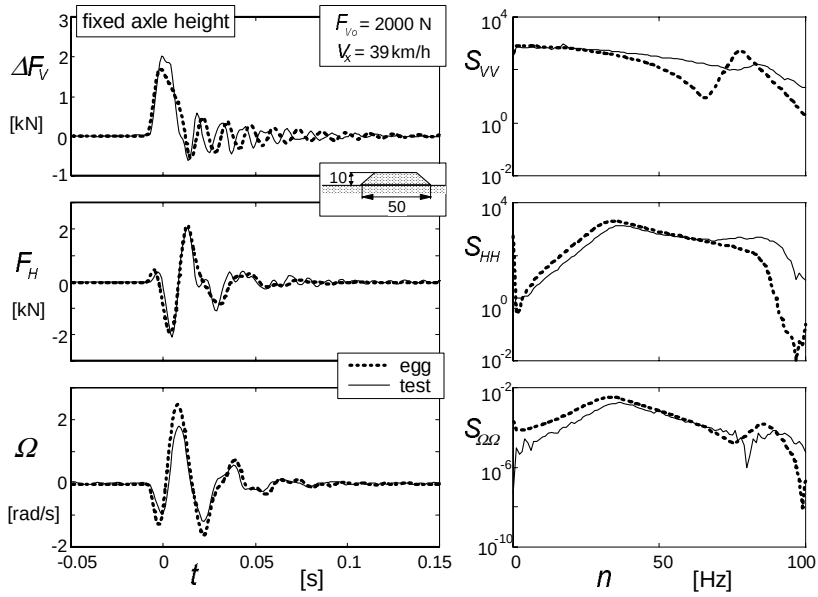

Fig. 9.64. Time traces and power spectra of vertical force, horizontal longitudinal force anf angular velocity for wheel running at given speed of 39 km/h and initial vertical load of 2000 N over trapezium cleat at constant axle height using SWIFT tyre parameters and obstacle parameters of Table 9.6. (Schmeitz).

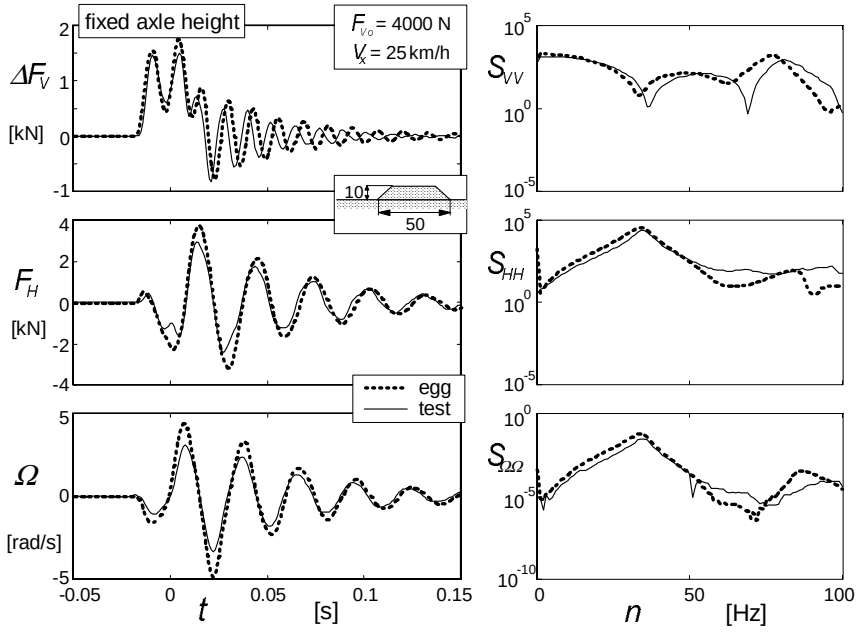

Fig. 9.65. Same as Fig.9.64 but at different speed and initial vertical load .

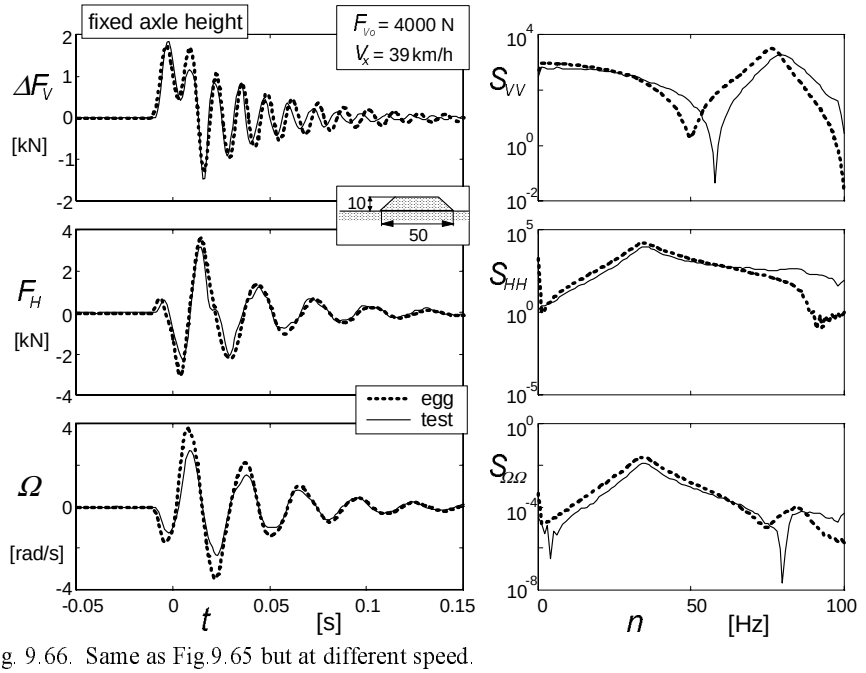

Fig. 9.66. Same as Fig.9.65 but at different speed.

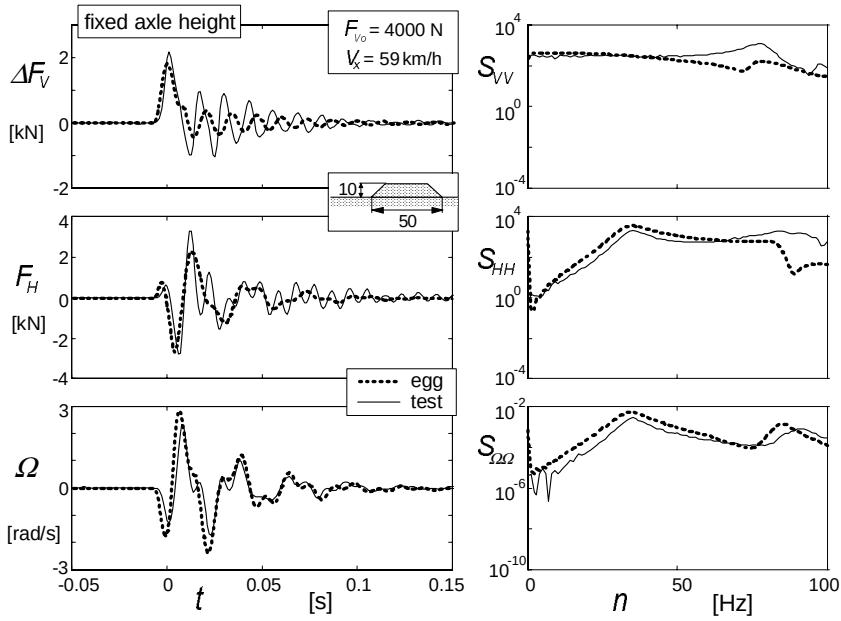

Fig. 9.67. Same as Fig.9.66 but at different speed.

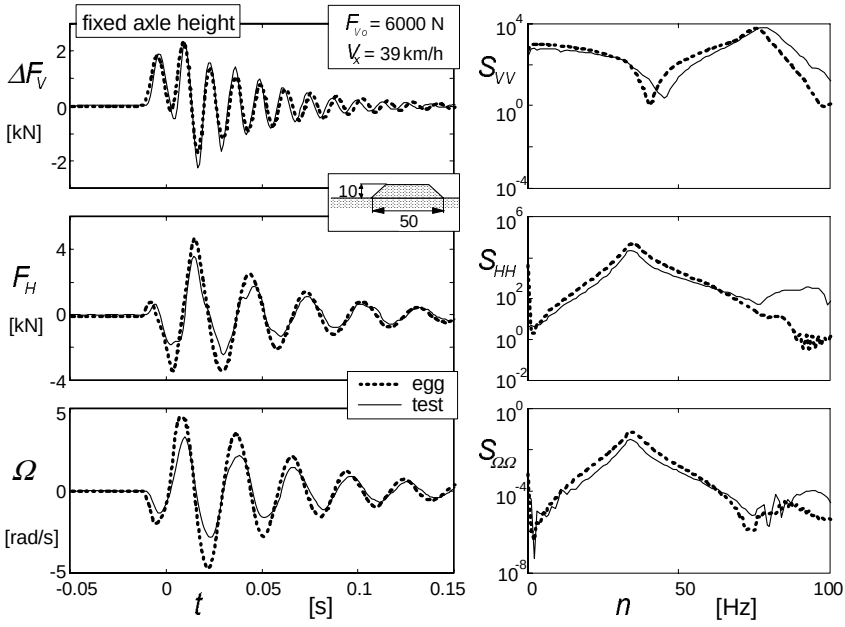

Fig. 9.68. Same as Fig.9.66 but at different initial vertical load .

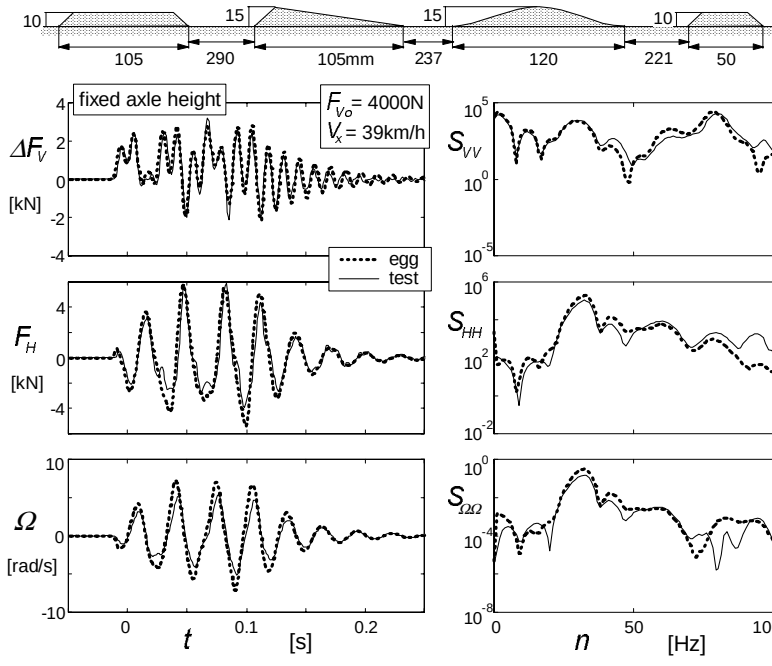

Fig. 9.69. Running over a series of cleats mounted on the drum surface, at constant axle height.

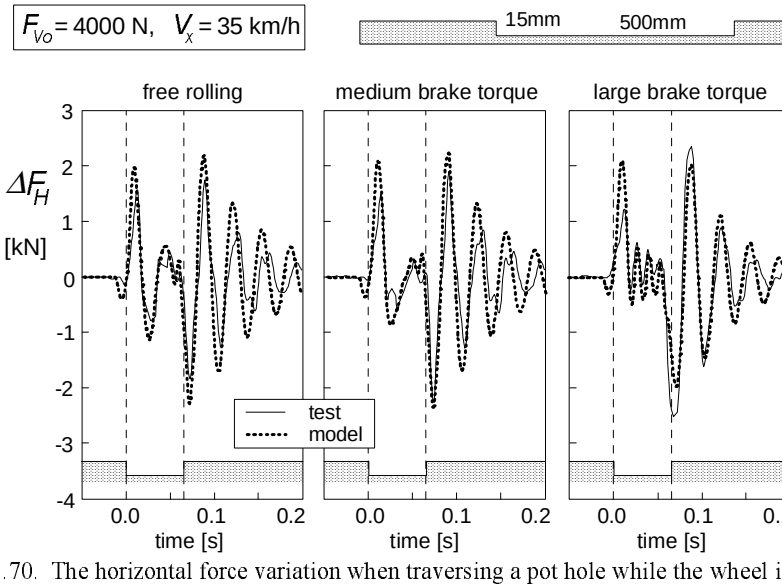

Fig. 9.70. The horizontal force variation when traversing a pot hole while the wheel is being braked at three different levels of brake torque (M_B = ca. 4, 375, 850Nm respectively, Zegelaar, 1998). Experiments on 2.5m drum, calculations using obstacle parameters according to Fig.9.54.

up to frequencies around 50Hz. Figure 9.69 demonstrates the application to a more general road surface profile. It shows the responses of the tyre when moving over a series of different types of cleats that resembles an uneven stretch of road.

Finally, in Fig.9.70 the test and simulation results conducted by Zegelaar (1998) have been depicted, representing a more complex condition where the tyre is subjected to a given brake torque (brake pressure) while the wheel rolls over a pot hole at fixed axle location. The complex longitudinal force response conditions that are brought about by load and slip variations induced by tyre modal vibrations and road unevennesses are simulated quite satisfactorily using the SWIFT theory including obstacle geometric filtering.

9.5.6. Effective Road Inputs at Wheel and Road Camber

In this subsection an attempt is made to deal with non-symmetric road unevennesses and cambered wheels. If one would be able to conduct an experiment with a tyre slowly rolling over an uneven road surface that locally shows a forward and transverse slope, e.g. an oblique cleat, with the surface being made very slippery so that frictional forces are avoided as much as possible, the effective road plane transverse slope may be assessed together with the forward slope and the effective road plane height. Again, the presumption is

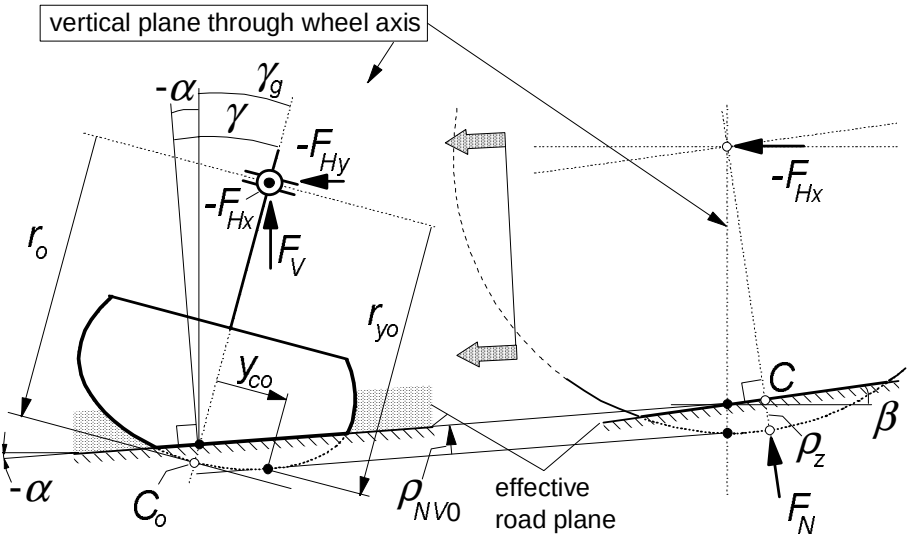

Fig. 9.71 . Situation with wheel camber γ and road camber α at a forward slope β.

that the resulting measured force is directed perpendicularly to to the effective road plane. Of course, the effective rolling radius variation must be assessed through a test on a friction surface to ensure that the wheel properly rolls and is not halted as a result of the rolling resistance. An alternative suggestion for the estimation of the effective transverse slope variation is: use a simple tyre model with camber stiffness and relaxation length (possibly including ply-steer and conicity force variation with load changes) and compare the dry surface test results with simulated force variations and minimize the difference through an optimisation technique.

As before, the method may be generalised for different loads by utilising the egg and follower technique. Two parallel ellipses are used now (or even ellipsoids that is: eggs with three dimensions), the (centre) planes of which are positioned at a constant lateral mutual distance of say 80% of the tread width $2b$ belonging to the nominal load. Both eggs touch the actual road surface and the resulting parallel basic profiles are to be traced by a four point follower. The four point heights and the transverse slopes front and rear and the forward slopes left and right are finally averaged to obtain the effective road plane input quantities. The aligning torque that shows up because of the warped contact surface may be modelled by taking into account the different roll angles of the front and rear 'axles' of the four point follower. The ultimate procedure is yet to be developed.

If the wheel shows an inclination angle with respect to the vertical (the global camber angle γ_g) it is probably best to define the assessed road inputs to occur at the horizontal coordinates of the lowest point of the undeformed tyre in the wheel centre plane C_o. Figure 9.71 depicts the situation. Assume that the effective road plane height and the effective slopes are available and were determined with an upright wheel ($\gamma_g = 0$) that is: vertical eggs. Figure 9.72 shows the detailed configuration in the vertical plane through the wheel spin axis. The problem is now to find the (uncorrected) normal tyre compression ρ_{z0} of the tyre that runs at a (global) camber angle at a given height with respect to a horizontal reference plane, cf. Fig.9.73.

In contrast to the situation without road and wheel camber as dealt with in the preceding sections, it is now necessary to know the actual location of the inclined effective road plane with the height defined below point C_o. It turns out that a for α corrected effective road plane height $-w_\alpha$ has to be introduced, as indicated in Fig.9.72. The correction is needed because of the finite lateral dimensions of the tyre (it is not a thin disc). We have to account for the actual undeformed contour of the tyre cross section, given by the free radius r_{yo} as a function of the lateral distance to the wheel centre plane y_{co}. The contour has been used before to compute the overturning couple M_x at camber, cf. Sec.4.3.5,

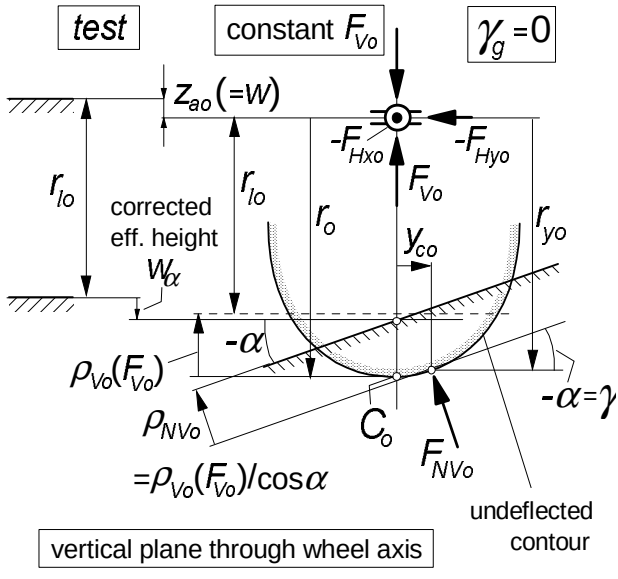

Fig. 9.72. Suggested test configuration performed at constant vertical wheel load F_{Vo} to assess effective road plane height and slopes (on frictionless surface). The for transverse slope corrected effective height w_α.

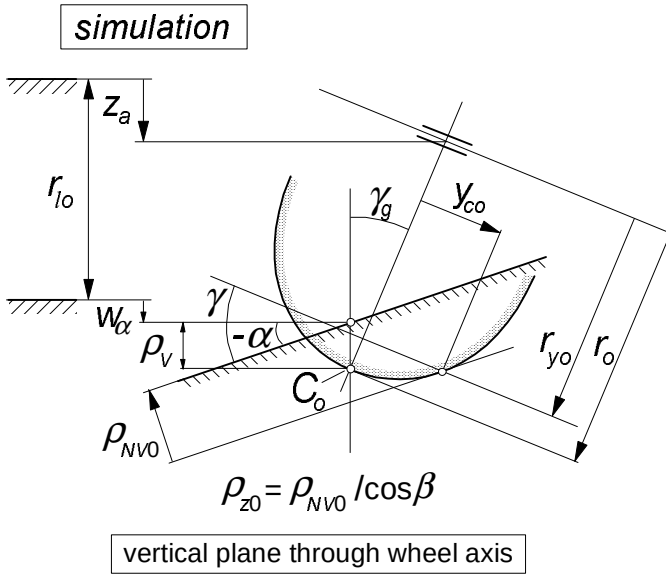

Fig. 9.73. The use of the (corrected) effective road inputs, which are calculated as function of the horizontal position of point C_o, in a simulation where a global wheel camber angle γ_g may occur.

Eq.(4.125). To simplify the matter, it is assumed that the tyre stiffness normal to the tyre tread surface is independent of the location at the cross section contour. The vertical tyre that is loaded against a horizontal surface with a normal force F_{Vo} shows a radial compression ρ_{Vo}. Figure 9.72 indicates that deflection. To achieve the same vertical force but now loaded against a surface with transverse slope angle α and possibly with a forward slope, the normal deflection ρ_{zo} projected against the vertical plane through the wheel spin axis producing ρ_{NVo} should be equal to:

$$\rho_{NVo} = \{r_{yo} - (r_o - \rho_{Vo} - z_{ao} + w_\alpha)\}\cos\alpha - y_{co}\sin\alpha \tag{9.259}$$

To get the same vertical force the following condition holds:

$$\rho_{NVo} = \frac{\rho_{Vo}(F_{Vo})}{\cos\alpha} \tag{9.260}$$

While by definition the uncorrected effective height would read:

$$w = z_{ao} \tag{9.261}$$

the corrected effective road plane height defined at horizontal coordinates of point C_o, Fig.9.72, now becomes by using (9.259, 260):

$$w_\alpha = w - \rho_{Vo}\tan^2\alpha - y_{co}\tan\alpha - (r_o - r_{yo}) \tag{9.262}$$

With the corrected height introduced we can handle the calculation of the normal tyre deflection at wheel (global) camber, cf. Fig.9.73. The vertical distance ρ_V is found to be:

$$\rho_V = r_o\cos\gamma_g - (r_{lo} - z_a + w_\alpha) \tag{9.263}$$

where r_{lo} is the loaded radius at nominal vertical load F_{vo}. The projected normal deflection then reads:

$$\rho_{NV0} = \rho_V\cos\alpha - (r_o - r_{yo})\cos\gamma + y_{co}\sin\gamma \tag{9.264}$$

At a forward slope defined according to Fig.9.71 the normal deflection (not corrected for tyre growth etc.) becomes:

$$\rho_{z0} = \frac{\rho_{NV0}}{\cos\beta} \tag{9.265}$$

Finally, the actual normal tyre compression is determined with tyre growth and the interaction with lateral and longitudinal deflection taken into account, analogous to Eq.(9.221):

$$\rho_z = \rho_{z0} + \Delta r\cos\gamma - q_{Fcx}\rho_x^2/r_o - q_{Fcy}\rho_y^2/r_o \tag{9.266}$$

In a dynamic situation, we deal with the belt rather than with the wheel rim motion. At given effective road plane, the normal deflection may be assessed by using in Eqs.(9.263-264) the belt centre height variation z_b and the belt camber angle γ_b instead of those of the wheel rim. As a result, the normal residual deflection ρ_{zr} is obtained. The normal force F_N may, finally, be calculated by using Eq.(9.220). This normal load, in its turn, governs the length l_s of the 4-point follower.

Chapter 10

MOTORCYCLE DYNAMICS

10.1. Introduction

The single track vehicle is more difficult to study than the double track automobile and poses a challenge to the vehicle dynamicist. Stability of motion is an important issue and it turns out that the stabilising actions of the human rider are essential to properly handle the vehicle. Steady-state cornering behaviour can be analysed in a straightforward manner together with the examination of the stability of the equilibrium motion. While for an automobile only the lateral and yaw degrees of freedom are minimally needed to perform such an analysis, a single track vehicle requires in addition the inclusion of the roll degree of freedom for the steady-state cornering study and the steer angle as a free motion variable to examine the stability. For better correspondence with reality also the torsion of the front frame with respect to the mainframe about an axis perpendicular to the steering axis is of importance. When the non-linear problem at higher cornering accelerations is investigated, a major difficulty is formed by the fact that the separation of lateral and vertical motions is not possible since due to the roll angle of the motorcycle a strong interaction between in-plane and lateral motions occur. This is in contrast to the situation of a double track vehicle where the roll angle remains relatively small.

Performance of the vehicle in terms of handling properties is a matter that can be studied theoretically only if a proper model of the stabilisation capabilities of the human rider is available. While in an automobile the driver normally uses the steering wheel to control the vehicle direction of motion, the pilot of a motor cycle has two or three quantities to his disposal to steer and stabilise the vehicle. These are: the steer angle or the steer torque and the lean angle (and possibly the lateral shift) of the upper torso.

In the past, a number of researchers studied the performance of the single track vehicle. Noteworthy is the very early theoretical study of Whipple (1899) on the stability of the motion of the bicycle with the tyres assumed to be rigid. Sharp (1971) was one of the first to investigate the motorcycle's stability using a proper tyre model. Later, the torsional compliance of the frame was introduced (Sharp, 1980a and Spiering, 1981) which appeared to have a marked effect on

the stability of the wobble mode (steering oscillations). In 1980,1983 Koenen reported on an elaborate study on the stability also at large lateral curving accelerations which involve large roll angles and interaction of in-plane and lateral dynamics of the complex system. As the model representing the vehicle becomes more complex and impacts from road obstacles become more demanding to model the tyre, e.g. the kick-back phenomenon, multi-body vehicle models and advanced dynamic tyre models become indispensable for proper and efficient research. We refer to the following publications: Iffelsberger (1991), Wisselman et al. (1993), Breuer et al. (1998), Sharp et al. (2001a) and Berritta et al. (2000). Significant experimental results relating to the influence of design parameters on the damping of the main oscillatory modes have been given by Bayer (1988), Takahashi et al. (1984) (tyre parameters), Hasegawa (1985) and Nishimi et al. (1985). In 1978, 1985 and 2001 Sharp published extensive reviews of the at these dates existing state of the art. We refer to these sources for further study.

In the present chapter we will first establish geometrical relationships of the vehicle also at large roll angles with the steer angle being kept small; then discuss modelling of tyre forces, derive the linear equations of motion using the Lagrangean method and study the motion at relatively small lateral accelerations. For the steady-state cornering motion the understeer coefficient will be assessed that provides information on the variation of the steer angle with increasing speed of travel at a given radius of turn. In addition, the associated steer torque will be determined. For the linear system the stability of motion with its various possibly unstable modes will be investigated. The effects of driving and braking as well as of the aerodynamic drag will be included. In Section 10.5.3 typical changes in vibrational modes that may occur at large roll angles are discussed.

A relatively simple rider model that accomplishes feed-back control will be introduced that is able to stabilise the vehicle motion. Step response to handling inputs of the rider may then be investigated successfully. Inputs considered are: steer torque and lean torque. The lateral offset of the centre of gravity will be treated as a constant small parameter that affects straight running behaviour. Important literature is available on rider behaviour both as an active controller and stabiliser and as a passive part of the structure. We refer to the publications: Weir (1972), Nishimi et al.(1985), Katayama et al. (1988,1997), Cossalter et al. (1998) and Biral et al. (2001). The first one studies stabilising feedback control, the second reference deals with passive rider model behaviour, the third couple of papers discuss, among other things, manoeuvring effort while the latter two papers address the problem of optimal manoeuvrability. Ruijs (1985) uses feed-back control loops to stabilise the unmanned motorcycle with a stabilising rider-robot.

Similar to the treatment of steady-state cornering behaviour of automobiles we will demonstrate the assessment of the handling diagram for the motorcycle also covering large lateral accelerations. From the diagram established, the steer angle required to negotiate a given steady-state cornering manoeuvre can be assessed. Also the steer torque is determined. Examples of results will be discussed. The responses to other inputs such as cross wind and transverse slope of the road surface have not been investigated. The introduction of such input quantities into the model may, however, be easily accomplished.

10.2. Model Description

In Fig.10.1 the motorcycle has been depicted while it moves at a roll angle φ of the mainframe and with a steer angle δ of the handlebar about a steering axis that, in the neutral upright position, shows a steering head (rake) angle ε with respect to a vertical line and a caster length t_c. The reference point A that lies on the line of intersection of the plane of symmetry of the vehicle and the road plane and is located in the upright position below the centre of gravity of the

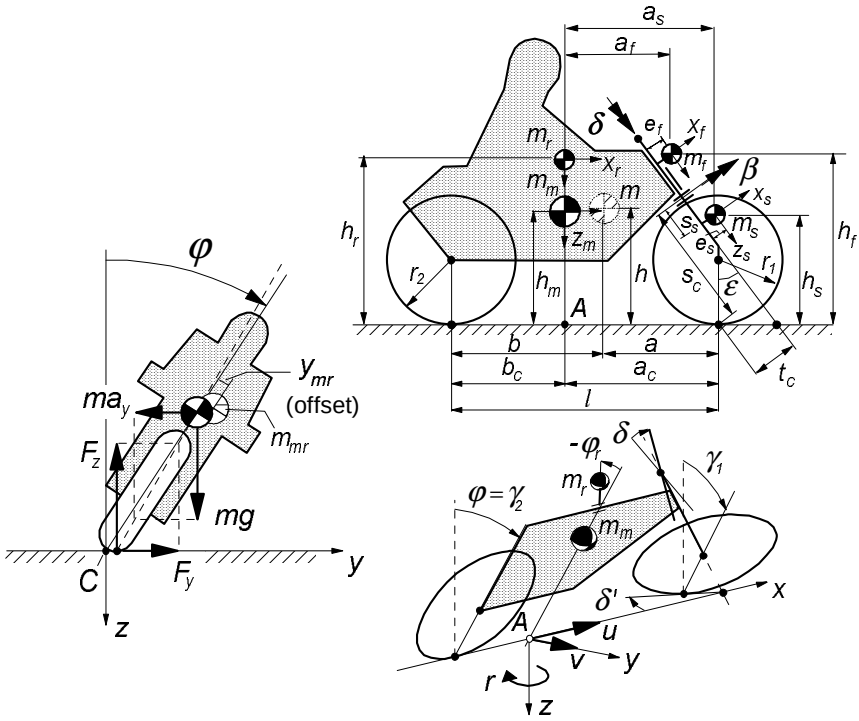

Fig. 10.1. Motorcycle model configuration.

mainframe, moves forwards with a velocity u and in lateral direction with a velocity v. The line of intersection moves over the road surface and shows a yaw angle ψ, the time rate of which is denoted by r. The mainframe roll angle φ is measured as the angle between the plane of symmetry and the normal to the road surface. As depicted in the figure, an additional degree of freedom may be introduced associated with the torsional flexibility of the front (steerable) frame, possibly including a portion of the mainframe, with respect to the centre part of the mainframe. To model this, an axis of rotation is introduced perpendicular to the steering axis about which (a part of) the front frame can rotate with twist angle β. The rider has a lean degree of freedom (relative angle φ_r about a longitudinal axis) of its upper torso (with mass m_r) and may exert (internal) moments about the steer and lean axes. Also, a small lateral shift y_m of the c.g. of mainframe and y_r of the rider may be included leading to a joint offset y_{mr}. The offsets are of the same order of magnitude as the roll angle and will be used in the steady-state analysis. Air drag is accounted for by the introduction of a longitudinal force F_d acting at a height h_d on the vehicle in the mainframe centre plane. Finally, the various feed-back control loops have been introduced in the equation for the steer angle to simulate possible rider control.

10.2.1. Geometry and Inertia

The geometrical dimensions of the motorcycle and the location of the centres of gravity of the four connected bodies (mainframe including lower part of the rider and rear wheel, upper torso of the rider, front upper frame and front subframe including front wheel) are defined by quantities given in the figure. The following relations exist between geometrical parameters:

$$\begin{aligned}
a_f &= a_c - \{h_f \sin\varepsilon - (e_f + t_c)\}/\cos\varepsilon \\
a_s &= a_c - \{h_s \sin\varepsilon - (e_s + t_c)\}/\cos\varepsilon \\
s_s &= s_c - \{h_s - (e_s + t_c)\sin\varepsilon\}/\cos\varepsilon \\
h_\beta &= s_c \cos\varepsilon + t_c \sin\varepsilon \\
s_k &= s_c - t_c/\tan\varepsilon \\
h_k &= t_c/\sin\varepsilon
\end{aligned} \tag{10.1}$$

The last three dimensions have not been indicated in the figure.

The masses of the mainframe, the front upper frame, the front subframe and the upper torso are denoted as m_m, m_f, m_s and m_r respectively. The magnitude of total mass m, the possibly shifted c.g. of $m_{mr} = m_m + m_r$, the wheel base l and the location of the centre of the total mass centre with respect to the rear and front wheel axles (distances a and b) and above the ground (height h) become:

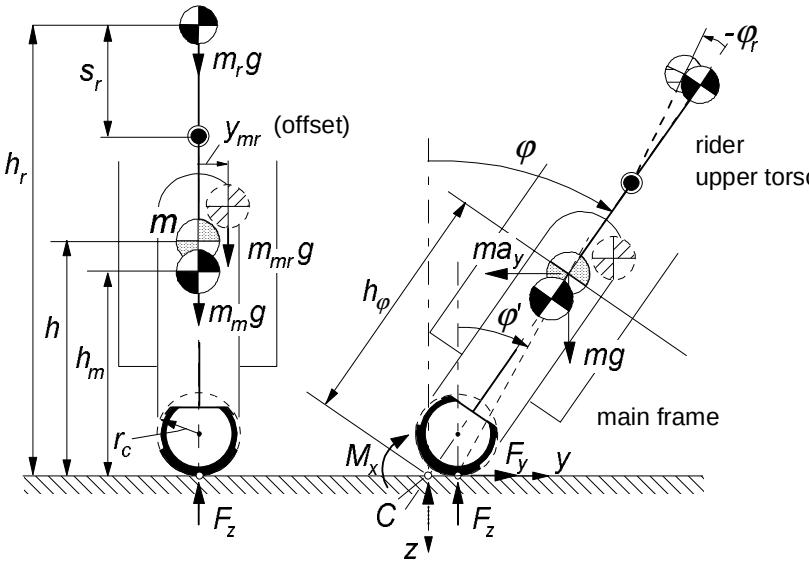

Fig. 10.2. Rear view of motorcycle with tyre cross section and possible c.g. offset indicated.

$$
\begin{aligned}
m &= m_m + m_f + m_s + m_r \\
m_{mr} &= m_m + m_r \\
l &= a_c + b_c \\
b &= \{m_{mr} b_c + m_f(a_f + b_c) + m_s(a_s + b_c)\}/m \\
a &= l - b \\
h &= (h_m m_m + h_f m_f + h_s m_s + h_r m_r)/m
\end{aligned}
\tag{10.2}
$$

The inertial quantities (provided with subscript 0) that would apply in case of a rigid rider (lean angle remains zero) may be retrieved by using the following equations where I_{rx} is moment of inertia of the rider's upper torso about its longitudinal axis; I_{rz} is assumed to be incorporated in the mainframe inertia:

$$
\begin{aligned}
m_{m0} &= m_{mr0} = m_m + m_r \\
h_{m0} &= (h_m m_m + h_r m_r)/m_{m0} \\
I_{mx0} &= I_{mx} + h_m^2 m_m + I_{rx} + h_r^2 m_r - h_{m0}^2 m_{m0} \\
I_{mxz0} &= I_{mxz} + I_{rxz}
\end{aligned}
\tag{10.3}
$$

Products of inertia, except I_{mxz} of the mainframe, will be neglected.

The cross sections of the tyres are assumed to have a finite crown radius r_{c1} and r_{c2} (front and rear). These radii are responsible for the creation of the major part of the tyre overturning couples $M_{x1,2}$. Moreover, the heights of the c.g.'s are affected by these crown radii when running at large roll angles. Figure 10.2

illustrates such a situation.

Important is the notion of the so-called contact centre or point of intersection C that lies below the wheel spin axis and on the line of intersection of wheel centre plane and road surface. We may refer to Fig.4.27 and the related discussion. For the rear wheel the centre plane coincides with the plane of symmetry of the (assumedly symmetric) mainframe. Rotation of the mainframe about the line of intersection gives rise to an increase of the normal load of the tyre. At constant vertical load, a simultaneous lift of the vehicle must occur. Consequently, the distance of the centre of gravity to the line of intersection will increase from h to h_φ as indicated in the figure. With a weighted average crown radius

$$r_c = (b/l)\, r_{c1} + (a/l)\, r_{c2} \tag{10.4}$$

we find:

$$h_\varphi = h + r_c(1 - \cos\varphi)/\cos\varphi \tag{10.5}$$

At large roll angles also the caster length t_c should be adapted. We find approximately with δ assumed small:

$$t_{c\varphi} = t_c + r_{c1} \sin\varepsilon (1 - \cos\varphi)/\cos\varphi \tag{10.6}$$

In the linear analysis restricted to small angles, these extensions are of no importance.

10.2.2. The Steer, Camber and Slip Angles

To determine the side force F_y and the moments M_x and M_z acting on the front and rear wheels, the respective slip and camber angles are needed as input. For the rear wheel these angles can be obtained in a straightforward way. The front wheel poses a problem because we have an attitude of the wheel plane that is defined by at least three successive rotations. In Fig.10.3 several triads have been introduced which are needed to define the orientation of mainframe and front wheel. The line of intersection of the mainframe centre plane and the road plane coincides with the x axis. The origin of the horizontal moving axes system (x, y, z) is the reference point A indicated in Fig.10.1 with forward and lateral velocity components u and v. Furthermore, this system rotates about the vertical axis with yaw rate $r = \dot{\psi}$. The mainframe rotates about the x axis giving rise to the roll angle φ. The rotated system of axes (x_φ, y_φ, z_φ) is attached to the mainframe. In the mainframe centre plane the steering axis is positioned at an angle of inclination (the rake angle ε) with respect to the z_φ axis. The triad (x_ε, y_ε, z_ε) is also attached to the mainframe but with a z_ε axis along the inclined steering axis. The system (x_δ, y_δ, z_δ) is attached to the upper part of the front frame that is

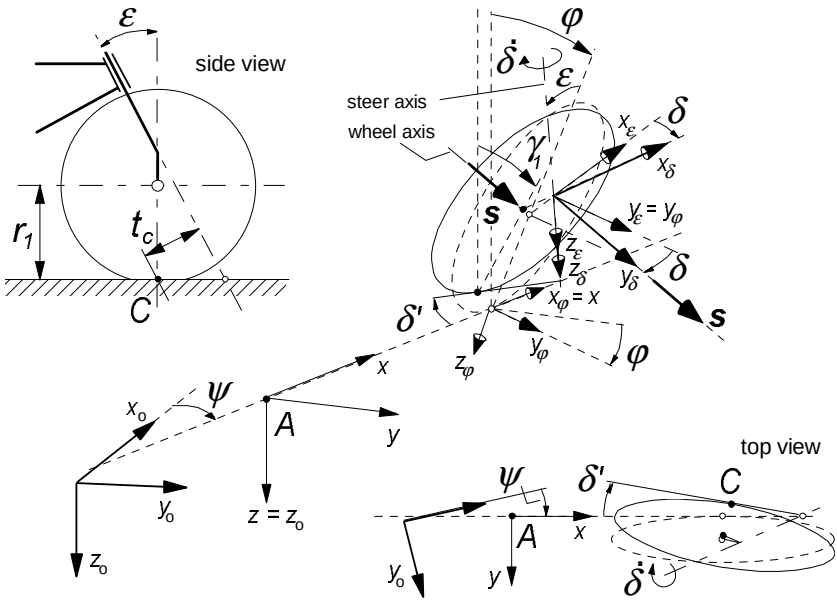

Fig. 10.3. View of front wheel assembly with various coordinate system triads to assess the ground steer angle δ' and camber angle γ_1 of the front wheel using the unit vector $\boldsymbol{s}$ along the wheel spin axis ($\beta = 0$).

rotated with steer angle δ with respect to the $(x_\varepsilon, y_\varepsilon, z_\varepsilon)$ frame. Finally, we may introduce the twist angle β (not considered in Fig.10.3, cf. Fig.10.1) giving rise to the system of axes $(x_\beta, y_\beta, z_\beta)$ with the y_β axis running along the wheel spin axis. We now introduce a unit vector $\boldsymbol{s}$ directed according to the wheel spin axis, that is along the y_β axis. The components of this vector along the axes of the moving horizontal system (x, y, z) will be now be determined by successive rotation transformations. The result of each successive step is indicated by a subscript that denotes the frame with respect to which the unit vector is regarded. We have

$$\boldsymbol{s}_\beta = \begin{pmatrix} 0 \\ 1 \\ 0 \end{pmatrix}, \quad \boldsymbol{s}_\delta = \begin{pmatrix} 1 & 0 & 0 \\ 0 & \cos\beta & -\sin\beta \\ 0 & \sin\beta & \cos\beta \end{pmatrix} \boldsymbol{s}_\beta, \quad \boldsymbol{s}_\varepsilon = \begin{pmatrix} \cos\delta & -\sin\delta & 0 \\ \sin\delta & \cos\delta & 0 \\ 0 & 0 & 1 \end{pmatrix} \boldsymbol{s}_\delta, \tag{10.7}$$

$$\boldsymbol{s}_\varphi = \begin{pmatrix} \cos\varepsilon & 0 & \sin\varepsilon \\ 0 & 1 & 0 \\ -\sin\varepsilon & 0 & \cos\varepsilon \end{pmatrix} \boldsymbol{s}_\varepsilon, \qquad \boldsymbol{s} = \begin{pmatrix} 1 & 0 & 0 \\ 0 & \cos\varphi & -\sin\varphi \\ 0 & \sin\varphi & \cos\varphi \end{pmatrix} \boldsymbol{s}_\varphi$$

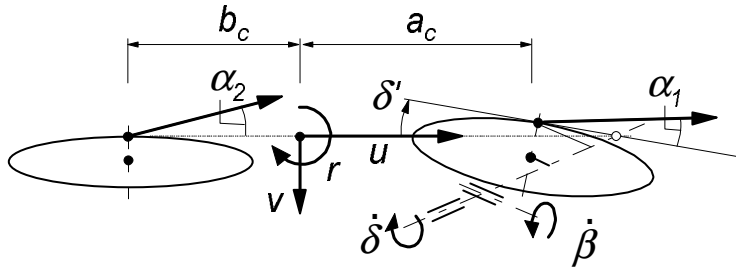

Fig. 10.4. Top view of the single track vehicle showing the front and rear slip angles.

In the subsequent analysis we will approximate the situation by assuming small steer and twist angles. This is certainly admissable. For the non-linear steady-state cornering problem, the roll angle should be allowed to attain magnitudes larger than 45°. Of course, the rake angle ε which is a system parameter, will be regarded to be large. With δ and β assumed small, the unit vector reduces to:

$$\boldsymbol{s} = \begin{pmatrix} -\delta\cos\varepsilon + \beta\sin\varepsilon \\ \cos\varphi - \sin\varphi(\delta\sin\varepsilon + \beta\cos\varepsilon) \\ \sin\varphi + \cos\varphi(\delta\sin\varepsilon + \beta\cos\varepsilon) \end{pmatrix} \tag{10.8}$$

which in case of a completely linear analysis, with also the roll angle assumed small, reduces to:

$$\boldsymbol{s} = \begin{pmatrix} -\delta\cos\varepsilon + \beta\sin\varepsilon \\ 1 - \varphi(\delta\sin\varepsilon + \beta\cos\varepsilon) \\ \varphi + \delta\sin\varepsilon + \beta\cos\varepsilon \end{pmatrix} \tag{10.9}$$

The ground steer angle δ' and the camber angle γ_1 can now easily be determined from the components of the unit vector. We find for the non-linear expressions:

$$\tan\delta' = -\frac{s_x}{s_y} = \frac{\delta\cos\varepsilon - \beta\sin\varepsilon}{\cos\varphi - \sin\varphi(\delta\sin\varepsilon + \beta\cos\varepsilon)} \tag{10.10}$$

$$\sin\gamma_1 = s_z = \sin\varphi + \cos\varphi(\delta\sin\varepsilon + \beta\cos\varepsilon) \tag{10.11}$$

and for the linearised approximations:

$$\delta' = \delta\cos\varepsilon - \beta\sin\varepsilon \tag{10.12}$$

$$\gamma_1 = \varphi + \delta\sin\varepsilon + \beta\cos\varepsilon \tag{10.13}$$

For the non-steered rear wheel we simply have a camber angle

$$\gamma_2 = \varphi \tag{10.14}$$

The slip angles are assumed to remain small and read at steady state by

considering Fig.10.4:

$$\alpha_1 = \delta' - \frac{1}{u}(v + a_c r)$$
$$\alpha_2 = -\frac{1}{u}(v - b_c r) \tag{10.15}$$

For the dynamic non-steady-state situation the linearised model will be employed. The slip angles then become including the time rate of changes of δ and β:

$$\alpha_1 = \delta \cos\varepsilon - \beta \sin\varepsilon - \frac{1}{u}(v + a_c r - t_c \dot{\delta} - s_c \dot{\beta})$$
$$\alpha_2 = -\frac{1}{u}(v - b_c r) \tag{10.16}$$

With the camber and slip angles now derived, we can formulate the resulting side force and moments. First, however, the normal loads are to be established. These are affected by the fore and aft load transfer caused by aerodynamic drag and braking or driving forces.

10.2.3. Air Drag, Driving or Braking and Fore and Aft Load Transfer

Apart from the forces and moments acting from road to tyres, we will consider the aerodynamic drag force F_d that is assumed to act in longitudinal backward direction in the pressure centre a distance h_d above the road surface (in upright position). We will here define the drag force to depend quadratically on the speed u as follows:

$$F_d = C_{dA} u^2 \tag{10.17}$$

Due to the action of the drag force F_d and the longitudinal tyre forces F_{xi}, load transfer arises from the front to the rear wheel. The increase of the rear normal load which (by neglecting the overal aerodynamic lift) is equal to the decrease of the front normal load.

The sum of the longitudinal tyre forces is denoted as $F_{x,tot}$. The remaining force for the acceleration of the vehicle in longitudinal direction becomes:

$$F_{ax} = F_{x,tot} - F_d \tag{10.18}$$

which results in the forward acceleration:

$$a_x = \frac{1}{m} F_{ax} \tag{10.19}$$

and from this the acceleration forces acting on the four individual masses $F_{axm} = a_x m_m$, $F_{axr} = a_x m_r$, $F_{axf} = a_x m_f$ and $F_{axs} = a_x m_s$.

With the moment arms h_φ (cf. Fig.10.2) and $h_{d\varphi}$ the amount of load transfer becomes:

$$\Delta F_z = \frac{1}{l}(h_{d\varphi} F_d + h_\varphi F_{ax})\cos\varphi \tag{10.20}$$

which for small roll angles reduces to:

$$\Delta F_z = \Delta F_{z0} = \frac{1}{l}(h_d F_d + h F_{ax}) \tag{10.21}$$

The resulting vertical wheel loads now become:

$$F_{z1} = F_{z1o} - \Delta F_z , \qquad F_{z2} = F_{z2o} + \Delta F_z \tag{10.22}$$

and at small roll angles:

$$F_{z1} = F_{z10} = F_{z1o} - \Delta F_{z0} , \quad F_{z2} = F_{z20} = F_{z2o} + \Delta F_{z0} \tag{10.23}$$

with the initial wheel loads:

$$F_{z1o} = \frac{b}{l} mg , \qquad F_{z2o} = \frac{a}{l} mg \tag{10.24}$$

The imposed braking force is assumed to be distributed over the front and rear wheels in proportion to the wheel loads as would occur in straight ahead motion, that is: according to the loads (10.23). We have at braking ($F_{x,tot} < 0$):

$$F_{x1} = \frac{F_{z10}}{mg} F_{x,tot} , \qquad F_{x2} = \frac{F_{z20}}{mg} F_{x,tot} \tag{10.25}$$

and at driving:

$$F_{x1} = 0 , \quad F_{x2} = F_{x,tot} \tag{10.26}$$

These forces will act as parameters in the formulae for the tyre forces as described in the subsequent subsection.

It may be noted that in the rolled position the longitudinal drag and acceleration forces will also produce a moment about the vertical z axis through reference point A. This gives rise to an increase at the rear and a decrease at the front of the side forces to be generated by the tyres almost in proportion to the changes in normal load (not exactly because of the effect of the pneumatic trails). This is essentially different from what happens with the automobile.

10.2.4. Tyre Force and Moment Response

Linear Model

We will take into account the transient response of the side force F_y and aligning torque M_z to changes in slip angle and camber angle. However, the non-lagging part of the response will be disregarded. On the other hand, the overturning couple M_x is assumed to respond instantaneously to changes in camber. For the transient responses the relaxation length σ will be used as parameter in the first-order differential equations. These equations describe the responses of the transient slip or deflection angles α' and γ' which in steady-state conditions become equal to the input slip and camber angles α and γ. We obtain for tyre i (i = 1 or 2):

$$\begin{aligned} \frac{1}{u}\sigma_{\alpha i}\dot{\alpha}_i' + \alpha_i' &= \alpha_i \\ \frac{1}{u}\sigma_{\gamma i}\dot{\gamma}_i' + \gamma_i' &= \gamma_i \end{aligned} \tag{10.27}$$

which gives rise to the side force at small slip and camber angles:

$$F_{yi} = C_{F\alpha i}\alpha_i' + C_{F\gamma i}\gamma_i' \tag{10.28}$$

For the aligning torque stiffness against wheel camber we introduce the effect of the longitudinal force F_{xi} by considering a finite crown radius r_{ci} assuming that the lateral shift of the line of action of the longitudinal force changes instantaneously with the camber angle. We find for the aligning torque:

$$M_{zi} = -C_{M\alpha i}\alpha_i' + C'_{M\gamma i}\gamma_i' - r_{ci}F_{xi}\gamma_i \tag{10.29}$$

Note, that we have disregarded here the other influences of the longitudinal force F_{xi} on the side force and the aligning torque as expressed e.g. by Eqs.(4.45-48).

Finally, we have the overturning couple indicated in Fig.10.2 assumed here to depend only on the camber angle. In the linearised version we have:

$$M_{xi} = -C_{Mx\gamma i}\gamma_i \tag{10.30}$$

Obviously, we have neglected here the small effect of the lateral distortion due to the side force. The coefficients are assumed to depend on the normal load as follows (omitting subscript i):

$$C_{F\alpha} = C_{F\alpha o}/(1 + d_5\gamma^2) \tag{10.32}$$

(in the linear model d_5=0) with

$$C_{F\alpha o} = d_1F_{zo} + d_2(F_z - F_{zo}) \tag{10.33}$$

$$C_{F\gamma} = d_3F_z \tag{10.34}$$

$$C_{M\alpha} = e_1F_z \tag{10.35}$$

$$C'_{M\gamma} = e_2 F_z \tag{10.36}$$

and

$$C_{Mxy} = e_3 F_z \quad \text{with} \quad e_3 = r_c \tag{10.37}$$

We introduce the pneumatic trails $t_{\alpha o}$ (>0) of the side force due to side slip and $t_{\gamma o}$ (<0) of the camber force:

$$t_{\alpha o} = \frac{C_{M\alpha}}{C_{F\alpha o}}, \quad t_{\gamma o} = -\frac{C'_{M\gamma}}{C_{F\gamma}} \tag{10.38}$$

Also the relaxion lengths depend on the normal load. This appears to occur in a way similar to that of the change in cornering stiffness. Experimental evidence shows that the relaxation length for side slip is close to the one for camber. The non-lagging part that (although small) exists in the response to camber changes is disregarded here. We define:

$$\sigma_\alpha = \sigma_\gamma = f_1 F_{zo} + f_2 (F_z - F_{zo}) \tag{10.39}$$

Non-Linear Model

For the non-linear force and moment description we will make use of the Magic Formula in a simplified version. The values of the parameters involved have been listed in Table 10.1 at the end of the present Section 10.2. The similarity method will be employed to incorporate the effect of the imposed fore and aft force F_x. We will assume here that the cornering stiffness $C_{F\alpha}$ is not affected by F_x and that the vertical shift is small with respect to D_0. We have for the side force (again omitting subscript i):

$$C = d_8 \tag{10.40}$$

$$K = C_{F\alpha} \tag{10.41}$$

$$D_0 = d_4 F_z / (1 + d_7 \gamma^2) \tag{10.42}$$

$$D = \sqrt{D_0^2 - F_x^2} \tag{10.43}$$

$$B = K/(CD_0) \tag{10.44}$$

$$S_{Hf} = C_{F\gamma} \gamma' / C_{F\alpha} \tag{10.45}$$

$$S_V = d_6 F_z \gamma' D / D_0 \tag{10.46}$$

$$S_H = S_{Hf} - S_V / C_{F\alpha} \tag{10.47}$$

$$\alpha'_{Feq} = (D_0/D)(\alpha' + S_{Hf}) - S_{Hf} \tag{10.48}$$

$$F_y = D\sin[C\arctan\{B(\alpha'_{Feq} + S_H)\}] + S_V \tag{10.49}$$

and for the aligning torque using the pneumatic trail and the side force solely due to side slip:

$$\alpha'_{eq0} = (D_0/D)\alpha' \tag{10.50}$$

$$F_{y\alpha} = D\sin[C\arctan(B\alpha'_{eq0})] \tag{10.51}$$

$$B_t = e_7 \tag{10.52}$$

$$C_t = e_8 \tag{10.53}$$

$$B_r = e_9/(1 + e_4\gamma^2) \tag{10.54}$$

$$C_r = e_{10}/(1 + e_5\gamma^2) \tag{10.55}$$

$$t_\alpha = t_{\alpha o}\cos[C_t\arctan(B_t\alpha'_{eq0})]/(1+e_5\gamma^2) \tag{10.56}$$

$$M_{zro} = C'_{M\gamma}\arctan(e_6\gamma')/e_6 \tag{10.57}$$

$$M_{zr} = M_{zro}\cos[C_r\arctan(B_r\alpha'_{eq0})] \tag{10.58}$$

$$M_z = -t_\alpha F_{y\alpha} + M_{zr} - r_c F_x \tan\gamma \tag{10.59}$$

in which the term with the product F_xF_y has been disregarded. Finally, we define for the overturning couple using formula (4.126) while neglecting the vertical and lateral tyre deflection:

$$M_x = -r_c F_z \tan\gamma \tag{10.60}$$

Since the non-linear analysis will be limited to steady-state conditions, the input slip and camber angles α and γ may be used directly instead of the transient angles α' and γ'.

As an example, in Figs.10.5 and 10.6, the steady-state characteristics for F_y and M_z versus α have been plotted for a number of γ values for the front and rear tyres for the two cases: free rolling and braking. The characteristics of the freely rolling tyre are similar to the experimentally found curves (extending from -6 to +6 degrees slip angle) reported by De Vries (1998a). The parameter values have been listed in Table 10.1.

The non-linear analysis may be improved by employing the full Magic Formula description as given in Chapter 4 or the special motorcycle version presented in Sec.10.6.1, covering large camber angles but restricted to moderate slip angles. In the present analysis these equations may be used for $\kappa=0$, with the similarity method employed to include the effects of the given longitudinal

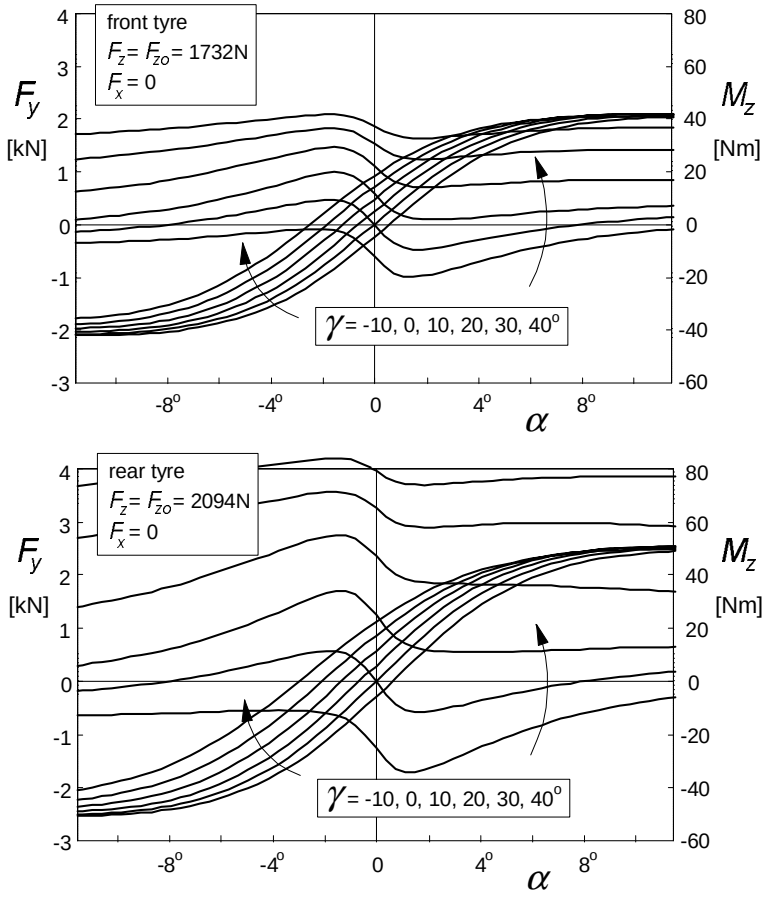

Fig. 10.5. Side force and aligning torque characteristics for the freely rolling front and rear motorcycle tyre model at a series of camber angles.

force F_x. If instead of the force F_x the longitudinal slip κ is imposed or results from wheel rotational dynamics with imposed braking or driving effort, the complete Magic Formula model with combined slip may be used. For the present study this is a less practical option.

In the diagrams of Figs. 10.5,6 the side force curves show a mainly sideways shift at increasing camber angle. The moment curves are moved upwards while their shape is changed. The upward shift is a consequence of the spin torque that results from the wheel inclination angle. At braking (Fig. 10.6) the aligning torque at camber is considerably increased in magnitude because of the direct contribution of F_x (<0) which is represented in (10.59) by the last term. It is observed, that due to the longitudinal force, the maximum level of the side force is reduced.

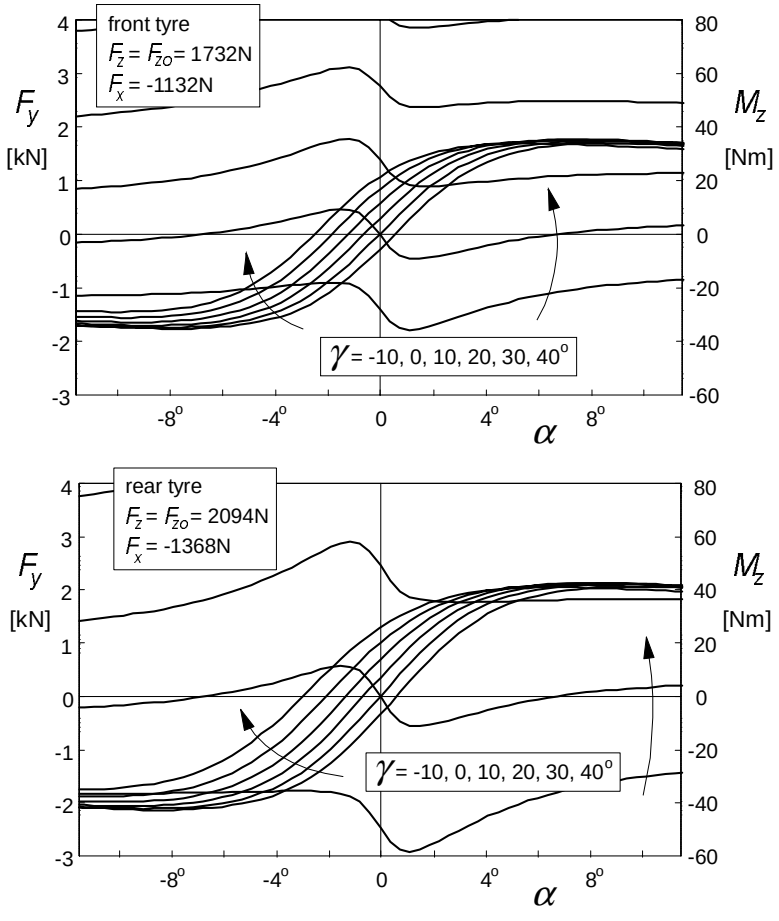

Fig. 10.6. Side force and aligning torque characteristics for the braked front and rear motorcycle tyre at a series of camber angles.

Table 10.1. Parameters of hypothetical front (,1) and rear (,2) motorcycle tyre model.

$d_{1,1}$	14	$d_{2,1}$	9	$d_{3,1}$	0.8	$f_{1,1}$	0.00015
$d_{1,2}$	13	$d_{2,2}$	4	$d_{3,2}$	0.8	$f_{1,2}$	0.00015
$e_{1,1}$	0.4	$e_{2,1}$	0.04	$e_{3,1}$ $(=r_{c1})$	0.08	$f_{2,1}$	0.0001
$e_{1,2}$	0.4	$e_{2,2}$	0.07	$e_{3,2}$ $(=r_{c2})$	0.1	$f_{2,2}$	0.0001
$d_{4,1}$	1.2	$d_{5,1}$	0.15	$d_{6,1}$	0.1	$d_{7,1}$	0.15
$d_{4,2}$	1.2	$d_{5,2}$	0.4	$d_{6,2}$	0.1	$d_{7,2}$	0.15
d_8	1.6	e_4	10	e_5	2	e_6	1.5
e_7	50	e_8	1.1	e_9	20	e_{10}	1

10.3. Linear Equations of Motion

For the dynamic analysis of the vehicle motion we restrict ourselves to small deviations from the rectilinear path. The differential equations will be kept linear with the forward speed u considered as a constant parameter. We will derive the equations using the modified equations of Lagrange (1.28) derived in Chapter 1. After adding the dissipation function D to include damping in the system, these equations read for the variables v and r (=dψ/dt) and subsequently for the remaining generalised coordinates q_j (here: j = 3, 4, 5 or 6):

$$\begin{aligned}
&\frac{d}{dt}\frac{\partial T}{\partial v} + r\frac{\partial T}{\partial u} = Q_v \\
&\frac{d}{dt}\frac{\partial T}{\partial r} - v\frac{\partial T}{\partial u} + u\frac{\partial T}{\partial v} = Q_r \\
&\frac{d}{dt}\frac{\partial T}{\partial \dot{q}_j} - \frac{\partial T}{\partial q_j} + \frac{\partial U}{\partial q_j} + \frac{\partial D}{\partial \dot{q}_j} = Q_j
\end{aligned} \tag{10.61}$$

The generalised forces are found from the virtual work (using Δ instead of δ):

$$\Delta W = \sum_{j=1}^{6} Q_j \, \Delta q_j \tag{10.62}$$

with q_j referring to the quasi coordinate y and to the generalised coordinates ψ, φ, φ_r, δ and β. To establish the equations we will assess successively the kinetic and potential energies, the dissipation function and the virtual work. The terms appearing in the resulting expressions will be restricted to terms of the second order of magnitude. The velocity u and the connected wheel speeds of revolution $\Omega_i = u/r_i$, the vehicle weight mg and the aerodynamic drag F_d and longitudinal force $F_{x,tot}$ are quantities of the zeroth order of magnitude whereas the variables v and the generalised coordinates are of the first order of magnitude. Also, the imposed lateral offset y_{mr} of the combined mainframe and rider mass centre is considered as a quantity of the first order of magnitude. Products of first order of magnitude quantities become terms of the second degree. Terms of higher degree will be neglected as these would give rise to second or higher degree terms in the final differential equations, which we intend to keep linear (only first degree terms).

The pitch angle θ of the mainframe which does not represent a degree of freedom is of the second order of magnitude and should be accounted for in the expressions for the energies. Expressed in terms of the generalised coordinates we find the second degree constraint equation, cf. Eqs.(10.1):

$$
\begin{aligned}
l\theta = & -h_k(\delta\sin\varepsilon+\beta\cos\varepsilon)(\varphi+\tfrac{1}{2}\delta\sin\varepsilon+\tfrac{1}{2}\beta\cos\varepsilon)+ \\
& -s_k(\varphi\beta+\delta\beta\sin\varepsilon+\tfrac{1}{2}\beta^2\cos\varepsilon)
\end{aligned}
\tag{10.63}
$$

The Kinetic Energy

Translational and angular velocities of the six bodies are to be expressed in terms of v and the generalised coordinates (and tentatively θ) and their time derivatives. We find for the longitudinal, lateral and vertical velocities of the c.g. of the mainframe plus rear wheel (except polar moment of inertia I_{wy2}) with mass m_m (body1):

$$
\begin{aligned}
u_m &= u - h_m r\varphi - h_m\dot{\theta} - y_m r \\
v_m &= v + h_m\dot{\varphi} \\
w_m &= -b_c\dot{\theta}
\end{aligned}
\tag{10.64}
$$

and for the angular velocities:

$$
\begin{aligned}
\omega_{mx} &= \dot{\varphi} \\
\omega_{my} &= \dot{\theta} \\
\omega_{mz} &= r
\end{aligned}
\tag{10.65}
$$

The velocities of the rider upper torso with mass m_r (body 2):

$$
\begin{aligned}
u_r &= u - h_r r\varphi - s_r r\varphi_r - h_r\dot{\theta} - y_r r \\
v_r &= v + h_r\dot{\varphi} + \dot{y}_r + s_r\dot{\varphi}_r \\
w_r &= -b_c\dot{\theta}
\end{aligned}
\tag{10.66}
$$

and for the angular velocities:

$$
\begin{aligned}
\omega_{rx} &= \dot{\varphi} + \dot{\varphi}_r \\
\omega_{ry} &= \dot{\theta} \\
\omega_{rz} &= r
\end{aligned}
\tag{10.67}
$$

The velocities of the front frame with mass m_f (body 3 with z axis parallel to steer axis):

$$
\begin{aligned}
u_f &= u - h_f r\varphi - e_f r\delta - h_f\dot{\theta} \\
v_f &= v + h_f\dot{\varphi} + e_f\dot{\delta} + a_f r \\
w_f &= -(b_c + a_f)\dot{\theta}
\end{aligned}
\tag{10.68}
$$

and

$$
\omega_{fx} = \dot{\varphi}\cos\varepsilon - r\sin\varepsilon
$$

$$\omega_{fy} = \dot{\theta} \tag{10.69}$$
$$\omega_{fz} = \dot{\varphi}\sin\varepsilon + r\cos\varepsilon + \dot{\delta}$$

For the front subframe plus front wheel (except polar moment of inertia $I_{wy1)}$ with mass m_s (body 4 with z axis parallel to steer axis):

$$u_s = u - h_s r\varphi - e_s r\delta + s_s r\beta - h_s\dot{\theta}$$
$$v_s = v + h_s\dot{\varphi} + e_s\dot{\delta} - s_s\dot{\beta} + a_s r \tag{10.70}$$
$$w_s = -(b_c + a_s)\dot{\theta}$$

and

$$\omega_{sx} = \dot{\varphi}\cos\varepsilon - r\sin\varepsilon + \dot{\beta}$$
$$\omega_{sy} = \dot{\theta} \tag{10.71}$$
$$\omega_{sz} = \dot{\varphi}\sin\varepsilon + r\cos\varepsilon + \dot{\delta}$$

For the front wheel angular velocities (bodies 5 and 6 only possessing polar moments of inertia $I_{wy1,2}$ possibly extended with effective moment of inertia $n_g I_{ey}$ of other rotating parts reduced to the wheel rotational speed):

$$\omega_{wy1} = -\Omega_1 + \gamma_1(\dot{\delta}' + r) \tag{10.72}$$

and for the rear wheel:

$$\omega_{wy2} = -\Omega_2 + \varphi r \tag{10.73}$$

where

$$\Omega_1 = \frac{u}{r_1}, \qquad \Omega_2 = \frac{u}{r_2} \tag{10.74}$$

with r_1 and r_2 denoting the front and rear wheel (effective rolling) radii. Due to symmetry of the undisturbed system, the Ω's do not need to be regarded as variables in our linearised system equations and non-holonomic constraint equations do not occur. The kinetic energy becomes, in general, summed over the six bodies:

$$T = \frac{1}{2}\sum_{k=1}^{6} m_k(u_k^2 + v_k^2 + w_k^2) + \tag{10.75}$$
$$+\frac{1}{2}\sum_{k=1}^{6}\{I_{xk}\omega_{xk}^2 + I_{yk}\omega_{yk}^2 + I_{zk}\omega_{zk}^2 - 2(I_{xyk}\omega_{xk}\omega_{yk} + I_{yzk}\omega_{yk}\omega_{zk} + I_{zxk}\omega_{zk}\omega_{xk})\}$$

The products of inertia will be neglected except $I_{zx1} = I_{mxz}$ of the mainframe. The velocities u_k etc. appearing in (10.75) correspond to the quantities given by the expressions (10.64-74). The time derivative of the pitch angle θ is obtained from expression (10.63).

The Potential Energy and the Dissipation Function

The potential energy is composed of contributions from torsional spring deflections: twist angle β and lean angle φ_r with stiffnesses c_β and $c_{\varphi r}$ respectively, and the heights of the centres of gravity of the various bodies. These heights become expressed in terms of the generalised coordinates and θ :

For body 1 with c.g. lateral offset y_m :

$$-z_m = h_m(1-\tfrac{1}{2}\varphi^2) + b_c\theta - y_m\varphi \tag{10.76}$$

For body 2 with c.g. lateral offset y_r :

$$-z_r = h_r - \tfrac{1}{2}(h_r - s_r)\varphi^2 - \tfrac{1}{2}s_r(\varphi+\varphi_r)^2 + b_c\theta - y_r\varphi \tag{10.77}$$

For body 3:

$$-z_f = h_f - \tfrac{1}{2}h_f\varphi^2 - e_f\delta\varphi - \tfrac{1}{2}e_f\delta^2\sin\varepsilon + (b_c+a_f)\theta \tag{10.78}$$

For body 4: (10.79)

$$-z_s = h_s - \tfrac{1}{2}h_s\varphi^2 - e_s\delta\varphi + s_s\beta\varphi - \tfrac{1}{2}e_s\delta^2\sin\varepsilon + s_s\delta\beta\sin\varepsilon + \tfrac{1}{2}s_s\beta^2\cos\varepsilon + (b_c+a_s)\theta$$

Furthermore, we have the torsional deflections φ_r and β. The complete potential energy is now written as follows:

$$U = -m_m g z_m - m_r g z_r - m_f g z_f - m_s g z_s + \tfrac{1}{2}c_{\varphi r}\varphi_r^{\,2} + \tfrac{1}{2}c_\beta\beta^2 \tag{10.80}$$

Again, Eq.(10.63) should be employed to express θ, appearing in the formulae (10.76-79), in terms of the generalised coordinates.

If we consider viscous damping to be present in the steer bearings and possibly also around the lean and twist axes we obtain for the dissipation function with k_δ, $k_{\varphi r}$ and k_β denoting the respective damping coefficients:

$$D = \tfrac{1}{2}k_\delta\dot{\delta}^2 + \tfrac{1}{2}k_{\varphi r}\dot{\varphi}_r^2 + \tfrac{1}{2}k_\beta\dot{\beta}^2 \tag{10.81}$$

The Virtual Work

Through the virtual work the generalised forces each associated with a generalised coordinate can be assessed. The forces which act from the environment upon the vehicle are the horizontal ground forces and moments, the aerodynamic forces and the gravitational force component in longitudinal direction in case of a forward slope or the dynamic longitudinal d'Alembert forces acting in the mass centres which are in equilibrium with the longitudinal forces generated by the tyres. The option of considering a forward slope that at given aerodynamic drag and driving or braking forces is just able to maintain a

constant forward velocity would make the analysis correct as in that case the coefficients of the linear equations are time independent (cf. Eq.(3.123) with (3.126) where this is not the case). The longitudinal acceleration a_x appearing in the ensuing equations may be considered equal to the longitudinal component of the acceleration due to gravity that would arise if the vehicle continuously runs over a road with equivalent forward slope.

With the various forces and moments that act upon the vehicle in and around the respective points of application the virtual work becomes:

$$\begin{aligned}\Delta W = {} & F_{x1}\Delta x_1 + F_{y1}\Delta y_1 + M_{z1}(\Delta\delta' + \Delta\psi) + M_{x1}\Delta\gamma_1 + \\ & + F_{x2}\Delta x_2 + F_{y2}\Delta y_2 + M_{z2}\Delta\psi + M_{x2}\Delta\varphi + \\ & - F_d\Delta x_d + M_\delta\Delta\delta + M_{\varphi r}\Delta\varphi_r + \\ & - a_x(m_m\Delta x_m + m_r\Delta x_r + m_r\Delta x_r + m_s\Delta x_s)\end{aligned} \tag{10.82}$$

The virtual displacements expressed in terms of the generalised coordinates turn out to read:

$$\begin{aligned}\Delta x_1 &= (\delta\cos\varepsilon - \beta\sin\varepsilon)(\Delta y + a_c\Delta\psi) + (t_c\delta + s_c\beta)\Delta\psi + h_\beta\beta\Delta\delta \\ \Delta x_2 &= 0 \\ \Delta y_1 &= \Delta y + a_c\Delta\psi \\ \Delta\delta' &= \cos\varepsilon\,\Delta\delta - \sin\varepsilon\,\Delta\beta \\ \Delta\gamma_1 &= \Delta\varphi + \sin\varepsilon\,\Delta\delta + \cos\varepsilon\,\Delta\beta \\ \Delta y_2 &= \Delta y - b_c\Delta\psi \\ \Delta x_d &= -h_d\varphi\,\Delta\psi - h_d\Delta\theta \\ \Delta x_m &= -(h_m\varphi + y_m)\Delta\psi - h_m\Delta\theta \\ \Delta x_r &= -(h_r\varphi + s_r\varphi_r + y_r)\Delta\psi - h_r\Delta\theta \\ \Delta x_f &= -(h_f\varphi + e_f\delta)\Delta\psi - h_f\Delta\theta \\ \Delta x_s &= -(h_s\varphi + e_s\delta - s_s\beta)\Delta\psi - h_s\Delta\theta\end{aligned} \tag{10.83}$$

where $\Delta\theta$ can be expressed in the generalised coordinates by taking the variation of θ (10.63).

Now, we may compare (10.82), after having substituted herein the expressions (10.83), with the formulation of the virtual work according to Eq.(10.62) which becomes:

$$\begin{aligned}\Delta W &= \sum_{j=1}^{6} Q_j\,\Delta q_j = \\ &= Q_y\Delta y + Q_r\Delta\psi + Q_\varphi\Delta\varphi + Q_{\varphi r}\Delta\varphi_r + Q_\delta\Delta\delta + Q_\beta\Delta\beta\end{aligned} \tag{10.84}$$

As a result, the generalised forces Q_j are obtained which are to be inserted at the

right-hand sides of the Lagrangean equations (10.61).

Complete Set of Linear Differential Equations

All the necessary preparations to set up the equations have been completed. To establish the equations, the operations with the energies as indicated in (10.61) can now be carried out. The resulting set of equations are completed with the four first-order differential equations for the transient slip and camber angles front and rear and the linear equations for the side forces, the aligning torques and the overturning couples together with expressions of the slip and camber angles all resulting from the analysis of Section 10.2. Note that the tyre model coefficients, $C_{F\alpha 1}$, $\sigma_{\alpha 1}$ etc., depend on the current vertical wheel load $F_{zi} = F_{zi0}$, Eqs(10.23, 10.33-39). The total order of the system turns out to be 14.

With a given speed of travel u and the total longitudinal tyre force $F_{x,tot}$, the air drag F_d, the vertical tyre loads F_{z10}, F_{z20} and the individual long-itudinal tyre forces $F_{x1,2}$ can be assessed using the equations (10.17, 18, 19, 21, 23, 24, 25, 26). The initial wheel loads (at stand-still) F_{z1o}, F_{z2o} are directly associated with the vehicle mass distribution, Eq.(10.24).

In the equations the imposed handlebar torque M_δ and lean torque $M_{\varphi r}$ appear in the right-hand members. The tyre side forces and moments are tentatively put on the right-hand side as well. In the equation for the steer angle the control terms have been added.

The equations for successively the variables v, r, φ, φ_r, δ, β, α_1', γ_1', α_2' and γ_2' become as follows:

v:

$$\begin{aligned}
&(m_m+m_f+m_s+m_r)(\dot v+ur)+(m_f a_f+m_s a_s)\dot r\ + \\
&\quad +(m_m h_m+m_f h_f+m_s h_s+m_r h_r)\ddot\varphi+m_r s_r\ddot\varphi_r+(m_f e_f+m_s e_s)\ddot\delta-m_s s_s\ddot\beta+ \\
&\quad -F_{x1}(\cos\varepsilon\,\delta-\sin\varepsilon\,\beta)=F_{y1}+F_{y2}
\end{aligned}\tag{10.85}$$

r:

$$\begin{aligned}
&(m_f a_f+m_s a_s)(\dot v+ur)+\{m_f a_f^2+m_s a_s^2+I_{mz}+(I_{fx}+I_{sx})\sin^2\varepsilon+(I_{fz}+I_{sz})\cos^2\varepsilon\}\dot r \\
&\quad +\{m_f h_f a_f+m_s h_s a_s-I_{mxz}+(I_{fz}+I_{sz}-I_{fx}-I_{sx})\sin\varepsilon\cos\varepsilon\}\ddot\varphi\ + \\
&\quad -\{I_{wy1}/r_1+(I_{wy2}+n_g I_{ey})/r_2\}u\,\dot\varphi\ + \\
&\quad +\{m_f e_f a_f+m_s e_s a_s+(I_{fz}+I_{sz})\cos\varepsilon\}\ddot\delta-(I_{wy1}/r_1)\,u\,\sin\varepsilon\dot\delta\ + \\
&\quad -(m_s s_s a_s+I_{sx}\sin\varepsilon)\ddot\beta-(I_{wy1}/r_1)\,u\,\cos\varepsilon\dot\beta\ + \\
&\quad -F_d h_d\varphi-F_{x1}\{(t_c+a_c\cos\varepsilon)\delta+(s_c-a_c\sin\varepsilon)\beta\}\ + \\
&\quad -a_x\{mh\varphi+m_r s_r\varphi_r+(m_f e_f+m_s e_s)\delta-m_s s_s\beta\}\ = \\
&\qquad\qquad = a_c F_{y1}-b_c F_{y2}+M_{z1}+M_{z2}+m_{mr}a_x y_{mr}
\end{aligned}\tag{10.86}$$

φ:

$$
\begin{aligned}
&(m_m h_m + m_f h_f + m_s h_s + m_r h_r)(\dot{v} + ur) + \{I_{wy1}/r_1 + (I_{wy2} + n_g I_{ey})/r_2\} u r + \\
&\quad + \{m_f h_f a_f + m_s h_s a_s - I_{mxz} + (I_{fz} + I_{sz} - I_{fx} - I_{sx}) \sin\varepsilon \cos\varepsilon\} \dot{r} + \\
&\quad + \{m_f h_f^2 + m_s h_s^2 + m_m h_m^2 + m_r h_r^2 + I_{mx} + I_{rx} + (I_{fx} + I_{sx}) \cos^2\varepsilon + (I_{fz} + I_{sz}) \sin^2\varepsilon\} \ddot{\varphi} + \\
&\quad - (m_m h_m + m_f h_f + m_s h_s + m_r h_r) g \varphi + (I_{rx} + m_r s_r h_r) \ddot{\varphi}_r - m_r s_r g \varphi_r + \\
&+ \{m_f e_f h_f + m_s e_s h_s + (I_{fz} + I_{sz}) \sin\varepsilon\} \ddot{\delta} + (I_{wy1}/r_1) u \cos\varepsilon \dot{\delta} - (t_c F_{z1} + m_f e_f g + m_s e_s g) \delta \\
&\quad - (m_s s_s h_s - I_{sx} \cos\varepsilon) \ddot{\beta} - (I_{wy1}/r_1) u \sin\varepsilon \dot{\beta} - (s_c F_{z1} - m_s s_s g) \beta = \\
&\qquad = M_{x1} + M_{x2} + m_{mr} g y_{mr}
\end{aligned}
\tag{10.87}
$$

φ_r:

$$
\begin{aligned}
&m_r s_r (\dot{v} + ur) + (I_{rx} + m_r s_r h_r) \ddot{\varphi} - m_r s_r g \varphi + \\
&\quad (I_{rx} + m_r s_r^2) \ddot{\varphi}_r + k_{\varphi r} \dot{\varphi}_r + (c_{\varphi r} - m_r s_r g) \varphi_r = M_r
\end{aligned}
\tag{10.88}
$$

δ:

$$
\begin{aligned}
&(m_f e_f + m_s e_s)(\dot{v} + ur) + (I_{wy1}/r_1) \sin\varepsilon\, ur + \{m_f e_f a_f + m_s e_s a_s + (I_{fz} + I_{sz}) \cos\varepsilon\} \dot{r} + \\
&\quad + \{m_f e_f h_f + m_s e_s h_s + (I_{fz} + I_{sz}) \sin\varepsilon\} \ddot{\varphi} - (I_{wy1}/r_1) u \cos\varepsilon \dot{\varphi} + \\
&\quad - (t_c F_{z1} + m_f e_f g + m_s e_s g) \varphi + \\
&\quad + (m_f e_f^2 + m_s e_s^2 + I_{fz} + I_{sz}) \ddot{\delta} + k_\delta \dot{\delta} - (t_c F_{z1} + m_f e_f g + m_s e_s g) \sin\varepsilon\, \delta + \\
&\quad - m_s e_s s_s \ddot{\beta} - (I_{wy1}/r_1) u \dot{\beta} - \{(s_c F_{z1} - m_s s_s g) \sin\varepsilon + F_{x1} h_\beta\} \beta + \\
&\quad + g_v v + g_r r + g_{d\varphi} \dot{\varphi} + g_\varphi \varphi + g_{d\delta} \dot{\delta} + g_\delta \delta = \\
&\qquad = -t_c F_{y1} + M_{z1} \cos\varepsilon + M_{x1} \sin\varepsilon + M_\delta
\end{aligned}
\tag{10.89}
$$

β:

$$
\begin{aligned}
&- m_s s_s \dot{v} - (m_s s_s a_s + I_{sx} \sin\varepsilon) \dot{r} - \{m_s s_s - (I_{wy1}/r_1) \cos\varepsilon\} u r + \\
&\quad - (m_s s_s h_s - I_{sx} \cos\varepsilon) \ddot{\varphi} + (I_{wy1}/r_1) u \sin\varepsilon \dot{\varphi} - (s_c F_{z1} - m_s s_s g) \varphi + \\
&\quad - m_s e_s s_s \ddot{\delta} + (I_{wy1}/r_1) u \dot{\delta} - (s_c F_{z1} - m_s s_s g) \sin\varepsilon\, \delta + \\
&\quad + (m_s s_s^2 + I_{sx}) \ddot{\beta} + k_\beta \dot{\beta} + \{c_\beta - (s_c F_{z1} - m_s s_s g) \cos\varepsilon\} \beta = \\
&\qquad = -s_c F_{y1} - M_{z1} \sin\varepsilon + M_{x1} \cos\varepsilon
\end{aligned}
\tag{10.90}
$$

transient slip and camber angles:

$$\sigma_{\alpha 1} \dot{\alpha}_1' + u \alpha_1' = u \alpha_1 \tag{10.91}$$

$$\sigma_{\gamma 1} \dot{\gamma}_1' + u \gamma_1' = u \gamma_1 \tag{10.92}$$

$$\sigma_{\alpha 2} \dot{\alpha}_2' + u \alpha_2' = u \alpha_2 \tag{10.93}$$

$$\sigma_{\gamma 2} \dot{\gamma}_2' + u \gamma_2' = u \gamma_2 \tag{10.94}$$

tyre forces and moments (coefficients depend on wheel load (10.23, 10.33-10.39)):

$$F_{y1} = C_{F\alpha 1}\alpha_1' + C_{F\gamma 1}\gamma_1' \tag{10.95}$$

$$F_{y2} = C_{F\alpha 2}\alpha_2' + C_{F\gamma 2}\gamma_2' \tag{10.96}$$

$$M_{z1} = -C_{M\alpha 1}\alpha_1' + C'_{M\gamma 1}\gamma_1' - r_{c1}F_{x1}\gamma_1 \tag{10.97}$$

$$M_{z2} = -C_{M\alpha 2}\alpha_2' + C'_{M\gamma 2}\gamma_2' - r_{c2}F_{x2}\gamma_2 \tag{10.98}$$

$$M_{x1} = -C_{Mx\gamma 1}\gamma_1 \tag{10.99}$$

$$M_{x2} = -C_{Mx\gamma 2}\gamma_2 \tag{10.100}$$

slip and camber angles:

$$\alpha_1 = (-v - a_c r + t_c\dot{\delta} + s_c\dot{\beta})/u + \cos\varepsilon\,\delta - \sin\varepsilon\,\beta \tag{10.101}$$

$$\gamma_1 = \varphi + \sin\varepsilon\,\delta + \cos\varepsilon\,\beta \tag{10.102}$$

$$\alpha_2 = (-v + b_c r)/u \tag{10.103}$$

$$\gamma_2 = \varphi \tag{10.104}$$

the rider feedback control gains, occurring in Eq.(10.89), depend on the speed of travel u and are assessed here by trial and error:

$$g_v = g_{vo}/u,\ \ g_r = g_{ro}/u,\ \ g_{d\varphi} = g_{d\varphi o}(1 - u/u_c)/u,$$
$$g_\varphi = g_{\varphi o},\ \ g_{d\delta} = g_{d\delta o}/u,\ \ g_\delta = g_{\delta o} \tag{10.105}$$

The steer torque M_δ is considered to act in addition to the stabilisation steer torque, that results from feedback control, and is represented by the terms containing the control gains in Eq.(10.89).

For the mass centre lateral offset we have introduced for abbreviation:

$$m_{mr}y_{mr} = m_m y_m + m_r y_r \quad \text{with} \quad m_{mr} = m_m + m_r \tag{10.106}$$

If the steer and roll angles remain sufficiently small so that it may be assumed that geometric linearity still prevails we may investigate the influence of larger wheel slip by using for the tyre side forces and moments the non-linear functions of α_i', γ_i', γ_i, wheel load F_{zi} and the braking/driving force F_{xi} according to the Eqs.(10.40-60).

For the baseline configuration of the linear vehicle model the rider is considered rigid ($c_{\varphi r}\to\infty$). With the rider upper torso released, the parameter values of Table 10.2 hold. The tyres parameter values have been chosen as listed in Table 10.1. The model configuration may be considered as typical for a heavy motor cycle. When a rigidly connected rider upper torso is considered (baseline configuration with $\varphi_r = 0$), the relevant parameters result from Eqs.(10.3).

For the linear system defined, the eigenvalues and the steady-state steer angle and steer torque per unit path curvature have been established for a series of values of the speed of travel u (=V). In addition, a number of parameters related

to both the vehicle construction and the tyres have been changed in value to examine their influence.

Table 10.2. Parameters of vehicle in baseline configuration but with rider upper torso released (in baseline configuration $c_{\varphi r} \to \infty$). Rider control gains g with cross-over velocity u_c.

m_m	300 kg	m_f	15 kg	m_s	25 kg	m_r	50 kg
I_{mx}	20 kgm^2	I_{mz}	20 kgm^2	I_{mxz}	4 kgm^2	I_{rx}	4.75kgm^2
I_{fx}	0.5 kgm^2	I_{fz}	0.3 kgm^2	I_{sx}	1.0 kgm^2	I_{sz}	0.7 kgm^2
I_{wy1}	1.0 kgm^2	I_{wy2}	1.0 kgm^2	I_{ey}	0.06 kgm^2		
a_c	0.9 m	b_c	0.6 m	e_f	0.05 m	e_s	0.05 m
s_c	0.7 m	t_c	0.1 m	r_1	0.3 m	r_2	0.3 m
h_m	0.55 m	h_f	0.8 m	h_s	0.4 m	h_d	0.75 m
s_r	0.4 m	h_r	0.9 m			k_δ	0 Nms/rad
k_β	50 Nms/rad	c_β	25kNm/rad	$k_{\varphi r}$	20 Nms/rad	$c_{\varphi r}$	350Nm/rad
g	9.81 m/s^2	n_g	1.5	ε	0.5 rad	C_{dA}	0.2 kg/m
u_c	15 m/s	g_{vo}	-500	g_{ro}	100	$g_{d\varphi o}$	-900
		$g_{\varphi o}$	-10	$g_{d\delta o}$	150	$g_{\delta o}$	50

10.4. Stability Analysis

Free Uncontrolled Motion

In a series of diagrams the variation of the eigenvalues as a function of speed has been presented. The diagram of Fig.10.7 represents the situation corresponding to the baseline configuration defined by Tables 10.1,2 but with the rider regarded as a rigid element of the mainframe body.The upper diagram gives the real part of the eigenvalues of this 12th order system versus speed indicating the degree of instability (if positive) or damping (stable, if negative). The second diagram presents the variation of the imaginary part of the eigenvalues that represent the frequencies of the different modes of vibration (in rad/s). The third diagram depicts the variation of the eigenvalues in the complex plane. Along the curves the speed changes as indicated.

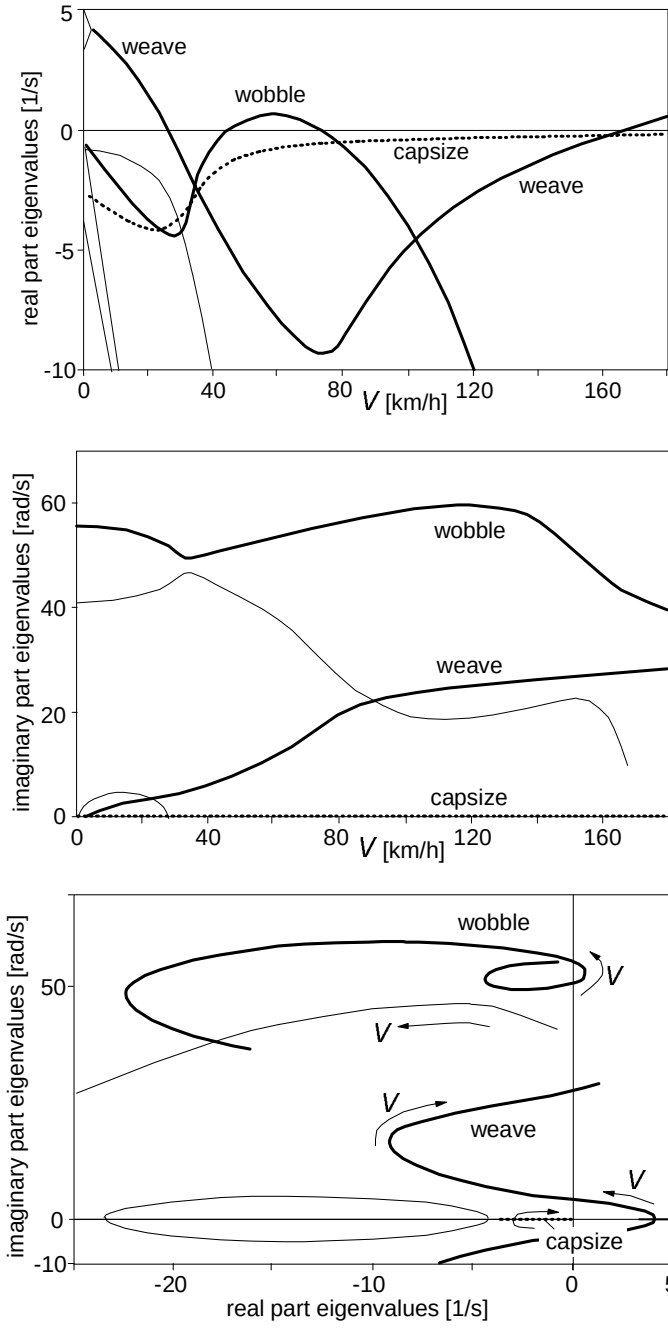

Fig. 10.7. Baseline configuration (rigid rider, with air drag,, zero forward acceleration, no control). Real and imaginary parts of eigenvalues versus speed of travel V.

The weave mode is a relatively low frequency oscillatory motion in which the whole vehicle takes part. This mode exhibits a possibly dangerous unstable yaw and roll motion at higher speeds (in our case above a speed of ca. 165km/h) with a frequency of 3 to 4 Hz. At low speeds the frequency decreases and the mode becomes unstable and constitutes the phenomenon where the uncontrolled vehicle falls over. At very low speed it is observed that the complex pair of roots with a positive real part changes into two positive real roots constituting the divergent unstable modes associated with capsizing of the whole machine and of the front frame about the inclined steer axis (the latter is observable with the motorcycle on its centre stand and with the front wheel clear of the ground). The frequency of the oscillation can be found from the two lower plots. In the high speed unstable range the frequency of the weave mode appears to be around 27 rad/s or ca. 4 Hz. The capsize mode can in certain cases become (moderately) unstable beyond a relatively low critical velocity. The eigenvalue remains real and, consequently, the motion does not show oscillations. In our case, this mode remains stable. The third mode that is of interest is the wobble mode which is a steering oscillation that can become unstable in a range of moderate speeds (in our case between ca. 45 and 70 km/h). The frequency in the unstable range appears here to take values around 55 rad/s or ca. 8 Hz as can be seen in the two lower plots with the imaginary part as the ordinate. The frequency is mainly influenced by the front frame inertia, the mechanical trail and the front tyre cornering stiffness. The remaining modes are well damped and consequently of less interest.

Starting out from the baseline configuration (with air drag) the effect of changes in several system parameters has been investigated. To get a clear picture of the role various parameters play in stabilising or destabilising this single track vehicle, their values have been changed drastically. Figure 10.8 shows the resulting stability characteristics. For clarity, the wobble mode curves have been shown separately in the lower diagram. From the results we may conclude the following:

1. The model shows that *absence of air drag* (case 1) slightly stabilises the weave mode and destabilises the wobble mode.
2. *Torsional rigidity of the mainframe* (case 2, large c) appears to be of crucial importance especially for the manner in which the wobble manifests itself. High stiffness or disregarding the torsional compliance gives rise to a (too) high critical speed. A more flexible frame (baseline configuration) causes the wobble to occur in a limited range of speed around 50km/h which turns out to be experienced also in reality.
3. Almost vanishing *relaxation lengths* (rapid tyre response) drastically suppresses the wobble instability.

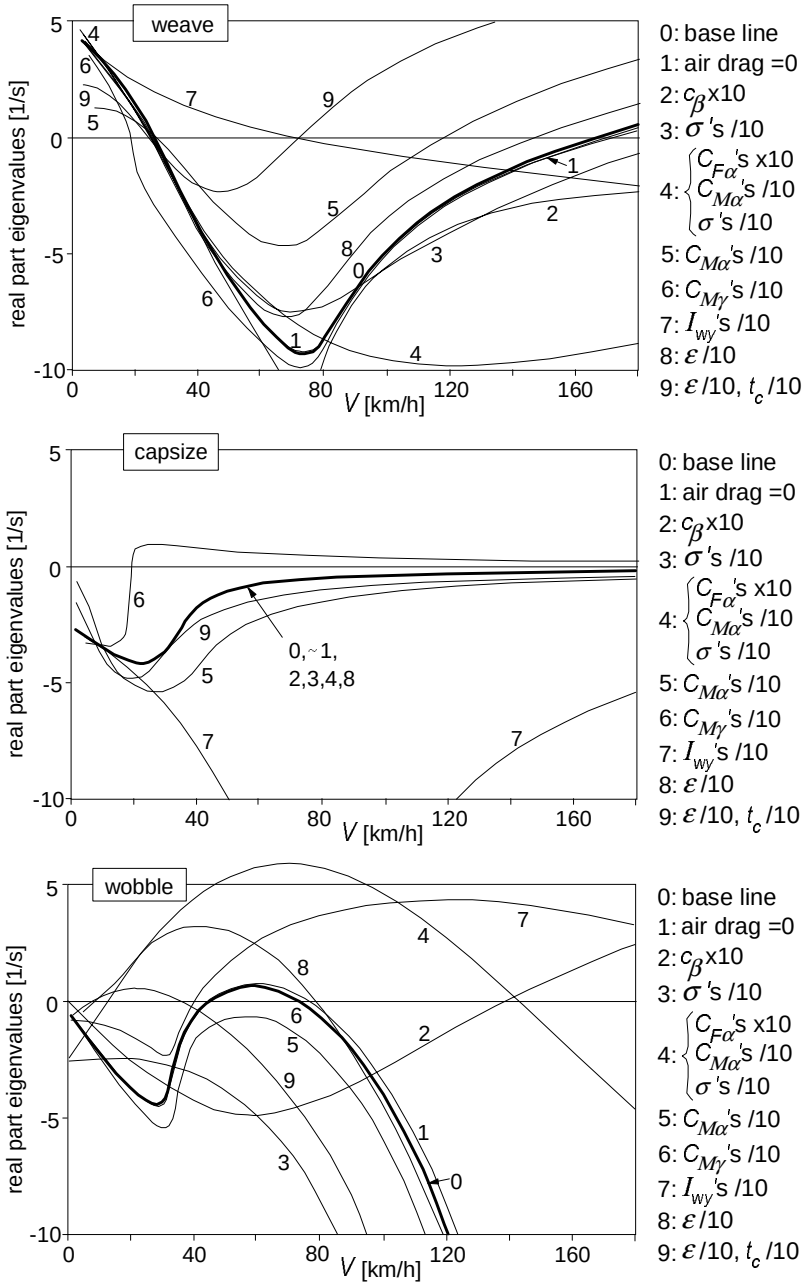

Fig. 10.8. Effect of drastic changes in model parameter values on stability characteristics.

4. Making the *tyre almost rigid* (with in addition to very small σ: very large cornering stiffness and very small pneumatic trail, case 4) would drastically suppress the high speed weave but gives rise to violent wobble over a large range of speed. A much larger camber force stiffness can not be technically realised even with a very stiff solid wheel. It would increase the low speed unstable weave range and stabilise the high speed weave; wobble is almost not affected (not shown).
5. Making only the *aligning torque stiffnesses* very small destabilises the high speed weave mode and stabilises the wobble mode. The capsize root is made more negative.
6. Even a considerable decrease of the *camber aligning moment stiffness* has very little effect, at least in the case of zero or very small longitudinal tyre forces. The same holds for the *overturning couple stiffness* that is: a small *crown radius* (not shown). The smaller camber aligning moment stiffness does have an influence on the capsize stability. As indicated in the diagram, capsize instability now shows up and occurs beyond a speed of around 20 km/h.
7. The fundamental role of the *gyroscopic coupling* terms becomes evident when the polar moments of the wheel are considerably reduced (case 7). First, the low speed unstable weave range is stretched to almost 70km/h and second, the wobble becomes violently unstable up to very high levels of speed. It may be concluded that the gyroscopic effect of the rotating wheels is largely responsible for the fact that the motorcycle is capable of moving in a stable manner.
8. Reduction of the *rake angle* to an almost vertical steer axis orientation with the caster length kept the same would strongly destabilise the wobble mode.
9. At the same time reducing the *caster length* as well (case 9) would strongly destabilise the weave mode which unveils the fundamental effect of introducing the steer axis backwards inclination.

Effects of more realistic levels of variation of the system parameters have been presented in the stability diagrams of Figs. 10.9. Comparison with the curves that represent the baseline configuration (0) reveals that (again, curve numbers correspond to list numbers below):

- A 20% smaller *front relaxation length* stabilises the wobble mode and has practically no effect on the weave and capsize modes.
- A smaller *rear relaxation length* stabilises the wobble mode in a lesser degree and stabilises the weave mode. No effect on the capsize mode.
- Moving the *centre of gravity* of the mainframe plus rider 10cm *forwards* turns out to strongly stabilise the weave mode. However, it destabilises the

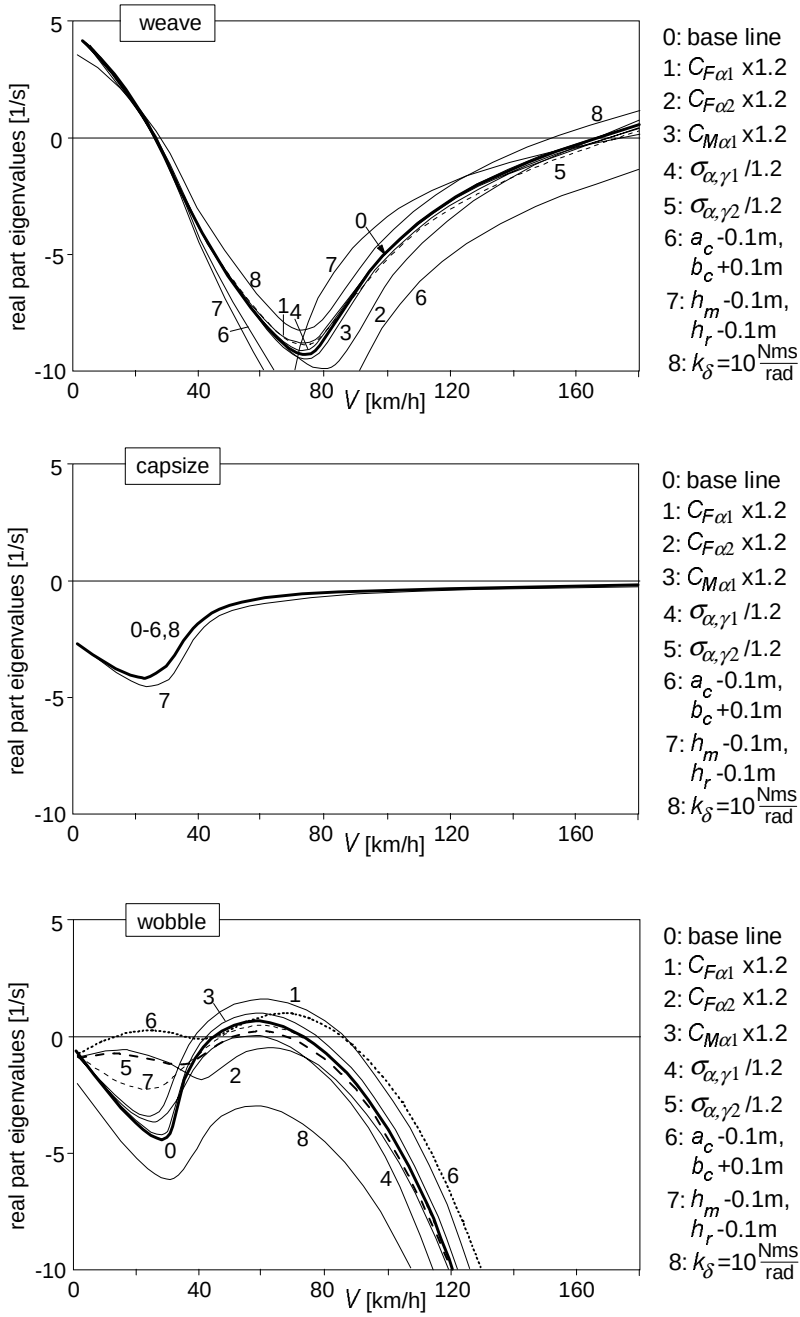

Fig. 10.9. Effect of realistic changes in parameter values on stability characteristics.

wobble. Capsize is not affected.

- *Lowering* both *centres of gravity* over 10cm stabilises both the weave and wobble modes a little. The capsize mode becomes more stable.
- Adding *steer damping* does, of course, stabilise the wobble mode. However, it adversely affects the weave mode stability.

For the free control situation we finally consider the influence of driving or braking and the addition of a degree of freedom: the rider lean angle measured with respect to the mainframe roll angle. Figure 10.10 shows the stability diagram of the baseline configuration at zero net acceleration force (10.18) $F_{ax} = 0$ (rear wheel driving force just withstands the air drag so that speed is

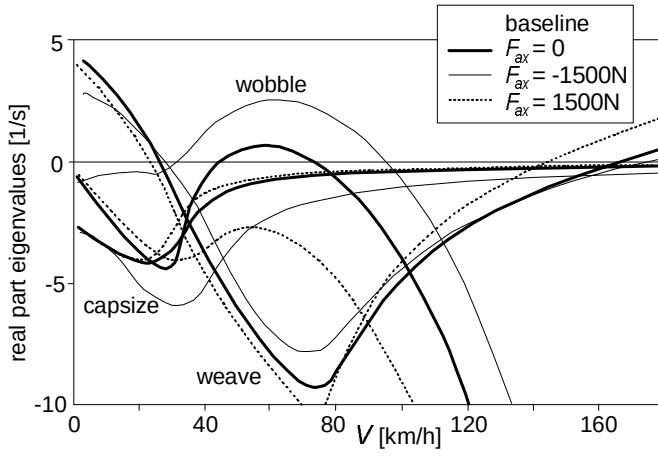

Fig. 10.10. Effect of the application of braking (F_{ax}, $F_{x1,2} < 0$) and driving forces (F_{ax}, $F_{x2} > 0$) on the stability diagram (baseline configuration).

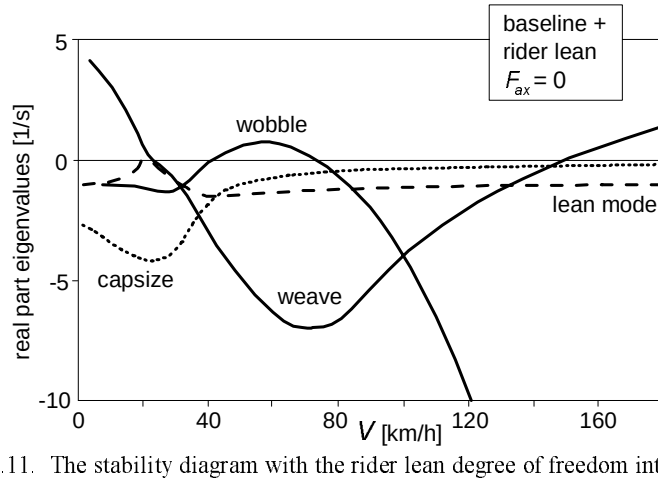

Fig. 10.11. The stability diagram with the rider lean degree of freedom introduced.

constant), at braking (10.25) F_{ax} = -1500N and at driving (10.26) F_{ax} = 1500N. It is observed that braking destabilises the wobble mode which is mainly due to the increased normal load at the front wheel that gives rise to larger relaxation length and cornering and aligning stiffnesses, the effects of which were shown in Fig.10.9. The terms with $F_{x1}\delta$ in Eq.(10.86) (destabilising) and with $h_\beta F_{x1}\beta$ in Eq.(10.89) (stabilising) have a smaller effect. The terms in Eqs.(10.85,89) with F_{x1} appear to largely neutralise the stabilising effects of the increased front wheel load.

When driving, the longitudinal force is generated at the rear wheel only. Obviously, wobble is completely suppressed. Weave, however, appears to show up already at considerably lower speeds.

As depicted in Fig.10.11, the introduction of the lean angle of the rider as an additional generalised coordinate with torsional stiffness and damping with respect to the mainframe gives rise to a decrease of the critical velocity for weave instability while the wobble mode is hardly affected. The lean angle is introduced to enable the study of the response of the vehicle motion to a step change in lean torque M_r which is defined to act between upper torso and mainframe about the longitudinal lean axis.

Step Responses of Controlled Motion

We will study the responses of the vehicle motion to a unit step of the imposed steer torque M_δ and of the lean torque M_r. This, as a first attempt to investigate the transient handing quality of the vehicle. First, the motorcycle must be stabilised in the range of speed we want to cover. For this, the various feed-back signals have been provided with gains defined by Eq.(10.105) and Table 10.2. In Fig.10.12 the six gains have been presented as a function of the speed of travel. Similar functions have been used by Ruijs (1985) in the feed-back control loops to stabilise the unmanned motorcycle with stabilising rider-robot. The peculiar change in sign that occurs in the gain from roll rate to steer torque is essential to stabilise both the low and the high speed weave.

The resulting stability diagram is presented in Fig.10.13. Comparison with Fig.10.10 shows that adopted feed-back gains considerably enlarges the stable velocity range especially at the low end. An additional control action using the lean torque (and as a consequence moving the rider c.g. laterally) would be necessary to further push back the low speed instability which here appears to correspond to an unstable lean mode. At such low speeds, steering would be almost ineffective to move the contact point laterally and thereby stabilise the motion.

In Fig.10.14 the resulting unit step responses have been shown for the case of zero F_{ax}. The figure depicts the variations of the yaw rate r, the steer angle δ,

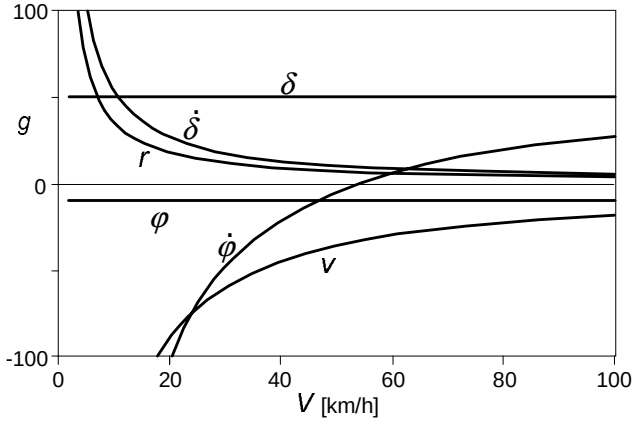

Fig. 10.12. Hypothetical rider steer torque feed-back stabilising control gains versus speed.

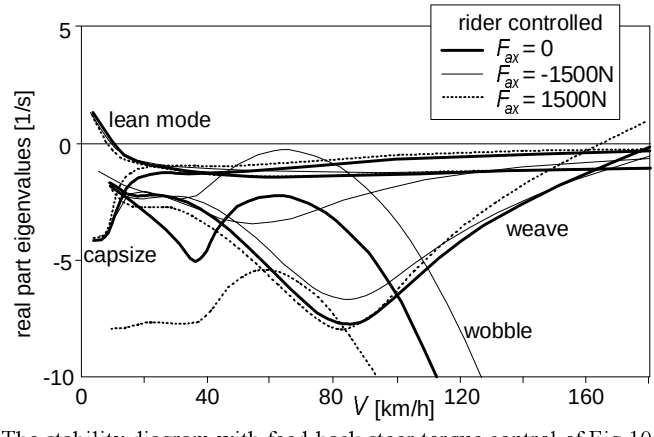

Fig. 10.13. The stability diagram with feed-back steer torque control of Fig.10.12 activated.

the mainframe roll angle φ and the upper torso roll angle $\varphi+\varphi_r$. Two values of speed have been considered: 35 and 70 km/h. The results are most interesting. We observe that as a result of a positive change in steer torque (to the right) first a positive steer angle arises with also positive yaw rate (to the right). After a short time, a change in sign occurs and a negative yaw rate is being developed with a negative steer angle. It is seen, that during this short transition time the roll angle begins to build up in the correct direction (to the left) that belongs to the final steady-state curving situation. This variation in the motion variables is similar to what would be observed in reality. The uncontrolled vehicle is stable at the speed V=35km/h (Fig.10.11). If at this speed the stabilisation controller would not be activated, the motorcycle exhibits a similar response but with angles and yaw rate becoming larger and with less damped wobble and weave vibrations.

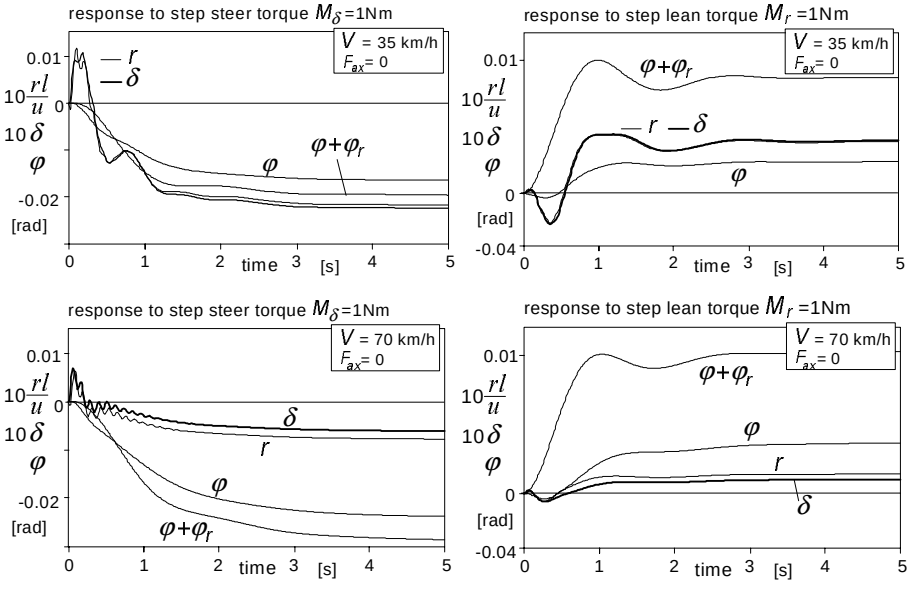

Fig. 10.14. The step responses of motion variables to unit steer and rider lean torque at zero forward acceleration, F_{ax} = 0 (with rider stabilising control).

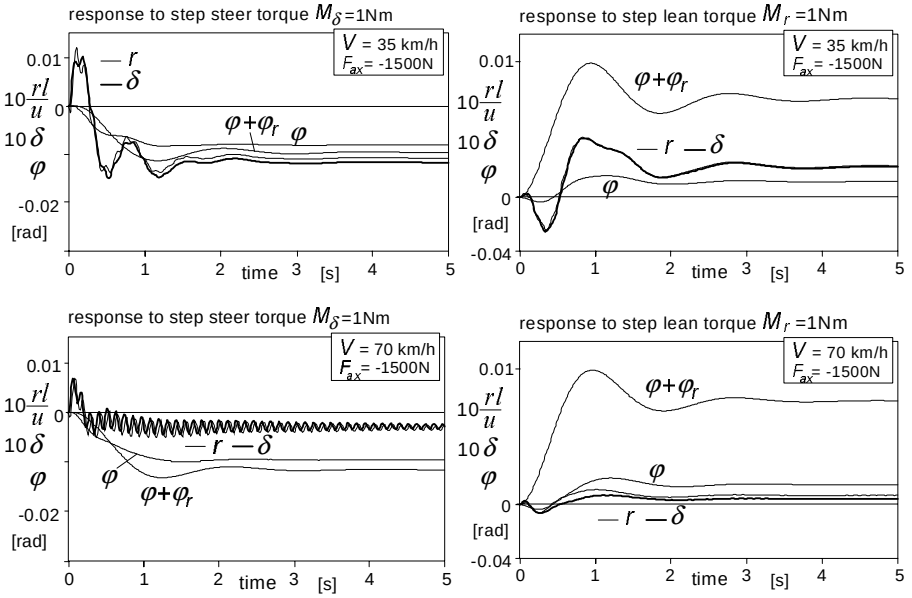

Fig. 10.15. The step responses of motion variables to unit steer and rider lean torque while braking, F_{ax} = -1500N (with rider stabilising control).

The lean torque response shows initially a negative roll angle which is the result of counteracting the imposed (internal) lean torque. After the initial phase, the angle becomes positive. Also the steer angle and with that the yaw rate turn out to become negative in the initial phase which causes the contact points to move in the right direction (to the left). The steady-state situation is reached after low frequency damped lean mode oscillations. If the controller is not activated, a very similar response with now low frequency damped weave oscillations (Fig.10.11) occurs. Now, it becomes clear that it is mainly the gyroscopic couple (plus camber aligning moment) that steers the front wheel initially in the right direction. Analysis shows that the hardly visible small positive steer angle peak right after the lean torque step change is due to the mechanical trail and the aligning stiffness of the front wheel (t_c and $C_{M\alpha 1}$).

At the higher speed of V=70km/h the responses show the same tendencies but with much smaller steer angles and yaw rates. The weave is more damped and the wobble less. Without controller the wobble becomes unstable and a violent steering oscillation at ca. 9Hz is developed.

With the lean degree of freedom disregarded, only the response to steer torque can be considered. The resulting motion responses turn out to get close to those depicted in the left-hand diagrams of Fig.10.14 with the curves for $\varphi+\varphi_r$ deleted. The low frequency oscillation that is predominant at the lower speed is now attributed to the weave mode. The uncontrolled system (Fig.10.7) is just stable at 35km/h and behaves similar to the controlled one albeit that somewhat larger weave and wobble vibrations and a larger steady-state response arise. At 70km/h the unstable wobble vibration develops again.

Figure 10.15 presents the results for the system while the brakes are applied (F_{ax} = -1500N). The course of the various signals show similar tendencies as occurs in the unbraked situation. The obvious differences are the lowly damped wobble vibration that is seen to occur at 70 km/h (cf. Fig.10.13) and the much smaller steady-state responses (cf. Fig.10.20 of next section). These differences are primarily due to the accompanied load transfer.

10.5. Analysis of Steady-State Cornering

When a steady-state cornering condition is reached equilibrium of forces and moments exists. We consider the equilibrium in lateral direction, about the vertical axis and about the line of intersection of mainframe centre plane and road plane; this in addition to the static equilibrium of forces in vertical direction. In the approximate analysis the small c.g. forward offsets of the steerable front and subframes e_f and e_s will be neglected. In addition, the twist angle β and the

rider lean angle φ_r will be disregarded. Instead, we will study the effect of a sideways shift y_{mr} of the centre of gravity of the combined mainframe and rider. Once the side forces and the roll angle have been assessed at a given lateral acceleration, the slip angles can be determined and from their difference with the given non-dimensional path curvature, l/R, the steer angle can be estimated. By considering the equilibrium about the steering axis the steer torque needed to maintain the curving motion is derived.

First, an approximate linearised theory is developed. The findings will be compared with the exact steady-state solutions of the linear differential equations (10.85-94) with the φ_r degree of freedom deleted. After that, the theory is extended to larger roll angles and the non-linear handling diagram is established for the steadily cornering motorcycle.

10.5.1. Linear Steady State Theory

The theoretical expressions for the coefficients concerning the steady-state turning behaviour and the c.g. lateral offset effects will be developed in several successive stages starting with the simplest case in which tyre moments, gyroscopic effects and air drag are disregarded and ending with the ultimate configuration in which all these items are included and driving or braking may be considered. First, the required roll and steer angles will be assessed and with these results the expression for the steer torque determined.

Wheel Moments and Air Drag Neglected

As an introduction, we will first discuss the simple case where the air drag, longitudinal tyre forces and all the tyre moments about the vertical axis are disregarded. That means that the aligning moment, the overturning couple and the spin (camber) moment are set equal to zero. Moreover, we neglect the gyroscopic couples.

For the lateral wheel forces we find as in Chapter 1, Section 1.3.2, Eq.(1.61) for the automobile with pneumatic trails neglected (equilibrium in lateral direction and about the vertical axis):

$$\frac{F_{y1}}{F_{z1o}} = \frac{F_{y2}}{F_{z2o}} = \frac{a_y}{g} \quad \left(= \frac{ur}{g} \right) \tag{10.107}$$

The roll angle φ_y needed to maintain equilibrium about the longitudinal x axis when a lateral offset y_{mr} of the centre of gravity of the combined mainframe and rider exists (cf. Figs.10.1,2) equals:

$$\varphi_y = -\frac{m_{mr} y_{mr}}{m h} \tag{10.108}$$

The additional roll angle of the motorcycle that arises while cornering becomes:

$$\varphi - \varphi_y = \frac{a_y}{g} \quad \left(= \frac{ur}{g} \right) \tag{10.109}$$

The front and rear camber angles read in terms of the roll angle and the ground steer angle, cf. Eqs.(10.12-14):

$$\gamma_1 = \varphi + \delta' \tan \varepsilon \tag{10.110}$$

$$\gamma_2 = \varphi \tag{10.111}$$

The slip angles result from Eq.(10.28), primes omitted, with (10.107-111). We find:

$$C_{F\alpha 1} \alpha_1 = (F_{z1o} - C_{F\gamma 1}) \varphi + C_{F\gamma 1} \delta' \tan \varepsilon - F_{z1o} \varphi_y \tag{10.112}$$

$$C_{F\alpha 2} \alpha_2 = (F_{z2o} - C_{F\gamma 2}) \varphi - F_{z2o} \varphi_y \tag{10.113}$$

These equations show the importance of the difference between camber stiffness (N/rad) and initial tyre load (N) in view of the sign of the slip angles. Obviously, in general, side slip is needed to accomplish lateral/yaw equilibrium. It may be realised, that at higher speeds the steer angle is much smaller than the roll angle, $|\delta'| << |\varphi|$.

With the wheel base $l = a_c + b_c$ and the Eqs.(10.15) we find the relationship between the ground steer angle δ' $(= \delta \cos \varepsilon)$ on the one side and the non-dimensional path curvature $l/R = lr/u$ and the difference of slip angles on the other:

$$\delta' = \frac{l}{R} + \alpha_1 - \alpha_2 \tag{10.114}$$

With the use of (10.112,113) the ground steer angle may now be written in terms of the non-dimensional path curvature l/R, the lateral acceleration a_y and the c.g. offset y_{mr}:

$$\zeta \delta' = \frac{l}{R} + \eta \frac{a_y}{g} + \eta_y \frac{m_{mr} y_{mr}}{m h} \tag{10.115}$$

where we have introduced the steer angle coefficient ζ which is a bit larger than unity:

$$\zeta = \zeta_{oo} = 1 + \frac{C_{F\gamma 1}}{C_{F\alpha 1}} \tan \varepsilon \tag{10.116}$$

the understeer coefficient η of the simplified system:

$$\eta = \eta_{oo} = \frac{F_{z1o}}{C_{F\alpha 1}} - \frac{F_{z2o}}{C_{F\alpha 2}} - \left(\frac{C_{F\gamma 1}}{C_{F\alpha 1}} - \frac{C_{F\gamma 2}}{C_{F\alpha 2}} \right) \tag{10.117}$$

and the c.g. offset coefficient η_y:

$$\eta_y = \eta_{yoo} = \frac{C_{F\gamma 1}}{C_{F\alpha 1}} - \frac{C_{F\gamma 2}}{C_{F\alpha 2}} \tag{10.118}$$

Since we have proportions occurring in the right-hand member of (10.117) which are all of the same order of magnitude it is evident that the understeer coefficient of the single track vehicle is quite different from its counterpart that is found for the automobile where only the first two terms appear in the simplified analysis while ζ is assumed equal to one. The ratio of camber and cornering stiffness front relative to rear is of decisive importance for the sign and magnitude of the understeer coefficient and consequently also for the difference in slip angle front and rear which follows from (10.114,115):

$$\zeta(\alpha_1 - \alpha_2) = (1-\zeta)\frac{l}{R} + \eta\frac{a_y}{g} + \eta_y \frac{m_{mr} y_{mr}}{m h} \tag{10.119}$$

where the first term in the right-hand member vanishes if the rake angle equals zero making ζ=1.

When the motorcycle moves straight ahead ($l/R = a_y = 0$) Eqs.(10.115,119) show that a steer angle and difference in slip angles would arise solely as a result of the c.g. offset and depend on the difference of the ratios of camber and side slip stiffnesses front and rear.

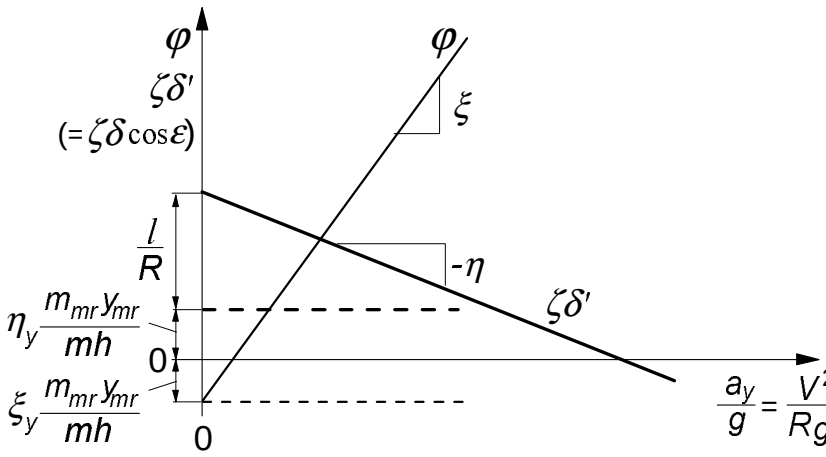

Fig. 10.16. The ground steer angle δ' and the roll angle φ due to path curvature $1/R$ and c.g.lateral offset y_{mr} and the variation with lateral acceleration a_y.

The general course of steer angle and roll angle versus speed of travel at given path curvature and c.g. lateral offset has been illustrated in Fig.10.16. The coefficients ξ and ξ_y will be defined below.

The actual steer angle δ of the handlebar about the inclined steer axis with rake angle ε is obtained from the ground steer angle δ' by dividing this angle by $\cos\varepsilon$ as has been formulated by Eq.(10.12) with twist angle β set equal to zero.

If fore and aft load transfer due to aerodynamic drag is considered, the lines of Fig.10.16 are not quite straight anymore. The understeer coefficient η corresponds to the slope of the line in the diagram if air drag is neglected. This may be compared with the theory for the automobile where ζ is taken equal to unity and air drag is disregarded (Fig.1.10). If, at high speed, air drag is not negligible, η is found as the slope of the characteristic that arises if $\zeta\delta'$ - l/R is plotted against a_y/g with the speed V held constant while the curvature increases with growing lateral acceleration. If we would plot $\zeta\delta'$ versus a_y/g, again, in this linear theory with constant speed, a straight line arises which now has a slope equal to $lg/V^2 + \eta$. For the sake of convenience the above definition for the degree of understeer has been adopted although a more proper definition might be $\eta' = (\partial\delta/\partial(a_y/g))_R = (\eta/\zeta)/\cos\varepsilon$.

Discussion of numerical results (Table 10.3) follows after more adequate approximations have been developed. For the simple theory developed so far the coefficients ξ and ξ_y appearing in the diagram are equal to unity. Below, we will see the effect of tyre width and gyroscopic couples on these roll angle coefficients.

Tyre Overturning and Gyroscopic Couples Included

Closer consideration of the roll equilibrium around the line of intersection reveals that instead of (10.109) we actually have with also the caster length t_c taken into account (cf. Eq.(10.88) with (10.2)):

$$mgh\varphi - mha_y - (I_{wy1}/r_1 + I_{wy2}/r_2)\,ur + F_{z1}t_c\delta + M_{x1} + M_{x2} - m_{mr}gy_{mr} = 0 \tag{10.120}$$

The third term represents the sum of gyroscopic couples. With Eqs.(10.13,14,30) we obtain for the roll angle:

$$\varphi = \frac{(mh + I_{wy1}/r_1 + I_{wy2}/r_2)\,a_y + (C_{Mxy1}\sin\varepsilon - F_{z1}t_c)\delta - m_{mr}gy_{mr}}{(mgh - C_{Mxy1} - C_{Mxy2})} \tag{10.121}$$

Inspection of the values of parameters as listed in Tables 10.1,2 leads to the conclusion that the steer angle δ has a negligible effect on the relationship between roll angle φ and y_{mr} and also between φ and lateral acceleration $a_y = ur$

if $\delta <<\sim 30(a_y/g)$. With δ expressed in radians it is expected that at not too low speed, this condition will soon be satisfied in the more interesting range of operation.

We will henceforth use the approximate expression for the roll angle with the δ term in (10.121) neglected:

$$\varphi = \xi \frac{a_y}{g} - \xi_y \frac{m_{mr} y_{mr}}{mh} \tag{10.122}$$

where the tilt coefficients ξ and ξ_y read:

$$\xi = g \frac{mh + I_{wy1}/r_1 + I_{wy2}/r_2}{mgh - C_{Mx\gamma 1} - C_{Mx\gamma 2}} \tag{10.123}$$

$$\xi_y = \frac{mgh}{mgh - C_{Mx\gamma 1} - C_{Mx\gamma 2}} \tag{10.124}$$

The quantities appear to be a little larger than unity due to the gyroscopic action and the width of the tyres (finite crown radii). The tilt coefficients become in the baseline configuration (Tables 10.1,2):

$$\xi = 1.21 \ , \quad \xi_y = 1.18 \tag{10.125}$$

An effective tilt angle φ' (the angle of the dashed line, through tyre contact point and mass centre, indicated in Fig.10.1 with respect to the vertical) may be defined. We have:

$$\varphi' = \frac{\varphi}{\xi_y} \tag{10.126}$$

With the additional moments about the x axis now introduced, we find for the understeer coefficient:

$$\eta = \eta_o = \frac{F_{z1o}}{C_{F\alpha 1}} - \frac{F_{z2o}}{C_{F\alpha 2}} - \xi \left(\frac{C_{F\gamma 1}}{C_{F\alpha 1}} - \frac{C_{F\gamma 2}}{C_{F\alpha 2}} \right) \tag{10.127}$$

and the c.g. offset coefficient:

$$\eta_y = \eta_{yo} = \xi_y \left(\frac{C_{F\gamma 1}}{C_{F\alpha 1}} - \frac{C_{F\gamma 2}}{C_{F\alpha 2}} \right) \tag{10.128}$$

while the steer angle coefficient ζ remains unchanged:

$$\zeta = \zeta_o = 1 + \frac{C_{F\gamma 1}}{C_{F\alpha 1}} \tan \varepsilon \tag{10.129}$$

The in Table 10.3 listed numerical values will be discussed later on.

Tyre Yaw Moments Included

Because of the obvious sensitivity to slight variations in tyre parameters we should examine the influence of the remaining (yaw) moments due to side slip and camber acting on the tyre. When taking into account the tyre aligning torques and the moment applied by the air drag force (assumed to act parallel to the x axis) we find for the tyre side forces from the equilibrium conditions:

$$F_{y1} = C_{F\alpha 1}\alpha_1 + C_{F\gamma 1}\gamma_1 = \frac{1}{l}\left(b m a_y - h_d F_d \varphi - M_{z1} - M_{z2}\right) \tag{10.130}$$

$$F_{y2} = C_{F\alpha 2}\alpha_2 + C_{F\gamma 2}\gamma_2 = \frac{1}{l}\left(a m a_y + h_d F_d \varphi + M_{z1} + M_{z2}\right) \tag{10.131}$$

in which the lateral acceleration a_y can, with (10.122), be expressed in terms of the roll angle φ and the c.g. offset y_{mr}. The aligning torques are:

$$M_{zi} = -C_{F\alpha i} t_{\alpha i}\alpha_i + C_{M\gamma i}\gamma_i \tag{10.132}$$

with camber aligning torque stiffness that without the action of the longitudinal tyre force is defined by (10.36). The camber angles can be expressed in terms of the roll angle and the slip angles by using the relations (10.109,110,113). We have:

$$\gamma_1 = \varphi + \delta' \tan\varepsilon = \varphi + \left(\frac{l}{R} + \alpha_1 - \alpha_2\right)\tan\varepsilon \tag{10.133}$$

$$\gamma_2 = \varphi \tag{10.134}$$

From the thus created two equations the two unknown slip angles α_i can be solved and expressed in terms of the known path curvature l/R, roll angle φ and c.g. offset y_{mr}. By substituting the expression (10.114):

$$\delta' = \frac{l}{R} + \alpha_1 - \alpha_2 \tag{10.114}$$

in the relationship (10.115):

$$\zeta\delta' = \frac{l}{R} + \eta\frac{a_y}{g} + \eta_y\frac{m_{mr} y_{mr}}{m h} \tag{10.115}$$

and using again (10.122) the steer angle, understeer and c.g. offset coefficients ζ, η and η_y can finally be assessed. The resulting expressions read:

$$\zeta = 1 + \left\{\frac{C_{F\gamma 1}}{C_{F\alpha 1}} + \left(\frac{1}{C_{F\alpha 1}} + \frac{1}{C_{F\alpha 2}}\right)\frac{t_{\alpha 1} C_{F\gamma 1} + C_{M\gamma 1}}{l^*}\right\}\tan\varepsilon \tag{10.135}$$

with the effective wheel base

$$l^* = l - t_{\alpha 1} + t_{\alpha 2} \tag{10.136}$$

and

$$\eta = \lambda_1 \frac{F_{z1o} - \xi C_{F\gamma 1}}{C_{F\alpha 1}} - \lambda_2 \frac{F_{z2o} - \xi C_{F\gamma 2}}{C_{F\alpha 2}} + \\ - \frac{\xi}{l^*}\left(\frac{1}{C_{F\alpha 1}} + \frac{1}{C_{F\alpha 2}}\right)\left(C_{M\gamma 1} + C_{M\gamma 2} + F_d h_d\right) \tag{10.137}$$

and

$$\eta_y = \xi_y \left\{ \lambda_1 \frac{C_{F\gamma 1}}{C_{F\alpha 1}} - \lambda_2 \frac{C_{F\gamma 2}}{C_{F\alpha 2}} + \\ + \frac{1}{l^*}\left(\frac{1}{C_{F\alpha 1}} + \frac{1}{C_{F\alpha 2}}\right)\left(C_{M\gamma 1} + C_{M\gamma 2} + F_d h_d\right) \right\} \tag{10.138}$$

in which the coefficients λ_1 and λ_2 have been introduced:

$$\lambda_1 = 1 + \frac{1}{l^*} \frac{C_{F\alpha 1} + C_{F\alpha 2}}{C_{F\alpha 2}} t_{\alpha 1} \tag{10.139}$$

$$\lambda_2 = 1 - \frac{1}{l^*} \frac{C_{F\alpha 1} + C_{F\alpha 2}}{C_{F\alpha 1}} t_{\alpha 2} \tag{10.140}$$

which are close to unity (around 1.03 and 0.95 respectively in the baseline configuration changing a little depending on load transfer).

In Table 10.4, appearing further on, the values that η and η_y take in the baseline configuration (Tables 10.1,2) for the cases without and with air drag (in the latter case at speeds 1 and 160 km/h) have been listed together with the current wheel loads and air drag force.

Driving and Braking Forces Included

Applying longitudinal forces to the tyres through braking or driving have three effects on the handling behaviour of the vehicle occurring through the tyres. First, we have the direct effect (only at braking) due to the sideways component of the front wheel longitudinal tyre force that arises as a result of the steer angle. Then, we have two indirect effects brought about by changes in tyre behaviour due to the longitudinal force (notably in the camber aligning torque coefficient $C_{M\gamma}$), and due to the induced load transfer. In addition, the longitudinal acceleration inertia forces acting in the mass centres exert a moment about the vertical z axis if we have a roll angle φ and possibly a c.g. lateral offset y_{mr}. The front and rear lateral tyre forces now become, instead of the right-most members of Eqs.(10.130,131):

$$F_{y1} = \frac{1}{l}\left\{b m a_y - l F_{x1}\delta' - (h_d F_d \varphi + M_{z1} + M_{z2} + m a_x h \varphi + m_{mr} a_x y_{mr})\right\} \quad (10.141)$$

$$F_{y2} = \frac{1}{l}\left\{a m a_y + (h_d F_d \varphi + M_{z1} + M_{z2} + m a_x h \varphi + m_{mr} a_x y_{mr})\right\} \quad (10.142)$$

with the tyre aligning torques according to (10.132) but with the total camber aligning torque stiffness now expressed as (according to (10.29)):

$$C_{M\gamma i} = C'_{M\gamma i} - r_{ci} F_{xi} \quad (10.143)$$

The same procedure is followed as before and we find the coefficients ζ, η and η_y augmented for the presence of vehicle acceleration a_x and longitudinal tyre forces F_{x1}. The terms that are to be added to the expressions (10.135,137,138) (for zero acceleration, $F_{ax}=0$, cf. (10.19)) read respectively:

$$\Delta\zeta_{Fx} = \lambda_1 \frac{F_{x1}}{C_{F\alpha 1}} \quad (10.144)$$

$$\Delta\eta_{Fx} = -\frac{\xi}{l^*}\left(\frac{1}{C_{F\alpha 1}} + \frac{1}{C_{F\alpha 2}}\right) m h a_x \quad (10.145)$$

$$\Delta\eta_{y,Fx} = \frac{\xi_y}{l^*}\left(\frac{1}{C_{F\alpha 1}} + \frac{1}{C_{F\alpha 2}}\right)\left(C_{Mx\gamma 1} + C_{Mx\gamma 2}\right)\frac{a_x}{g} \quad (10.146)$$

Numerical Results

For the parameter values of the baseline configuration the various handling coefficients have been presented in Tables 10.3 and 10.4 together with the calculated air drag, wheel loads and possibly braking or driving forces (for a given acceleration force F_{ax}). Table 10.3 shows the values obtained when using the simpler expressions for the coefficients which result when the gyroscopic and overturning couples and/or the aligning torques are neglected, according to the theories covered by the Eqs.(10.107-118) and (10.120-129). The influence of air drag results here from the induced load transfer. Table 10.4 presents the results when all the moments are accounted for and also braking and driving may be considered. The equations concerned are (10.130-140) and (10.141-146). First of all, when we compare the different stages of approximation, it is observed that the influence of the various wheel and tyre moments is essential in generating more correct values of understeer and c.g. offset coefficients, η and η_y.

Table 10.3. Handling coefficients with tyre aligning moments neglected.
F_{z1o}= 1732N, F_{z2o}= 2094N, cos ε = 0.878; Eqs(10. 116-118,123-129).

V	F_d	F_{z1}	F_{z2}	ξ	ξ_y	ζ_o	η_{oo}	η_o	η_{yoo}	η_{yo}
km/h	N	N	N	-	-	-	-	-	-	-
0	0	1732	2094	1.214	1.18	1.031	0	0	0	0
160	0	1732	2094	1.214	1.18	1.031	0	0	0	0
160	395	1534	2291	1.217	1.183	1.03	0.013	0.016	-0.01	-0.01

Table 10.4. Handling coefficients with tyre aligning moments and driving and braking included.
F_{z1o} = 1732N, F_{z2o} = 2094N, cosε = 0.878; Eqs.(10.123,124,135-138,144-146).

V	F_d	F_{ax}	F_{x1}	F_{x2}	F_{z1}	F_{z2}	ξ	ξ_y	ζ	η	η_y
km/h	N	N	N	N	N	N	-	-	-	-	-
1	0	0	0	0	1732	2094	1.214	1.18	1.034	0	0.014
160	0	0	0	0	1732	2094	1.214	1.18	1.034	0	0.014
160	395	0	0	395	1534	2292	1.217	1.183	1.033	0	0.023
1	0	1500	0	1500	1137	2689	1.222	1.188	1.028	0	0
1	0	-1500	-912	-588	2327	1499	1.207	1.173	1.008	0	0.034
160	395	1500	0	1895	940	2886	1.225	1.19	1.026	0	0
160	395	-1500	-615	-490	2129	1697	1.209	1.176	1.016	0	0.042

The steer angle coefficient ζ is much less affected by the tyre moments while the roll angle coefficients ξ and ξ_y are influenced considerably by the gyroscopic and/or overturning couple coefficients; note that these coefficients take the value one in the simplest approximation according to Eqs.(10.108,109).

The last two columns of Table 10.4 indicate that for the conditions considered the understeer coefficient shows large changes but keeps the same negative sign, which means: steering less to the right for a right-hand turn if speed is increased. In automobile terms one would speak of an oversteered vehicle. However, the steer angle does not serve as an input quantity and the speed where the steer angle changes sign is not a critical speed beyond which instability occurs. It is the steer torque that acts as the input variable and when at a given path radius a change in sign of the steer torque would arise at a certain velocity, the system

becomes unstable because in that situation the last term of the characteristic equation of the system becomes negative. We then have divergent instability corresponding to the capsize mode that becomes unstable beyond a critical speed as illustrated in the diagram of Fig.10.8, case 6 with very small camber aligning stiffness.

The sign of the c.g. offset coefficient appears to change from positive to negative in the case of accelerating at low speed. When the rider hangs to right-hand side (y_{mr}>0 making φ<0) while moving straight ahead, steering to the right is normally required to compensate for the camber forces pointing to the left. This appears to be true except when the rear wheel driving force produces sufficient positive yaw moment through the finite crown radius.

As was already clear from the relevant expressions, the influence of speed on the coefficients occurs if air drag is included in the model. At the high speed of 160km/h the effect of air drag becomes quite noticeable. This would be much less at a speed of say 100km/h because of the quadratic speed influence.

As was to be expected, the longitudinal tyre forces have a large effect on the two coefficients. When driving with F_{ax}=1500N, coefficient η changes from -0.0177 to -0.0204. At the high speed, much more driving force at the rear wheel is needed to overcome the air drag and realise the aimed acceleration. Oversteer has increased a lot with respect to the situation at zero acceleration (first and third row). The driving force and the opposite inertia force form a couple around the vertical axis (because of the roll angle) that tries to turn the vehicle more into the curve. At braking more understeer arises caused by the forward inertia force exerting an outward couple about the z axis and the sideways component of the front wheel braking force that does the same, trying to straighten the vehicle's path.

As an example we might further analyse the case represented by the last row of Table 10.4. If the motorcycle would be negotiating a circular path with a radius of 200 times the wheel base, l/R = 0.005, R = 300m, at V = 160km/h (=44.4m/s) the lateral acceleration becomes $a_y = V^2/R$ = 6.58m/s^2 = 0.67g. As a consequence, the roll angle becomes $\varphi = \xi a_y/g$ = 1.209×0.67 = 0.81rad = 46°. The ground steer angle takes the value: $\delta' = (l/R + \eta a_y/g)/\zeta$ = -0.0027/1.016 = -0.00266 rad = -0.15° and the handlebar steer angle $\delta = \delta'/\cos\varepsilon$ = -0.17°. It is obvious that with this high lateral acceleration the assumption of linearity is not valid. A smaller path curvature would have been a better choice. If the centre of gravity of the mainframe plus rider is located a distance y_{mr}= 1cm to the right of the vehicle centre plane, a roll angle $\varphi = -\xi_y\, m_{mr} y_{mr}/mh$ = -1.176×350×0.01/(390×0.59) = -0.018rad = -1.03° results at straight line running. The ground steer angle is predicted to amount to $\delta' = \eta_y\, m_{mr} y_{mr}/mh$ = 0.0423×350×0.01/(390×0.59) = 6.38×10^{-4}rad = 0.036° and the handlebar steer angle δ = 0.041°.

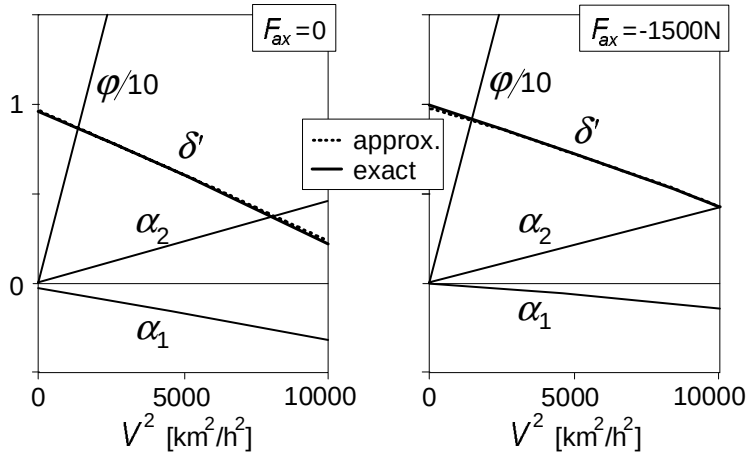

Fig. 10.17. Steer, roll and slip angles per unit non-dimensional path curvature l/R versus speed squared $V^2 = a_y R$ (left: non-accelerating, right: braking) according to the exact and approximate theories.

In Figs.10.17,18 this case where the brakes are applied is further examined for speeds ranging from 1 to 100km/h also showing the variation of the slip angles.

In Fig.10.17 the left-hand diagram is presented for the non-accelerating vehicle with air drag included (rows 1 and 3 of Table 10.4) showing the variation of the roll angle and the ground steer angle versus speed squared. In addition, the variation of the front and rear slip angles has been depicted. The almost straight lines result from computations with the steady-state version of the differential equations (10.85-94) with the rider lean degree of freedom deleted. An additional (dotted) line shows the variation of the ground steer angle according to the approximate analytical results corresponding to those listed in Table 10.4. Only very slight differences appear to occur between the approximate (β disregarded and δ term in Eq.(10.121) neglected) and exact results for the ground steer angle, slip angles and roll angle. According to the exact computations, the twist angle β amounts to ca. 0.5% of the roll angle φ. Note that the difference in slip angles α_2-α_1 practically equals l/R minus the ground steer angle δ' (ζ being very close to unity). We may calculate the slip angles following the analytical approach through an explicit expression by using the equations (10.148,149) for the lateral tyre force components caused by side slip, given later on.

The right-hand diagram of Fig.10.17 refers to the situation that arises when the brakes are applied (fifth and last row of Table 10.4). Again, an excellent correspondence between the approximate and exact solutions occurs. Obviously, the vehicle performs now in a less oversteered manner as was already concluded from the less negative value of η in Table 10.4. The front slip angle is less negative to make the side force more positive to counteract the sideways

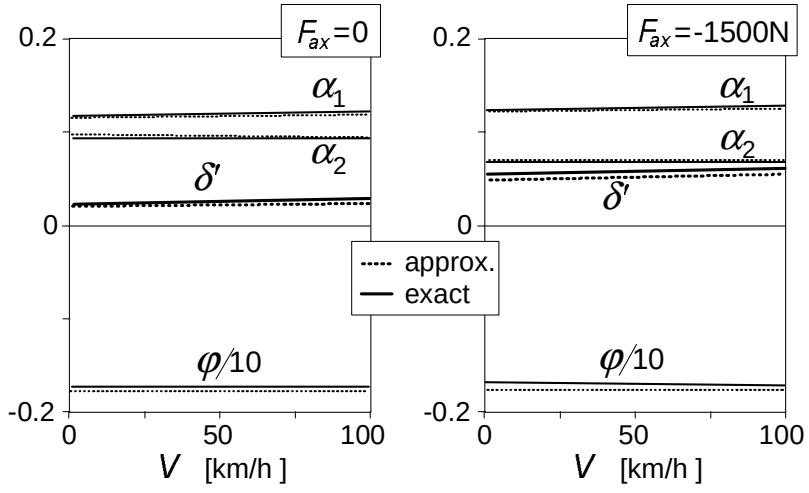

Fig. 10.18. Steer, roll and slip angles and the steer torque per m lateral c.g. offset y_{mr} that occur at straight line motion (according to the exact and approximate theories).

component of the front wheel braking force. At the same time, the rear slip angle is made slightly larger to help compensate for the positive yaw moment that arises from the braking forces their points of application being shifted to the right because of the finite crown radii. Under this condition of braking, β appears to become somewhat smaller.

Finally, Fig.10.18 shows the variation of the various angles per unit lateral c.g. offset. It is seen that the influence of speed is very small and that the agreement between approximate and exact results is good. Both slip angles are positive thereby neutralising the camber forces which point to the left because of the negative roll angle that arises to compensate for the c.g. location lateral offset. At braking, the centre of gravity remains above the line connecting the contact points of the tyres. The forward load transfer reduces the rear camber force which allows a decrease of the rear slip angle. As α_1 increases only a little to balance both the increased camber force and the sideways component of the front wheel braking force, the steer angle needs to become larger to keep α_1-δ' equal to α_2. In both cases, β is equal to ca. 5% of φ and will have a relatively large effect on the actual value of steer angle of the handle bar δ (cf. Eq.(10.12)).

The Steer Torque

By considering Eq.(10.89) with β neglected the following steady-state expression for the steering couple is obtained:

$$\begin{aligned} M_\delta = \; & t_c F_{y1} + \\ & - t_c F_{z1} \gamma_1 + \\ & + (1/r_1) I_{wy1} a_y \sin\varepsilon + \\ & - M_{x1} \sin\varepsilon + \\ & - M_{z1} \cos\varepsilon + \\ & + (m_f e_f + m_s e_s)(a_y - g\gamma_1) \end{aligned} \tag{10.147}$$

Like we did with the steer angle, we wish to develop an expression for the steer torque in terms of path curvature l/R, lateral acceleration a_y and c.g. offset y_{mr}. For this, first the relationship with a_y, φ, γ_1 and δ' will be established. With the aid of relationships assessed before the desired expression can be derived.

In the first term of expression (10.147) the side force of the front wheel appears which is determined using Eq.(10.141). For this, but also for the fifth term of (10.147), the sum of aligning torques is needed. The torque due to side slip follows by multiplying the side force due to side slip $F_{y\alpha i}$ with the pneumatic trail $t_{\alpha i}$.This part of the side force is found by subtracting from the total side force the part due to camber. The also appearing side force due to side slip of the rear wheel can be eliminated by employing the expression for the sum of side slip forces obtained from (10.130,131,141,142):

$$F_{y\alpha 1} + F_{y\alpha 2} = ma_y - lF_{x1}\delta' - C_{F\gamma 1}\gamma_1 - C_{F\gamma 2}\varphi \tag{10.148}$$

The following relation for the front wheel side slip force is finally obtained:

$$\begin{aligned} F_{y\alpha 1}(l - t_{\alpha 1} + t_{\alpha 2}) = \; & bma_y - (l + t_{\alpha 2}) F_{x1}\delta' - (h_d F_d + mha_x)\varphi - m_{mr} y_{mr} a_x + \\ & + t_{\alpha 2}(ma_y - C_{F\gamma 1}\gamma_1 - C_{F\gamma 2}\varphi) - C_{M\gamma 1}\gamma_1 - C_{M\gamma 2}\varphi - lC_{F\gamma 1}\gamma_1 \end{aligned} \tag{10.149}$$

The expression for $F_{y\alpha 1}$ can be used to determine the slip angle α_1 (= $F_{y\alpha 1}/C_{F\alpha 1}$) or directly the aligning torque due to side slip $M_{z\alpha 1}$ by multiplying -$F_{y\alpha 1}$ with the pneumatic trail $t_{\alpha 1}$. Similarly, we obtain $M_{z\alpha 2}$. The remaining part of the aligning torque due to wheel camber $M_{z\gamma 1}$ is obviously found by multiplying the camber aligning torque stiffnes $C_{M\gamma i}$ (10.143) with the camber angle γ_i. The resulting expression for the steer torque turns out to read:

$$M_\delta = \frac{t_c + t_{\alpha 1}\cos\varepsilon}{l^*}\Big\{(b+t_{\alpha 2})ma_y - (l+t_{\alpha 2})C_{F\gamma 1}\gamma_1 - t_{\alpha 2}C_{F\gamma 2}\varphi +$$
$$- C_{M\gamma 1}\gamma_1 - C_{M\gamma 2}\varphi - lF_{x1}\delta' - (h_d F_d + mha_x)\varphi - m_{mr}y_{mr}a_x\Big\} +$$
$$- \Big\{t_c(F_{z1} - C_{F\gamma 1}) - C_{Mx\gamma 1}\sin\varepsilon + C_{M\gamma 1}\cos\varepsilon\Big\}\gamma_1 +$$
$$+ \frac{1}{r_1}I_{wy1}\sin\varepsilon\, a_y + (m_f e_f + m_s e_s)(a_y - g\gamma_1) \qquad (10.150)$$

The front wheel camber angle γ_1 may be written in terms of φ and δ' with Eq.(10.133). On their turn, φ and δ' can be expressed in l/R, a_y and y_{mr} with the use of Eqs.(10.122) and (10.115). At this stage we may improve the result for M_δ by approximately accounting for the term with δ in (10.121) which we neglected. Due to a steer angle, the contact point shifts sideways and a roll angle is needed to keep the motorcycle in balance. The approximate correction for φ becomes:

$$\Delta\varphi = -\frac{b\,t_c}{lh\cos\varepsilon}\delta' \qquad (10.151)$$

with the steer angle equation

$$\zeta\delta' = \frac{l}{R} + \eta\frac{a_y}{g} + \eta_y\frac{m_{mr}y_{mr}}{mh} \qquad (10.115)$$

and the roll angle equation (10.122) the corrected roll angle can be assessed:

$$\varphi = \xi\frac{a_y}{g} - \xi_y\frac{m_{mr}y_{mr}}{mh} - \frac{b\,t_c}{lh\cos\varepsilon}\delta' \qquad (10.152)$$

and also the front wheel camber angle:

$$\gamma_1 = \varphi + \delta'\tan\varepsilon \qquad (10.133)$$

Especially at low speeds and when the front brake is applied, the improvement can become considerable. Obviously, this is due to the camber aligning torque in which the longitudinal force may play a predominant role, cf. Eq.(10.143).

It is possible now to write Eq.(10.150) in the following non-dimensional form:

$$\frac{M_\delta}{F_{z1o}l} = \mu_R\frac{l}{R} + \mu_a\frac{a_y}{g} + \mu_y\frac{m_{mr}y_{mr}}{mgh} \qquad (10.153)$$

The expressions for the steer torque coefficients are too elaborate to be reproduced here. Numerically, however, their values can be easily assessed directly from the original Eq.(10.150) together with Eqs.(10.122, 152, 133).

In Fig.10.19 the general course of the non-dimensional steer torque (10.152)

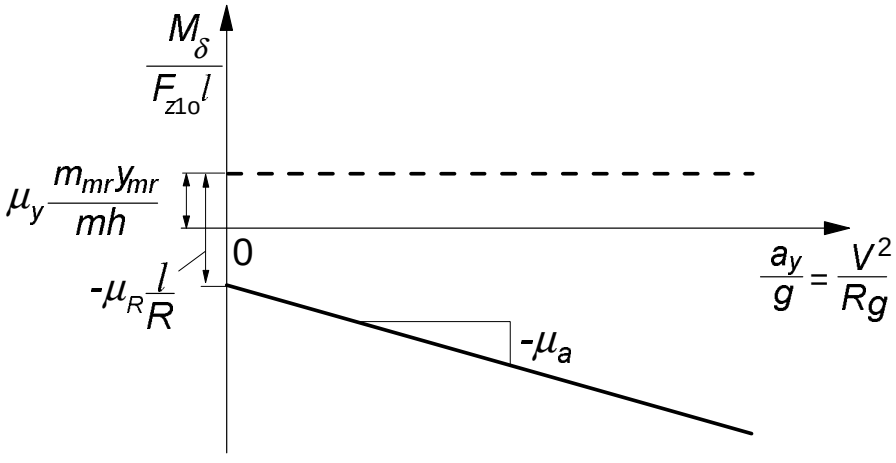

Fig. 10.19. The non-dimensional steer torque due to path curvature $1/R$ and c.g.lateral offset y_{mr} and the variation with lateral acceleration a_y or speed V.

has been depicted. The initial value at speed nearly zero is governed by the coefficients μ_R and μ_y while the slope equals μ_a.

Numerical Results

For the baseline configuration, and the various conditions examined in Table 10.4, the values for the three steer torque coefficients have been listed in Table 10.5.

Table 10.5. Steer torque coefficients; Eq.(10.152).

V	F_d	F_{ax}	F_{x1}	F_{x2}	F_{z1}	F_{z2}	μ_R	μ_a	μ_y
km/h	N	N	N	N	N	N	-	-	-
1	0	0	0	0	1732	2094	-0.05	-0.01	0.1118
160	0	0	0	0	1732	2094	-0.05	-0.01	0.1118
160	395	0	0	395	1534	2292	-0.04	-0.01	0.1104
1	0	1500	0	1500	1137	2689	-0.03	-0.01	0.080
1	0	-1500	-912	-588	2327	1499	-0.02	-0.05	0.1729
160	395	1500	0	1895	940	2886	-0.03	-0.01	0.079
160	395	-1500	-615	-490	2129	1697	-0.03	-0.04	0.1624

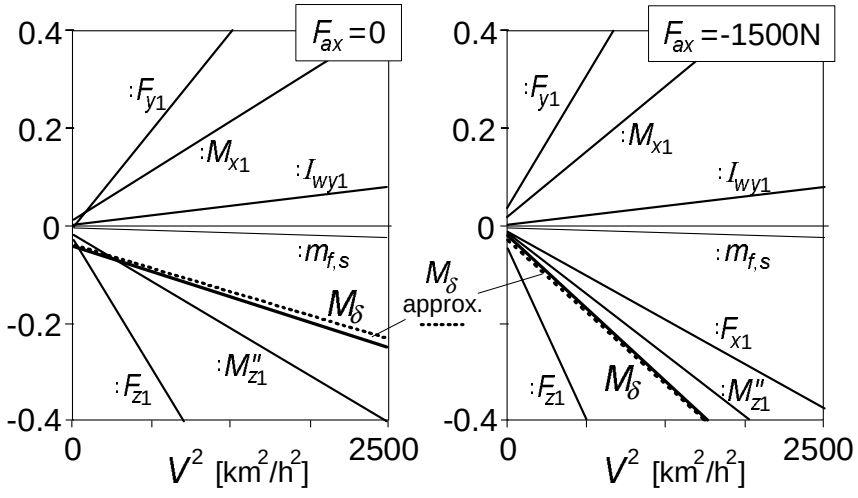

Fig. 10.20. The non-dimensional steer torque ($M_\delta/(F_{z1o}l)$ and its components (cf. Eq.(10.147)) per unit non-dimensional path curvature l/R. In M''_{z1} the F_{x1} contribution is omitted.

Figure 10.20 depicts the variation of the steer moment with the speed squared computed according to the approximate analytical equation (10.150) (dotted line) and with the exact equations (10.85-94) (including β but with $\varphi_r = 0$) together with contributing components. These components correspond with the terms of expression (10.147) and with the relevant terms of Eq.(10.89). In the contribution from the front wheel aligning torque (10.59) we distinguish the part

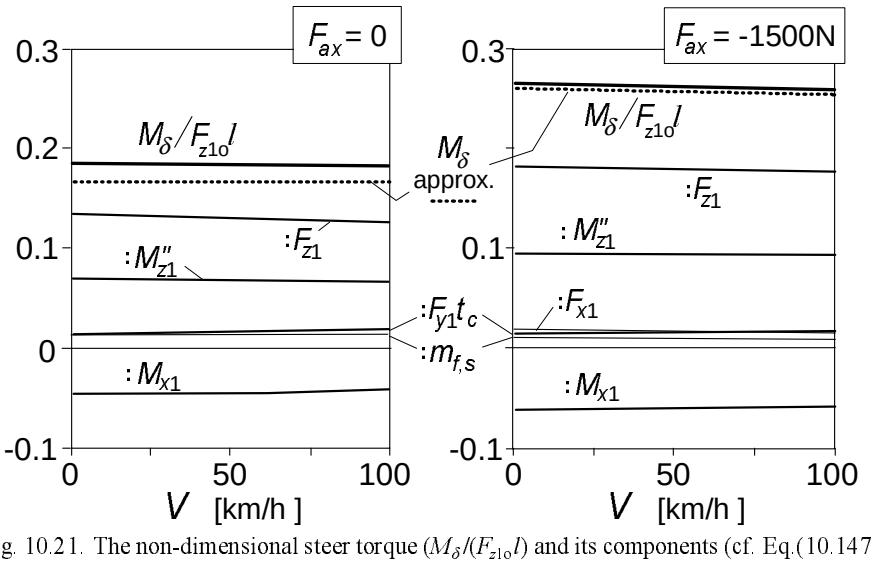

Fig. 10.21. The non-dimensional steer torque ($M_\delta/(F_{z1o}l)$ and its components (cf. Eq.(10.147)) per m c.g. lateral offset y_{mr}. In M''_{z1} the F_{x1} contribution is removed.

directly attributed to F_{x1} and the remaining part indicated with M''_{z1}. The component indicated in the diagram by :F_{x1} contains the former part plus the term with F_{x1} already appearing in the β coefficient in Eq.(10.89). In both cases examined (without and with braking) the approximate total moment closely follows the course of the exact solution. The difference is largely due to the fact that in the approximate theory the twist angle has been neglected.

In all cases, the initial torque ($V \to 0$) at cornering is negative ($\mu_R < 0$) which means that when turning to the right an anti-clockwise steer torque is required. This appears to be mainly due to the direct action of the front normal load the axial component of which ($F_{z1}\gamma_1$) forms with the arm t_c a moment about the steering axis. Also the tyre aligning torque with the negative slip angle of the front wheel (Fig.10.17) helps to make the steer torque negative. In the braking case, the front wheel brake force considerably increases the negative steer torque. The weights of the steerable front and subframes have an almost negligible effect, while the gyroscopic action and the front wheel side force have a tendency to make the steer torque positive.

Finally, Fig.10.21 gives the moment response to lateral offset of the centre of mass of the combined rider and mainframe. The approximation is less good then we have seen so far. The deviation is largely due the omission of the twist compliance. Because of the small side forces in this straight ahead motion we see only a very small direct effect of F_{y1}. At braking, the tyre torques become larger in magnitude due to the increased front slip angle and steer angle (camber), cf. Fig.10.18.

As an illustration, we consider again the case that the motorcycle runs in a curve with a radius of 200 times the wheel base, $l/R = 0.005$, $R = 300$m, at $V =$ 160km/h (= 44.4m/s) the lateral acceleration becomes $a_y = V^2/R = 6.58\text{m/s}^2 = 0.67g$. The vehicle is being braked and the last row of Table 10.5 applies. As a consequence, the non-dimensional torque becomes $M_\delta/(F_{z1o}\,l) = \mu_R\, l/R + \mu_a a_y/g =$ -0.029×0.005 - 0.0363×0.67 = -0.0245 or in dimensional form: $M_\delta =$ -0.0245×1732×1.5= -63.7Nm. At 50km/h we would obtain: $M_\delta/(F_{z1o}\,l) =$ -0.0245×0.005 - 0.0451×0.0655 = -0.63×0.005 = -0.0031 and M_δ= -8.05Nm The value -0.63 corresponds to the value found in Fig.10.20 at V=50km/h.

For a c.g. offset of 1cm one would find a steer torque at straight ahead running at 160km/h: $M_\delta/(F_{z1o}\,l) = \mu_y m_{mr} y_{mr}/mh$ = 0.1624×350×0.01/ (390×0.59) = 0.0025 and M_δ= 0.0025×1732×1.5 = 6.5Nm. The value 100×0.0025 = 0.25 may be predicted from Fig.10.21, where y_{mr}= 1m, at 160km/h.

10.5.2. Non-Linear Analysis of Steady-State Cornering

In this section the so-called handling diagram will be established for the motorcycle. In that diagram the variation of the (ground) steer angle can be found as a function of the lateral acceleration for a given speed of travel or for a selected value of path curvature. As an additional information, the variation of the associated steer torque will given. The diagram is similar to the handling diagrams established for the motorcar in Chapter 1. The relatively large roll angle calls for special attention to assess the equilibrium condition for the front and for the rear tyre.

A Simple Approximation

To introduce the problem we will again first neglect all the tyre moments and the gyroscopic couples as well as the air drag. We then have the equilibrium conditions stated before:

$$\frac{F_{y1}}{F_{z1}} = \frac{F_{y2}}{F_{z2}} = \frac{a_y}{g} \quad \left(= \frac{ur}{g} \right) \tag{10.153}$$

while the roll angle and the front and rear camber angles become with δ neglected with respect to the large φ:

$$\tan\varphi = \frac{a_y}{g} \tag{10.154}$$

and

$$\gamma_1 = \varphi \tag{10.155}$$

$$\gamma_2 = \varphi \tag{10.156}$$

Consequently, for a given roll angle φ we know the lateral acceleration, both side forces and the camber angles. From the non-linear tyre side force characteristic that holds for the camber angle at hand and the vertical load (here equal to the static load) it must now be possible to assess the slip angle that produces together with the camber angle the desired side force. When we do this for both the front and rear wheels the difference in slip angles can be found and the handling curve can be drawn. At a given path curvature the ground steer angle is then easily found by using the approximate relationship:

$$\delta' = \frac{l}{R} + \alpha_1 - \alpha_2 \tag{10.157}$$

Figure 10.22 shows the normalised side force characteristics according to the

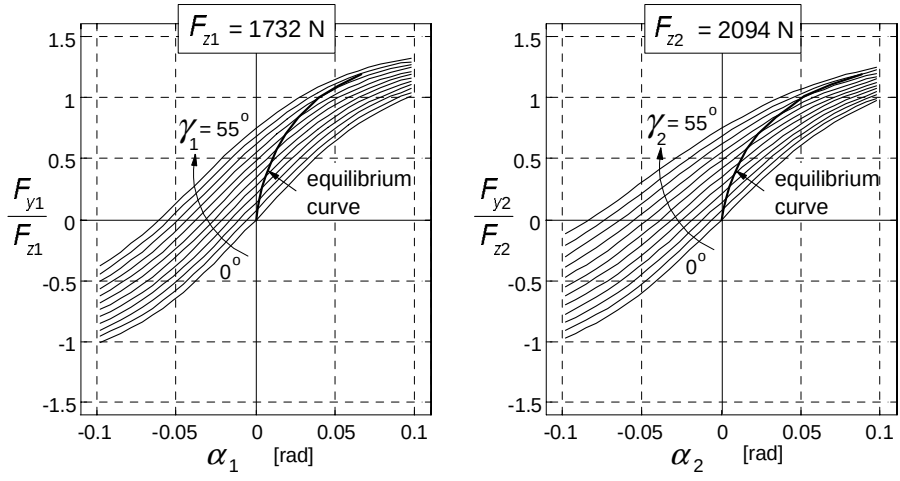

Fig. 10.22. Tyre side force diagrams at a series of camber angles γ. Simplified situation where wheel loads remain unchanged (no air drag) and tyre moments and gyroscopic couples are left out of consideration. Equilibrium curves have been shown where the tyre side force agrees with the roll angle ($\approx\gamma_{1,2}$).

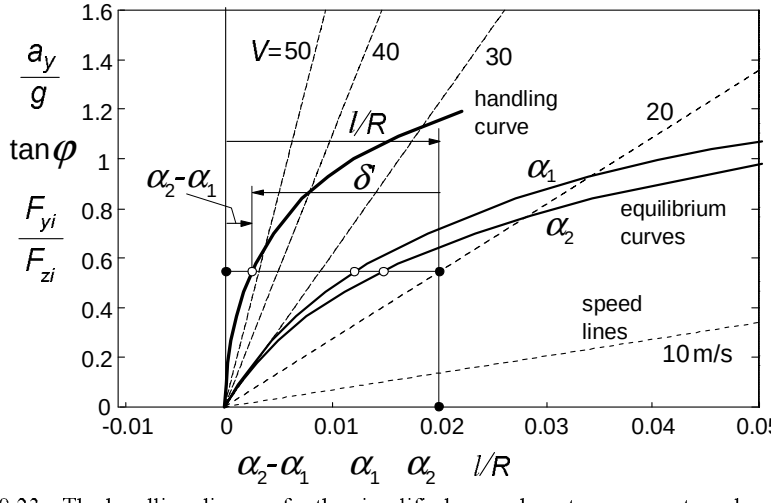

Fig. 10.23. The handling diagram for the simplified case where tyre moments and gyroscopic couples are deleted and air drag is disregarded. The normalised side force versus slip angle curves (in this simplified case equal to the equilibrium curves) have been depicted as well.

baseline configuration together with the equilibrium curves where the camber angle equals the roll angle belonging to the side force. In Fig.10.23 the resulting handling curve with speed lines forming the handling diagram has been presented. The speed lines indicate the relationship between lateral acceleration

and path curvature for given values of speed:

$$\frac{l}{R} = \frac{gl}{V^2}\frac{a_y}{g} \tag{10.158}$$

In the figure, the equilibrium curves of Fig.10.22 have been reproduced. By horizontal subtraction of these curves the handling curve is obtained. The horizontal distance between selected speed line and the handling curve equals the ground steer angle. The slope of the handling curve with respect to the vertical axis at zero lateral acceleration corresponds to the understeer coefficient in the linear theory $\eta/\zeta = \partial\delta'/\partial(a_y/g)$ at constant l/R. By using Eq.(10.10) with twist angle neglected and steer angle assumed small with respect to the roll angle we find the actual steer angle:

$$\delta = \frac{\delta'}{\cos\varepsilon}\cos\varphi \tag{10.159}$$

The theory given above turns out to be too crude to give a reasonably accurate result. To improve the analysis, the tyre moments and the gyroscopic couples should be accounted for. We may also include the effect of air drag and braking or driving forces.

To set up the equations for the steady-state cornering situation, we need to consider the conditions for equilibrium in the directions of the x, y and z axes and about these three axes and for the steer torque: about the steering axis. We will do this for the general case with air drag introduced and with braking or driving forces acting on the front and rear wheels and possibly with a given sideways shift of the centre of gravity. The twist angle β is neglected and the lean angle φ_r is disregarded since at steady-state turning its effect is similar to that of the c.g. lateral offset. The steer angle δ is considered small with respect to the roll angle. Also the wheel slip angles are assumed to be relatively small (smaller than ca. 10 degrees).

Equilibrium Conditions for the Complex Configuration

The condition of equilibrium in longitudinal direction can be met by making the driving force equal to the air drag force. This means that $F_{x,acc} = 0$ or $F_{x2} = F_d$. When a different driving force or when braking forces are applied, equilibrium can only be assured ($a_x = 0$) when the vehicle runs on an upward or downward slope. If this is not the case, we may speak of a quasi equilibrium situation in the longitudinal direction. We have the equation (where the small longitudinal component of the side force $F_{y1}\,\delta'$ has been neglected):

$$m\,a_x = F_{x,acc} = F_{x1} + F_{x2} - F_d \tag{10.160}$$

In lateral direction equilibrium occurs if

$$m a_y = F_{y1} + F_{y2} + F_{x1}\delta' \tag{10.161}$$

and in vertical direction if

$$m g = F_{z1} + F_{z2} \tag{10.162}$$

About the x axis we have the condition:

$$\begin{aligned} &-m a_y h_\varphi \cos\varphi + m g h_\varphi \sin\varphi + m_{mr} g y_{mr} \cos\varphi + \\ &-(I_{wy1}\Omega_1 + I_{wy2}\Omega_2) r \cos\varphi + F_{z1} t_{c\varphi} \delta \cos\varphi + M_{x1} + M_{x2} = 0 \end{aligned} \tag{10.163}$$

about the y axis:

$$\begin{aligned} &m a_x h_\varphi \cos\varphi - m_{mr} a_x y_{mr} \sin\varphi + \\ &\qquad + a F_{z1} - b F_{z2} + h_{d\varphi} F_d \cos\varphi = 0 \end{aligned} \tag{10.164}$$

and about the z axis:

$$\begin{aligned} &m a_x h_\varphi \sin\varphi + m_{mr} y_{mr} a_x \cos\varphi + \\ &\quad + a F_{y1} - b F_{y2} + a F_{x1}\delta' + M_{z1} + M_{z2} + h_{d\varphi} F_d \sin\varphi = 0 \end{aligned} \tag{10.165}$$

The wheel normal loads $F_{z1,2}$ are found from the Eqs.(10.162) and (10.164). The longitudinal tyre forces $F_{x1,2}$ are distributed according to Eq.(10.25) and as before, the acceleration force $F_{x,acc}$ is used as parameter in the handling diagrams to be developed.

With M_{ya} introduced for abbreviation:

$$M_{ya} = m a_x h_\varphi \cos\varphi - m_{mr} y_{mr} a_x \sin\varphi + h_{d\varphi} F_d \cos\varphi \tag{10.166}$$

where h_φ and $h_{d\varphi}$ are defined by Eq.(10.5) with if relevant h replaced by h_d, we obtain the loads:

$$\begin{aligned} F_{z1} &= \frac{1}{l}(b m g - M_{ya}) \\ F_{z2} &= \frac{1}{l}(a m g + M_{ya}) \end{aligned} \tag{10.167}$$

The two side forces are found from the Eqs.(10.161) and (10.165). If we introduce for abbreviation:

$$M_{za} = m a_x h_\varphi \sin\varphi + m_{mr} a_x y_{mr} \cos\varphi + M_{z1} + M_{z2} + h_{d\varphi} F_d \sin\varphi \tag{10.168}$$

we obtain:

$$\begin{aligned} F_{y1} &= \frac{1}{l}(b m a_y - l F_{x1}\delta' - M_{za}) \\ F_{y2} &= \frac{1}{l}(a m a_y + M_{za}) \end{aligned} \tag{10.169}$$

with (from Eq.(10.10) with $\beta = 0$)

$$\delta' = \delta \frac{\cos\varepsilon}{\cos\varphi} \tag{10.170}$$

From Eq.(10.163) an expression for the lateral acceleration can be obtained. After using Eq.(10.60) for M_{xi} and the corrected effective rolling radii $r_{i\varphi}$:

$$r_{i\varphi} = r_i - r_{ci} + r_{ci}\cos\varphi \tag{10.171}$$

and neglecting the very small contribution of δ to the moment about the x-axis we find by using the factor β_x defined as

$$\beta_x = \frac{m h_\varphi}{m h_\varphi + \frac{1}{r_{1\varphi}} I_{wy1} + \frac{1}{r_{2\varphi}} I_{wy2}} \tag{10.172}$$

for the lateral acceleration $a_y = ur$:

$$\frac{a_y}{g} = \beta_x \left[\left(1 - \frac{r_{c1} F_{z1} + r_{c2} F_{z2}}{m g h_\varphi \cos\varphi} \right) \tan\varphi + \frac{m_{mr} y_{mr}}{m h_\varphi} \right] \tag{10.173}$$

The Handling Diagram

For a given $\tan\varphi$ and y_{mr} the corresponding lateral acceleration a_y can be computed by using (10.173). If we disregard, as a first step, the influence of δ' and the aligning torques $M_{z1,2}$ in Eqs.(10.169,168) we can calculate the front and rear side forces $F_{y1,2}$ belonging to a_y. With the approximation (10.155,156) the camber angles are taken equal to the roll angle of the main frame. It is then possible through iteration to assess the values for the slip angles $\alpha_{1,2}$ belonging to the calculated F_y's and the known camber angles $\gamma_{1,2}$ with the loads obtained from (10.167,166). From the slip angles and the camber angles established, the aligning torques $M_{z1,2}$ can be estimated for the next computation step (for a given next incremented roll angle φ) by extrapolation. Also the ground steer angle δ' is estimated for the next step. This is done by using the equations (10.157) after having selected a value for the forward speed $V = u$. Now, a more accurate value for the side forces that belong to the equilibrium state can be found from Eqs.(10.169) with (10.168). For a series of successive values of φ the values of α_1 and α_2 may be computed in this way, resulting, when plotted against a_y/g, in the equilibrium curves for the front and rear wheels (equivalent to the effective axle characteristics of Chapter1). From the difference α_1 - α_2 the handling curve is obtained. If air drag $F_d = C_{dA} u^2$ and/or a front wheel longitudinal force F_{x1} are

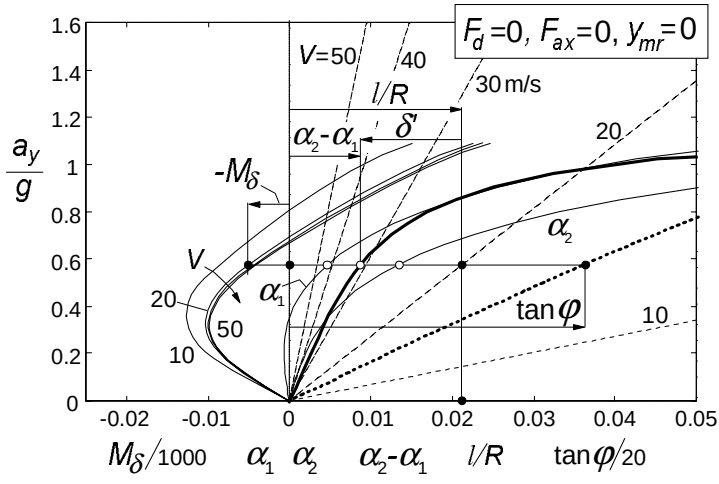

Fig. 10.24. Handling diagram for complex model with all tyre moments and gyroscopic couples included. Air drag = 0 which makes the diagram valid for all speeds V. Curves for roll angle, front and rear slip angles and steer torque (different for each speed).

considered, the handling curve changes with speed and the handling diagram holds only for the selected value of speed u. If air drag and front wheel braking are disregarded, a generally valid single handling curve with a series of speed lines arises as depicted in Fig.10.24. The slope at $a_y = 0$ is $(\partial\delta'/\partial(a_y/g))_R = \eta/\zeta$.

In these diagrams also the slip angles and the actual roll angle have been plotted (in abscissa direction). As an additional information, the diagram contains curve(s) for the steer torque M_δ possibly changing with speed of travel $V\,(\approx u)$. How this quantity is assessed will be discussed in the subsection below.

The Steer Torque

The steer torque that is applied to the handle bar by the rider in a steady turn can be found by considering the equilibrium about the steering axis. The resulting expression is similar to the one given by Eq.(10.147) but now extended to cover large roll angles. We find with the caster length $t_{c\varphi}$ according to Eq.(10.6):

$$\begin{aligned} M_\delta = \; & t_{c\varphi} F_{y1} \cos\gamma_1 - t_{c\varphi} F_{z1} \sin\gamma_1 + \\ & + (1/r_{1\varphi}) I_{wy1}\, ur \sin\varepsilon \cos\varphi + \\ & - M_{x1} \sin\varepsilon - M_{z1} \cos\varepsilon \cos\gamma_1 + \\ & + (m_f e_f + m_s e_s)(ur \cos\gamma_1 - g \sin\gamma_1) \end{aligned} \tag{10.174}$$

with the aligning torque according to Eq.(10.59):

$$M_{z1} = -t_{\alpha 1} F_{y\alpha 1} + M_{zr1} - r_{c1} F_{x1} \tan\gamma_1 \tag{10.175}$$

In the computations, we can use the correct expression for the camber angle γ_1 according to Eq.(10.13) with $\beta = 0$ because the steer angle δ is now available. This δ dependency causes the moment to change with path curvature and thus produces different curves for each speed value even if air drag is disregarded (Fig.10.24). The slope of the steer torque curve with respect to the vertical at $a_y = 0$ corresponds to $\mu_a F_{z1o} l$, cf. Table 10.5.

Results and Discussion of the Non-Linear Handling Analysis

For a number of situations the handling diagram has been established for the baseline configuration and presented in the diagrams of the Figs.10.24-28. The following cases have been examined:

1. No air drag, no braking or driving forces, no off-set of c.g. (Fig.10.24).
2. With air drag and a rear wheel driving force necessary to withstand the air drag so that the forward acceleration equals zero (F_{ax}=0: neutral situation) (V=30m/s=108km/h) (Fig.10.25).
3. Braking: total deceleration force -F_{ax}=1500N (V=108km/h) (Fig.10.26).
4. Hard braking: total deceleration force -F_{ax} = 2500N (V = 108km/h) (Fig.10.27).
5. Neutral but now with lateral shift y_{mr} = 5cm of the combined mass of main frame and rider (V=108km/h) (Fig.10.28).

The following interesting observations may be made:

6. The tyre/wheel moments have a considerable influence on the resulting handling characteristic, Fig.10.24. Much more oversteer appears to occur when compared with Fig.10.23. This was already concluded from the linear theory.
7. Air drag does not change handling behaviour very much if the speed is not much higher than 100 km/h. The steer torque at the speed of 108 km/h appears to reach a peak, decreases and changes in sign in the higher lateral acceleration range (Fig.10.25) where F_{y1} and M_{x1} in (10.174) become dominant.

– Braking causes the ground steer angle to become larger while the steer torque changes towards the negative direction especially at higher lateral accelerations (Fig.10.26, note the change in scale for the steer torque).
– Hard braking (Fig.10.27) tends to change the slope of the handling curve into understeer at large lateral accelerations. Also, the maximum lateral acceleration that can be reached is reduced. Larger steer angles arise in the higher a_y range of operation. Also the steer torque increases considerably in magnitude.

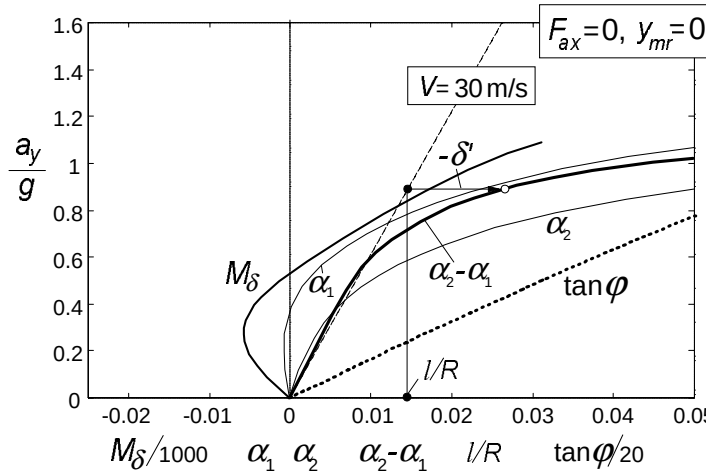

Fig. 10.25. The handling diagram with air drag considered and zero forward acceleration, (V = 108km/h).

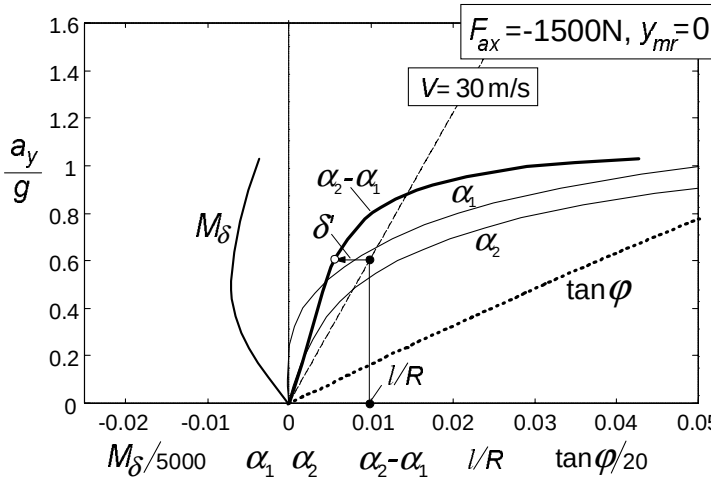

Fig. 10.26. The handling diagram at braking (V = 108 km/h).

– The lateral c.g. shift of 5cm gives rise to large changes in the diagram as indicated in Fig.10.28. It shows that the changes are largely due to horizontal shifts of the curves. We may compare the graph with that of Fig.10.25. Initially, at zero lateral acceleration (corresponding to Figs.10.18,21) a negative roll angle occurs while the ground steer angle and the steer torque are positive (which corresponds to $(\eta_y/\zeta)m_{mr}y_{mr}/mh$ and $(\mu_y m_{mr}y_{mr}/mh)F_{z1o}\,l$ respectively). At a certain level of the lateral acceleration the steer torque reaches a minimum.

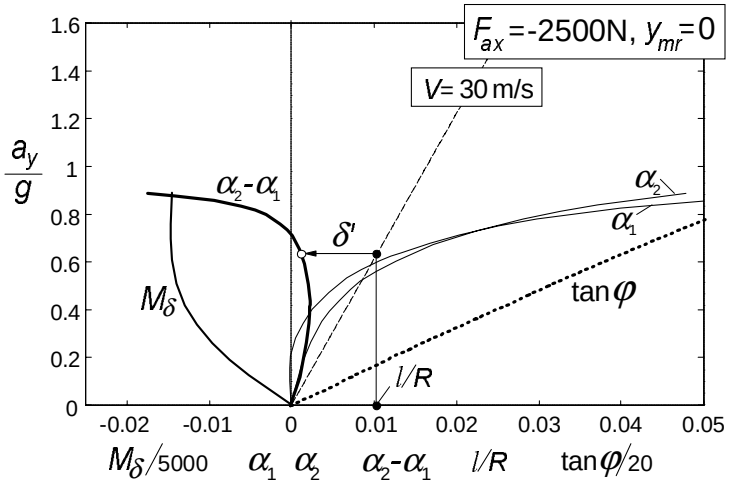

Fig. 10.27. The handling diagram at hard braking (V = 108 km/h).

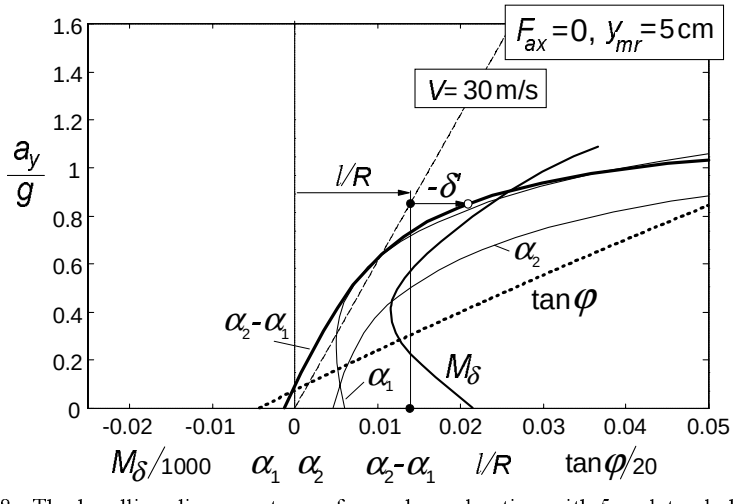

Fig. 10.28. The handling diagram at zero forward acceleration with 5cm lateral shift of the centre of gravity of combined rider and mainframe mass (V = 108 km/h).

The path curvature where these minima of the steer moment or maxima of $-M_\delta$ occur constitutes the boundary of monotonous instability. At larger curvature the capsize mode becomes unstable. This is analogous to what was found for the automobile where the input is the steer angle and its maximum at a given speed of travel corresponds to the boundary of divergent (monotonous) instability (cf. Fig.1.20).

10.5.3. Modes of Vibration at Large Lateral Accelerations

The free vibrations that occur after a slight disturbance in a high lateral acceleration cornering manoeuvre is considerably complex in nature. Koenen (1980, 1983) studied the eigenvalues and eigenvectors of the linear homogeneous differential equations that result after linearisation of the non-linear set of equations at given steady-state levels of operation. The original non-coupled in-plane and lateral out-of-plane modes of vibration appear to strongly interact with each other at larger roll angles. The weave mode occurring at straight ahead running intertwines with the bounce and pitch modes and form three different modes of vibration in which both the in-plane and lateral degrees of freedom play a role. As a result, unstable cornering weave oscillations may arise. Similarly, the wobble mode may interact with the wheel hop mode of the front wheel which manifests itself by a violent combined steering and vertical wheel oscillation. As an example, we present in Fig.10.29 the set of root loci in the complex plane (the eigenvalues) for both the case of straight ahead motion where we have uncoupled in-plane and out-of plane vibrations and the case where the motorcycle moves

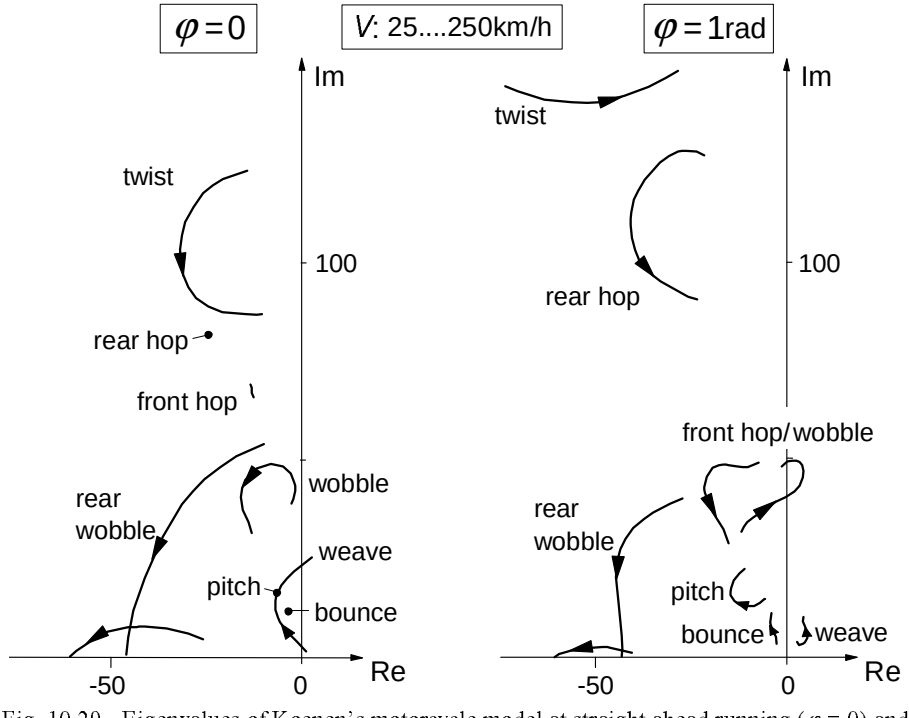

Fig. 10.29. Eigenvalues of Koenen's motorcycle model at straight ahead running (φ = 0) and at a roll angle of one radian. The speed varies from 25 to 250 km/h.

along a circular path at an average roll angle of one radian (from Koenen's work). The bounce, pitch and hop modes appear to become almost speed independent at vanishing roll angle. In a curve, all the modes do depend on the speed of travel. In the sharp high lateral acceleration curving motion considered, the cornering weave root loci appear to be shifted completely to the right-hand side of the imaginary axis. The wobble mode is destabilised as well. The higher frequency twist mode (flexible frame torsion mode) keeps an individual course.

10.6. Motorcycle Magic-Formula Tyre Model

For single track vehicles that may corner at possibly very large roll angles a modified set of equations has been developed. To properly cover large camber angles De Vries (1998a) has adapted the original Magic Formulae. Additional changes have been introduced regarding the aligning torque and combined slip and the resulting complete set has been listed below. The scaling factors λ and Eqs.(4.E1-E8) still apply. The equations of the remaining set which have been modified are indicated by means of an asterisk (*). The resulting characteristics appear to be quite accurate also at large camber angles (>30deg.) but then limited to slip angles less than ca. 6 degrees (for the cases considered).

One of the notable alterations is introduced in the formula for the lateral force, Eq.(10.E19). Here the slip angle and the camber angle have been treated in a more equally valued and independent manner than in the original equation (4.E19). A vertical shift did not appear to be necessary anymore. The sum of the two shape factors C_y and C_γ is not allowed to exceed the value 2 to prevent the side force from becoming negative at large slip and camber angles. Figure 10.30 illustrates the structure of the formula generating the F_y vs α characteristic for a given value of γ. It is seen that with respect to the situation of Fig.4.7, the basic sine curve is shifted sideways as a result of the presence of a camber angle.

Another feature that differs from the original model concerns the creation of the aligning torque. The part M_z' is now obtained by multiplying the pneumatic trail with the side force that is attributed to the side slip and not to the camber angle (indirectly through camber induced side slip). This may, especially at large camber angles, be closer to the actual mechanism. This part of the side force, denoted with $F_{y,\gamma=0}$, is obtained from the same Eqs.(10.E19-28) by setting $\gamma=0$.

Examples of computed characteristics compared with experimentally assessed curves for both pure slip at various camber angles and combinedslip conditions are presented in Section 10.6.2, Figs.10.30,31.

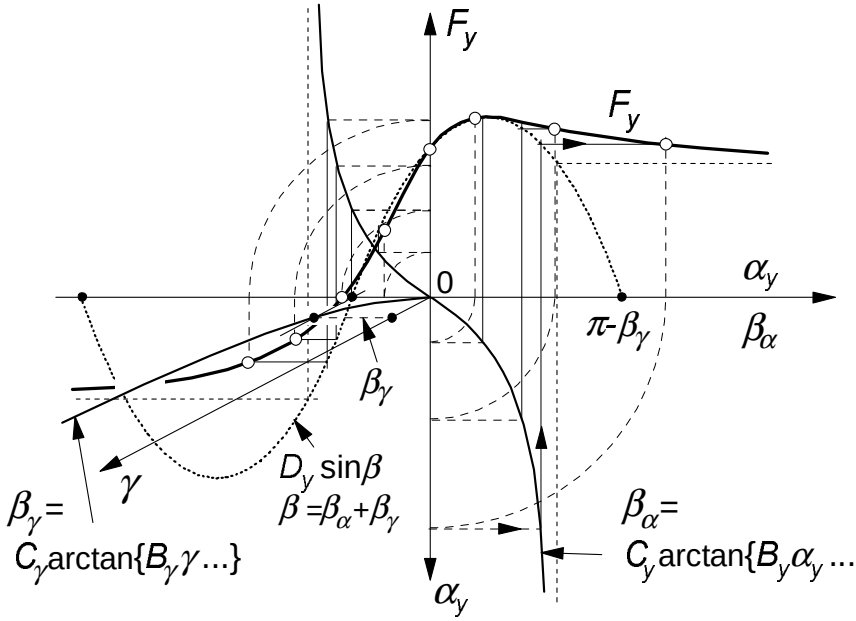

Fig. 10.30. The structure of the for motorcycle tyres adapted Magic Formula rendering the side force versus slip angle characteristic for a given camber angle.

10.6.1. Full Set of Tyre Magic Formula Equations

Longitudinal Force (pure longitudinal slip)

$$F_{xo} = \left[D_x \sin[C_x \arctan\{B_x\kappa_x - E_x(B_x\kappa_x - \arctan(B_x\kappa_x))\}] + S_{Vx}\right] \cdot \operatorname{sgn} V_{cx} \qquad (10.E9)$$

$$\kappa_x = \kappa + \qquad (10.E10)$$

$$C_x = p_{Cx1} \cdot \lambda_{Cx} \qquad (10.E11)$$

$$D_x = \mu_x \cdot F_z \qquad (10.E12)$$

$$\mu_x = (p_{Dx1} + p_{Dx2} df_z) \cdot \lambda_{\mu x} \qquad (>0) \qquad (10.E13)$$

$$E_x = (p_{Ex1} + p_{Ex2} df_z + p_{Ex3} df_z^2) \cdot \{1 - p_{Ex4} \operatorname{sgn}(\kappa_x)\} \cdot \lambda_{Ex} \qquad (\leq 1) \qquad (10.E14)$$

$$K_{x\kappa} = F_z \cdot (p_{Kx1} + p_{Kx2} df_z) \cdot \exp(p_{Kx3} df_z) \cdot \lambda_{Kx\kappa}$$
$$(= B_x C_x D_x = \partial F_{xo} / \partial \kappa_x \quad \text{at } \kappa_x = 0) \quad (= C_{F\kappa}) \qquad (10.E15)$$

$$B_x = K_{x\kappa}/(C_x D_x + \varepsilon_x) \tag{10.E16}$$

$$S_{Hx} = -(q_{sy1} F_z \lambda_{My} + S \qquad \text{(cf. (10.E70))} \qquad *(10.E17)$$

$$S_{Vx} = F_z \cdot (p_{Vx1} + p_{Vx2}\, df_z) \cdot \{|V_{cx}|/(\varepsilon_{Vx} + |V_{cx}|)\} \cdot \lambda_{Vx} \cdot \lambda'_{\mu x} \tag{10.E18}$$

Lateral Force (pure side slip)

$$F_{yo} = D_y \sin[C_y \arctan\{B_y\alpha_y - E_y(B_y\alpha_y - \arctan(B_y\alpha_y))\} + \\ + C_\gamma \arctan\{B_\gamma\gamma - E_\gamma(B_\gamma\gamma - \arctan(B_\gamma\gamma))\}] \qquad *(10.E19)$$

$$(C_y + C_\gamma < 2)$$

$$\alpha_y = \alpha^* + \tag{10.E20}$$

$$C_y = p_{Cy1} \cdot \lambda_{Cy} \qquad (>0) \tag{10.E21}$$

$$D_y = \mu_y \cdot F_z \tag{10.E22}$$

$$\mu_y = p_{Dy1} \cdot \exp(p_{Dy2} df_z) \cdot (1 - p_{Dy3}\gamma^2) \cdot \lambda_{\mu y} \qquad (>0) \qquad *(10.E23)$$

$$E_y = (p_{Ey1} + p_{Ey2}\gamma^2) + (p_{Ey3} + p_{Ey4}\gamma)\,\mathrm{sgn}(\alpha_y)\} \cdot \lambda_{Ey} \qquad (\le 1) \qquad *(10.E24)$$

$$K_{y\alpha o} = p_{Ky1} F'_{zo} \sin[p_{Ky2} \arctan\{F_z/((p_{Ky3} + p_{Ky4}\gamma_y^2) F'_{zo})\}] \lambda_{Ky\alpha} \qquad *(10.E25)$$

$$(= B_y C_y D_y = \partial F_{yo}/\partial\alpha_y \text{ at } \alpha_y = 0 \text{ if } \gamma = 0) \quad (= C_{F\alpha})$$

$$K_{y\alpha} = K_{y\alpha o} \cdot (1 - p_{Ky5}\gamma^2) \qquad *(10.E26)$$

$$B_y = K_{y\alpha}/(C_y D_y + \varepsilon_y \tag{10.E27}$$

$$S_{Hy} = p_{Hy1} \cdot \lambda_{Hy} \qquad *(10.E28)$$

$$C_\gamma = p_{Cy2} \cdot \lambda_{C\gamma} \qquad *(10.E29)$$

$$K_{y\gamma} = (p_{Ky6} + p_{Ky7} df_z) \cdot F_z \cdot \lambda_{Ky\gamma} \\ (= B_\gamma C_\gamma D_y = \partial F_{yo}/\partial\gamma \text{ at } \alpha_y = \gamma = 0) \quad (= C_{F\gamma}) \qquad *(10.E30)$$

$$E_\gamma = p_{Ey5} \cdot \lambda_{E\gamma} \qquad *(10.E31)$$

$$B_\gamma = K_{y\gamma}/(C_\gamma D_y + \varepsilon \qquad *(10.E32)$$

Aligning Torque (pure side slip)

$$M_{zo} = M'_{zo} + M_{zro} \tag{10.E33}$$

$$M'_{zo} = -t_o \cdot F_{yo,\gamma=0} \qquad *(10.E34)$$

$$t_o = t(\alpha_t) = D_t \cos[C_t \arctan\{B_t\alpha_t - E_t(B_t\alpha_t - \arctan(B_t\alpha_t))\}] \cdot \cos'\alpha \tag{10.E35}$$

$$\alpha_t = \alpha^* \qquad *(10.E36)$$

$$M_{zro} = M_{zr}(\alpha_r) = D_r \cos[\arctan(B_r\alpha_r)] \tag{10.E37}$$

$$\alpha_r = \alpha^* + S_{Hr} \qquad *(10.E38)$$

$$\gamma_z = \gamma \cdot \lambda_{\gamma z} \qquad *(10.E39)$$

$$S_{Hr} = q_{Hz1} + q_{Hz2} df_z + (q_{Hz3} + q_{Hz4} df_z)\gamma_z \qquad *(10.E40)$$

$$B_t = (q_{Bz1} + q_{Bz2} df_z + q_{Bz3} df_z^2) \cdot (1 + q_{Bz4}\gamma_z + q_{Bz5}|\gamma_z|) \cdot \lambda_{K\gamma\alpha}/\lambda_{\mu y} \quad (>0) \tag{10.E41}$$

$$C_t = q_{Cz1} \qquad (>0) \tag{10.E42}$$

$$D_{to} = F_z \cdot (R_o/F'_{zo}) \cdot (q_{Dz1} + q_{Dz2} df_z) \cdot \lambda_t \tag{10.E43}$$

$$D_t = D_{to} \cdot (1 + q_{Dz3}|\gamma_z| + q_{Dz4}\gamma_z^2) \tag{10.E44}$$

$$E_t = (q_{Ez1} + q_{Ez2} df_z + q_{Ez3} df_z^2) \cdot \left\{1 + (q_{Ez4} + q_{Ez5}\gamma_z)\frac{2}{\pi}\arctan(B_t C_t \alpha_t)\right\} \ (\leq 1)$$

$$*(10.E45)$$

$$B_r = q_{Bz9} \cdot \lambda_{Ky}/\lambda_{\mu y} \qquad *(10.E46)$$

$$D_r = F_z R_o \{(q_{Dz6} + q_{Dz7} df_z)\lambda_{Mr} + (q_{Dz8} + q_{Dz9} df_z)\gamma_z \lambda_{K\gamma z} + (q_{Dz10} + q_{Dz11} df_z)\gamma_z|\gamma_z|\} \cos'\alpha \cdot \lambda_{\mu y} \qquad *(10.E47)$$

$$K_{z\alpha o} = D_{to} K_{y\alpha o} \quad (= \sim -\partial M_{zo}/\partial\alpha_y \text{ at } \alpha_y = \gamma = 0) \quad (= C_{M\alpha}) \tag{10.E48}$$

$$K_{z\gamma o} = F_z R_o (q_{Dz8} + q_{Dz9} df_z)\lambda_{K\gamma z} \quad (= \sim \partial M_{zo}/\partial\gamma \text{ at } \alpha = \gamma = 0) \quad (= C_{M\gamma}) \tag{10.E49}$$

Longitudinal Force (combined slip)

$$F_x = G_{x\alpha} \cdot F_{xo} \tag{10.E50}$$

$$G_{x\alpha} = \cos[C_{x\alpha} \arctan(B_{x\alpha}\alpha_S)]/G_{x\alpha o} \quad (>0) \tag{10.E51}$$

$$G_{x\alpha o} = \cos[C_{x\alpha} \arctan(B_{x\alpha} S_{Hx\alpha})] \tag{10.E52}$$

$$\alpha_S = \alpha^* + S_{Hx\alpha} \tag{10.E53}$$

$$B_{x\alpha} = (r_{Bx1} + r_{Bx3}\gamma^2)\cos[\arctan(r_{Bx2}\kappa)] \cdot \lambda_{x\alpha} \quad (>0) \tag{10.E54}$$

$$C_{x\alpha} = r_{C:} \tag{10.E55}$$

$$S_{Hx\alpha} = r \tag{10.E57}$$

Lateral Force (combined slip)

$$F_y = G_{y\kappa} \cdot F_{yo} + S_{Vy\kappa} \tag{10.E58}$$

$$G_{y\kappa} = \cos[C_{y\kappa} \arctan(B_{y\kappa}\kappa_S)]/G_{y\kappa o} \quad (>0) \qquad *(10.E59)$$

$$G_{y\kappa o} = \cos[C_{y\kappa} \arctan(B_{y\kappa} S_{Hy\kappa})] \qquad *(10.E60)$$

$$\kappa_S = \kappa + S_{Hy\kappa} \tag{10.E61}$$

$$B_{y\kappa} = (r_{By1} + r_{By4}\gamma^2)\cos[\arctan\{r_{By2}(\alpha^* - r_{By3})\}] \cdot \lambda_{y\kappa} \quad (>0) \qquad *(10.E62)$$

$$C_{y\kappa} = r_{Cy1} \tag{10.E63}$$

$$S_{Hy\kappa} = r_{Hy1} \tag{10.E65}$$

$$S_{Vy\kappa} = D_{Vy\kappa} \sin[r_{Vy5} \arctan(r_{Vy6}\kappa) \tag{10.E66}$$

$$D_{Vy\kappa} = \mu_y F_z \cdot (r_{Vy1} + r_{Vy2} df_z + r_{Vy3}\gamma) \cdot \cos[\arctan(r_{Vy4}\alpha^*)] \tag{10.E67}$$

Normal Load

$$F_z = p_{z1} \cdot (F'_{zo}/R_o) \cdot \max(\rho_z, 0) \cdot \lambda_{Cz} \quad (\geq 0)$$
$$(C_{Fz} = \partial F_z/\partial \rho_z = p_{z1}\lambda_{Cz} F'_{zo}/R_o) \tag{10.E68}$$

Overturning Couple

$$M_x = F_z R_o \cdot (q_{sx1} - q_{sx2}\gamma + q_{sx3} F_y/F'_{zo}) \cdot \lambda_{Mx} \qquad *(10.E69)$$

Rolling Resistance Moment

$$M_y = -F_z R_o \cdot (q_{sy1} + q_{sy2} F_x / F'_{zo}) \cdot \lambda_{My} \qquad *(10.E70)$$

Aligning Torque (combined slip)

$$M_z = M'_z + M_{zr} + s \cdot F_x \qquad (10.E71)$$

$$M'_z = -t \cdot F'_y \qquad (10.E72)$$

$$t = t(\alpha_{t,eq}) = D_t \cos[C_t \arctan\{B_t \alpha_{t,eq} - E_t(B_t \alpha_{t,eq} - \arctan(B_t \alpha_{t,eq}))\}] \cdot \cos'\alpha \qquad (10.E73)$$

$$F'_y = F_{y,\gamma=0} - S_{Vy\kappa} \qquad (10.E74)$$

$$F_{y,\gamma=0} = G_{y\kappa} \cdot F_{yo,\gamma=0} \qquad (10.E75)$$

$$M_{zr} = M_{zr}(\alpha_{r,eq}) = D_r \cos[\arctan(B_r \alpha_{r,eq})] \qquad (10.E76)$$

$$s = R_o \cdot \{s_{sz1} + s_{sz2}(F_y / F'_{zo}) + (s_{sz3} + s_{sz4} df_z)\gamma\} \cdot \lambda_s \qquad (10.E77)$$

$$\alpha_{t,eq} = \sqrt{\alpha_t^2 + \left(\frac{K_{x\kappa}}{K'_{y\alpha}}\right)^2 \kappa^2} \cdot \mathrm{sgn}(\alpha_t) \qquad (10.E78)$$

$$\alpha_{r,eq} = \sqrt{\alpha_r^2 + \left(\frac{K_{x\kappa}}{K'_{y\alpha}}\right)^2 \kappa^2} \cdot \mathrm{sgn}(\alpha_r) \qquad (10.E79)$$

10.6.2. Measured and Computed Motorcycle Tyre Characteristics

As an example and similar to the presentation of the car and the truck tyre characteristics in Chapter 4, the characteristics of a 160/70 ZR17 motorcycle tyre have been collected in the diagrams of Fig.10.31 and 32. Again, at braking,the moment is difficult or impossible to model more accurately.

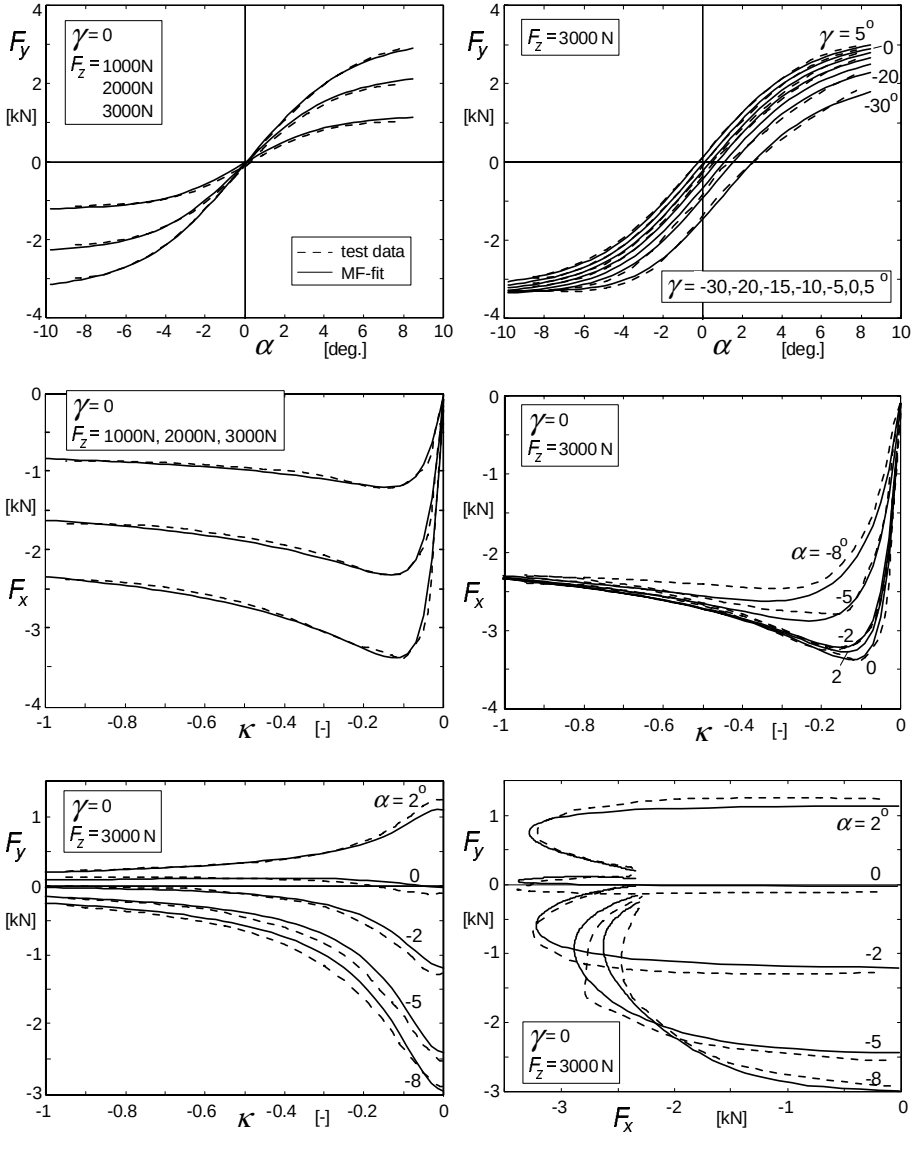

Fig. 10.31. Force characteristics of a 160/70 ZR17 motorcycle tyre. Modified Magic Formula computed results compared with data from measurements conducted with the Delft Tyre Test Trailer.

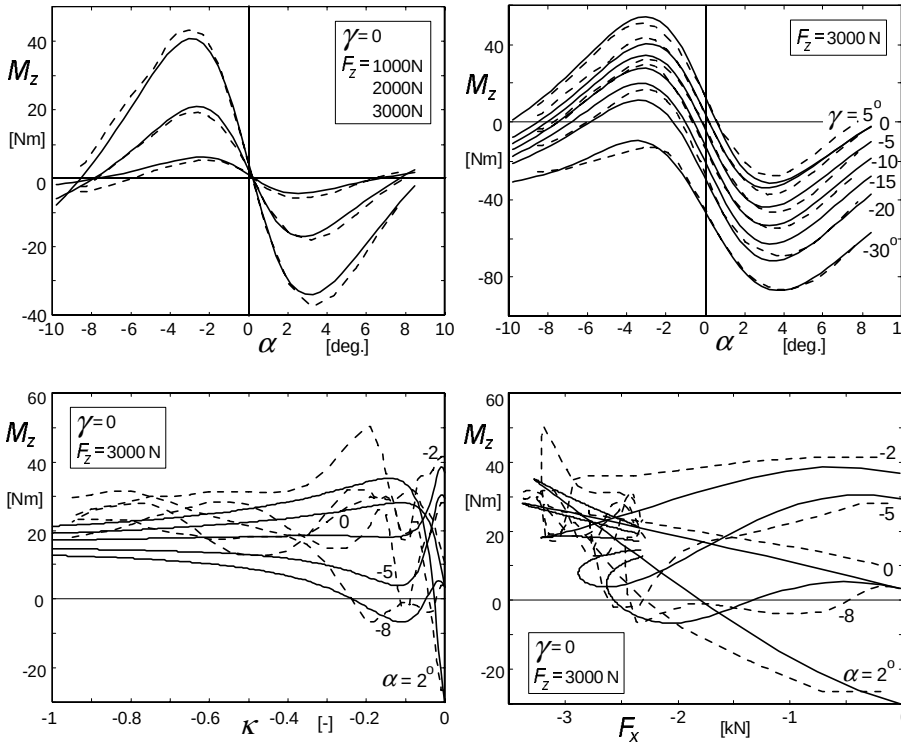

Fig. 10.32. Aligning torque characteristics of a 160/70 ZR17 motorcycle tyre. Modified Magic Formula computed results compared with data from measurements conducted with the Delft Tyre Test Trailer.

References

Abramowitz, M., and Stegun, I.A. (1965): *Handbook of mathematical functions.* Dover, New York, 1965.

Badalamenti, J.M., and Doyle, G.R. (1988): Radial-interradial spring tire models. *J. of Vibration, Acoustic, Stress and Reliability in Design*, 110, 1, 1988.

Bakker, E., Nyborg, L., and Pacejka, H.B. (1987): Tire Modeling for Use in Vehicle Dynamics Studies. *SAE Paper* No. 870421, 1987.

Bakker, E., Pacejka, H.B., and L.Lidner (1989): A New Tire Model with an Application in Vehicle Dynamics Studies. *SAE Paper* No. 890087, 1989.

Bandel, P., and Monguzzi, C. (1988): Simulation model of the dynamic behavior of a tire running over an obstacle.*Tire Science and Technology*, TSTCA, 16, 2, 1988.

Bandel, P., and Bernardo, C. di (1989): A Test for Measuring Transient Characteristics of Tires. *Tire Science and Technology*, 17, 2, 1989.

Bayer, B. (1988): Flattern und Pendeln bei Krafträdern. *Automobil Industrie*, 2, 1988.

Bayle, P., Forissier, J.F., and Lafon, S (1993): A New Tyre Model for Vehicle Dynamics Simulation. *Automotive Technology International*, 1993.

Becker, G., Fromm, H., and Maruhn, H. (1931): *Schwingungen in Automobil-lenkungen ('Shimmy').* Berlin, 1931.

Bergman, W. (1965): Theoretical prediction of the effect of traction on cornering force. *SAE Transactions*, 614, 1965.

Bernard, J.E., Segel, L., and Wild, R.E. (1977): Tire shear force generation during combined steering and braking maneuvres. *SAE Paper* 770852, 1977.

Berritta, R., Biral, F., and Garbin, S. (2000): Evaluation of motorcycle handling and multibody modelling and simulation. In: *Proceedings of 6th Int. Conference on High Tech. Engines and Cars*, Modena, 2000.

Besselink, I.J.M. (2000): *Shimmy of Aircraft Main Landing Gears.* Dissertation, TU Delft, 2000.

Biral, F., and Da Lio, M. (2001): Modelling drivers with the optimal maneuvre method. In: Proceedings of *ATA 2001*, The Role of Experiments in the Automotive Product Development Process, Florence, 2001.

Böhm, F. (1963): Der Rollvorgang des Automobil-Rades. *ZAMM* 43, T56-T60, 1963.

Borgmann, W. (1963): *Theoretische und experimentelle Untersuchungen an Luftreifen bei Schräglauf.* Dissertation, Braunschweig, 1963.

Breuer, T., and Pruckner, A. (1998): Advanced dynamic motorbike analysis and driver simulation. In: *13th European ADAMS Users' Conference*, Paris, 1998.

Brockman, R.A., and Braisted, W.R. (1994): Critical Speed Estimation of Aircraft Tires. *Tire Science and Technology* 22, 2, 1994.

Bruni, S., Cheli, F., and Resta, F. (1996): On the identification in time domain of the parameters of a tyre model for the study of in-plane dynamics. In: Proceedings of *Proceedings of 2nd Colloquium on Tyre Models for Vehicle Analysis*, eds. F.Böhm and H.P.Willumeit, Berlin 1997, Suppl. Vehicle System Dynamics, 27, 1996.

Chiesa, A., and Rinonapoli, L. (1967): Vehicle Stability Studied with a Nonlinear Seven Degree of Freedom Model. *SAE Paper* 670476, 1967.

Clark, S.K. (1982): A brief history of tire rolling resistance. In: *Proceedings of the Rubber Division Symposia*, 1, Chicago, 1982.

Cossalter, V., Da Lio, M., Biral, F., and Fabbri, L. (1998): Evaluation of motorcycle maneuvrability with the optimal maneuvre method. *SAE Paper* 983022, 1998.

Davis, D.C. (1974): A radial-spring terrain-enveloping tire model. *Vehicle System Dynamics*, 3, 1974.

Dijks, A. (1974): A Multifactor Examination of Wet Skid Resistance of Car Tires. *SAE Paper* 741106, 1974.

Dugoff, H., Fancher, P.S., and Segel, L. (1970): An analysis of tire traction properties and their influence on vehicle dynamics performance. In: *Proceedings FISITA Int. Auto. Safety Conference, SAE Paper* 700377, 1970.

Fiala, E. (1954): Seitenkräfte am rollenden Luftreifen. VDI Zeitschrift, 96, 1954.

Frank, F. (1965a): Grundlagen zur Berechnung der Seitenführungskennlinien von Reifen. *Kautchuk und Gummi*, 18, 8, 1965.

Frank, F. (1965b): *Theorie des Reifenschräglaufs*, Dissertation, Braunschweig, 1965.

Freudenstein, G. (1961): Luftreifen bei Schräg- und Kurvenlauf . *Deutsche Kraftfahrzeugforschung und Str. Verk. techn.*, 152, 1961.

Fritz, W. (1977): *Federhärte von Reifen und Frequenzgang der Reifenkräfte bei periodischer Vertikalbewegung der Felge*. Dissertation, Karlsruhe, 1977.

Fromm, H. (1941): *Kurzer Bericht über die geschichte der Theorie des Radflatterns*. Bericht 140 der Lilienthal Gesellschaft, 1941; NACA TM 1365, 1954.

Gillespie, T.D. (1992): *Fundamentals of Vehicle Dynamics*. SAE, 1992.

Gipser, M., Hofer, R., and Lugner, P. (1997): Dynamical Tire Forces Response to Road Unevennesses. In: Proceedings of *Proceedings of 2nd Colloquium on Tyre Models for Vehicle Analysis*, eds. F.Böhm and H.P.Willumeit, Berlin 1997, Suppl. Vehicle System Dynamics, 27, 1996.

Goncharenko, V.I., Lobas, L.S., and Nikitina, N.V. (1981): Wobble in guide wheels. *Soviet Applied Mechanics*, 17, 8, 1981.

Gong, S. (1993): *A Study of In-Plane Dynamics of Tires*. Dissertation, TU Delft, 1993.

Gong, S., Savkoor, A.R., and Pacejka, H.B. (1993): The influence of boundary conditions on the vibration transmission properties of tires. *SAE Paper* 931280, 1993.

Gough, V.E. (1963): Tyres and air suspension. *Advances in Automobile Engineering*, ed. G.H. Tidbury, Pergamon Press, Oxford, 1963.

Guntur, R.R. (1975): *Adaptive brake control systems*. Dissertation, TU Delft, 1975.

Guo, K.H. (1994): The Effect of Longitudinal Force and Vertical Load Distribution on Tire Slip Properties. *SAE Paper* 945087, 1994.

Guo, K.H., and Liu, Q. (1997): Modelling and Simulation of Non-Steady State Cornering Properties and Identification of Structure Parameters of Tyres. In: *Proceedings of 2nd Colloquium on Tyre Models for Vehicle Analysis*, Berlin 1997, eds. F.Böhm and H.P.Willumeit. Suppl. Vehicle System Dynamics, 27, 1996.

Hadekel, R. (1952): The mechanical characteristics of pneumatic tyres. *S & T Memo* 10/52, British Ministry of Supply, TPA 3/TIB, 1952.

Hartog, J.P. den (1940): *Mechanical Vibrations*, New York, 1940.

Hasegawa, A. (1985): Analysis of controllability and stability of motorcycles - Analysis of stability of high speed driving. In: *Proceedings of 10th Int. Tech. Conf. on Experimental Safety Vehicles*, 1985.

Henker, E. (1968): Dynamische Kennlinien von PKW Reifen. *Wissenschaftlich-Technische Veröffentlichungen aus dem Automobilbau* (IFA-DDR) Heft 3, 1968.

Higuchi, A., and Pacejka, H.B. (1997): The Relaxation Length Concept at Large Wheel Slip and Camber. In: *Proceedings of 2nd Colloquium on Tyre Models for Vehicle Analysis*, Berlin 1997, eds. F.Böhm and H.P.Willumeit. Suppl. Vehicle System Dynamics, 27, 1996.

Higuchi, A. (1997): *Transient response of tyres at large wheel slip and camber*. Dissertation, TU Delft, 1997.

Ho, F.H., and Hall, M.F. (1973):An experimental study of the pure-yaw frequency response of the 18x5.5 type VII aircraft tires. AFFDL-TR-73-79, 1973.

Iffelsberger, L. (1991): Application of vehicle dynamic simulation in motorcycle development. *Safety Environment Future*, Forschungshefte Zweiradsicherheit, 7, 1991.

Jagt, P. van der, Pacejka, H.B., and Savkoor, A.R. (1989): Influence of tyre and suspension dynamics on the braking performance of an anti-lock system on uneven roads. In: *Proceedings of EAEC Conference*, Strassbourg, C382/047 IMechE 1989.

Jagt, P. van der (2000): *The Road to Virtual Vehicle Prototyping*. Dissertation. TU Eindhoven, 2000.

Jenkinson, D. (1958): *The Racing Driver*. Batsford Ltd., London, 1958.

Jianmin, G., Gall, R., and Zuomin, W. (2001): Dynamic Damping and Stiffness Characteristics of the Rolling Tire. *Tire Science and Technology* 29, 4, 2001.

Katayama, T, Aoki, A., and Nishimi, T. (1988): Control behaviour of motorcycle riders. *Vehicle System Dynamics*, 17, 1988.

Katayama, T, Nishimi, T., Okoyama, T., and Aoki, A. (1997): A simulation model for motorcycle rider's behaviours. In: *Proceedings of SETC '97*, Yokohama, SAE of Japan, 1997.

Keldysh, M.V. (1945): *Shimmy of the front wheel of a three-wheeled landing gear*. Tr. Tsentr. Aerogidrodinamicheskogo Inst., 564, 1945.

Klotter, K. (1960): *Technische Schwingungslehre II.* Berlin, 1960.

Kluiters, M.A.M. (1969): *An investigation into F-28 main gear vibrations.* Fokker Report X-28-430, 1969.

Kobiki, Y., Kinoshita, A., and Yamada, H. (1990): Analysis of interior booming noise caused by tire and power train-suspension system vibration. *Int. J. of Vehicle Design*, 11, 3, 1990.

Koenen, C., and Pacejka, H.B. (1980): Vibrational Modes of Motorcycles in Curves. In: *Proceedings of the Int. Motorcycle Safety Conference*, Wash. D.C., Motorcycle Safety Foundation, Vol.II, 1980.

Koenen, C. (1983): The dynamic behaviour of a motorcle when running straight ahead and when cornering. Dissertation, TU Delft, 1983.

Koiter, W.T., and Pacejka, H.B. (1969): On the skidding of vehicles due to locked wheels.In: *Proceedings of the Symposium onHandling of Vehicles under Emergency Conditions*, Inst. of Mech. Engnrs. 1968-69, 183 Pt 3H, 19, 1969.

Kortüm, W., and Lugner, P. (1994): *Systemdynamik und Regelung von Fahrzeugen.* Springer Verlag, Berlin, 1994.

Krylov, N., and Bogoljubov, N. (1947): *Introduction to Non-Linear Mechanics.* Princeton, 1947.

Laerman, F.J. (1986): Seitenführungsverhalten von Kraftfahrzeugreifen bei schnellen Radlaständerungen. Dissertation, Braunschweig, *VDI-Fortschritt Berichte*, 12, 73, 1986.

Lee, Jung-Hwan (2000): Analysis of Tire Effect on the Simulation of Vehicle Straight Line Motion. *Vehicle System Dynamics*, 33, 2000.

Leipholz, H. (1987): *Stability theory, an introduction to the stability of dynamic systems and rigid bodies.* John Wiley & Sons, B.G.Teubner, Stuttgart, 1987.

Lippmann, S.A., Piccin, W.A., and Baker, T.P. (1965,67): Enveloping characteristics of truck tires - a laboratory evaluation. *SAE Paper* 650184, 1965.

Lippmann, S.A., and Nanny, J.D. (1967): A quantitative analysis of the enveloping forces of passenger car tires. *SAE Paper* 670174, 1967.

Magnus, K. (1955): Ueber die Verfahren zur Untersuchung nicht-linearer

Schwingungs- und Regelungs-Systeme. *VDI-Forschungsheft* 451 B, 21, 1955.

Mastinu, G. (1997): A Semi-Analytical Tyre Model for Steady and Transient State Simulations. In: *Proceedings of 2nd Colloquium on Tyre Models for Vehicle Analysis*, Berlin 1997, eds. F.Böhm and H.P.Willumeit. Suppl. Vehicle System Dynamics, 27, 1996.

Maurice, J.P., Berzeri, M., and Pacejka, H.B. (1999): Pragmatic Tyre Model for Short Wavelength Side Slip Variations. *Vehicle System Dynamics*, 31, 2, 1999.

Maurice, J.P. (2000): *Short wavelength and dynamic tyre behaviour under lateral and combined slip conditions*. Dissertation, TU Delft, 2000.

Metcalf, W.H. (1963): Effect of a Time-Varying load on Side Force Generated by a Tire Operating at Constant Slip Angle. *SAE Paper* 713c, 1963.

Milliken, W.F. et al. (1956): *Research in Automobile Stability and Control and Tire Performance*. The Inst. of Mech. Engnrs, London, 1956.

Milliken, W.F., and Milliken, D.L. (1995): *Race Car Vehicle Dynamics*. SAE 1995.

Mitschke, M. (1982): *Dynamik der Kraftfahrzeuge*, Band A, *Antrieb und Bremsung*. Springer Verlag, Berlin 1982.

Mitschke, M. (1990): *Dynamik der Kraftfahrzeuge*, Band C, *Fahrverhalten*. Springer Verlag, Berlin 1990.

Moreland, W.J. (1954): The story of shimmy. *J. of the Aeronautical Sciences*, December 1954.

Mousseau, C.W., and Clark, S.K. (1994): An analytical and experimental study of a tire rolling over a stepped obstacle at low velocity. *Tire Science and Technology*, TSTCA, 16, 2, 1994.

Nishimi, T., Aoki, A, and Katayama, T. (1985): Analysis of straight-running stability of motorcycles. In: *Proceedings of 10th Int. Tech. Conf. on Experimental Safety Vehicles*, 1985.

Nordeen, D.L., and Cortese, A.D. (1963): Force and moment characteristics of rolling tires. *SAE paper* 713A, 1963; *SAE Transactions* 325, 1964.

Oertel, Ch. (1997): On modelling contact and friction - calculation of tyre response on uneven roads. In: Proceedings of *Proceedings of 2nd Colloquium on Tyre Models for Vehicle Analysis*, eds. F.Böhm and H.P.Willumeit. Suppl. Vehicle System Dynamics, 27, 1996.

Olley, M. (1947): Road manners of the modern car. *J. Inst. Auto. Engnrs.*,15, 1947.

Oosten, J.J.M. van, and Bakker, E. (1993): Determination of Magic Tyre Model Parameters. In: *Proceedings of 1st Colloquium on Tyre Models for Vehicle Analysis*, ed. H.B. Pacejka, Delft 1991, Suppl. Vehicle System Dynamics, 21, 1993.

Oosten, J.J.M. van, Unrau, J.H., Riedel, G., and Bakker, E. (1996): TYDEX

Workshop: Standardisation of Data Exchange in Tyre Testing and Tyre Modelling. In: *Proceedings of 2nd Colloquium on Tyre Models for Vehicle Analysis*, eds. F.Böhm and H.P.Willumeit, Berlin 1997, Suppl. Vehicle System Dynamics, 27, 1996.

Pacejka, H.B. (1958): *Study of the lateral behaviour of an automobile moving upon a flat level road.* Cornell Aeronautical Laboratory Report YC-857-F-23, 1958.

Pacejka, H.B. (1965): Analysis of the wheel shimmy phenomenon. In: *Proceedings of the Auto. Division of I.Mech.E.*, 180, Part 2A, Inst. of Mech. Engnrs., 1965-66.

Pacejka, H.B. (1966): *The wheel shimmy phenomenon.* Dissertation, TU Delft, 1966.

Pacejka, H.B. (1971): The Tyre as a Vehicle Component. Chapter 7 of: *Mechanics of Pneumatic Tires*, ed. S.K. Clark, N.B.S. Monograph 122, Washington D.C., 1971 (new edition 1981).

Pacejka, H.B. (1972): Analysis of the Dynamic Response of a String-Type Tire Model to Lateral Wheel-Plane Vibrations. *Vehicle System Dynamics*, 1, 1, 1972.

Pacejka, H.B., and Fancher,P.S. (1972a): Hybrid simulation of shear force development of a tire experiencing longitudinal and lateral slip. In: *Proceedings of XIV FISITA Int. Auto. Tech. Congress*, London, 1972.

Pacejka, H.B. (1973a): Approximate dynamic shimmy response of pneumatic tyres. *Vehicle System Dynamics*, 2, 1973.

Pacejka, H.B. (1973b): Simplified analysis of steady-state turning behaviour of motor vehicles. *Vehicle System Dynamics*, 2, p.161,173,185; 1973.

Pacejka, H.B. (1974): Some recent investigations into dynamics and frictional behavior of pneumatic tires. In: *Proceedings of G.M. Symposium Physics of Tire Traction*, eds. D.F. Hays and A.L. Browne, Plenum Press, New York 1974.

Pacejka, H.B., Van der Berg, J., and Jillesma, P.J. (1977): Front Wheel Vibrations. In: *Proceedings of 5th VSD-2nd IUTAM Symposium*, eds. A. Slibar and H. Springer, Vienna 1977, Swets and Zeitlinger, Lisse 1978.

Pacejka, H.B. (1981): Analysis of Tire Properties. Chapter 9, *Mechanics of Pneumatic Tires*, ed. S.K. Clark, DOT HS-805 952, 1981.

Pacejka, H.B. (1981a): In-Plane and Out-of-Plane Dynamics of Pneumatic Tyres. *Vehicle System Dynamics*, 10, 1981.

Pacejka, H.B. (1986): Non-Linearities in Road Vehicle Dynamics. *Vehicle System Dynamics*, 15, 5, 1986.

Pacejka, H.B., and Sharp, R.S. (1991): Shear Force Development by Pneumatic Tyres in Steady State Conditions: A Review of Modelling Aspects. *Vehicle System Dynamics*, 20, 1991.

Pacejka, H.B., and Takahashi, T. (1992): Pure Slip Characteristics of Tyres on Flat and on Undulated Road Surfaces. In: *Proceedings of AVEC'92*, Yokohama, SAE of

Japan, 1992.

Pacejka, H.B., and Bakker, E (1993): The Magic Formula tyre model. In: *Proceedings of 1st Colloquium on Tyre Models for Vehicle Analysis*, Delft 1991, ed. H.B. Pacejka, Suppl. Vehicle System Dynamics, 21, 1993.

Pacejka, H.B. (1996): The Tyre as a Vehicle Component. In: *Proceedings of XXVI FISITA Congress*, ed. M. Apetaur, Prague, 1996.

Pacejka, H.B., and Besselink, I.J.M. (1997): Magic Formula Tyre Model with Transient Properties. In: *Proceedings of 2nd Colloquium on Tyre Models for Vehicle Analysis*, eds. F.Böhm and H.P.Willumeit, Berlin 1997, Suppl. Vehicle System Dynamics, 27, 1996.

Pevsner, Ja. M. (1947): *Theory of the stability of automobile motions*. (In Russian). Masjgiz, Leningrad, 1947.

Radt, H.S., and Pacejka, H.B. (1963): Analysis of the Steady-State Turning Behavior of an Automobile. In: *Proceedings of the Symposium on Control of Vehicles*, Inst. of Mech. Engnrs., London, 1963.

Radt, H.S., and Milliken, W.F. (1983): Non-dimensionalizing Tyre Data for Vehicle Simulation. *Road Vehicle Handling*, Inst. of Mech. Engnrs. (C133/83), 1983.

Reimpell, J., and Sponagel, P. (1986): *Fahrwerktechnik: Reifen und Räder*. Vogel Buchverlag, Würzburg 1986.

Riekert, P., and Schunck, T.E. (1940): Zur Fahrmechanik des Gummi-bereiften Kraftfahrzeugs. *Ingenieur Archiv* 11, 210, 1940.

Rocard, Y. (1949): Dynamique général des vibrations. Paris, 1949.

Rogers, L.C., and Brewer, H.K. (1971): Synthesis of tire equations for use in shimmy and other dynamic studies. *J. of Aircraft*, 8, 9, 1971.

Rogers, L.C. (1972): Theoretical tire equations for shimmy and other dynamic studies. *AIAA J. of Aircraft*, 1972.

Ruijs, P.A.J., and Pacejka, H.B. (1985): Research in Lateral Dynamics of Motorcycles. In: *Proceedings of 9th IAVSD Symposium on the Dynamics of Vehicles on Roads and Tracks*, ed. O. Nordström, Linköping 1985, Suppl. Vehicle System Dynamics,15, 1986.

SAE J670e 1976: *Vehicle Dynamics Terminology*. SAE J670e, Society of Automotive Engineers, Inc.,Warrendale, PA, July 1976.

Saito, Y. (1962): A study of the dynamic steering properties of tyres. In: *Proceedings IX FISITA Congress*, London, 1962.

Sakai, H (1981): Theoretical and experimental studies on the dynamic cornering properties of tyres. *Int. J. of Vehicle Design*, 2(1-4), 1981.

Sakai, H. (1989): Study on Cornering Properties for Tire and Vehicle. *The 8th annual meeting of the Tire Society*, Akron, 1989.

Sakai, H. (1990): Study on Cornering Properties of Tire and Vehicle. *Tire Science and Technology*, TCTCA, 18(3), 1990.

Savkoor, A.R. (1970): The lateral flexibility of a pneumatic tyre and its application to the lateral contact problem. In: *Proceedings FISITA Int. Auto. Safety Conference, SAE Paper* 700378, 1970.

Schlippe, B. von, and Dietrich, R. (1941): *Das Flattern eines bepneuten Rades.* Bericht 140 der Lilienthal Gesellschaft, 1941: NACA TM 1365, 1954.

Schlippe, B. von, and Dietrich, R. (1942): *Zur Mechanik des Luftreifens.* Zentrale für wissenschaftliches Berichtwesen, Berlin-Adlershof, 1942.

Schlippe, B. von, and Dietrich, R. (1943): Das Flattern eines mit Luftreifen versehenen Rades. In: *Jahrbuch der deutsche Luftfahrtforschung*, 1943.

Schmeitz, A.J.C., and Pauwelussen, J.P. (2001): An Efficient Dynamic Ride and Handling Tyre Model for Arbitrary Road Unevennesses. VDI-Berichte, 1632, 2001.

Segel, L. (1956): Theoretical Prediction and Experimental Substantiation of the Response of the Automobile to Steering Control. In: *Proceedings of Auto. Division of I.Mech.E.*, 7, 1956-57.

Segel, L. (1966): Force and moment response of pneumatic tires to lateral motion inputs. *Transactions ASME, J. of Engineering for Industry*, 88B, 1966.

Segel, L., and Wilson, R. (1976): Requirements on describing the mechanics of tires used on single-track vehicles. In: *Proceedings of IUTAM Symposium on the Dynamics of Vehicles,* TU Delft 1975, ed. H.B. Pacejka, Swets and Zeitlinger, Lisse 1976.

Segel, L., and Ervin, R.D. (1981): The Influence of Tire Factors on the Stability of Trucks and Tracktor Trailers. *Vehicle System Dynamics*, 10, 1, 1981.

Sekula, P.J., et al. (1976): Dynamic indoor tyre testing and Fourier transform analysis. *Tire Science and Technology*, 4, 2, 1976.

Sharp, R.S. (1971): The Stability and Control of Motorcycles. *J. of Mech. Engng. Sci.*, 13, 5, I.Mech.E., 1971.

Sharp, R.S. (1978): A Review of Motorcycle Steering Behaviour and Straight Line Stability Characteristics. SAE Paper 780303, 1978.

Sharp, R.S., and Jones, C.J. (1980): A comparison of tyre representations in a simple wheel shimmy problem. *Vehicle System Dynamics*, 9, 1, 1980.

Sharp, R.S., and Alstead, C.J. (1980a): The Influence of Structural Flexibilities on the Straight-Running Stability of Motorcycles. *Vehicle System Dynamics*, 9, 1980.

Sharp, R.S. (1985): The lateral dynamics of motorcycles and bicycles. *Vehicle System Dynamics*, 14, 4-6, 1985.

Sharp, R.S., and El-Nashar, M.A. (1986): A generally applicable digital computer based mathematical model for the generation of shear forces by pneumatic tyres.

Vehicle System Dynamics, 15, 1986.

Sharp, R.S. (2001): Stability, Control and Steering Responses of Motorcycles. *Vehicle System Dynamics*, 35, 4-5, 2001.

Sharp, R.S., and Limebeer, D.J.N. (2001a): A motorcycle model for stability and control analysis. Multibody System Dynamics, 6, 2, 2001.

Smiley, R.F. (1957): *Correlation and extension of linearized theories for tire motion and wheel shimmy*. NACA Report 1299, 1957.

Smiley, R.F. (1958): *Correlation, evaluation and extension of linearized theories for tire motion and wheel shimmy*. NACA (NASA) Tech. Note 4110, 1958.

Sperling, E. (1977): *Zur Kinematik und Kinetik elastischer Räder aus der Sicht verschiedener Theorien*. Dissertation, TU Munich, 1977.

Spierings, P.T.J. (1981): The Effects of Lateral Front Fork Flexibility on the Vibrational Modes of Straight Running Single Track Vehicles. *Vehicle System Dynamics*, 10, 1980.

Stoker, J.J. (1950): *Non-Linear Vibrations*. New York, 1958.

Strackerjan, B. (1976): Die Querdynamik von Kraftfahrzeugreifen. In: Proceedings of: *VDI-Schwingungstagung*, 1976.

Takahashi, T, Yamada, T., and Nakamura, T. (1984): Experimental and theoretical study of the influence of tires on straight-running motorcycle weave response. SAE Paper 840248, 1984.

Takahashi, T., and Pacejka, H.B. (1987): Cornering on uneven roads. In: *Proceedings of 10th IAVSD Symposium on the Dynamics of Vehicles on Roads and Tracks*, ed. M. Apetaur, Prague 1987, Suppl. Vehicle System Dynamics, 17, 1988.

Tanguy, G. (1986): Antiskid Systems and Vehicle Suspension. *SAE Paper* 865134, 1986.

Troger, H., and Zeman, K. (1984): A non-linear analysis of the generic types of loss of stability of the steady-state motion of a tractor-semi-trailer. *Vehicle System Dynamics*, 13, 1984.

Valk, R. van der, and Pacejka, H.B. (1993): An analysis of a civil aircraft main landing gear shimmy failure. *Vehicle System Dynamics*, 22, 1993.

Vries, E.J.H. de, and Pacejka, H.B. (1998a): Motorcycle tyre measurements and models. In: *Proceedings of 15th IAVSD Symposium on the Dynamics of Vehicles on Roads and Tracks*, ed. L.Palkovics, Budapest 1997, Suppl. Vehicle System Dynamics 28, 1998.

Vries, E.J.H. de, and Pacejka, H.B. (1998b): The effect of tire modelling on the stability analysis of a motorcycle.. In: *Proceedings AVEC'98*, Nagoya, SAE of Japan, 1998.

Weir, D.H. (1972): Motorcycle handling dynamics and rider control and the effect of

design configuration on response and performance. Dissertation, UCLA, 1972.

Whipple, F.J.W. (1899):The Stability of the Motion of a Bicycle. *Quart. J. of Pure and Applied Mathematics*, 30, 1899.

Whitcomb, D.W., and Milliken, W.F. (1956): Design Implications of a General Theory of Automobile Stability and Control. In: *Proceedings of Auto. Division of I.Mech.E.*, 7, 1956-57.

Willumeit, H.P. (1969):Theoretisch Untersuchungen an einem Modell des Luftreifens. Dissertation, Berlin, 1969.

Winkler, C.B. (1998): Simplified Analysis of the Steady-State Turning of Complex Vehicles. *Vehicle System Dynamics*, 29, 3, 1998.

Wisselman, D., Iffelsberger, D., and Brandlhuber, B. (1993): Einsatz eines Fahrdynamik-Simulationsmodells in der Motorradentwicklung bei BMW. *ATZ*, 95, 2, 1993.

Zegelaar, P.W.A., Gong, S., and Pacejka, H.B. (1993): Tyre Models for the Study of In-Plane Dynamics. In: *Proceedings of 13th IAVSD Symposium on the Dynamics of Vehicles on Roads and Tracks*, ed. Z. Shen, Chengdu 1993, Suppl. Vehicle System Dynamics 23, 1994

Zegelaar, P.W.A., and Pacejka, H.B. (1995): The In-Plane Dynamics of Tyres on Uneven Roads. In: *Proceedings of 14th IAVSD Symposium on the Dynamics of Vehicles on Roads and Tracks*, ed. L. Segel, Ann Arbor 1995, Suppl. Vehicle System Dynamics 25, 1996

Zegelaar, P.W.A., and Pacejka, H.B. (1997): Dynamic Tyre Responses to Brake Torque Variations. In: *Proceedings of 2nd Colloquium on Tyre Models for Vehicle Analysis*, eds. F.Böhm and H.P.Willumeit, Berlin 1997, Suppl. Vehicle System Dynamics, 27, 1996.

Zegelaar, P.W.A. (1998): *The dynamic response of tyres to brake torque variations and road unevennesses*. Dissertation, TU Delft, 1998.

List of Symbols

a	distance front axle to c.g.; half of contact length
a_x	longitudinal acceleration
a_y	lateral acceleration
a_μ	slip velocity dependency coefficient for friction
A_r	rolling resistance coefficient
b	distance rear axle to c.g.; half contact width
B	stiffness factor in 'Magic Formula'
B_1	brake force of rolling wheel
c	stiffness; factor
c_c	lateral carcass stiffness per unit length
c_{gyr}	non-dimensional gyroscopic coefficient
$c_{px,y}$	tread element stiffness per unit length of circumference
c'_{px}	tread element longitudinal stiffness per unit area
C	cornering stiffness ; sum front and rear
C_i	cornering stiffness, sum left and right
C	contact centre (point of intersection)
C	shape factor in 'Magic Formula'
C_{dA}	air drag coefficient
C_{Fy}	lateral stiffness of standing tyre
C_{Fx}	longitudinal stiffness of standing tyre
$C_{F\alpha}$	cornering stiffness
$C_{F\kappa}$	longitudinal slip stiffness
$C_{F\gamma}$	camber stiffness for side force
$C_{F\varphi}$	spin stiffness for side force
C_{gyr}	tyre gyroscopic coefficient
$C_{M\alpha}$	aligning torque stiffness
$C_{M\gamma}$	camber stiffness for aligning torque
$C_{M\varphi}$	spin stiffness for aligning torque
$C_{M\psi}$	torsional yaw stiffness of standing tyre
$C_{Mx\gamma}$	overturning couple stiffness against camber
$C_{cx,y}$	carcass horizontal stiffness of standing tyre
C_{gyr}	gyroscopic coefficient
df_z	normalized change in normal load, Eq.(4.E2)
d_t	tread depth
D	peak factor in 'Magic Formula'; dissipation function
E	curvature factor in 'Magic Formula'

e	caster length; tread element deflection
f	trail of c.g.
f_r	rolling resistance coefficient
F_{ax}	force for forward acceleration
F_d	air drag force
$F_{x,tot}$	sum of longitudinal tyre forces
F_x	longitudinal tyre force
F_y	lateral tyre force
F_z	vertical (normal) tyre force (load) (>0), in Chap.9 F_z<0
F_r	rolling resistance force (>0)
F_N	tyre normal force (>0)
F_{No}	reference vertical load, nominal load (= $\|F_{zo}\|$)
F_V	tyre vertical force
F_H	tyre longitudinal horizontal force
g	acceleration due to gravity; feedback rider control gain
G	weighting factor
h	height
i	√-1
i_z	radius of inertia
H	height; sharpness factor in 'Magic Formula'
H	transform; Hurwitz determinant
j	√-1
I	moment of inertia
I_w	wheel polar moment of inertia
I_p	wheel polar moment of inertia
k	radius of inertia; viscous damping coefficient
K	centrifugal force; force acting in belt, wheel centre
l	wheel base
l_s	shift; two-point follower length
l_b	length of basic curve
l_f	offset
$\boldsymbol{l}$	unit vector along line of intersection
m	mass; fraction of $2a$ where adhesion occurs
m_c	contact patch mass (dummy)
m_t	tyre mass
m_m	mass of mainframe (including lower part of rider)
m_{mr}	mass of mainframe plus rider
m_r	mass of upper torso
$M_{B,D}$	brake, drive torque
M_x	overturning couple

M_y	rolling resistance moment
M_z	(self) aligning torque
M_z'	(self) aligning torque due to lateral deflections
M_z^*	aligning torque due to longitudinal deflections
$M_{z,gyr}$	gyroscopic couple
M_δ	steer torque
n	number of elements; frequency [Hz]
$\boldsymbol{n}$	unit vector normal to the road $=(0,0,-1)^T$
n_{st}	steer system ratio
p	Laplace variable [1/m]
p_i	inflation pressure
q	average vehicle yaw resistance arm; generalized coordinate
q	contact force per unit length of circumference, vector
Q	generalized force
r	yaw rate; tyre (loaded) radius
r_c	radius of carcass (belt), unloaded; cross section crown radius
r_{yo}	free tyre radius varying along cross section contour, $r_{yo} = r_{yo}(y_{co})$
r_e	effective rolling radius of freely rolling wheel
r_f	free unloaded tyre radius
r_l	loaded radius
r_o	free unloaded tyre radius ($=R_o$)
R	radius of curvature
R_o	free unloaded tyre radius ($=r_o$)
s	forward position of neutral steer point; half track width;
s	Laplace variable; travelled distance
s_{sx}	κ (practical slip component)
s_{sy}	$\tan\alpha$ (practical slip component)
$\boldsymbol{s}$	unit vector along wheel spin axis
S	wheel slip point; impulse; string tension force
$S_{V,H}$	vertical, horizontal shift
t	pneumatic trail; time
t_c	caster length
t_r	rise time
$\boldsymbol{t}$	unit vector in road plane perpendicular to line of intersection $\boldsymbol{l}$
T	kinetic energy; moment acting around belt, wheel centre
u	forward velocity of c.g.; longitudinal deflection
v	lateral velocity of c.g.; lateral deflection
U	potential energy
V	speed of travel of c.g. (with x, y components)
V	speed of travel of wheel centre (with x, y components)

V_c	speed of contact centre C (with x, y components)
V_g	speed of sliding (with x, y components)
V_o	reference velocity $=\sqrt{gR_o}$
V_r	wheel linear speed of rolling ($= V_{cx} - V_{sx}$)
V_s	wheel slip velocity of slip point S (with x, y components)
V_x	longitudinal speed component of wheel centre
V_s^*	velocity of contact patch mass (with x, y components)
w	vertical road (effective) profile (positive downwards)
W	work
x,y,z	longitudinal, lateral, vertical displacement
x,y,z	coordinates with respect to moving axes system, z axis vertical
x^o,y^o,z^o	global coordinates
$\bar{x},\bar{y},\bar{z}$	global coordinates
X	longitudinal horizontal tyre force
X,Y,Z	global coordinates
y_{co}	distance from wheel centre plane
y_{mr}	lateral offset of m_{mr} c.g.
α	wheel (side) slip angle; axle (side) slip angle
α	road transverse slope angle
α'	transient tyre slip angle
α_a	virtual axle slip angle
β	vehicle side slip angle; tyre yaw torsion angle
β	road forward (eff.) slope angle
β_{gyr}	gyroscopic wheel coupling coefficient, Eq.(6.35)
γ	camber (wheel inclination) angle
γ'	transient tyre camber angle
Γ	unit step response function
δ	steer angle of front wheels
δ_o	$\approx 1/R$, steer angle at $V \to 0$
Δ	increment
ε	roll steer coefficient; rake angle of steering axis
ε	string length ratio, Eq.(5.153); eff. roll. radius gradient $-\partial r_e/\partial d_t$
ε_γ	camber stiffness reduction factor
ε_{NL}	non-lagging part
ε	small quantity to avoid singularity
ζ	damping ratio; spin factor (=1 if spin influence is disregarded)
ζ_h	height ratio, Eq.(6.36)
ζ_α	cornering stiffness load transfer coefficient
ζ_γ	camber stiffness load transfer coefficient

η	understeer coefficient; effective rolling radius gradient $-\partial r_e/\partial \rho_z$
η_y	c.g. offset steer coefficient
θ	tyre model parameter, Eqs.(3.6,24,46)
θ	angular displacement about η axis; pitch angle
θ_c	string model composite parameter, Eq.(5.160)
κ	longitudinal wheel slip
κ'	transient longitudinal tyre slip
κ^*	damping coefficient due to tread width
λ	wavelength; root characteristic equation
λ	fraction of $2a$ where adhesion occurs; user scaling factor
μ	coefficient of friction
ρ	tyre radial (vertical) deflection
$\rho_{x,y,z}$	tyre longitudinal, lateral, normal deflection
σ	relaxation length; load transfer coefficient
σ	theoretical slip, vector, Eq.(3.34)
σ^*	intersection length in string model with tread elements
σ_c	string model length parameter, Eq.(5.153)
σ_c	contact patch relaxation length
τ	roll camber coefficient
φ	body roll angle; spin slip
φ'	transient spin slip
φ_t	turn slip
ϕ	phase angle
ψ	yaw angle; steer angle
ψ_{cl}	compliance steer angle
ψ_{io}	toe angle
ω	frequency [rad/s]
ω_o	undamped natural frequency
$\omega_{1,2}$	natural frequencies
ω_n	damped natural frequency
ω_s	path frequency [rad/m]
Ω	wheel speed of revolution
ξ,η,ζ	moving axes system, η axis along spin axis, ξ horizontal

Subscripts and superscripts

a	axle; from belt to wheel rim centre
b	belt; from belt centre to rim
c	compliance (steer)
c	contact patch; from contact patch centre to belt; crown; contour

D	drag
e	effective
eff	effective (cornering stiffness)
eq	equivalent
f	free, unloaded; of front frame
g	global
i	1: front, 2: rear
L,R	left, right
m	of mainframe
mr	of mainframe plus rider
NL	non-lagging
o	original; initial; average
o	unloaded; nominal; at vanishing speed; natural
r	roll; rolling; rolling resistance; of residual spring; of rider
s	slip; from road surface to contact patch; of front sub-frame
sl	at verge of total sliding
sf	side force (steer)
ss	steady state
st	static
stw	steering wheel
t	transition from adhesion to sliding
w	wheel
x,y,z	forward (longitudinal), lateral (to the right), downward
zr	residual (torque)
ξ,η,ζ	along, around ξ,η,ζ axes
1,2	front, rear; leading, trailing edge

Appendix 1

Sign Conventions for Force and Moment and Wheel Slip

	SAE	adapted SAE (Pacejka, this book)	ISO	adapted ISO (Besselink, 2000)
side angle (top view)	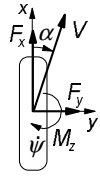	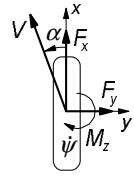	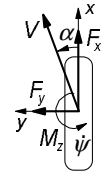	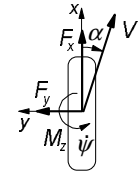
inclination/ camber angle (rear view)	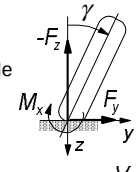	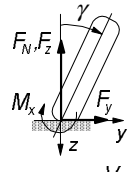	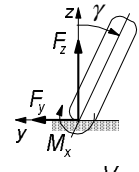	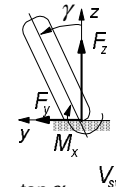
side slip	$\tan\alpha = \frac{V_{sy}}{V_x}$	$\tan\alpha = -\frac{V_{sy}}{V_x}$	$\tan\alpha = \frac{V_{sy}}{V_x}$	$\tan\alpha = -\frac{V_{sy}}{V_x}$
longitudinal slip	$\kappa = -\frac{V_{sx}}{V_x}$	$\kappa = -\frac{V_{sx}}{V_x}$	$\kappa = -\frac{V_{sx}}{V_x}$	$\kappa = -\frac{V_{sx}}{V_x}$
turn slip	*not defined*	$\varphi = -\frac{\dot{\psi}}{V_x}$	*not defined*	$\varphi = -\frac{\dot{\psi}}{V_x}$

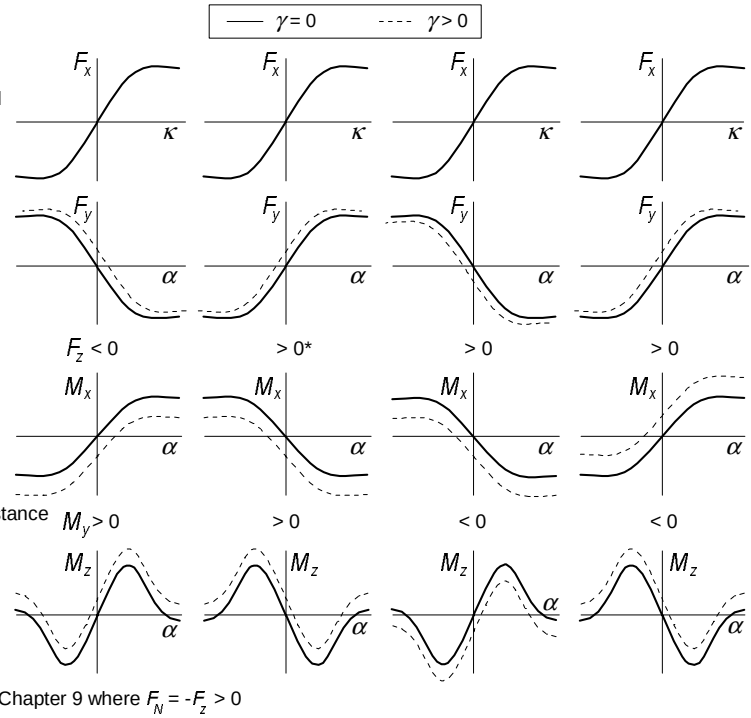

*except for Chapter 9 where $F_N = -F_z > 0$

Appendix 2

TreadSim

A Matlab program for the calculation of steady-state force and moment response to side slip, longitudinal slip, camber and turnslip using a brush model with up to three rows of tread elements and a flexible carcass. Cf. Chapter 3, Section 3.3 and Figs.3.35,38.

```
%   **  TreadSim.m  **

%   **  tread element following model   **
%   **  one, two or three rows   **

%   **  stationary response to lateral, longitudinal, camber and turn slip   **
%   **  carcass rigid with only lateral compliance effect in Mz   **
%   **  or
%   **  carcass lateral, yaw and bending compliance   **
%   **  with approximate slip speed dependent friction coefficient   **
%   **  conicity, ply-steer, correction factors for lateral roll and camber distortion  **
%   **  calculation of forces Fx, Fy and moment Mz (and t)
%       as function of kappa, alpha or a/R
%      (with kappa, a/R =aphit, gamma or alpha as changing motion parameter)
%   **  option for making deformation picture for one set of motion variables**

clf;
picture=1;  % if =1 then single set of values of motion variables is given and diagrams of
            % force distribution and of carcass and tread elements deformation are produced
rigid=0;        % =1 if carcass is rigid, else =0
if rigid ==1
iitend=1;       % =1 (no iterations at rigid carcass!)
else
iitend=5;           % =5....25 (number of iterations depends on carcass compliance)
end;
n=20;                       % number of elements -1
nrow=3;                     % number of rows (1 or 2 or 3)
a=0.1;                      % half contact length [m]

if picture ==1              % single set of values of motion variables
  alphapict= 4;             % slip angle in degrees
  gammapict= 0;             % camber angle in degrees
  Rpict= 1.00000000;        % turnslip = a/Rpict,  path curvature radius Rpict in m
  kappapict= -0.0;          % long. slip (from -1 to ....)
  n=30;
end;
                    % if running variable (abscissa) (then =1 else =0)
alpharuns=0;                % slip angle
```

```
kapparuns=1;                    % longitudinal slip ratio
aphitruns=0;                    % non-dimensional turnslip (aphit=a/R)

            % if not chosen as running variable but as changing parameter (then =1, else =0)
gammapar=0;
aphitpar=0;
alphapar=1;
kappapar=0;

      % side slip angle: alpha range and step [deg] (if chosen as running variable)
alphdegminr=-25.01;
alphdegmaxr=25;
g1a=0.05; g2a=0.2;        % deltalphdegr=g1a*abs(alphadeg)+g2a (varying alpha increment)
      % longidinal slip ratio: kappa range and step [-] (if chosen as running variable)
kappaminr=-0.99;          % negative: braking
kappamaxr= 0.8;           % positive: driving
g1k=0.1; g2k=0.01;% deltakappar=g1k*abs(kappa)+g2k  (varying kappa increment)
      % non-dim. turnslip: aphit (=a/R) range and step [-] (if chosen as running parameter)
aphitminr=0.01;
aphitmaxr=0.7;
g1t=0.01; g2t=0.01;       % deltaphitr=g1t*abs(aphit)+g2t   (varying aphit increment)

                        % constant motion parameters
      % (overruled if chosen as changed parameter or as running variable)
alphadeg=0;           % [deg]     (slip angle)
gammadeg=0;               % [deg]     (camber angle)
R=10000000;               % [m]       (aphit=a/R;   non-dimensional turnslip)
kappa=0;              % [-]         (long. slip ratio)

aphit=a/R;
jmax=1;
deltgamdeg=0; gamdegmin=gammadeg;
deltalphdeg=0; alphdegmin=alphadeg;
deltaphit=0; aphitmin=aphit;
deltakappa=0; kappamin=kappa;

      % changed motion parameters (number, minimum, step)

if gammapar==1            % **gamma** as changed motion parameter [deg]:
jmax=6; gamdegmin=-5; deltgamdeg=5;
end;
if aphitpar==1            % **aphit (=a/R)** as changed motion parameter [-]:
jmax=12; aphitmin=-0.3; deltaphit=0.1;
end;
if alphapar==1            % **alpha** as changed motion parameter [deg]:
jmax=5; alphdegmin=0.000001-2; deltalphdeg=2;
end;
if kappapar==1            % **kappa** as changed motion parameter [-]:
jmax=1; kappamin=-0.0; deltakappa=-0.05;
```

```
end;

% system parameters

re=0.3;                 % effective rolling radius [m]
Fz=3000;                % normal load [N]
Vc=30;                  % speed of contact centre [m/s]
mu0=1;                  % friction coefficient [-]
amu=0.03;               % speed dependency coefficient for mu [s/m]
                        % ( mu=mu0/(1+amu*Vbi) ); 0.03
CFkappaFz=15;           % long. slip stiffness over Fz [-]
CFkappa=CFkappaFz*Fz;     %[N/-]    from this: cp=(1/(nrow*2*a*a))*CFkappa;
%  cornering stiffness coeff. CFalpha/Fz [-] is calculated if alpharuns=1 for last param. case
%  a (half contact length) defined above
b=0.08;                 % half contact width [m]
brow=0.05;              % half effective contact width [m]
 if nrow==1
 brow=0;
end;
alphadegply=0;          % ply-steer equivalent slip angle [deg]
gammadegcon=0;          % conicity equivalent camber angle [deg]

      %stiffnesses of tyre carcass at contact patch at base of tread elements
      % (as if measured on bare tyre)
y0=0.00;        % initial lateral off-set (vo) , if rigid: Mz=Mz-c*Fx*Fy-y0*Fx  (0.005)

if rigid==0
 cyaw= 6000.000;   % [Nm/rad]    8000
 cbend=4000.000;   % [mN]        8000
 clat= 100000;           % [N/m]       suggested:  clat=Fz/(0.15*a)    200000
 else
 cyaw= 10000000;         % [Nm/rad]
 cbend=10000000;         % [mN]
 clat= 10000000;         % [N/m]
 c=1/100000;         % c=(1-epsyFy)/clat ,
                         % Mz=Mz-c*Fx*Fy-y0*Fx, (0.5/200000),   c is used if 'rigid'
end;
      %resulting stiffness of tread elements, per row, per unit of circumfernce
cp=(1/(nrow*2*a*a))*CFkappa;
theta=(1/3)*CFkappa/(mu0*Fz); % not used

      % correction parameters
epsyprime=0.0;   % reduction factor for moment arm of Fx causing yaw distortion (slope);
            % arm =~(1-epsyprime)*ymeff   (0.5)
             % where ymeff represents effective lateral displacement of belt in contact zone
epsyrgamma=4;   % moment (Mz) arm for Fx due to sideways rolling caused by camber =
           %  ygamroll=epsyrgamma*gamma*b; if abs(ygamroll)>b: ygamroll=b*sign(gamma)
epsyFy=0.0; % reduction factor moment(Mz)arm for Fx due to sideways rolling caused by
Fy
```

```
            % and the counter effect of longitudinal deflection
            % total moment {Mz) arm= ymeff= ym0+ydefl(1-epsyFy)+ygamroll
epsdrgam=0.0;     % coefficient for reduced change eff. rolling radius left/right
                  % caused by camber
            % delta_re_Right=~ -(1-epsdrgam)*gamma*brow; suggestion: epsdrgam
% (=epsxgamma)=epsgamma
epsgamma=0.0;   % reduced camber curvature coefficient (will be >0) due to distorsion
     % (=epsygamma)
            % resulting camber contactline curvature (at mu=0)
            % 1/Rgamma=(1/re)*(1-epsgamma)*sin(gamma)

        % end of parameter settings

        % start of computation
a2=a*a; a3=a2*a;
nCFa=0;  CFalphaFz='?';

if picture==1
   jmax=1;
   alphadegmin=alphapict;
   gamdegmin=gammapict;
   aphitmin=a/Rpict;
   kappamin=kappapict;
end;

          % **  begin gamma, aphit(=a/R), alpha or kappa-loop (as motion parameter) **
for j=1:jmax
gammadeg=gamdegmin+(j-1)*deltgamdeg;
aphit=aphitmin+(j-1)*deltaphit;
alphadeg=alphdegmin+(j-1)*deltalphdeg;
kappa=kappamin+(j-1)*deltakappa;

alpha=alphadeg*pi/180;
gamma=(gammadeg+gammadegcon)*pi/180;
singam=sin(gamma);
cs0=alphadegply*pi/180;              % initial belt slope due to ply-steer
cc0=(1/re)*(1-epsgamma)*singam;% initial belt lateral curvature due to camber and conicity
ym0=-0.5*cc0*a2;         % initial belt lateral position at contact centre resulting from camber
                         % at mu=0. This is a guess; then, y0i=cs0*a at leading edge (x=a)
ygamroll=epsyrgamma*singam*b;  % moment arm of Fx due to sideways rolling at camber
 if abs(ygamroll)>b
 ygamroll=b*sign(gamma);
 end;

cs=cs0;
cc=cc0;
ym=ym0;
Fy=0; Mzprime=0; Fym1=0; Mzm1=0;
if alpharuns==1
```

```
alphadeg=alphdegminr;
imax=round((log(abs(1-g1a*alphdegminr/g2a))+log(abs(1+g1a*alphdegmaxr/g2a)))/g1a)+2;
end;
if kapparuns==1
kappa=kappaminr;
imax=round((log(abs(1-g1k*kappaminr/g2k))+log(abs(1+g1k*kappamaxr/g2k)))/g1k)+2;
end;
if aphitruns==1
aphit=aphitminr;
imax=round((log(abs(1-g1t*aphitminr/g2t))+log(abs(1+g1t*aphitmaxr/g2t)))/g1t)+5;
end;

if picture==1
  alphadeg=alphapict;
  alpha=alphadeg*pi/180;
  kappa=kappapict;
  aphit=a/Rpict;
  alphadegminr=alphapict;
  kappaminr=kappapict;
  aphitminr=a/Rpict;
  imax=1;
end;

for ia=1:imax        % **  begin kappa or alpha or a/R (if running variable) ia-loop **

if alpharuns==1
alpha=pi*alphadeg/180;
Fym1=Fy;                % needed for calculation of cornering stiffness
end;
R=a/(aphit+0.0001);
Fy=0; Mzprime=0;        % initial value for iteration

                        % **  begin carcass deflection iteration, iit-loop **
for iit=1:iitend
slope=Mzprime/cyaw;
cs=cs0+slope;           % belt slope at contact centre w.r.t. wheel plane
curve=Fy/cbend;
cc=cc0-curve;           % belt lateral curvature in contact zone
ydefl= Fy/clat;
ym=ym0+ydefl;      % belt lateral position at contact centre w.r.t. wheel plane
yFyroll=-epsyFy*ydefl;
ymeff=ym+ygamroll+yFyroll;    %effective moment (Mz) arm for Fx

for iLR=1:nrow    % **  begin left (iLR=1) and right row (iLR=2) loop (if one row: nrow=1)
  if nrow==1
    ibLR=0; bLR=0;
  end;
  if nrow==2
    ibLR=(2*iLR-3); bLR=ibLR*brow;
```

```
  end;
  if nrow==3
    ibLR=(iLR-2); bLR=ibLR*brow;   % left: bLR=-brow,  mid: bLR=0,  right: bLR=+brow
  end;

psidot= -Vc/R;

Vcx=Vc*cos(alpha);
Vsx= -Vcx*kappa;
Vsy= -Vcx*tan(alpha);
Vr=Vcx-Vsx;
omega=Vr/re;
VcxLR=Vcx-bLR*psidot;
VsxLR=Vsx-bLR*psidot+bLR*omega*(1-epsdrgam)*singam;
VsyLR=Vsy;
VrLR=Vr;


deltat=2*a/(n*VrLR);
deltax=2*a/n;
xi=a; x(1)=a;
ei=0; exi=0; eyi=0; Fxim1=0; Fyim1=0; Mzim1=0;
px(1)=0; py(1)=0; pz(1)=0; p(1)=0;
sliding=0;
                        % **  begin i-loop: passage through contact length
for  i=2:n+1
eim1=ei; exim1=exi; eyim1=eyi;
xi=xi-deltax; xi2=xi*xi;
x(i)=xi;
dybdximean=cs+cc*(xi+0.5*deltax);
ybi=ym +cs*xi+0.5*cc*xi*xi+bLR;
ybieff=ymeff+cs*xi+0.5*cc*xi*xi+bLR;
Vbxi=VsxLR;
Vbyimean=VsyLR + (xi+0.5*deltax)*psidot - VrLR*dybdximean;
Vbi=sqrt(Vbxi*Vbxi+Vbyimean*Vbyimean); Vb(i)=Vbi;      % belt point velocity
mu=mu0/(1+amu*Vbi);
pzi=0.75*Fz*(a2-xi2)/(a3*nrow); pz(i)=pzi;      % vertical pressure distribution (qz)
deltasxi=deltat*Vbxi;
deltasyi=deltat*Vbyimean;

if sliding>0                  % element is sliding
ei=mu*pzi/cp;
 if i==2
 eim1=0.00001;
 exim1=-eim1*Vbxi/Vbi;
 eyim1=-eim1*Vbyimean/Vbi;
 end;
gi=0.5*eim1*((exim1-deltasxi)*(exim1-deltasxi)+(eyim1-deltasyi)*...
      (eyim1-deltasyi)-ei*ei)/(exim1*(exim1-deltasxi)+eyim1*(eyim1-deltasyi));
```

```
exi=(1-gi/eim1)*exim1-deltasxi;
eyi=(1-gi/eim1)*eyim1-deltasyi;
ein=sqrt(exi*exi+eyi*eyi);
exi=(ei/ein)*exi;   %correction
eyi=(ei/ein)*eyi;   %correction
pxi=(exi/ei)*mu*pzi;
pyi=(eyi/ei)*mu*pzi;
 if gi<0                    % element starts to adhere to the road
 sliding=0;
 exi=-deltasxi+exim1;
 eyi=-deltasyi+eyim1;
 ei=sqrt(exi*exi+eyi*eyi); e(i)=ei;
 pii=cp*ei;
 pxi=cp*exi;
 pyi=cp*eyi;
  if pii>mu*pzi
  pxi=(exi/ei)*mu*pzi;
  pyi=(eyi/ei)*mu*pzi;
  pii=mu*pzi;
  sliding=1;
  end;
 end;
else                        % element is adhering to the road
exi=-deltasxi+exim1;
eyi=-deltasyi+eyim1;
ei=sqrt(exi*exi+eyi*eyi); e(i)=ei;
pii=cp*ei;
pxi=cp*exi;
pyi=cp*eyi;
 if pii>mu*pzi              % element starts to slide
 sliding=1;
  if i==2
  eim1=0.00001;
  exim1=-eim1*Vbxi/Vbi;
  eyim1=-eim1*Vbyimean/Vbi;
  end;
 ei=mu*pzi/cp;
 gi=0.5*eim1*((exim1-deltasxi)*(exim1-deltasxi)+(eyim1-deltasyi)*...
      (eyim1-deltasyi)-ei*ei)/(exim1*(exim1-deltasxi)+eyim1*(eyim1-deltasyi));
 exi=(1-gi/eim1)*exim1-deltasxi;
 eyi=(1-gi/eim1)*eyim1-deltasyi;
 ein=sqrt(exi*exi+eyi*eyi);
 exi=(ei/ein)*exi;  %correction
 eyi=(ei/ein)*eyi;  %correction
 pxi=(exi/ei)*mu*pzi;
 pyi=(eyi/ei)*mu*pzi;
 end;
end;
```

```
pii=sqrt(pxi*pxi+pyi*pyi);
Fxi=Fxim1+pxi*2*a/n;
Fyi=Fyim1+pyi*2*a/n;
Mzi=Mzim1+(xi*pyi -ybieff*pxi)*2*a/n;
py(i)=pyi;
Fxim1=Fxi;
Fyim1=Fyi;
Mzim1=Mzi;

if picture==1
 if ibLR==-1
 yL(1,i)=mu*pzi; yL(2,i)=pxi; yL(3,i)=pyi; yL(4,i)=pii; yL(5,i)=0;
 xelL(3*i-2)=xi; xelL(3*i-1)=xi+exi ; xelL(3*i)=xi;
 yelL(3*i-2)=ybi-bLR; yelL(3*i-1)=ybi-bLR+eyi ; yelL(3*i)=ybi-bLR;
 ey(i)=eyi;
 else
  if ibLR==0
  yM(1,i)=mu*pzi; yM(2,i)=pxi; yM(3,i)=pyi; yM(4,i)=pii; yM(5,i)=0; yM(6,i)=pzi;
yM(7,i)=1000*Vbi;
  xelM(3*i-2)=xi; xelM(3*i-1)=xi+exi ; xelM(3*i)=xi;
  yelM(3*i-2)=ybi-bLR; yelM(3*i-1)=ybi-bLR+eyi ; yelM(3*i)=ybi-bLR;
  ey(i)=eyi;
  else
  yR(1,i)=mu*pzi; yR(2,i)=pxi; yR(3,i)=pyi; yR(4,i)=pii; yR(5,i)=0;
  xelR(3*i-2)=xi; xelR(3*i-1)=xi+exi ; xelR(3*i)=xi;
  yelR(3*i-2)=ybi-bLR; yelR(3*i-1)=ybi-bLR+eyi ; yelR(3*i)=ybi-bLR;
  eyR(i)=eyi;
  end;
 end;
end;

end;                    % **  end i-loop (passage through contact length)

if ibLR==-1
 FxL=Fxi; FyL=Fyi; MzL=Mzi;
else
if ibLR==0
 FxM=Fxi; FyM=Fyi; MzM=Mzi;
else
 FxR=Fxi; FyR=Fyi; MzR=Mzi;
end;
end;
end;                    % **  end iLR-loop (one, two or three rows of elements)

if nrow==1
 Fx=FxM;
 Fy=FyM;
 Mz=MzM;
else
```

```
 if nrow==2
 Fx=FxL+FxR;
 Fy=FyL+FyR;
 Mz=MzL+MzR;
 else
 Fx=FxL+FxR+FxM;
 Fy=FyL+FyR+FyM;
 Mz=MzL+MzR+MzM;
 end;
end;

Mzprime=Mz+Fx*ymeff*epsyprime;   % for torsion (slope) calculation

end;                    % **  end iit-loop (carcass deflection iteration)

if rigid==1
   Mz=Mz-c*Fx*Fy-y0*Fx;
else
   Mz=Mz-y0*Fx;
end;

t=-Mz/Fy;                    % pneumatic trail

yfx(ia,j)=Fx;
yfy(ia,j)=Fy;
ymz(ia,j)=Mz;
yt(ia,j)=t;

if kapparuns==1
xa(ia,j)=kappa;
end;
if alpharuns==1
xa(ia,j)=alphadeg;
end;
if aphitruns==1
xa(ia,j)=aphit;
end;
if alpharuns==1            % calculation of CFalpha/Fz (take deltalphadegr small!)
      if nCFa==0
            if ia>1
                  if alpha>0
                  if gamma==0
                              if abs(aphit)<0.001
                                    if kappa==0
                                          CFalphaFz=(Fy-Fym1)/(Fz*pi*deltalphdegr/180);
                                          nCFa=1;
                                    end;
                              end;
                        end;
```

```
                end;
            end;
        end;
else
 CFalphaFz='?';
end;

if alpharuns==1
 deltalphdegr=g1a*abs(alphadeg)+g2a;
 alphadeg=alphadeg+deltalphdegr;
end;
if kapparuns==1
 deltakappar=g1k*abs(kappa)+g2k;
 kappa=kappa+deltakappar;
end;
if aphitruns==1
 deltaphitr=g1t*abs(aphit)+g2t;
 aphit=aphit+deltaphitr;
end;

end;            % **  end running variable ia-loop

end;            % **  end motion parameter j-loop


if picture==1
xelL(1)=a; xelL(2)=a ; xelL(3)=a;
yelL(1)=0; yelL(2)=0 ; yelL(3)=ym +cs*a+0.5*cc*a*a;
xelL(3*(n+1)+1)=-a; yelL(3*(n+1)+1)=0;
xelL(3*(n+1)+2)=a; yelL(3*(n+1)+2)=0;
xelM(1)=a; xelM(2)=a ; xelM(3)=a;
yelM(1)=0; yelM(2)=0 ; yelM(3)=ym +cs*a+0.5*cc*a*a;
xelM(3*(n+1)+1)=-a; yelM(3*(n+1)+1)=0;
xelM(3*(n+1)+2)=a; yelM(3*(n+1)+2)=0;
xelR(1)=a; xelR(2)=a ; xelR(3)=a;
yelR(1)=0; yelR(2)=0 ; yelR(3)=ym +cs*a+0.5*cc*a*a;
xelR(3*(n+1)+1)=-a; yelR(3*(n+1)+1)=0;
xelR(3*(n+1)+2)=a; yelR(3*(n+1)+2)=0;
  if rigid==1
    yc=Fy*c;
          for i=3:3*(n+1)
      yelL(i)=yelL(i)+yc;
      yelM(i)=yelM(i)+yc;
      yelR(i)=yelR(i)+yc;
    end;
     end;
                % plots picture of force distribution and deformations
if nrow~=2
figure(1);
```

```
plot(x,yM);
xlabel('x  [m]');
ylabel('d.blue: mu*pz, l.blue: p, green: px, red: py, sepia: pz[N/m], black: Vb[mm/s]');
text(-0.1,16500,...
      ['alpha= ',num2str(alphapict),' deg, gamma= ',num2str(gammapict),' deg, kappa= ',....
       num2str(kappapict),', R= ',num2str(Rpict),'m']);
text(-0.1,18500,...
      ['cyaw= ',num2str(cyaw),', cbend= ',num2str(cbend),', clat= ',...
       num2str(clat),', cp= ',num2str(cp)]);
text(-0.1,14500,['theta= ',num2str(theta)]);
text(-0.1,12500,['epsyprime= ',num2str(epsyprime),...
      ', epsyrgamma= ',num2str(epsyrgamma)]);
text(-0.1,10500,['epsyFy= ',num2str(epsyFy),', epsgamma= ',num2str(epsgamma)]);
text(-0.1,8500,['epsdrgam= ',num2str(epsdrgam),', y0= ',num2str(y0*1000),'mm']);
 if nrow==1
   text(0.03,12500,['SINGLE ROW']);
 else
   text(0.03,12500,['MIDDLE ROW']);
 end;
axis([-0.11,0.11,-5000,20000]);
grid;

figure(2);
plot(xelM,-yelM);
xlabel('x and longitudinal deflections [m]');
ylabel('lateral deflections  [m]');
text(-0.1,0.007,['alpha= ',num2str(alphapict),' deg, gamma= ',num2str(gammapict),...
      ' deg, kappa= ', num2str(kappapict),', R= ',num2str(Rpict),'m']);
 if rigid==1
   text(-0.1,0.009,['** RIGID **,  c= ',num2str(c),'m/N']);
 else
   text(-0.1,0.009,['cyaw= ',num2str(cyaw),', cbend= ',num2str(cbend),...
      ', clat= ',num2str(clat),', cp= ',num2str(cp)]);
 end;
text(-0.02,0.005,['Fy= ',num2str(round(Fy)),'N,  Mz= ',num2str(round(Mz)),'Nm']);
 if nrow==1
   text(-0.1,0.005,['SINGLE ROW']);
 else
   text(-0.1,0.005,['MIDDLE ROW']);
 end;
axis([-0.11,0.11,-0.04,0.01]);
end;
if nrow~=1
figure(3);
plot(x,yR);
xlabel('x  [m]');
ylabel('d.blue: mu*pz,  l.blue: p,  green: px,  red: py  [N/m]');
text(-0.1,16500,['alpha= ',num2str(alphapict),' [deg], gamma= ',num2str(gammapict),...
      ' [deg], kappa= ',num2str(kappapict),' [-], R= ',num2str(Rpict),' [m]']);
```

```
text(-0.1,18500,['cyaw= ',num2str(cyaw),', cbend= ',num2str(cbend),...
        ', clat= ',num2str(clat),', cp= ',num2str(cp)]);
text(-0.1,12500,['RIGHT ROW']);
axis([-0.11,0.11,-5000,20000]);
grid;
figure(4);
plot(xelR,-yelR);
xlabel('x and longitudinal deflections [m]');
ylabel('lateral deflections  [m]');
text(-0.1,0.007,['alpha= ',num2str(alphapict),' [deg], gamma= ',num2str(gammapict),...
        ' [deg], kappa= ',num2str(kappapict),' [-], R= ',num2str(Rpict),' [m]']);
 if rigid==1
   text(-0.1,0.009,['** RIGID **,  c= ',num2str(c),'m/N']);
 else
text(-0.1,0.009,['cyaw= ',num2str(cyaw),', cbend= ',num2str(cbend),', clat= ',num2str(clat),...
        ', cp= ',num2str(cp)]);
 end;
text(-0.1,0.005,['RIGHT ROW,   brow/a= ',num2str(brow/a)]);
axis([-0.11,0.11,-0.04,0.01]);

figure(5);
plot(x,yL);
xlabel('x  [m]');
ylabel('d.blue: mu*pz,  l.blue: p,  green: px,  red: py  [N/m]');
text(-0.1,16500,['alpha= ',num2str(alphapict),' deg, gamma= ',num2str(gammapict),...
        ' deg, kappa= ', num2str(kappapict),', R= ',num2str(Rpict),'m']);
text(-0.1,18500,['cyaw= ',num2str(cyaw),', cbend= ',num2str(cbend),...
        ', clat= ',num2str(clat),', cp= ',num2str(cp)]);
text(-0.1,14500,['theta= ',num2str(theta)]);
text(-0.1,12500,['epsyprime= ',num2str(epsyprime),...
        ', epsyrgamma= ',num2str(epsyrgamma)]);
text(-0.1,10500,['epsyFy= ',num2str(epsyFy),', epsgamma= ',num2str(epsgamma)]);
text(-0.1,8500,['epsdrgam= ',num2str(epsdrgam),', y0= ',num2str(y0*1000),'mm']);
text(0.03,12500,['LEFT ROW']);
axis([-0.11,0.11,-5000,20000]);
grid;

figure(6);
plot(xelL,-yelL);
xlabel('x and longitudinal deflections [m]'); ylabel('lateral deflections  [m]');
text(-0.1,0.007,['alpha= ',num2str(alphapict),' deg, gamma= ',num2str(gammapict),...
        ' deg, kappa= ', num2str(kappapict),', R= ',num2str(Rpict),'m']);
 if rigid==1
   text(-0.1,0.009,['** RIGID **,  c= ',num2str(c),'m/N']);
 else
text(-0.1,0.009,['cyaw= ',num2str(cyaw),', cbend= ',num2str(cbend),', clat= ',num2str(clat),...
        ', cp= ',num2str(cp)]);
 end;
text(-0.02,0.005,['Fy= ',num2str(round(Fy)),'N,  Mz= ',num2str(round(Mz)),'Nm']);
```

```
text(-0.1,0.005,['LEFT ROW']);
axis([-0.11,0.11,-0.04,0.01]);
end;
                                        %    end if picture

else
            % plots with running variable
if alpharuns==1
xmin=alphdegminr; xmax=alphdegmaxr; xtext='slip angle  alpha  [deg]';
Fxmin=-mu0*Fz; Fxmax=mu0*Fz; Fymin=-mu0*Fz; Fymax=mu0*Fz;
Mmin=1.1*0.1*a*Fymin; Mmax=0.9*0.1*a*Fymax;
tmin=-0.2*a; tmax=0.6*a; ax=0.25; ay=0;
partext1=['CFkap= ',num2str(CFkappaFz),'*Fz, CFalf= ',num2str(CFalphaFz),'*Fz'];
end;
if kapparuns==1
xmin=kappaminr; xmax=kappamaxr; xtext='longitudinal slip ratio  kappa  [-]';
Fxmin=-mu0*Fz; Fxmax=mu0*Fz; Fymin=-mu0*Fz; Fymax=mu0*Fz;
Mmin=1.1*0.1*a*Fymin; Mmax=0.9*0.1*a*Fymax;
tmin=-0.2*a; tmax=0.6*a; ax=-0.25; ay=0;
partext1=['CFkap= ',num2str(CFkappaFz),'*Fz'];
end;
if aphitruns==1
xmin=0; xmax=aphitmaxr; xtext='non-dim. turn slip  aphit= a/R  [-]';
Fxmin=-mu0*Fz; Fxmax=mu0*Fz; Fymin=-mu0*Fz/3; Fymax=mu0*Fz;
Mmin=1.1*a*Fymin/6; Mmax=0.9*0.8*a*Fymax;
tmin=-a; tmax=0.2*a; ax=0.25; ay=0;
partext1=['CFkap= ',num2str(CFkappaFz),'*Fz'];
end;

xl=xmax-xmin; Fxl=Fxmax-Fxmin; Fyl=Fymax-Fymin; Ml=Mmax-Mmin; tl=tmax-tmin;

if kappapar==1
      if alpharuns==1
            partext0=['a/R= ',num2str(aphit),', gamma= ',num2str(gammadeg),' [deg]'];
      else
       partext0=['alpha= ',num2str(alphadeg),', gamma= ',num2str(gammadeg),' [deg]'];
  end;
      if jmax==1
      partext=['kappa= ',num2str(kappamin)];
  else
     partext=['kappamin= ',num2str(kappamin), ', deltakappa=',num2str(deltakappa),' [-]'];
  end;
elseif gammapar==1
      if alpharuns==1
            partext0=['a/R= ',num2str(aphit),', kappa= ',num2str(kappa)];
      elseif kapparuns==1
            partext0=['alpha= ',num2str(alphadeg),' [deg]',', a/R= ',num2str(aphit)];
      else
            partext0=['alpha= ',num2str(alphadeg),' [deg]',', kappa= ',num2str(kappa)];
```

```
        end;
        if jmax==1
       partext=['gamma= ',num2str(gamdegmin)],' [deg]';
   else
        partext=['gammamin= ',num2str(gamdegmin), ', deltagamma=',...
       num2str(deltgamdeg),' [deg]'];
   end;
elseif alphapar==1
        if kapparuns==1
                partext0=['a/R= ',num2str(aphit),', gamma= ',num2str(gammadeg),' [deg]'];
        else
       partext0=['kappa= ',num2str(kappa),', gamma= ',num2str(gammadeg),' [deg]'];
   end;
        if jmax==1
       partext=['alpha= ',num2str(alphdegmin),' [deg]'];
   else
       partext=['alphamin= ',num2str(alphdegmin), ', deltaalpha=',...
       num2str(deltalphdeg),' [deg]'];
   end;
elseif aphitpar==1
   if alpharuns==1
       partext0=['kappa= ',num2str(kappa),', gamma= ',num2str(gammadeg),' [deg]'];
        else
        partext0=['alpha= ',num2str(alphadeg),' [deg]',', gamma= ',num2str(gammadeg),' [deg]'];
   end;
        if jmax==1
       partext=['aphit= ',num2str(aphitmin)];
   else
       partext=['aphitmin= ',num2str(aphitmin), ', deltaaphit=',num2str(deltaphit),' [-]'];
   end;
else
        if alpharuns==1
                partext0=['a/R= ',num2str(aphit),', kappa= ',num2str(kappa)];
        elseif kapparuns==1
                partext0=['alpha= ',num2str(alphadeg),' [deg]',', a/R= ',num2str(aphit)];
        else
                partext0=['alpha= ',num2str(alphadeg),' [deg]',', kappa= ',num2str(kappa)];
        end;
        partext=['gamma= ',num2str(gamdegmin),' [deg]'];
end;
if rigid==0
   texttitle= ['Vc= ',num2str(Vc),'m/s, mu0= ',num2str(mu0),', amu= ',num2str(amu),....
        ', cyaw= ',num2str(cyaw),', cbend= ',num2str(cbend),', clat= ',num2str(clat)];
else
   texttitle= ['Vc= ',num2str(Vc),'m/s , mu0= ',num2str(mu0),' , amu= ',num2str(amu),....
        ' , c= ',num2str(c),' , y0= ',num2str(y0),'      (rigid carcass)'];
end;
partext2= ['a=',num2str(a),', b=',num2str(b),', brow=',num2str(brow), ', Fz=',num2str(Fz),...
 ', plyst=',num2str(alphadegply),', conic=',num2str(gammadegcon),',iitend=',num2str(iitend)];
```

```
figure(1);
plot(xa,yfy); ylabel('side force  Fy [N]'); xlabel(xtext);
title(texttitle);
text(xmin+0.02*xl, Fymin+(0.95-1.5*ay)*Fyl,['nr rows= ',num2str(nrow)]);
text(xmin+0.02*xl, Fymin+(0.9-1.5*ay)*Fyl,['theta= ',num2str(theta)]);
text(xmin+(0.27+ax)*xl, Fymin+0.205*Fyl,partext0);
text(xmin+(0.27+ax)*xl, Fymin+0.13*Fyl,partext);
text(xmin+(0.27+ax)*xl, Fymin+0.055*Fyl,partext1);
text(xmin+(0.27+ax)*xl, Fymin+0.01*Fyl,partext2);
axis([xmin,xmax,Fymin,Fymax]);
grid;

figure(2);
plot(xa,yfx); ylabel('longitudinal force  Fx [N]'); xlabel(xtext);
title(texttitle);
text(xmin+0.02*xl, Fymin+0.95*Fyl,['nr rows= ',num2str(nrow)]);
text(xmin+0.02*xl, Fymin+0.9*Fyl,['theta= ',num2str(theta)]);
text(xmin+(0.27-ax)*xl, Fymin+0.205*Fyl,partext0);
text(xmin+(0.27-ax)*xl, Fymin+0.13*Fyl,partext);
text(xmin+(0.27-ax)*xl, Fymin+0.055*Fyl,partext1);
axis([xmin,xmax,Fxmin,Fxmax]);
grid;

figure(3);
plot(xa,ymz); ylabel('align.torque  Mz [-]'); xlabel(xtext);
title(texttitle);
text(xmin+0.02*xl, Mmin+0.95*Ml,['nr rows= ',num2str(nrow),', nr elem= ',num2str(n)]);
text(xmin+0.02*xl, Mmin+0.9*Ml,['theta= ',num2str(theta)]);
text(xmin+0.52*xl, Mmin+0.95*Ml,['epsyprime= ',...
      num2str(epsyprime),', epsyrgamma= ',num2str(epsyrgamma)]);
text(xmin+0.52*xl, Mmin+0.88*Ml,['epsyFy= ',...
      num2str(epsyFy),', epsgamma= ',num2str(epsgamma)]);
text(xmin+0.52*xl, Mmin+0.81*Ml,['epsdrgam= ',...
      num2str(epsdrgam),', y0= ',num2str(y0*1000),'mm']);
text(xmin+0.02*xl, Mmin+(0.275+ay)*Ml,partext0);
text(xmin+0.02*xl, Mmin+(0.205+ay)*Ml,partext);
text(xmin+0.02*xl, Mmin+(0.13+ay)*Ml,partext1);
text(xmin+0.02*xl, Mmin+(0.055+ay)*Ml,partext2);
axis([xmin,xmax,Mmin,Mmax]);
grid;

figure(4);
plot(xa,yt); ylabel('pneum. trail [m]'); xlabel(xtext);   % (xamean,ytdiff)
title(texttitle);
text(xmin+0.02*xl, tmin+0.95*tl,['nr rows= ',num2str(nrow)]);
text(xmin+0.02*xl, tmin+0.205*tl,partext0);
text(xmin+0.02*xl, tmin+0.13*tl,partext);
text(xmin+0.02*xl, tmin+0.055*tl,partext1);
axis([xmin,xmax,tmin,tmax]);
```

```
grid;

figure(5);
plot(yfx,yfy); ylabel('side force [N]'); xlabel('longitudinal force [N]');
title(texttitle);
text(Fxmin+0.03*Fxl, Fymin+0.95*Fyl,['nr rows= ',num2str(nrow)]);
text(Fxmin+0.03*Fxl, Fymin+0.205*Fyl,partext0);
text(Fxmin+0.03*Fxl, Fymin+0.13*Fyl,partext);
text(Fxmin+0.03*Fxl, Fymin+0.055*Fyl,partext1);
text(Fxmin+0.03*Fxl, Fymin+0.01*Fyl,partext2);
axis([1.2*Fxmin,1.2*Fxmax,Fymin,Fymax]);
grid;

figure(6);
plot(yfx,ymz); ylabel('aligning torque [Nm]'); xlabel('longitudinal force [N]');
title(texttitle);
text(Fxmin+0.03*Fxl, Mmin+0.95*Ml,['nr rows= ',num2str(nrow)]);
text(Fxmin+0.52*Fxl, Mmin+0.95*Ml,['epsyprime= ',num2str(epsyprime),...
      ', epsyrgamma= ',num2str(epsyrgamma)]);
text(Fxmin+0.52*Fxl, Mmin+0.88*Ml,['epsyFy= ',num2str(epsyFy),...
      ', epsgamma= ',num2str(epsgamma)]);
text(Fxmin+0.52*Fxl, Mmin+0.81*Ml,['epsdrgam= ',num2str(epsdrgam),...
      ', y0= ',num2str(y0*1000),'mm']);
text(Fxmin+0.03*Fxl, Mmin+0.205*Ml,partext0);
text(Fxmin+0.03*Fxl, Mmin+0.13*Ml,partext);
text(Fxmin+0.03*Fxl, Mmin+0.055*Ml,partext1);
text(Fxmin+0.03*Fxl, Mmin+0.0*Ml,partext2);
%axis([1.2*Fxmin,1.2*Fxmax,Mmin,Mmax]);
grid;

end;
clear;
```

Appendix 3

SWIFT parameters

App. 3.1. Parameter values of *Magic Formula* and *SWIFT* model

Table A3.1. (205/60R15 91V, 2.2 bar. ISO sign definition. Also, cf. App.3.2)

$R_o(=r_o) = 0.313$m ,	$F_{zo}(=F_{No}) = 4000$N ,	$m_o = 9.3$kg ,	$V_o = 16.67$m/s	
$p_{Cx1} = 1.685$	$p_{Dx1} = 1.210$	$p_{Dx2} = -0.037$	$p_{Ex1} = 0.344$	$p_{Ex2} = 0.095$
$p_{Ex3} = -0.020$	$p_{Ex4} = 0$	$p_{Kx1} = 21.51$	$p_{Kx2} = -0.163$	$p_{Kx3} = 0.245$
$p_{Hx1} = -0.002$	$p_{Hx2} = 0.002$	$p_{Vx1} = 0$	$p_{Vx2} = 0$	
$r_{Bx1} = 12.35$	$r_{Bx2} = -10.77$	$r_{Cx1} = 1.092$	$r_{Hx1} = 0.007$	
$q_{sx1} = 0$	$q_{sx2} = 0$	$q_{sx3} = 0$		
$p_{Cy1} = 1.193$	$p_{Dy1} = -0.990$	$p_{Dy2} = 0.145$	$p_{Dy3} = -11.23$	$p_{Ey1} = -1.003$
$p_{Ey2} = -0.537$	$p_{Ey3} = -0.083$	$p_{Ey4} = -4.787$	$p_{Ky1} = -14.95$	$p_{Ky2} = 2.130$
$p_{Ky3} = -0.028$	$p_{Hy1} = 0.003$	$p_{Hy2} = -0.001$	$p_{Hy3} = 0.075$	
$p_{Vy1} = 0.045$	$p_{Vy2} = -0.024$	$p_{Vy3} = -0.532$	$p_{Vy4} = 0.039$	
$r_{By1} = 6.461$	$r_{By2} = 4.196$	$r_{By3} = -0.015$	$r_{Cy1} = 1.081$	$r_{Hy1} = 0.009$
$r_{Vy1} = 0.053$	$r_{Vy2} = -0.073$	$r_{Vy3} = 0.517$	$r_{Vy4} = 35.44$	$r_{Vy5} = 1.9$
$r_{Vy6} = -10.71$				
$q_{Bz1} = 8.964$	$q_{Bz2} = -1.106$	$q_{Bz3} = -0.842$	$q_{Bz4} = 0$	$q_{Bz5} = -0.227$
$q_{Bz9} = 18.47$	$q_{Bz10} = 0$	$q_{Cz1} = 1.180$	$q_{Dz1} = 0.100$	$q_{Dz2} = -0.001$
$q_{Dz3} = 0.007$	$q_{Dz4} = 13.05$	$q_{Dz6} = -0.008$	$q_{Dz7} = 0.000$	$q_{Dz8} = -0.296$
$q_{Dz9} = -0.009$	$q_{Ez1} = -1.609$	$q_{Ez2} = -0.359$	$q_{Ez3} = 0$	$q_{Ez4} = 0.174$
$q_{Ez5} = -0.896$	$q_{Hz1} = 0.007$	$q_{Hz2} = -0.002$	$q_{Hz3} = 0.147$	$q_{Hz4} = 0.004$
$s_{sz1} = 0.043$	$s_{sz2} = 0.001$	$s_{sz3} = 0.731$	$s_{sz4} = -0.238$	
$q_{Iay} = 0.109$	$q_{ma} = 0.237$	$q_{cbx0,z} = 121.4$	$q_{kbx,z} = 0.228$	$q_{cb\theta 0} = 61.96$
$q_{Iaxz} = 0.071$	$q_{mb} = 0.763$	$q_{cby} = 40.05$	$q_{kby} = 0.284$	$q_{cb\gamma,\psi} = 20.33$
$q_{Iby} = 0.696$	$q_{mc} = 0.108$	$q_{ccx} = 391.9$	$q_{kcx} = 0.910$	$q_{cc\psi} = 55.82$
$q_{Ibxz} = 0.357$		$q_{ccy} = 62.7$	$q_{kcy} = 0.910$	$q_{kb\theta} = 0.080$
$q_{Ic} = 0.055$				$q_{kb\gamma,\psi} = 0.038$
				$q_{kc\psi} = 0.834$
$q_{V1} = 7.1\times 10^{-5}$	$q_{sy1} = 0.01$	$q_{a1} = 0.135$	$B_{reff} = 9$	$q_{Fcx1} = 0.1$
$q_{V2} = 2.489$	$q_{sy3} = 0$	$q_{a2} = 0.035$	$D_{reff} = 0.23$	$q_{Fcy1} = 0.3$
$q_{Fz1} = 13.37$	$q_{sy4} = 0$	$q_{bvx,z} = 3.957$	$F_{reff} = 0.01$	$q_{Fcx2} = 0$
$q_{Fz2} = 14.35$		$q_{bv\theta} = 3.957$		$q_{Fcy2} = 0$

App. 3.2. Non-Dimensionalization (with some remarks)

The quantities listed in Table A3.1 are non-dimensional. They are used in the following equations:

Magic Formula: Eqs.(4.E1-E78), except (4.E68, E70)

SWIFT: Eqs.(9.131-236), except (9.177-182).

The inertia quantities have been made non-dimensional by dividing by the reference mass m_o or the reference moment of inertia I_o. For m_o the total tyre mass has been taken. The quantity I_o is defined as:

$$I_o = m_o R_o^2 \quad [\text{kg.m}^2] \tag{A3.1}$$

Consequently, we have the non-dimensional parameters shown in the list above:

$$q_{ma} = \frac{m_a}{m_o}\text{, etc. and } \quad q_{Iay} = \frac{I_{ay}}{m_o R_o^2}\text{, etc.} \tag{A3.2}$$

As has been introduced already in connection with Eqs.(9.213-216) the non-dimensionalization of the stiffnesses and damping coefficients is realized by dividing the linear (translational) stiffnesses and damping coefficients by:

$$c_{to} = \frac{F_{zo}}{R_o} \text{ [N/m]} \quad \text{and} \quad k_{to} = \sqrt{\frac{m_o F_{zo}}{R_o}} \text{ [Ns/m]} \tag{A3.3}$$

and the rotational stiffnesses and damping coefficients by:

$$c_{ro} = F_{zo} R_o \text{ [Nm/rad]} \quad \text{and} \quad k_{ro} = \sqrt{m_o F_{zo} R_o^3} \text{ [Nms/rad]} \tag{A3.4}$$

As a consequence, we have for example:

$$q_{cbx} = \frac{c_{bx}}{c_{to}}\text{, etc. and } \quad q_{kbx} = \frac{k_{bx}}{k_{to}}\text{, etc.} \tag{A3.5}$$

$$q_{cb\psi} = \frac{c_{b\psi}}{c_{ro}}\text{, etc. and } \quad q_{kb\psi} = \frac{k_{b\psi}}{k_{ro}}\text{, etc.} \tag{A3.6}$$

Remarks. In (9.131,132) the factors $k_{bx,z}\Omega$ are set equal to zero as rolling resistance has been accounted for already by the moment M_y (9.236,230, 231). The mass m_a is the mass of that part of the tyre that, according to the model, moves with the wheel rim or axle. The quantity I_{ay} is the moment of inertia of that part of the tyre that rotates about the η axis as if it were attached as a rigid body to the wheel rim. The tyre inertia that is allocated to the belt is denoted with subscript b. The inertia denoted with subscript c is assumed to move with the contact patch. The interaction parameters q_{Fcx2} and q_{Fcy2} have been chosen equal to zero. They would have taken values 0.94 and 1.56 if $q_{Fcx1} = q_{Fcy1} = 0$.

App. 3.3. Estimation of SWIFT Parameter Values

using a limited set of (semi-static) measurements
(Contributed by I.J.M. Besselink, TNO-Automotive)

In Chapter 9 the SWIFT tyre model has been described. In order to assess the parameters of this tyre model a number of different tests are required, e.g. dynamic braking, yaw oscillation, dynamic cleat experiments on the drum. A full measurement programme to determine all parameters of the SWIFT model will be extensive and time consuming. Also the dedicated measurement equipment to perform high frequency testing may not be available or not suited to handle very large tyres (e.g. truck or aircraft tyres).

Using the experience gained from a number of full measurement programmes executed on passenger car tyres, a procedure has been developed to make sensible first estimates for the SWIFT parameters. This description applies to SWIFT-Tyre as implemented by TNO Automotive in a number of simulation codes (e.g. ADAMS, DADS or MATLAB/Simulink). The following steps can be distinguished:

(1) Force and moment testing

Fitting of the Magic Formula: $F_x, F_y, M_x, M_y, M_z = f(F_z, \kappa, \alpha, \gamma, V_x)$.

The software program MF-Tool, also developed by TNO Automotive, may be used to fit the Magic Formula parameters. This program requires that the measurement data is provided in the form of TYDEX files, a standardised format as developed by the international TYDEX (*Ty*re *D*ata *Ex*change) workgroup, cf. Oosten et al.(1996).

Note: the contribution of the forward velocity V_x is present in the rolling resistance formula (9.231):

$$f_r = q_{sy1} + q_{sy3}|V_x/V_o| + q_{sy4}(V_x/V_o)^4 \tag{9.231}$$

that is used in connection with Eqs.(9.230,236). Of course, in cases such as moving on wet roads, the friction coefficient may be formulated as functions of the speed, cf. Eq.(4.E23).

(2) Loaded radius/effective rolling radius

The tyre normal deflection ρ_z is the difference between the free tyre radius of the rotating tyre r_Ω and the loaded tyre radius r_l:

$$\rho_z = r_o + \Delta r - r_l = r_\Omega - r_l \tag{9.218}$$

The following set of equations needs to be fitted:

a) centrifugal growth of the tyre free radius Δr (coefficient q_{V1})

$$\Delta r = q_{V1} r_o (\Omega r_o / V_o)^2 \tag{9.219}$$

b) vertical force-deflection equation (coefficients: q_{v2}, q_{Fcx1}, q_{Fcy1}, q_{Fz1} and q_{Fz2})

$$F_z = \left\{ 1 + q_{V2} |\Omega| \frac{r_o}{V_o} - \left(q_{Fcx1} \frac{F_x}{F_{zo}} \right)^2 - \left(q_{Fcy1} \frac{F_y}{F_{zo}} \right)^2 \right\} \left(q_{Fz1} \frac{\rho_z}{r_o} + q_{Fz2} \frac{\rho_z^2}{r_o^2} \right) F_{zo} \tag{9.217}$$

c) effective rolling radius, similar to (9.232), (coefficients: B, D, F_{reff})

$$r_e = r_o + \Delta r - \frac{F_{zo}}{C_{Fz}} \left\{ D_{reff} \arctan\left(B_{reff} \frac{C_{Fz}}{F_{zo}} \rho_z \right) + F_{reff} \frac{C_{Fz}}{F_{zo}} \rho_z \right\} \tag{A3.7}$$

with the vertical stiffness of the standing tyre at nominal load F_{zo} as derived from Eq.(9.217):

$$C_{Fz} = \frac{F_{zo}}{r_o} \sqrt{q_{Fz1}^2 + 4 q_{Fz2}} \tag{9.232b}$$

Notes: (1) F_{zo}, V_o and r_o=R_o are reference parameters: they are just used to make the coefficients dimensionless. (2) An additional parameter q_{re0} may be introduced that multiplied with r_o in Eqs.(9.218, 232) gives an improved value for the free unloaded radius.

The measurement data for assessing the loaded and the effective rolling radius typically consists of values for r_l, r_e, V, F_x, F_y, F_z carried out for a number of different vertical loads, forward velocities and possibly longitudinal and/or lateral forces. Based on the relation V=Ωr_e it is sufficient to specify two out of three variables: forward velocity V, angular velocity Ω and effective rolling radius r_e. The data for F_x and F_y can be considered optional for passenger car tyres, but generally should be included for racing tyres.

Fitting of the parameters is generally done in two steps. In order to obtain maximum accuracy for the loaded radius the equations (9.219) and (9.217) are fitted first. In a second step the coefficients for the effective rolling radius, as given by equation (9.232,232a), are determined.

(3) Contact length

In SWIFT the following formula is used for the contact length formula, a represents half of the contact length (coefficients: q_{a1} and q_{a2})

$$a = \left(q_{a1}\sqrt{\frac{F_z}{F_{zo}}} + q_{a2}\frac{F_z}{F_{zo}} \right) r_o \tag{9.207}$$

Consequently, measurement data should provide half the contact length as a function of the vertical load F_z. If no or only very limited data is available the following formula may give a good estimate (where ρ_z is the tyre deflection):

$$a = p_{a1}\left(p_{a2}\sqrt{\frac{\rho_z}{r_o}} + \frac{\rho_z}{r_o} \right) r_o \tag{A3.8}$$

This formula was proposed by Besselink (2000) and better acknowledges the fact that the contact length is a geometrical property and primarily a function of the tyre deflection. The suggested parameter values for a passenger and light truck tyres are respectively:

p_{a1} =0.35 and p_{a2}=2.25 (on a flat surface)

p_{a1} =0.45 and p_{a2}=1.25 (on an external drum with a diameter of 2.5m).

It has been found that this formula is valid for a fairly wide range of tyres and can also be used for different tyre pressures without changing the coefficients, see Fig.A3.1. This figure also clearly illustrates that on an external drum the contact length is shorter compared to the situation on a flat road surface.

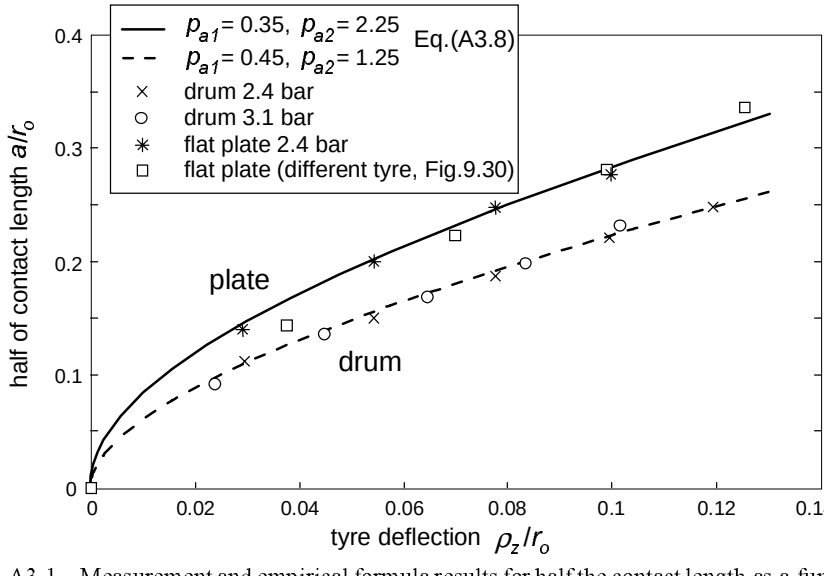

Fig. A3.1. Measurement and empirical formula results for half the contact length as a function of tyre deflection, passenger car tyres.

(4) Relaxation lengths, overall longitudinal and lateral stiffness

Apart from an accurate representation of the high frequency responses, it is important that the low frequency, transient behaviour (i.e. relaxation effects of the tyre) is included correctly. Measurements of the relaxation lengths can be used to assess the resulting longitudinal and lateral stiffness of the tyre carcass (that is excluding the tread) at ground level. For *SWIFT* the following equations hold for the longitudinal and lateral relaxation lengths respectively, cf. Eqs(9.15) and (9.51) with $m = 1$ (at vanishing slip) and the relatively small effect of the torsional compliance $1/c_\psi$ neglected:

$$\sigma_x = \frac{C_{F\kappa}}{c_x} + a \tag{A3.9}$$

$$\sigma_y = \frac{C_{F\alpha}}{c_y} + a \tag{A3.10}$$

where:

σ_x longitudinal relaxation length
$C_{F\kappa}$ longitudinal slip stiffness of the tyre
c_x longitudinal carcass stiffness at ground level
σ_y lateral relaxation length
$C_{F\alpha}$ cornering stiffness of thye tyre
c_y lateral carcass stiffness at ground level
a half of the contact length

In the lateral direction all parameters may be known (σ_y, $C_{F\alpha}$, c_y, a), but usually the left and right hand side of Eq.(A3.10) turn out not to be the same in magnitude. In general the relaxation length based on the lateral stiffness and contact length is too short compared to the measurements on a rolling tyre. Since the aim of the tyre model is to have an accurate description of the tyre under rolling conditions, Eqs.(A3.9,10) are used to calculate the resulting carcass stiffnesses of the tyre model in lateral and longitudinal direction (c_x and c_y respectively).

In the next step (5), the resulting compliances at ground level will be divided and distributed over the various parts of the tyre model.

(5) Carcass compliances

In *SWIFT* the rigid belt ring is elastically suspended with respect to the rim in all directions. The contact patch is elastically attached to the ring. Normally the

various stiffness values are determined from dynamic experimental results. By using these values, it is possible to calculate their respective contribution to the overall carcass deflection at ground level when it is assumed that a longitudinal or lateral force is applied and that the rim is held fixed, cf. Fig.A3.2.

Table A3.2. Distribution of longitudinal and lateral carcass compliance components.

longitudinal at ground level	*tyre 1*	*tyre 2*	*tyre 3*	*rule of thumb*
rigid ring translation (*a*)	27%	28%	31%	30%
rigid ring rotation (*b*)	63%	62%	60%	60%
contact patch translation (*c*)	10%	10%	9%	10%

lateral at ground level	*tyre 1*	*tyre 2*	*tyre 3*	*rule of thumb*
rigid ring translation (*a*)	34%	25%	28%	25%
rigid ring rotation (*b*)	62%	56%	55%	55%
contact patch translation (*c*)	4%	19%	18%	15%

Table A3.2 shows the relative contributions *a*, *b* and *c* that have been assessed for three different tyres. Based on these data it may be concluded that although the compliance values themselves are different, the relative contributions to the overall carcass deflection are fairly constant. Since under

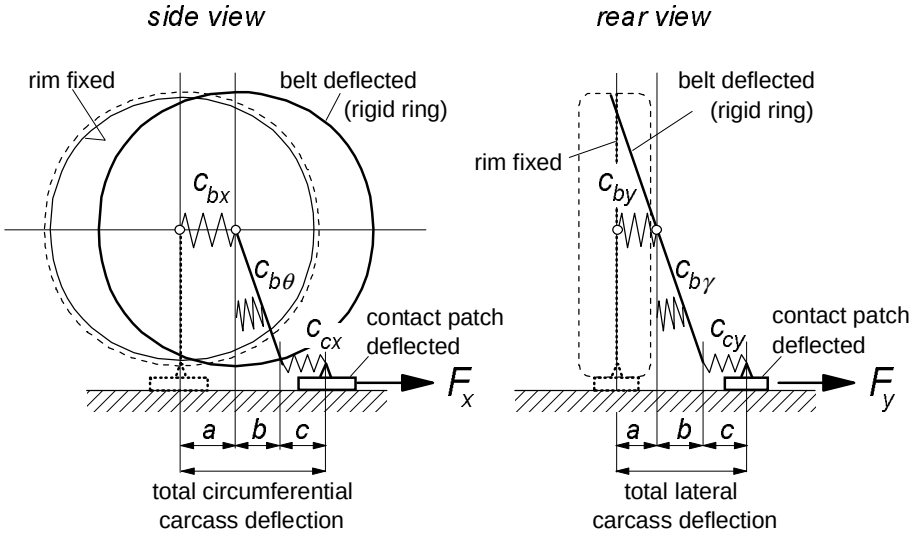

Fig. A3.2. Longitudinal and lateral deflections of the rigid ring and contact patch.

step (4) the overall longitudinal and lateral carcass stiffnesses have been determined, it is now possible to assess approximate individual stiffness values using the suggested "rule of thumb".

Additional measurement data (e.g. yaw stiffness or FEM model results) may also be used to enhance the estimates or to gain additional confidence in the stiffness/deflection distribution.

(6) Carcass inertia

In the SWIFT tyre model the tyre is not considered as a single rigid body. A part of the tyre near the rim is assumed to be rigid and fixed to the rim. The other part that represents the belt, is considered to move as a rigid ring. Consequently, the total tyre mass has to be divided and a distribution has to be made over the inertia of the ring and the inertia of the part rigidly attached to the rim. The latter part is further regarded as a part of the wheel body. An estimate of this division can be made based on past experience or on a detailed weight break-down provided by the tyre manufacturer. The following rough initial estimate is suggested:

75% of the tyre mass is assigned to the tyre belt

85% of the tyre moments of inertia is assigned to the tyre belt

Tentatively, the contact patch body is considered as an additional small mass.

(7) Carcass damping

Generally, the exact amount of damping of the tyre is very difficult to assess experimentally. For instance, it is observed that a large difference in vertical damping exists between a tyre that stands still and a tyre that rolls: under rolling conditions the apparent damping may be a factor 10 smaller compared to the damping of a tyre standing still, also cf. Jianmin et al. (2001). A simple model with finite contact length and provided with radial dry friction dampers (Pacejka, 1981a) may explain this phenomenon.

Based on experience, the following guideline may be provided: when the tyre is not in contact with the ground (and the rim is fixed) the damping will be relatively low. Typical values of the damping coefficients lie in the range of 1 to 6% of the corresponding critical damping coefficients. Generally, the modes that contain a large translational component are more heavily damped than the modes with a large rotational component.